UNIVERSIDADE
BEIRA INTERIOR

Frost Detection in Refrigeration Systems through Sensor Technology Integration

Martim Lima de Aguiar

Tese para obtenção do Grau de Doutor em
Engenharia Mecânica
(3º ciclo de estudos)

Orientador: Prof. Doutor Pedro Miguel de Figueiredo Dinis Oliveira Gaspar
Orientador: Prof. Doutor Pedro Nuno Dinho Pinto da Silva

Júri:
Prof. Doutor José Carlos Páscoa Marques
Prof. Doutor Rui António Pitarma Sabino da Cunha Ferreira
Prof. Doutor Adélio Manuel Rodrigues Gaspar
Prof. Doutor Pedro Miguel de Figueiredo Dinis Oliveira Gaspar
Prof. Doutor Christian Johann Losso Hermes

Março de 2026

Declaração de Integridade

Eu, Martim Lima de Aguiar, que abaixo assino, estudante com o número de inscrição D2151 de Engenharia Mecânica da Faculdade de Engenharia, declaro ter desenvolvido o presente trabalho e elaborado o presente texto em total consonância com o Código de Integridade da Universidade da Beira Interior.

Em particular, declaro assumir integralmente a autoria do presente trabalho, afirmando não ter incorrido em qualquer forma de fraude académica, cujas tipologias conheço e reconheço, tendo observado rigorosamente as exigências de referenciação de frases, excertos, imagens e demais formas de criação intelectual. Asseguro ter conduzido todo o trabalho de forma ética, com respeito pelos outros e com orientação pelo bem comum, não tendo recorrido a qualquer prática de fabricação ou falsificação de resultados.

Declaro, ainda, que o recurso a ferramentas de inteligência artificial generativa e a modelos de linguagem de grande dimensão ocorreu nos termos descritos na secção *Disclaimer on the usage of LLM tools*

Universidade da Beira Interior, Covilhã 22/05/2026

Assinado por: **Martim Lima de Aguiar**
Num. de Identificação: 14229673
Data: 2026.05.22 20:52:43+01'00'

_____

Martim Lima de Aguiar

Disclaimer on the usage of LLM tools

The same way the internet revolutionized how scientific research is conducted, Large Language Models (LLMs) are reshaping the way we process, structure, and communicate knowledge. When the internet first became widespread, many questioned its legitimacy as a research tool, yet today, it is an essential part of every scientist's workflow. A similar transformation is now unfolding with Artificial Intelligence (AI).

Although most of the experimental and analytical work presented in this thesis had already been completed when LLMs became widely accessible, these tools still played a positive and ethically conscious role in the later stages of this work. Their main contributions were in enhancing the clarity and coherence of written text, improving readability, assisting in refining existing code, and supporting creative brainstorming when exploring new ideas. They acted as a creativity enhancer rather than a replacer, helping but without substituting human reasoning or critical judgment.

Importantly, these models were not used to generate data, fabricate results, or replace scientific reasoning. All data, figures, and analyses presented herein were obtained experimentally. The LLMs served as a complementary instrument, much like an advanced spell checker, amplifying human capability rather than replacing it.

When employed with integrity, such tools can foster transparency, reproducibility, and accessibility in research. Yet, as with any powerful technology, they also come with caveats. It is unethical to use LLMs to generate unverified facts, produce references that do not exist, or fabricate information, practices that would constitute academic misconduct. Conversely, these same tools can also help to combat such malpractice, by assisting researchers in verifying sources and cross-checking citations.

The purpose of including this section is to contribute to openness and clarity in the use of emerging AI tools within academia. Just as a researcher today could choose to avoid the internet and rely solely on printed libraries (at the cost of efficiency and reach) one could also avoid using LLMs. However, the potential of these technologies is far too great to be ignored. The responsibility, therefore, lies not in rejecting them, but in defining and demonstrating good practices for their ethical use.

As professionals and innovators in technology, it is our duty to stand at the forefront of such transformations, not as passive users but as contributors to the standards and ethics that will shape their responsible integration into research and education.

Agradecimentos

Um trabalho desta natureza nunca é fruto de um esforço isolado. Constrói-se com o contributo de quem nos rodeia, pela partilha de conhecimento e ideias, mas também dos que ofereceram apoio, paciência e amizade. A todos, o meu reconhecimento.

Ao Professor Doutor Pedro Miguel de Figueiredo Dinis Oliveira Gaspar, que me lançou este desafio, pela orientação, pela liberdade para explorar ideias e pelo acesso a recursos que me permitiram chegar mais longe. A diversidade dos projetos que partilhámos inspirou-me a seguir o seu exemplo de dedicação e energia. Acima de tudo, foi sempre generosamente disponível e genuinamente dedicado ao meu percurso.

Ao Professor Doutor Pedro Nuno Dinho Pinto da Silva, pela partilha de conhecimento, pela orientação que me levou a ir além do óbvio e por, na altura certa, saber dizer o necessário para me recentrar no que realmente importava.

À equipa do LITecS, que tive a felicidade de ver crescer, pela cultura de trabalho, pelas *side quests* e pelo ambiente de inovação, colaboração e amizade que continuamos a construir juntos.

À minha Mãe, por ter despertado e nutrido em mim a chama da curiosidade, ao meu Pai, por me ter ensinado a arte do engenho e o engenho da arte, e ao Simão, por me mostrar que a criatividade é muitas vezes rebelde.

À Raquel, pelo carinho, paciência e apoio, mesmo quando nem sempre era claro como o dar.

À restante família, cujo apoio ultrapassou a distância e a ausência.

Ao Daniel, amigo e sócio nesta travessia, pela amizade e entreajuda, ao João, que, mesmo só a ver me ajudou bastante, e ao Joni, com quem tive o privilégio de forjar aventuras.

Aos meus amigos das caminhadas, das viagens, dos jantares, da escalada e da ADPP, por me ajudarem a sair da rotina, por tornarem o caminho mais leve e por me lembrarem, com mais ou menos subtileza, que uma tese não se escreve sozinha.

A todos os que, de uma forma ou de outra, contribuíram para que este trabalho fosse possível, o meu sincero bem-haja.

Resumo alargado

A formação de gelo em evaporadores de sistemas de refrigeração é um fenómeno que degrada a sua eficiência energética, levando a um aumento do consumo de energia e a custos operacionais mais elevados. Para mitigar este problema, os sistemas de refrigeração recorrem a ciclos de descongelação que, na sua maioria, são ativados por temporizadores. Esta abordagem, embora simples, é ineficiente, pois os ciclos são dimensionados para as piores condições de funcionamento, resultando em descongelações desnecessárias ou excessivas na maioria das situações. Uma alternativa mais eficiente é a descongelação por-demanda, que ativa o ciclo apenas quando a acumulação de gelo o justifica. A implementação desta estratégia requer, no entanto, métodos fiáveis e de baixo custo para a deteção de gelo, uma área onde ainda existe espaço para inovação.

Neste contexto, a presente tese foca-se no desenvolvimento de sensores resistivos para a deteção da formação de gelo, explorando-os como uma solução económica e de fácil integração. O trabalho aborda o ciclo completo de desenvolvimento, desde a conceção teórica, passando pela prototipagem e testes experimentais, até à validação final. Ao longo da investigação, foram desenvolvidas e avaliadas várias famílias de sensores, simples e com materiais entre os elétrodos tais como cerâmica, tecido e encapsulados. Também foram produzidos sensores por fabrico aditivo.

Para validar objetivamente o desempenho destes sensores, foi desenvolvido um método de visão computacional para quantificar a formação de gelo na superfície do permutador de calor. Para além de ser um método adicional de deteção da formação de gelo, serviu como uma referência independente para correlacionar e validar os sinais dos sensores resistivos. Adicionalmente, foi implementado um detetor de conclusão de descongelação baseado na medição da humidade absoluta, que valida a conclusão do ciclo de descongelação.

A investigação demonstrou que a posição no permutador e a colocação do sensor são fatores críticos para a sua fiabilidade. Por esse motivo, o método de visão computacional foi expandido para criar mapas da formação de gelo, permitindo analisar a distribuição espacial do gelo e identificar as zonas mais representativas para a instalação dos sensores. O estudo do sensor com melhor desempenho, o FMRS4, incluiu o desenvolvimento de algoritmos de processamento de sinal para a deteção da nucleação de gelo e da conclusão da descongelação. Estes algoritmos foram validados experimentalmente em doze ciclos de congelação-descongelação, demonstrando uma

elevada fiabilidade na deteção de ambos os eventos, desde que o sensor estivesse corretamente posicionado.

O trabalho explorou ainda aspetos complementares, como a mitigação de efeitos eletroquímicos que afetam as medições e a compensação da dependência do sinal com a temperatura. Foi também investigado o conceito de um módulo de deteção autónomo em termos energéticos, alimentado por um gerador termoelétrico que aproveita os gradientes de temperatura do próprio sistema de refrigeração. Os resultados confirmaram a viabilidade de gerar energia suficiente para alimentar um sensor de baixo consumo e o seu sistema de comunicação sem fios.

Em suma, esta tese contribui para o avanço de tecnologias de deteção de gelo, apresentando uma solução de baixo custo com potencial para otimizar as operações de descongelação, resultando em sistemas de refrigeração mais sustentáveis e eficientes.

Palavras-chave

Formação de gelo; sensores para a deteção de gelo; sensores; visão computacional; gelo eficiência energética; evaporadores; sistemas de refrigeração; descongelação

Abstract

Frost formation on refrigeration system evaporators degrades thermal performance and increases energy consumption. Conventional defrosting methods, typically time-controlled, are inefficient and lead to unnecessary energy use. This thesis addresses this issue by developing and validating a cost-effective resistive sensor for demand-defrost applications. An iterative design-build-test methodology was employed to evaluate various sensor configurations, such as the air gap, ceramic medium, and fabric-medium designs. To provide an objective benchmark, a computer vision method was developed to quantify frost accumulation, complemented by an absolute humidity-based detector for validating defrost completion. The FMRS4 sensor demonstrated the most repeatable performance, consistently detecting both frost nucleation and defrost completion when sensor placement is adequate. Signal processing algorithms, including a Frost Nucleation Detector and a Defrost Completion Detector, were successfully developed and implemented. The study also highlights the importance of sensor placement, utilising frost formation maps derived from CV analysis to identify optimal sensor placement. Furthermore, strategies to mitigate electrochemical effects and compensate for temperature dependency were developed, and the feasibility of an energy-autonomous sensor powered by a thermoelectric generator was demonstrated. The research culminates in a validated sensor technology that offers a practical pathway towards more intelligent and energy-efficient refrigeration systems.

Keywords

Frost formation; Demand defrost; Resistive sensors; Computer vision; Refrigeration systems; Energy efficiency; Evaporators; Heat exchangers; Signal processing.

Index

List of Figures

List of Tables

List of Symbols

$\widetilde{ADC}$	Temperature-compensated ADC value [–].
$\overline{ADC}$	Moving-averaged, temperature-compensated ADC [–].
$\overline{AH1}$	Smoothed inlet AH [g·m⁻³].
$\overline{AH2}$	Smoothed outlet AH [g·m⁻³].
$\overline{\Delta AH}$	Smoothed AH difference [g·m⁻³].
Δt_{dry}	Time difference between DCD and HBDCD events [min].
Δt_{nuc}	Time difference between FND and CVFND events [min].
Δt_{op}	Operation execution time [s].
A	Area [m²].
ADC	Raw ADC sample value [–].
ADC^{trig}	Stored reference value of $\overline{ADC}$ at defrost start [–].
$AH1$	Absolute humidity at HX inlet [g·m⁻³].
$AH2$	Absolute humidity at HX outlet [g·m⁻³].
C	Capacitance [F].
C^{ADC}	Classified slope output ∈ {−1, 0, +1} [–].
$\bar{C}^{ADC}$	Moving average of the last M slope-classifier values [–].
C_S	Capacitance of the reference capacitor [F].
C_X	Capacitance of the sensing electrodes [F].
CC^{DCD}	DCD consensus classifier [–].
CV_{th}	CVG threshold after which a defrosting is initiated [–].
$CVFND$	CV-based Frost Nucleation Detector [–].
CVG	Whole HX surface CV based frost metric [–].
CVT	Targeted-Tile CV frost metric [–].
d	Distance between electrodes [m].
DCD	Defrost Completion Detector [–].
DOS	Door-Open Sensor state [–].
dT/dx	Temperature gradient in the direction of heat flow [K·m⁻¹].
E_{op}	Energy required for a given operation [mJ].
E_{tot}	Total energy consumption over the analysed period [mJ].
F	Flow rate [L/h]
f_i	Predefined threshold value.
FT	Binarization threshold applied to the image in the CV method [/]
FND	Frost Nucleation Detector [–].
h	Convective heat transfer coefficient [W·m⁻²·K⁻¹].

h	Slope horizon for CVT (number of samples) [−].
$HBDCD$	Humidity-Based Defrost Completion Detector [−].
I_{op}	Current drawn during operation [mA].
k	Thermal conductivity of the material [$W \cdot m^{-1} \cdot K^{-1}$].
K	Average-slope window length [−].
M	Consensus window length [−].
min	Minute [min].
n	Number of charge-transfer cycles [−].
n	Number of frosted pixels [−].
n	ADC bit depth [-]
N	Total number of pixels [−].
N	Moving-average window length for AH [−].
$N\mathrm{R}^{\mathrm{FND}}$	Negative-run indicator [−].
P	Persistence window length [−].
P_{elec}	Electrical power generated by the TEG [W].
P_m	Power during the measurement phase [mW].
P_{op}	Electrical power consumption for a given operation [mW].
P_s	Power during the sleep phase [mW].
P_t	Power during the transmission phase [mW].
q	Heat transfer rate [W].
Q	Moving-average window length applied to ΔAH [−].
$\dot{Q}_c$	Heat flow on the cold side [W].
$\dot{Q}_h$	Heat flow on the hot side [W].
r	Frost-density coefficient [−].
$R(T)$	Resistance measured at temperature T [Ω].
$R(T_{ref})$	Resistance referenced to T_{ref} [Ω].
$R_{s_{max}}$	Maximum expected resistance of the sensor [Ω].
$R_{s_{\min}}$	Minimum expected resistance of the sensor [Ω].
R_{air}	Resistance of the air parcel within the measured volume [Ω].
R_f	Fixed resistor [Ω].
R_{load}	Load resistor used to test the TEG-HX [Ω].
R_s	Resistance of the FDS [Ω].
R_{water}	Resistance of the water parcel within the measured volume [Ω].
$RH1$	Inlet-air relative humidity at sample n [%].
$RH2$	Outlet-air relative humidity at sample n [%].

S	Frosted-surface coefficient [–].
s	Second [s].
T	Local temperature at the sensor [°C].
t_{CVFND}	Timestamp of CVFND [min].
t_{DCD}	Timestamp of DCD [min].
t_{FND}	Timestamp of FND [min].
t_{HBDCD}	Timestamp of HBDCD [min].
T_{ref}	Reference temperature for normalisation [°C].
$TA1$	Inlet-air temperature [°C].
$TA2$	Outlet-air temperature [°C].
u	Standard uncertainty (1σ)
U	Expanded uncertainty
U	Update window length for CVFND [–].
u_{acc_F}	Standard uncertainty from accuracy for Flow rate
u_{acc_I}	Standard uncertainty from accuracy for Current
$u_{acc_{RH}}$	Standard uncertainty from accuracy for Relative Humidity
$u_{acc_{TA}}$	Standard uncertainty from accuracy for Air Temperature
$u_{acc_{TWF}}$	Standard uncertainty from accuracy for Working Fluid Temperature
u_{ADC}	Standard uncertainty of ADC in LSB counts
$u_{ADC,V}$	Standard uncertainty of ADC in Volts
u_{ADC_I}	Standard uncertainty from ADC for Current
$u_{\widehat{ADC}}$	Standard uncertainty of the compensated ADC signal
$u_{\overline{ADC}}$	Standard uncertainty of the smoothed ADC signal
u_{avg}	Standard uncertainty of the average
u_{CVG}	Standard uncertainty of the CV method
u_{dom}	Largest other standard uncertainty
u_F	Combined standard uncertainty for Flow rate
$u_{F,TEG}$	Combined standard uncertainty for Flow rate (TEG)
u_I	Combined standard uncertainty for Current
u_P	Standard uncertainty of power
$u_{P_{elec}}$	Standard uncertainty of TEG electrical power
$u_{\dot{Q}}$	Standard uncertainty of heat flow
u_{res}	Standard uncertainty related to resolution
$u_{res,TEG}$	Standard uncertainty from resolution for Flow rate (TEG)
u_{res_F}	Standard uncertainty from resolution for Flow rate

$u_{res_{RH}}$	Standard uncertainty from resolution for RH
$u_{res_{TA}}$	Standard uncertainty from resolution for Air Temperature
$u_{res_{TWF}}$	Standard uncertainty from resolution for Working Fluid Temperature
u_{RH}	Combined standard uncertainty for RH
u_{TA}	Combined standard uncertainty for Air Temperature
u_{TWF}	Combined standard uncertainty for Working Fluid Temperature
u_y	Combined standard uncertainty of y
u_{x_i}	Standard uncertainty of input x_i
$u_{\Delta AH}$	Standard uncertainty of the difference in absolute humidity
$u_{\overline{\Delta AH}}$	Standard uncertainty of the smoothed difference in absolute humidity
$u_{\Delta T}$	Standard uncertainty of temperature difference
$u_{\Delta\overline{ADC}}$	Standard uncertainty of the local slope
$u_{\Delta\overline{ADC}^{avg}}$	Standard uncertainty of the average slope
$u_{\overline{AH}}$	Standard uncertainty of the smoothed AH
u_{AH}	Standard uncertainty of the AH
$u_{V_{load}}$	Standard uncertainty of voltage across load resistor
V_{in}	Input voltage [V].
V_{load}	Voltage across R_{load} [V].
V_{op}	Operating voltage (ESP32) [V].
V_{out}	Output voltage [V].
V_R	Excitation voltage [V].
V_S	Voltage measured after charge transfer [V].
W	Moving-average window length [–].
α	Temperature coefficient used in compensation [°C⁻¹].
$\Delta\overline{\mathrm{ADC}}$	Local finite-difference slope of $\overline{\mathrm{ADC}}$ [–].
$\Delta\overline{ADC}^{avg}$	Average of slopes over a window of length K [–].
ΔAH	Difference in absolute humidity between HX outlet and inlet [g·m⁻³].
ΔCVT	Local slope estimate of CVT over a horizon h [–].
ΔT	Temperature difference [K]
$\Delta T_{h-c\ AVG}$	Average temperature difference between TEG-HX hot and cold sides [K].
Δt_m	Duration of the measurement phase [s].
Δt_s	Duration of the sleep phase [s].
Δt_t	Duration of the transmission phase [s].
ε	Stability tolerance threshold [g·m⁻³].
ε_r	Relative permittivity of the medium between electrodes [–].

ε_0	Electric constant (vacuum permittivity), 8.854×10^{-12} F·m^{-1}.
ζ	Tolerance around ADC^{trig} [–].
θ_{CV}	CV slope threshold for nucleation [–].
θ_s	Slope threshold for classification [–].
Λ	Validity band limits for $\overline{\Delta AH}$ [g·m^{-3}].
τ	Sampling period [s].
φ^{ADC}	State variable for locked negative-trend [–].
φ^{DCD}	DCD state variable encoding drainage/ drying/ stabilisation sequence [–].
ψ	$\overline{\Delta AH}$ threshold for AL-HX to be considered dry [g · m^{-3}].

List of Acronyms

3D	Three Dimensional
AC	Alternated Current
ADC	Analog-to-Digital Converter
AGRS	Air Gap Resistive Sensors
AH	Absolute Humidity
AL-HX	Air-to-Liquid Heat Exchanger
AM	Additive Manufacturing
AMRS	Additive Manufactured Resistive Sensor
C920	Camera Logitech C920
CAD	Computer-Aided Design
CAM	Computer-Aided Manufacturing
CFC	Chlorofluorocarbons
CFRS	Conductive Filament Resistive Sensor
CMRS	Ceramic-Medium Resistive Sensors
CNC	Computer Numerical Control
COP	Conference of the Parties
CRE	Commercial Refrigeration Equipment
CSV	Comma Separated Value
CV	Computer Vision
CVFND	Computer-Vision Frost Nucleation Detector
CVG	Computer Vision Global frost metric
CVT	Computer Vision Tile/Targeted frost metric
DC	Direct Current
DCD	Defrost Completion Detector
DoE	Design of Experiment
DOS	Door Opening Sensor
DXF	Drawing Exchange Format
EDRS	Encapsulated Double electrode water medium Resistive Sensor
EEI	Energy Efficiency Index
ESRS	Encapsulated Single electrode water medium Resistive Sensor
EWRS	Encapsulated Water medium Resistive Sensor
FDS	Resistive Frost Detection Sensor
FFM	Frost Formation Map
FMRS	Fabric Medium Resistive Sensors
FND	Frost Nucleation Detector

FS	Flow Sensor
GHG	Greenhouse Gas
GND	Ground
GPIO	General Purpose Input Output
GUI	Graphical User Interface
GWP	Global Warming Potential
HBDCD	Humidity-Based Defrost Completion Detector
HCFCs	Hydrochlorofluorocarbons
HMI	Human-Machine Interface
HVAC	Heating Ventilation and Air Conditioning
HVACR	Ventilation, Air Conditioning, and Refrigeration
HX	Heat Exchanger
IDE	Integrated Development Environment
IIR	International Institute of Refrigeration
IoT	Internet of Things
IPCC	Intergovernmental Panel on Climate Change
IR	Infrared
IRA	Illumination Recognition Area
LED	Light Emitting Diode
LLMs	Large Language Models
LSB	Least Significant Bit
MP	Megapixels
NaN	Not a Number
NCQG	New Collective Quantified Goal
NO	Normally Open
ODP	Ozone Depleting Potential
PETG	Polyethylene Terephthalate Glycol
PLA	Polylactic Acid
PLL	Phase-Locked Loop
PSU	Power Supply Unit
PWM	Pulse Width Modulation
RDCs	Refrigerated display cabinets
RFD	Resistive Frost Detection
RGB	Reed Green and Blue
RH	Relative Humidity
ROI	Region of interest
RSS	Root Sum Squared

STL	Stereolithography
SW	Switch
T	Temperature
TA	Air Temperature
TE	Thermoelectric
TEG	Thermoelectric Generators
TEG-HX	Thermoelectric Generator Heat Exchanger
TE-HX	Thermoelectric Heat Exchanger
TEPS	Tube-Encircled Photoelectric Sensor
TFT	Thin-Film Transistor
TPU	Thermoplastic Polyurethane
TRL	Technology Readiness Level
TWF	Working Fluid Temperature
UBI	University of Beira Interior
UN	United Nations
UNFCCC	United Nations Framework Convention on Climate Change
USB	Universal Serial Bus
WSNs	Wireless Sensor Networks

Chapter 1

Introduction

The technical problem of energy inefficiency in refrigeration is deeply embedded in a larger historical and societal context. To fully grasp the significance of the solutions proposed in this thesis, it is important to first explore the decades of scientific discovery, international policy, and growing societal need that have elevated this engineering challenge into a global imperative.

1.1. Framework

As the 21st century unfolds, the world faces an escalating climate emergency. The year 2024 was the warmest on record, reaching + 1.55 °C ± 0.13 °C above pre-industrial levels [1]. While these climate changes have not occurred suddenly within the human timeframe, they are rapid when considered in geological and evolutionary contexts, and therefore demand humanity's joined efforts to reduce the leading causes of environmental degradation.

1.1.1. Humanity's commitment to environmental protection

In 1938, Guy Stewart Callendar stood before the Royal Meteorological Society in London to propose a theory relating the burning of fossil fuels to a growing change in climatic conditions [2]. Although the theory was disregarded at the time, evidence stacked up, and 34 years later, on June 1st, 1972, the United Nations (UN) initiated a major conference in Stockholm on international environmental issues, marking the starting point in the development of a series of international environmental politics.

The Montreal protocol was adopted in 1987 to restrict and limit the usage of chemicals with Ozone Depletion Potential (ODP), shaking the Heating, Ventilation, Air Conditioning, and Refrigeration (HVACR) industry. This global agreement demanded the phase out of high-performance synthetic refrigerants, starting with chlorofluorocarbons (CFCs) and, with later amendments, hydrochlorofluorocarbons (HCFCs), which were the most used refrigerants in refrigeration and air conditioning machines at the time [3]. The refrigeration industry was consequently obliged to innovate and seek environmentally friendly alternative refrigerants and technologies to comply with the new international standards. This shift demanded retrofitting or ultimately replacing refrigeration equipment, which will later be argued to be an opportunity to implement additional upgrades to increase sustainability within the

sector. Nowadays, it is possible to confirm that international efforts returned positive results: the ozone decline has largely halted at extrapolar latitudes and transitioned to a slow ozone increase in both hemispheres. Kofi Annan, the former UN Secretary-General, characterized the Protocol as not only "*the most successful environmental treaty in history*", but also "*perhaps the most successful international agreement to date*" [4].

The Intergovernmental Panel on Climate Change (IPCC) was established on December 6, 1988, to provide a clear scientific assessment of the current state of knowledge on climate change and its potential environmental and socio-economic impacts. Its first report, published in 1990, laid the groundwork for the creation of the United Nations Framework Convention on Climate Change (UNFCCC), adopted in May 1992. This international treaty aims to reduce global warming and address the impacts of climate change, setting emissions reduction targets for industrialized countries. The UNFCCC was endorsed by 154 states at the United Nations Conference on Environment and Development in June 1992, also known as the Earth Summit, in Rio de Janeiro, and it came into effect on March 21, 1994.

Since its beginning, signatory nations have convened annually at the Conference of the Parties (COP) to evaluate progress in combating climate change. At COP3, held in December 1997, the Kyoto Protocol was established, legally mandating emission reduction targets for developed countries. Similarly, COP21, in December 2015, saw the adoption of the Paris Agreement. This agreement aims to limit the global average temperature increase to well below 2°C above pre-industrial levels and to pursue efforts to limit the temperature increase even further to 1.5°C, a threshold that was already surpassed in 2024 [1].

The most recent Conferences of the Parties continue to demonstrate growing international ambition. COP28, held in Dubai in 2023, culminated in the Outcome of the First Global Stocktake, which for the first time explicitly called for a global transition away from fossil fuels. The decision also established collective targets to triple renewable energy capacity and double the annual rate of energy efficiency improvements by 2030, marking a significant acceleration of the decarbonization agenda [5]. COP29, held in Baku in 2024, built upon this progress by adopting the framework for the New Collective Quantified Goal (NCQG) on climate finance, which will succeed the former USD 100 billion annual commitment and set a new benchmark for global climate investment. These decisions reaffirm the commitment of the 198 Parties to the Convention to strengthen mitigation, adaptation, and finance mechanisms in the face of escalating climate challenges [6].

The urgency to mitigate climate change comes from its rapid and unprecedented damage to biodiversity, escalating the frequency and severity of natural disasters, and posing threats to global communities and ecosystems. This is creating a crisis with impacts on human health, jeopardizing food and water security, and exerting pressure on the economy.

1.1.2. Feeding a growing population amidst a climate emergency.

Simultaneously, humanity's overexploitation of natural resources is manifesting in critical shortages, with the World Bank projecting a 40% global water deficit by 2030 [7]. The issue of water scarcity allied with climate change and geopolitical instability is intensifying the challenge of food security, it is estimated that between 638 and 720 million people faced hunger in 2024 [8]. With the global population expected to reach 9.7 billion by 2050 [9], if current consumption trends persist, it's estimated that food production will need to increase by over 50% to ensure sufficient nutrition for everyone [10]. Increasing demand for food, together with climate-induced disruptions to agricultural productivity pushes the earth's biocapacity limits. In 2025, the Earth Overshoot Day was on July 24th, meaning that between January 1st and July 24th, humanity's demand for biological regeneration was equivalent to the planet's entire annual regeneration capacity [11]. This is particularly relevant, as from 2004 to 2014 in the EU-27, the ecological footprint was primarily driven by food consumption, exceeding regional biocapacity [12]. The UN Sustainable Development Goal 2 advocates for food security through sustainable practices [13], reinforcing the need for efficiency, not only in agricultural practices, but also in food preservation methods. Avoiding food spoilage is an important contribution to safeguard the global food supply without increasing production capacity and therefore sacrificing sustainability. An estimated 13% of the world's food is lost in the supply chain from post-harvest to retail [14], and a further 19% of food is wasted in households, food services, and retail [15]. This is also an economic burden, as food loss and food waste cost close to 900 billion EUR per year in the period from 2010 to 2016 [16]. Lower temperatures contribute to maintaining food quality and extending the shelf-life of perishable goods from post-harvest to consumption [17]. Foods requiring refrigeration amount to 1661 million tonnes annually, 46% of total food production, after accounting for agricultural and post-harvest losses. However, only 47% of this quantity is refrigerated, mostly in developed nations. In developing nations, 23% of food loss is caused by a lack of an adequate cold chain. According to the International Institute of Refrigeration (IIR), 526 million tonnes of food could be saved yearly if properly refrigerated, which is enough to nourish 950 million individuals. This is a particularly significant number considering it surpasses the number of humans facing

hunger in 2024 [18]. The cold chain reduces food loss through a series of refrigeration steps, including pre-cooling, cold storage, refrigerated transport, and refrigerated display during marketing [19].

1.1.3. The impact of temperature on food preservation

Refrigeration slows physical, chemical, and biological mechanisms that, if not controlled, cause food decay, ultimately leading to food waste [17].

The physical factors that most affect food preservation are temperature and humidity. Adequate refrigeration provides a controlled environment that should maintain low and constant temperatures. Temperature inconsistencies in refrigeration units have been found to cause food safety issues [20], while extended thermal oscillation intervals result in greater loss of food mass [21]. Refrigeration systems play the role of avoiding heat spoilage while being properly setup to avoid freezing damage. These systems can regulate humidity levels to minimize changes in moisture content, which affects the rate of mass loss, texture, appearance, and microbial stability of food products [22].

Chemical factors that affect food preservation can also be mitigated by using lower and stable storage temperatures along the supply chain. Browning reactions, such as the Maillard reaction and other non-enzymatic browning processes, can be mitigated using adequate temperatures [23]. Low temperatures also slow oxidation reactions in food products, preventing or delaying oxidative spoilage [24]. Mitigating these and other chemical reactions that usually happen in food products, reduces changes in pigments, deterioration of flavours and odours, degradation of essential nutrients such as vitamins, minerals, fats, and bioactive compounds, helping to preserve the nutritional value of food.

Biological factors that lead to a decay in food quality can also be limited through proper refrigeration. Low temperatures reduce the rate at which bacteria, moulds, and yeasts that thrive at higher temperatures grow, thereby decreasing the risk of spoilage and foodborne illnesses [25]. Cold temperatures also slow down the activity of natural enzymes in food, which can cause undesirable changes in flavour, colour, and texture, such as enzymatic browning in fruits and vegetables [26].

The importance of refrigeration and maintaining consistent, low temperatures for ensuring food security and food safety, and for reducing food loss, is evident. However, refrigeration systems consume energy to function that originates in large amount from the burning of fossil fuels. Given the urgent need to increase energy efficiency and

minimize CO_2 emissions, the responsibility to improve refrigeration systems is particularly laid on the developed nations where their use is most prevalent. To further discuss efficiency in refrigeration machines, an understanding of their working principles is needed.

1.1.4. Vapor-compression refrigeration systems

To reduce the temperature within a refrigerated volume, a refrigeration system transfers heat from a low-temperature region to a higher-temperature region, a process that requires additional energy to obey the second law of thermodynamics. In this section, the vapor-compression refrigeration cycle will be analysed based on insights from [27]. Among the various refrigeration technologies, vapor-compression refrigeration systems are the most common, due to a balance of simplicity, efficiency, and versatility across a wide range of applications. These systems are most characterized by the sequential operation of four main components: the evaporator, condenser, compressor, and expansion valve, as depicted in Figure 1 (a).

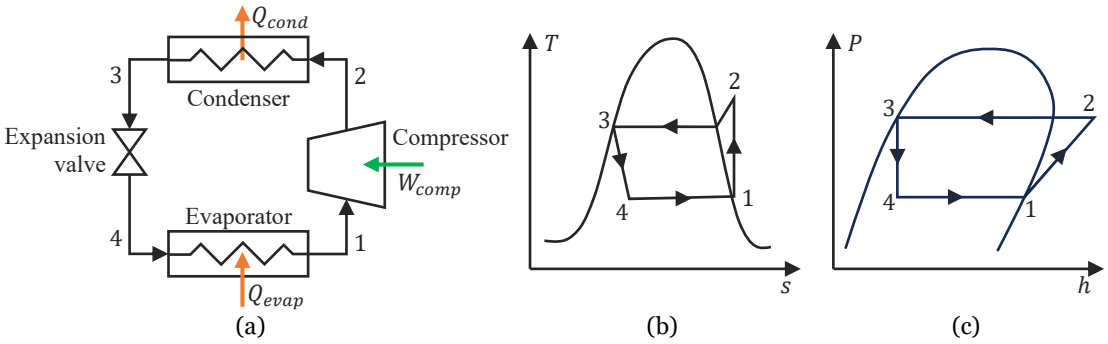

Figure 1 – Basic vapor-compression refrigeration system (a), corresponding ideal T-s diagram (b), and ideal Log P-h diagram (c) adapted from [27].

Heat is absorbed in the evaporator ($\dot{Q}_{evap}$) and rejected in the condenser ($\dot{Q}_{cond}$). This process requires compressor work input ($\dot{W}_{comp}$), usually via electrical power and unfolds consecutively with variations in temperature and entropy, as shown in Figure 1 (b), and variations in pressure and enthalpy, as shown in Figure 1 (c), as follows:

I. (1-2) Reversible adiabatic compression: The low-pressure refrigerant vapour is drawn to the compressor, where it is compressed from the evaporation pressure to the condensation pressure, typically reaching a superheated vapour state at the compressor outlet. This process requires compressor work input (W_{comp}), usually supplied by an electric motor-driven compressor.

II. (2-3) Idealised internally reversible heat rejection at constant pressure: Upon reaching the condenser coil, the high-pressure refrigerant rejects heat (Q_{cond}) to the external cooling medium at approximately constant pressure. In the ideal cycle, this process is represented as internally reversible. However, real heat rejection is externally irreversible because heat transfer requires a finite temperature difference between the refrigerant and the cooling medium. During condensation of a pure refrigerant, the phase change occurs at approximately constant saturation temperature.

III. (3-4) Irreversible adiabatic expansion: The high-pressure liquid refrigerant then passes through the expansion valve, where its pressure is abruptly reduced undergoing an expansion at constant enthalpy. This causes a decrease in the refrigerant's temperature, preparing it to absorb heat.

IV. (4-1) Idealised internally reversible heat absorption at constant pressure: The low-pressure, low-temperature refrigerant then enters the evaporator, where it absorbs heat from the refrigerated space (Q_{evap}). This heat absorption increases the refrigerant enthalpy and vapour quality at approximately constant pressure. For a pure refrigerant undergoing evaporation, the saturation temperature remains approximately constant. A temperature increase only occurs if the refrigerant becomes superheated after complete evaporation. The heat is absorbed from an external fluid, usually the air inside or circulating through the refrigerated volume. The saturated refrigerant vapour at evaporation pressure is then drawn back to the compressor, closing the cycle.

This cyclic process of compression, condensation, expansion, and evaporation results in the continuous transfer of heat from a lower to a higher temperature location, refrigerating the designated space. For a steady-flow control-volume formulation with negligible kinetic and potential energy changes, the first law of thermodynamics becomes Equation (1):

$$\dot{Q}_{in} + \dot{W}_{in} + \dot{m}h_{in} = \dot{Q}_{out} + \dot{W}_{out} + \dot{m}h_{out} \quad (1)$$

In which,

- $\dot{Q}$ represents the rate of heat transfer, [kW].
- $\dot{W}$ represents the rate of work, [kW].
- $\dot{m}$ is the mass flow rate of refrigerant, [kg/s].
- h is the enthalpy, [kJ/kg].

This equation holds for all the phases of a vapor-compression refrigeration system previously detailed, yet the system can be further divided, allowing each phase to be analysed using the first law of thermodynamics:

I. (1-2) Reversible adiabatic compression: there is no heat transfer between the compressor and its surroundings, and no work is produced by the compressor. The only work interaction is the compressor work input ($\dot{W}_{comp}$), resulting in the simplification shown in Equation (2):

$$\dot{W}_{comp} + \dot{m}h_1 = \dot{m}h_2$$
$$\dot{W}_{comp} = \dot{m}(h_2 - h_1) \quad (2)$$

II. (2-3) Idealised internally reversible heat rejection at constant pressure: in this phase, there is only heat transfer out of the system ($\dot{Q}_{cond}$) with no heat transfer into the system, and no rate of work input or output, resulting in Equation (3):

$$\dot{m}h_2 = \dot{Q}_{cond} + \dot{m}h_3$$
$$\dot{Q}_{cond} = \dot{m}(h_2 - h_3) \quad (3)$$

III. (3-4) Irreversible adiabatic expansion: in the expansion valve, the refrigerant expands, the work done by the system can be considered negligible, and no heat transfer is observed therefore simplifications observed in Equation (4) can be made:

$$\dot{m}h_3 = \dot{m}h_4$$
$$h_3 = h_4 \quad (4)$$

IV. (4-1) Idealised internally reversible heat absorption at constant pressure: finally, in the evaporator heat absorption ($\dot{Q}_{evap}$) is observed, but no heat is transferred out of the system and no rate of work is input or output, resulting in Equation

$$\dot{Q}_{evap} + \dot{m}h_4 = \dot{m}h_1$$

$$\dot{Q}_{evap} = \dot{m}(h_1 - h_4) \tag{5}$$

For the complete refrigeration cycle, the energy balance is expressed as shown in Equation (6):

$$\dot{Q}_{evap} + \dot{W}_{comp} = \dot{Q}_{cond} \tag{6}$$

And the coefficient of performance (COP) becomes that of Equation (7):

$$COP = \frac{\dot{Q}_{evap}}{\dot{W}_{comp}}$$

or

$$COP = \frac{\dot{Q}_{evap}}{\dot{Q}_{cond} - \dot{Q}_{evap}} \tag{7}$$

In practical vapor-compression refrigeration cycles, deviations from the ideal theoretical cycle occur mainly due to pressure and temperature drops and heat interactions with the surroundings. The refrigerant vapour entering the compressor is superheated, and irreversibilities during compression alter its entropy. The refrigerant leaving the condenser may experience subcooling, which can increase the refrigeration effect, while pressure drops in the circuit generally reduce performance and require careful management to minimize compressor workload.

From this energy analysis of the vapor-compression refrigeration cycle, it is clear how the cycle's efficiency can be compromised by various factors. Power consumption is intrinsically tied to the amount of heat that the system must absorb from the refrigerated chamber ($\dot{Q}_{evap}$). The equations show that irreversibilities, thermal loads, and heat-transfer limitations increase the required compressor work ($\dot{W}_{comp}$), thus increasing energy consumption. Understanding these relationships allows for a more directed approach to mitigating losses and improving the overall energy efficiency of refrigeration systems.

1.1.5. Efficiency and sustainability in the refrigeration sector

Refrigeration is an energy-heavy industry, yet the challenge of energy efficiency and sustainability begins even before powering these systems. If food spoils, the energy and resources invested in its production, packaging, transportation, and storage are all wasted, undermining sustainability efforts. In fact, 8 – 10% of global Greenhouse Gas (GHG) emissions are associated with food that is wasted before consumption [16].

Although refrigeration systems significantly reduce food loss before consumption, they also pose environmental challenges. The efficiency and sustainability of these systems are evaluated through several parameters: the quality of refrigeration, which ensures stable and appropriate temperatures; refrigerant sustainability, by using refrigerants with low associated environmental impact; and energy efficiency, addressing both electrical and thermal efficiencies.

The quality of refrigeration directly impacts food preservation. As previously discussed, maintaining proper temperature, temperature stability, and adequate humidity extends the shelf life and quality of perishable products, thereby reducing the likelihood of losses before consumption.

Refrigerant sustainability concerns include refrigerant leaks and end-of-life disposal practices that lead to atmospheric emissions of gases with high ODP and Global Warming Potential (GWP). Refrigerant leakage of up to 15% per year in commercial refrigeration plants is not uncommon [25], contributing to environmental harm. Shifting towards more sustainable refrigerants has been the tendency, mainly forced by intergovernmental agreements. There are a variety of energy-efficient CFC and HFC-free refrigeration technologies providing no justifiable reasons for the commercial sector to delay a swift transition [28]. However, 80% of the global-warming impact of refrigeration plants is attributed to energy consumption, rather than refrigerant leakage [25].

Energy efficiency in refrigeration systems is determined by their thermal performance, which is enhanced by improving the electrical efficiency of components, increasing heat transfer efficiency in heat exchangers, improving control methods, reducing heat losses through insulation, and minimizing thermal loads [29].

The IIR [29] estimated the energy consumption in the global cold chain to be 281 TWh/year, with 83 TWh/year of the 281 TWh/year at the retail sales stage. Energy consumption in reach-in coolers in Australia, Brazil, China, EU, India, Japan, Mexico,

South Africa, and the U.S. is projected to increase from 83 TWh in 2013 to 175 TWh by 2035 if the current trend continues, although there is an estimated energy savings potential at 45 to 56 TWh in 2035 if efficiency is pursued.

Refrigerated display cabinets (RDCs) hold a dominant position in the global Commercial Refrigeration Equipment (CRE) market, accounting for 50% of the market value, as illustrated in Figure 2 [30].

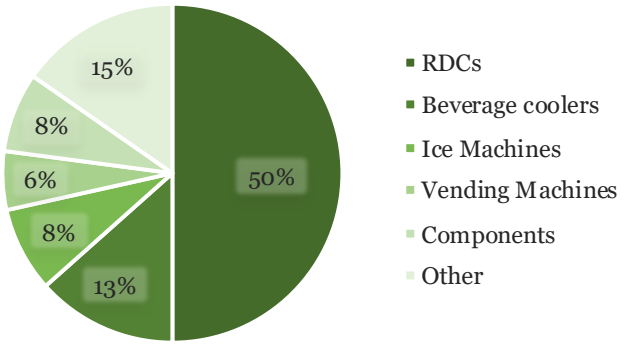

Figure 2 – Worldwide market value distribution of commercial refrigeration equipment by product type, adapted from [30].

Historically, the energy efficiency of CRE has substantially improved. The daily energy consumption per total display area in refrigerated display cabinets saw a decrease of 30% from 2005 to 2013, and 40% from 1997 to 2013. Moreover, the average EEI for newly sold storage cabinets saw a notable enhancement of about 40% from 2015 to 2020 [29]. Despite this increase in efficiency, CRE systems account for half of the energy consumption in supermarkets [31].

The substantial role that RDCs play in the global CRE market, combined with their significant energy consumption and the potential for energy savings and efficiency improvements, is the reason for the focus on these systems. By concentrating on RDCs, which are widely used during the retail phase of the cold chain, this thesis aims to contribute to a sector where even marginal gains can lead to significant global environmental benefits and energy consumption reductions. To accomplish this, it is essential to first attain a basic understanding of what RDCs are and how they operate.

Refrigerated Display Cabinets, represent a category of CRE used in grocery stores, supermarkets, and convenience stores. These units are available in various forms such

as glass-door cabinets, service counters, and open multideck, which is represented in Figure 3.

Figure 3 – Generic multideck RDC, adapted and rendered from the CAD model in [32].

RDCs are built to store and display perishable food products, featuring either integral or remote compressors and condenser coils, evaporator coils, expansion valves, fans, control systems, lighting, and air curtain or transparent doors equipped with anti-condensation glass or condensation removal systems. These components work together to provide adequate temperature and humidity, increasing the freshness and safety of the displayed food products, with an appealing and facilitated consumer access.

Figure 4 (a) shows a cut view of a remote multideck RDC with air curtains, displaying the typical arrangement of internal components. These systems use an air curtain, which is created between a discharge air grille and a return air grille to minimize cold air loss while displaying and providing ease of access to refrigerated products. As displayed in Figure 4 (b), air is drawn into the system by a fan that pulls it from the return air grille and forces it through the evaporator coil, where heat is removed, lowering its temperature. This air is then directed vertically across the back cabinet, escaping through the perforated back panel and around the refrigerated products. Finally, the remaining chilled air that did not escape through the back panel is expelled through the discharge air grille and directed back toward the return grille. This high velocity air discharge creates a circulating air curtain that captures and recycles the air that has passed over the displayed products, minimizing cold air loss and maintaining a consistent temperature.

The energy consumption of open RDC is one of the highest among CRE, as their compact and open nature poses significant challenges to an efficient design. Despite this, they are often preferred to other CRE due to their higher marketing potential [31].

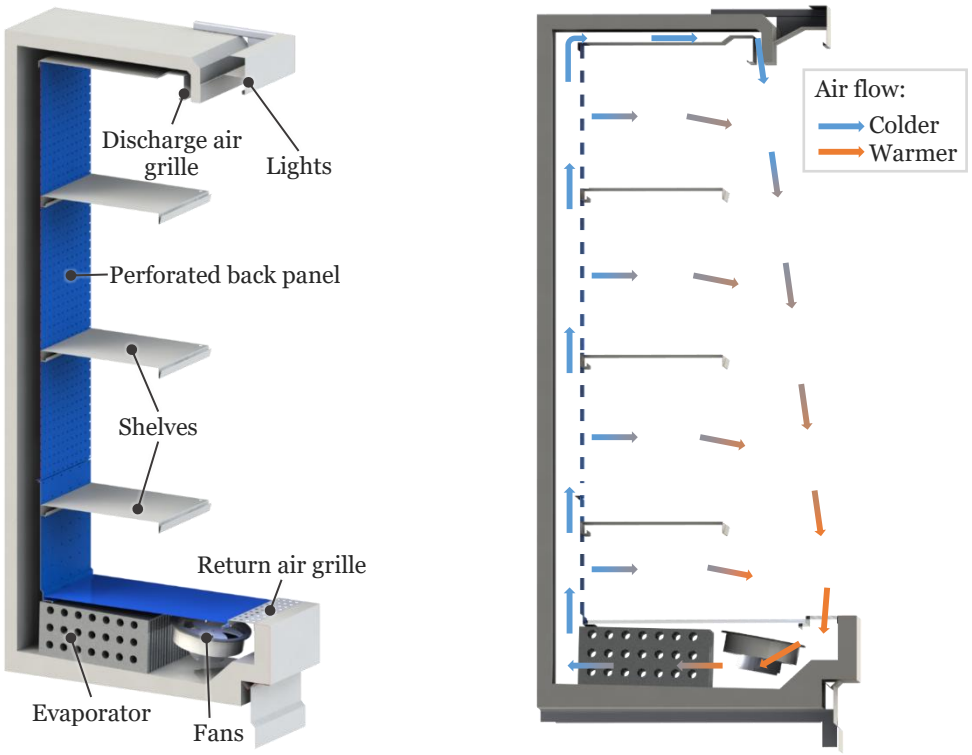

Figure 4 – Rendered cut view of an RDC CAD model from [32], with labelled components (a) and represented airflow dynamics (b).

Although techniques like multi-flow air curtains can help reduce thermal losses [31], cold air inevitably escapes the system [33], particularly when the air curtain is disrupted by people passing by or removing products [34], events that are both common and necessary in commercial settings. To address these challenges and enhance the efficiency of refrigeration systems, a variety of energy-saving design options have been developed. Table 1 summarizes some energy-saving design options for commercial refrigeration systems, which include components and modifications that can lead to significant efficiency improvements and cost implications.

Table 1 – Energy-saving design options for commercial refrigeration systems, adapted from [29].

Option	Potential Efficiency Improvement	Indicative Additional Cost	Applicable to
Fan/motors			
PSC fan motor for evaporator	< 15%	< 5%	All
PSC fan motor for condenser	< 5%	1%	Integral

Option	Potential Efficiency Improvement	Indicative Additional Cost	Applicable to
ECM fan motor for evaporator	2% – 35%	< 5%	All
ECM fan motor for condenser	< 15%	1.5%	Integral
Cabinet doors			
Optimized cabinet airflow	5%	< 10%	All
Variable-speed drive	10%	15%	All
High-performance door with low infiltration	20% – 45%	5% – 10%	Transparent doors
Cabinet lighting			
Super T8 lighting	< 2.5%	< 1%	Vertical no door units
Light-emitting diode (LED) lighting	10% – 35%	1.5%	Vertical
LED lighting with occupancy sensors	5% – 40%	5% – 20%	Vertical
Insulation			
Night curtains	5%	< 5%	Vertical no door units
Increase cabinet insulation thickness 13 mm	< 10%	< 5%	All
VIPs	< 25%	30% – 90%	All
Pipe insulation	< 5%	N/A	All
Heat exchanger			
Optimized evaporator design	< 5%	< 2%	All
Optimized condenser design	5% – 12.5%	< 3%	Integral
Optimized air fins	10%	< 0%	All
Compressors			
High-efficiency reciprocating compressor	5% – 10%	< 1.5%	Integral
Variable-speed drive	40%	2 ×	All
Motor efficiency controllers	10%	N/A	All
Dynamic demand controllers	40%	Variable	All
Control			
EEVs	20%	< 20%	All
Improved evaporator pressure control	2% per K increase	1.5% – 35%	All
Leak minimization			
Improved leak tightness	20%	10%	All
Leak detection	15%	10%	All
Refrigerant			
High-efficiency refrigerant	Variable	N/A	All
Refrigerants with nanoparticles	20%	10%	All
Defrost			
Hot gas, reverse cycle	5%	< 5%	Freezers
Off-cycle	10%	< 0%	Refrigerator
On-demand control	10%	< 5%	All
Others			
Radiant reflectors	8%	< 0%	All
Improved glazing	5%	5%	All
Anti-sweat heater control	5%	< 0%	All
Refrigerant line trim heaters	10% – 25%	< 0%	All

Substantial performance enhancements can be achieved with high-efficiency variable-speed compressors, advanced controls, ECM fans, and enhanced insulation. Additionally, alternative refrigeration cycles like subcooling, ejector-enhanced, and vapor-injection cycles can offer further performance gains. For larger systems, employing methods like evaporative condensing and parallel compression can be a cost-effective method to enhance performance. These remote systems also help reduce the load on the building's Heating, Ventilation and Air Conditioning (HVAC) system by rejecting heat outdoors. In developed economies, there has been a shift towards using CO_2 as a refrigerant due to its lower environmental impact compared to HFCs, leading to the adoption of sophisticated configurations such as booster and cascade refrigeration systems. Intermittent defrosting contributes to the continuous operation of refrigeration systems, as accumulated frost in the evaporator adds thermal resistance, increasing power consumption and if not properly removed, might block airflow entirely [35]. Advanced options like hot-gas defrost and reverse-cycle, though more expensive, improve energy efficiency. Systems that employ demand defrosting—defrosting based on actual need rather than a set schedule—can offer further efficiency improvements, but widespread adoption remains limited. Recent innovations in frost prediction and sensing technologies can contribute to a more efficient and sustainable refrigeration industry.

1.1.6. Concluding remarks:

As the 21st century progresses, the pressing climate emergency necessitates a unified effort to mitigate environmental degradation, influenced by rising global temperatures and intensified climate events. The historical context provided highlights the ongoing shift towards sustainable practices, particularly in the refrigeration sector, due to its substantial energy consumption and impact on ozone depletion.

RDCs, which dominate the CRE market, exemplify the dual challenge of enhancing energy efficiency while ensuring marketable food preservation. Innovations in RDC technology have marked substantial progress towards efficiency, although cost remains a barrier to updating refrigeration systems with new efficient technologies. The ongoing phase-out of refrigerants with ODP and high GWP presents a unique opportunity, as regulatory pressures necessitate the retrofitting or complete replacement for implementation of more sustainable refrigerants. This transition phase offers an ideal moment to integrate energy-efficient solutions. Businesses should therefore seize this opportunity to enhance their systems' efficiency while aligning with mandatory environmental standards and reduce operational costs in a competitive market.

Among the various areas with potential for further improvement, the integration of frost detection technologies stands out. Demand defrosting promises substantial reductions in energy consumption but has yet to be widely adopted by the industry. This points towards the need to further research and develop this technology, which will be the focus of this thesis.

1.2. Objectives and work relevance

Increasing efficiency and sustainability in refrigeration systems is of the utmost importance, as it results in multiple wins: increasing food security and food safety, decreasing the environmental impact associated with food loss, and decreasing power consumption of the refrigeration sector. For this, refrigeration should balance energy consumption with food quality loss. Optimizing the operation of supermarket refrigeration systems can result in energy savings without extra loss of food quality. This helps in maintaining the quality attributes of food products under varying ambient conditions [36].

The primary goal of this thesis is to contribute to the scientific progress of efficiency in refrigeration systems. Given the substantial role that RDCs play in the global CRE market, combined with their significant energy consumption and the potential for energy savings and efficiency improvements, this research focuses on RDCs as a representative and impactful system within the food retail sector. By concentrating on RDCs this work aims to contribute to a sector where even marginal efficiency gains can lead to substantial global reductions in energy consumption and environmental benefits.

The plan to achieve this goal will start by understanding frost formation and the effectiveness of using sensors for cost-effective detection. This will be achieved through the development of sensors for defrost control, enabling defrosting to be initiated based on measured frost accumulation rather than fixed schedules. As a result, unnecessary defrost cycles can be reduced, lowering energy consumption and limiting temperature disturbances that may affect refrigerated product preservation and refrigeration quality.

This exploration extends beyond a theoretical approach and into the design, prototyping, and experimental testing of a selection of frost-detection resistive sensors, along with the development of required supporting equipment and testing methods. Finally, control methods will be employed, tested and discussed. The significance of this work lies in its potential to offer practical, cost-effective solutions for improving the energy efficiency and operational reliability of refrigeration systems, which can help reduce the

environmental impact of cooling technologies used in food preservation. To accomplish the outlined objectives, the following tasks will be performed:

- Literature review: Conduct a review of existing studies on frost formation and technologies related to frost detection, defrosting methods and defrost control.
- Study the sensing principles of the resistive frost detection sensor to understand its detection mechanisms and develop the most suitable design configurations. This process follows a cyclic and iterative approach, beginning with theoretical conceptualization, followed by design, prototyping, testing, and performance evaluation, leading to refinement of the concept and subsequent redesign.
- Manufacturing process: Develop a replicable method for the manufacturing of selected resistive sensors.
- Experimental setup for testing: Design and implement an experimental setup to test the selected sensors' performance in detecting frost. This includes setting up frost formation environments, independent evaluating methods to assess sensor accuracy and reliability, and sensing capabilities to understand the conditions in which frost formation and defrosting is occurring.
- Data analysis and model development: Analyse the collected data to assess the effectiveness of resistive sensors in detecting frost formation. Use this data to implement frost-formation and defrost-completion detectors.
- Evaluation of results: Compare the performance of the developed sensors and independent frost and defrosting detection models.
- Recommendations and Future Work: Provide recommendations based on the research findings for the practical implementation of resistive sensors in commercial refrigeration systems. Outline areas for future research to continue advancing frost detection and defrosting technologies.

The successful completion of this work aims to advance frost sensing technologies that have the potential to optimize defrosting operations in RDCs, thereby contributing to the development of more sustainable and energy-efficient cooling solutions. This research addresses a challenge in supermarket refrigeration, where defrosting inefficiencies represent a major source of energy waste. Beyond technical innovation, the outcomes of this thesis support broader objectives of environmental sustainability, reducing greenhouse gas emissions, and promoting food security in the face of global climate challenges.

1.3. Innovative aspects

At the heart of this thesis lies the development of resistive sensors for frost detection is its core and defining contribution. The work followed an iterative and experimental path, where each design was conceived, fabricated, and tested to reveal the underlying principles governing resistive sensing in frosting environments. This continuous cycle of design, experimentation, and refinement allowed the gradual evolution of sensor architectures, leading to increasingly robust and accurate detection solutions. The approach combined theoretical understanding with practical implementation, transforming conceptual ideas into validated prototypes.

Additive manufacturing played a supporting role in the fabrication of components for the experimental setup, facilitating rapid iteration and adjustment of test conditions. Its main innovative contribution, however, lies in its application to sensor development. This technology enables the creation of precise, small-scale geometries that would otherwise be difficult to manufacture by hand, while offering excellent reproducibility and design flexibility at low cost. By adapting the sensor architecture to the constraints and advantages of additive manufacturing, this work demonstrated a practical path toward producing accessible, customizable, and globally replicable sensors, marking a shift toward more sustainable and democratized fabrication methods in sensing technologies.

To interpret and validate sensor data, dedicated detectors were developed to process sensor signals and extract event detection in the frost–defrost cycle. These algorithms transformed continuous analog data into actionable triggers, enabling the detection of frost nucleation and defrost completion.

Complementing the resistive frost sensing approach, this work also introduced computer-vision-based and humidity-based frost and defrost completion detection methods. The computer-vision method provided an independent and objective means of assessing frost accumulation, while also demonstrating potential for standalone application in larger or more open refrigeration environments. The absolute humidity–based approach offered a metric for quantifying mass transfer during defrosting, proving valuable as both a validation and diagnostic tool for frost management.

An additional innovative contribution was the demonstration of an energy-autonomous sensing concept that explored the use of thermoelectric power generation to support low-energy monitoring modules. Although often overlooked as a practical power source due to its limited efficiency, the thermoelectric generator becomes highly suitable for this

application, where minimal energy demand coincides with large, readily available temperature gradients. In such conditions, it can provide sufficient power for sensor operation without the need for wiring or external supply, enabling a fully self-contained, plug-and-play solution. While still conceptual, this approach represents a promising step toward reliable, self-sufficient, and easily deployable frost detection systems.

Finally, the scientific and technological advances achieved throughout this thesis have been disseminated through peer-reviewed publications and protected through intellectual property rights. The work generated 14 scientific publications, comprising 6 journal articles, 6 international conference papers, and 2 book chapters, spanning topics from resistive sensor design and computer vision methods to electrochemical mitigation and energy-autonomous sensing. Meanwhile, 3 other scientific papers and 1 book chapter have been prepared and are currently undergoing the submission process. The publications reference is listed below:

1.3.1. International peer review journals

1. M. L. d. Aguiar, P. D. Gaspar, P. D. Silva and A. M. Martinez, Medium materials for improving frost detection on a resistive sensor, Energy Reports, vol. 6, pp. 263-269, 12 2020. https://doi.org/10.1016/j.egyr.2020.11.258

2. M. L. d. Aguiar, P. D. Gaspar and P. D. Silva, Additive Manufacturing of a Frost-Detection Resistive Sensor for Optimizing Demand Defrost in Refrigeration Systems, Sensors, vol. 24, no. 24, 2024, p. 8193. https://doi.org/10.3390/s24248193

3. M. L. d. Aguiar, P. D. Gaspar and P. D. Silva, Mitigating Electrochemical Effects in Resistive Frost-Detection Sensors, Applied Sciences, vol. 15, no. 8, 2025, p. 4110. https://doi.org/10.3390/app15084110

4. M. L. d. Aguiar, P. D. Gaspar and P. D. Silva, “Image recognition method for frost sensing applications,” Energy Reports, vol. 8, no. 3, pp. 234-240, 2022. https://doi.org/10.1016/j.egyr.2022.01.049

5. M. L. d. Aguiar, P. D. Gaspar and P. D. Silva, “Optimized Placement of Frost-Measuring Sensors in Heat Exchangers via Image Processing of Frost Formation Pattern,” Sensors, vol. 23, no. 11, p. 5253, 2023. https://doi.org/10.3390/s23115253

6. M. L. d. Aguiar, P. D. Gaspar and P. D. Silva, Thermoelectric-Powered Remote Sensor for Frost Detection, Electronics, vol. 13, n.º 14, p. 2683, 2024. https://doi.org/10.3390/electronics1314268313

7. M. L. d. Aguiar, P. D. Gaspar and P. D. Silva, A Computer Vision Framework for Frost Quantification and Nucleation Detection on Evaporators, International Journal of Refrigeration, [IN SUBMISSION PROCESS]

8. M. L. d. Aguiar, P. D. Gaspar and P. D. Silva, Mass Transfer Analysis via Absolute Humidity Sensing for Detecting Defrost Completion in Evaporators, International Journal of Heat and Mass Transfer, [IN SUBMISSION PROCESS]

9. M. L. d. Aguiar, P. D. Gaspar and P. D. Silva, A Signal Processing Framework for Frost Nucleation and Defrost Completion Detection using Resistive Sensors, Applied Thermal Engineering, [IN SUBMISSION PROCESS]

1.3.2. Proceedings of International conferences:

1. M. L. d. Aguiar, P. D. Gaspar and P. D. Silva, Frost Measurement Methods for Demand Defrost Control Systems: A Review, Lecture Notes in Engineering and Computer Science, vol. 2236, p. 671-677, 2018. http://hdl.handle.net/10400.6/7405

2. M. L. d. Aguiar, P. D. Gaspar and P. D. Silva, Current status and future trends of computational methods to predict frost formation, +AGRO 2018 - International Congress on Organizational Management, Energy Efficiency and Occupational Health and Safety in Agrifood Industry, CEi – Center for Innovative Companies, Castelo Branco, Portugal, October 3-4, 2018. http://hdl.handle.net/10400.6/7407

3. M. L. d. Aguiar, P. D. Gaspar and P. D. Silva, Further development and experimental testing of a resistive sensor for monitoring frost formation in refrigeration systems, The 25th IIR International Congress of Refrigeration (ICR 2019), Montreal, Canada, August, 24-30, 2019. https://doi.org/10.18462/iir.icr.2019.0562

4. M. L. d. Aguiar, P. D. Gaspar and P. D. Silva, Optimization and further experimental testing of a resistive sensor for monitoring frost formation in refrigeration systems, 6th IIR International Conference on Sustainability and the Cold Chain (ICCC 2020). Nantes, France, August, 26-28, 2020, 77-84.

5. M. L. d. Aguiar, P. D. Gaspar and P. D. Silva, Testing of a resistive sensor with fabric medium for monitoring frost formation in refrigeration systems, Procedia Environmental Science, Engineering and Management, 8(1), 205-214, 2021. http://procedia-esem.eu/pdf/issues/2021/no1/23_02.23.Gaspar.02_21.pdf

6. M. L. d. Aguiar, P. D. Gaspar and P. D. Silva, "Analysis of the frost formation pattern in heat exchangers for proper placement of frost measuring sensors," in The 26th IIR International Congress of Refrigeration (ICR 2023), Paris, France, 2023. https://doi.org/10.18462/iir.icr.2023.0399

1.3.3. Book chapters

1. M. L. d. Aguiar, P. D. Gaspar and P. D. Silva, "Frost Measurement Sensors for Demand Defrost Control Systems: Purposed Applications in Evaporators," in Transactions on Engineering Technologies, Singapore, Springer Singapore, 2019, pp. 159-171. https://doi.org/10.1007/978-981-32-9531-5_12

2. M. L. d. Aguiar, P. D. Gaspar and P. D. Silva, "Frost Measuring and Prediction Systems for Demand Defrost Control", In Novel Technologies and Systems for Food Preservation. Hershey, PA: IGI Global Scientific Publishing, pp. 24-50, 2019. https://doi.org/10.4018/978-1-5225-7894-9.ch0022019

3. M. L. d. Aguiar, P. D. Gaspar and P. D. Silva, "Frost Detection in Food Refrigeration Systems Through Computer Vision Integration", In Comprehensive Food Refrigeration, Major Reference Work, Elsevier, London, UK, 2027. [IN SUBMISSION PROCESS]

1.3.4. Patent applications

In addition, two patent applications were submitted, one already granted at the national level (PT 116073 A) and another under provisional protection, as follows:

1. P.D. Gaspar, Aguiar, M.L.d., P.D. Silva, "Sensor resistivo para a deteção de gelo", Patente PAT n.º 116073, Boletim da Propriedade Industrial n.º 12/2024, Instituto Nacional da Propriedade Industrial (INPI), 17/01/2024.

2. M.L.d. Aguiar, P.D. Gaspar, P.D. Silva, "Additive Manufacturing-Based Resistive Sensor for Frost Detection", Pedido Provisório de Patente, Instituto Nacional da Propriedade Industrial (INPI), 20/11/2024.

These publications document the progressive maturation of the research, innovation, and form a body of work that advances the state of the art in frost detection using resistive sensors. This is achieved by combining thermodynamics, material science, sensor design, data processing, and advanced manufacturing. This certificates the innovative aspects that contribute to the future development of intelligent, efficient, and accessible refrigeration systems.

1.4. Structure of the thesis

This thesis is structured to follow a coherent progression from contextualization and problem definition to technological development, validation, and future perspectives. It begins with an introduction, Chapter 1, that frames the environmental and societal relevance of refrigeration efficiency within the global challenges of sustainability and food security.

After establishing this context, the discussion included in Chapter 2 narrows to the technical understanding of refrigeration systems, room for improvement and the problem of frost formation in evaporators. Frost formation mechanisms and their impact on system performance and energy consumption are analysed. The literature analysis section concludes by compiling existing defrosting strategies—both traditional and demand-based—and identifying resistive sensing as a promising and underexplored approach for direct frost detection.

Building on this foundation, the experimental setup chapter, Chapter 3, presents the auxiliary systems developed for this research. It details the design, components, instrumentation, and data-acquisition architecture of the frost-formation setup, enabling controlled and repeatable frost–defrost cycles. This setup serves as the basis for all subsequent experimental work.

The Chapter 4 is devoted to the design and development of resistive frost detection sensors—the core of this thesis. It first discusses the underlying principles of resistive sensing, the electrical, chemical and mechanical factors influencing its performance, and the mitigation of phenomena such as electrolysis and temperature-induced resistance drift. It then describes the systematic, iterative development of sensor families that explore different electrode geometries and medium materials. These include air-gap, ceramic-medium, fabric-medium, and additively manufactured configurations, each evaluated experimentally and compared to determine the most effective design. The encapsulated sensor concept, a complementary development, is referenced later in the complementary works section.

To validate and complement resistive sensing, a computer vision method for frost detection was developed in Chapter 5. The optical setup and image processing pipeline, designed to quantify frost growth across the heat exchanger and correlate it with sensor signals, are described. The method includes full-surface and localized analyses, as well as a frost distribution mapping approach for frost pattern analysis.

The following chapter, Chapter 6, focuses on testing and validating the best-performing resistive sensor configuration. It introduces the signal-processing framework and the implementation of dedicated detectors for frost nucleation and defrost completion. The results of these tests, complemented by independent validation through computer vision and humidity-based measurements, provide a comprehensive assessment of the sensor's reliability and accuracy. This chapter represents the culmination of the experimental phase, demonstrating the practical viability of resistive frost sensing for demand-defrost control.

Subsequently, an exploratory concept of an energy-autonomous demand-defrost control module is presented in Chapter 7. This study evaluates the feasibility of using thermoelectric generation to power a self-sufficient sensor unit, introducing a pathway toward fully independent, plug-and-play frost-detection solutions.

The final chapter, Chapter 8, integrates the findings of all previous sections. It presents general conclusions and specific insights derived from each phase of the work, with an assessment of technological maturity and intellectual property outcomes. The section on future works outlines promising directions for further development in sensing, algorithmic control, and system integration, while complementary works summarize related but secondary and unfinished studies arising from this research.

Annexes provide supporting information, such as experimental data, repeated test results, and the software code used for data acquisition and user interface operation.

Overall, the thesis follows a logical trajectory: it first establishes why frost detection matters, develops a setup for generating frost, then the principles of detecting it, sensor design and preliminary testing, auxiliary tools to assess sensor performance, detection algorithms and a more in-depth analysis of sensor performance, ending with conclusions and where the field can go next.

Chapter 2

The problem of frost formation in evaporators

Frost formation is a complex transient phenomenon involving simultaneous heat and mass transfer processes that significantly affect the efficiency and durability of refrigeration systems. To understand its impact, it is first necessary to examine the mechanisms governing frost formation, growth and densification, as well as their influence on heat exchanger (HX) performance.

The literature review conducted in this chapter led to four publications, which reviewed sensing [37, 38] and prediction [39, 40] technologies for frost detection.

2.1. Understanding frost formation

The phenomenon of frost formation is initiated by a sequence of water-phase changes, beginning when the air temperature drops below its dew point, causing moisture in the air to condense on the chilled surface. As these surfaces cool the condensed water further below its freezing point, this water transitions to ice, marking the onset of frost accumulation [41]. The process of frost formation on a cold surface can be described through a series of steps, as shown in Figure 5.

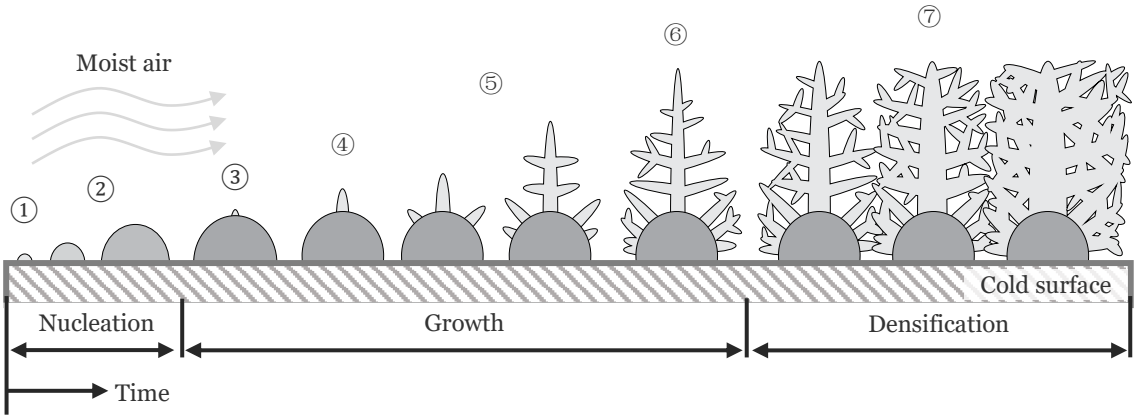

Figure 5 – Schematic representation of the frost formation on a chilled surface, designed from [42, 43].

It begins with the nucleation of a frost embryo on the cold surface ①. This embryo is a concentration of water molecules that are transformed into a frost nucleus. As the embryo grows ②, its surface area increases, raising its surface temperature above that

of the plate, increasing its energy-removal demands to sustain growth. Once the energy needed to maintain this growth exceeds what is required to initiate nucleation elsewhere, the growth of the initial embryo stops, and secondary nucleation occurs ③. As the new embryo continues to grow ④, it requires more energy removal, leading to the formation of additional nucleation sites on the surface of the original embryo ⑤. This cycle of nucleation and merging continues until the supercooling and supersaturation levels near zero ⑥. After this point, the frost layer acts as a porous medium, absorbing water vapor, which contributes to the thickening and densification of the frost ⑦ [42, 43].

The real process of frost formation, growth and densification on the surface of a frozen water droplet is illustrated in Figure 6.

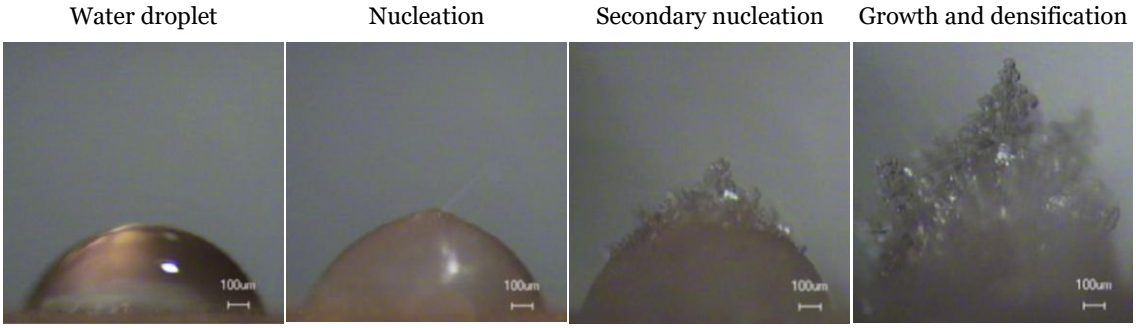

Figure 6 – Process of frost formation, starting from a water droplet (a), in which after freezing, primary nucleation is visible (b), followed by secondary nucleation (c) and frost growth and densification (d), adapted from [44].

This figure portrays the progression through several stages, starting with the water droplet laying on a surface (a). After freezing, nucleation on its cold surface occurs (b), marking the initial formation of ice crystal embryos. These embryos grow, and secondary nucleation occurs, leading to the development and expansion of ice crystals (c). Finally, the growth of the frost crystal slows down, and the densification of the frost crystal begins (d).

2.2. Factors affecting frost formation, growth and densification

Several parameters influence frost formation and growth on HX surfaces, but the most influential are those relating to temperature and humidity. Two thermodynamic drivers govern the process, supersaturation and supercooling. Supersaturation is the difference between the actual amount of water vapour in the air and the maximum amount the air can hold near the cold surface, which determines how much vapour is available to

condense or deposit as frost [45, 46]. Supercooling is the extent to which the HX surface is colder than the air's dew-point temperature, providing the thermal driving force for phase change. When the surface is below both the dew point and 0 °C, the ice-point temperature becomes the relevant reference, as it represents the saturation condition of water vapour with respect to ice [47]. Frost can initiate by condensation followed by freezing or by direct desublimation, the prevailing path is set by the supersaturation and supercooling levels [46, 47].

Absolute Humidity (AH) modulates supersaturation, so higher AH generally enhances frost growth. Higher air velocity and turbulence increase convective heat and mass transfer coefficients, accelerating deposition [45, 48]. The flow regime (laminar vs. turbulent) further shifts growth rates and patterns [49, 48]. HX surface conditions reshape local transport and nucleation, as fin shape and spacing alter local flow and temperature fields [50], while air cleanliness, defined by the presence of particulates or impurities, modifies nucleation density and adhesion behaviour [51].

The processes of heat and mass transfer within the frost layer, which is a porous medium, help understanding frost growth and densification. The diffusivity of water vapour in air and the thermal conductivity of the frost influences the distribution of temperature and humidity within the frost layer. Higher heat fluxes are associated with increased frost growth, while higher mass fluxes indicate densification. Effective heat and mass transfer, water vapour and the removal of latent heat, facilitate frost growth and densification [52, 45].

For the nucleation step of frost formation to occur, the Gibbs free energy barrier must be exceeded. This Gibbs energy change for nucleation varies with several factors, represented in Figure 7, such as the contact angle θ, contact area between parent phase, i, and new phase j, A_{ij}, contact area between cold surface s and new phase j, A_{js}, new phase volume, temperature change, vapour pressure, among others. [45, 53].

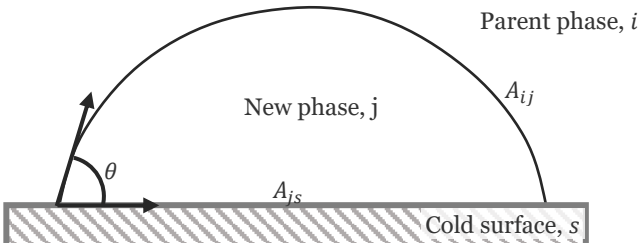

Figure 7 – Representation of factors that influence the Gibbs energy change, adapted from [53].

Surfaces with lower energy and with higher contact angles, require a higher degree of supersaturation for nucleation. The contact angle determines how easily water can spread over the surface, influencing the likelihood of frost nucleation. Surface roughness enhances this process by increasing the contact area between the frost embryo and the substrate, thereby reducing the required supersaturation degree. Particles on the surface can also act as nucleation sites, especially if they have higher surface energy than the cold surface, promoting earlier frost formation [53].

The factors influencing frost formation, growth, and densification directly impact HX performance by modifying the frost's thermal and physical properties. As frost accumulates and its density changes, it progressively impedes airflow and reduces heat transfer efficiency.

2.3. Why frost impacts heat exchanger performance in refrigeration systems

Frost formation on HX affects the performance and efficiency of refrigeration systems, air conditioners, and heat pumps. The mechanisms driving frost formation and the resulting constraints on HX design are complex, involving coupled effects of thermodynamics, fluid dynamics, and material science. In systems operating at subfreezing temperatures, a frost layer develops on the fin surfaces [45, 50], as illustrated in Figure 8.

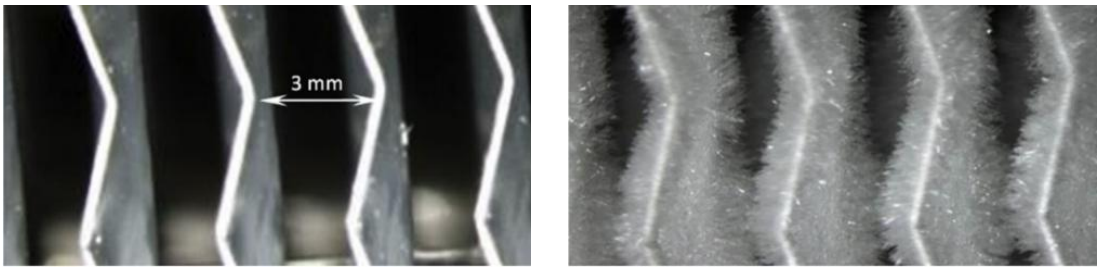

(a) (b)

Figure 8 – Visualization of the fins' surface before (a) and after (b) the frost formation process [50].

Frost is a porous medium composed of ice crystals and air, with an effective thermal conductivity (k_f) lower than that of solid ice and orders of magnitude lower than that of metallic HX surfaces. The effective k_f increases as porosity decreases, since ice has a much higher thermal conductivity ($\sim 2.2\ \mathrm{W/m \cdot K}$) than air ($\sim 0.024\ \mathrm{W/m \cdot K}$). Therefore, frost density is a factor in determining the conductive heat transfer across the layer. According to Fourier's law:

$$q = -k \cdot A \cdot \frac{dT}{dx} \tag{8}$$

where:

- q is the heat transfer rate [W],
- k the thermal conductivity of the material [$\mathrm{W/m \cdot K}$],
- A is the cross-sectional area perpendicular to the heat flow [$\mathrm{m^2}$],
- $\frac{dT}{dx}$ is the temperature gradient in the direction of the heat flow [K/m].

An increase in frost thickness (δ) or decreasing its effective thermal conductivity k_f increases the conductive thermal resistance, thereby reducing the heat flux for a given temperature difference. At the same time, frost accumulation reduces the free-flow cross-sectional area ($A_{\min}$) for air. From the continuity equation, for a fixed mass flow rate, a reduced $A_{\min}$ increases air velocity (V), which in turn increases the convective heat transfer coefficient (h) via:

$$q = h \cdot A \cdot \Delta T \tag{9}$$

where:

- h is the convective heat transfer coefficient, [$\mathrm{W/m^2 \cdot K}$].
- A is the area through which heat is being transferred, [$\mathrm{m^2}$].
- ΔT is the temperature difference between the surface and the fluid, [K].

Higher velocity enhances turbulence, partially compensating for the added thermal resistance in the early stages of frosting. This explains why, initially, total cooling capacity may remain stable despite the presence of frost.

As frost continues to grow, its density typically increases due to crystal packing and recrystallization, which raises k_f, but the dominant effect becomes the increased thermal resistance from greater thickness and the airflow restriction. This leads to a decline in both convective and conductive heat transfer, a rise in air-side pressure drop, and a reduction in evaporator cooling capacity.

Experimental and numerical studies show that the relative importance of these effects depends on operating conditions. Higher supercooling degrees increase the vapour mass flux to the surface, accelerating frost growth and often producing less dense, dendritic

morphologies that clog fin passages more rapidly. Conversely, higher surface temperatures can favour denser frost, which has better conductivity but still impedes airflow over time. Simulations indicate that fan airflow reduction due to increased pressure drop is often the dominant cause of capacity loss, with conductive resistance playing a secondary role [45, 54].

Non-uniform frost growth, caused by evaporator geometry, uneven airflow, or refrigerant maldistribution, can lead to localized blockages and exacerbate performance degradation. Ultimately, the interplay between frost morphology, density, and distribution determines whether the initial airflow acceleration effect is short-lived or sustained, reinforcing the need for frost management strategies and defrost control to maintain efficiency and avoid premature system degradation.

The presence of frost requires HX design considerations, imposes operational limitations, and necessitates defrost cycles, which consume additional energy and place mechanical stress on the system, ultimately increasing operational costs and reducing overall performance.

2.4. Mitigating the consequences of frost formation in HX

To mitigate the adverse effects of frost, defrost methods are employed to restore HX performance. These methods frequently require additional energy input and/or introduce undesirable thermal loads and temperature fluctuations, which can adversely affect the preservation of stored goods [43].

2.4.1. Classification of defrost methods

Defrost strategies can be broadly classified into restraint frost techniques, that are employed to slow frost formation, or frost removal methods that are applied after frost accumulation requires removal to restore system performance. This classification is detailed in Figure 9:

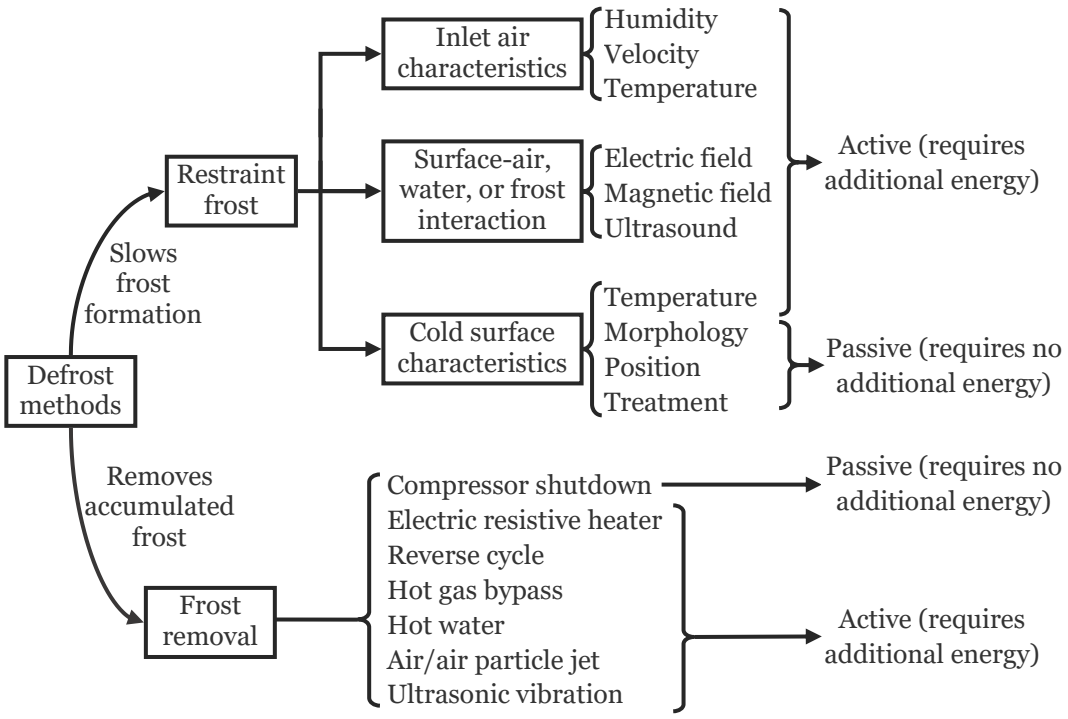

Figure 9 – Classification of available defrost methods.

Restraint frost methods aim to delay frost formation by altering the characteristics of the inlet air, such as humidity, velocity, and temperature [50, 55], or by modifying the properties of the cold surface, such as surface temperature and fin geometry [56], hydrophobic [57, 58] and superhydrophobic [59] surface properties and coatings, and fin layout, geometry and perforation [60, 61]. Influencing air–surface interactions through external electric [62], magnetic [63], or ultrasonic [64] fields can also delay frost nucleation and decrease the rate of frost accumulation.

In contrast, frost removal methods act upon the frost after it has formed to restore normal operating conditions, employing techniques such as compressor shutdown [65], electric resistive heating [66], reverse-cycle operation [67, 68], hot gas bypass [69], hot water application [70], mechanical removal via air jets or particle jets [71], and ultrasonic [44, 72] or piezoelectric vibration [73]. Both restraint and removal methods can be classified as passive, when no additional energy input is required, or active, when extra power is needed to remove or reduce frost [74]. In commercial refrigeration, the most widely adopted approaches use electric resistive heaters or reverse-cycle operation, however, despite the availability of more advanced strategies, few alternatives have achieved widespread adoption due to the complexity, cost, and reliability [75, 76]. The energy consumption of frost removal methods relies on the control approaches used to trigger defrosting at the most appropriate time, which is when frost is present, to avoid both the consequences of excessive defrosts and insufficient defrosting.

A study on open multideck RDCs demonstrated that the optimal defrost interval varied substantially throughout the day and across seasons, depending on ambient conditions such as Relative Humidity (RH). For the refrigeration system analysed, this interval ranged from approximately 2 hours under warm, humid conditions to about 10.5 hours under cooler, drier ones [77], following the trend shown in Figure 10.

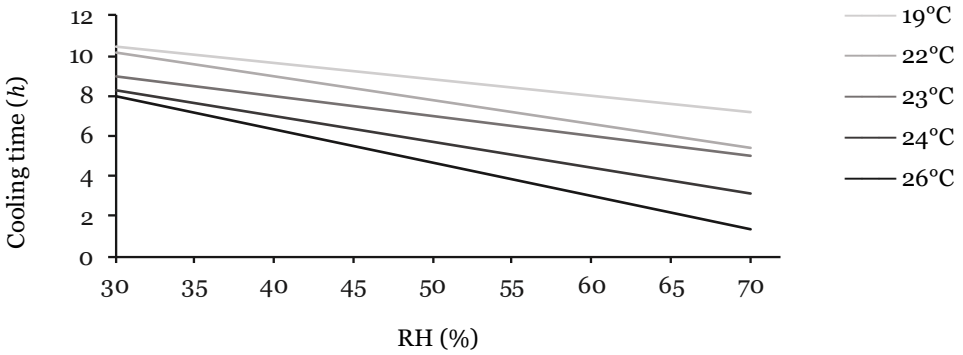

Figure 10 – Optimum time between defrosts in relation to air temperature and RH, adapted from [77].

The dynamic nature of frost formation in HXs demands control approaches that adapt defrost operations to varying environmental and operational conditions. These strategies aim to improve upon traditional time-controlled methods by reducing unnecessary defrost cycles when conditions are less favourable to frost accumulation, thereby increasing energy efficiency and decreasing temperature fluctuations within the refrigerated space. Conversely, when ambient conditions promote rapid frost buildup, they increase the frequency of defrost operations to prevent excessive blockage of the HX, mitigating efficiency losses and avoiding potential system damage.

2.4.2. Control approaches for defrosting

Defrost control strategies can be categorised according to the primary trigger that initiates the defrosting operation. After the literature review, four categories are considered: time-based control, system-symptom monitoring, prediction-based methods, and direct frost sensing. This categorization is shown in Figure 11.

Time-based control triggers defrost operations at fixed intervals, regardless of actual frost accumulation. These can be defined as scheduled cycles (fixed daily or hourly patterns) or interval-based cycles determined by the elapsed time since the previous defrost [78].

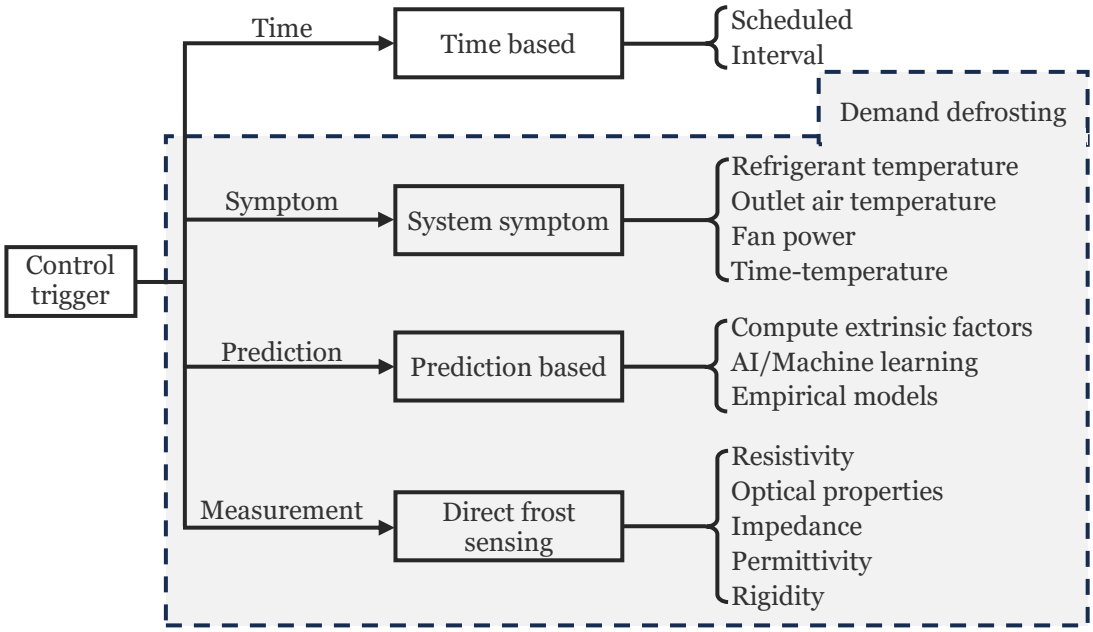

Figure 11 – Classification of defrost control triggers.

In time-controlled systems, intervals must be set for the worst case, resulting in excessive defrosting during most operating periods. Demand defrosting addresses this limitation by dynamically adjusting defrost intervals according to actual system and environmental conditions.

2.5. Demand defrosting

Demand defrosting refers to all control strategies that go beyond purely time-based defrost operations. Instead of triggering defrosts on a fixed schedule based on worst-case conditions, these methods adjust initiation to the actual likelihood or measured presence of frost. Approaches such as system-symptom monitoring, prediction-based control, and direct frost measurement can be applied individually or in combination to determine both the start and end of a defrost cycle. Compared to simple time control, demand defrosting reduces unnecessary cycles when frost formation potential is low and increases frequency when conditions favour rapid buildup, leading to improved energy efficiency, better temperature stability, and enhanced system reliability [79].

2.5.1. Indirect frost detection through system symptoms

In system-symptom monitoring, frost is not detected directly but inferred from measurable changes in system performance. One such indicator is the refrigerant, coil, or outlet-air temperature. As frost builds up on the HX surface, it forms a thermal insulating layer that reduces the heat transfer rate from the air to the refrigerant. This drop in heat transfer can lead to different outlet-air temperature responses: if airflow

remains close to nominal, the outlet air temperature may increase due to reduced heat transfer; if airflow is restricted, the outlet-air temperature tends to decrease because of diminished air volume passing through the coil [80]. Another common indicator is the air-side pressure drop. Frost accumulation between fins reduces the free-flow area, forcing air through smaller gaps and, for a fixed fan speed, increasing the measured pressure drop across the HX [81]. On the refrigerant side, frost buildup also affects the degree of superheat. With less heat transferred into the refrigerant, it has less opportunity to gain sensible heat after complete evaporation, reducing the temperature difference between the actual refrigerant temperature and its saturation temperature [82]. Finally, fan electrical power consumption can be another indicator, as frost narrows the airflow passages and increases aerodynamic resistance, the fan must work harder to maintain airflow, resulting in higher power draw [83].

Time–temperature control augments fixed time intervals with a temperature criterion [79]. In this method, when a threshold coil, refrigerant, or air-outlet temperature is reached, a timer is started. Once the timer expires, a defrost cycle is initiated and continues until another temperature threshold is met. A common variation uses temperature only to terminate defrost, with initiation still based on fixed time intervals. This approach is inexpensive, more adaptive than pure time control, and remains simple and robust, which explains its status as the most widely used demand defrost method in commercial equipment [74, 79].

Measured system symptoms can be used to trigger defrosts directly through simple logic or threshold settings. This approach is appealing because it can reuse existing sensors and adapt to changing operating conditions. However, it requires calibration and can be affected by interferences that lead to false positives or false negatives [80, 81]. More advanced control strategies use these system symptoms, alone or combined with environmental measurements, to estimate the frost state in the HX.

2.5.2. Frost prediction through model-based estimation

Prediction-based demand defrost seeks to estimate frost formation, allowing the system to initiate defrost at the optimal time. One approach is extrinsic-factor computation, which uses measured environmental and operating conditions—such as ambient temperature, relative humidity, air velocity, and coil surface temperature—to calculate a frost accumulation index or predict the time to reach a critical frost level [84]. Another method involves empirical models, which are mathematical relationships tuned to the specific system based on experimental data; these models can predict frost growth rates under different conditions with relatively low computational requirements [85, 86].

More advanced solutions employ AI or machine learning (ML) techniques, where algorithms are trained on historical operating data to recognize patterns that precede frost buildup and forecast when a defrost will be needed [87]. These AI/ML approaches can also fuse ambient condition data with system-symptom signals—such as pressure drop or superheat—to improve robustness and adaptability [88]. When properly calibrated and supplied with representative training data, prediction methods can reduce defrost frequency and energy consumption while maintaining performance. However, just as with the system symptom based defrost control method, they require careful tuning and extensive validation to avoid false positives and false negatives, both of which can undermine system efficiency and reliability. A demand defrost method that helps avoid false readings is the direct measurement of frost on the HX. The resulting measurements can be used directly as a trigger by applying a threshold or fed as a reliable input into a prediction algorithm to project frost growth over time or to extend the effective monitored area.

2.5.3. Direct frost detection through dedicated sensors

Direct methods detect the frost itself on the HX, making them the most unambiguous trigger source for defrost control. These sensors measure frost properties, with reported approaches including optical properties [89, 90], computer vision [91], electrical permittivity [92], mechanical rigidity [93], and electrical resistivity [94], among others. Such techniques provide immediate information on frost presence and, in some cases, its morphology or thickness, enabling initiation and termination of defrost cycles. As they sense frost directly, these methods have the potential for reliable demand defrost control in commercial HXs. The following section describes the working principles of these sensors and evaluates their suitability for real-world integration.

2.6. Sensors for frost detection and their working principles

Direct frost measurement techniques must detect or respond to material properties in a way that enables a reliable distinction between air, water and frost or ice. These measurements must also be repeatable, robust, cost-effective, and suitable for integration into compact evaporators. This section focuses on sensor types with practical potential for frost detection, whether they are already implemented in commercial refrigeration systems, and that are viable for application in evaporators. Direct methods requiring human intervention, such as cathetometer telescopes [95], micrometres [46], or vernier gauges [96], are excluded from this review. Although they can provide accurate

results, such instruments are impractical for integration into commercial refrigeration systems.

2.6.1. Photoelectric sensors

Photoelectric sensors operate with an emitter–receiver pair positioned across a narrow passage where frost can form in line with the accumulation occurring in the rest of the HX, as shown schematically in Figure 12. When powered, the emitter sends a constant light beam to the receiver. As frost accumulates between them, it progressively attenuates the beam, gradually lowering the receiver's electrical output from a value characteristic of air to one indicating frost blockage. This change provides a measurement of frost formation with sufficient accuracy for defrost control [97].

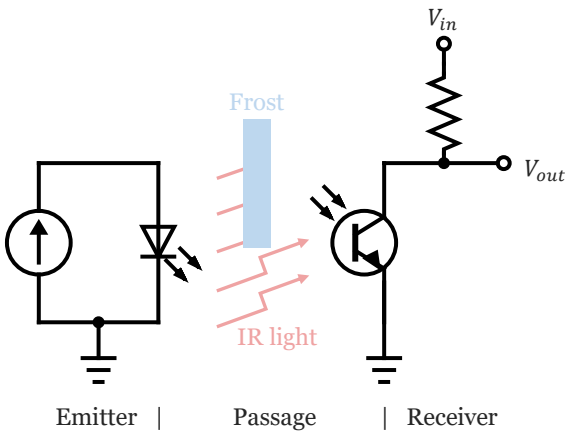

Figure 12 – Circuit of the photoelectric sensor, drawn based on [97].

In [97] and [89], a Tube-Encircled Photoelectric Sensor (TEPS) was developed for defrost control. This compact device, shown in Figure 13, is mounted directly on the refrigerant tube, allowing a correlation to be established between the frost accumulating on the tube and that on the HX surface.

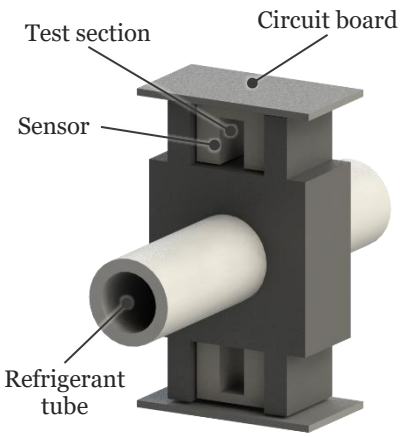

Figure 13 – TEPS sensor installed on the refrigerant tube, drawn from [97].

When compared with timed defrost, the difference is evident. Figure 14 presents a comparison between the two methods for a specific test: each black dot represents a time-triggered defrost in the default control system, while each orange dot represents a defrost initiated by the TEPS sensor.

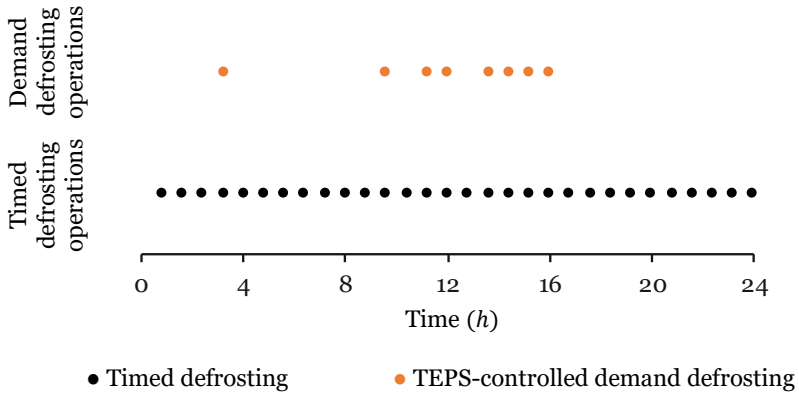

Figure 14 – Comparison between the number of operations for timed defrosting control versus demand defrosting control using the TEPS sensor, adapted from [97].

This example illustrates the adaptive behaviour of demand defrosting but should be interpreted as a single case result rather than a general rule. In this test, the TEPS-based control triggered only eight defrost cycles compared to thirty under time-based control. Specifically, within the same 24 h period, four defrosting operations were initiated between 12 h and 16 h, while no operations were triggered between 16 h and 24 h. However, under different environmental or operational conditions, the number of demand-defrost events could vary substantially. This variability represents the dynamic nature of frost accumulation and shows the importance of demand defrost strategies over fixed-time approaches.

2.6.2. Fibre optic sensors

Nowadays, one of the most advanced ice sensing technologies is the fibre-optic method [90], which was developed for application on aircraft wings to detect ice formation. This sensor operates by exploiting the distinct reflective properties of water, frost, and ice. As illustrated in Figure 15 (a), an Infrared (IR) Light Emitting Diode (LED) transmits light through an optical fibre bundle to the sensor tip, shown in Figure 15 (b). When ice forms on the surface, it reflects the light back into the system, as represented in Figure 15 (c), where the reflected signal travels through the return fibre bundle and is detected by phototransistors.

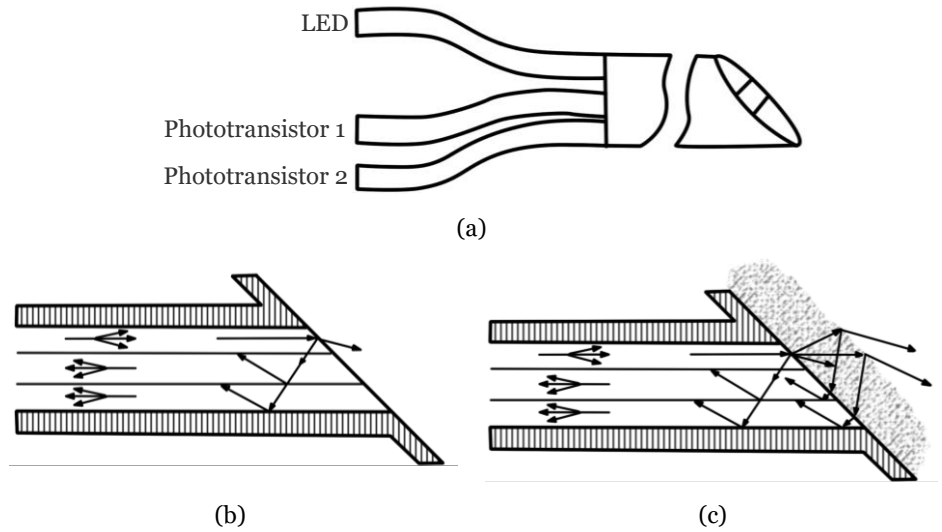

Figure 15 – Sensor scheme (a) and sensor tip operation without (b) and with (c) ice, adapted from [90].

As different conditions produce ice layers with varying thicknesses and morphologies—each associated with distinct reflective coefficients—the measured values change accordingly. This variability can be both a limitation and an opportunity: on one hand, it may introduce measurement errors if not properly accounted for; on the other hand, when correctly interpreted, it can enable the estimation of both frost thickness and morphology, from the optical intensity measured over time as illustrated in Figure 16.

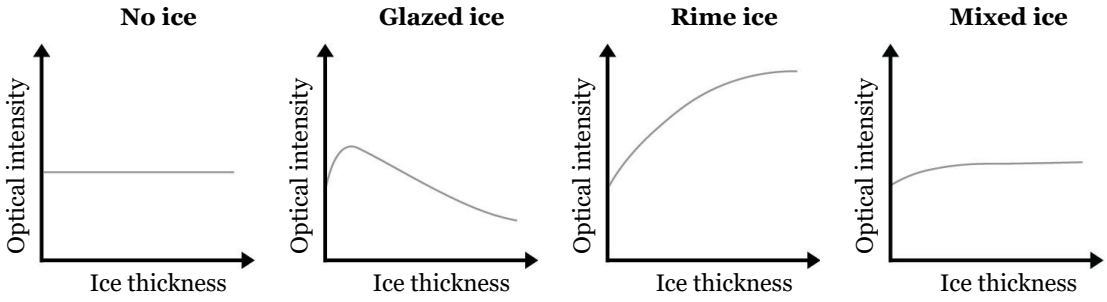

Figure 16 – Common curve shapes for different measurements using the fibre optic, adapted from [90].

Tapered optical fibre sensors can also be used to detect condensed water and frost in refrigeration systems [98] by the same principles the scattering loss to the medium surrounding the tapered fibre allows for the differentiation between liquid water and frost. The cost and fragility of the optic fibre cable are considerations that must be taken into account when implementing this sensor.

2.6.3. Piezoelectric sensors

Piezoelectric sensors operate based on the principle of mechanical resonance in piezoceramic materials. When an alternating sinusoidal voltage is applied to a

piezoceramic resonator, the material oscillates at its natural resonant frequency. This frequency is sensitive to both the stiffness and the mass of the medium in contact with the sensor surface. Figure 17 shows the piezoelectric transducer used in these experiments.

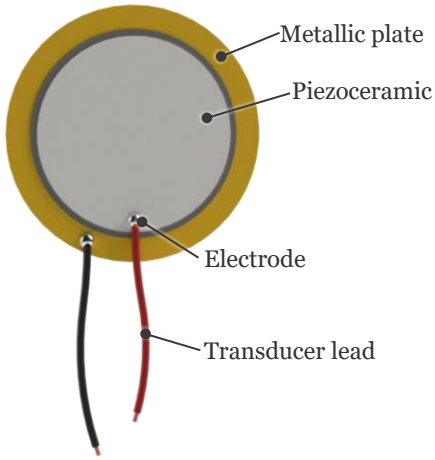

Figure 17 – Bottom view of the piezoelectric transducer, drawn based on [93].

As described in [93], the resonant frequency of the piezoceramic transducer decreases when additional mass is added, when liquid water accumulates on its surface, and increases when the surrounding medium becomes stiffer, as occurs during ice formation. In the transition from water to ice, these two opposing effects coexist: while the added mass tends to lower the frequency, the stiffness increase dominates, resulting in a net frequency rise. This behaviour enables the detection of ice and the tracking of its accumulation through continuous monitoring of the resonant frequency.

In the referenced experimental study, the authors tested this principle using a small piezoceramic disc excited by an electronic oscillator circuit. The transducer was exposed to controlled icing conditions where successive layers of water and ice were deposited on its surface. The resonant frequency was tracked by a microprocessor-based circuit that identified frequency peaks corresponding to the transducer's fundamental mode.

The results, shown in Figure 18, demonstrate that a consistent correlation between resonant frequency and layer thickness can be established, allowing frost thickness to be quantitatively estimated from frequency measurements. The formation and thickening of ice films led to a steady increase in frequency, confirming the strong correlation between the resonant frequency and the mechanical properties of the surface layer.

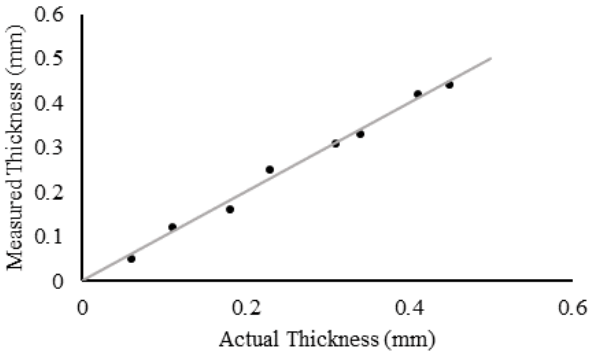

Figure 18 – Results for the piezoelectric ice detection system, adapted from [93].

The measured data revealed a nearly linear increase in resonant frequency with ice thickness, validating the sensor's capability for quantitative estimation. Within the tested range of 0.06 mm to 0.45 mm, the resonant frequency rose by over 10 kHz, while the presence of comparable water layers caused a smaller but measurable decrease.

Although not yet directly investigated for applications in evaporators, the piezoceramic resonator can, in theory, be mounted directly on fins or refrigerant tubes, providing a compact and robust sensing solution. The associated measurement system requires an oscillator or phase-locked loop circuit to continuously track resonant frequency, and the sensor packaging must ensure mechanical stability against ambient vibrations and airflow disturbances. Although the study focused on ice detection, the same underlying principle applies to frost, as both materials increase the effective stiffness of the sensor's surface. However, the stiffness of frost is expected to differ from that of solid ice due to its porous and less homogeneous structure, even though it still produces an overall increase in stiffness compared with liquid water. Therefore, its inherent simplicity, low power consumption, and sensitivity to phase changes make the piezoceramic resonator a candidate for integration into compact evaporators.

2.6.4. Capacitive sensors

Capacitive sensors detect air, water, ice or frost by monitoring changes in the electric capacitance that result when the dielectric environment near the sensor electrodes changes: air, water, ice and frost each have different relative permittivities, so replacing or overlaying the sensor surface with one of these media produces a measurable change in capacitance [99, 92]. This concept can be represented by a parallel-plate capacitor as shown in Figure 19, with air (a) or frost (b) between the electrodes. Because the frost alters the local electric-field distribution and the effective dielectric constant experienced by the electrodes, the capacitance changes.

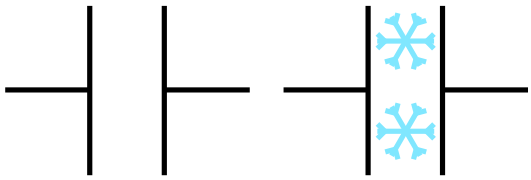

(a) (b)

Figure 19 – Representation of the capacitive sensor without (a) and with (b) frost, based on [100].

In the idealized parallel-plate approximation, the capacitance can be expressed as shown in Equation (10).

$$C = \varepsilon_0 \cdot \varepsilon_r \cdot \frac{A}{d} \tag{10}$$

Where:

- C is the capacitance $[F]$,
- ε_0 is the electric constant of $8.854 \times 10^{-12}\ F \cdot \mathrm{m}^{-1}$,
- ε_r is the relative permittivity of the medium between the electrodes $[-]$,
- A is the electrode overlap area $[\mathrm{m}^2]$,
- d is the separation [m].

Replacing the medium (air, water, ice or frost) changes ε_r and therefore also changes C. A parallel-plate capacitor inherently samples the dielectric strictly within the volume bounded by its facing electrodes because the dominant electric-field lines are confined between the plates, as shown in Figure 20 (a). To overcome this limitation, sensor designs therefore move to planar, open electrode geometries that exploit fringing fields as shown in Figure 20 (b) [99]

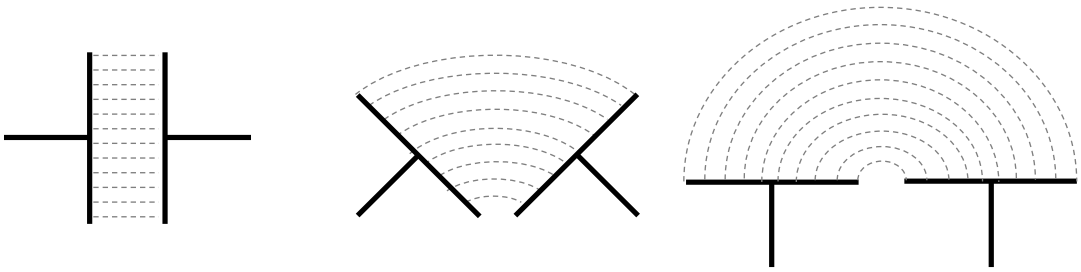

(a) (b) (c)

Figure 20 – Transition from a parallel plate capacitor to a planar capacitive sensor, adapted from [101].

The fringing-field penetration depth and the sensing volume are controlled by electrode geometry, which permits designing of sensitivity and sensing depth to the expected frost morphology. When the sensor is placed perpendicular to the monitored frost surface, the measured capacitance typically increases with frost accumulation, as represented in Figure 21.

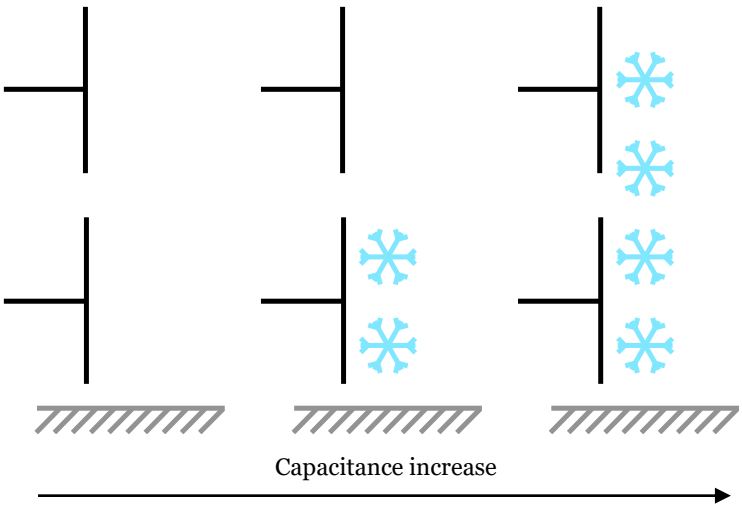

Figure 21 – Progression of frost relative to a planar capacitive sensor, mounted perpendicularly to the frost formation surface based on [100].

For instance, in [92] a road ice capacitive sensor was developed with the concentric geometry seen in Figure 22 (a) suited for field robustness, while [99] and [102] used an interdigitated approach represented in Figure 22 (b), offering improved sensitivity to thin frost layers, even achieving the distinction between condensation, nucleation, growth and densification of frost using this principle.

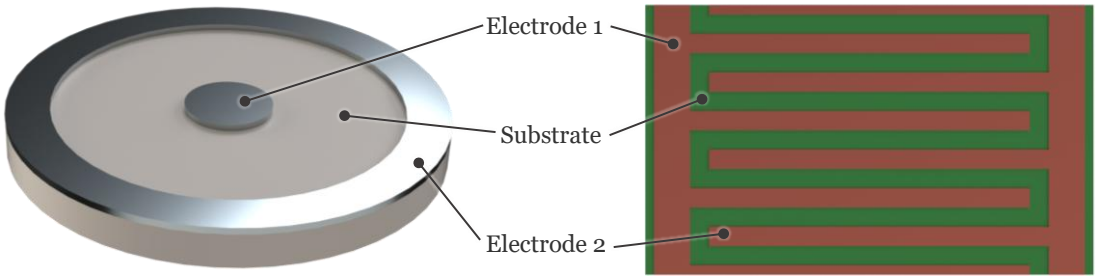

(a) (b)

Figure 22 – Electrode configurations: concentric (a) and interdigitated electrodes (b), based on the designs of [92] and [99, 102], respectively.

The ice-detection system developed by [92] uses a charge-transfer capacitive measurement circuit to read the sensor's capacitance. The setup, shown in Figure 23 consists of a sensing capacitor C_X, a reference capacitor C_S, and three electronic switches

S_1 , S_2 and S_3 . A reference voltage source V_R excites the electrodes at selectable frequencies through S_1.

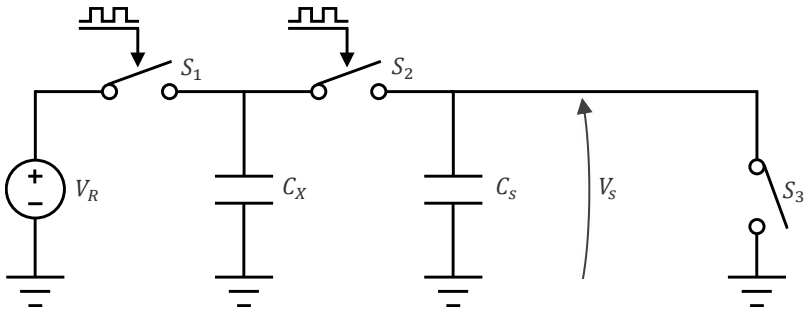

Figure 23 – Diagram of the circuit to read capacitive sensors, drawn from [92].

When S_2 closes, the charge stored in C_X is transferred to the reference capacitor C_S. This operation is repeated n times to improve accuracy before C_S is discharged by S_3. The resulting voltage V_S across C_S is amplified and digitized by the Analog to Digital Converter (ADC) of a microcontroller. The sensor capacitance is then obtained from the relation shown in Equation (11).

$$C_X = \frac{C_S}{n} \cdot \frac{V_S}{V_R} \tag{11}$$

Where:

- C_X is the capacitance of the sensing electrodes,
- C_S is the capacitance of the reference capacitor,
- V_S is the voltage measured after charge transfer,
- V_R is the excitation voltage,
- n is the number of charge-transfer cycles.

The characteristic capacitive signal observed in [99, 100] follows a reproducible sequence that is schematized in Figure 24. It starts with a stable dry baseline, a progressive rise in capacitance during frost accumulation, a pronounced peak when defrosting results in water, and a return toward the dry baseline as the surface drains and dries. Both the absolute change and its time derivative can be used to detect and discriminate these stages in practical control logic.

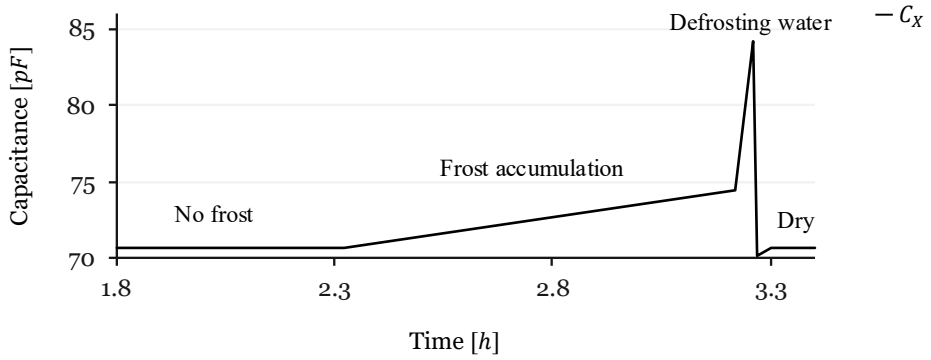

Figure 24 – Schematic capacitive response for a single frost–defrost cycle: simplified overlay of an original plot to highlight the main stages. Made from the observed trends in [99, 100].

These studies show that capacitive sensing delivers phase discrimination [99, 102]. Quantitative thickness estimation from a single-frequency, road-type geometry is only weakly observable [92], but after system-specific calibration of interdigitated electrode geometry, extraction of multi-frequency features and, where available, fusion with temperature references—trend-level tracking of frost growth and densification becomes feasible [102]. For HX integration, electrodes on flexible substrates can be bonded to fins or tubes and read synchronously at multiple frequencies to separate phases and partially compensate for the permittivity dependence on temperature and frequency [99, 102]. Because capacitive sensors are sensitive to contamination and liquid films, practical layouts should include shielding, drainage-aware placement, and on-board temperature sensing, for compensation [92, 100]. This approach also admits miniaturization pathways microsensor integration for compact, high-resolution deployments [103].

2.6.5. Computer vision

In recent years, computer vision (CV) has emerged as a cost-effective method for sensing applications due to its lower hardware costs, versatility, and ability to extract rich spatial information from visual data. Unlike point-based sensors that provide only local measurements, vision systems can monitor large areas simultaneously, offering detailed insight into surface conditions, texture evolution, and spatial non-uniformities. This capability makes CV attractive for frost detection. The method developed in [91] applies image-recognition techniques to quantify frost accumulation directly from images of the outdoor coil surface. When frost forms, the surface brightness increases due to light scattering by the ice crystals, allowing frost detection through analysis of image grey values.

The setup, illustrated in Figure 25, consists of a fixed camera positioned to capture images of the evaporator surface. The camera may be placed front-facing the coil, as

shown in Figure 25 (a), or at an inclination angle α, as shown in Figure 25 (b). A front-facing configuration generally facilitates image processing, as it minimizes perspective distortion and simplifies segmentation of frosted regions. However, the camera may obstruct airflow or interfere with the equipment layout. The angled configuration can overcome this limitation by positioning the camera outside the airflow path, though it requires additional image correction or calibration to interpret the captured area.

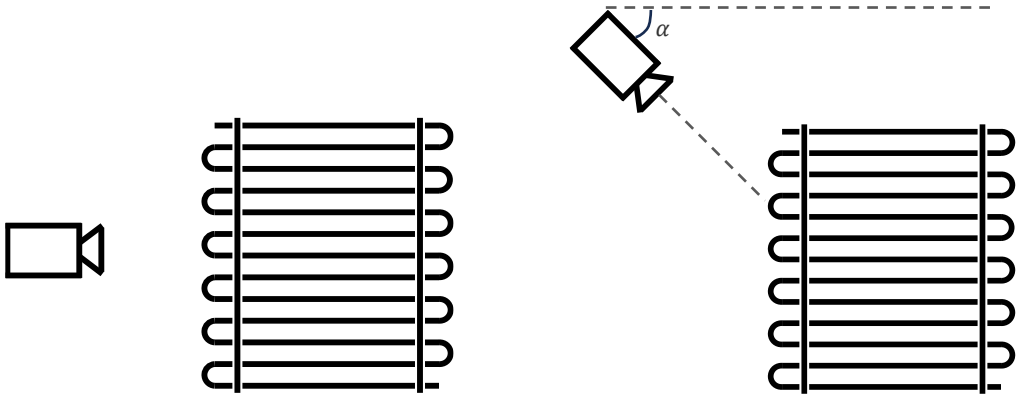

Figure 25 – Front-facing (a) and angled (b) position of the camera relative to the evaporator (drawn from the experimental setup of [91]).

Each captured image is then converted from colour to grayscale, where each pixel has an intensity value ranging from 0 (black) to 255 (white). Frosted areas appear brighter, corresponding to higher grey values.

By comparing each pixel's value with a predefined threshold f_i, the algorithm distinguishes frosted from non-frosted regions. This process is illustrated in Figure 26, where the original image captured by the camera is shown in Figure 26 (a), and the processed grayscale image highlighting the detected frosted region is shown in Figure 26 (b).

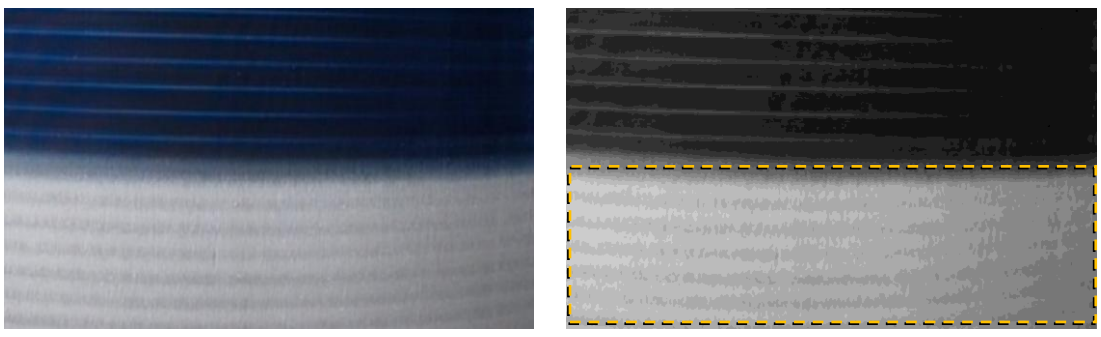

Figure 26 –Camera (a) and corresponding grayscale image (b) with frost region (adapted from [91]).

The ratio between the number of frosted pixels n and the total number of pixels N defines the frosted-surface coefficient S, while the mean grey value of the frosted pixels determines the frost-density coefficient r. Their product yields the frost-degree parameter, $F = S \cdot r$, which varies between 0 and 1, indicating no frost and fully frosted, respectively.

This method was experimentally validated on four evaporators with different geometries and operating capacities, under standard frosting conditions. The parameter F increased consistently with frost growth, confirming its reliability as an indicator of frost accumulation [91]. Additional experiments examined the influence of camera angle, image resolution, illumination level, and coil-surface temperature. The results showed that F was largely unaffected by image resolution or coil temperature, but highly sensitive to illumination changes, which could introduce false readings. To address this, the authors introduced an Illumination Recognition Area (IRA), a fixed non-frosted region used as a reference to compensate for variations in ambient light. By adjusting the image-processing thresholds according to the brightness of the IRA, the method became robust to illumination changes and maintained accuracy under different lighting conditions.

Because image-recognition-based detection directly quantifies surface frost, it eliminates the uncertainty inherent to indirect methods. Moreover, it can operate automatically using low-cost cameras and lightweight image-processing algorithms, making it suitable for integration into defrost-control systems. In practice, the F parameter can be used as a direct trigger for defrost initiation once a calibrated threshold is exceeded, or as an input to adaptive algorithms predicting the optimal timing of defrost cycles.

When incorporated into broader frost-detection or defrost-control frameworks, computer-vision systems such as that proposed in [91] can serve as a validation or supervisory layer. In the context of the present work, such a system could complement other sensors by providing visual ground-truth data for calibration and by verifying the spatial uniformity of frost formation across the HX surface. Since the F parameter correlates with both frost coverage and density, it may also help refine sensor-placement strategies and in training data-driven control models. Ultimately, combining local sensor measurements with image-based observations might enable a robust and adaptive defrost-control strategy, improving both energy efficiency and operational reliability.

2.6.6. Resistive sensor

Resistive frost detection sensors operate on the principle that air, water, ice and frost exhibit distinct electrical resistivities. When two electrodes are positioned within or near the evaporator surface and a voltage is applied across them, the measured resistance, R_s, varies according to the medium between the electrodes. As condensation begins, liquid water forms a conductive bridge, leading to a sharp decrease in resistance. As this water subsequently freezes, the conductivity drops again, producing a rise in the measured resistance. This transition can be tracked over time, using the circuit shown in Figure 27, providing a direct and cost-effective indication of frost [94, 104].

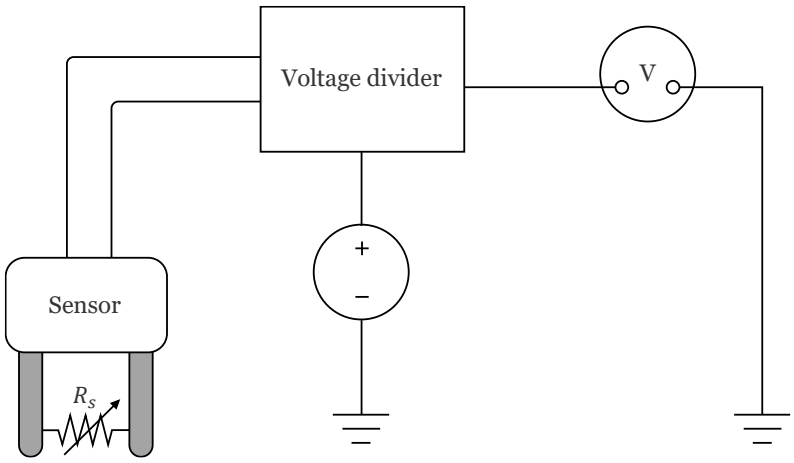

Figure 27 – Setup for water and ice detection using a resistive sensor (drawn from the description of [104]).

In the voltage divider circuit used to read the sensor, lower R_s (water) yields a higher output voltage, as R_s rises during freezing, the output voltage decreases. The general arrangement of the sensor is shown in Figure 28. It consists of two copper electrodes, each 1.5 mm^2 in cross-section and 150 mm in length, embedded in a 3D-printed frame whose width is designed to fit snugly between the evaporator fins.

The 10 mm electrode gap was selected to match the fin spacing in the evaporator, ensuring good thermal and physical coupling to the heat-exchange surface. The sensor connects to a voltage divider that converts resistance variations into a measurable voltage signal. In [104], eight identical sensors were installed along the coil between the refrigerant inlet and outlet, enabling the monitoring of frost formation and propagation. During operation, the electrical signal evolves through three distinct stages corresponding to the transitions between air, water, and ice or frost.

Figure 28 –Sensor prototype CAD model, redrawn from [104].

The results, presented in Figure 29, show the voltage evolution measured across four of these sensors during a typical frosting cycle. In dry-air conditions, the differential voltage remained between 9 mV and 32 mV. Once condensation initiated on the surface, the signals from sensors 2 and 4 rose sharply to approximately 6 to 7 V, indicating the formation of a water bridge between the electrodes. Sensors 1 and 3 responded slightly later as condensation propagated along the coil. As freezing occurred, the conductivity decreased in sensors 1 and 2, indicating frost detection in their regions. This sequential behaviour reflects the transition from air to water and then to frost in two of the four sensors, demonstrating the sensor's ability to detect frost.

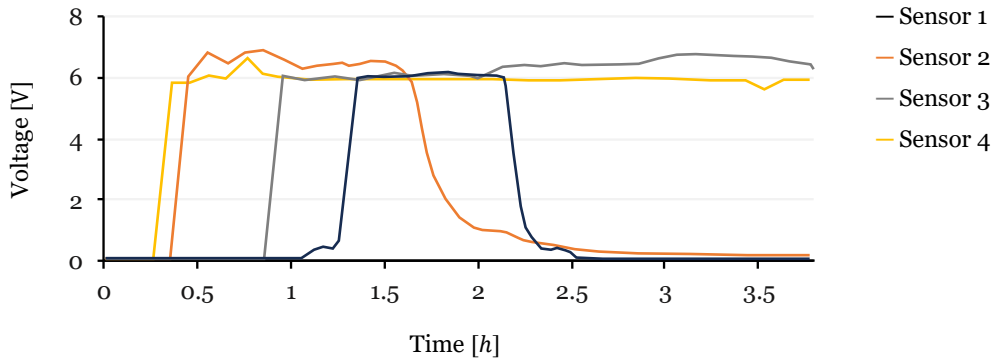

Figure 29 –Experimental results from the resistive frost detection sensor showing voltage variation over time (adapted from [104]).

The authors reported repeatability in condensation and frost detection, confirming the sensor's potential under repeated frosting–defrosting cycles. Although the configuration does not inherently allow for frost-thickness measurement, the electrode configuration could be adapted to provide an indirect estimate of layer height, for instance, by arranging electrodes at varying depths or using a distributed array.

From a practical standpoint, resistive sensors offer several advantages. They are inexpensive to fabricate, require simple readout electronics, and can be easily integrated onto the fins or tubes of HXs. Their direct response to phase transitions makes them a compelling solution for real-time frost monitoring and defrost-control applications. However, this technology is still in its early stages of development, and further research is needed to better correlate the electrical signal with the physical properties of the frost layer.

2.6.7. Comparison between sensors

The comparative analysis of the reviewed direct frost detection methods highlights distinct trade-offs between maturity, complexity, and potential for further development. Photoelectric and fibre-optic sensors provide accurate and fast responses, relying on the optical attenuation or reflection caused by frost and ice; however, their implementation in compact evaporators is limited by alignment constraints, susceptibility to surface contamination, and relatively high cost. Piezoelectric sensors offer a mechanically robust alternative with clear frequency-based signatures of phase transitions, yet their sensitivity to mounting conditions and vibration restricts their reliability in industrial refrigeration environments. Capacitive sensors, on the other hand, have demonstrated reliability and strong phase discrimination, with the ability to track frost growth and densification with repeatability. When properly shielded and compensated for temperature and contamination effects, they provide stable performance. Their flexible electrode geometries also allow close integration with HX fins, making them perhaps the most promising and field-ready technique. CV complements these methods by offering wide-area frost quantification with high accuracy and strong reliability once illumination compensation is implemented. However, despite its robustness, this approach is less suitable for compact refrigeration systems due to space constraints, and higher processing requirements. Although it still holds considerable potential for commercial applications where space is less restrictive, within the context of this work it remains more effective as a supervisory or validation tool rather than as a primary integrated sensor. Resistive sensing, in contrast, stands out as the simplest and most cost-effective technique, capable of detecting phase transitions directly through measurable electrical resistance variations. Although it remains in an early stage of research, its low cost, compactness, and adaptability for miniaturization also make it promising for integration into evaporators. With proper optimization of electrode geometry and materials, resistive sensors could achieve the accuracy and reliability required for autonomous demand-defrost control, representing both a practical and innovative direction for further development.

Among all reviewed techniques, the resistive sensor and the capacitive sensor emerge as the two most viable candidates for continued development. While capacitive sensing offers maturity, proven reliability, and accurate monitoring of frost evolution, resistive sensing provides unmatched simplicity, compactness, and cost effectiveness, with significant room for innovation. The resistive sensor's minimal hardware combined with its direct response to condensation and frost, make it viable for miniaturization and distributed integration. Its potential for advancement and novelty is high. For this reason, the resistive sensor was selected as the primary focus of this work.

2.6.8. Concluding remarks

Different methods for demand defrosting have been developed so far, and although many solutions exist nowadays, defrosting operations in refrigeration systems are still widely time controlled. The consequence is unnecessary energy consumption and temperature fluctuations that affect the conservation state of foods due to excessive defrosting operations.

Directly measuring frost on the evaporator may be the solution to minimize the impact of this problem. Cost effective, compact, simple, reliable, and still accurate enough to command defrost operations sensors can be developed. The necessity to measure the frost thickness is not one of high precision, but one precise enough to command the defrosting operations when frost accumulation becomes a problem.

Outside factors during frost formation can impact the frost characteristics, such as crystal morphology and consequent density, translucency, reflection coefficient, stiffness, capacitance, electrical resistance, etc. These variations could induce errors in measurements that should be studied to be minimized before implementation in commercial systems.

Resistive sensing approaches have the potential to be a solution to this problem. Their simplicity, cost effectiveness, and ability to directly detect phase changes make them particularly suitable for integration into existing refrigeration systems without significant design alterations. Such sensors can provide an input for demand-defrost control while remaining compact and inexpensive to manufacture. Unlike other methods that rely on complex measurement systems, resistive sensors can be miniaturized and distributed across the evaporator, allowing localized detection and faster response to frost formation.

For these reasons, the development of a resistive frost detection sensor represents a promising path toward more efficient and sustainable refrigeration. However, to design and validate such a sensor, it is important to control the conditions under which frost forms. The behaviour of resistive elements depends on operational parameters of the refrigeration system, therefore, a dedicated frost formation setup is required to generate reproducible frosting–defrosting cycles, allowing systematic testing, calibration, and optimization of the sensor. This experimental platform will make it possible to understand how measurements correlate with the different stages of frost evolution and to develop a sensor that is both practical and robust against the variability of operating conditions.

Chapter 3

Frost formation experimental setup

The goal of this chapter is to establish the experimental foundation for the development and testing discussed in the following chapters. The tools and their most relevant specifications will be presented, along with the materials and methods used in the development and testing of frost detection resistive sensors.

3.1. Experimental setup overview

As this is the first chapter addressing the practical work, it is relevant to provide a simplified overview of the experimental setup. This will help the reader understand how the different circuits, sensors and actuators work together. Figure 30 displays a schematic overview of the experimental setup:

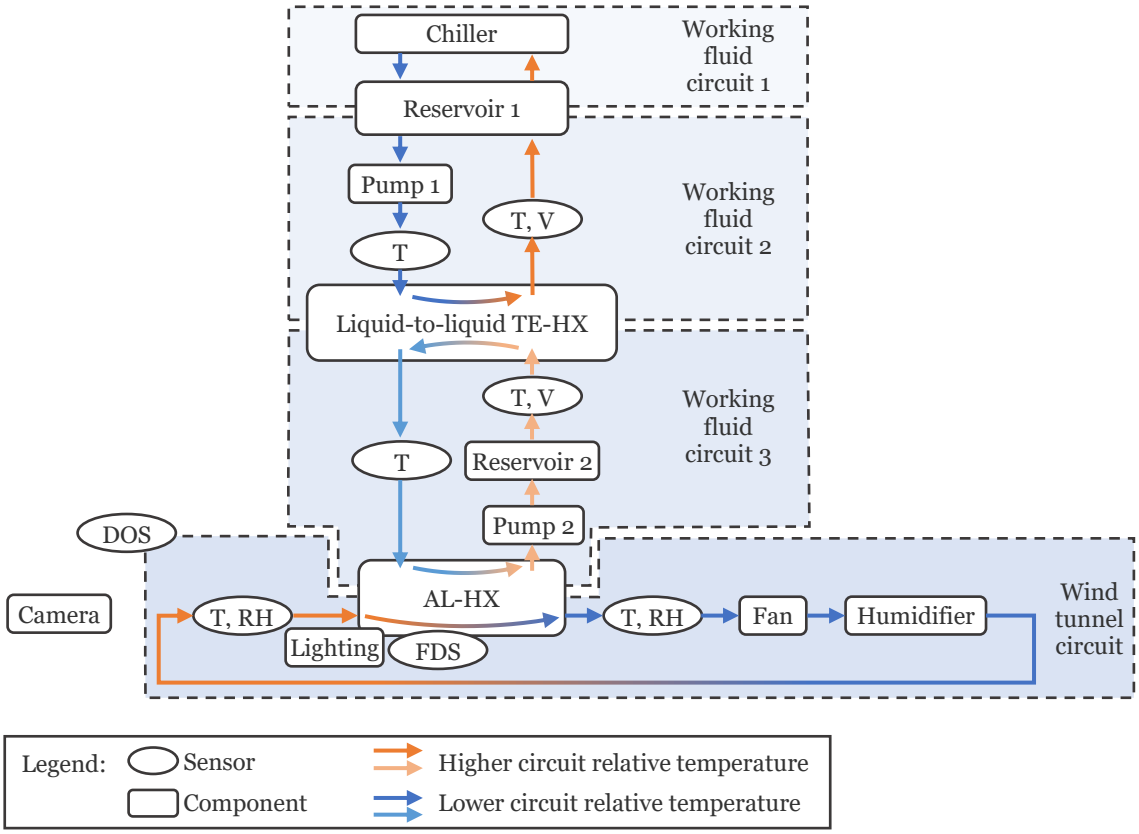

Figure 30 – Simplified overview of the experimental setup, with main components, sensors and actuators.

The working fluid is an ethylene-glycol/water solution in a concentration of 40% by volume. The three working fluid circuits, wind tunnel circuit, main components, sensors, actuators and the interaction between them are represented. Orange and blue arrows

indicate the variation of working fluid temperatures relative to the temperature differences within the circuit, with different shades used to distinguish between the different working fluid circuits, indicating fluid exchange between circuits 1 and 2, and no fluid exchange between circuits 2 and 3.

The experimental setup consists of an Air-to-Liquid HX (AL-HX) in which a resistive frost detection sensor (FDS) can be mounted. A camera is positioned to face the intake end of the AL-HX, enabling periodical image acquisition to corroborate the sensor measurements by processing the images using a CV method to detect frost formation. The AL-HX absorbs heat from the air to promote frost formation on the surface where the sensor is mounted. This low temperature is achieved through a cascading cooling system in which the working fluid circulating in the AL-HX is first cooled in a liquid-to-liquid thermoelectric heat exchanger (TE-HX), which further lowers its temperature below that of the secondary working-fluid circuit connected to the chilled reservoir. The reservoir temperature is maintained by the chiller, providing thermal stability and supplying cold working fluid to the TE-HX, enabling the AL-HX to reach the conditions required for controlled frost generation.

The air circuit is closed to maintain the lowest temperature possible, therefore, to achieve sufficient absolute humidity (AH) for frost formation (since AH decreases as water condenses and frost forms), a humidifier is included in series with a fan that recirculates the air through both the AL-HX and the humidifier.

Parameters are continuously monitored throughout the system to understand the operation conditions and better understand frost formation:

- The temperature of the working fluid is measured at both the inlet and outlet of all heat exchangers (TE-HX and AL-HX).
- Flow rates are measured in working fluid circuits 2 and 3.
- In the wind tunnel, temperature and relative humidity are monitored at the inlet and outlet of the AL-HX.

Data collected from system working parameters allows for the analysis of the conditions of frost formation, facilitating further analysis in post-processing and system troubleshooting when necessary. With an overview of the system, it is now possible to advance to the subject matter of this chapter.

3.2. Software, and online libraries

The development and implementation of the frost detection sensors and the associated experimental setup required the use of various software tools for design, prototyping, programming, data processing, and data visualization. The following sections provide an overview of the software tools used and their purposes for each specific application in this thesis.

3.2.1. Computer-aided design

Computer-Aided Design (CAD) was a tool for the design and optimization of parts to ensure compatibility and functionality within the experimental setup. The CAD models were helpful in the production of parts, in visualizing the physical layout of the components and in studying their interactions. This facilitated the design process by allowing for simulations and adjustments before physical production.

Some of the CAD models were further processed for part production using various Computer Numerical Control (CNC) technologies, such as Additive Manufacturing (AM), routing, and laser cutting. These models contributed to accuracy and reliability in the production of the experimental setup components. SolidWorks was selected as the primary CAD software for this thesis. It was employed to create 3D models and prototypes of the system components and sensor hardware. Additionally, some off-the-shelf components had their CAD models available online. Besides the manufacturers' websites, libraries such as the GrabCAD Community Library [105] were consulted to download these CAD files. The components obtained from these libraries are mentioned throughout this document, and credit is given to their authors.

Finally, the CAD models were rendered using the SolidWorks PhotoView 360 to visual representations of the components, which will be and have been presented throughout this document. These rendered models enhance the visualization of the system components.

3.2.2. Computer-aided manufacturing

Computer-Aided Manufacturing (CAM) software converted the virtual designs into G-code, which the manufacturing machines could interpret and execute. This software allowed for the customization of various parameters, specific to each manufacturing technology employed, to meet the design requirements and ensure that the produced parts matched the intended specifications.

For this project, several CAM software tools were utilized for different CNC manufacturing technologies:

- Slic3r and Ultimaker Cura: These programs were used for preparing additive manufacturing jobs. They converted CAD models into G-code, allowing customization and analysis of printing parameters such as material type, layer height, and density, thus optimizing the printed parts.
- Esprit Software: This software was used for CNC cutting of metallic parts. It converted CAD models into G-code, allowing customization of machining parameters such as toolpaths, spindle speed, feed rate, and depth of cut, ensuring accurate production of the model geometries.
- Since the laser cutting was outsourced, a Drawing Exchange Format (DXF) file was saved from SolidWorks and provided to the manufacturer, who then proceeded with the CAM processing.

These CAM tools allowed the transition from virtual CAD models to the physical parts produced via various CNC manufacturing techniques. Configurations and settings for these processes will be provided in future sections when relevant.

3.2.3. Firmware development

The data acquisition system was designed to capture data from a variety of sensors, including the resistive frost detection sensors, temperature sensors for air and refrigerant, humidity sensors, and flow sensors, which will be later detailed within this chapter. This data was collected via the Arduino microcontroller and then sent to a computer running MATLAB through serial communication for further processing and analysis.

The Arduino Integrated Development Environment (IDE) was selected for programming this data acquisition system. The Arduino IDE provides a well-documented platform for writing, compiling, and uploading code to the Arduino microcontrollers. It facilitates the integration of multiple sensors, data collection, and communication with other components of the system. Additionally, the IDE is user-friendly, and many cost-effective sensor libraries are readily available, streamlining the development process.

The use of these libraries helped with the development of the data acquisition system, and their usage can be consulted in Annex B.1. The Arduino microcontroller was programmed using the Arduino IDE, for capturing data from the array of sensors and

transmitting it via serial to the MATLAB interface for data visualization, processing and recording. The program developed for the data acquisition will be detailed later.

3.2.4. MATLAB

MATLAB version R2018b was used for data processing and analysis. After capturing the image, receiving the frost sensor and experimental setup working parameters through serial communication, this software was used to facilitate the processing, visualization, and interpretation of data. MATLAB's set of tools and functions enabled all the calculations and image analysis, providing awareness into the performance of the frost detection sensors. Post-processing scripts are available from Annex B3 to Annex B5. The processed data was then used to refine sensor designs, understand, troubleshoot and optimize the experimental setup.

3.2.5. MATLAB App Developer

MATLAB App Developer was employed to create a user-friendly interface for monitoring and controlling the experimental setup. This tool allowed for the design of a custom Graphical User Interface (GUI) that facilitated real-time data visualization and system control. The application provided an intuitive platform to observe sensor readings, control experimental parameters, and analyse data trends, enhancing the overall understanding of testing conditions. This GUI will be detailed later, and the code developed is available in Annex B.2.

3.2.6. Adobe Photoshop CC and Illustrator CC

Adobe Photoshop CC and Illustrator CC were used to create and refine visual content for the thesis. These tools enabled the production of schemes, diagrams, and illustrations that visually represented the concepts, designs, and results discussed in the thesis. Photoshop was used for image editing, while Illustrator was used for creating vector graphics and some schematics. The use of these software tools improved the quality and clarity of the visual elements of the thesis.

3.2.7. Microsoft Excel and Microsoft Word

Microsoft Excel and Word were used for data analysis and the writing of this document. Excel was employed for data analysis, posterior data plotting and table creation. This pursued clarity in data visualization, contributing to effective analysis and communication of findings. Word was utilized for writing and formatting this document, and for creating some of the diagrams and flowcharts.

3.3. Prototyping tools used for the development of this thesis

This section details the prototyping tools used in the development of this thesis, focusing on the methods and equipment employed throughout the project. The tools are categorized into four main areas: AM, CNC machining, electronic prototyping, and workshop prototyping tools. Each category provides an overview of the tools and techniques used for the development and assembly of the experimental setup.

3.3.1. Additive manufacturing

AM played an important role in the development and assembly of the experimental setup. It was used in almost every prototyping phase of the experimental setup, as will be mentioned further. This includes sensor housings, structural parts, joining sections, and full components. This section outlines the 3D printers and materials used.

3.3.1.1. Equipment

The initial stages of the experimental setup development utilized a RepRap Kossel Mini, which was the available machine at the time. As the project progressed, an Artillery Sidewinder X1 was acquired, which enhanced the printing capabilities in volume, materials, and quality.

Table 2 – Specifications of the 3D printers used in the development of the experimental setup.

Feature	Sidewinder	Genius	Kossel
	General		
Brand	Artillery		RepRap
Model	Sidewinder X1	Genius Pro	Kossel Mini
Materials	PLA, PETG, TPU		PLA, PETG
Build Volume	$300 \times 250 \times 400$ mm	$220 \times 220 \times 250$ mm	$\varnothing 180 \times 250$ mm
Extruder	Direct drive		Bowden
Max. temperature	240 ^{o}C		240 ^{o}C
	Bed		
Voltage	220 V AC		12 V DC
Surface	Carborundum coated glass		
Max. temperature	130 ^{o}C		
	Other features		
Z-axis	Dual		Triple V-Slot carriage
Max. printing speed	150 mm/s		320 mm/s
Connectivity	USB, SD Card		USB
HMI	TFT colour touch screen		LCD Screen
Failure Detection	Filament run-out sensor		None

The acquisition of an Artillery Genius Pro followed which increased the production capacity. These machines provided the versatility and precision needed to produce acceptable quality prototypes and functional parts. Table 2 summarizes the main features and specifications of the 3D printers used in this project.

Although the additive manufacturing equipment used in the development of the experimental setup varied significantly, the main differences observed were related to quality and printing volume. These differences will be discussed later, as early development parts had to be divided into sections for production due to the limitations in printing volume.

3.3.1.2. Materials

Overall, the materials used in the mentioned machines included Polylactic Acid (PLA), Polyethylene Terephthalate Glycol (PETG), and Thermoplastic Polyurethane (TPU). Although material properties can vary slightly across different manufacturers, it is possible to make general assumptions about the expected properties of these materials. However, it is important to allow for a margin of variation even within the same type of material, due to differences in composition and pigment.

In summary, all parts that required mechanical strength, such as those subjected to pressure or traction and low temperatures, were produced using PETG. This choice was made because PLA was found to become brittle over time when in contact with the working fluid and exposed to the low temperatures in the experimental setup. For some of the components that did not require high mechanical performance, PLA was used due to its ease of printing. TPU was selected for flexible components, such as custom gaskets, due to its elasticity.

3.3.2. CNC machining

A CNC Vertical Machining Centre was also used to develop the experimental setup. The Litz CV-1000 was utilized to produce the HX plates for the TE-HX. Table 3 summarizes the main features and specifications of the Litz CV-1000, which was used for developing the experimental setup for this thesis.

Table 3 – Specifications of the Litz CV-1000 used in the development of the experimental setup.

Feature	Specification
General	
Brand	Litz
Model	Cv-1000
Maximum spindle speed [RPM]	12000
Number of tools	20
Table dimensions [mm]	560×1000
Maximum table load capacity [kgf]	750
Spindle nose to worktable surface [mm]	$135 - 735$
Cutting feedrate [mm/min]	$1 - 10000$
Travel	
X [mm]	1020
Y [mm]	560
Z [mm]	600
B (4th axis)	360°
C (5th axis)	−30° to +120°
Rapid traverse speeds	
X [m/min]	24
Y [m/min]	24
Z [m/min]	18

This equipment was used to facet and mill two aluminium plates with a thickness of 10.0 mm to produce the TE-HX, utilizing a 5.0 mm end mill. The milling process machined the plates with enough accuracy so that they aligned with the remaining components, as will be later discussed in this section.

3.3.3. Electronic prototyping

For the development of resistive sensors and the data acquisition hat for the Arduino, various sensors and circuits were produced using a range of electronic tools and tested using specialized equipment. A DSUNYK 8586 soldering station with a hot air blower was utilized for soldering components. Voltage and resistance measurements, as well as troubleshooting, were conducted using a Keysight U1253B multimeter. Circuit development and testing were supported by a B&K Precision 1660 power supply. These tools were used for assembly, measurements, and testing throughout the development process.

3.3.4. Workshop prototyping tools

In addition to specialized equipment, various general prototyping tools were used for the development of the experimental setup. These included hand and power tools for material shaping, assembly, and disassembly. Adhesives, paints, and resins were used for bonding and sealing components. General machining tools supported various modifications and maintenance tasks. These tools provided the flexibility and manual capability required to address diverse needs throughout the development process.

3.4. Frost formation setup components

This section details the development and assembly of the experimental setup for the frost formation, focusing also on the components and their specifications when relevant. Each subsection provides an overview of the hardware components and their specifications. The frost formation setup, previously schematized in Figure 30, comprises two HXs (TE-HX and AL-HX) and four circuits (three working fluid circuits and one wind tunnel circuit):

- Circuit 1 - This circuit connects the chiller to reservoir 1 and is responsible for dissipating heat from it. It links to circuit 2 through the reservoir 1, allowing the working fluid to be shared between the two circuits.
- Circuit 2 - This circuit absorbs heat from the TE-HX and releases it into reservoir 1. It includes a pump, a flow meter, and TE-HX inlet and outlet temperature sensors.
- TE-HX - The TE-HX contains four Peltier thermoelectric modules powered by four independent power supply units (PSUs), forcing heat from the cold side to the hot side of the TE-HX. A current sensor is connected in series with each PSU so that power consumption can be monitored.
- Circuit 3 - Connected to circuit 2 at the TE-HX, this circuit only exchanges heat, not fluids, between the two systems. The powered TE-HX lowers the temperature in this circuit, which then connects to the AL-HX in the wind tunnel. It includes a pump, a small reservoir, a flow meter, a temperature sensor between the TE-HX outlet and the AL-HX inlet, and another temperature sensor between the AL-HX outlet and the TE-HX inlet.
- Wind Tunnel Circuit - This circuit circulates air through the AL-HX. The air in contact with the cold surface condenses and/or forms frost. After passing through the AL-HX, the air goes through a temperature and humidity sensor, a fan, a humidifier, and returns to the AL-HX inlet, where another temperature and humidity sensor is placed. The tunnel has doors at both ends, allowing for

accelerated defrosting by turning off the TE-HX, working fluid pumps 1 and 2, and maximizing the fan power to force warmer outside air through the AL-HX.

This setup results in a method of frost formation, providing a controlled environment for experimental observations and measurements. With this understanding of the frost formation setup, some components need further clarification.

3.4.1. Complementary material and construction methods

Melamine-laminated chipboard was used as the structural base to which all other components were fastened. A variety of mechanical fasteners were employed to assemble the 3D-printed parts and secure them to the wooden base. Transparent PVC tubing (Ø 16 mm) connected the components of the working fluid circuits, except for circuit 1, and was complemented by spring-steel hose clamps, fittings, and valves for fluid circuit connections.

Different adhesives were used according to function: epoxy glue for sensor assembly and for sealing waterproof adapters, hot glue as a temporary fixing method during assembly, and an adhesive sealant to bond the polycarbonate and acrylic plates forming the wind tunnel. Acrylic sheets were used for the main body of the air tunnel, while polycarbonate was employed for the recirculation section, which was later added to the design. Hinged doors were designed and 3D printed to fit the polycarbonate panels to provide access. The choice of polycarbonate over acrylic for the recirculation component was based primarily on material availability at the time of assembly.

3.4.2. Working fluid circuit 1

The main components of the working fluid circuit 1 are the chiller and reservoir 1. As the chiller encompasses the pumps and temperature control systems, it will be addressed as a single unit. As previously mentioned, the working fluid is an ethylene-glycol/water solution in a concentration of 40% by volume. The specific chiller used in this setup is the MTA TAE EVO 031, and the unit is depicted in Figure 31.

Figure 31 – Picture of the MTA TAE EVO 031 chiller used, with inlet and outlet ports visible on the bottom left corner.

The role of the chiller is to remove heat from reservoir 1, maintaining the desired temperature for the experiment. This temperature control is essential for the successful operation of the entire system. Table 4 presents the main specifications of the chiller.

Table 4 – Main specifications of the MTA TAE EVO 031 chiller used.

Feature	Specification
Model	
Brand	M.T.A. SRL
Model	TAE EVO 031
Year of construction	2003
System settings	
Voltage [V]	400
Phases	3
Frequency [Hz]	50
Max absorption [A]	11.0
Installed power [kW]	6.0
Protection rating	IP54
Refrigerant circuit	
Refrigerant	R407C
Refrigerant charge [kg]	2.600
Max refrigerant working pressure [MPa]	2.8
Max refrigerant temperature [°C]	65.0
Working fluid circuit	
Pump pressure [kPa]	300
Max working fluid pressure [kPa]	600
Inlet temperature range [°C]	−5 to 35
Minimum outlet temperature [°C]	−10
Weight [kg]	200

Although the chiller can reach -10°C, it is consistently set to a minimum of -6°C to avoid issues that have arisen in the past at lower output temperatures during prolonged testing. This adjustment helps in maintaining the reliability and longevity of the equipment.

As previously described, the chiller is connected to a reservoir that consists of a plastic barrel, as shown in Figure 32. This reservoir is placed on a tray to collect condensation, as its surface gets below the dew point and the freezing point of water during testing.

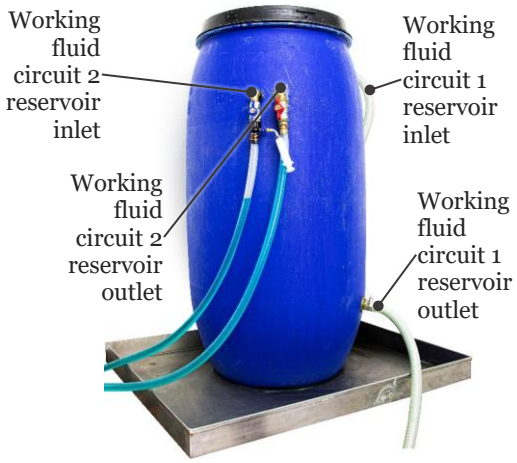

Figure 32 –Reservoir 1, with indication of reservoir inlet and outlet for working fluid circuits 1 and 2.

Reservoir 1 is used to stabilize the temperature within the system. With a volume of 0.2 m^3 and filled with working fluid, it acts as a thermal buffer. This volume ensures that temperature fluctuations are minimized when the chiller alternates between on and off states. By slowly absorbing and releasing heat, reservoir 1 helps maintain a consistent temperature throughout the system, preventing sudden changes that could affect the performance and stability of the experimental setup.

As the inlet from working fluid circuit 1 is positioned above the refrigerant level in reservoir 1, and the chiller's working fluid pump can generate 300 kPa of pressure, turbulence is observed at the top of the barrel. This turbulence results in the mixture of air bubbles, which can be drawn into the outlet of working fluid circuit 2, leading to the accumulation of air within this circuit. Therefore, the initial design focus of working fluid circuit 2 must address this issue.

3.4.3. Working fluid circuit 2

Since working fluid circuit 2 is sensitive to air in the system, a method was developed to minimize air intake. This solution involves a weighted PET bottle with a PETG 3D printed clamping lid that clamps to the outlet tube of working fluid circuit 2. This design

ensures the tube reaches the bottom of the reservoir where turbulence does not introduce as much air bubbles. The rendered view of this solution is shown in Figure 33:

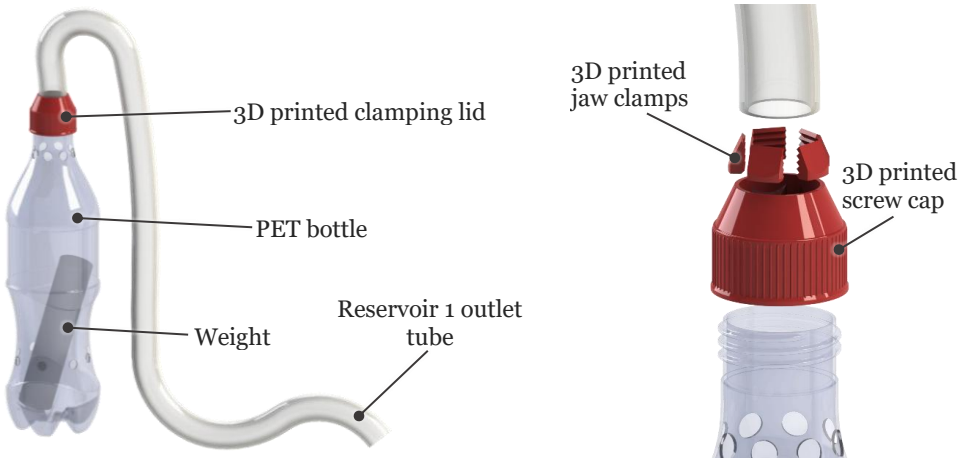

Figure 33 – Rendered view of the solution to minimize air intake in working fluid circuit 2, showing the weighted bottle connected to the tube (a) and the detail of the 3D printed clamping lid (b).

The tube then connects to a valve, which allows the circuit to be isolated from the reservoir to prevent a full reservoir spillage in case of an accidental leak when the experimental setup is unattended for extended periods. Within the reservoir outlet valve, there is a smaller air purge valve that enables air to be removed from working fluid circuit 2 using a suction method, such as a syringe. Valves and the air purge system with the syringe are shown in Figure 34, which is a close-up section of Figure 32.

Figure 34 – Picture of valves and air purge system.

The reservoir outlet valve is then linked to the pump. This pump is a Phobya DC12-220 with the specifications presented in Table 5.

Table 5 – Specifications of the Phobya DC12-220 pump.

Feature	Specification
Voltage [V]	8 – 12
Power consumption [W]	6.5
Maximum Flow [L/h]	400
Maximum pressure [kPa]	220

The pump then connects to a temperature sensor, placed before the intake on the hot side of the TE-HX. To ensure the sensor is in contact with the working fluid to measure its temperature, an adapter was custom-designed and 3D-printed using PETG, allowing the sensor to contact the working fluid directly. Due to the nature of FFF production, porosity was expected in the part. To address this issue, epoxy resin was applied to seal the pores and secure the sensor, making it watertight. A rendered (a) and cut (b) view of the 3D-printed adapter for the temperature sensor is shown in Figure 35.

(a) (b)

Figure 35 – Rendered (a) and rendered cut (b) views of the custom-made adapter with fitted temperature sensor.

After the working fluid temperature is measured, it is forced through the hot side of the TE-HX, where it absorbs heat, allowing for a further lowering of temperature in working fluid circuit 3. Upon exiting the TE-HX outlet, the working fluid passes through another temperature sensor and then through a flow meter before being returned to the reservoir via another valve. The flow meter required connectors, which were also specifically designed and 3D-printed for this setup. Epoxy resin was then applied to seal any pores. Figure 36 shows the connector.

(a) (b)

Figure 36 – Custom made tube (a) and threaded flow meter (b) connectors for the flow meter.

There is no exchange of fluids between working fluid circuit 2 and working fluid circuit 3. The only thermal connection between the two circuits is in the TE-HX in which heat is exchanged between the two circuits.

3.4.4. Thermoelectric heat exchanger

As frost formation varies according to surface temperature, achieving temperatures lower than −6°C that the chiller could reach was necessary for rapid frost formation. To achieve this, thermoelectric modules were introduced to further decrease the working fluid temperature to create the TE-HX. Figure 37 shows the assembled TE-HX within the experimental setup. The blue working fluid is visible inside the TE-HX.

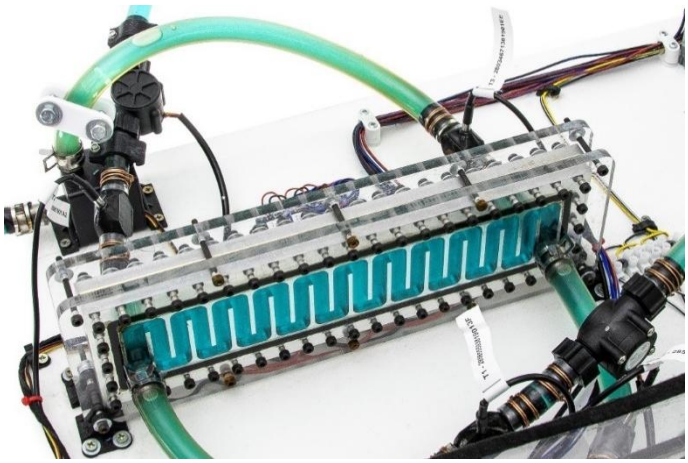

Figure 37 –TE-HX within the experimental setup.

The thermoelectric modules rely on the Peltier effect, which involves the absorption and release of heat when an electric current flows through the junctions of different conductive materials. The designed solution employed four thermoelectric modules to reduce the temperature of the working fluid passing through the AL-HX. The specifications of the used modules are presented in Table 6.

Table 6 – Specifications of the thermoelectric module selected.

Feature	Specification
Reference	TEC1-12710
Type	Thermoelectric module
Dimensions [mm]	$40.0 \times 40.0 \times 3.3$
Max voltage [V]	12.0
Max power [W]	89.0
Max current [A]	10.5
Resistance [Ω]	1.08

Thermoelectric modules operate on the coupled Seebeck–Peltier effects, in which an applied electrical current drives heat absorption at one junction and heat release at the opposite side. Electrically, each module behaves approximately as a resistive element; doubling the applied voltage doubles the current, and since power is proportional to the voltage and current, the electrical input increases with the square of the voltage. This self-limiting resistive behaviour means that although the modules are rated for nearly 90 W each, they are not operated at their maximum rating, as doing so would rapidly reduce efficiency and accelerate thermal stress. The direction of heat pumping depends on the polarity of the applied current, which determines which face of the module is cooled and which is heated. In the TE-HX, four TEC1-12710 modules were clamped between two machined aluminium HX plates and covered with a transparent acrylic lid, as illustrated in Figure 38.

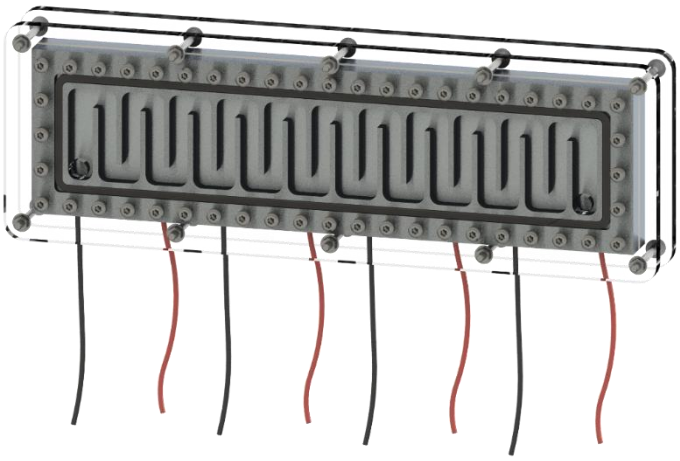

Figure 38 – Rendered view of the assembled TE-HX.

The TE-HX consists of several components, some of which were custom-produced. Given the number of parts, their features, and specifications, Table 7 outlines the main components for reference. In this subsection, these components will be referred to in

figures and text using circled numbers to ensure clarity and uniformity, as indicated in the component list of Table 7.

Table 7 – Main components of the TE-HX.

Component	Number
TE-HX subsystem fastener M4 × 60 hex socket screw	①
TE-HX subsystem fastener M4 washer	②
TE-HX subsystem fastener M4 nut	③
TE-HX module fastener M4 × 16 mm hex socket screw	④
Acrylic lid	⑤
Custom made gasket	⑥
Machined aluminium HX plate	⑦
Peltier TE cell	⑧
Thermal insulant	⑨
Thermal paste	⑩

The TE-HX is separated into three main subsystems, as shown in Figure 39. The first two are equal and opposite: the HX modules, highlighted in yellow, each connected to a closed working fluid circuit that flows in counter-current to that of the opposite HX module.

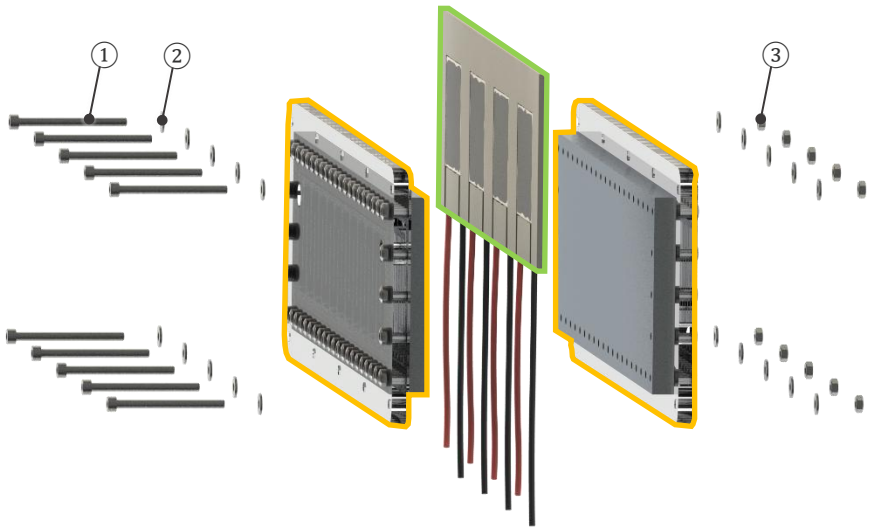

Figure 39 – Rendered view of the TE-HX, separated into modules.

This means that the working fluid of circuit 2 crosses the HX from left to right and that of circuit 3 crosses the HX from right to left (as schematized previously in Figure 30). The TE module, highlighted in green, contains four Peltier cells and functions by creating

a temperature difference between its surfaces when powered, thereby actively driving additional heat transfer between the two circuits. These three modules are held together by 10 screws ①, washers ② and nuts ③.

Each HX module is assembled as shown in the exploded view of Figure 40.

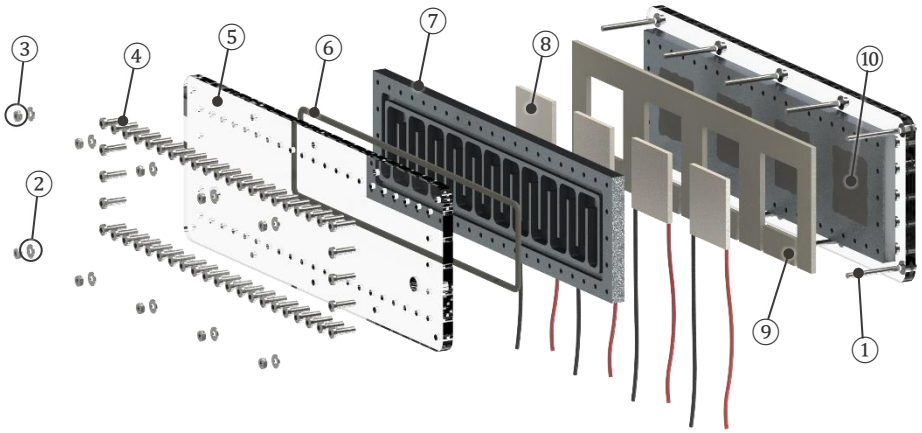

Figure 40 – Rendered view of the TE-HX, showing the four Peltier cells, machined aluminium plates, lids, and fixtures.

Each HX module is separated by removing the screws ④, allowing the acrylic lid ⑤ to be detached. This lid is sealed against the HX ⑦ with a gasket ⑥.

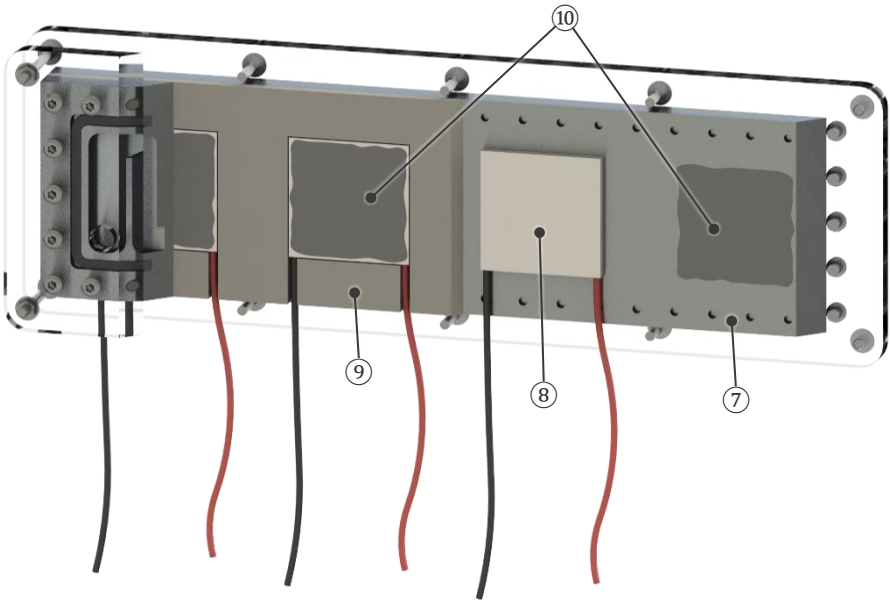

Figure 41 – Rendered cut view of the assembled TE-HX.

The TE module is clamped between the two HX modules, as shown in the cut view of Figure 41. The Peltier cells ⑧, are held in place by a thermally insulating rubber ⑨ to reduce undesired heat exchange caused by the thermal gradient created by the powered

TE module. This rubber also aligns the cells without blocking direct contact between them and the two HX aluminium plates, which is further enhanced by applying thermal paste ⑩ on both sides. The four Peltier cells are connected in parallel to a 5 V PSU.

Figure 42 – Rendered view of the HX aluminium plate.

The HX is comprised of an aluminium plate, represented in Figure 39, which was machined from 10 mm aluminium plates to produce the thermally conductive part of the TE-HX. The milling process used a 5.0 mm end mill to cut a channel ⑪ with a 13.5 × 7.0 mm section, that follows a serpentine path, to increase surface area and therefore heat transfer coefficient. All the holes ⑫ were threaded for the M4 screws so that a lid could be uniformly tightened against the aluminium plate.

A 5 mm channel ⑬ was cut to add a custom-made gasket, which was constructed out of a rubber cord, which was cut to size and joined diagonally, as represented in Figure 43, using cyanoacrylate glue as per manufacturer instructions. When assembling, a small amount of Vaseline was applied to the gasket channel and gasket surface to improve the seal.

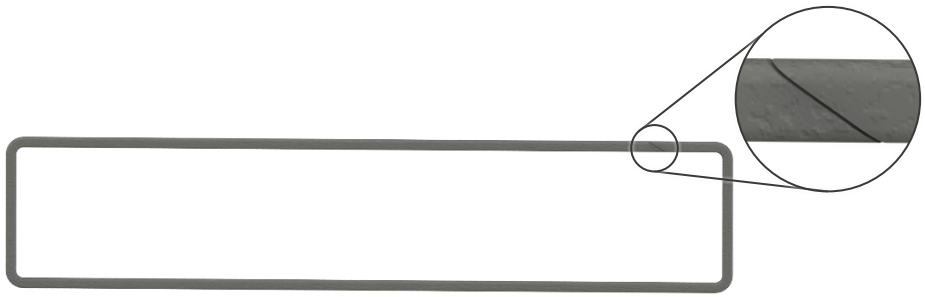

Figure 43 – Rendered representation of the gasket.

When assembled, this gasket creates a watertight seal between the HX plate and the acrylic lids.

These acrylic lids were used as HX covers and were produced by laser cutting 10 mm acrylic sheets using a CNC laser cutter. ⌀ 4.0 mm ⑭ and ⌀ 4.5 mm ⑮ holes were included

to allow screws to assemble the TE-HX, and a G1/4 thread was tapped into the inlet and outlet holes ⑯ to enable tube fittings to be screwed in. The acrylic lids, shown in Figure 44, provide a see-through view of the working fluid, facilitating troubleshooting and the purging of air from the TE-HX circuits.

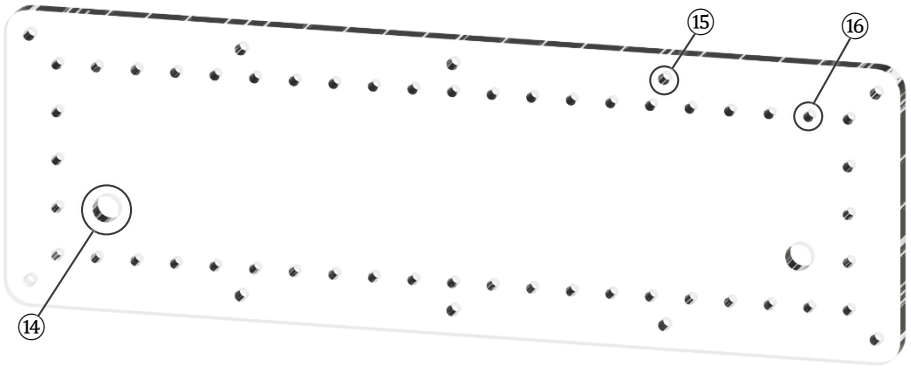

Figure 44 – Rendered view of the acrylic lid.

The TE-HX was designed and assembled to ensure reliability over time under liquid fluid circulation. Considerations were made to ensure it was watertight, robust, and leak-proof during testing. This construction had no observed leaks during operation or standby throughout the years this study took place, withstanding the experimental testing temperatures, pressures and standby times. Additionally, the TE-HX performs its main objective of absorbing heat from working fluid circuit 3, thereby lowering its temperature.

3.4.5. Working fluid circuit 3

The lowest temperature in the entire experimental setup, when in steady state, is measured at the TE-HX outlet in working fluid circuit 3. This temperature sensor is positioned after the outlet and before the AL-HX. This HX, an Alphacool ST30, is placed in the wind tunnel and allows heat exchange between working fluid circuit 3 and the wind tunnel circuit. The specifications of the HX can be analysed in Table 8.

Several considerations must be taken from the specifications. Firstly, the wind tunnel section must be close to the 124 mm height of the AL-HX. Additionally, the sensor placement in this HX will require fitting between fins with a density of 0.6 fins/mm. Imperial G1/4 adapters were acquired to fit the HX inlet and outlet. The black colour of the AL-HX creates a greater contrast for visualizing frost formation, aiding the application of a CV method.

Table 8 – Specifications of the Alphacool ST30 HX.

Feature	Specification
Dimensions	
Length [mm]	157
Height [mm]	124
Depth [mm]	30
Front HX area [mm]	120×120
HX performance characteristics	
Cooling Channels	12
Material	Copper
Fin Density (fins per mm)	0.6
Operational limits	
Pressure Tested [kPa]	80
Maximum Working Temperature [°C]	60
Mounting and other characteristics	
Inlet and outlet threads	G1/4"
Mounting thread size	M3
Weight [g]	420
Colour	Black

The AL-HX outlet connects to the pump, a Phobya DC12-400, which forces the circulation of the working fluid across this circuit. The pump specifications are presented in Table 9:

Table 9 – Specifications of the Phobya DC12-400 pump.

Feature	Specification
Voltage [V]	$8 - 12$
Power consumption [W]	18
Maximum Flow [L/h]	800
Maximum pressure [kPa]	400

It is important to note that the pump used in this circuit has twice the maximum flow rate of the pump used in working fluid circuit 2. This will result in significantly different ΔT values at the hot and cold sides of the TE-HX. Figure 45 displays part of the experimental setup, with working fluid circuit components visible.

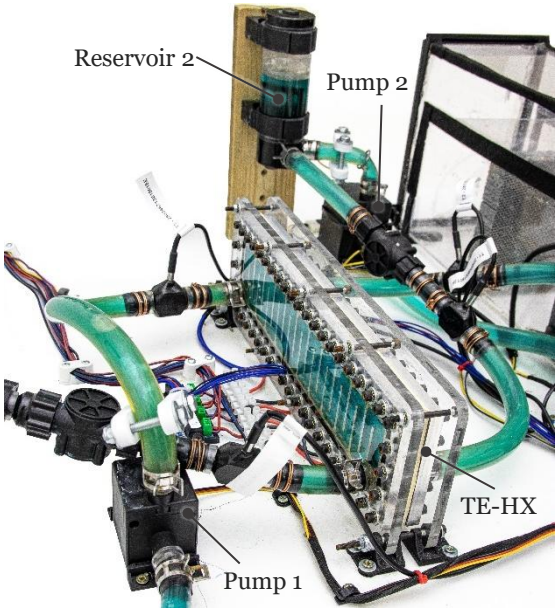

Figure 45 – Components from the working fluid circuits 2 and 3.

If flow reduction is desired by restricting the tube, it should be done right at the pump outlet to avoid pressurizing the entire circuit, which is not rated for the high pressures the pump can achieve. This is particularly relevant for the AL-HX, which is only pressure tested up to 80 kPa.

The pump outlet leads to reservoir 2, a Phobya Balancer 150, whose specifications can be found in Table 10.

Table 10 – Specifications of the Phobya Balancer 150 reservoir.

Feature	Specification
Diameter [mm]	50
Height [mm]	150
Inlet and Outlet Ports	G1/4"
Pressure Tested [kPa]	200
Volume [cm^3]	250

This reservoir serves several functions: it collects air from the circuit, facilitates the process of topping up the working fluid, allows for fluid expansion, and compensates for fluid losses due to small leaks and evaporation.

Reservoir 2 then connects to a flow meter and a temperature sensor before returning to the TE-HX cold side inlet, completing working fluid circuit 3. This circuit absorbs heat from the air in the wind tunnel and releases it into working fluid circuit 2. The heat

absorption occurs in the AL-HX, which acts as the connection between the two circuits. This setup ensures lower temperatures are possible to achieve, resulting in a controlled velocity at which frost is formed in the wind tunnel circuit.

3.4.6. Wind tunnel circuit

While the working fluid circuits ensure that temperatures within the AL-HX are sufficient for frost formation, the wind tunnel circuit maintains the appropriate air conditions for frost to form. In steady operation, the cooling provided by the TE-HX must balance the total thermal loads from the surroundings, leakage, fan work, and latent heat associated with condensation and frosting. For this to happen, the wind tunnel circuit is closed (except during defrosting) to control humidity and temperature during tests. The configuration of the wind tunnel circuit and its components is illustrated in Figure 46.

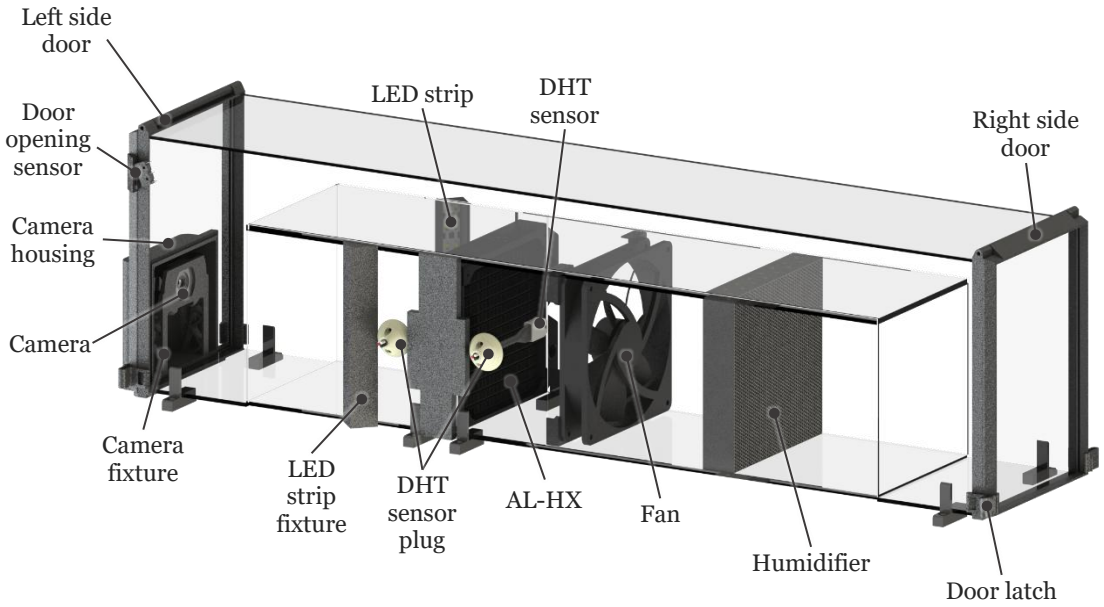

Figure 46 – Rendered view of the wind tunnel circuit.

As the acrylic walls do not provide substantial thermal insulation, heat is exchanged with the surroundings while the air circulates, resulting in an increased temperature. A small increase in the temperature of the recirculated air between the AL-HX outlet and inlet is desirable, as a warmer intake air can hold more water vapour, and thus promote more frosting on the AL-HX surface. However, the inlet air temperature must remain low enough to preserve supercooling and avoid any risk of melting. The air circulation path is illustrated in Figure 47.

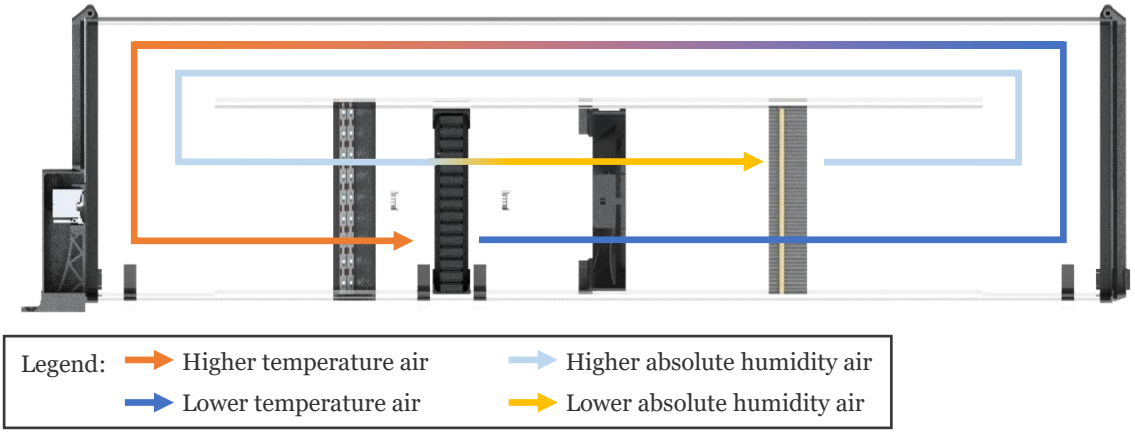

Figure 47 – representation of the air flow direction, temperature and humidity.

The air crosses the AL-HX, where it releases heat to the working fluid, and in the process water vapour condenses or freezes, effectively dehumidifying the air. After the HX, the air crosses a DHT temperature and humidity sensor before going through the fan. This fan is a Noctua NF-A14 whose specification can be seen in table 11

Table 11 – Specifications of the Noctua NF-A14 fan.

Feature	Specification
Dimensions	
Size [mm]	$140 \times 140 \times 25$
Mounting hole spacing [mm]	124.5×124.5
Working parameters	
Max. angular velocity [RPM]	1500
Min. angular velocity [RPM]	300
Max. airflow [m^3/h]	140.2
Max. static pressure [Pa]	20.4
Power and control	
Connector	4 pin
Speed control	PWM
Power [W]	1.6
Voltage [V]	12

This fan pushes the air through a humidifier, whose function is to compensate for the air dehumidifying effect of the AL-HX, due to condensation and frost formation. To reintroduce this humidity, a rectangular-shaped honeycomb structure was designed, and 3D printed, as shown in the rendered image of Figure 48 (a). This structure consists of multiple hexagonal cells arranged in a compact and uniform grid, designed to maximize surface area for enhanced moisture absorption and efficient humidification by increasing

contact between the air and the humidifying medium. The humidifier has several circular holes running vertically where cotton wicks are placed, for even moisture accumulation and distribution, as shown in the cut view of Figure 48 (b).

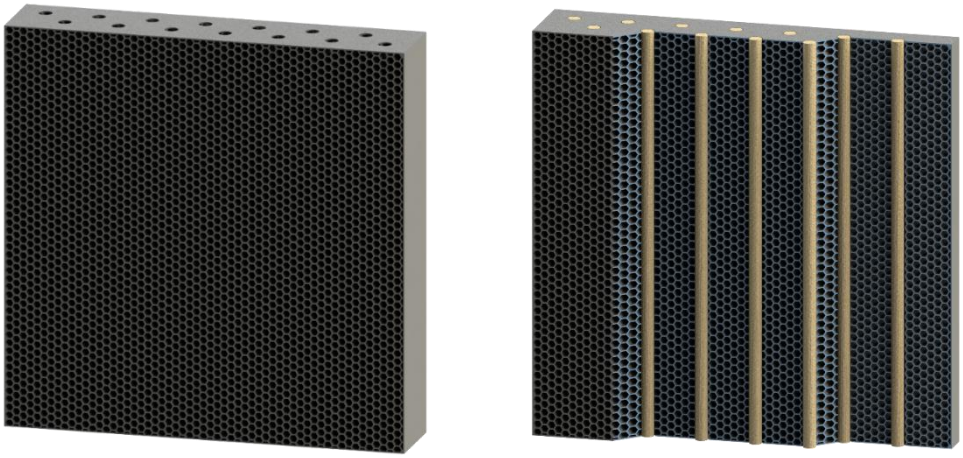

(a) (b)

Figure 48 – Rendered view of the humidifier (a) and rendered cut view (b) in which the cotton wicks are visible.

This humidifier was produced in PLA, and although the rendered CAD model displays the hexagonal cells, the production method imported a solid rectangle, as shown in Figure 50 (a). The hexagonal cells were produced as infill, which results in an even print, a more reliable part, and a better finish. Additionally, the crisscrossed production of infill and increased layer height results in a more accentuated wall texture and higher porosity, which facilitates the accumulation of water, as is visible in Figure 49.

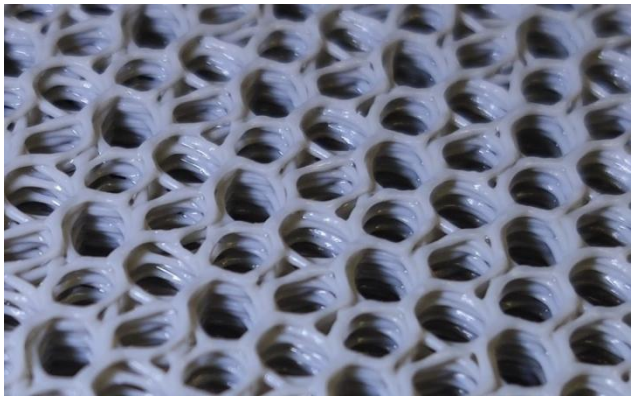

Figure 49 – Close up of the humidifier cells in which porosity and water accumulation is visible.

To achieve the desired results, certain slicing parameters had to be adjusted, as detailed in Table 12.

Table 12 – Slicing parameters for the humidifier.

Slicing parameter	Value
Fill Density	25%
Layer Height	0.28
Fill Pattern	Honeycomb
Perimeters	0
Solid top layers	0
Solid bottom layers	0

Since the printed part has no top layers, bottom layers or perimeters, it consists solely of the infill, as shown in Figure 50 (b).

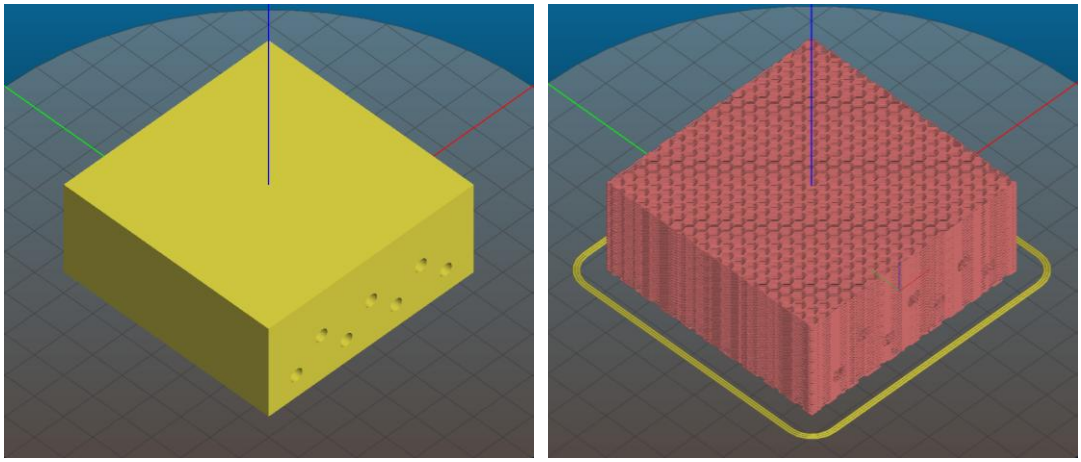

(a) (b)

Figure 50 – CAD model of the humidifier section loaded into the Slic3r environment (a) and toolpath visualization after slicing (b).

In Figure 50, it is also evident that the printed model represents only one quarter of the complete humidifier. This segmentation was necessary because the available printer at the time, the Kossel Mini, lacked the build volume to produce the entire part at once. Consequently, the humidifier was divided into four separate sections, which were later joined using cyanoacrylate glue.

After passing through the humidifier, the air circulates back to the AL-HX, passing through another DHT sensor at the AL-HX intake, which is seen in Figure 51.

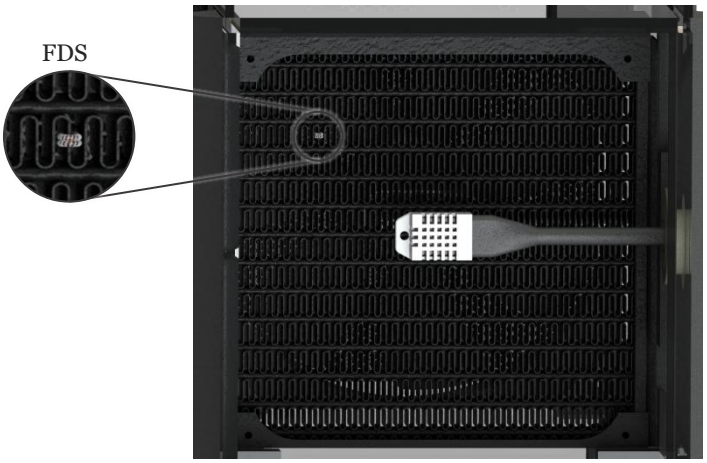

Figure 51 – Rendered front view of the intake of the AL-HX.

Some additional components serve as accessories to the wind tunnel circuit without directly influencing air characteristics:

A camera is positioned facing the intake front of the HX to measure frost, as detailed in a later chapter. The camera is centred with the HX to minimize distortion and is held by a 3D printed support that aligns it with the HX. To prevent the camera from significantly disrupting airflow, the door on the camera side includes a housing that places the camera outside the main airflow zone, avoiding a transparent acrylic between the camera and the HX surface in which fogging could occur, affecting frost measurements using image processing techniques.

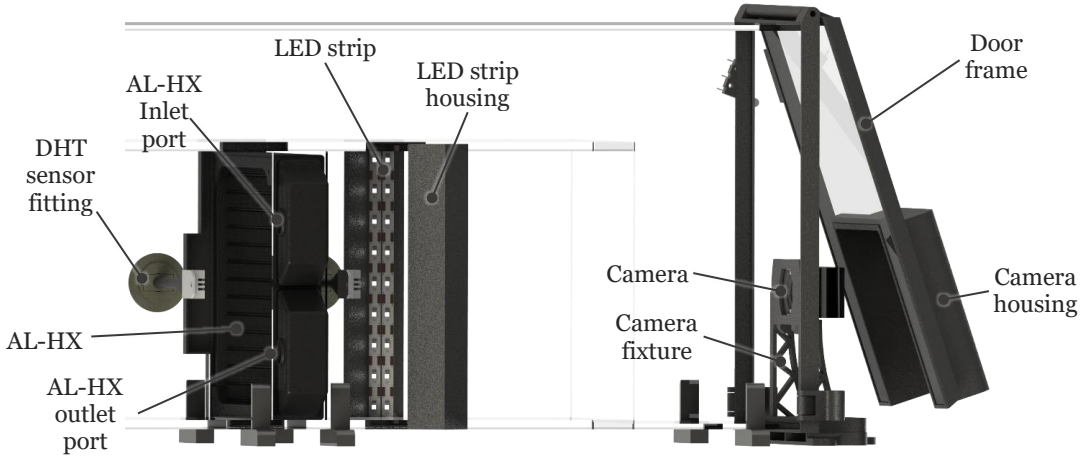

Figure 52 – Close-up rendered view of the left section of the wind tunnel.

Two pairs of LED strips are placed at a 45° angle on each side of the HX, pointing towards the HX. These LEDs provide constant illumination for uniform camera readings regardless of external lighting conditions. These components are highlighted in Figure 52.

The acrylic tunnel was built in two phases. The first phase involved constructing the core of the wind tunnel, which was initially open. The second phase arose from the need to close the wind tunnel, adding a channel to recirculate air back to the HX intake, and two doors. A picture of the assembled wind tunnel is shown in Figure 53:

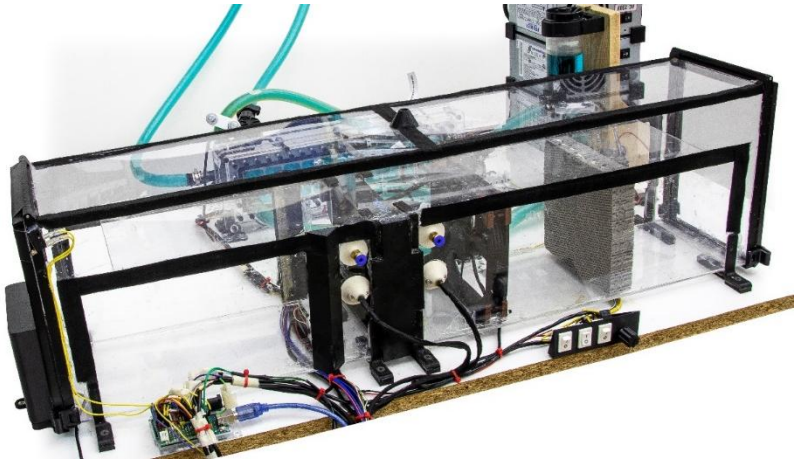

Figure 53 – Picture of the assembled wind tunnel within the experimental setup.

These doors provide access to the tunnel components, facilitating humidifier recharges, sensor placement, defrosting, and maintenance. The door frames, printed in PETG, are fitted with 3 mm acrylic sheets cut to size. Two latches on each side of the doors ensure they remain closed against the frame. The left door features a protrusion to house the camera, and it includes a sensor to log door openings for later analysis.

This experimental setup effectively forms frost, but for meaningful analysis and system optimization, sensing, system control, and data acquisition are needed. These processes allow the collection, processing and interpretation of data from experimental testing, forming the basis for further analysis and insights. In this document, data acquisition setup will be detailed in two different parts, one detailing the system operational parameters, which are parameters within the experimental setup that were thought to be relevant to monitor its working state, and in the data acquisition of frost detection systems which will detail how frost formation is detected in the frost sensing technologies developed within the scope of this work.

3.5. Auxiliary sensors and data acquisition

The data acquisition setup consists of a microcontroller, to which all the sensors are connected. The sensors have already been briefly presented at the beginning of this chapter, in Figure 30, but Figure 54, now with a better understanding of the experimental setup, provides additional information.

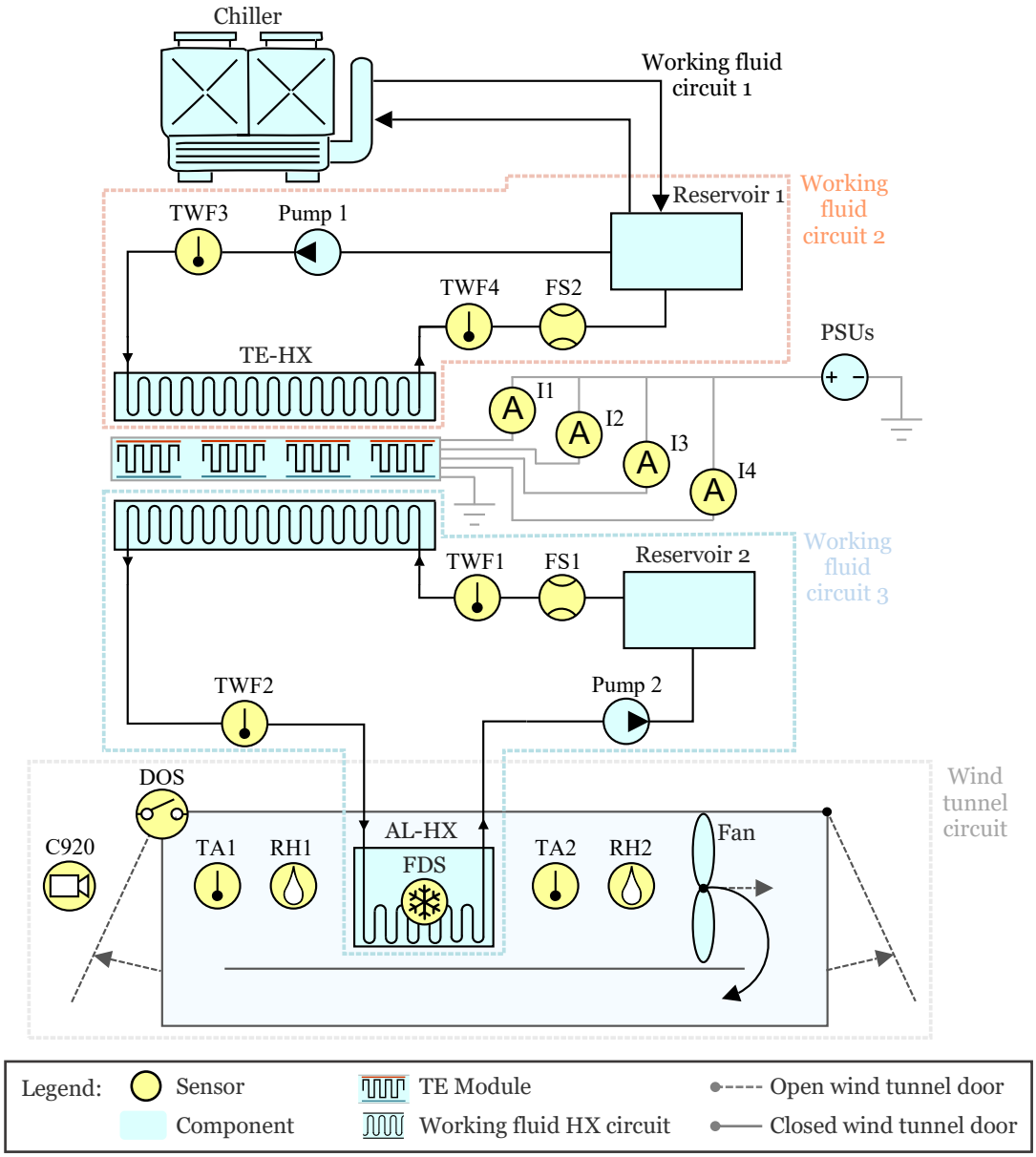

Figure 54 – Detailed overview of the experimental setup focused on sensors for data acquisition.

To properly understand this figure and its symbols, Table 13 lists the sensors used, their location and reference. Despite the significant number of measurements taken, only seven different types of sensors are responsible for all the measurements: DS18B20 for working fluid temperature measurements; FS300A for working fluid flow measurements; ACS712 ELC-20A for thermoelectric module current consumption; DHT22 for air temperature and humidity measurements; and AVL32553 for door opening measurements. The next chapters will focus on frost detection, with custom-made resistive sensors and a Logitech C920 camera for frost detection using CV. The FDS reference of the frost detection sensor is generic, as each of the developed sensors will have its own reference showcasing the type of resistive sensor.

Table 13 – Sensors within the experimental setup.

Reference	Measurement	Sensor
	Working fluid circuit 3	
TWF3	TE-HX inlet working fluid temperature	DS18B20
TWF4	TE-HX outlet working fluid temperature	DS18B20
FS2	Flow	FS300A
	TE-HX	
I1	Thermoelectric module 1 current	ACS712 ELC-20A
I2	Thermoelectric module 2 current	ACS712 ELC-20A
I3	Thermoelectric module 3 current	ACS712 ELC-20A
I4	Thermoelectric module 4 current	ACS712 ELC-20A
	Working fluid circuit 2	
TWF2	AL-HX inlet working fluid temperature	DS18B20
TWF1	AL-HX outlet working fluid temperature	DS18B20
FS1	Flow	FS300A
	Wind tunnel circuit	
TA1	AL-HX inlet air temperature	DHT22
TA2	AL-HX outlet air temperature	DHT22
RH1	AL-HX inlet air relative humidity	DHT22
RH2	AL-HX outlet air relative humidity	DHT22
DOS	Door opening sensor	AVL32553
FDS	Frost detection sensor	Custom made
C920	Frost detection camera	Logitech C920

To ensure the scientific rigor and reliability of the data collected from this experimental setup, a comprehensive error and uncertainty analysis was conducted. This analysis quantifies the contributions of all primary measurement instruments, establishing the standard uncertainties ($k = 1$) for key measurements: air and working fluid temperatures ($0.289\ °C$), relative humidity ($1.155\ \%RH$), current ($0.122\ A$), and flow rate ($4.12\ L/h$), with the microcontroller ADC contributing a standard uncertainty of $1.155\ LSB$. The full methodology is detailed in Annex C. This validation underpins the confidence in the measurements that form the basis for all subsequent experimental work presented in this thesis.

This section details the acquisition system, starting with the microcontroller to which all sensors (except for the camera) are connected.

3.5.1. Microcontroller Arduino Uno Rev3

The Arduino Uno Rev3 is an open-source development platform and was chosen for this project due to its versatility, adequate accuracy, and ease of use. One of the objectives of this work is to develop a reliable, low-cost system, and the Arduino platform is affordable, allowing for easy and fast prototyping. It also has robust support and extensive documentation available from the Arduino community, which facilitates the integration of various sensors and components. Its compatibility with a wide diversity of cost-effective devices makes it a good choice for the data acquisition setup.

However, for industrial applications, a more robust and custom embedded system should be selected. This solution, while sacrificing ease of iteration and versatility, would provide a definitive setup that does not require frequent changes or sensor trials. In such a scenario, the system would be embedded in a custom PCB, offering a stable and resilient configuration tailored to industrial requirements. The same programming platform and sensors could be used, as both Arduino and other manufacturers offer these compatible solutions, lowering costs even further.

The Arduino Uno Rev3 has a 10-bit ADC, providing a resolution of 1024 discrete levels for analog input, which is sufficient for capturing the nuances in sensor data. The previously mentioned Arduino IDE is also a straightforward programming environment suitable for developing and managing the experimental setup data acquisition. Relevant specifications for the Arduino Uno Rev3 are provided in Table 14.

Table 14 – Arduino Uno Rev3 microcontroller specifications [106, 107].

Specification	**Value**
Microcontroller	ATmega328P
Operating voltage [V]	5
Input voltage [V]	6 to 20
Digital I/O pins	14 (6 PWM)
Analog input pins	6
ADC input resolution [bits]	10
ADC input resistance [MΩ]	100
ADC integral non-linearity [LSB]	± 0.5
ADC absolute accuracy [LSB]	± 2
ADC conversion time [µs]	65 to 260
Flash Memory [kB]	32
Clock Speed [MHz]	16
Dimensions [mm]	$68.6 \times 53.4 \times 15.4$

To facilitate the integration of all the data-acquisition sensors listed in Table 13 in a straightforward and easy-to-troubleshoot manner, a shield for the Arduino Uno was developed. This shield, shown in Figure 55 (a), is color-coded, to facilitate sensor connection and troubleshooting. The color-coding ensures that each sensor can be quickly and correctly identified, streamlining the troubleshooting process and enhancing the overall reliability of the data acquisition system. This shield mounts into the Arduino Uno as shown in Figure 55 (b).

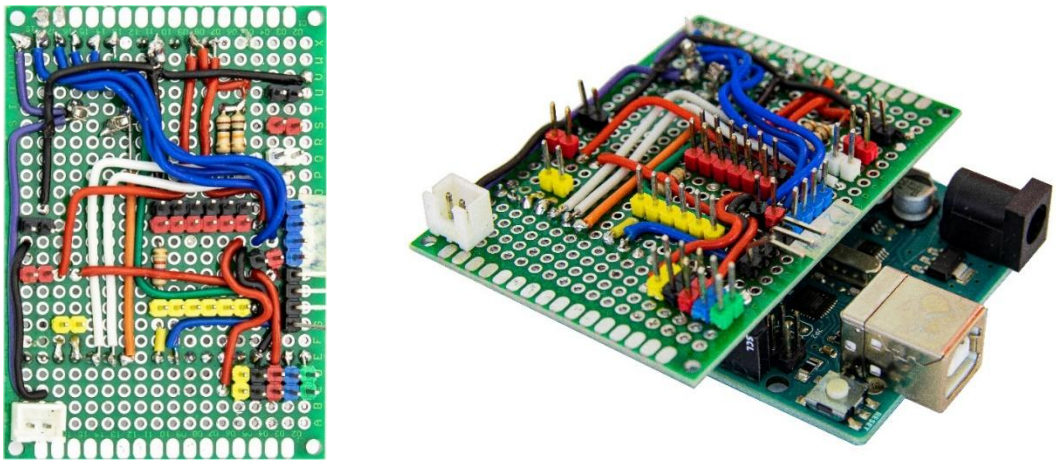

(a) (b)

Figure 55 – Developed hat for the Arduino Uno (a) and hat mounted on the Arduino microcontroller (b).

Table 15 details the sensor connections to the Arduino Uno, specifying the pin type for each sensor and the corresponding General Purpose Input Output (GPIO) pin it connects to. Additionally, the table indicates the sensor each port is associated with, for identification. The colour of the cable or header is also provided in the table, along with the number of available header connections for non-ground (GND) or Voltage Common Collector (VCC) pins.

Additionally, two sensors require a pullup resistor on the data pin, DS18B20 requires a 4.8 $k\Omega$ resistor, and DHT22 requires a 30 $k\Omega$ resistor.

Table 15 – Sensor connection mapping to Arduino pins via shield.

Sensor	Sensor Pin	Arduino Pin	Colour
DS18B20	VCC	VCC	Red
	GND	GND	Black
	DATA	8	Yellow (6×)
FS300A	VCC	VCC	Red
	GND	GND	Black
	DATA	2 (FS1), 3 (FS2)	Yellow (2×)
ACS712 ELC-20A	VCC	VCC	Red
	GND	GND	Black
	OUT	A1 (I1), A2 (I2), A3 (I3), A4 (I4)	Blue (4×)
DHT22	VCC	VCC	Red
	GND	GND	Black
	DATA	4 (RH1/TA1) 5 (RH2/TA2)	White (2×)
AVL32553	COM	GND	Black
	NO	9	Blue
FDS	VCC	6	Orange (1×)
	GND	GND	Black
	DATA	A5	Purple (1×)

Besides the sensors within the air tunnel that have already been shown in Figure 46 and in Figure 51, the sensors from the working fluid circuits 2 and 3 are shown in Figure 56 (a), and sensors from the intake end of the wind tunnel circuit are shown in Figure 56 (b):

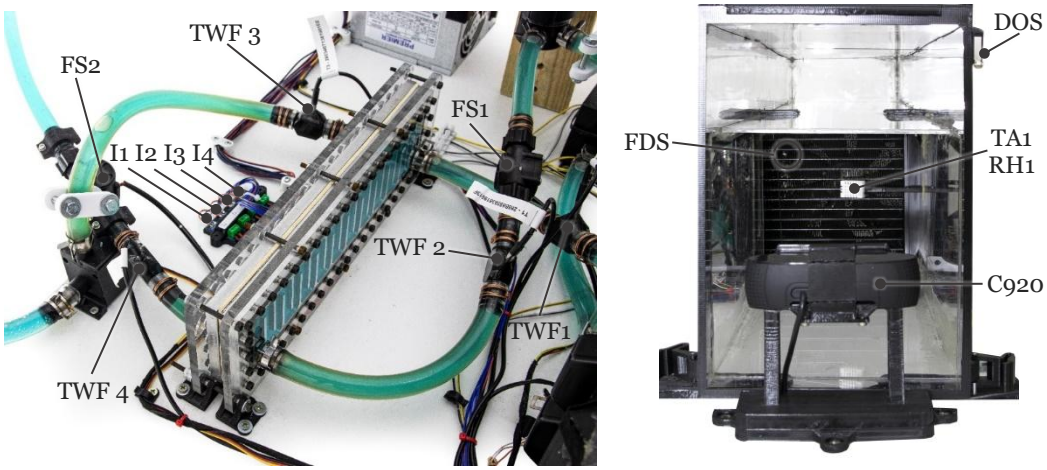

(a) (b)

Figure 56 – Sensors within the experimental setup, in working fluid circuits 2 and 3 (a) and in the intake end of the wind tunnel circuit (b).

Following the overview of the microcontroller, it is necessary to analyse each sensor individually, along with its specifications.

3.5.2. Working fluid temperature measurement sensor DS18B20

The DS18B20 sensor was chosen for liquid temperature measurement due to its waterproof housing, and range of operating temperature, which ensures durability in a low-temperature liquid environment. Detailed specifications for the DS18B20 sensor are provided in Table 16.

Table 16 – DS18B20 temperature sensor specifications [108].

Specification	Value
Operating Voltage [V]	3.0 to 5.5
Operating Temperature Range [°C]	−55 to 125
Accuracy [°C]	±0.5
Resolution	User-selectable 9 to 12 bits
Communication protocol	1-Wire
Waterproof housing	Yes
Dimensions [mm]	∅ 6 × 37

Its operating voltage and communication protocol mean it is compatible with the Arduino platform, and this facilitates integration into the data acquisition setup.

To read this sensor, the OneWire [109] and DallasTemperature [110] libraries were added to the Arduino IDE. The sensor addresses were specified in hexadecimal to retrieve the temperature values. The sensor position according to the diagram of Figure 54, and the corresponding addresses are provided in Table 17.

Table 17 – DS18B20 temperature sensor addresses [108].

Sensor	Address	Hexadecimal
TWF1	285B55593819013F	0x28, 0x5B, 0x55, 0x59, 0x38, 0x19, 0x01, 0x3F
TWF2	2853B23238190111	0x28, 0x53, 0xB2, 0x32, 0x38, 0x19, 0x01, 0x11
TWF3	28034671381901EE	0x28, 0x03, 0x46, 0x71, 0x38, 0x19, 0x01, 0xEE
TWF4	28BFF368381901A2	0x28, 0xBF, 0xF3, 0x68, 0x38, 0x19, 0x01, 0xA2

This sensor also requires the abovementioned 4.8 $k\Omega$ pullup resistor on the data bus.

3.5.3. Working fluid flow measurement sensor FS300A

The FS300A flow sensor was selected for its capability to measure low flow rates, aligning with the expected flow rates of the experimental setup. Additionally, it is rated to operate at temperatures below the expected range of the experimental conditions, ensuring reliable performance throughout the testing process. The most relevant specifications are presented in Table 18.

Table 18 – FS300A flow sensor specifications [111].

Specification	**Value**
Operating Voltage [V]	3.0 to 5.5
Connector	G3/4"
Fluid Pressure [MPa]	$\leq$ 1.75
Working Temperature [℃]	-25 ～80
Output Pulse Frequency [Hz]	$27 \times Q$
High Signal Voltage [V]	$>$ 4.5
Low Signal Voltage [V]	$<$ 0.5
Rated Flow Rate [L/h]	60 ～3600
Precision at rated flow rate	2%

The signal voltage values for the FS300A flow sensor given in Table 18 are specified for an operational voltage of 5 V. For the output pulse frequency, F represents the flow rate in L/h. To obtain F, the number of output pulses, OP, is measured over a period, Δt, and Q is given by Equation (12).

$$F = \frac{60 \cdot OP}{7.5 \cdot \Delta t} \tag{12}$$

Where:

- F represents the flow rate in [L/h],
- OP is the number of output pulses [-],
- Δt is the acquisition period [s],
- 7.5 is the pulse constant [Hz per L/min].

This sensor is also compatible with the Arduino platform, facilitating its integration into the experimental setup. For lower flow rates, it is recommended to increase the sampling

time. A low pulse count can lead to irregular values that are correct and accurate on average but appear erratic over short intervals.

3.5.4. Thermoelectric current sensor ACS712ELC-20A

The ACS712 ELC-20A current sensor was selected for its ability to measure current up to 20 A, with sufficient accuracy to calculate the power consumption of the TE-HX. This sensor outputs an analog voltage that is proportional to the current passing through it, allowing the Arduino to measure this current in a straightforward manner. Specifications for the ACS712 ELC-20A current sensor are provided in Table 19.

Table 19 – ACS712 ELC-20A current sensor specifications [112].

Specification	Value
Current Sensing Range [A]	±20
Sensitivity [V/A]	0.1
Operating Voltage [V]	4.5 to 5.5
Output Voltage [V]	0 to 5
Response Time [µs]	5
Bandwidth [kHz]	80
Operating Temperature [°C]	−40 to 85
Dimensions [mm]	$27 \times 11 \times 14$

Because this sensor reads from −20 A up to 20 A, and the Arduino can only measure positive voltages, the sensor returns 0.5 V to 2.5 V corresponding to −20 A to 0 A, and 2.5 V to 4.5 V corresponds to the positive current values of 0 A to 20 A. This means a −2.5 V offset must always be included in the readings. When testing the sensors, a small calibration factor had to be applied to obtain the most precise values. The Arduino output conversion into current was then given by Equation (13).

$$I = \frac{Reading \cdot Calibration\ factor - Offset}{Sensitivity} \tag{13}$$

where:

- I is the current being used by the thermoelectric cell [A].
- $Reading$ is the value that results in the conversion of the ADC returned measurements in volt [V].
- $Calibration\ factor$ is determined empirically [V].

- $Offset$ is to set the reading of 2.5 V to the actual 0 V it represents [V].
- $Sensitivity$ is the sensor's Volt per Ampere sensitivity [V/A].

Replacing the abovementioned values, Equation (14) is obtained.

$$I = \frac{\frac{5}{ADC} \cdot 0.004887586 - 2.5}{0.1} \tag{14}$$

Replacing the measured values in ADC, an instant calculated reading of current within the Arduino is obtained. As the reason behind this measurement is to calculate power consumption, the power equation can be applied to the sum of the current of each thermoelectric module, returning in this way the power consumption of the TE-HX from Equation (15),

$$P = U \cdot \sum_{n=1}^{4} I_n \tag{15}$$

where:

- P is the total TE-HX power consumption [W].
- U is the operating voltage, in volt [V].
- $\sum_{n=1}^{4} I_n$ represents the sum of the currents I_1, I_2, I_3 and I_4

It was chosen to apply the power calculation in post-processing, as individual current measurements could prove useful for understanding system workings and troubleshooting.

3.5.5. Air temperature and humidity measurement sensor DHT22

The DHT22 sensor was selected for measuring air temperature and relative humidity due to its ability to maintain constant accuracy within the expected range in the wind tunnel circuit. Specifications for the DHT22 sensor are provided in Table 20.

Table 20 – DHT22 temperature and humidity sensor specifications [113].

Specification	Value
Operating Voltage [V]	3.3 to 6.0
Output	Digital via single bus
Temperature Range [°C]	−40 to 80
RH Range [%]	0 to 100
Temperature accuracy [°C]	±0.5
Temperature resolution [°C]	0.1
RH accuracy [%]	±2
RH resolution [%]	0.1
Average Sensing Period [s]	2
Dimensions [mm]	$15.3 \times 7.8 \times 25.3$

This sensor integrates with Arduino systems, guaranteeing compatibility and ease of use. The DHT library [114] was installed in the Arduino IDE to allow sensor communication and data acquisition. This sensor provides monitoring of air temperature and RH, which is important for understanding frost formation dynamics.

As this sensor measures RH, it is expected that the measured values can increase after the air crosses the AL-HX. This occurs because, although the air loses water content due to frost and condensation, its temperature decreases, which consequently reduces its capacity to hold moisture. Absolute humidity, on the other hand, is always expected to decrease after the air crosses the HX. Absolute humidity can be calculated from relative humidity [115] from Equation (16).

$$AH = \frac{216.74 \cdot \frac{RH}{100} \cdot 6.112 \cdot e^{\frac{17.67 \times T}{T + 243.5}}}{T + 273.15} \tag{16}$$

where:

- AH is absolute humidity [g/m^3],
- RH is relative humidity [%],
- T is the temperature [°C].

This equation includes the Bolton [115] empirical formula for the saturation vapour pressure with an accuracy of 0.1% within the temperature range of -30°C to 35°C.

3.5.6. Door sensor AVL32553

The AVL32553 sensor is a microswitch that interrupts the circuit when the left wind tunnel door is opened, enabling the logging of door openings. This functionality ensures that defrosting events are registered and allows for conditional control of the fan speed. When the door opens, indicating defrosting, the fan speed increases to maximum, and the defrosting process is logged. Specifications for the AVL32553 sensor are provided in Table 17.

Table 21 – AVL32553 door sensor specifications [116].

Specification	Value
Actuator	Roller lever
Rated load [N]	0.59
DC Voltage Rating [V]	30
Current rating [A]	5
Cycles at rated load	50 000
Protection Rating	IP40

To ensure this switch interrupts the circuit when the door is open, it is wired in a normally open (NO) configuration, meaning the switch is closed when the door is shut. Additionally, because the circuit remains open otherwise, a pull-up resistor is included. This simple circuit is also straightforward to integrate with the Arduino platform.

3.5.7. Sensor testing and calibration

All sensor measurements were tested and double-checked against reliable sensors or through calibration methods. Temperature and humidity measurements were compared to those of the EL-USB-2 data logger, while flow meter accuracy was verified by measuring a volume of water over a set period of steady state water flow and comparing it to sensor readings. Current sensors were cross verified with measurements taken using the Keysight U1253B multimeter, ensuring all sensor measurements fell within their accuracy windows. These measures contribute towards an accurate data acquisition and reliable system monitoring and control.

3.5.8. Data acquisition

The microcontroller samples all sensors and emits a comma-separated line every $t = 3\ s$. Between these 3 s publishes, some signals are continuously accumulated to allow time-averaging, while others are scheduled to respect device latencies. A ring of helper

functions updates a `valueArray[20]` whose elements are printed in a fixed order. Delimiter is `", "` and the serial link runs at 9600 baud, synchronized to MATLAB.

For working fluid temperature measurements, the four DS18B20s share an OneWire bus on digital pin 8 and are addressed by their 64-bit ROM codes, already shown in Table 17 to ensure repeatable channel mapping (T1–T4). Each cycle proceeds non-blocking: `temperatureRead()` issues a conversion start early, allowing the ~750 ms conversion at 12-bit resolution to complete in the background; later in the same 3 s window `temperatureCalc()` retrieves temperatures with `getTempC(address)` and writes them to the array. This avoids blocking the loop and guarantees fresh data each publish.

For air temperature and RH, the two DHT22 sensors connected to digital pins 5 and 4 provide intake/outlet air measurements. Because DHT22 updates are slow, readings are taken once per 3 s window in `DHTCalc()`. If either Temperature or RH read returns NaN, the corresponding entries are set to 0 so downstream parsing remains robust.

The two flow meters with interrupt counting are connected to pins 2 and 3, increment pulse counters via rising edge. At publish time, pulses accumulated over the last t seconds are converted to volumetric flow using Equation (12). Counters are reset after each conversion to ensure non-overlapping windows.

The current in the TE modules is read in four analog channels ($A1$–$A4$) which measure the current drawn by each TE module. Each raw sample is converted by equations (13) and (14). `currentRead()` runs continuously between publishes, accumulating running sums and a sample count; at publish time `currentCalc()` divides by the count to produce window-averaged currents for all four modules. Electrical power per module is then obtained in post-processing.

The frost detection sensor has a gated, oversampled read. The resistive frost sensor is read on $A5$. To mitigate electrode polarization, electrolysis and to standardize the sampling instant, the sensor is enabled on digital pin 6 just before acquisition, then read as the final operation in the 3 s cycle, and then disabled again. Reading it last exploits the compute time of the prior calculations as a short on-time, allowing the signal to settle before sampling. Five consecutive `analogRead()` calls are issued; storing the last value is a way to flush any ADC multiplexer settling and to reduce transient noise.

A door switch as fan state proxy on pin 9 (`INPUT_PULLUP`) is sampled each cycle. Its logic state is placed into the stream as the fan-state channel (closed door → frosting → fan set

to low; open door → defrost → fan set to high). The same state is mirrored on $A0$ (used here as a digital output) to signal the fan controller that a defrost is underway.

The Arduino microcontroller prints the 20 element `valueArray` as a single CSV line. This output string can be represented in the form of a measurement vector, $z(t)$, as shown in Equation (17). The vector $z(t)$ corresponds directly to the variable `valueArray` in the Arduino code (see Annex B.1).

$$z(t) = [FDS, FS2, FS1, TWF1, TWF2, TWF3, TWF4, TA1, TA2, RH1, RH2, I1, I2, I3, I4, DOS, 0, 0, 0, 0] \quad (17)$$

Each element corresponds to the sensor references summarized in Table 13. The last four entries are reserved for future use and are currently set to zero. In practice, this array is transmitted as a comma-separated string, with each field directly matching the order above.

In the earliest validation runs, only the frost-sensor signal was acquired, the Arduino streamed a single channel to the serial monitor, and data were copied into Excel for offline analysis. As the study progressed, characterizing sensor behaviour required correlating it with the conditions under which frost formed. The acquisition, therefore, expanded to include air temperatures and humidity at the HX intake/outlet, working-fluid temperatures in circuits 2 and 3, flow rates in both liquid circuits, fan speed state, and the electrical current of each TE module. This required a different approach to allow for data visualization during testing, and a straightforward approach to data storage for analysis and post-processing.

3.5.9. Data storage visualization and GUI

To handle this multi-channel stream and enable real-time visualization, the implemented acquisition was connected to a MATLAB App Designer GUI where the data are parsed, displayed, annotated, and logged to a CSV file. The MATLAB side opens the Arduino's serial port, reads one CSV line per publish, and converts it to numeric form. In the script provided in Annex B.2, each acquisition cycle produces a single record, in the format shown in Equation (18), which is appended to the dataset matrix M.

$$b(t) = [t_s, z(t), C920] \quad (18)$$

Where:

- $b(t)$ is the data record vector at time t,
- t_s is the timestamp of the acquisition cycle $[s]$,
- $z(t)$ corresponds to the `valueArray` from the Arduino data acquisition system,
- $C920$ is the computed image acquisition metric that will be later addressed.

This same logic is embedded in the App Designer GUI, so that the host-side timestamp provides a common time base across all plots. When a test is terminated by pressing Stop, the application finalizes the session by generating three outputs: a CSV file containing the complete dataset M, a .txt file with the notes recorded during the test, and two synchronized image folders containing the raw RGB and the processed binarized frames acquired by the C920 camera. The file names are automatically generated using the session start time in the format yyyymmdd_HHMMSS, which is applied consistently across all outputs. For example, a session starting at 2024-01-15 14:32:08 would produce 20240115_143208.csv, 20240115_143208_Notes.txt, and two corresponding image directories (20240115_143208_RGB/ and 20240115_143208_BW/), this way that all files remain uniquely identifiable and cross-referenced.

The developed GUI, shown in Figure 57 provides Start/Stop controls for starting and finishing data acquisition, a running timer, and a notes field to manually input the relevant observations.

Every 3 s, the GUI refreshes all the values. The last measurements are displayed over a schematic of the setup. It is possible to read the values of working-fluid temperatures for circuits 2 and 3, TE module currents, intake and outlet air temperature and RH, flow rates and fan state (as a proxy of DOS). Plots display the values over time. On the right the plots of airside and liquid-side temperatures, air RH for intake and outlet and flow for working fluid circuits 2 and 3 are stacked. On the left, a plot of the fan state is displayed as a binary trace (Max/Min), matching the door-controlled two-level operation.

On the top right, a CV panel shows the last snapshot of the raw RGB picture of the HX intake and a binarized image used for frost quantification. The CV processing pipeline will be addressed in a later chapter.

At the bottom, a full-width plot overlays the frost sensor signal and the CV-derived frost metric over time, for comparison between sensor-measured and actual frost formation in the intake end of the HX. This display is used for analysing sensor response against a CV metric developed for this purpose across complete frost–defrost cycles.

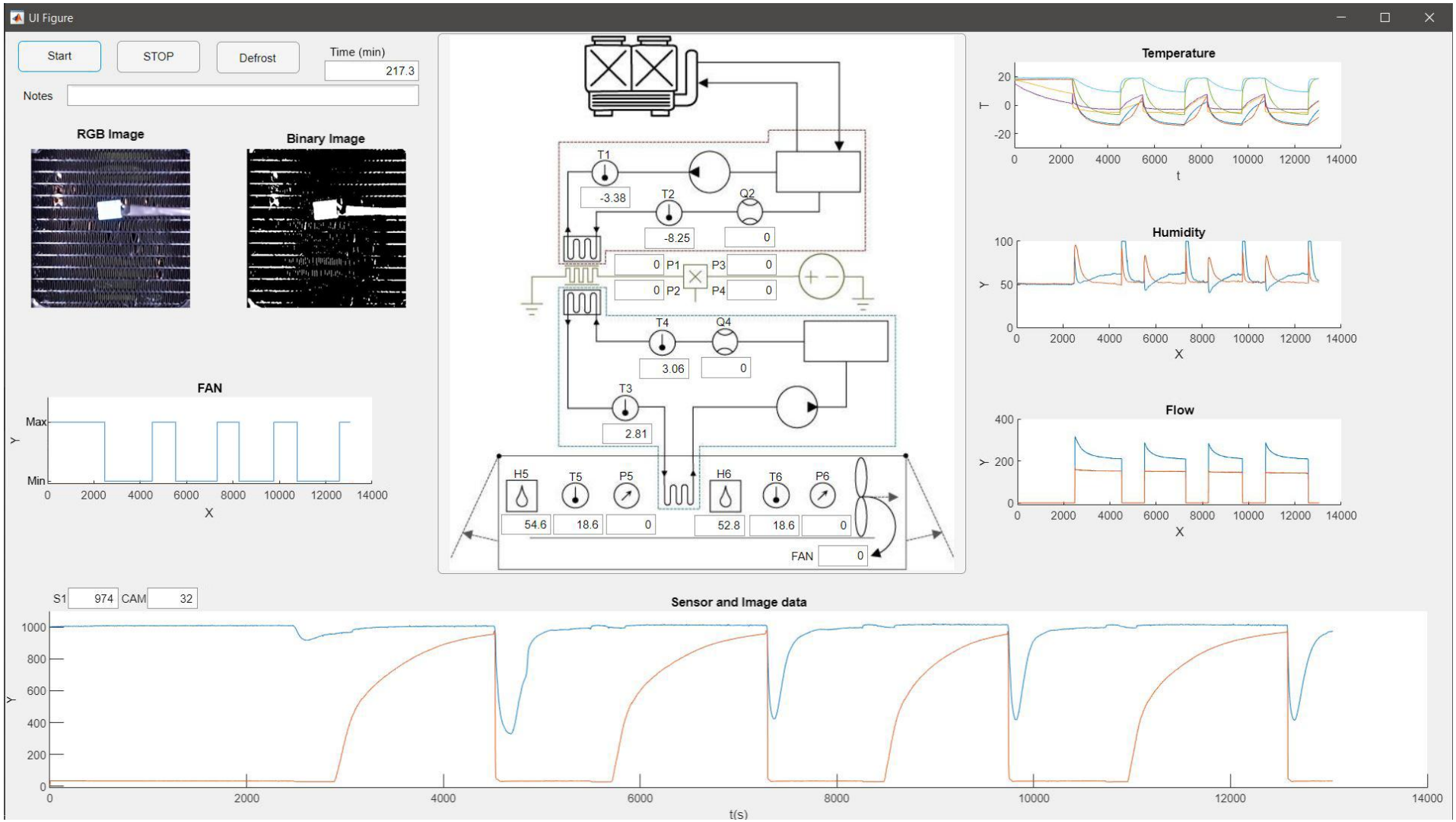

Figure 57 – Screen capture of the GUI developed in MATLAB App Designer, during a test run.

3.6. Experimental procedures

The control of the experimental setup is organized so that each subsystem operates under a well-defined scheme. The chiller is set to a fixed temperature of 6 °C, for this it must be switched on approximately one hour before testing to allow the working fluid in reservoir 1 to reach the target temperature. The chiller is only switched off after the tests are completed, requiring no further intervention in this working fluid circuit.

In working fluid circuits 2 and 3, the TE-HX modules are switched on individually when cooling is required. The pumps from both circuits are connected to the same switch (SW) to ensure they always operate simultaneously. Power to the pumps, along with the fan and lighting, is distributed through a dedicated 12 V DC accessories PSU connected to a switching board equipped with three switches, as shown in Figure 58. Besides the pump switch, the remaining two switches control the LED lighting and the fan. The fan speed is automatically set to maximum when the tunnel door is open, for defrosting and drying, and to minimum during frosting, when the tunnel door is closed.

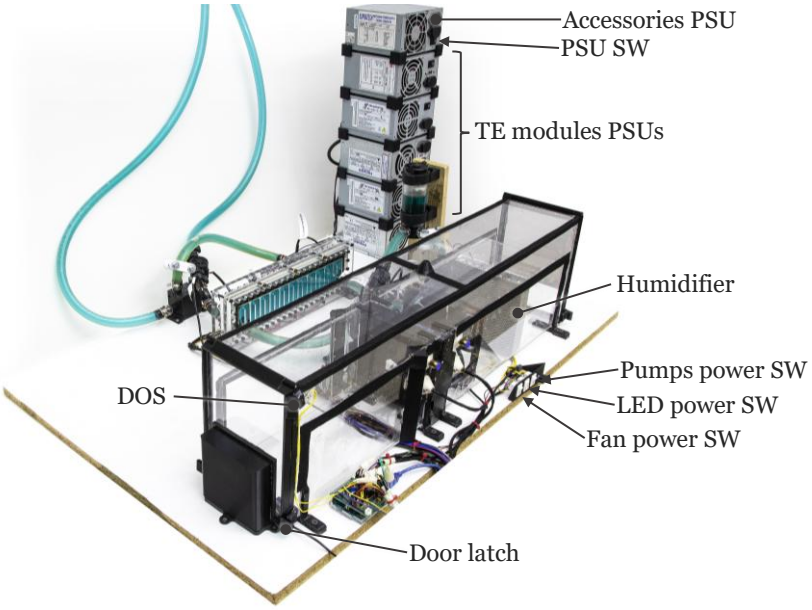

Figure 58 – Experimental setup and main controls and steps activated during test runs.

The experimental procedure, represented in the flowchart of Figure 59, begins one hour before the test with the activation of the chiller. During this waiting period, trapped air is purged from the working fluid circuit 2 and the valves are opened. The humidifier is saturated by immersion in water, so that the fabric and cavities are fully wetted.

Once the working fluid in circuit 1 reaches the target temperature, the experiment can commence. The humidifier is placed inside the wind tunnel and both doors are closed.

The CV lighting is switched on, the fan switch is activated, and data acquisition is started. Finally, the pumps are powered, followed by the TE-HX.

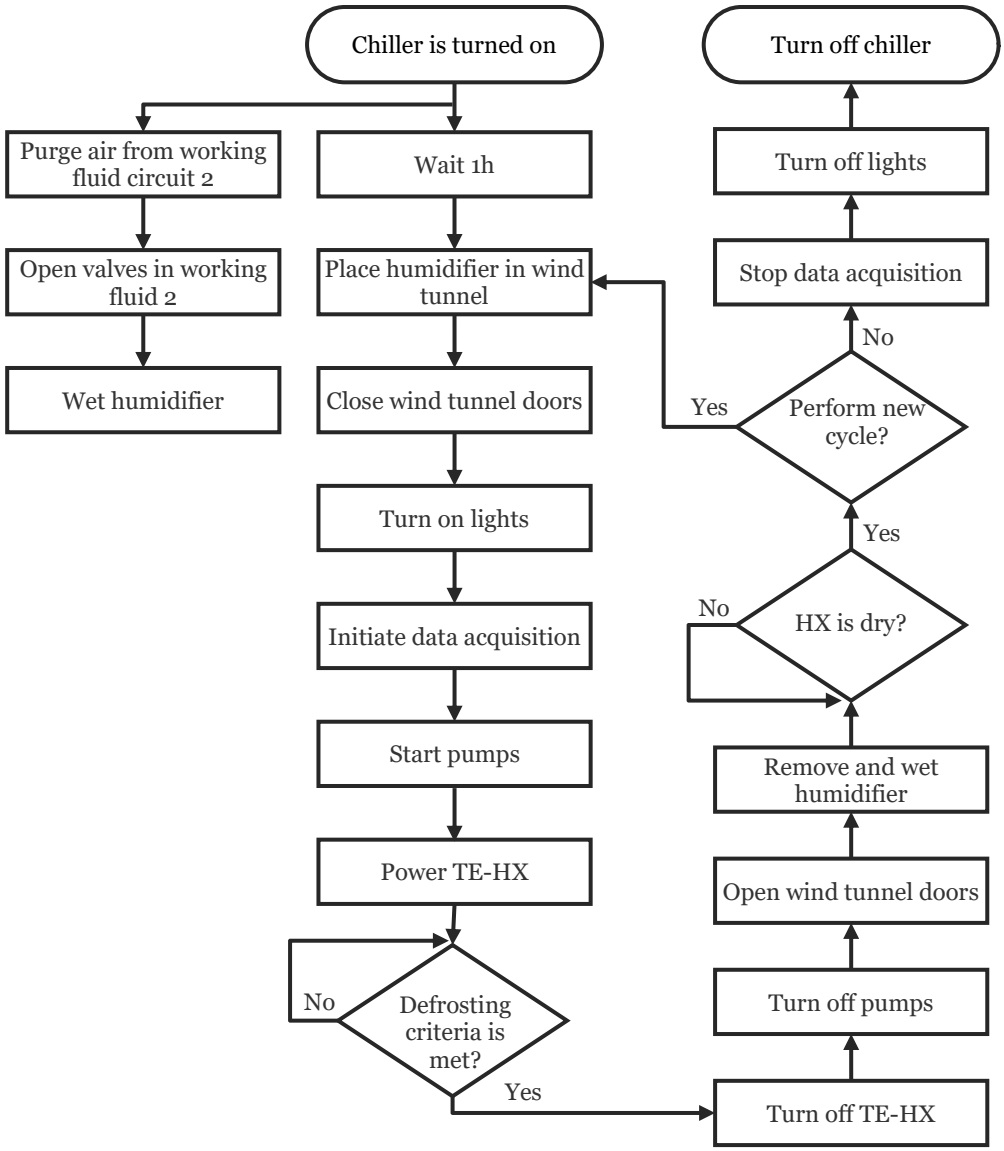

Figure 59 – Flowchart of the experimental procedure for frosting – defrosting cycles in the experimental setup.

With all the components working, frost is allowed to accumulate on the HX until one of three criteria is met, depending on the test being performed: a fixed time interval, a predetermined CV threshold, or, in the initial sensor validation tests, the visual observation of significant frost accumulation near the sensor. When the defrosting criterion is reached, the TE-HX modules and pumps are switched off, the wind tunnel doors are opened, as shown in Figure 60, and the humidifier is removed to be again saturated with water.

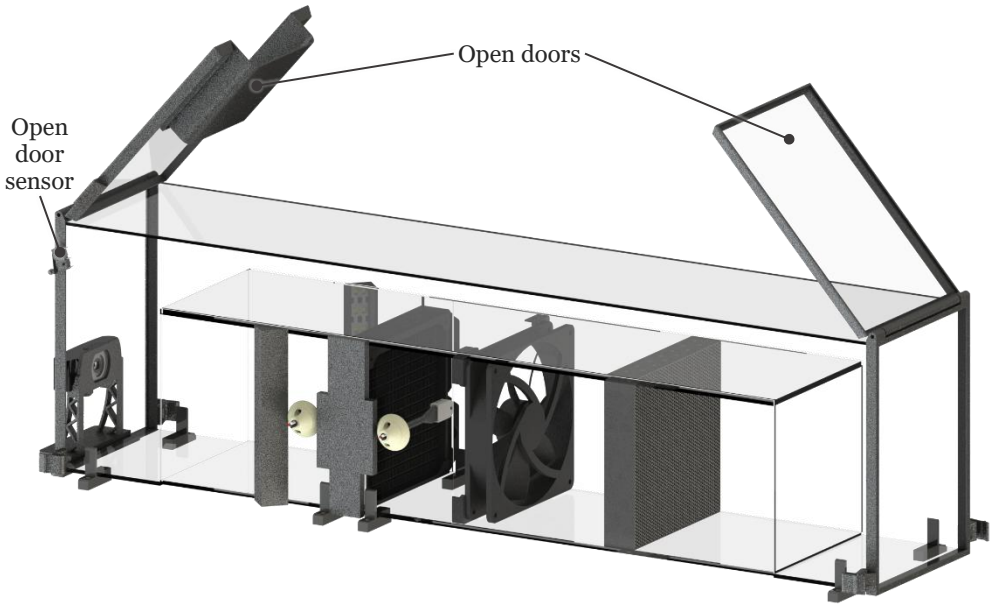

Figure 60 – Wind tunnel with both doors open, in defrosting configuration, before humidifier removal.

The open door automatically sets the fan to maximum speed, drawing warmer ambient air into the HX, which accelerates the melting of frost and the subsequent drying of the system, resetting it to a state in which the next cycle can be performed. Defrosting stops when HX is dry, which is determined to be when one of three criteria is met, depending on the test being performed: a fixed time interval, resistive sensor detects no water or dry HX is visually observed.

3.7. Data analysis

The datasets generated by the acquisition application were stored in CSV format and subsequently processed in Microsoft Excel. Depending on the objective of each experiment, post-processing ranged from simple visualization of raw signals to more structured operations, such as compiling results from multiple runs or averaging selected intervals to reduce noise and emphasize trends.

For interpretation, sensor signals were always analysed in context. The fan state was included in the plots since it switches to maximum speed whenever the tunnel door is opened, marking the onset of defrosting. These intervals were shaded in the charts so that the timing of defrosting was highlighted, because the initiation of defrosting strongly influences sensor behaviour.

Since the sensor measurements were recorded as 10-bit ADC values, ranging from 0 to 1023, this signal is referred to as the sensor-derived frost metric. When available, the computer-vision frost metric was also incorporated into the plots, enabling direct

comparison between the resistive sensor response and the actual frost observed on the HX. This combination of sensor data and visual evidence improved understanding of transient phenomena and clarified effects that were not always intuitive from the sensor signals alone. The benefits of this integrated analysis will be illustrated in the following sections.

3.8. Concluding remarks

With the frost formation setup components, supporting hardware, and acquisition procedures established, the experimental framework required to study the phenomena is now in place. The instrumentation, sensor integration, and data acquisition system provide a platform for collecting and interpreting the relevant measurements, contributing to the observation of frost–defrost cycles with sufficient detail to understand the underlying processes and to validate new sensing approaches. This concludes the development of the auxiliary setup dedicated to frost formation and monitoring. The following chapter will focus on frost sensing, through the design, development, and testing of resistive frost detection sensors.

Chapter 4

Design and development of resistive frost detection sensors

With the setup for frost generation established, this chapter shifts focus to the development of resistive frost detection sensors. Several hypotheses regarding resistive frost detection have been studied and tested, making it now opportune to examine the fundamental principles behind their operation and to present the design process that guided their evolution.

The work presented in this chapter resulted from a progressive research effort documented through several publications. The earliest contribution [117] laid the foundation for the concept, testing electrode configurations and materials under different conditions to evaluate the feasibility of resistive frost sensing. Building on this, the air-gap resistive sensor was formally developed and experimentally validated in [118], demonstrating the first successful implementation of the concept on an HX. Subsequent research explored the influence of different materials placed between electrodes on detection performance. The study in [119] compared ceramics and fabrics to enhance water retention and improve the consistency of frost detection, establishing the basis for the introduction of fabric-medium resistive frost detection sensors. These designs were further refined and validated in [120], where the fabric-medium resistive frost detection sensors were developed and tested, achieving improved sensitivity, repeatability, and robustness over previous designs. In [121], this line of research was extended through the application of AM techniques to produce AM resistive frost detection sensors. This work included the concept of Design for Additive Manufacturing (DfAM) into the sensor geometries, optimizing FDS placement and material usage to improve detection performance and energy efficiency in refrigeration systems.

Finally, the work developed in [122] investigated the electrochemical effects that affect the measurement quality and durability of resistive frost-detection sensors. It analysed the influence of electrolysis on both FDS readings and electrode integrity, and proposed mitigation strategies to reduce these effects, thereby improving the long-term reliability of the FDSs under cyclic conditions.

The characterization and validation of the resistive sensors presented in this chapter are supported by an evaluation of their measurement uncertainty. The analysis addresses the propagation of error from the primary measurements through the signal conditioning and temperature compensation algorithms. As detailed in Annex C, the standard uncertainty of the final processed signal is found to be approximately 0.15 LSB to 0.29 LSB, depending on the region of operation, confirming that the signal's stability is sufficient for the detection algorithms later applied.

4.1. Understanding the principles behind resistive frost detection sensors

The principle of resistive sensing relies on the fact that different materials exhibit distinct electrical resistivities, which vary according to their composition and physical state. By measuring the resistance and determining the resistivity, it is possible to infer the type of material present. In this context, the goal is to distinguish between water, air, ice or frost, each of which has vastly different electrical resistivities.

4.1.1. The resistivity of water in its different physical states

The resistivity of water across its different physical states can vary due to several factors, such as temperature and the presence of impurities, in addition to the physical state itself [99]. This variability is illustrated in Table 22.

Table 22 – Electrical properties of water [99].

Material	$\rho_{\min}\,[\Omega \cdot m]$	$\rho_{\max}\,[\Omega \cdot m]$
Water	$1.00E+03$	$2.00E+01$
Frost	$3.33E+08$	$3.33E+04$
Ice	$1.00E+08$	$2.00E+06$
Air	$3.33E+14$	$1.00E+09$

The table shows that the resistivity values of water, ice, frost, and air differ by several orders of magnitude, allowing for effective differentiation among them. Figure 61 represents those values visually.

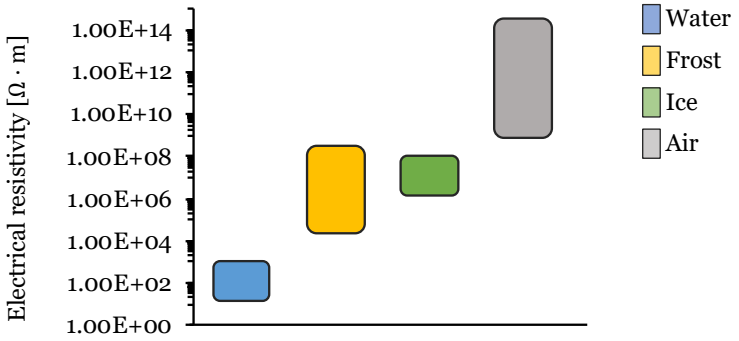

Figure 61 – Representation of the resistivity of water, frost, ice and air, based on [99].

The main challenge lies in detecting and distinguishing air, ice, and frost, as all exhibit very high resistivities and within a range of values that changes by several orders of magnitude. These resistivities vary not only with the ratio of ice crystals to air in the case of frost, but also strongly depend on temperature and the presence of impurities.

1) The water accumulated in the HX is condensed from the air and, therefore, resembles distilled water. However, impurities within the HX can rapidly increase the conductivity of the water.

Air, while having variable resistivities depending on ambient conditions, consistently exhibits much higher resistivity compared to water, ice, or frost. This makes its detection straightforward, as any measurement above a certain threshold can reliably be identified as air. The detection challenge lies mostly with ice and frost, which have resistivities that fall between those of water and air. Particularly frost, as discussed in previous chapters, is a complex structure made up of ice crystals and trapped air, with its density, and consequently resistivity, varying according to porosity, which can increase over time.

As a preliminary approach, distinguishing between water and air allows the assumption that any remaining material is likely ice or frost. The resistivity of ice also varies with temperature, which could be addressed initially by conducting tests at consistent temperatures and later incorporating temperature measurements as an input. The presence of impurities aids in frost detection, as pure ice is a poor conductor with conductivity primarily of an ionic nature rather than electronic [123].

4.1.2. Resistive sensors

The resistive sensor functions by measuring the resistance R of a given sample. This can be used to calculate the resistivity ρ_{res} of the material, along a given length L and sample cross-section area A. This resistance is given by Equation (19):

$$R = \rho_{res} \frac{L}{A} \tag{19}$$

Where:

- R is the resistance, in [Ω].
- ρ_{res} is the resistivity of the material, in [Ω · m].
- L is the length of the material, in [m].
- A is the cross-sectional area, in [m^2].

This is visually represented in Figure 62.

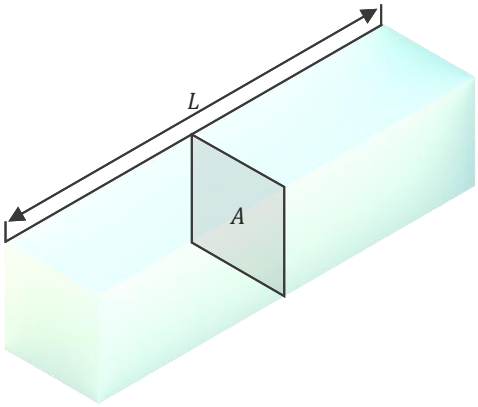

Figure 62 – Representation of L and A on a given sample of material.

To obtain the resistivity of the sample shown in Figure 62, its resistance must first be measured. For this purpose, two electrodes made of a material with high electrical conductivity should be positioned at the extremities of the L dimension, as illustrated in Figure 63.

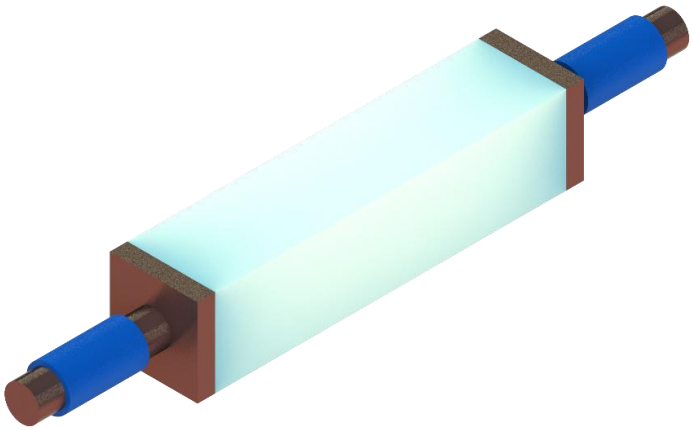

Figure 63 – Electrode placement to measure the resistivity of a given sample of material.

As the distance between electrodes is a known constant, the cross-section area does not vary as significantly as the resistivity across materials, it is safe to assume that the measured volume of a given sample between electrodes, represented in Figure 64, is constant.

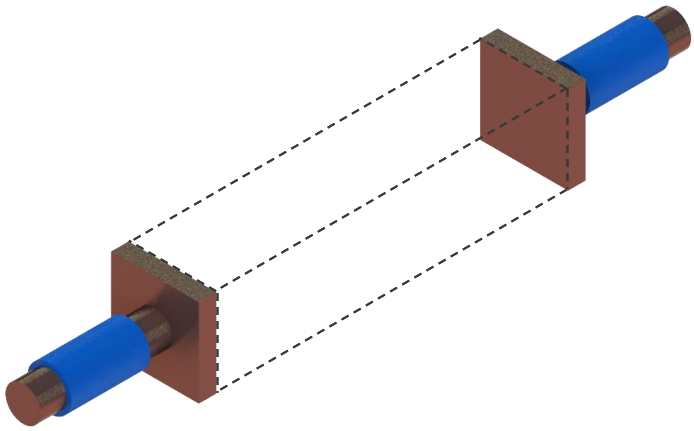

Figure 64 –Resistive FDS measured volume, which remains constant across measurements.

This constancy allows for the ratio of length L to cross-sectional area A in Equation (19) to be replaced by a constant C, which is unique to each FDS, resulting in Equation (20).

$$R = \rho_{res} \cdot C \tag{20}$$

Where:

- R is the resistance, in [Ω].
- ρ_{res} is the resistivity of the material, in [Ω · m].
- C is a constant characteristic of each FDS, given by the ratio of L to A [m^{-1}].

This indicates that for each FDS, R is directly proportional to ρ_{res}. Consequently, a simple resistance measurement will suffice to infer the resistivity characteristic for that specific FDS.

It is important to note that this relationship applies to the measured volume between electrodes. Within this volume, there could be air, water, ice, or a combination of both. In cases where a mixture is present, the resistance of the sample should indicate a transition phase or suggest that the space between the electrodes is only partially occupied by materials other than air. Given the significant differences in the resistivity of water, ice, and air, the measured resistance will tend to be closer to the resistivity of

either the less resistive material that bridges the two electrodes or the most resistive material that completely separates them. To better understand this effect, two examples are provided in Figure 65.

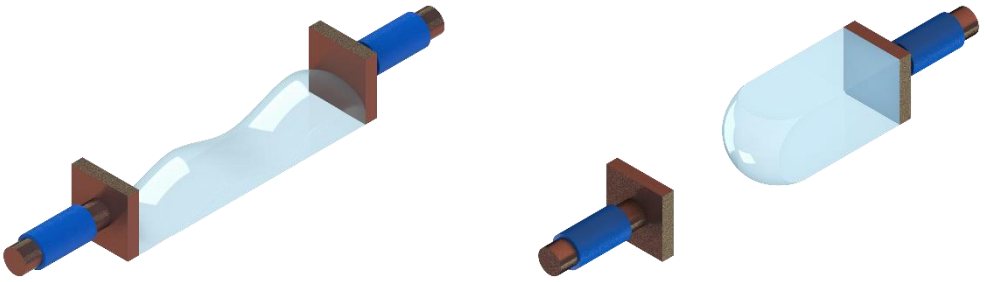

(a) (b)

Figure 65 – Representation of the measured volume with water bridging the two electrodes (a) and partially occupied by water but separated by air (b).

In the example shown in Figure 65 (a), water bridges the gap between the two electrodes, creating a continuous water connection at the bottom of the measured volume. Since water does not fully occupy the measured volume, air fills the remaining space. In this scenario, both the resistances of air (R_{air}) and water (R_{water}) form parallel connections between the electrodes, resulting in their resistances being in parallel, as represented in the equivalent circuit of Figure 66 (a).

Conversely, in the example depicted in Figure 65 (b), air connects the left electrode to a region of water, while water connects the right electrode to the same air region. Here, the resistance of the air (R_{air}) is in series with the resistance of the water (R_{water}), as illustrated in Figure 66 (b).

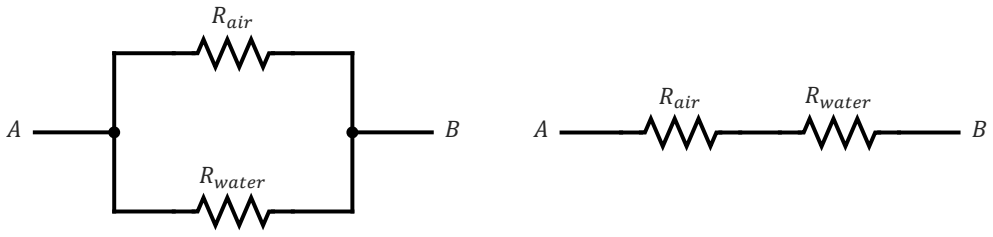

(a) (b)

Figure 66 – Representation of the electrical circuit between electrodes with air and water resistances in parallel (a) and in series (b).

This way, it is possible to calculate the equivalent resistance in both situations. For the first situation, depicted in Figure 65 (a) and Figure 66 (a), resistances are in parallel therefore Equation (21) applies.

$$\frac{1}{R_s} = \frac{1}{R_{air}} + \frac{1}{R_{water}} \tag{21}$$

When solving for R_s, Equation (22) is obtained:

$$R_s = \frac{R_{air} \cdot R_{water}}{R_{air} + R_{water}} \tag{22}$$

In which:

- R_s is the equivalent resistance within the measured volume, in [Ω],
- R_{air} is the resistance of the air parcel of the measured volume, in [Ω],
- R_{water} is the resistance of the water parcel of the measured volume, in [Ω].

Because the resistivity of water is much less than that of the air ($\rho_{res_{water}} \ll \rho_{res_{air}}$) in this case the equivalent resistance R_s will be lower, but very close to R_{water}.

On the other hand, the situation depicted in Figure 65 (b) and Figure 66 (b), displays resistances that are in series, therefore to calculate the equivalent resistance within the measured volume Equation (23) applies.

$$R_S = R_{air} + R_{water} \tag{23}$$

Because the resistivity of air is much greater than that of the water ($\rho_{res_{air}} \gg \rho_{res_{water}}$) in this case the equivalent resistance R_s will be very close to that of the air R_{air}.

This shows the importance of the FDS design, as if the electrodes do not facilitate a bridge of water deposition and frost accumulation between the electrodes, the resistance of the air will overwhelm that of the other materials and therefore render the FDS useless.

4.1.3. Resistance measuring circuit

To measure R_s, it is useful to treat it as a variable resistor. To interface this with a microcontroller capable of reading analog voltages, a circuit is needed to convert the fluctuations in R_s into corresponding voltage fluctuations. The simplest method to achieve this is through a voltage divider circuit, shown in Figure 67.

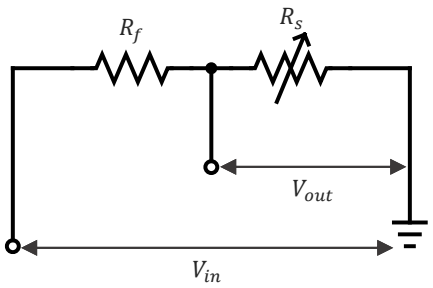

Figure 67 – Voltage divider circuit.

In this case, this circuit places a known fixed resistor (R_f) in series with the unknown R_s. The two resistors could be arranged in either order, but the configuration where R_s is on bottom was chosen as in this configuration the current flowing through the FDS electrodes is always limited by R_f, and because an increase in V_{out} corresponds to an increase in the sensor's resistivity, which simplifies direct interpretation.

The output voltage, V_{out} will be a variable fraction of V_{in}, varying according to the relation between R_f and R_s. This relation is given in Equation (24):

$$V_{out} = V_{in} \frac{R_s}{R_s + R_f} \tag{24}$$

Where:

- V_{out} is the output voltage [V].
- V_{in} is the input voltage [V].
- R_s is the variable resistance of the frost measuring sensor [Ω].
- R_f is a fixed resistance [Ω].

This setup results in a variable voltage drop across R_s to change along with its resistance. By measuring this voltage drop (V_{out}), the microcontroller can directly infer the value of R_s, calculating it by solving Equation (24) for R_s, as shown in Equation (25)

$$R_s = \frac{V_{out} \cdot R_f}{V_{in} - V_{out}} \tag{25}$$

This in turn allows for the determination of the resistivity of the material between the sensor's electrodes.

The reading of the V_{out} was performed using the Arduino's 10-bit ADC, which returns a value between 0 and 1023 corresponding to a voltage reading between $0\,\mathrm{V}$ and $5\,\mathrm{V}$. Therefore, the read voltage can be calculated from the ADC output using Equation (26).

$$V_{out} = \frac{ADC}{1023} \cdot 5 \tag{26}$$

Where:

- V_{out} is the output voltage [V],
- ADC is the raw returned value from the ADC [−].

As ADC has a linear relationship with V_{out}, it was often preferred throughout this document to use the ADC value directly instead of converting it to voltage or resistance. This approach provides a clearer understanding of the raw sensor data, resulting in more straightforward comparisons between measurements and retaining higher precision, as there is no loss of accuracy due to the conversion process.

To select an appropriate value for R_f it is important to balance the various factors that come into play in a real-world scenario. While testing different values and comparing results is often necessary to fine-tune the system, establishing a reasonable starting value is a good practice. One important consideration is that the voltage divider does not provide a linear response when measuring R_s. This non-linearity occurs because the relationship between V_{out} and R_s is not a simple linear function. As R_s changes, V_{out} changes in a non-linear way, particularly at the extremes of the ADC range. This non-linearity must be accounted for in the design and calibration of the system to ensure the most accurate measurements possible within the desired range.

To illustrate this effect, Figure 68 shows the variation of R_s with the corresponding ADC value for a 10-bit ADC. In this example, a value of 20 kΩ was selected for R_f, as it was the first value selected, as will be discussed later. Additionally, the change in R_s relative to the previous ADC value (ΔR_s) is also plotted. This represents the difference in R_s between two consecutive ADC values. This plot allows for the visualization of how much R_s changes for every increment in the ADC value, helping to understand the sensitivity of the resistance measurement in relation to the ADC output, across its range.

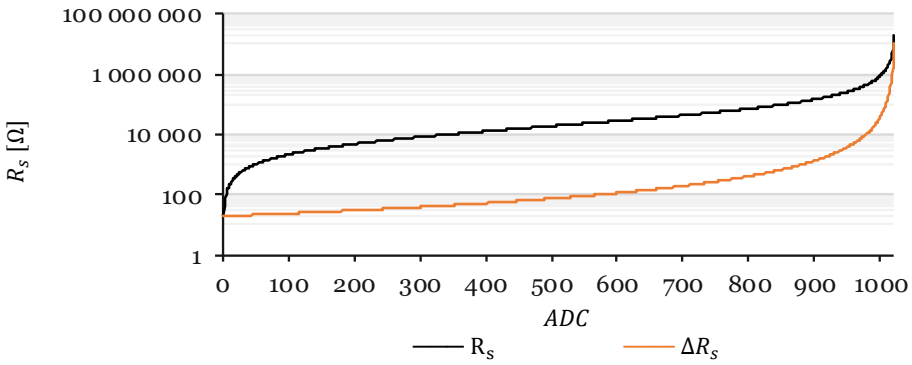

Figure 68 – Plot of R_s and ΔR_s using a 10-bit ADC and a R_f with a value of 20 $k\Omega$.

The $R_s - ADC$ curve follows an increasing, nonlinear trend that becomes sharply exponential as the ADC value approaches its upper limit. At low ADC readings, where the V_{out} is small compared to the V_{in}, the denominator of Equation (25) remains large, so the calculated R_s increases slowly and nearly linearly with ADC. As the ADC rises, V_{out} approaches V_{in}, causing the denominator to shrink and R_s to grow rapidly. Near the top of the range, this produces a steep, asymptotic rise where small changes in ADC correspond to very large changes in R_s, resulting in poor resolution for large resistances. Conversely, the low-ADC region offers better resolution for smaller resistances. This characteristic curve shape is determined by the voltage-divider equation itself and is independent of the chosen reference resistor value, which only scales the resistance axis.

The orange curve represents ΔR_s, which starts at a low value, indicating a higher measurement resolution. As the ADC value increases, ΔR_s increases in a close to exponential fashion, meaning that the changes in resistance between consecutive ADC values become more significant. However, as the ADC value reaches its higher range ($900 \leq ADC \leq 1022$), ΔR_s increases in a super exponential manner, indicating that small changes in ADC readings correspond to large changes in R_s.

This is better illustrated in Table 23, in which 5 samples of ADC increments are presented across the ADC range.

This table displays how ΔR_s for a single ADC step remains within the same order of magnitude slightly more than half the ADC range, before sharply increasing. The increase spans two orders of magnitude up to ADC values around 900 and escalates up to six orders of magnitude in the last ADC increment. This pattern reveals that the sensor offers greater resolution at lower resistance values, where small fluctuations in ADC yield minor changes in resistance. Conversely, at higher ADC values, the same fluctuations result in much larger variations in measured resistance. This behaviour must be

considered when interpreting sensor measurements, especially in the higher resistance range.

Table 23 – ADC values and respective V_{out}, R_s and ΔR_s.

ADC	V_{out} [V]	R_s [Ω]	ΔR_s [Ω]
0.00	0.00	0.00	19.57
1.00	0.00	19.57	
100.00	0.49	2166.85	24.04
101.00	0.49	2190.89	
500.00	2.44	19120.46	74.94
501.00	2.45	19195.40	
900.00	4.40	146341.46	1363.45
901.00	4.40	147704.92	
1021.00	4.99	10210000.00	10230000.00
1022.00	5.00	20440000.00	

For different values of R_f, the curve shown in Figure 68 retains its characteristic shape, but the values of R_s and ΔR_s increase for the same ADC measurement value. This allows to increase the measurement resolution for higher values of R_s, at the cost of a lower resolution for lower values of R_s.

One approach to finding the starting point for R_f that best mitigates non-linear effects and ensures better resolution is to choose an R_f value close to the geometric mean of the minimum $R_{s_{\min}}$ and maximum $R_{s_{max}}$ resistances. The geometric mean is selected because it balances the influence of both extremes—low and high resistances—on the measurement system. In a voltage divider circuit, when R_f is near the geometric mean of $R_{s_{\min}}$ and $R_{s_{max}}$, it helps maintain a more consistent voltage output range, thus improving the sensitivity and accuracy of the sensor readings across the entire range of R_s. This approach minimizes the skew that can occur if R_f is significantly lower or higher than the typical range of R_s, which could otherwise lead to poor resolution caused by the non-linearity in the sensor's response.

The formula for the geometric mean applied to this case is given in Equation (27)

$$R_f = \sqrt{R_{s_{min}} \cdot R_{s_{max}}} \tag{27}$$

Where:

- R_f is the fixed resistance [Ω].
- $R_{s_{\min}}$ is the minimum expected resistance of the FDS [Ω].
- $R_{s_{max}}$ is the maximum expected resistance of the FDS [Ω].

Given that the FDS is expected to measure values with significantly different resistances—due to the varying resistivity of water, frost, and air—an approach that prioritizes accuracy within a range of interest can be implemented. In this case, the FDS can be designed to achieve higher accuracy within this range and allow it to saturate for extreme values outside of this range.

This method can be helpful for measuring very high-resistivity materials such as air, where the FDS might struggle with precision. By allowing the FDS to saturate at these higher resistivity values, it can be assumed that air is the material between the electrodes whenever the FDS reaches these higher values. This strategy simplifies the measurement process by focusing on the range where data is most critical, while still accounting for the presence of less conductive materials.

The value of R_f is constrained by the input resistance of the Arduino, as values too close to this threshold could cause instability. Additionally, it is important to consider that higher R_f values increase the system's susceptibility to noise and parasitic currents. To enhance the sensitivity and resolution of this sensor, a higher-bit ADC could be employed, along with an operational amplifier. Furthermore, the implementation of an adaptive resistance network — a system that automatically switches R_f to the optimal value from several predefined resistors — could be used to optimize the FDS sensitivity across different ranges of R_s.

The first value for R_f will be calculated later, after the FDS design has been discussed in detail. At that stage, better estimates for $R_{s_{\min}}$ and $R_{s_{max}}$ will be available. The FDS design will provide the measured volume dimensions L and A, which, combined with the resistivity of the different materials, will allow for a more accurate estimation of R_f

4.2. Data acquisition

The data acquisition strategy was standardized across all tests to ensure the collection of comparable data. A reading interval of $\tau = 3\ s$ was chosen, allowing sufficient time for the program to cycle through all FDSs in the experimental setup, while maintaining a high acquisition rate. This allows for a thorough analysis of irregularities and fast transition phases.

4.2.1. Initial approach

For measuring and acquiring resistance data, the Arduino platform was chosen, as discussed earlier. The FDS was connected to a voltage divider, as shown in Figure 67, with the V_{in} supplied by the Arduino's 5 V port. Data readings were taken at 3 s intervals ($\tau = 3\ s$), following the flowchart outlined in Figure 69, in which t represents the timer variable used to capture the current timestamp. The high data acquisition rate was selected to capture detailed information.

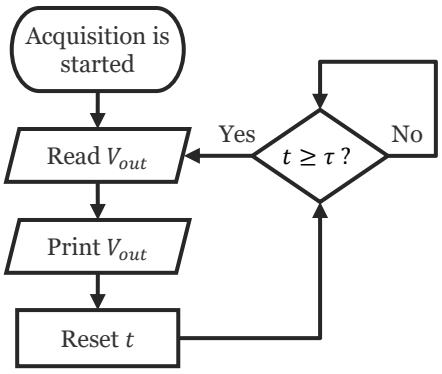

Figure 69 – Flowchart of the initial data acquisition approach.

Upon testing this acquisition method with distilled water, the FDS readings were somewhat erratic. Additionally, when the sensor was saturated with water, small bubbles were observed between the electrodes. This occurred due to electrolysis, where the applied electric field between FDS electrodes caused water to decompose into hydrogen and oxygen gases [124].

4.2.2. How electrolysis affects sensor measurements

When a voltage is applied to the sensor electrodes, the negatively charged electrode becomes the cathode, and the positively charged electrode becomes the anode. The dissociation of water molecules in an electric field between two noble metal electrodes occurs through the following chemical reactions at each electrode [124]:

- At the cathode, a reduction reaction takes place where water molecules gain electrons, producing hydrogen gas and hydroxide ions, as shown in chemical Equation (28):

$$4H_2O(l) + 4e^- \rightarrow 2H_2(g) + 4OH^-(aq) \quad (28)$$

- At the anode, an oxidation reaction occurs, where water molecules lose electrons to the anode, resulting in the production of oxygen gas and hydrogen ions, as shown in chemical Equation (29)

$$2H_2O(l) \rightarrow O_2(g) + 4H^+(aq) + 4e^- \quad (29)$$

These chemical reactions generate ions that increase water conductivity and produce gases with varying resistivities between the sensor electrodes, making the use of a resistive FDS highly impractical. To address this issue, a deeper understanding of the molecular and ionic interactions that occur between the FDS electrodes during measurements is necessary.

Naturally, H^+ and OH^- ions are present in equal but very small quantities in distilled neutral water as water molecules are more stable than their dissociated forms. They are a product of the self-ionization of water, which occurs due to interactions between water molecules. This phenomenon is described by the following chemical Equation (30):

$$H_2O(l) \rightleftharpoons H^+(aq) + OH^-(aq) \quad (30)$$

When the FDS is powered, ion migration occurs, although at a low rate due to the electrolyte being distilled (condensed) water, which has very few free ions. Ion migration refers to the movement of ions in response to the electric field generated by the applied voltage across the electrodes. When the electric field is applied, both the naturally present H^+ ions and those generated at the anode migrate toward the cathode, where they gain electrons and form hydrogen gas, as shown in Equation (31):

$$2H^+(aq) + 2e^- \rightarrow H_2(g) \quad (31)$$

Conversely, OH^- ions produced at the cathode, along with naturally occurring OH^- ions in the water, migrate towards the anode, where they lose electrons to produce H_2O, and O_2 as shown in chemical Equation (32):

$$4OH^-(aq) \rightarrow O_2(g) + 2H_2O(l) + 4e^- \quad (32)$$

Although oppositely charged ions migrate through the same medium in opposite directions between the FDS electrodes under the influence of the electric field, they typically do not combine to form water, as described in Equation (30). Instead, they continue migrating toward the electrode that attracts them, generating an ionic current. However, if the electric field ceases, the ions will tend to combine and form water, due to the reversible nature of Equation (30). This happens because without the dominant electric field, their charges will be sufficient to attract each other. This understanding lays the basis for addressing the issue, with the solution focusing on the control aspect of the FDS measurements.

4.2.3. Solving the electrolysis problem

Two methods for mitigating this effect were proposed. The first method involves using alternating polarities to power the sensor. This method alternates the electric field, causing the ions to move in both directions, to neutralize the electrolysis process, and would require some redesigning, and slightly increased complexity.

The second approach involves using Pulse Width Modulation (PWM) to control the voltage supplied to the FDS. Figure 70 illustrates how PWM is applied to V_{in}, where the voltage alternates between 'ON' (during measurement periods) and 'OFF' (during idle periods). The duty cycle represents the percentage of time the voltage is 'ON' within one period. In this approach, the FDS is powered only for short intervals, minimizing the time available for electrolysis to begin. During the longer 'OFF' periods, the ions have time to recombine into water, thereby reducing the impact of electrolysis.

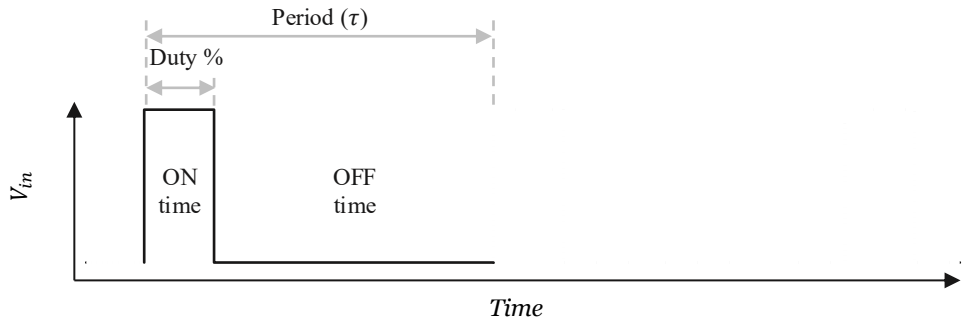

Figure 70 – PWM applied to V_{in} with a duty cycle of 20%.

This means that using this strategy, not only does electrolysis have minimal time to occur, but any products of electrolysis that do form are reversed during the 'OFF' periods.

A lower duty cycle and longer period enhance this effect. In Figure 70, a duty cycle of 20% is used for visualization purposes; however, to test this approach, the duty cycle should be minimized. Experimental iterations determined that an ON time of 50 ms was sufficient for FDS readings. This corresponds to a 1.7% duty cycle for $\tau = 3\ s$ which reduces the time the water is exposed to the electric field by 98.3%. Given the electrochemical reactions previously described, the consequences of electrolysis are expected to significantly decrease, likely beyond the proportional reduction in exposure time. The resulting 1.7% duty cycle PWM waveform is visually represented in Figure 71.

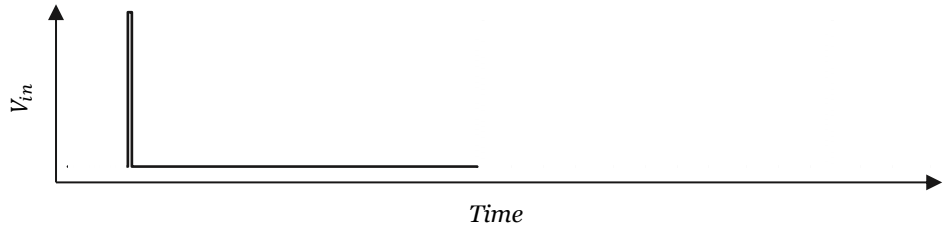

Figure 71 – PWM waveform applied to V_{in} with a duty cycle of 1.7%.

Additionally, the choice of a higher τ value further amplifies this effect. A τ in the minutes range is far more than sufficient for frost detection in any refrigeration system, reducing the duty cycle and exposure time to several orders of magnitude compared to the initial continuous reading method.

This PWM method was selected for testing due to its straightforward implementation and proven effectiveness. To apply this approach, the acquisition program was modified from the configuration shown in Figure 69 to the PWM-based FDS reading method schematized in the flowchart of Figure 72.

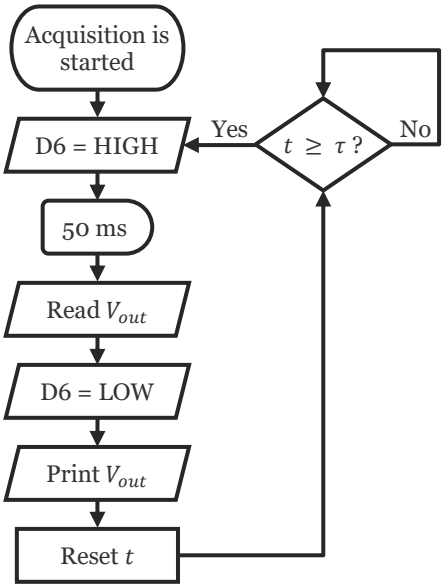

Figure 72 – Flowchart illustrating the data acquisition process with the implementation of the PWM-based FDS reading method.

In this configuration, the voltage divider V_{in} was connected to the $GPIO$ pin $D6$ instead of the Arduino's 5 V output. This pin is programmed to supply 5 V for 50 ms during each reading cycle, after which it is turned off for the remainder of the interval. Testing was conducted to validate the effectiveness of this method.

4.2.4. Experimental testing for the PWM-based sensor reading method

To validate this theory, an experiment was designed using two identical sensors, as the one shown in Figure 73. Each sensor was encapsulated in a glass flask filled with distilled water, and consisted of two parallel copper electrodes, 35 mm in length and 2.25 mm in diameter, spaced 5 mm apart. Additionally, the sensors were designed larger than the final intended size to improve the visualization of results during this analysis.

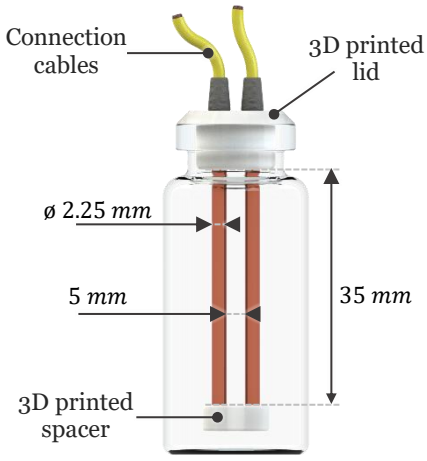

Figure 73 – Schematic of the sensor developed for testing the effects of electrolysis in the continuous vs PWM-based sensor reading method.

Copper was selected for material used as it was the most common electrode material used in the development of this work. This is due to its good electrical properties, availability, low cost, and ease to work with (shaping, and soldering). This means that, due to copper not being a noble metal, in this experiment, it is expected that more chemical reactions happen when an electric field is present, apart from those already discussed. If this sensor were to be implemented, and electrode material were to become a problem in long-term testing, noble metals could be considered.

When submerged in distilled water and no electric field is present, no reaction between copper and distilled water is expected, apart from very minor oxidation caused by the presence of oxygen due to the self-ionisation of water [125].

The two flask-encased sensors were mounted into a 3D-printed jig base to ensure proper alignment during testing, as shown in Figure 74. The sensor on the right, connected by blue cables, operated under the initial continuous-power approach, where the sensor remained powered without interruption. The sensor on the left, connected by green cables, utilized the PWM-based sensor reading method.

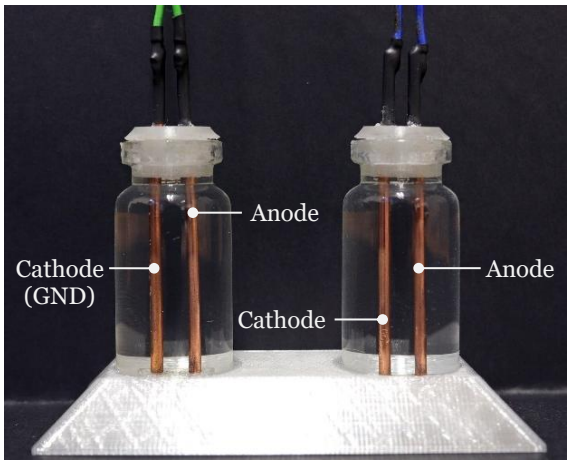

Figure 74 – Image of the experimental setup for testing the effects of electrolysis in the continuous vs PWM-based sensor reading method.

To facilitate observation, a camera was positioned on a tripod facing this setup to capture images of the sensors every 5 minutes, allowing for later analysis. A black background was used to enhance the visibility of the chemical reactions.

Data was collected via Arduino and transferred to MATLAB, which generated a CSV file for further analysis in Microsoft Excel. The data was post-processed to a 60-second interval to reduce excess data that did not contribute to the visualization of results. The experiment was conducted over a period of 5 hours and 45 minutes. The results, as shown

in Figure 75, demonstrate a clear distinction between the two sensor measurement methods.

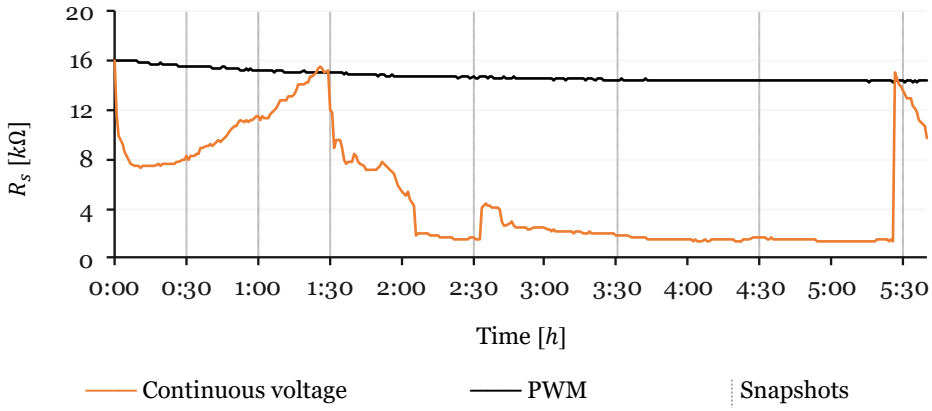

Figure 75 – Comparison of measurement results between continuous voltage sensor readings and PWM-based sensor readings.

The measurements obtained using the continuously powered sensor method were highly erratic, the resistance values fluctuated unpredictably between a maximum of 16.0 $k\Omega$ and a minimum of 1.4 $k\Omega$. The curve exhibited irregular, sharp drops and jumps, showing considerable instability throughout the measurement process.

In contrast, the PWM-based sensor reading method produced a much more stable curve, displaying a concave downward shape with a decreasing slope, showing a stabilizing tendency. The resistance started at 16.1 $k\Omega$ and gradually decreased to 14.4 $k\Omega$, where it stabilized. This behaviour may be explained by a slight increase in ion concentration that reduces water resistivity, even with the very low duty cycle. The resistivity then appears to stabilise as equilibrium is reached between ion formation during the 50 ms pulses and ion recombination as previously shown in Equation (30).

As seen in Figure 76, during testing with the PWM-based sensor method, no visible changes occurred in the electrodes or the water, a positive outcome consistent with the experiment's objectives. It should also be noted that in the top row of Figure 77, from $t = 0{:}00\ h$ to $t = 1{:}30\ h$, the time interval between pictures is $0{:}30\ h$, whereas in the bottom row, from $t = 2{:}30\ h$ to $t = 5{:}30\ h$, the interval is $1{:}00\ h$. The snapshots are highlighted in the graph of Figure 75 facilitate the analysis.

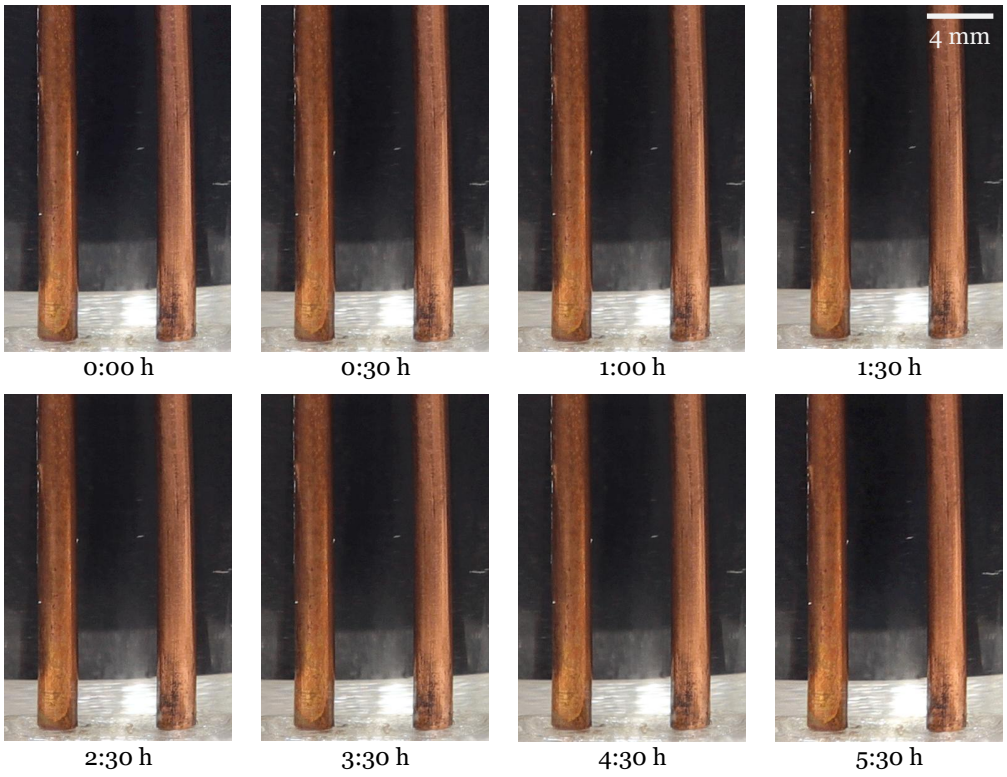

Figure 76 – Sensor electrodes during PWM-based sensor reading method.

The results from the continuously powered sensor reading method reveal markedly different outcomes, as shown in Figure 77.

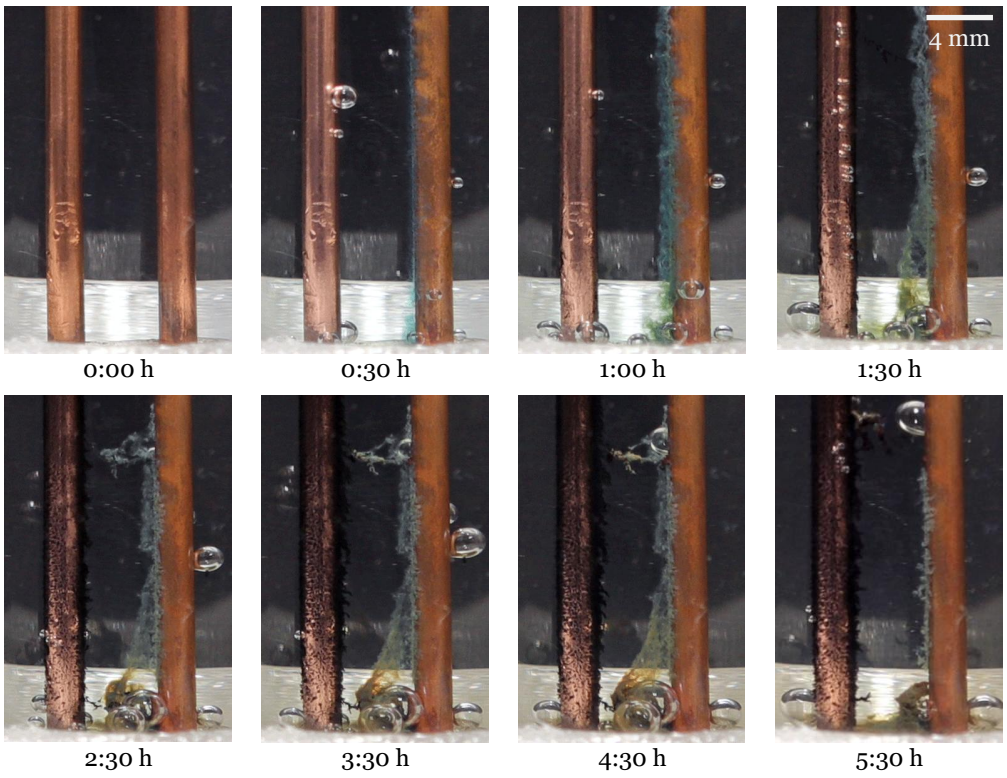

Figure 77 – Sensor electrodes during the continuously powered sensor reading method.

Multiple electrochemical reactions occur both at the electrodes and within the water, developing over time as follows:

$t = 0{:}30\ h$ At this time, gas bubbles are observed forming near both electrodes, a blue substance is noticeably present on the left side of the anode, and the cathode has developed a polished, reflective surface. All three phenomena were already present at $t = 0{:}05\ h$; however, at that earlier time, the polished surface was fully formed, while the blue substance and gas bubbles were nearly imperceptible, only becoming more noticeable around $t = 0{:}20\ h$.

$t = 1{:}00\ h$ The blue layer on the anode grows significantly, and gas bubbles production continues, but significantly more at the cathode, where hydrogen gas bubbles dislodge and flow to the surface at smaller sizes, contrary to the oxygen bubble that grows on the electrode surface. The lower part of the blue precipitate spreads to about half the distance between electrodes and starts darkening in colour.

$t = 1{:}30\ h$ The blue layer on the anode continues to expand toward the cathode and begins dislodging from the electrode, precipitating into the solution. Simultaneously, the cathode develops a progressively darker appearance as a black material starts to coat the entire electrode surface.

$t = 2{:}30\ h$ The upper portion of the blue material dislodges from the anode and connects to the top region of the cathode. The bottom section also detaches and bends toward the cathode, where it begins to darken, particularly near the cathode. Meanwhile, the black substance continues to accumulate around the cathode surface, with a more significant buildup on the side facing the anode.

$t = 3{:}30\ h$ Gas production and the formation of both blue and black materials at both electrodes nearly stop, with only slight gas production still observable at the bottom.

$t = 4{:}30\ h$ Gas production, as well as the formation of both blue and black materials, is still not observed.

$t = 5{:}30\ h$ The blue material has almost completely precipitated to the bottom, severing the connection between the cathode and anode, leaving only water between them. Gas bubble formation resumes at this stage.

It should again be noted, as seen in Figure 77, that the images in the top row of Figure 77 from $t = 0{:}00\ h$ to $t = 1{:}30\ h$, the time interval between pictures is $0{:}30\ h$, whereas in the bottom row, from $t = 2{:}30\ h$ to $t = 5{:}30\ h$, the interval is $1{:}00\ h$.

These electrochemical reactions and their impact on sensor measurements can now be compared to the sensor measured data of graph of Figure 75, noticing the snapshots marked by the vertical bars to facilitate analysis. The following explanation is based on the understanding that the materials involved are distilled water and copper under an applied voltage that creates an electric field between sensor electrodes.

Based on the observed colours of the materials deposited on the sensor electrodes—black and blue—two compounds are identified as the likely candidates. The black material is Copper (II) oxide (CuO), while the blue material is Copper (II) hydroxide ($Cu(OH)_2$) [126]. These observations help explain the electrochemical phenomena occurring during the experiment, as detailed below:

- Cathode acquires a polished, reflective surface:

As the electrodes were previously exposed to air, a thin layer of Cu_2O (Copper(I) oxide) is present on both. When the sensor is powered, electrons flow into the anode, facilitating a reduction reaction, as described by Equation (33):

$$Cu_2O(s) + H_2O(l) + 2e^- \rightarrow 2Cu(s) + 2OH^-(aq) \qquad (33)$$

Since copper without an oxide layer has a polished, metallic appearance, this reaction results in a reflective surface.

- Presence of Copper (II) Hydroxide, $Cu(OH)_2$, and Copper(II) Oxide, CuO.

When noble metals are used as electrodes, only OH^- and H^+ ions migrate between the anode and cathode. However, when copper electrodes are used, oxidation at the anode occurs, and Cu^{2+} ions form, as shown in Equation (34):

$$Cu(s) \rightarrow Cu^{2+}(aq) + 2e^{-} \quad (34)$$

These copper ions migrate toward the cathode, where they are expected to gain electrons and form copper again. However, upon encountering OH^{-} ions, they react to form $Cu(OH)_2$, as described in Equation (35):

$$Cu^{2+}(aq) + 2OH^{-}(aq) \rightarrow Cu(OH)_2(s) \quad (35)$$

This reaction occurs at both electrodes. Near the anode, Cu^{2+} ions form and migrate toward the cathode, while OH^{-} ions form at the cathode and migrate toward the anode. Due to the low voltage and current (4.2 V and 0.3 mA, respectively), there is a higher concentration of OH^{-} ions near the cathode and Cu^{2+} ions near the anode.

$Cu(OH)_2$ can remain stable in pure water without transforming into CuO. However, in the presence of OH^{-} ions (as in alkaline solutions), this transformation occurs more rapidly [126]. Under these conditions, copper ions dissolve, forming $Cu(OH)_4^{2-}$, which eventually leads to the formation of CuO, as described in Equation (36):

$$Cu(OH)_2(s) + 2OH^{-}(aq) \rightarrow Cu(OH)_4^{2-}(aq) \rightarrow CuO(s) + 2OH^{-}(aq) + H_2O(l) \quad (36)$$

This explains the presence of Copper (II) Hydroxide near the cathode and Copper (II) Oxide near the anode.

- Oxygen (O_2) and Hydrogen (H_2) Gas Bubbles

Gas bubbles formed from oxygen and hydrogen are expected, as explained in the water electrolysis reactions given in chemical equations (28), (29), (31) and (32). However, the observed oxygen production is visually lower than expected, due to the disproportionate consumption of oxygen molecules in the formation of CuO and $Cu(OH)_2$.

These reactions are the key chemical processes observed during the experiment. With this understanding, the behaviour of the curve in the continuous voltage sensor readings, shown in Figure 75, can be explained as follows:

$t = 0{:}30\ h$ Ions dissolving in the distilled water rapidly decrease the water resistivity.

$t = 1{:}00\ h$ Resistivity slowly increases as Copper (II) oxide and Copper (II) hydroxide form on the electrodes, neutralizing ions and thus increasing water conductivity.

$t = 1{:}30\ h$ Resistivity reaches a local maximum.

$t = 2{:}30\ h$ Resistivity drops abruptly as Copper (II) hydroxide dislodges from the electrode, creating a connection between the cathode and anode.

$t = 3{:}30\ h$ Resistivity remains low as electron movement occurs primarily through the bridging connection between electrodes, which halts gas production and the formation of $Cu(OH)_2$ and CuO.

$t = 4{:}30\ h$ The connection between the cathode and anode persists, keeping resistivity low, with minimal gas production and copper oxide/hydroxide formation.

$t = 5{:}30\ h$ The material bridging the electrodes detaches and precipitates towards the bottom of the flask. As the water had time for ions to cancel out, its resistivity is high, and therefore a spike in resistance is observed. Gas and ion production resume, resulting in a drop in resistivity once again.

This explanation highlights the dynamics of continuous monitoring and its impact on electrode degradation, as the anode loses copper ions during electrolysis, accelerating the deterioration process. The experiment demonstrates how the control method directly affects sensor reliability and emphasizes the need to account for the effects of electrolysis when using a resistive sensor in a water medium. The PWM control solution effectively addresses this issue by minimizing the duration in which electrolysis occurs between the sensor electrodes.

The use of noble metals would largely mitigate some of the negative effects of electrolysis, as they are far less prone to oxidising and dissolving into the water under the potentials used. Additionally, this would not significantly increase the sensor cost for most of the developed sensors. The small sensor electrodes have a volume of approximately $0.0015\ \mathrm{mm}^3$, and for a metal such as platinum, with a density of $21.45\ \mathrm{g/cm}^3$ and a 5 year historical price peak of 34.56 € on February 6th, 2021 [127], the raw material cost would amount to approximately 1.1 € per sensor electrode.

4.3. Temperature effects on resistive measurements

During frosting–defrosting cycles, the local temperature at the FDS in the present setup can vary between approximately $-10\,°C$ and $20\,°C$. The electrical pathways between electrodes are influenced not only by the phase of water, which is the primary basis of the FDS operation, but also by temperature. In aqueous environments, ionic mobility increases with temperature, leading to higher conductivity. For many dilute salt solutions and natural waters, conductivity rises by roughly 2% per °C, while for pure water the increase can reach up to 5.5% per °C. Although this variation is not strictly linear, the degree of non-linearity remains relatively small across a ΔT of 30 °C [128, 129]

Without compensation, these intrinsic temperature effects confound the interpretation of resistance variations as being solely due to phase changes (liquid water, frost, or air) bridging the electrodes. In practice, this means that changes attributed to frost formation may in fact arise from temperature-driven conductivity shifts, thereby interfering with the accuracy of the readings.

To address this, resistive sensors are commonly corrected using a linear temperature compensation model, where the measured resistance $R(T)$ at temperature T is expressed relative to a reference temperature T_{ref} as shown in Equation (37):

$$R(T) = \frac{R(T_{ref})}{1 + \alpha \cdot (T - T_{ref})} \tag{37}$$

In which:

- $R(T)$ is the resistance measured at temperature T,
- $R(T_{ref})$ is the equivalent resistance referenced to T_{ref},
- α is the temperature coefficient of conductivity, expressed in $°C^{-1}$,
- T is the local temperature at the FDS,
- T_{ref} is the chosen reference temperature for normalization.

To apply the compensation model, the temperature coefficient of conductivity, α, must be determined. For this purpose, a test was performed in which the system was turned on gradually, ensuring that no condensation occurred on the FDS surface. In this way, the variation of the electrical signal could be attributed solely to temperature effects.

Figure 78 shows the evolution of the resistance ratio during this test. The ratio r was calculated according to Equation (38) and used instead of raw ADC values, since compensation must be applied in resistance space rather than directly on ADC counts.

$$r = \frac{ADC}{1023 - ADC} \tag{38}$$

While this reduces the intuitive readability of the signal, it provides the correct basis to apply the compensation equation and to extract α.

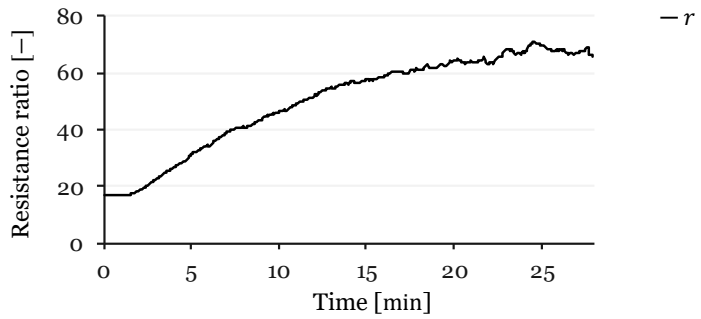

Figure 78 – Evolution of r during a controlled cooling test.

During this same test, the temperatures were recorded at four locations of the HX setup: $TA1$, the air inlet temperature, $TA2$, the air outlet temperature, $TWF1$, the working fluid AL-HX inlet temperature, and $TWF2$, the working fluid AL-HX outlet temperature. These measurement points are illustrated in Figure 54 of the Frost formation experimental setup chapter, and their evolution over this test is shown in Figure 79.

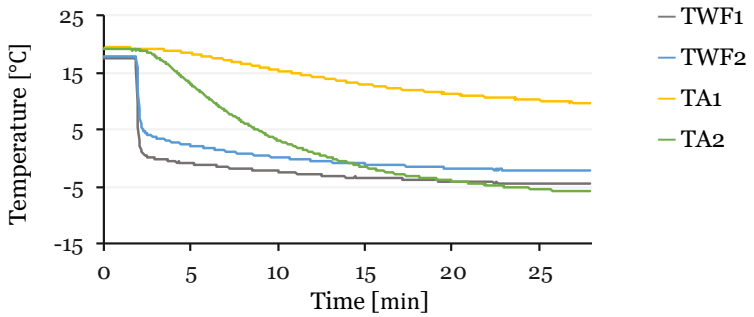

Figure 79 – Temperature profiles during the controlled cooling test.

To quantify the influence of these temperatures on the FDS output, a regression data analysis was performed in Microsoft Excel using the four temperature variables as predictors and the resistance ratio as the dependent variable. The results of this regression are summarized in Table 24.

Table 24 – Regression coefficients for four-temperature model.

Variable	Coefficient	Std. Error	t Stat	P-value	Lower 95%	Upper 95%
Intercept	81.03	0.98	82.49	<0.001	79.1	82.96
TWF1	0.3	0.12	2.44	0.02	0.06	0.54
TWF2	-0.66	0.15	-4.28	<0.001	-0.96	-0.36
TA2	-1.06	0.04	-28.51	<0.001	-1.13	-0.99
TA1	-1.92	0.06	-29.57	<0.001	-2.05	-1.79

The regression analysis using the four temperature points indicates an excellent fit, with $R^2 = 0.998$, Adjusted $R^2 = 0.996$, $F - statistic = 38417$, and a $standard\ error$ of 1.00. These results confirm that the combined influence of these four temperature measurements explains nearly all the variance in the resistance ratio signal. The resulting regression model can be expressed as shown in Equation (39):

$$\hat{r} = 81.03 + 0.30 \cdot TWF1 - 0.66 \cdot TWF2 - 1.06 \cdot TA2 - 1.92 \cdot TA1 \qquad (39)$$

This equation was then used to compute the predicted resistance ratio and compared to the measured resistance ratio, with results shown in Figure 80. The two curves overlap almost entirely, with the predicted signal appearing as a smoothed version of the measured resistance. The only significant divergence occurs briefly at minute two, where the regression exhibits a slight momentary drop. This behaviour coincides with the abrupt decrease in working fluid temperatures observed in Figure 79 during system startup. Aside from this transient deviation, the predictive model closely reproduces the measured FDS response.

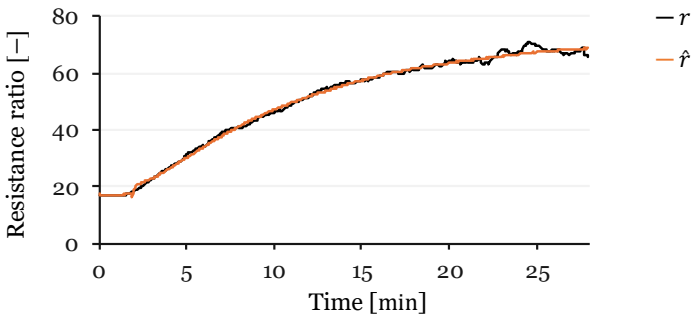

Figure 80 – Measured vs. predicted resistance ratio using four-temperature regression model.

In practical applications, the use of multiple auxiliary temperature FDSs increases system complexity, cost, and the likelihood of maintenance issues. For a resistive FDS to be more applicable in real-world systems, it must remain as simple as possible while still

providing effective compensation for temperature effects. Therefore, the strategy was to reduce the number of input variables and assess whether a single representative temperature could provide a sufficiently accurate correction.

Among the four available measurements, $TA2$ was selected to be tested as the sole predictor. This choice is justified as the outlet air temperature reflects the combined effect of both the inlet air temperature and the refrigerant-side surface temperatures of the HX. The FDS itself is subject to these same interactions, making $TA2$ physically more representative of the conditions influencing the FDS resistance. This is reflected in the temperature plots of Figure 79, where the outlet air temperature is the measurement that most closely resembles the profile of the resistance ratio during the test. A linear regression was performed using only TA2 as the predictor variable and the resistance ratio as the response variable. The regression outcomes are presented in Table 25:

Table 25 – Regression coefficients for the $TA2$ model.

Variable	Coefficient	Std. Error	t Stat	P-value	Lower 95%	Upper 95%
Intercept	55.3	0.07	757.81	<0.001	55.16	55.44
TA2	-1.97	0.01	-237.51	<0.001	-1.99	-1.95

Despite relying on a single predictor, the model exhibits excellent fidelity, with $R^2 = 0.995$, Adjusted $R^2 = 0.990$, $F - statistic = 56411$, and a $standard\ error$ of 1.65, showing only a modest loss compared to the four temperature model. The model still captures most of the variability in the signal. The resulting regression model for this simplified approach is given in Equation (40).

$$\hat{r} = 55.30 - 1.97 \cdot TA2 \tag{40}$$

The comparison of the measured resistance ratio with the values predicted by the regression model based solely on TA2 is shown in Figure 81. The predicted curve closely overlaps the experimental data, with discrepancies largely within the measurement noise and comparable to the four-temperature model.

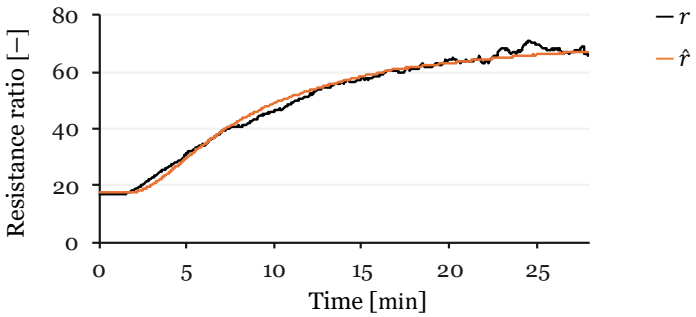

Figure 81 – Measured vs. predicted resistance ratio using TA2-only regression model.

From the simplified regression using outlet air temperature as the sole predictor, a slope of $\beta = -1.97$ (resistance ratio per °C) was obtained in the model $\hat{r} = a + \beta T$. Because temperature compensation is applied in resistance space, the relevant temperature coefficient is the logarithmic sensitivity of the resistance ratio to temperature, defined in Equation (41).

$$\alpha \equiv \frac{1}{\hat{r}} \cdot \frac{dr}{dT} \tag{41}$$

With $dr/dT = \beta$ from the regression, the temperature coefficient follows directly as shown in Equation (42).

$$\alpha = \frac{\beta}{\hat{r}} \tag{42}$$

This expression was not fixed at a single reference point but instead evaluated for each data point using Equation (43).

$$\alpha(ADC) = -1.97 \cdot \frac{1023}{ADC \cdot (1023 - ADC)} \tag{43}$$

To ensure reliable values, only points satisfying $ADC < 990$ and $TA2 > 2$°C were considered. The first condition excludes cases where the ADC output approaches saturation, since at very high values of ADC the resistance ratio tends to diverge and amplifies numerical noise (which is seen for higher values of r in Figure 78). The second condition imposes a margin above the freezing point, so that the measured variations can be attributed solely to the intrinsic conductivity of liquid water. The 98 valid $\alpha(ADC)$

values were then averaged to obtain the representative coefficient for temperature compensation of $\alpha = -0.045\ °C^{-1}$.

This result is expected, as it lies between the typical values for aqueous films of $-0.02\ °C^{-1}$ and the value for aqueous films of ultrapure water of $-0.055\ °C^{-1}$. Because the water on the sensor is condensed rather than ultrapure, trace impurities such as dissolved CO_2, surface ions or particulate residues increase baseline conductivity and its temperature sensitivity, placing the coefficient toward the more negative end of that interval. The negative sign reflects that, as temperature rises, conductivity increases and the measured resistance decreases.

With α determined, the remaining parameter to obtain in Equation (37) is T_{ref}. It should be chosen near the temperatures of greatest interest, which corresponds to where the signal is in the window of frost nucleation, minimizing both linearization error and noise amplification by the compensation factor. However, the denominator in Equation (37) must not be zero. To improve numerical robustness, a safety margin over the operating range was determined to be m = 0.2, so that Equation (44) is true:

$$1 - \alpha \cdot \left(T_{max} - T_{ref}\right) \geq m, \qquad \left(m \in (0,1)\right) \tag{44}$$

This can be rearranged to Equation (45):

$$T_{ref} \geq T_{max} - \frac{1 - m}{\alpha} \tag{45}$$

Which can be calculated for a $T_{max} = 20°C$ and an $\alpha = -0.045$ to return the value of $T_{ref} = 2.22\ °C$. From this, the corrected resistance is obtained from Equation (46):

$$r_{corr} = \frac{r}{1 + \alpha(T - T_{ref})} \tag{46}$$

Which is calculated from ADC values as shown in Equation (47):

$$r_{corr} = \frac{\frac{ADC}{1023 - ADC}}{1 - 0.045 \cdot (T - 2.22)} \tag{47}$$

And can be solved for ADC so that Equation (48) returns the temperature compensated ADC reading:

$$\widetilde{ADC} = \frac{1023 \cdot ADC}{\left(1 - 0.045 \cdot (T - 2.22)\right) \cdot (1023 - ADC) + ADC} \tag{48}$$

This formulation provides a means of converting raw ADC readings into temperature-compensated values. While the compensation does not fully eliminate the complex thermally induced effects present in aqueous films, it reduces their influence and isolates the resistance changes to phase transitions.

In later chapters, this $\widetilde{ADC}$ signal is used as the input for frost-detection algorithms based on the FDS, so that the triggering logic responds primarily to frost nucleation and growth rather than to temperature-driven conductivity shifts.

With the principles affecting frost detection, data acquisition procedures and the respective strategies for compensation defined, the next step is to address the design considerations for resistive FDS.

4.4. Sensor design considerations

The most straightforward solution for resistive frost sensing involves using a two-electrode FDS in the configuration shown in Figure 82 (a). It becomes a variable resistor, whose resistance (R_s) varies according to the resistivity of the medium between electrodes, as represented in the overlaid circuit of Figure 82 (b).

This FDS is positioned at the intake end of the AL-HX, and when the electrode temperature falls below the dew point, condensation will occur on its surface.

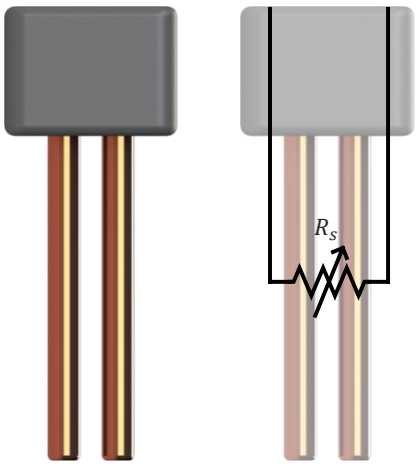

Figure 82 – Simplified representation of the FDS (a) with overlaid circuit representation (b).

If the electrodes are placed close enough together, as shown in Figure 83 (a), water will bridge the gap between them, as shown in Figure 83 (b) thereby decreasing the FDS overall electrical resistance. Should this water freeze, as illustrated in Figure 83 (c), the FDS electrical resistance will increase due to the lower electrical conductivity of ice. After defrosting, and before condensation, when the HX is dry, only air is between the FDS electrodes, and this is when resistivity is expected to be the highest.

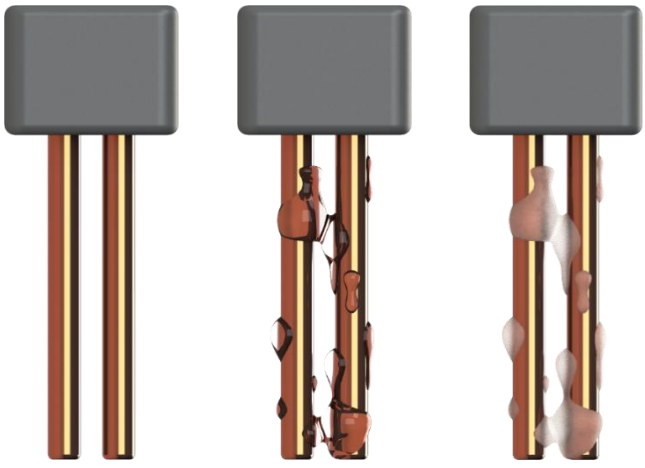

Figure 83 – Basic FDS (a) with the accumulation of water (b) and phase change of this water to ice (c).

From this short analysis some design choices are important to consider: the electrode material, the distance between electrodes, the number of electrodes, electrode shapes and FDS placement.

4.4.1. Electrode material

The two primary requirements for the electrode material are high thermal and electrical conductivity. Once the electrical conductivity is compared to that of the surrounding

media, which is ice, distilled water, or air, the specific choice of metal becomes less critical, as most common conductive metals exhibit similarly high conductivity relative to these materials. At least one electrode must be electrically insulated from the HX, as many HXs are made of bare metal and thus electrically conductive. The electrode temperature needs to be as close as possible to that of the HX surface to ensure that its surface reflects the conditions of the HX, in terms of condensation and frost formation. To achieve this, the electrode material must be a good conductor of heat and close to the HX surface. Additionally, the electrode must be exposed to frost and moisture so that electrical conductivity between the electrodes is possible when a bridge is formed by water droplets resulting from condensation. For this bridge to form, the electrodes must be positioned close enough to allow the condensation droplets to span the gap between them. In some sensor configurations, additional medium materials were used to improve this effect.

4.4.2. Distance between electrodes

The distance between electrodes is an important factor in the design of the resistive frost detection sensors. First, the distance must be close enough to allow condensation droplets to bridge the gap between the electrodes before precipitating, as illustrated in Figure 84 (a). If this distance is too large, droplets may form on the electrodes but fail to bridge them, resulting in a FDS resistivity close to that of air (as previously represented in Figure 65 (b) and Figure 66 (b)). This scenario, depicted in Figure 84 (b), would cause the FDS resistance to be very high, incorrectly indicating the absence of water.

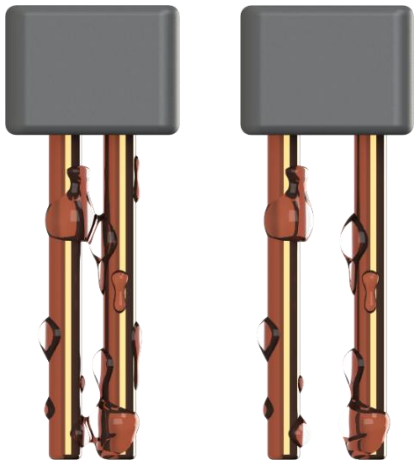

(a) (b)

Figure 84 – Impact of electrode distance in allowing (a) or not allowing (b) the formation of condensation droplets to bridge the gap between electrodes.

Another important consideration is that the FDS resistance should not be so high that it becomes difficult to read, as this would complicate the data acquisition system, which is

intended to be simple and low-cost. Reducing the distance between electrodes decreases the length L of the measured volume, which, as shown in Equation (78), results in lower FDS resistance for a given resistivity. This way, a shorter distance between electrodes has the added benefit of improving the readability of the FDS.

Finally, the electrode spacing also affects the overall FDS size. One of the design goals is to maintain a low footprint, enabling placement in tight spaces between HX fins without significantly impacting HX performance. Closer electrodes lead to a smaller sensor, which aligns with this objective. However, this spacing is constrained by the need to maintain a safe distance between electrodes to prevent them from touching and creating an unintended connection. Ensuring this safe distance allows the sensor to measure conductivity without forming a direct electrical connection between the electrodes.

4.4.3. Number of electrodes

The number of electrodes is not a critical factor in the design of frost detection sensors, but it can enhance their accuracy. The minimum requirement is obviously two electrodes, as depicted in Figure 85 (a), even if one electrode is the HX itself. Adding more electrodes, as shown in Figure 85 (b), has the potential to increase the sensor surface area where condensation and frost formation can occur, and it increases the cross-sectional area (A), which according to Equation (78), results in lower resistance.

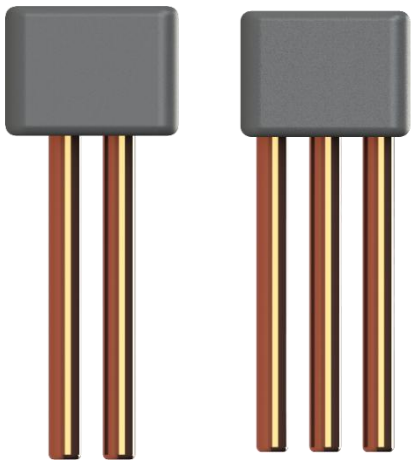

(a) (b)

Figure 85 – Sensor with two (a) and three (b) electrodes.

If more than two electrodes are used, they should be connected in an alternating pattern. This is so that each electrode is adjacent to another electrode to which it is not wired. However, it is important to consider that increasing the number of electrodes will also enlarge the overall footprint of the sensor.

4.4.4. Sensor placement

Regarding sensor placement, all FDS configurations were installed at the intake end of the HX, as this area is most susceptible to frost formation. Three distinct position-oriented sensor configurations were hypothesized, as illustrated in Figure 86.

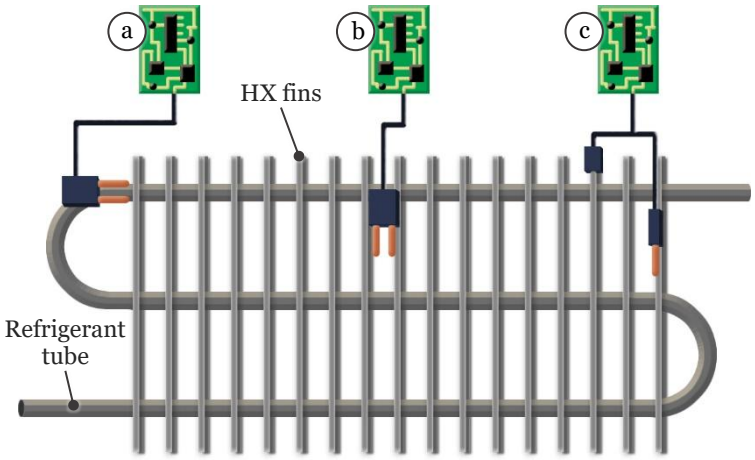

Figure 86 – Three different position-oriented sensor configurations.

The configuration shown in Figure 86 (a) involves placing the FDS in the refrigerant tube. This can be done either among the fins or outside the finned region. In this configuration, the sensor benefits from being in contact with the colder refrigerant tube, which partially compensates for losses in heat transmission and approximates the FDS temperature to that of the HX surface. When within the finned region, the sensor directly measures frost formation in the HX surface, though there is the drawback of positioning the electrodes slightly below the intake surface of the HX, leading to exposure to air that is marginally less humid and at a slightly lower temperature. Additionally, while the FDS has a small footprint, together with the wiring, it still affects the airflow through the HX. If the sensor is placed outside the finned region, as seen with the TEPS sensor [97], it avoids disturbing the airflow but may not fully represent the HX surface in terms of frost formation. However, as proven by the results achieved by the TEPS sensor, this can be effective if a relationship between frost formation in the refrigerant tube and the rest of the HX is set up.

The configuration shown in Figure 86 (b) involves a module with two (or more) electrodes, like configuration (a), but placing it between or on the HX fins. This sensor configuration improves contact with the intake air, which results in more pronounced condensation and frost formation. However, to improve measurements, the sensor electrodes must be at a temperature close to that of the fin surface at the HX front end. Despite its benefits, this configuration causes the greatest disturbance in airflow, so the sensor must be made as compact as possible to mitigate this issue.

The configuration shown in Figure 86 (c) is a compact adaptation of the configuration shown in (b). It uses the HX itself as one of the electrodes, requiring only a single additional electrode in the HX, reducing the number of minimum applied electrodes by half. This configuration offers the advantage of directly using the HX, however it connects the whole refrigeration system to the acquisition circuit. This setup only requires a single electrode to be placed for the detection of condensation and frost formation on its surface, as the HX itself serves as the second electrode. This configuration also requires more complex installation procedures due to the connection of the HX to the sensor's circuit. The most common configuration developed and tested was the configuration shown in Figure 86 (b) for its good balance of simplicity, ease of installation and accuracy.

4.4.5. Medium material between electrodes

Another technique employed to enhance FDS accuracy was the introduction of various medium materials between the sensor electrodes. These different mediums were theorized or tested with the objective of mitigating challenges encountered during the sensor's development. The mediums are classified as shown in the diagram in Figure 87.

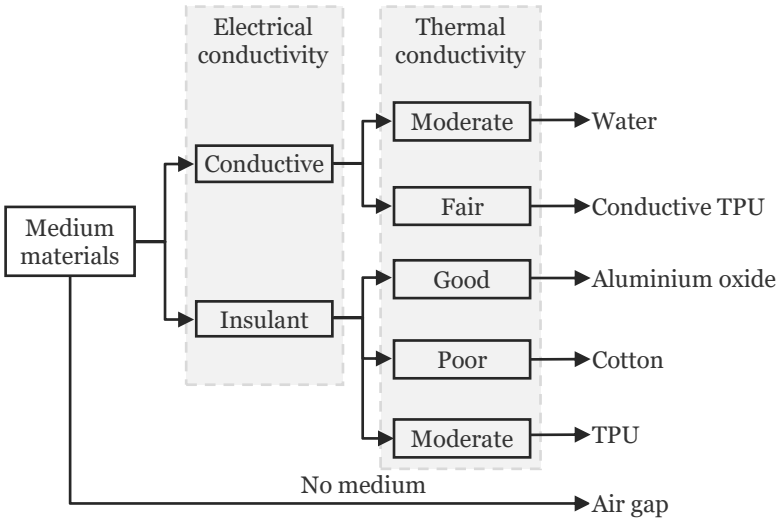

Figure 87 – Diagram of the classification of medium materials tested.

This classification is helpful when designing resistive frost detection sensors as the electrical conductivity of the medium directly affects the resistance measured by the sensor, while the thermal properties of the medium influence the sensor's temperature, impacting condensation and frost formation on its surface, where detection occurs. These factors will impact the sensor design, as strategies for using or mitigating medium properties must be utilized. Figure 88 presents a simplified representation of the FDS sensors incorporating the mediums previously described.

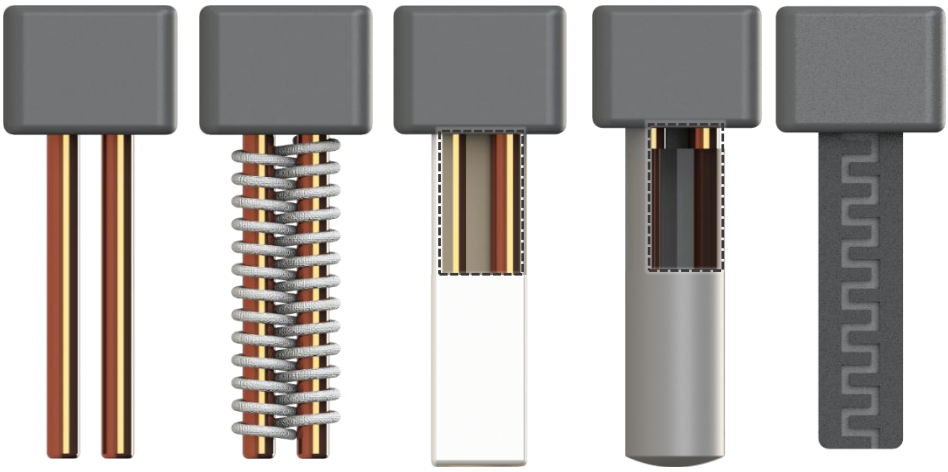

(a) (b) (c) (d) (e)

Figure 88 – Representation of different mediums used in the development of resistive sensors, for the Air Gap Resistive Sensors (a), Fabric-Medium Resistive Sensors (b), Ceramic-Medium Resistive Sensors (c), Encapsulated Water Resistive Sensors (d) and Additively Manufactured Resistive Sensors (e).

The FDS, as discussed thus far, operates with air as the primary medium between the electrodes when water and frost are not present. Therefore, the bare electrodes remain exposed, and this type of sensor will be designated as an Air Gap Resistive Sensor (AGRS), represented in Figure 88 (a). However, when a small distance between electrodes is insufficient to reliably accumulate water or when additional resilience against interferences such as vibrations—which may cause water droplets to precipitate—is needed, a medium material can be introduced between the electrodes.

For instance, a string of porous, electrically insulating material, such as a cotton fabric, can be intertwined between the sensor electrodes, as shown in Figure 88 (b). This material serves the purpose of capturing moisture from the electrodes and surroundings and bridging the electrodes through capillarity. However, since this material typically does not conduct heat well, it may act as a thermal insulator and decrease condensation on the electrode surfaces. To mitigate this, a porous, high-resistivity material with a good thermal conductivity, such as a porous alumina (Al_2O_3), ceramic can be used. In this scenario, represented in Figure 88 (c), the electrodes (seen in the cut section within the dashed line) are embedded within the ceramic body.

To eliminate the sensor's dependence on moisture accumulation, an encapsulated sensor was also conceptualized. This Encapsulated Water Medium Resistive Sensor (EWRS) can be configured with either a single electrode—where the capsule itself serves as the second electrode or with two internal electrodes. As the development of this sensor was not fully pursued, its development is only approached in the Complementary Works section of the Conclusions and Future Works chapter.

Finally, the last proposed sensing medium consists of a flexible, electrically insulating polymer base, on which a flexible, electrically conductive polymer layer is printed to form the electrodes. Fabricated via multi-material FFF AM using the Filaflex 95A [130] and the Conductive Filaflex [131] material, which is a TPU filled with carbon nanoparticles, produced by Recreus. This Additively Manufactured Resistive Sensor (AMRS), shown in Figure 88 (e), replaces metallic electrodes with a conductive polymer, enabling more complex geometries thanks to the flexibility and precision of the AM process. In this configuration, the absorption of water or the presence of frost within the interstitial spaces between the printed electrodes alters its resistivity. This approach improves sensor reproducibility and design freedom for miniaturized components.

4.5. Resistive sensor technologies developed and tested

Although the previously discussed design considerations were accounted for in each sensor iteration, sensors were categorized based on the medium placed between the electrodes. Table 26 compiles the sensor designations and corresponding references, which will be used onward to refer to each of the developed FDS or FDS family.

Table 26 – Compilation of references given to the sensors developed and tested within this thesis.

Reference	Designation
Air Gap Resistive Sensors	
AGRS1	Air Gap Resistive Sensor No. 1
AGRS2	Air Gap Resistive Sensor No. 2
AGRS3	Air Gap Resistive Sensor No. 3
AGRS4	Air Gap Resistive Sensor No. 4
AGRS5	Air Gap Resistive Sensor No. 5
AGRS6	Air Gap Resistive Sensor No. 6
Fabric-Medium Resistive Sensors	
FMRS1	Fabric-Medium Resistive Sensor No. 1
FMRS2	Fabric-Medium Resistive Sensor No. 2
FMRS3	Fabric-Medium Resistive Sensor No. 3
FMRS4	Fabric-Medium Resistive Sensor No. 4
FMRS5	Fabric-Medium Resistive Sensor No. 1
Encapsulated Water Resistive Sensors	
EWRS1	Encapsulated Water Resistive Sensor
EWRS2	Encapsulated Water Resistive Sensor
Ceramic-Medium Resistive Sensors	
CMRS	Ceramic-Medium Resistive Sensor
Conductive Polymer Resistive Sensor	
AMRS1	Additively Manufactured Resistive Sensor No. 1

Sensor development followed the order in the table, and began with the AGRS family, which served as the foundation for the development of all other sensors by incorporating medium materials to address issues identified during their development and testing.

4.6. Testing and evaluation procedures

Testing performed in this chapter was conducted before the implementation of an external verification metric based on CV. Consequently, sensor performance was assessed visually, with defrost cycles manually triggered when significant frost accumulation was observed on the HX surface. At this stage, the data presented correspond to uncompensated raw measurements.

Electrolysis mitigation using PWM-based control was also not yet implemented. While this may introduce some erratic behaviour in the signal during water phases, these effects were not sufficient to compromise the overall assessment of sensor viability. As later confirmed, electrolysis influenced short-term signal stability but did not alter the classification of sensors as viable or non-viable, because these sensors are not submerged in water except partially for short periods during defrosting.

The number of tests performed for each sensor was not fixed but adapted dynamically according to performance. Sensors that demonstrated consistent and repeatable detection were subjected to more extensive testing to confirm reliability, whereas those showing poor or inconsistent response in early trials were discontinued sooner. A performance threshold equivalent to successful detection in at least four out of five tests was considered indicative of acceptable repeatability. Sensors failing two or more detection tests were excluded from further development.

The development methodology for these sensors followed an iterative design-test-analyse cycle. Each sensor prototype was designed, fabricated, and subjected to functional testing until exclusion. The underlying causes of failure were then analysed, leading to a redesign aimed at mitigating identified limitations. This iterative process was repeated as necessary.

4.7. AGRS - Air Gap Resistive Sensors

AGRS consist of two or more electrodes separated by nothing but air, as represented in Figure 89.

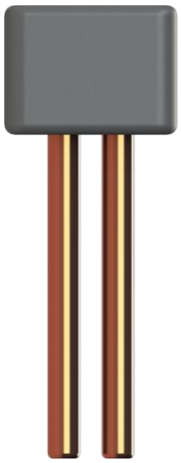

Figure 89 – Simplified representation of a two-electrode AGRS.

As previously described, they rely on water condensation bridging the electrodes and later freezing on their surface to change the overall sensor resistance, which is measured to detect the presence of frost.

4.7.1. AGRS1

The AGRS1 was the first sensor designed and tested within this work and is represented in Figure 90. It follows the simplistic approach of having two parallel copper electrodes glued to a 3D printed compliant clamp, represented in grey in Figure 90 (a).

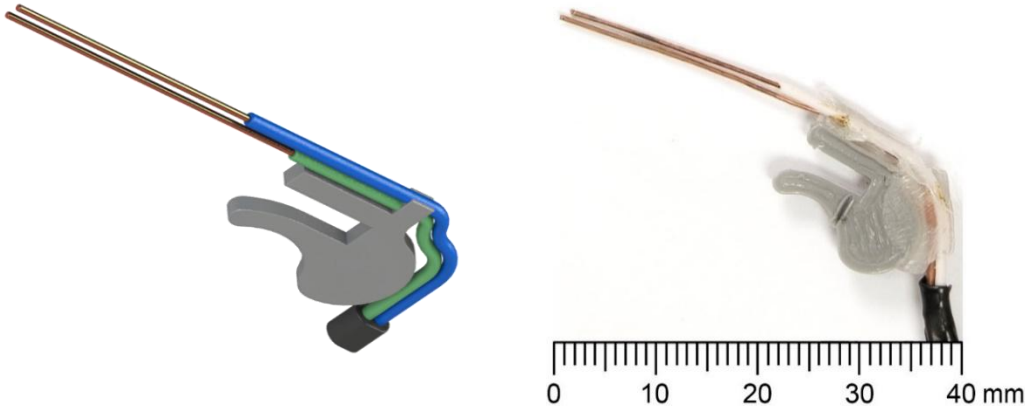

(a) (b)

Figure 90 – Rendered view of the CAD model (a) and picture (b) of the sensor AGRS1.

The clamp is designed to attach to the HX refrigerant tube that goes through the fins. The sensor is positioned from the back of the HX, with the electrodes extending through the fins and protruding 18.0 mm from the front intake of the HX as shown in Figure 91.

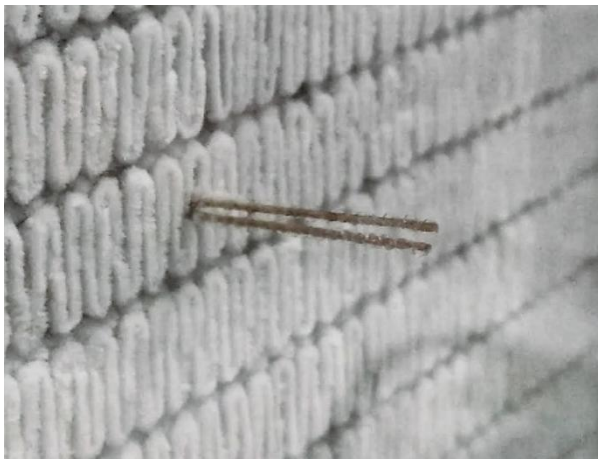

Figure 91 – AGRS1 electrodes protruding from the HX surface.

The parallel electrodes are separated by a 0.6 mm air gap and are expected to accumulate water and frost between electrodes. The main sensor specifications are detailed in Table 27.

Table 27 –AGRS1 specifications.

Feature	Specification
Sensor configuration	
Number of electrodes	2
Electrode shape	Cylindrical
Electrode relative position	Parallel
Dimensions	
Electrode section	Ø0.5 mm
Electrode length	25.0 mm
Distance between electrodes	0.6 mm
Material	
Electrode material	Copper
Medium between electrodes	None
Placement	
Placement within HX	Between fins
Fixture method	3D printed compliant clamp
Electrode position (airflow)	Aligned with airflow
Electrode position (HX Surface)	Perpendicular to HX surface

The two 25 mm straight copper electrodes with a diameter of 0.5 mm each, are perpendicular to the HX surface, which means they are aligned with the airflow. This sensor was placed in the HX and tested to evaluate its performance.

The AGRS1 sensor was tested in three separate tests, producing mixed results that suggest the underlying principle of frost sensing is viable but requires refinement. The results of each test were as follows:

In the first test, shown in Figure 92, the sensor initially showed high resistivity, indicating that although water condensation on the electrodes was observed, no conductive bridge was formed. At $t = 10.8$ min, a brief drop in resistivity suggested the detection of water, but this was short-lived, lasting only until $t = 11.3$ min. This irregularity was likely due to a droplet that either dried, precipitated, or quickly froze. The sensor successfully detected water again at $t = 15.3$ min, with frost detection occurring at $t = 22.1$ min as resistivity increased. Defrosting was initiated at $t = 23.6$ min, followed by a drop in resistivity at $t = 24.1$ min, indicating the detection of melting water. The process concluded with the detection of air at $t = 34.4$ min, signifying the end of defrosting. Despite the initial fluctuation, this test demonstrated the sensor's ability to detect water, frost, and the dry state of the HX after defrosting.

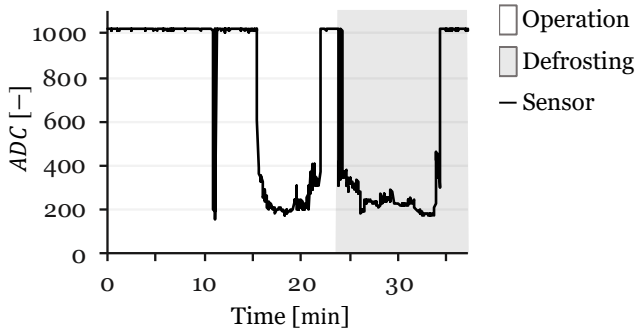

Figure 92 – Results for the first test of the AGRS1.

The second test, with results displayed in Figure 93 showed similar performance, with water detected at $t = 10.9$ min. Frost was detected at $t = 23.5$ min as resistivity increased, followed by a brief detection of water at $t = 25.0$ min, lasting until $t = 25.7$ min. Defrosting began at $t = 41.0$ min, with resistivity dropping at $t = 41.3$ min as water was detected due to the melting frost. The sensor detected air at $t = 65.9$ min, marking the end of defrosting, although a brief fluctuation occurred at $t = 66.3$ min before stabilizing to air detection at $t = 67.1$ min. The test was successful, detecting the transition between water, frost, and the dry HX state, despite minor fluctuations.

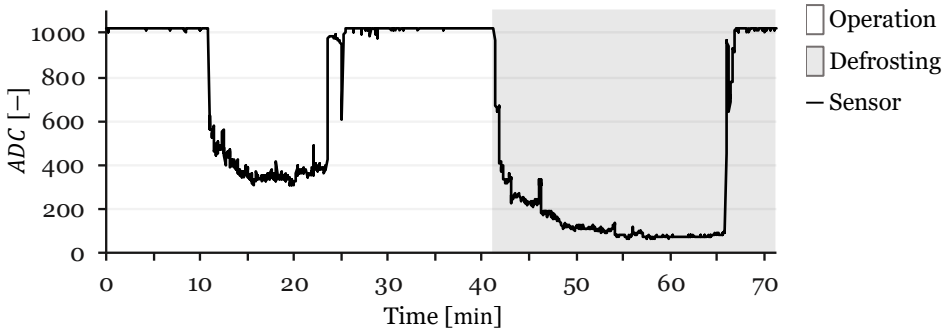

Figure 93 – Results for the second test of the AGRS1.

The third test, shown in Figure 94 highlighted some challenges in the sensor design. Although frost formation was visually observed, the sensor failed to detect it. Minor fluctuations in resistivity were observed after $t = 20.0$ min, likely due to condensation on the frost surface briefly connecting the electrodes. Defrosting was initiated at $t = 40.0$ min, as frost blocked the HX, even though it was not detected by the sensor. Water was finally detected at $t = 44.5$ min, after all frost had melted, and air detection at $t = 53.8$ min indicated the end of defrosting. The delayed water detection after defrosting suggests issues with sensor placement, which may hinder proper water deposition and frost detection if the sensor is not in adequate contact with the HX surface.

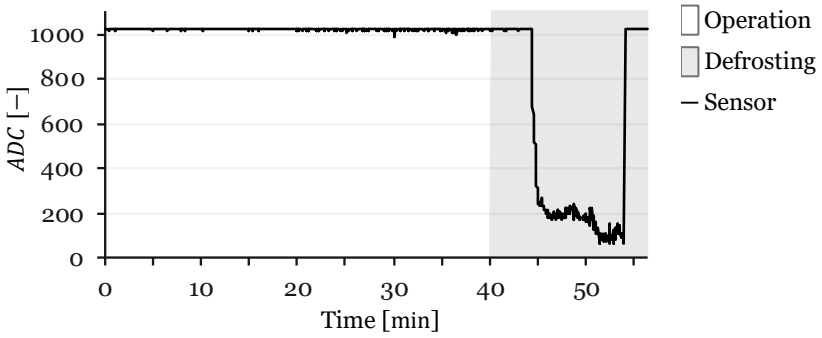

Figure 94 – Results for the third test of the AGRS1.

Overall, the AGRS1 sensor demonstrated its potential in frost detection but exhibited sensitivity to position changes and temperature gradients along its electrodes. These factors led to inconsistent water and frost detection, highlighting the need for design improvements to enhance heat exchange between the sensor electrodes and the HX without creating an electrical connection. This sensitivity also caused short, unexpected bursts of water detection, attributed to the varying temperatures along the sensor's length, which resulted in condensation in some electrode regions while others were

under frosting conditions. The following versions addressed these challenges to improve the sensor's reliability and accuracy.

4.7.2. AGRS2

The AGRS2 is a variation of the AGRS1, it is also made from two parallel copper electrodes with a diameter of 0.5 mm, separated by an air gap of approximately 0.6 mm. This sensor is differentiated by the shorter length of the electrodes, that only offset 1.0 mm from the intake face of the evaporator. Shorter electrodes result in this sensor having less contact with the warmer intake air, and therefore an expected lower temperature gradient on its electrodes. Figure 95 shows the sensor CAD model (a) and the tested sensor (b).

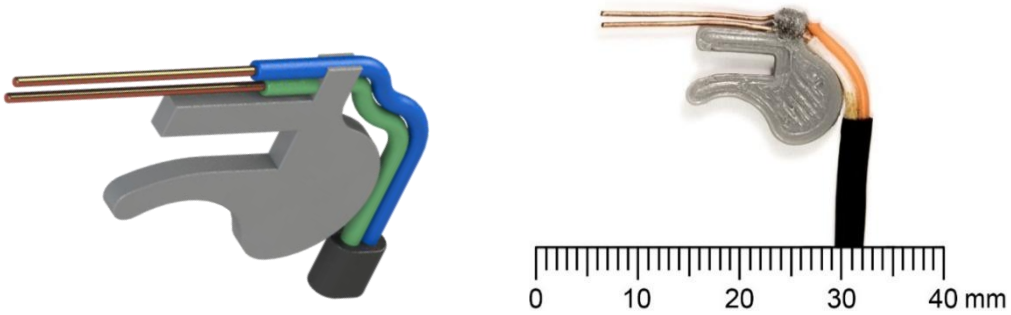

(a) (b)

Figure 95 – Rendered view of the CAD model (a) and picture (b) of the AGRS2.

As this sensor is very similar to AGRS1, except for the electrode length, its specifications also closely resemble those of this sensor, as shown in Table 28.

The AGRS2 was tested in three trials, yielding less favourable results compared to the AGRS1. The smaller electrodes, intended to mitigate the temperature gradient issue observed in AGRS1, ultimately made it more difficult to bridge the electrodes with water, impacting the sensor's performance.

Table 28 –AGRS2 specifications.

Feature	Specification
Sensor configuration	
Number of electrodes	2
Electrode shape	Cylindrical
Electrode relative position	Parallel
Dimensions	
Electrode section	∅0.5 mm
Electrode length	17.0 mm
Distance between electrodes	0.6 mm
Material	
Electrode material	Copper
Medium between electrodes	None
Placement	
Placement within HX	Between fins
Fixture method	3D printed compliant clamp
Electrode position (airflow)	Aligned with airflow
Electrode position (HX Surface)	Perpendicular to HX surface

In the first test, represented in Figure 96, the sensor failed to detect both water accumulation, frost, and defrosting, with sensor resistivity remaining high throughout the entire test duration. At $t = 26.6$ min, defrosting was initiated, but no changes in resistivity were observed, indicating that the sensor was unable to detect the presence of water or frost. This failure was attributed to the sensor's shorter electrodes, which struggled to detect water accumulation between them, even though water was observed on the HX surface. Despite being positioned in the same region of the HX as the AGRS1, the placement did not facilitate adequate water accumulation, leading to the decision to reposition the sensor in a lower HX region for subsequent testing.

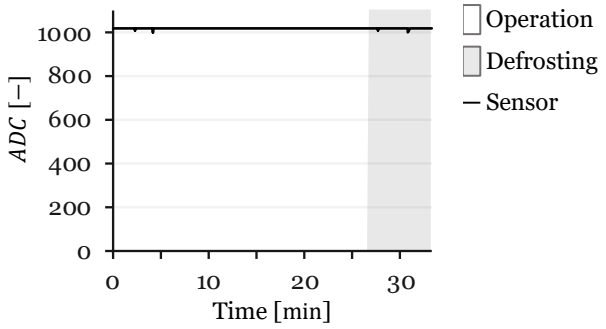

Figure 96 –Results for the first test of the AGRS2.

The second test, shown in Figure 97 demonstrated some improvement, but the sensor still faced challenges. Up until $t = 14.9$ min, the sensor detected no water, with resistivity remaining high. At $t = 14.9$ min, a drop in resistivity indicated water detection. However, at $t = 33.1$ min, frost was observed to be significantly accumulated in the HX, yet no frost detection occurred as resistivity remained low. Defrosting was initiated, and after almost 20 minutes, a brief spike in resistivity at $t = 52.6$ min suggested dry HX detection, but it quickly returned to low resistivity, indicating water at $t = 53.0$ min. Finally, at $t = 54$ min, high resistivity signalled dry HX detection. The inability to detect frost, despite its presence, highlighted the sensor's limited thermal contact with the HX surface, which made it difficult to release enough heat for water to freeze between the electrodes. Conversely, the warm intake air was sufficient to dry the sensor.

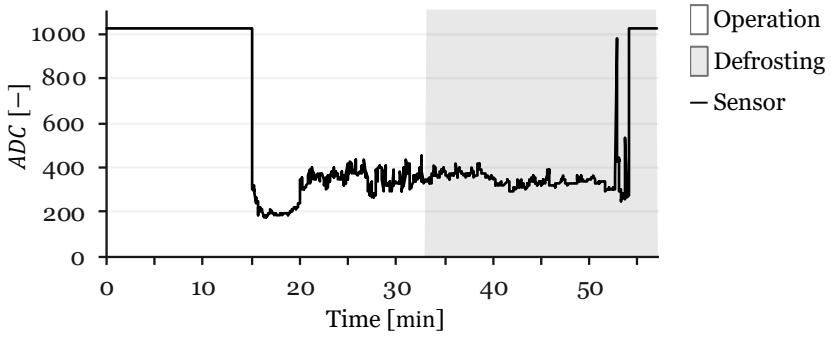

Figure 97 –Results for the second test of the AGRS2.

In the third test, represented in Figure 235 of the Annex A, similar results to the second test were observed.

The AGRS2 performance shows the impact of sensor position and electrode orientation relative to the HX. In the first test, the sensor detected nothing, but when repositioned, it could only detect water and failed to detect frost, even when the HX was blocked with frost. This was partly due to the shorter electrodes, which were positioned mostly below the HX surface, in a region with lower humidity (as air dehumidifies at the HX front), making it less exposed to water and frost formation. When placed in a region prone to water accumulation, the sensor struggled to detect frost and primarily detected water.

4.7.3. AGRS3

The sensor AGRS3 is also made from two parallel copper electrodes with a diameter of 0.5 mm, however the electrodes are positioned vertically, parallel to the intake face of the HX. The electrodes are separated by an air gap of approximately 0.6 mm. This sensor has a higher contact area with the intake air and less contact with the HX. The sensor CAD

model is shown in Figure 98 (a) and the tested sensor in Figure 98 (b). The goal of this sensor is to assess if it is possible to have enough heat transfer through the sensor wiring to have condensation and frost forming on its electrodes at the front end of the HX where air has the most humidity.

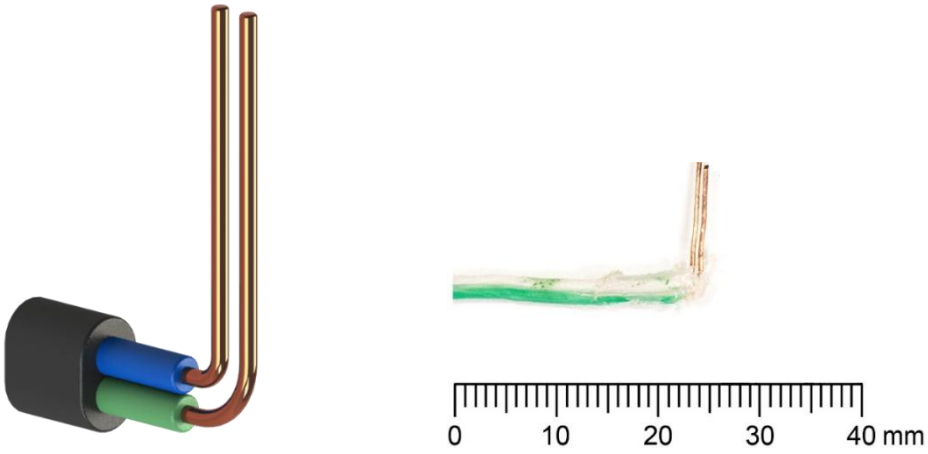

(a) (b)

Figure 98 – Rendered view of the CAD model (a) and picture (b) of the AGRS3.

The AGRS3 has the characteristics presented in Table 29.

Table 29 –AGRS3 specifications.

Feature	Specification
Sensor configuration	
Number of electrodes	2
Electrode shape	Cylindrical
Electrode relative position	Parallel
Dimensions	
Electrode section	Ø0.5 mm
Electrode length	11.0 mm
Distance between electrodes	0.6 mm
Material	
Electrode material	Copper
Medium between electrodes	None
Placement	
Placement within HX	Front of HX surface
Fixture method	Cable wedged between fins
Electrode position (airflow)	Perpendicular to airflow
Electrode position (HX Surface)	Parallel to HX surface

The AGRS2 consisted of two parallel cylindrical copper electrodes, each with a diameter of 0.5 mm and a length of 11.0 mm, separated by an air gap of approximately 0.6 mm. The

electrodes were positioned vertically, parallel to the HX front surface, which increased their exposure to the intake air. Both electrodes were made of copper. The sensor was mounted at the front of the HX surface, with the connection cable wedged between fins to secure it in place and improve thermal contact. In this configuration, the electrodes were oriented perpendicular to the airflow and parallel to the HX surface, emphasizing contact with the intake air.

The AGRS2 sensor underwent two tests, as expected neither of which yielded successful results. In the first test, shown in Figure 99, the sensor failed to detect frost or the defrosting process, with the measured resistivity remaining consistently high throughout the test. At $t = 22.4$ min, defrosting was initiated, but the sensor did not register any change in resistivity, indicating a failure to detect water. Despite the formation of water on the HX surface, the sensor, positioned in front of the HX, was unable to detect it. This issue was attributed to insufficient heat transfer between the sensor electrodes and the HX, as the copper cables wedged between the fins did not conduct enough heat to surpass the heat exchange between the electrodes and the warmer intake air.

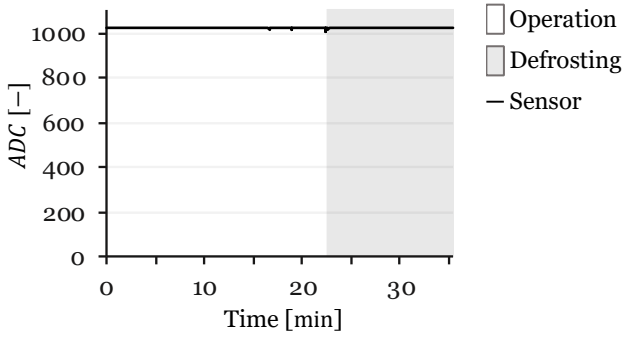

Figure 99 – Results for the first test of the AGRS3.

The second test, referenced in Figure 236 (Annex A), produced similar results. No detection of water, frost, or defrosting was observed. This configuration places the sensor electrodes in front of the HX, to exposing them to air with higher moisture content. However, the setup relied on heat conduction through the copper cables, which proved inadequate for lowering the sensor electrode temperature sufficiently to induce condensation, due to constant contact with the warmer intake air. As a result, the sensor remained ineffective in detecting the intended changes. These findings led to the development of AGRS4, which aims to increase the electrode surface area, and AGRS5 and AGRS6, which were designed with improved heat exchange between the electrodes and the HX fins.

4.7.4. AGRS4

The reasoning behind the AGRS4 was to go back and place the sensor between fins to increase its heat transfer to the HX and increase the sensed volume. Figure 100 shows the sensor CAD model (a) and a picture of the sensor (b).

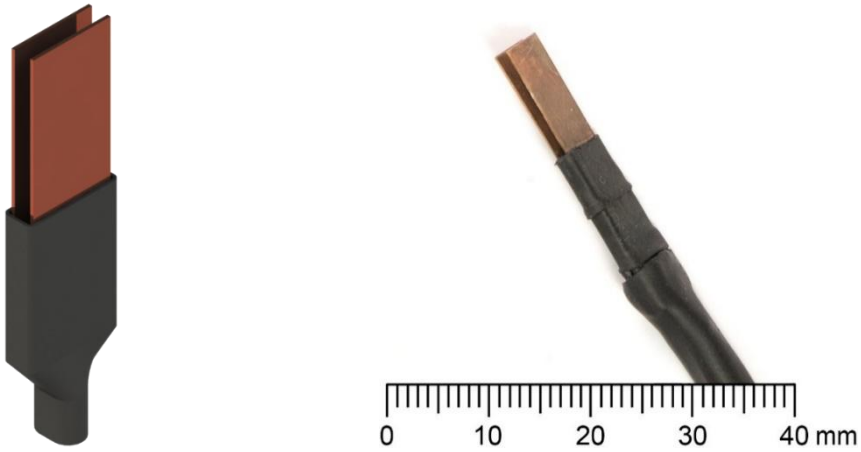

(a) (b)

Figure 100 – Rendered view of the CAD model (a) and picture (b) of the AGRS4.

This sensor is built with two equal and parallel copper plates, and is placed within the HX fins, perpendicularly to the HX front face. Sensor specifications are displayed in Table 30.

Table 30 –AGRS4 specifications.

Feature	Specification
Sensor configuration	
Number of electrodes	2
Electrode shape	Plates
Electrode relative position	Parallel
Dimensions	
Electrode section	6.0 × 0.2 mm
Electrode length	11.0 mm
Distance between electrodes	1.3 mm
Material	
Electrode material	Copper
Medium between electrodes	None
Placement	
Placement within HX	Between fins
Fixture method	Wedged between fins
Electrode position (airflow)	Aligned with airflow
Electrode position (HX Surface)	Perpendicular

Because having a larger footprint meant blocking the airflow between the fins in which this sensor is wedged in between, the airflow between sensor electrodes is not facilitated. The larger electrode area also means that AGRS4 has an increased surface in which to exchange heat between the air and sensor surface, increasing sensor temperature. Finally, the electrical insulation around the sensor electrodes, to avoid short circuiting as it is in physical contact with the fins it is wedged between, means decreased thermal conductivity, and facilitates water deposition, shielded from lower temperatures. This means that once this sensor detects water, it is difficult to either freeze or dry it, as shown in Figure 101.

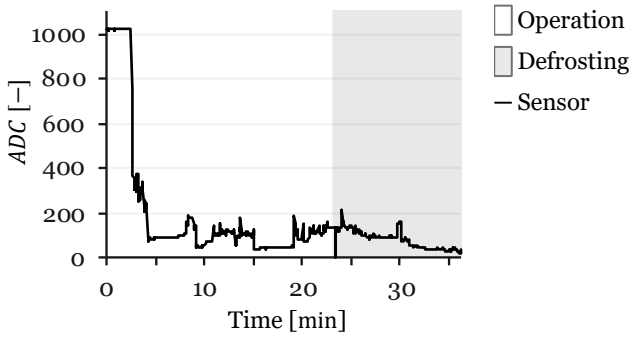

Figure 101 – Results for the first test of the AGRS4.

Figure 237 in Annex A confirms the results obtained in the first test. After water detection is performed, the water neither freezes nor dries between the sensor electrodes. After these results, sensors with improved heat exchange with the HX, but also with a design that allows placement without blocking airflow between electrodes, were designed and built, resulting in AGRS5 and AGRS6.

4.7.5. AGRS5

The AGRS5 was developed to improve thermal contact with the HX and to promote more reliable water detection. This design combined a clamp-shaped electrode that fixed directly onto an HX fin with a cylindrical electrode facing the intake air. The objective was to ensure that condensation and frost would consistently form between the two electrodes, while maintaining a compact footprint suitable for integration between fins. Figure 102 shows the sensor CAD drawing (a) and tested sensor (b).

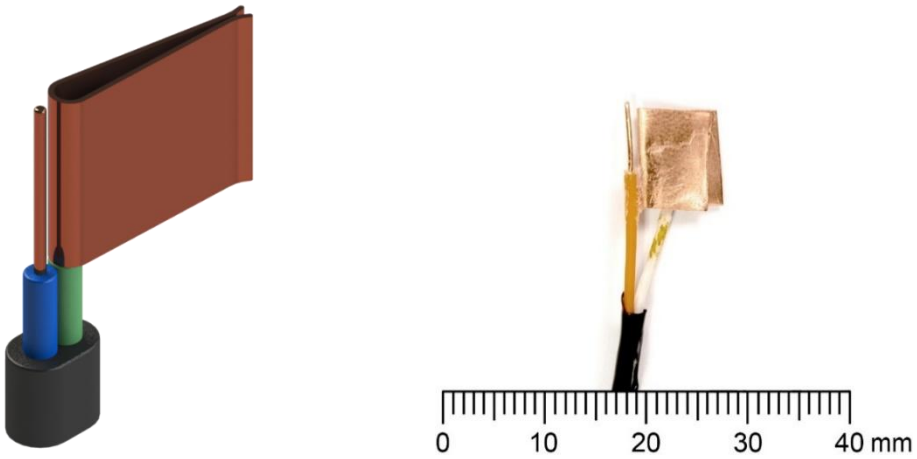

(a) (b)

Figure 102 – Rendered view of the CAD model (a) and picture (b) of the AGRS5.

The sensor consisted of two copper electrodes arranged in parallel and separated by an air gap of approximately 0.6 mm. The clamp electrode, with a rectangular section of 6.0 × 0.4 mm and a length of 6.0 mm ensured firm attachment and thermal contact with the HX fin. The second electrode was a cylindrical copper wire, 0.5 mm in diameter and 6.0 mm long, positioned in front of the clamp electrode. The sensor was clamped directly on the HX fin, with electrodes oriented perpendicular to the airflow and parallel to the HX surface. The sensor specifications are shown in Table 31.

Table 31 –AGRS5 specifications.

Feature	Specification
Sensor configuration	
Number of electrodes	2
Electrode shape	Clamp/Cylindrical
Electrode relative position	Parallel
Dimensions	
Electrode section	6.0 × 0.4 mm/Ø0.5 mm
Electrode length	6.0 mm
Distance between electrodes	0.6 mm
Material	
Electrode material	Copper
Medium between electrodes	None
Placement	
Placement within HX	On fin
Fixture method	Clamped on fin
Electrode position (airflow)	Perpendicular to airflow
Electrode position (HX Surface)	Parallel

The AGRS5 was subjected to five separate tests to evaluate its performance. In four out of five cases, the sensor successfully detected all phases of the frost–defrost cycle, demonstrating improved reliability compared to previous AGRS configurations. Additionally, tests 1 to 4 were conducted consecutively: full detection was achieved in tests 1, 2, and 4, while test 3 resulted in only partial detection, with water and dry states identified during defrosting but no frost formation detected.

In the first test shown in Figure 238-Annex A, the sensor correctly detected water accumulation, the transition to frost, the initiation of defrosting, and the final dry HX state. All detection stages were clearly identifiable.

The second test shown in Figure 103 reinforced these results. Water was detected at $t \in [9, 17[$ min, reaching saturation at 17 min. Frost detection followed at $t = 20$ min, after which defrosting was initiated at $t = 22$ min. The sensor detected water at the start of the defrosting operation and subsequently identified a dry HX at $t = 33$ min.

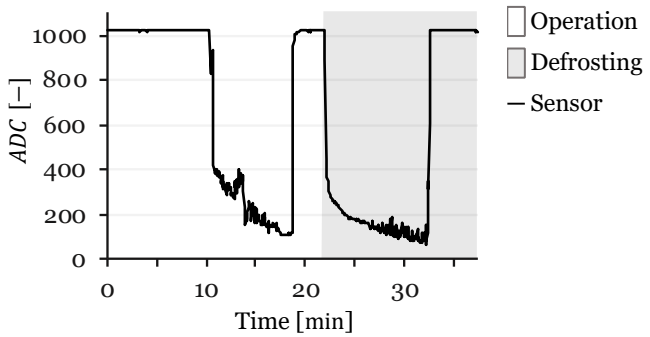

Figure 103 – Results for the second test of the AGRS5.

In the third test, shown in Figure 104, the sensor failed to detect water formation, as condensation froze too quickly before a conductive bridge could be established between electrodes. Consequently, water detection was not achieved, and defrosting had to be initiated based on visual observation. Water was detected when defrosting was initiated at $t = 32$ min and the dry HX state at $t = 45$ min. This again highlights a limitation of the air gap sensor configuration, as it fails under conditions where water freezes immediately before forming a conductive bridge between electrodes.

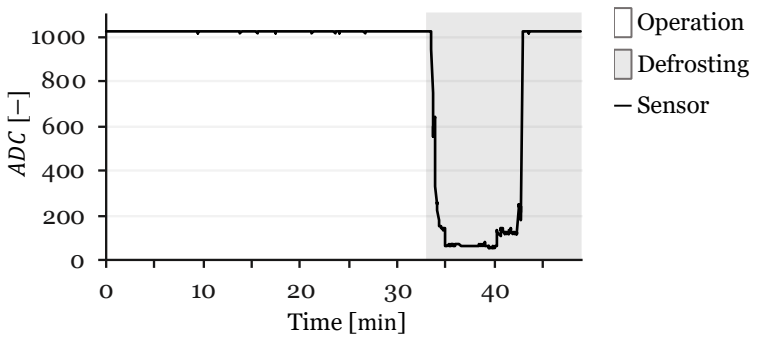

Figure 104 – Results for the third test of the AGRS5.

The fourth test, shown in Figure 105 showed similar behaviour to tests 1 and 2. Water was detected at $t \in [7, 11[\ \text{min}$, followed by frost detection at $t = 11\ \text{min}$. Defrosting began at $t = 17$ min, immediately triggering water detection. A dry HX reading was first obtained at $t = 20$ min; however, residual humidity or weak water bridges caused the ADC values to remain high but below saturation (around 900) and unstable throughout $t \in [23, 34[$ min. Full dry HX detection was achieved at $t = 34$ min. Despite this minor irregularity, all main cycle stages were identified correctly.

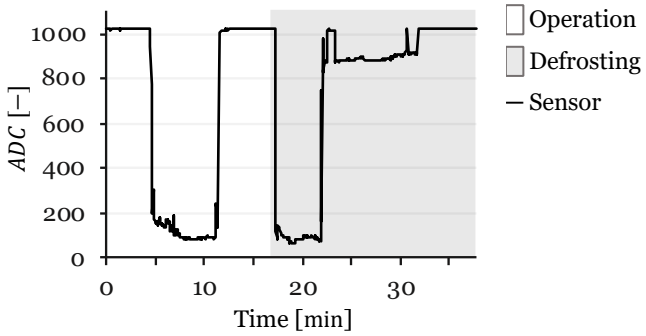

Figure 105 – Results for the fourth test of the AGRS5.

Finally, the fifth test results, shown in Figure 239-Annex A confirmed the detection pattern of this design, with the sensor successfully detecting water, frost, and the dry HX state throughout the cycle.

Based on these results, the design was adapted to address situations where water was not consistently detected. The next iteration repositioned and reconfigured the second electrode to ensure that incoming airflow always passed between both electrodes, while maintaining the clamp electrode. This led to the development of AGRS6, described in the following section.

4.7.6. AGRS6

The AGRS6 was developed as a variation of the AGRS5, aiming to further improve water detection. In this design, the second cylindrical electrode was replaced with a copper plate positioned at an angle of approximately 45° facing the air intake. The intent was to increase airflow interaction with the sensor by ensuring that the incoming air passed directly between the two electrodes. As in previous designs, the electrodes were separated by an air gap of approximately 0.6 mm. The CAD model (a) and the tested sensor (b) of the AGRS6 are shown in Figure 106.

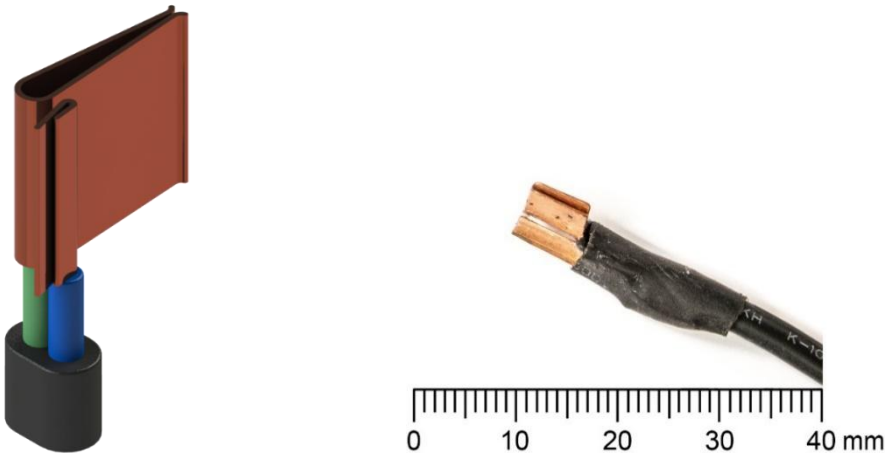

(a) (b)

Figure 106 – Rendered view of the CAD model (a) and picture (b) of the AGRS6.

The sensor consisted of two copper electrodes arranged in parallel, separated by a 0.6 mm air gap. The clamp electrode ensured mechanical fixation and thermal contact with the HX fin, while the second electrode was a copper plate with a rectangular section of 6.0 × 0.8 mm, oriented at an angle of 45° relative to the airflow. The electrodes were each 6.0 mm in length and made of copper. The sensor was mounted directly on the HX fin, clamped in place with electrodes positioned perpendicular to the airflow and parallel to the HX surface. The sensor specifications are shown in Table 32.

The AGRS6 was tested to evaluate whether the angled plate electrode could enhance water detection. However, the results showed that this design was ineffective. The 45° orientation of the plate increased airflow velocity between the electrodes, preventing droplet accumulation and causing condensation to be blown away before forming a conductive bridge.

Table 32 –AGRS6 specifications.

Feature	Specification
Sensor configuration	
Number of electrodes	2
Electrode shape	Clamp/Plate
Electrode relative position	Parallel
Dimensions	
Electrode section	6.0 × 0.8 mm/Ø0.5 mm
Electrode length	6.0 mm
Distance between electrodes	0.6 mm
Material	
Electrode material	Copper
Medium between electrodes	None
Placement	
Placement within HX	On fin
Fixture method	Clamped on fin
Electrode position (airflow)	Perpendicular to airflow
Electrode position (HX Surface)	Parallel

Figure 107 presents the results of the testing of this sensor. The behaviour was consistent across attempts and no meaningful detection was achieved. Throughout the entire test, the sensor registered no signal variations, failing to identify water and frost alike. Defrosting was initiated at $t = 31$ min due to significant frost accumulation being visually observed, but no water was detected during the defrosting and drying process.

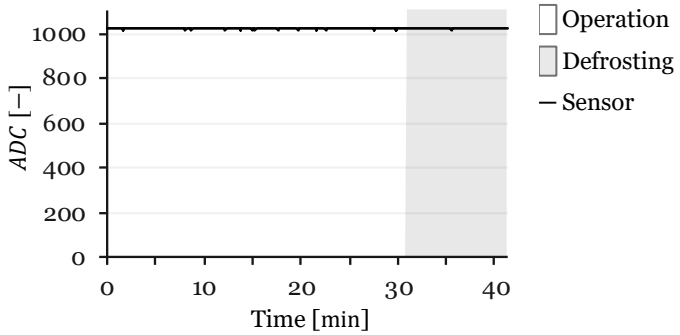

Figure 107 – Results for the first test of the AGRS6.

This outcome highlights that while the AGRS5 design demonstrated promising results, the modification implemented in AGRS6 increased airflow between the electrodes, which in turn prevented droplet bridging as water was blown away. As a result, the design was deemed ineffective and not pursued further.

4.7.7. Air gap resistive sensors – concluding remarks

The development and testing of AGRS1– AGRS6 highlighted both the potential and the limitations of air gap resistive sensors for frost detection. The initial prototypes (AGRS1 and AGRS2) demonstrated that, while the principle was viable, reliable detection depended strongly on electrode placement, length, and thermal contact with the HX. AGRS3 further confirmed that insufficient heat exchange with the HX surface made condensation and frost detection ineffective, as electrodes exposed primarily to the warmer intake air failed to cool sufficiently. AGRS4 attempted to address this by increasing electrode surface area and embedding the sensor between fins, but this configuration resulted in water being retained between electrodes without freezing or drying, preventing clear transitions between states.

The most promising results were achieved with AGRS5, where the clamp electrode ensured good thermal contact with the HX fin, and the facing cylindrical electrode allowed water and frost accumulation to be consistently detected. In four out of five tests, the sensor successfully identified all stages of the frost–defrost cycle, and even in the failed case the limitation was identified as rapid freezing before bridging occurred. Figure 108 shows the AGRS5 at the beginning of frost accumulation (a) and with significant frost accumulation (b) before defrosting, where the frost layer forming on the sensor surface is easily observable.

(a) (b)

Figure 108 – Images of the AGRS5 during frost nucleation (a) and significant frost accumulation (b).

AGRS6, developed as a further variation, attempted to improve airflow interaction by replacing the cylindrical electrode with an angled plate on the side of the clamp electrode, but the resulting increase in airflow velocity prevented droplet retention and rendered the sensor ineffective.

Overall, the air gap sensors confirmed that ensuring proper thermal contact with the HX is essential for reliable detection. However, the recurring challenge of retaining water between electrodes without premature freezing or drying pointed toward the need for alternative approaches to increase sensor reliability. These results pointed towards the importance of introducing a porous medium capable of enhancing and stabilizing the water bridge between electrodes, guiding the development of the next iteration of resistive sensors.

4.8. CMRS - Ceramic-Medium Resistive Sensors

The development of the CMRS was motivated by the limitations observed in the air gap configurations, particularly the difficulty of retaining water between electrodes long enough to form a stable conductive bridge. The design concept was to introduce a medium that would be porous and thermally conductive, granting effective heat transfer between the HX fins and the electrodes, while at the same time being electrically insulating.

For this purpose, porous alumina ceramic was selected. Alumina presents a combination of properties suited to this application. It is a material with a high electrical resistivity ($\approx 10^{14}\ \Omega \cdot c$m), good thermal conductivity for a ceramic (typically $\sim 25 - 35\ \mathrm{W \cdot m^{-1} \cdot K^{-1}}$), chemical stability, and the possibility of creating a porosity [132]. Porous alumina allows water to be absorbed and held in its structure, thereby allowing for water bridging between electrodes [133]. These characteristics make alumina a suitable ceramic for this application.

The concept was to embed two electrodes within a porous ceramic medium. In this configuration, the ceramic acts simultaneously as a thermal conductor and as an electrical insulator, preventing any short-circuiting between the electrodes even when placed in direct contact with a bare metal HX. By allowing sufficient thermal conductivity, the ceramic surface can follow the cooling dynamics of the HX, promoting frost formation on its surface under the same conditions as the fins. At the same time, the porous structure facilitates the absorption of condensed water, allowing liquid to establish an electrical connection between the embedded electrodes. This concept is illustrated in Figure 109, where (a) shows a rendered view of the sensor and (b) presents a cut view of the design, highlighting the embedded electrodes within the ceramic body.

(a) (b)

Figure 109 – CAD model of a concept of a ceramic medium resistive sensor.

A practical challenge of this approach lies in the high sintering temperatures required for alumina, which preclude embedding metallic electrodes during the green state. This will complicate production if this medium is viable.

To test this concept, porous alumina samples were produced following a conventional powder-processing route. Alumina powder was first homogenized using the planetary mono mill Pulverisette 6 and sieved with a Retsch sieve shaker to ensure uniform particle size distribution. To introduce porosity, sodium chloride ($NaCl$) particles were incorporated into the alumina powder mixture as a sacrificial pore former. The mixture was pressed into green pellets, which were then dried and sintered in a Termolab electric furnace. The sintering cycle consisted of heating from room temperature to 600 °C at 2 °C/min with a 30 min hold, followed by heating to 1300 °C at 5 °C/min with a 120 min hold, and finally cooling at −5 °C/min down to 100 °C. After processing, the discs reached final dimensions of approximately 12.0 mm in diameter and 2.6 mm in thickness with a porosity of 26.74% .

To enable electrical characterization, a clamp with two copper plate electrodes connected to the ADC was designed and fabricated via AM. This fixture enabled resistance measurements over time when distilled water was placed on the ceramic surface, allowing verification of whether a conductive water bridge could form across the sample. A rendered view of the clamp design and the produced fixture are shown in Figure 110 (a) and (b), respectively.

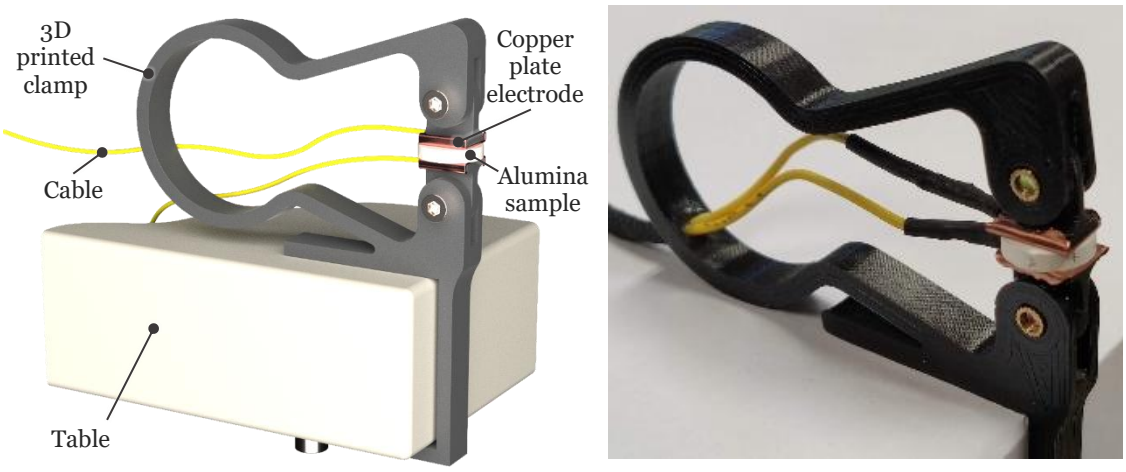

(a) (b)

Figure 110 – Rendered view (a) and picture (b) of the clamp fixture used for electrical characterization of the ceramic samples.

The alumina disc was placed in the clamp fixture and connected to the ADC. A short stabilization period of approximately two minutes was allowed prior to testing to ensure thermal and electrical equilibrium between the sample and the measurement setup. During this period, the readings remained stable. Distilled water was then slowly added dropwise onto the sample surface over the course of one minute. The water was rapidly absorbed by the porous structure, and the ADC signal dropped almost immediately as liquid absorbed by the sample bridged the electrode pads, confirming the high-water uptake rate of the alumina porous sample. Once water addition was stopped, the ADC values gradually increased over time, reflecting partial drying of the surface. These results, presented in Figure 111, demonstrate that the porosity achieved in the processed alumina promoted fast absorption and electrical response to water, validating this medium as suitable for the condensation and defrosting phases of frost formation.

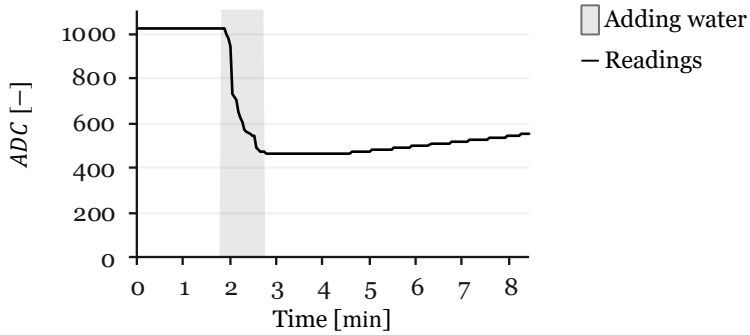

Figure 111 – ADC response of the porous alumina sample during the water absorption test.

The wetted samples were subsequently subjected to cyclic freeze-thaw testing to evaluate their structural integrity under repeated phase-change conditions. Each cycle consisted

of wetting, freezing, returning to ambient conditions, drying, and re-wetting. All tested samples eventually fractured, with the number of cycles to failure ranging from a minimum of two to a maximum of ten. Figure 112 shows the control half-sample that remained intact (a), a sample broken into two parts after four cycles (b).

(a) (b)

Figure 112 – Control (a) and tested (b) sample of porous alumina ceramics after four freeze–thaw cycles.

This outcome highlights a critical limitation of porous ceramic media for frost sensing in refrigeration systems. The inherent rigidity of ceramics, combined with the volumetric expansion of water upon freezing, leads to progressive structural degradation. This cyclic phenomenon is intrinsic to evaporators operating at subzero temperatures, making ceramics inherently vulnerable to fracture under repeated frost-defrost cycles. Although porous alumina provided advantageous properties such as good thermal conductivity and high electrical insulation, its lack of mechanical compliance rendered it unsuitable for this application. These findings indicate the need for alternative materials capable of accommodating volumetric variations during phase-change, even if this requires sacrificing some of the favourable properties offered by ceramics.

4.9. FMRS - Fabric-Medium Resistive Sensors

The shortcomings of both the AGRS and CMRS families—namely, unreliable water retention and structural fragility under frost cycling—highlighted the need to explore alternative media. The fabric-medium resistive sensor builds upon the air-gap configuration by wrapping a cotton string around both electrodes. This textile medium electrically insulates the metal electrodes while taking advantage of the capillary effect to absorb and distribute moisture, thereby forming a conductive fluid bridge and reducing resistivity when humid.

Cotton is a sustainable and organic material that acts as an electrical insulator when dry, with a surface resistivity on the order of $10^9\,\Omega$, while its thermal conductivity is

approximately $0.0633\ \mathrm{W \cdot m^{-1} \cdot K^{-1}}$ for dry fabrics [134]. Its low thermal conductivity remains a limitation, however, because the cotton string is very thin, the electrodes are separated from the HX surface by only a minimal barrier, allowing heat transfer to still occur. Additionally, the absorbent nature of cotton enables it to take up moisture not only from the sensor electrodes, but also from the surrounding environment, directly from the HX surface. This capillary action should contribute to a rapid moisture uptake and lateral distribution across the gap, establishing a conductive bridge between electrodes when wet, while maintaining electrical insulation in the dry state. Additionally, as the relative amount of absorbed water increases, the effective thermal conductivity rises, asymptotically approaching the thermal conductivity of water itself [135].

This FMRS concept is illustrated in Figure 113, where the electrodes are entwined by a cotton string in a figure-eight arrangement. In this configuration, the string alternates between wrapping each electrode and crossing at the midpoint, so that the cotton fibres are consistently oriented from one electrode toward the other. This crossing pattern provides electrical insulation by maintaining separation, while simultaneously enhancing capillary-driven water distribution between the electrodes, thereby promoting the formation of a conductive bridge during condensation and defrosting events.

Figure 113 – Simplified representation of a two electrode FMRS.

From this concept, FMRS were developed, following the same procedures as for the AGRS, with the added step of applying the cotton string as described. The individual sensors are detailed in the following subsections.

4.9.1. FMRS1

The FMRS1 was the first prototype designed to test the feasibility of a fabric medium in resistive frost sensing. It consisted of two parallel cylindrical copper electrodes, around which a cotton sewing thread was tightly wound in a figure-eight pattern. The use of cotton introduced electrical insulation between electrodes while relying on its capillarity to promote water bridging when moisture was present. Because cotton has poor thermal conductivity, and to take advantage of the fact that the AGRS is electrically insulated from the surface it comes in contact with, the sensor was positioned directly on the refrigerant tube of the HX, for maximum thermal contact with the lower temperature part of the HX. The electrodes were kept short and curved around the intake-side tubing, simultaneously facing the airflow while remaining in contact with the HX tube. The rendered CAD model (a) and the tested sensor (b) are shown in Figure 114.

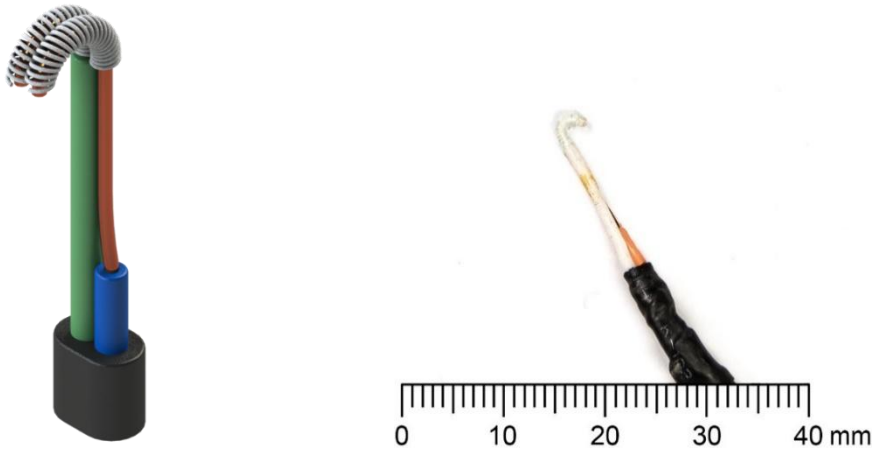

(a) (b)

Figure 114 – Rendered view of the CAD model (a) and picture (b) of the FMRS1.

The sensor consisted of two copper electrodes with a diameter of 0.5 mm and a length of 6.0 mm, separated by a 0.3 mm gap and wrapped in cotton thread. The assembly was clamped directly on the refrigerant tube between fins. Electrodes were oriented towards the intake end of the HX. The sensor specifications are summarized in Table 33.

Table 33 –FMRS1 specifications.

Feature	Specification
Sensor configuration	
Number of electrodes	2
Electrode shape	Cylindrical
Electrode relative position	Parallel
Dimensions	
Electrode section	∅0.5 mm
Electrode length	6.0 mm
Distance between electrodes	0.3 mm
Material	
Electrode material	Copper
Medium between electrodes	Cotton sewing thread
Placement	
Placement within HX	On refrigerant tube
Fixture method	Clamped on refrigerant tube
Electrode position (airflow)	Curved, perpendicular to airflow
Electrode position (HX Surface)	On HX surface

The first test results are shown in Figure 115. Initially, only a very slight water detection was observed at $t \in [15, 16[$ min, with the ADC value decreasing marginally from ~1022 to ~1011. Frost detection followed, with values remaining near saturation (~1023). Defrosting was initiated at $t = 20$ min, at which point water was immediately detected, with ADC values dropping until $t = 22$ min. The sensor then gradually returned to high values, reaching ~1022 by $t = 25$ min, corresponding to a dry HX state. Although the water detection during the frosting phase was weak, the full frost–defrost cycle was captured, confirming the concept's viability.

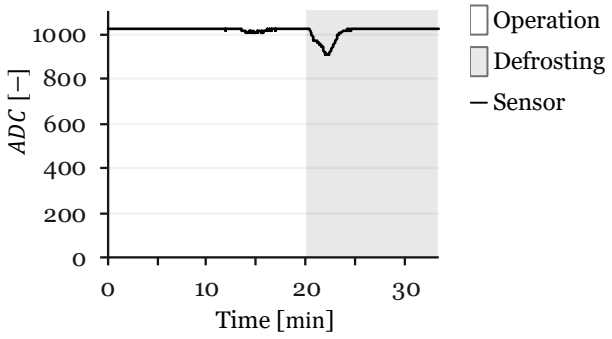

Figure 115 – Results for the first test of the FMRS1.

In the second test, shown in Figure 116, fluctuations at the beginning were negligible and likely measurement noise. Frost accumulation was visually confirmed, and defrosting was manually initiated at $t = 34$ min. Water was immediately detected as ADC values dropped, followed by a rise beginning at $t = 41$ min, reaching dry HX detection at $t = 45$ min. Fluctuations occurred during drying, reflecting residual melting before complete evaporation.

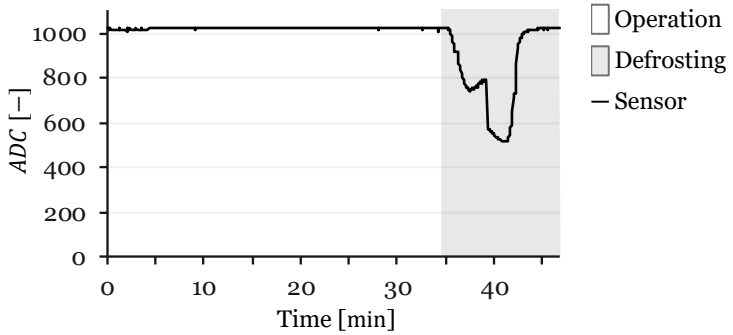

Figure 116 – Results for the second test of the FMRS1

Overall, while FMRS1 did not consistently detect water formation during the frosting phase, it identified water, frost, and drying stages during defrosting. These results provided a proof of concept for fabric-medium resistive sensors and justified further development into alternative configurations.

4.9.2. FMRS2

The FMRS2 was developed as a variation of FMRS1, with the main difference being its placement on the HX fin rather than on the refrigerant tube. While the tubing offers the lowest temperatures in the HX, the fins extend further toward the intake side, bringing the sensor into closer contact with the humid incoming air. Since the fins and tubes are metallic and thermally connected, the temperature difference between them is small, and this configuration aims to investigate whether positioning the sensor on the fins could improve detection. The sensor maintained the same construction principle as FMRS1, with two parallel copper electrodes wrapped in cotton thread, but with increased electrode length to enhance thermal contact with the fin. The CAD rendered view (a) and the tested sensor (b) are shown in Figure 117.

(a) (b)

Figure 117 – Rendered view of the CAD model (a) and picture (b) of the FMRS2.

The sensor was composed of two parallel cylindrical copper electrodes with a diameter of 0.5 mm, bent around the fin with a length of 18.0 mm, and a separation of 0.3 mm. The electrodes were tightly wrapped in cotton sewing thread and clamped around a fin on the intake side of the HX. Electrodes were oriented towards the airflow and in contact with the fin surface. The specifications are summarized in Table 34.

Table 34 –FMRS2 specifications.

Feature	Specification
Sensor configuration	
Number of electrodes	2
Electrode shape	Cylindrical
Electrode relative position	Parallel
Dimensions	
Electrode section	∅0.5 mm
Electrode length	18.0 mm
Distance between electrodes	0.3 mm
Material	
Electrode material	Copper
Medium between electrodes	Cotton sewing thread
Placement	
Placement within HX	On fin
Fixture method	Clamped on refrigerant fin
Electrode position (airflow)	Curved, parallel to airflow
Electrode position (HX Surface)	Around fin, intake side

The first test results are shown in Figure 118. No water detection was observed during the frosting phase. At $t = 27$ min, defrosting was initiated as significant frost accumulation was observed. During the defrosting process, a slight drop in ADC values indicated limited water detection. This behaviour suggests that the tightly bound cotton thread reduced its ability to absorb and retain moisture, acting more as a barrier than as a conductive medium.

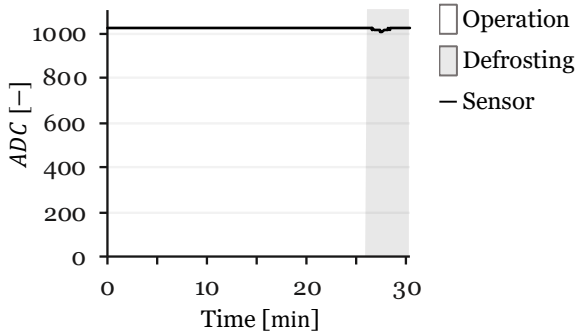

Figure 118 – Results for the first test of the FMRS2.

In the second test, shown in Figure 119, the sensor again failed to detect water during the frosting phase. A gradual decrease in ADC values was observed from ~1015 at the beginning of the test to ~998 by the time defrosting was initiated at $t = 22$ min, however this variation was too low and gradual to indicate effective detection. Once defrosting began, the signal dropped sharply to ~381, showing clear water detection. The ADC values then rose rapidly, stabilizing to dry HX detection at $t = 28$ min.

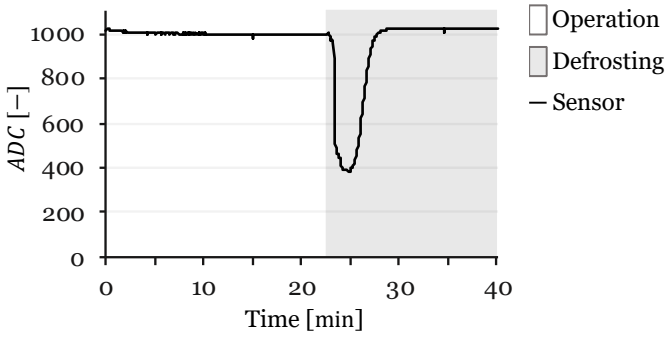

Figure 119 – Results for the second test of the FMRS2.

Overall, FMRS2 confirmed that water could be detected reliably during defrosting, when melting produced larger amounts of water. However, it consistently failed to detect water formation during the frosting phase, likely due to the cotton string restricting absorption and shielding the electrodes from condensation. This points to the need for improved design, with looser spacing or partial exposure of the electrodes to enhance both heat exchange and water interaction.

4.9.3. FMRS3

The FMRS3 was developed to increase heat exchange between the sensor and the HX by directly coupling one electrode to the fins. For this purpose, a wavy copper plate was inserted between the fins, for thermal contact with the HX surface. This plate extended into one of the electrodes, for good heat conduction but requiring the second electrode to remain insulated from the HX. Both electrodes were placed at the intake end of the HX, aligned vertically and parallel to the HX surface, and thus positioned in direct contact with the intake airflow. The electrodes were manufactured from a copper sheet, cut into rectangular sections, with one end wrapped to form the electrode and the other shaped into waves to wedge securely between fins. To address the excessive thermal resistance observed in FMRS2, a thicker cotton rope thread was used as the medium. The larger fibre diameter reduced overlap between consecutive turns and exposed more of the copper surface, while still maintaining good electrical insulation between electrodes. Figure 120 shows the CAD model (a) and the produced FMRS3 sensor (b).

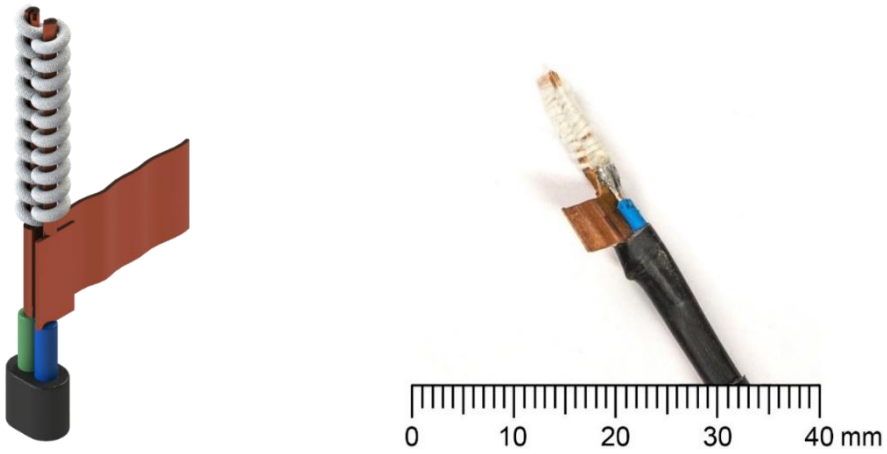

(a) (b)

Figure 120 – Rendered view of the CAD model (a) and picture (b) of the FMRS3.

The sensor consisted of two parallel rectangular copper electrodes separated by 0.5 mm and wrapped by a cotton rope thread. Each electrode measured 13.0 mm in length with a section of 1.1 × 2.4 mm. The sensor was wedged between fins, so that the electodes laid in the intake end of the HX surface, with orientation perpendicular to the airflow and parallel to the HX face. The sensor specifications are presented in Table 35.

Table 35 –FMRS3 specifications.

Feature	Specification
Sensor configuration	
Number of electrodes	2
Electrode shape	Rectangular
Electrode relative position	Parallel
Dimensions	
Electrode section	1.1 × 2.4 × 12.0 mm
Electrode length	13.0 mm
Distance between electrodes	0.5 mm
Material	
Electrode material	Copper
Medium between electrodes	Cotton rope thread
Placement	
Placement within HX	In front of HX
Fixture method	Clamp wedged between fins
Electrode position (airflow)	Perpendicular
Electrode position (HX Surface)	Parallel

The FMRS3 was tested in two separate frost–defrost cycles. In the first test, with results plotted in Figure 121, water detection during frosting was negligible, with sensor readings remaining close to an ADC value of ~1022. Defrosting was initiated at $t = 29$, after which a minor fluctuation down to an ADC value of ~1015 at $t \in [32, 33[$ was measured.

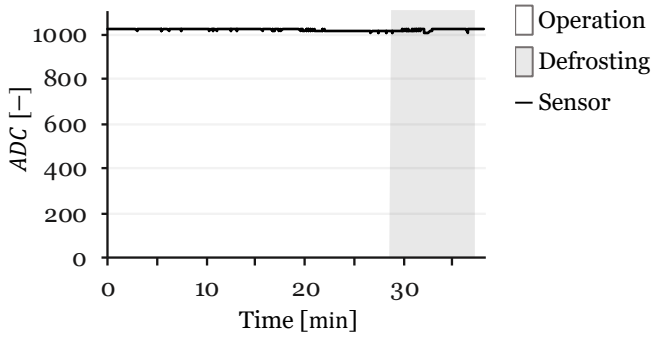

Figure 121 – Results for the first test of the FMRS3.

The second test, shown in Figure 122, exhibited even worse results. Defrosting was initiated at $t = 17$ min due to significant frost accumulation, but only negligible variations were observed, barely indistinguishable from measurement noise. No meaningful water detection occurred before or during defrosting, and the output curve remained essentially flat.

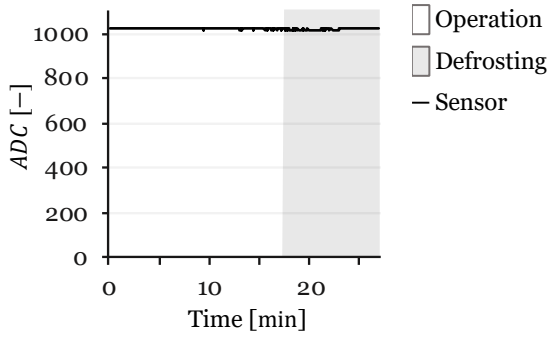

Figure 122 – Results for the second test of the FMRS3.

These results point towards the failure in achieving a good thermal conductivity with this sensor, which is most likely due to the wedge method of fixing the sensor between fins, and the increased footprint of the intake side surface area of the sensor. Furthermore, during defrosting, water does not drip directly onto the electrodes. In contrast, FMRS2, placed between fins, achieved stronger responses during defrosting despite its limitations. Thus, this configuration points towards a better path in placing the sensor clamped on the HX fins, taking full advantage of its electrical insulation. The thicker, more loosely spaced cotton wrapping may still offer potential when combined with an in-fin placement like FMRS2.

4.9.4. FMRS4

The FMRS4 was developed as a variation of FMRS2, maintaining the placement around a HX fin but introducing a different fabric medium configuration. Instead of tightly wound cotton sewing thread, the same thin cotton rope thread used in the FMRS3 was loosely wound in a figure-eight pattern, as represented in the CAD model of Figure 123 (a). This resulted in complete electrode coverage by the fabric medium and the presence of protruding microfibers visible in the tested sensor, shown in Figure 123 (b). These fibres extended outward from the main thread, which increased the effective contact surface and enhanced the potential for moisture absorption directly from the surrounding HX fins. The design also aimed to preserve medium porosity, thereby improving condensation bridging while still providing electrical insulation. Furthermore, the use of longer electrodes, similarly to FMRS2, increased the thermal contact area with the fin, with only the tip being exposed to the warmer intake air.

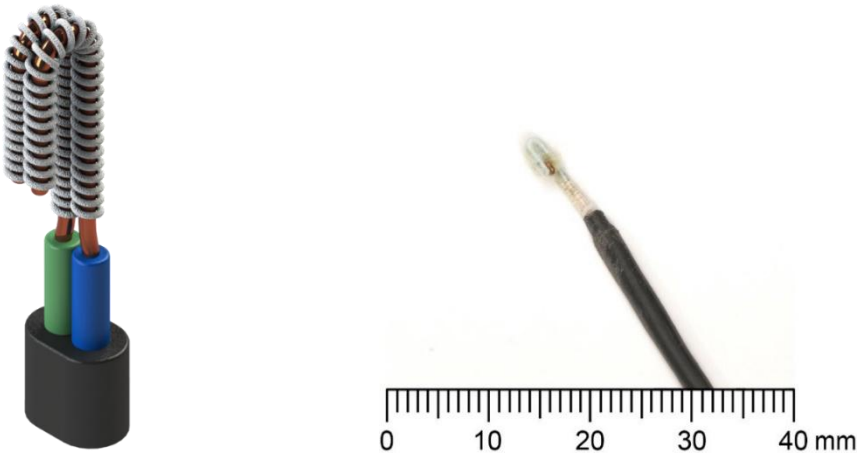

(a) (b)

Figure 123 – Rendered view of the CAD model (a) and picture (b) of the FMRS4.

The FMRS4 consists of two parallel cylindrical copper electrodes with a diameter of 0.5 mm and a length of 14.0 mm. The electrodes were spaced by an air gap of approximately 0.4 mm and insulated using a thin cotton rope thread as the fabric medium. The sensor was clamped onto a fin of the HX, positioned around the intake side so that the electrodes were curved parallel to the airflow while remaining in direct thermal contact with the fin. The sensor specifications are presented in Table 36.

Table 36 –FMRS4 specifications.

Feature	Specification
Sensor configuration	
Number of electrodes	2
Electrode shape	Cylindrical
Electrode relative position	Parallel
Dimensions	
Electrode section	Ø0.5 mm
Electrode length	14.0 mm
Distance between electrodes	0.4 mm
Material	
Electrode material	Copper
Medium between electrodes	Thin cotton rope thread
Placement	
Placement within HX	On fin
Fixture method	Clamped on refrigerant fin
Electrode position (airflow)	Curved, perpendicular to airflow
Electrode position (HX Surface)	Around fin, intake side

The FMRS4 yielded the most promising results among the fabric-based sensors. Across five consecutive frost–defrost cycles, the sensor consistently detected water accumulation, frost formation, and subsequent drying. This represents the first configuration to achieve reliable detection across all cycles. The signal was also distinct from that of the air gap sensors. Water detection during frosting was characterized by irregular fluctuations and moderate noise, whereas defrosting exhibited smoother and more continuous transitions.

In the first test, shown in Figure 124, water detection began almost immediately at $t = 1$ min, as ADC values gradually decreased from ~1020 to ~564 at $t = 9$ min. The descent was irregular, showing oscillations. Frost detection followed at $t = 11$ min, accompanied by a short spike, after which the values increased steadily, stabilizing at ~1022 at $t = 27$ min. Defrosting was initiated at $t = 33$ min due to visual observation of significant frost accumulation. The sensor immediately detected water, with a sharp drop in signal to ~358 at $t = 35$ min, stabilizing briefly before a sharp rise indicated complete drying at $t = 40$ min.

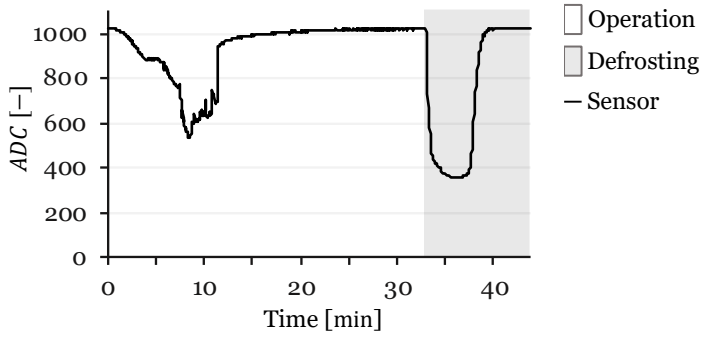

Figure 124 – Results for the first test of the FMRS4.

The second test, shown in Figure 125, also started with water detection almost immediately, with ADC values decreasing gradually from ~1023 at the beginning of the test to ~996 at $t = 7$ min. At this point, a sharp drop occurred, reaching ~895, marking the lowest sensitivity to water detection among all FMRS4 tests. Despite this being the weakest water detection result for the frosting phase, the drop was still significant and well above the responses observed in previous FMRS designs. From $t \in [7, 31[$ min, the signal showed irregular fluctuations with a slight overall positive slope, stabilizing near ~990. Defrosting was initiated at $t = 47$ min after significant frost accumulation was visually confirmed. Immediately upon defrost initiation, the ADC value dropped sharply to ~190, continuing to decrease more gradually until reaching ~158 at $t = 53$ min. Following this low plateau, a sharp recovery occurred, and by $t = 55$ min the sensor had

returned to 1023, indicating a fully dry HX. The signal remained stable for the remainder of the test.

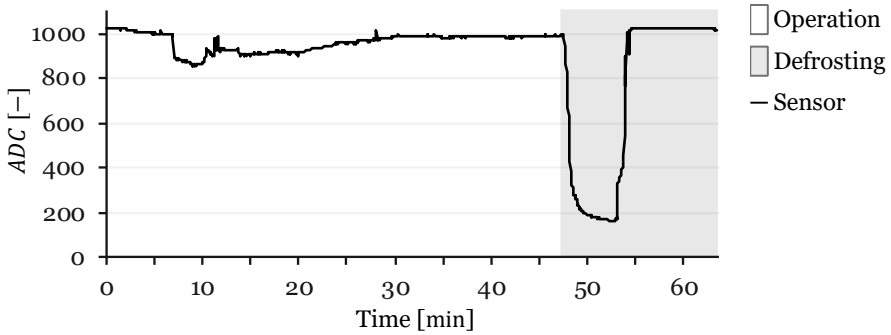

Figure 125 – Results for the third test of the FMRS4.

The third test, illustrated in Figure 240-Annex A showed water detection during the frosting phase, followed by some signal noise, while the defrosting stage behaved consistently with previous tests, displaying a sharp drop and recovery as the HX dried. The fourth test, shown in Figure 241-Annex A exhibited similar dynamics, with early water detection, a gradual decrease in signal, and a distinct response during defrosting, ending with stabilization as the HX reached a dry state. Finally, the fifth test, shown in Figure 242-Annex A presented delayed water detection but followed the same characteristic pattern: signal decrease during frosting, a sharp drop during defrosting, stabilization, and final recovery. Overall, all five tests confirmed the repeatability of FMRS4, consistently detecting frosting and defrosting events despite minor variations in sensitivity and timing.

A key feature of fabric medium sensors that is easily seen in this FMRS4 was the difference in signal morphology between frosting and defrosting. During frosting, the sensor response was irregular, with small oscillations superimposed on the overall negative slope, likely reflecting electrochemical effects, together with intermittent condensation and localized freezing within the cotton fibres. In contrast, during defrosting, the curve followed a smoother trajectory: a sharp initial drop, stabilization near a low plateau, followed by a rounded recovery curve until saturation at near 1023. This behaviour is attributable to the absorption capacity of cotton, which temporarily retains meltwater before gradually drying, producing a slower and more continuous recovery signal compared to the abrupt transitions seen in air gap sensors, whose droplet accumulation between electrodes is of a more erratic and unpredictable nature.

This distinction in curve morphology suggests that fabric-medium resistive sensors may offer reliable frost and defrost detection, but also richer information about the phase of

the cycle. Such signal patterns could potentially be used by data-driven approaches, such as machine learning or neural networks, to automatically classify sensor states (water accumulation, frost, defrosting, drying) based on curve shape alone. While this was not pursued within the present work, the results indicate that FMRS introduces an additional layer of interpretability compared to air gap sensors.

4.9.5. FMRS5

FMRS5 was developed as a variation of FMRS2, with the primary modification being the use of four electrodes instead of two. The electrodes were arranged in an alternating configuration ($1 - 2 - 1 - 2$). The aim of this design was to increase the surface area of contact with both the fin and the surrounding airflow, thereby enhancing moisture capture and potentially improving detection sensitivity. As with FMRS2, the electrodes were wrapped with cotton sewing thread. Figure 126 shows the CAD model (a) and the produced sensor (b).

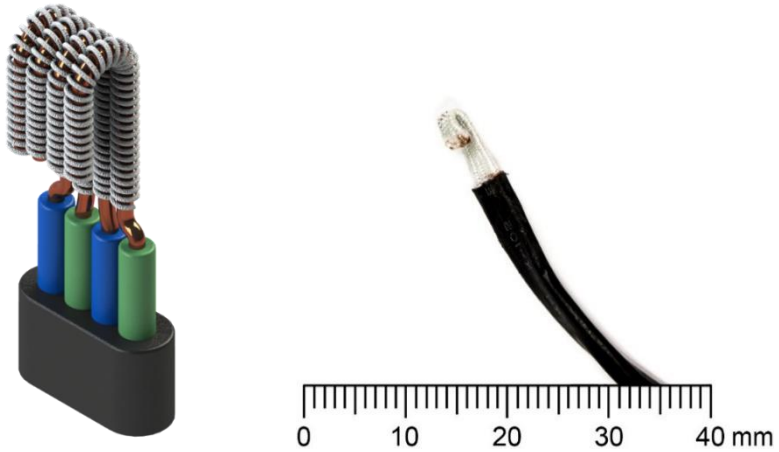

(a) (b)

Figure 126 – Rendered view of the CAD model (a) and picture (b) of the FMRS5.

The FMRS5 consists of four parallel cylindrical copper electrodes, each with a diameter of 0.5 mm and a length of 12.0 mm, arranged in an alternating configuration with 0.3 mm spacing. The electrodes are wrapped with cotton sewing thread, which serves as the insulating and moisture-absorbing medium. The sensor is designed to be clamped onto a refrigerant fin, with the electrodes curved perpendicular to the airflow and positioned around the fin on the intake side of the HX. The sensor specifications are presented in Table 37.

Table 37 –FMRS5 specifications.

Feature	Specification
Sensor configuration	
Number of electrodes	4
Electrode shape	Cylindrical
Electrode relative position	Parallel
Dimensions	
Electrode section	∅0.5 mm
Electrode length	12.0 mm
Distance between electrodes	0.3 mm
Material	
Electrode material	Copper
Medium between electrodes	Sewing cotton thread
Placement	
Placement within HX	On fin
Fixture method	Clamped on refrigerant fin
Electrode position (airflow)	Curved, perpendicular to airflow
Electrode position (HX Surface)	Around fin, intake side

In general, results for FMRS5 the sensor displayed clearer water detection than FMRS2, particularly during frosting phases, though performance was inconsistent and worse than that of the FMRS4, highlighting new challenges introduced by the larger electrode footprint.

For the first test, shown in Figure 127, the sensor began at an ADC value of 1023 and showed a slow decline starting at $t = 3$ min. The signal gradually decreased to ~882 by $t = 36$ min, followed by a sharp increase to ~940 at $t = 41$ min. From there, the curve rose more slowly, stabilizing at ~994 by $t = 67$ min. Defrosting was initiated at $t = 94$ min, after which a sharp drop occurred, reaching ~318 at $t = 96$ min. The signal then rose steadily, reaching 1008 at $t = 102$ min, marking full drying of the HX. This unusually long cycle was attributed to the sensor placement in a section of the HX that froze more slowly than others, and that is the reason for the late defrost, as frost formation was only significantly visible near the sensor at that time.

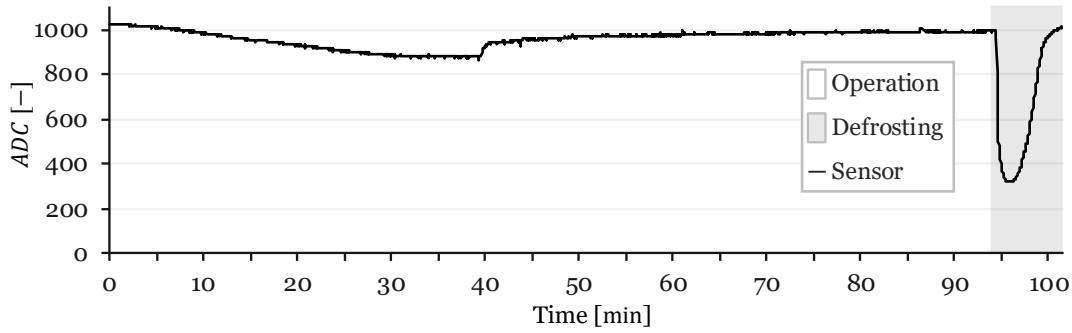

Figure 127 – Results for the first test of the FMRS5.

The results after repositioning the sensor are shown in Figure 128, water detection occurred much earlier. ADC values decreased slightly from ~1012 at $t = 2$ min to ~936 at $t = 7$ min, stabilizing until $t = 16$ min, when a rise began, meaning frost detection. Full saturation was reached by $t = 22$ min. Defrosting was initiated at $t = 30$ min, with an immediate sharp drop to ~243 at $t = 33$ min. A further decrease to ~158 occurred at $t = 35$ min, followed by a stable plateau. The signal then recovered sharply, rising to ~731 at $t = 42$ min, and finally reached 1023 at $t = 46$ min, indicating a dry HX. Compared to Test 1, the shorter freezing and drying times reflected a more favourable placement of the sensor within the HX.

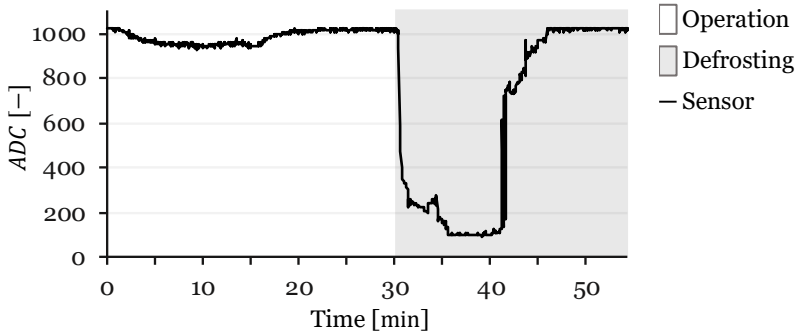

Figure 128 – Results for the second test of the FMRS5.

The third test, shown in Figure 129, was made with the same sensor position, however it revealed a worse behaviour. Water detection started almost immediately, with the signal dropping progressively to ~113 by $t = 14$ min. The sensor then stabilized at this low value, failing to clearly distinguish the frost phase before defrosting was initiated at $t = 23$ min due to significant frost accumulation around the sensor. Unlike previous tests, the signal did not drop further during defrosting but instead fluctuated slightly before beginning to rise at $t = 25$ min. However, the curve never returned to full saturation, indicating incomplete drying. This behaviour suggests that the larger electrode arrangement and tightly wound fabric may have led to water entrapment within the

cotton, shielding liquid from both freezing and evaporation, and thereby limiting the sensor's frost detection and recovery.

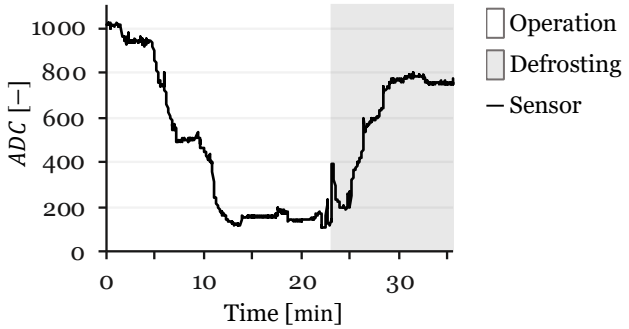

Figure 129 – Results for the third test of the FMRS5.

FMRS5 demonstrated that increasing the number of electrodes can improve water sensitivity but also introduces new challenges. The expanded footprint increased moisture accumulation, which extended freezing and drying times and even inhibited full recovery. Moreover, the larger geometry made integration between HX fins more difficult, especially in compact HX. While FMRS5 outperformed FMRS2, its drawbacks suggest that smaller, less intrusive sensors such as FMRS4 are preferable for reliable operation.

4.9.6. Fabric medium resistive sensors – concluding remarks

The development of the FMRS demonstrated that introducing a fabric medium between electrodes addressed some of the limitations observed in the AGRS designs and CMRS concept. Cotton, as a porous and absorbent material, enabled water uptake and distribution through capillary action, thereby creating stable thermal conductive bridges between electrodes during both frosting and defrosting phases. Unlike the developed and tested AGRS configurations, where water bridging was inconsistent, and CMRS concept, which suffered structural degradation under freeze–thaw cycling, the fabric medium provided mechanical compliance and durability under repeated testing.

Among the tested configurations, FMRS4, shown in Figure 130, installed on the HX surface in dry (a) and with significant frost accumulation (b), showed the most consistent and reliable performance.

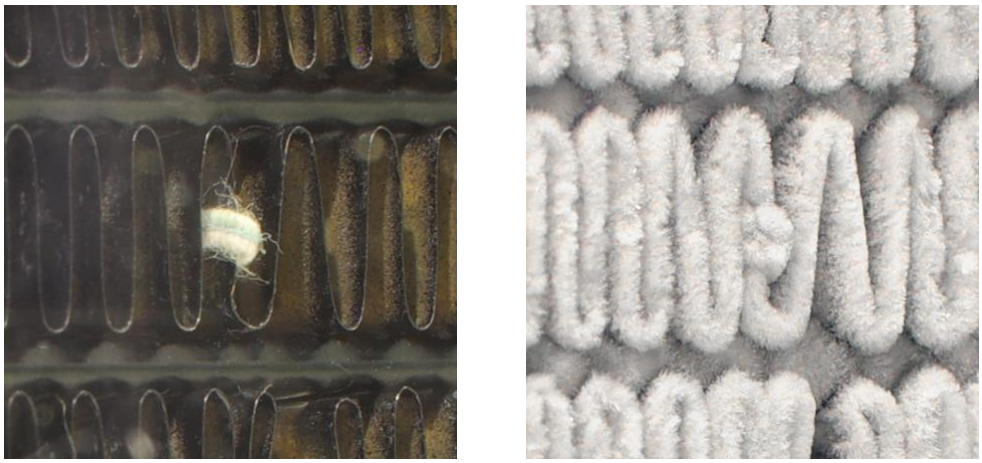

(a) (b)

Figure 130 – FMRS4 installed on the HX surface under dry conditions (a) and with significant frost accumulation (b).

This design successfully detected all five frost–defrost cycles. The thicker fibres and loosely tied cotton string, shown in the microscopic image in Figure 131 (a) allowed for increased porosity, promoting condensation and moisture absorption, while still offering electrical insulation when dry. In contrast, tightly wrapped designs (FMRS1, FMRS2 as shown in Figure 131 (b) and FMRS5) exhibited reduced sensitivity during frosting phases, as excessive insulation limited water penetration and extended drying times.

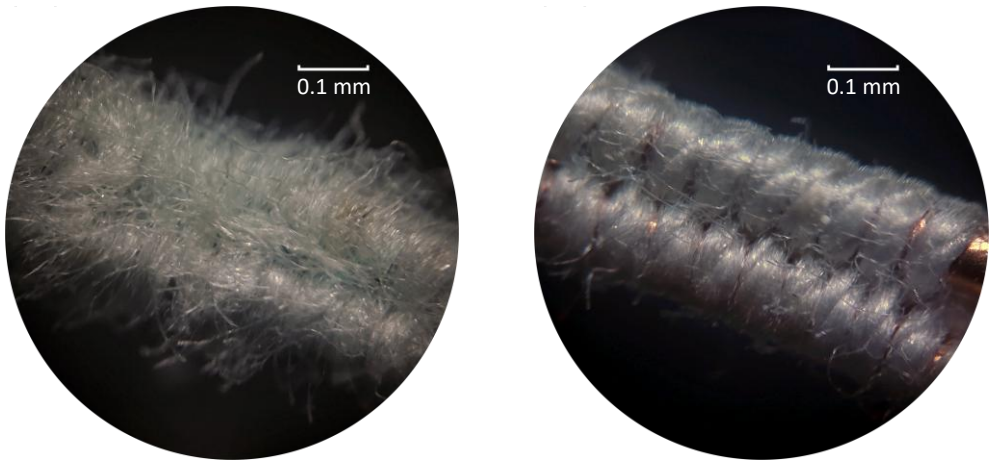

(a) (b)

Figure 131 – Close up view of the sensor electrodes for the FMRS4 (a) and FMRS2 (b).

The sensor's ability to absorb water was influenced by the type of fabric string used. The sensor employing a thinner fibre, denser, high twist thread tightly wound around the sensor electrodes, shown in Figure 132 (a), exhibited reduced sensitivity to water condensation. In contrast, the sensor using a thicker, looser cotton rope with thicker and

more dispersed fibres, shown in Figure 132 (b), displayed greater hydrophilicity and was more effective in detecting water during both condensation and defrosting phases.

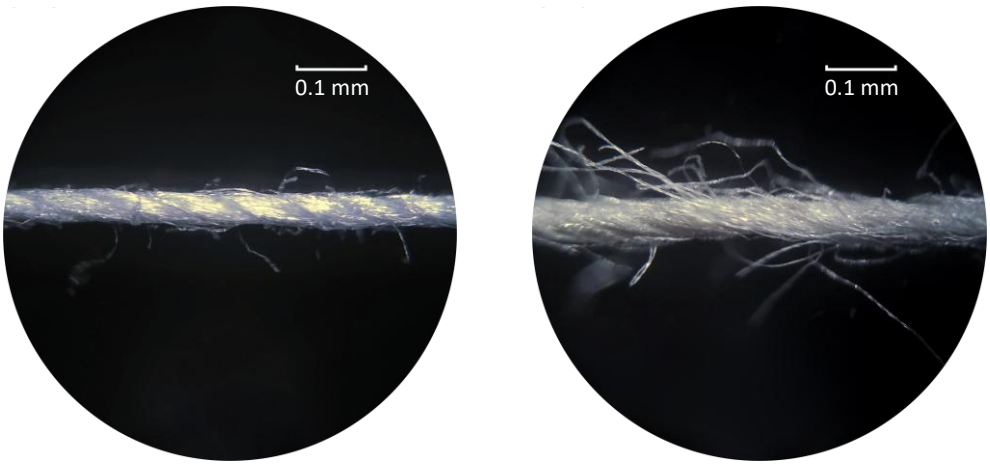

(a) (b)

Figure 132 – Close up view of the fabric mediums used, the sewing thread (a) and cotton rope thread (b).

Sensor placement was again shown to be a relevant consideration: sensors located directly on fins demonstrated better results than those positioned in front of the HX (FMRS3), which suffered from minimal water contact.

An important distinction observed in the FMRS compared to the AGRS is the morphology of the electrical signal during frosting and defrosting events. In FMRS, the presence of the absorbent medium introduced a smoother and more gradual response during defrosting, as absorbed water was released and dried in a smooth curve detection rather than in abrupt accumulations. Conversely, water detection during frosting was characterized by similarly noisier and irregular fluctuations, reflecting the heterogeneous absorption and condensation dynamics. Such differences in signal morphology may offer additional diagnostic potential, as they provide distinguishable patterns for identifying frosting versus defrosting phases.

Overall, these results highlight that fabric medium resistive sensors can combine the necessary electrical insulation, water absorption, and mechanical robustness required for reliable frost detection. However, performance strongly depends on electrode configuration, fabric properties, and placement within the HX. The findings indicate that optimal designs should control fabric tightness to allow water absorption without excessive shielding, ensure adequate thermal contact with the fins, and maintain a compact footprint to facilitate integration in tightly packed fin geometries.

4.10.AMRS - Additively Manufactured Resistive Sensors

AMRS1 was developed to explore the use of AM for resistive frost sensors. AM using FFF enables cost-effective fabrication and easy replication with dimensional precision worldwide, making sensors reproducible with widely available equipment.

Looking at the available materials for FFF 3D printing, flexibility is a desirable property, as it allows the sensor to conform closely to the HX surface when pressed or stretched against the fins, increasing the effective contact area and improving heat transfer. Among the main FFF materials, TPU stands out with the highest thermal conductivity (0.26 ± 0.05 $W \cdot m^{-1} \cdot K^{-1}$ [136]), making it a relatively poor insulator and therefore suitable for promoting thermal coupling with the HX. Together with the sensor's thin profile, this reduces overall thermal resistance and enables faster thermal response to surface changes. Manufacturing constraints also influence design: the minimum electrode width is 0.6 mm, set by the nozzle diameter of the available printer, while the minimum sensor thickness along the Z-axis is limited to 0.2 mm by the chosen layer height.

The AMRS1, is shown in Figure 133 (c) with the rendered CAD model, while Figure 133 (d) presents the printed and fabricated sensor.

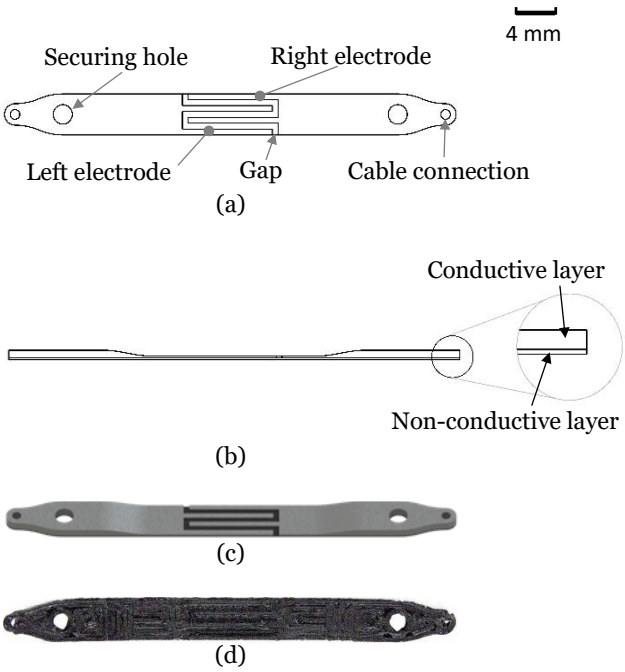

Figure 133 –Front (a) and side (b) view of the drawing, render (c) and picture (d) of the AMRS1 sensor.

This sensor was produced using a dual-material process, with an electrically insulating Filaflex TPU95A [130] base layer and a conductive Filaflex TPU92A [131] from Recreus for the interdigitated electrode pattern. The conductive filament exhibits an average resistivity on the order of 3.9 $\Omega \cdot cm$ [137]. This provides sufficient electrical conductivity for resistive sensing applications, even if it is lower than that of copper. The interdigitated layout, visible in Figure 133 (a), increases the electrode contact surface, enhancing sensitivity to water and frost bridging. The dual-material structure, shown schematically in Figure 133 (b), results in a thin and flexible sensor that can be stretched directly around a fin for improved contact with the HX.

The AMRS1 consisted of four interdigitated electrodes printed in conductive TPU, separated by 0.5 mm, embedded onto a flexible insulating TPU substrate. The sensing region had a total thickness of 0.4 mm, with electrodes 0.6 mm wide and 0.2 mm thick. At the extremities, electrode thickness increased to 0.8 mm to improve the conductor section and electrical contact in the cable contact hole. Two mounting holes were incorporated at each end to allow the sensor to be wrapped around a fin and secured by a non-conductive rod. The specifications are summarized in Table 38.

Table 38 –AMRS1 specifications.

Feature	Specification
Sensor configuration	
Number of electrodes	4
Electrode shape	Rectangular
Electrode relative position	Parallel
Dimensions	
Electrode section	0.6 × 0.2 mm
Electrode length	10.0 mm
Distance between electrodes	0.5 mm
Material	
Electrode material	Filaflex conductive TPU92A
Medium between electrodes	Filaflex TPU95A
Placement	
Placement within HX	On fin
Fixture method	Stretched around HX fin
Electrode position (airflow)	Curved, perpendicular to airflow
Electrode position (HX Surface)	Around fin, intake side

Four tests were carried out for the AMRS1, in all of which the sensor successfully detected the different phases of condensation, frost formation, defrosting, and drying. An

interesting characteristic consistently observed was that the ADC values decreased at the onset of frost formation, instead of increasing as seen with previous resistive sensors developed. After this initial drop, the signal began to rise gradually as frost accumulation increased, potentially indicating a measure of the amount of frost formed within the HX.

One possible explanation for this behaviour is that frost forming and expanding between the interdigitated electrodes might alter the electrical contact between them, potentially creating new conduction paths or bringing electrode regions into closer contact. This effect could explain the initial drop in ADC values upon frost onset, followed by a later increase as frost progressively insulated the electrodes. While this hypothesis requires further investigation, the phenomenon was observed across all four tests, highlighting a distinct response pattern specific to the AMRS1 design.

In the first test, shown in Figure 134, the ADC value began at ~1010 and gradually decreased to ~950 , corresponding to the presence of condensation bridging the electrodes. At $t = 12$ min, a sharp drop in ADC values was observed, coincident with the observed frost formation. The signal reached its minimum and stabilized at ~820 by $t = 21$ min. As frost continued to accumulate, ADC values slowly began to rise, indicating progressive insulation by the frost layer. At $t = 47$ min, defrosting was initiated after observable significant frost accumulation, and the ADC value sharply decreased from ~860 to 448, showing immediate water detection. The values remained low during the presence of liquid water before gradually recovering, reaching ~1010 after ~3.5 min once the HX dried. This test confirmed the ability of the AMRS1 to detect all frost–defrost phases, with its distinct behaviour of dropping ADC values upon frost onset.

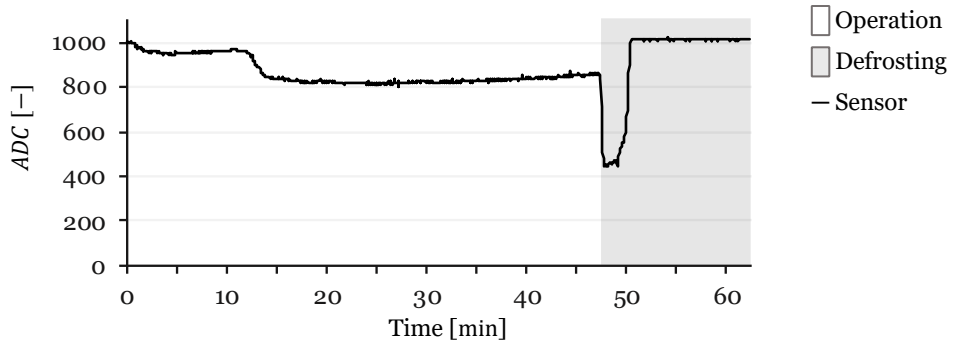

Figure 134 – Results for the first test of the AMRS1.

Tests 2 and 3 presented very similar behaviours to the first test. In Test 2, shown in Figure 243 – Annex A, the ADC signal decreased during condensation, reached a minimum as frost formed, and then gradually increased as frost accumulated. Defrosting caused a sharp signal drop, followed by recovery as the HX dried. In Test 3, shown in

Figure 244 – Annex A, a similar trend was observed, with a clear drop marking frost initiation, a gradual rise during frost accumulation, and a sharp decrease followed by recovery during defrosting. Both tests confirmed the repeatability of the sensor response, consistently detecting condensation, frost, defrosting, and drying phases.

The fourth test again confirmed the same detection sequence but exhibited a slightly different profile. From the beginning of the test, the ADC values followed a continuous negative slope with no clear plateau for saturation of water detection, suggesting that frost may have formed before water saturation. At $t = 7$ min, a sharp drop marked frost initiation, with a minimum reached by $t = 11.6$ min after which the signal began to rise gradually as frost accumulation progressed. Defrosting was initiated at $t = 51$ min, leading to a sharp decrease from ~965 to ~535, corresponding to water detection. As in the previous tests, values remained low during the presence of liquid water before recovering to ~1010 within ~3.5 min, indicating a dry HX. This result reinforces the repeatability of AMRS1 while highlighting that the dynamics of frost formation can influence the signal profile.

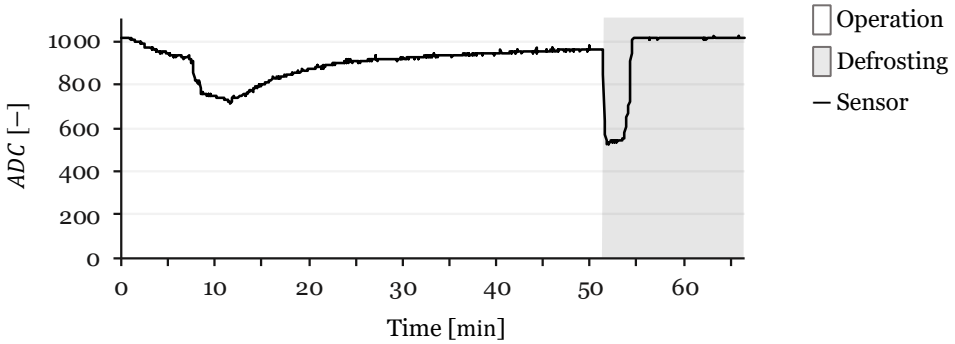

Figure 135 – Results for the fourth test of the AMRS1.

Across the four consecutive tests, the sensor detected condensation, frost formation, defrosting, and drying phases. A distinctive behaviour observed in all tests was the initial drop in ADC values at the onset of frost formation, in contrast to previous resistive sensors developed, where frost increased the sensor resistance. After reaching a minimum, frost accumulation gradually increases resistance again.

This unique signal morphology may provide additional information about the dynamics of frost onset compared to earlier designs. However, this effect must be fully understood before the sensor can be reliably used. As with the other sensors developed, AMRS1 also reached a saturation point beyond which it could not differentiate between moderate and severe frost accumulation. Even so, its ability to consistently capture the complete frost–defrost cycle, coupled with the advantages of low-cost additive manufacturing and

flexible TPU-based design, makes it a promising direction for further exploration. Figure 136 illustrates the AMRS1 mounted on the HX surface, shown under slight condensation (a) and with significant frost accumulation (b), where it is possible to observe that frost forms directly on the sensor surface as intended, confirming proper thermal coupling with the HX fins.

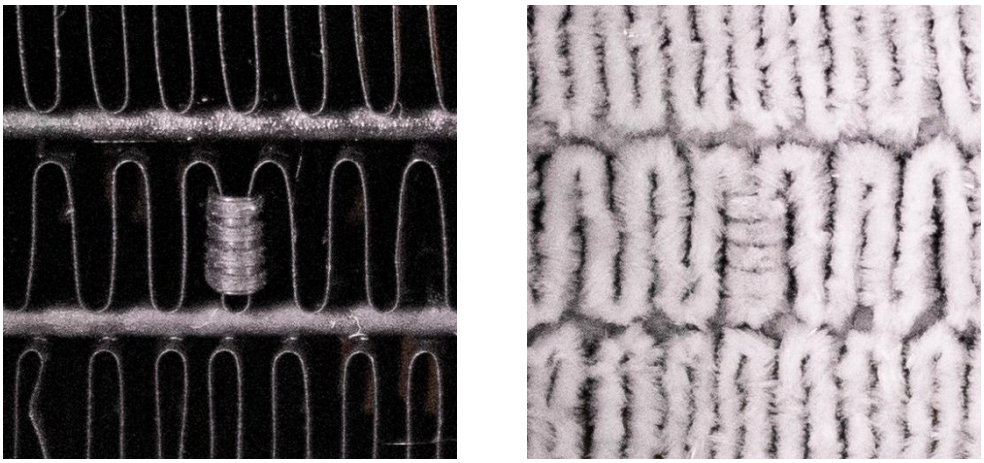

(a) (b)

Figure 136 – AMRS1 installed on the HX surface under slight condensation (a) and with significant frost accumulation (b).

The AMRS1 demonstrated that additive manufacturing can be a viable pathway for developing frost detection sensors, combining low fabrication cost, global reproducibility, and the flexibility to adapt to HX geometries without obstructing airflow.

4.11. Comparison between resistive sensor technologies

At the end of this chapter, and after discussing the principles and development of different types of resistive sensors, a comparative analysis is due. To objectively compare the different resistive sensor prototypes, a weighted scoring system was established and summarized in Table 39. Each sensor was evaluated against five criteria: frosting detection, defrosting detection, electrical insulation, fabrication, and installation.

Frosting detection evaluates the ability to detect both condensation and the transition to frost nucleation. Defrosting detection evaluates sensitivity to meltwater and the dry HX state. Together, these two criteria represent reliability and repeatability, which are the essential requirements for a viable frost sensor. Since a sensor that cannot reliably detect these phases is of no practical use, both criteria were assigned the highest weight of 3.

Electrical insulation considers risks of short circuits or unintended conduction when installed in direct contact with the HX. Here, exposed electrodes received lower scores,

while configurations with insulating mediums (fabric, ceramic) excelled due to their inherent insulation. Additively manufactured sensors were scored in between, as their conductive paths are embedded in a non-conductive matrix and inherently held apart from each other. This criterion was assigned a weight of 2.

Fabrication accounts for the ease and cost of manufacturing the sensor. Since all designs are very cost-effective and relatively simple to produce, this factor was given a lower weight of 1.

Installation reflects the practicality of mounting the sensor on the HX. Sensors that required insertion through the HX fins or had bulky geometries received penalties, while those that could be easily mounted without damaging the HX or disrupting airflow scored higher. This criterion was also given a weight of 1.

The scores assigned to each sensor for every criterion were 0 (none), 1 (low), 2 (average), 3 (good) and 4 (excellent). To calculate the final percentage, each score was multiplied by its respective weight, summed across all criteria, and normalized against the maximum achievable score, resulting in a performance index expressed as a percentage. This allows direct comparison of overall suitability across designs.

Table 39 –Weighted comparison between sensor designs.

Criteria / Sensor	Weight	AGRS1	AGRS2	AGRS3	AGRS4	AGRS5	AGRS6	FMRS1	FMRS2	FMRS3	**FMRS4**	FMRS5	CMRS1	AMRS1
Frosting	3	2	1	0	1	3	0	1	1	0	**4**	3	0	4
Defrosting	3	3	1	0	1	4	0	3	3	0	**4**	3	3	4
Electrical insulation	2	1	1	2	1	2	2	3	3	4	**3**	3	4	2
Fabrication	1	3	3	3	2	3	2	3	3	2	**3**	3	1	4
Installation	1	3	3	4	3	4	4	3	3	4	**3**	1	0	2
Total (%)		58	35	28	33	80	25	60	60	35	**90**	70	45	85

From this comparative evaluation, FMRS4 emerges with the best score, achieving 90% of the maximum score. FMRS4 distinguished itself through excellent sensitivity to both frosting and defrosting, high repeatability across multiple cycles, intrinsic electrical safety, and accurate response.

AMRS1 emerged as another promising approach, with a score of 85% scoring highest in fabrication due to the AM potential for cost-effective reproducibility and scalability while achieving great detection performance. However, its exposed electrodes and complexity of installation resulted in a worse score that did not yet match FMRS4, with design modifications might be possible to improve it enough to achieve or even surpass FMRS4.

Among the air-gap resistive sensors, AGRS5 achieved the best overall score of 80%, showing that clamped fin integration improved both thermal coupling and reliability. However, even this improved configuration still missed frost events in certain conditions, limiting its robustness compared to FMRS4. The remaining AGRS designs underperformed, AGRS2 and AGRS3 due to poor water bridging, AGRS4 due to persistent wet state, or AGRS6 due to ineffective electrode geometries.

The remaining fabric-medium sensors highlighted how sensor position, wrapping technique and selected thread affected performance. FMRS1 and FMRS2 performed poorly due to tight wrapping and the use of less absorbent thread, which insulated the electrodes and restricted water uptake. FMRS3, placed in front of the HX and exposed directly to intake air, received limited water during both condensation and defrosting, underscoring the importance of positioning the sensor between fins. FMRS5, which employed four electrodes, offered somewhat better detection than the earlier designs but was slower to respond, bulkier, and more complex to install. Its added complexity did not yield a proportional performance gain.

In summary, the comparative analysis highlights FMRS4 as the most suitable sensor for further development. It combined signal morphology, robustness, and ease of implementation, achieving results that no other configuration matched. AMRS1 remains a promising alternative for future research due to its manufacturability advantages and reliability, but it requires further research to fully understand its signal profile and does not outperform FMRS4 in its current state.

The work presented so far has focused on the development and comparative assessment of resistive FDS for demand defrosting control, to identify which concepts are most viable for reliable frost detection. This stage of the research has provided qualitative insights into which sensor designs work and why, primarily through analysis of their signal behaviour across frost–defrost cycles, with reference timings obtained from visual inspection and manual observation, which were then compared against the sensor measurements.

However, to progress further, it is necessary to quantify sensor sensitivity to frost beyond qualitative observation. As indicated in Chapter 2, one suitable tool for this purpose is CV, which can provide quantitative ground truth data on frost accumulation against which sensor signals can be correlated. The next chapter introduces the application of CV for frost detection, enabling a more rigorous evaluation of sensor performance.

Chapter 5

Computer vision method for frost detection

Having developed and tested different resistive sensor configurations in the previous chapter, the FMRS4 sensor design was selected to proceed with further analysis. However, to properly evaluate the accuracy and reliability of this sensor, it is necessary to establish a tool that objectively verifies when frost is present on the HX. Until now, validation has relied primarily on visual inspection; however, this approach is inherently subjective and lacks a consistent criterion for determining the onset and progression of frost. To overcome this limitation, a CV method was developed as part of the acquisition system.

The work developed in this chapter resulted in three publications. The first study [138] introduced the CV method applied to frost measurement, establishing a procedure to quantify frost accumulation and compare it with resistive sensor outputs. This initial validation demonstrated the feasibility of image-based frost detection as an objective reference. The following works [139] expanded this approach by analysing the spatial distribution of frost formation across the HX surface to evaluate local frost intensity and identify optimal regions for sensor placement. The research presented in [140] consolidated these results by developing a frost formation map, providing a spatial reference that supports both optimized sensor positioning and diagnosis of HX performance issues.

The validity of the quantitative metrics derived from the computer vision method is substantiated by an uncertainty analysis. This includes a visual sensitivity analysis that evaluates the impact of the binarization threshold on the final frost metric, as well as an empirical measurement of the system's stability and noise under different lighting conditions. As shown in Annex C, the empirical stability analysis determined the standard uncertainty of the global frost metric to be approximately 1.1 LSB ($10-bit$ equivalent) under stable, illuminated conditions. This assessment confirms the robustness and repeatability of the CV method as an objective reference for frost quantification.

In this way, the CV system acts as a quantitative metric for confirming whether the resistive sensor outputs correctly reflect actual frost presence.

5.1. Underlying principle

The principle of the computer vision method employed in this work mirrors the way humans naturally evaluate frost on a HX. When observing the surface, the perception of frost stems not only from its three-dimensional growth, which gives volume and texture to the deposit, but also from its characteristic white appearance, which contrasts strongly with the dark background of the AL-HX. This effect results from the scattering of incident light by frost at the numerous air–ice interfaces within its porous structure, whereas a clean HX surface absorbs more light and therefore appears darker. Consequently, despite its inherently three-dimensional nature, visual inspection of frost accumulation can be simplified to assessing the proportion of white versus dark regions in the image of the HX.

To mimic this process artificially, the image must be reduced to two categories: frost (white) and no frost (non-white). This can be achieved by processing the captured image so that only black and white pixels remain, which can then be counted and their proportion used to quantify frost. Figure 137 illustrates this principle using a cropped close-up of the HX during frost formation. The first image (a) shows the original snapshot, where frost is visible in the fin surface. In the second image (b), the same region is converted to grayscale, removing colour information and retaining only intensity values. The third (c) and fourth (d) images apply successive contrast enhancements until the surface is represented exclusively by black and white pixels, resulting in a fully binarized image. In theory, this transformation enables frost accumulation to be quantified directly by calculating the proportion of white pixels in the image.

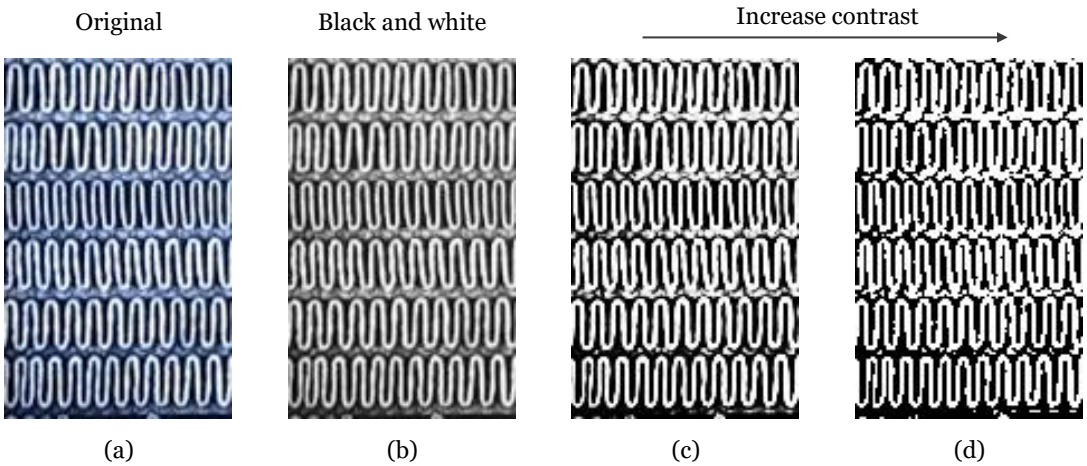

Figure 137 – Stepwise image processing of a cropped HX region, with the original (a), grayscale (b), contrast-enhanced (c) and binarized (d) steps shown.

The meaning of this binarization is further clarified in Figure 138, which magnifies a 5 × 5 pixel region from the binarized image in its upper right corner. In this zoomed view, nine pixels are black and sixteen are white, corresponding to 36% black and 64% white in that region. This simple exercise demonstrates the principle of the method: the proportion of white pixels provides an objective measure of frost coverage at the pixel level. While this example considers only a small section, the same calculation can be extended to the entire HX surface to obtain a global frost coverage metric.

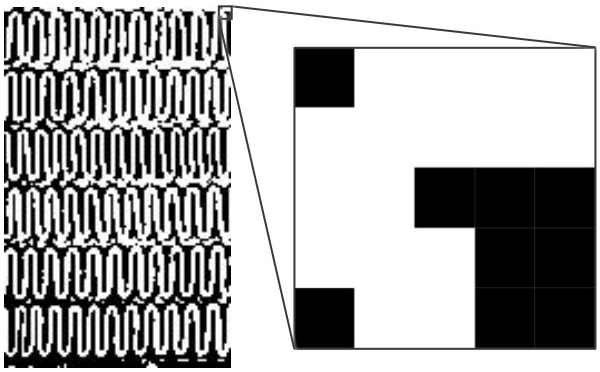

Figure 138 –Zoomed 5 × 5 pixel region from Figure 137 (d), showing 36% black (no frost) and 64% white (frost) pixels.

The application of this principle is demonstrated on a larger scale in Figure 139 and Figure 140, which show the entire HX during progressive frosting. In Figure 139, the original camera images depict four stages: (a) no frost, (b) low frost coverage, (c) moderate frost coverage, and (d) heavy frost, nearly blocking the HX.

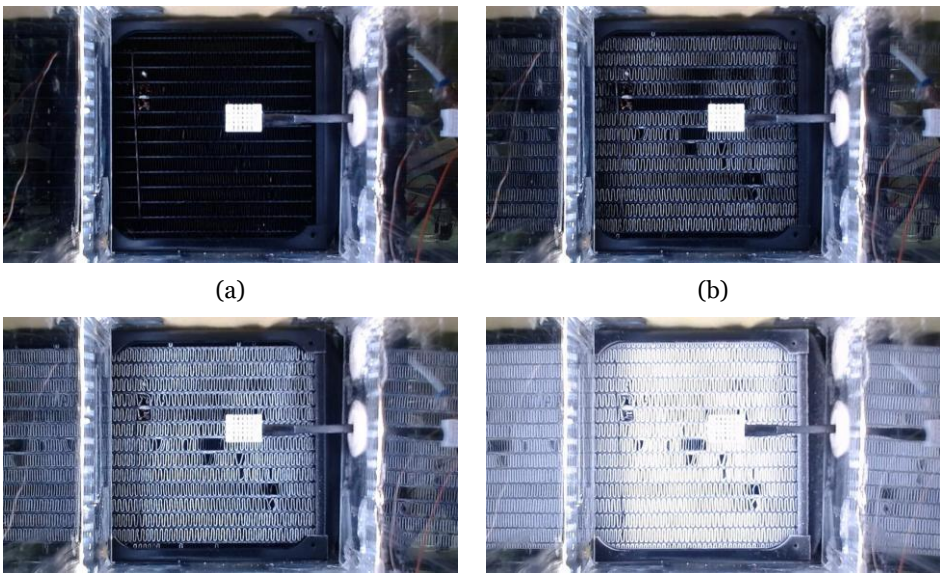

(a) (b)

(c) (d)

Figure 139 – Original images of the HX during testing with no (a), low (b), moderate (c) and significant (d) frost accumulation.

In Figure 140, the same images are processed in Adobe Photoshop using a fixed threshold of 128 on the 0 – 255 grayscale scale, corresponding to a 50% threshold. This is so that all four images are binarized under the same criterion, with white pixels corresponding to frost and black pixels corresponding to unfrosted regions.

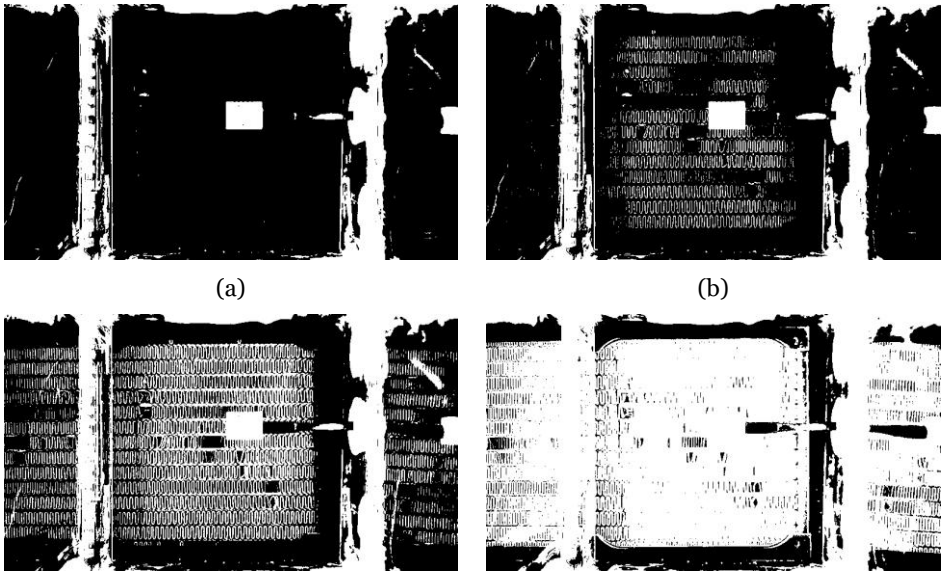

(a) (b)

(c) (d)

Figure 140 – Binarized versions of Figure 139 using a fixed threshold of 128 in Photoshop.

The results of this quantification are presented in Table 40, which reports the total number of pixels in each image, the division into black and white pixels, and the corresponding percentages. The values show a clear and consistent progression: from 18% frost coverage in image (a), to 28% in (b), 43% in (c), and finally 71% in (d).

Table 40 – Pixel quantification from Figure 140, showing progression of frost coverage.

Image	Total pixels	Black pixels	White pixels	Black pixels (%)	White pixels (%)
(a)	358302	294381	63921	82	18
(b)	358302	259708	98594	72	28
(c)	358302	204466	153836	57	43
(d)	358302	104355	253947	29	71

This demonstrates that the method provides an objective means of correlating the visual appearance of frost with a measurable parameter corresponding to the proportion of white pixels in the image. While the illustrative examples were prepared using Adobe Photoshop, which is a convenient tool for visually and intuitively manipulating images in a controlled way, applying this method in practice requires an automated approach under controlled acquisition conditions. For this purpose, both the lighting, camera and

HX must remain fixed relative to each other, and the images should be cropped to the relevant region of interest (ROI) to avoid noise from surrounding elements, which is clearly seen in the example of Figure 140. In this way, the conceptual demonstration is translated into a reproducible experimental setup, which is detailed in the following section.

5.2. Experimental setup

The setup described in the Frost formation experimental setup chapter already introduced the components required for image acquisition. In that section, the placement of the camera and the HX illumination system, were briefly presented. However, given their importance for the CV methodology, these components, highlighted in Figure 141 are here described in greater detail.

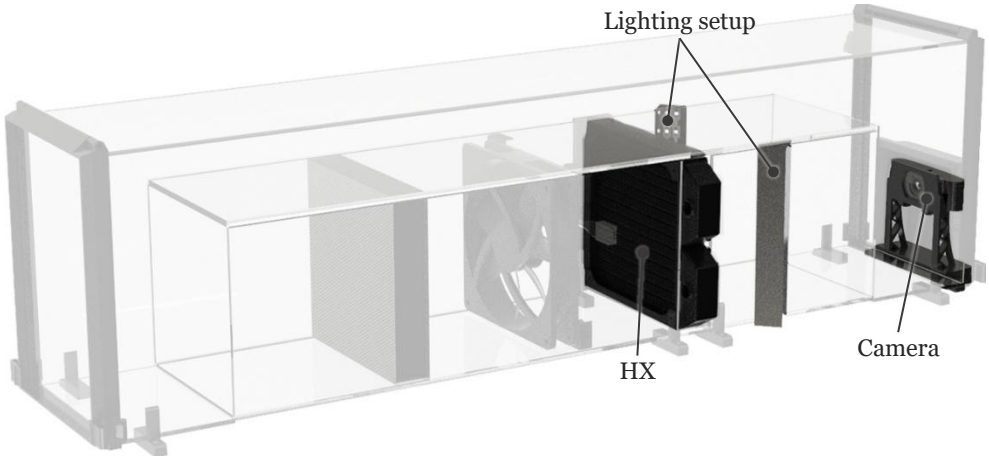

Figure 141 – Wind tunnel circuit, highlighting HX and CV components.

The frost detection camera used in this work was a Logitech C920, mounted inside the wind tunnel, and its main specifications are summarized in Table 41.

Table 41 – Logitech C920 camera for frost detection specifications [141].

Specification	Value
Connection type	USB-A
Image resolution [MP]	15
Still image resolution	1920 × 1080
Image quality settings customization	Yes
Diagonal field of view (FOV)	78°
Focus type	Auto
Cable length [mm]	1 500
Dimensions [mm]	94.0 × 43.3 × 71.0

The camera was positioned facing the intake end of the HX, fixed via a custom 3D-printed support that was fastened to the experimental setup base. This configuration ensured that the camera remained aligned with the AL-HX surface, with no possibility of displacement relative to the object of interest. This is important, since any movement of the camera relative to the HX would alter the region of interest and compromise the consistency of image processing across multiple tests. To prevent condensation on the acrylic walls from obscuring the field of view, the tunnel door at the camera side was designed with a dedicated housing. This placed the camera inside the tunnel volume itself, so that condensation formed on the door did not interfere with image acquisition. Illumination was provided by four LED light strips mounted in pairs to a support glued to the acrylic walls at an angle of 45° relative to the HX surface, directing light towards the region of interest. All these components are visible in the exploded view of Figure 142.

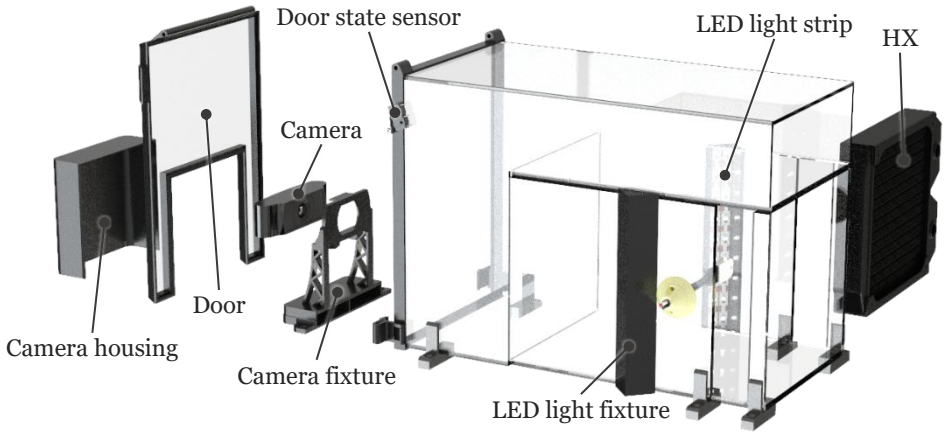

Figure 142 – Exploded rendered view of the wind tunnel section, highlighting the components used for CV.

The acrylic walls of the tunnel allowed the LED light to pass through, illuminating the AL-HX surface evenly without introducing additional obstructions into the airflow path. The power of the LEDs was sufficient to dominate over both laboratory artificial lighting and natural daylight entering the room, thereby minimizing noise from external light sources. This was done so that controlled and repeatable illumination conditions would improve consistency in results. The LED strips were manually activated at the beginning of each test and kept unchanged until the conclusion of the test session.

5.3. Image processing pipeline overview

The CV method implemented in the developed MATLAB application follows a sequential image-processing pipeline designed to extract a quantifiable measure of frost coverage.

At each acquisition cycle, occurring at $\tau = 3\ s$ intervals, an image of the AL-HX surface is captured. This sampling interval was intentionally selected to be more frequent than strictly necessary for most of the frosting phase, as frost growth typically develops on the order of tens of minutes. Nevertheless, oversampling provides a tool for analysis in post-processing, while allowing dataset reduction by down-sampling, whereas insufficient sampling cannot be compensated for in post-processing. Moreover, although frosting is a relatively slow process, defrosting occurs much more rapidly and involves fast transitions in surface state and appearance. The chosen three-second interval, therefore, ensures that these dynamic events are adequately captured. Figure 143 presents six consecutive images— RGB (a) and processed (b)—acquired over a 15 *s* window during a defrosting event. The visible changes in surface condition within such a short period highlight the need for a high acquisition rate to accurately characterize these transient phenomena.

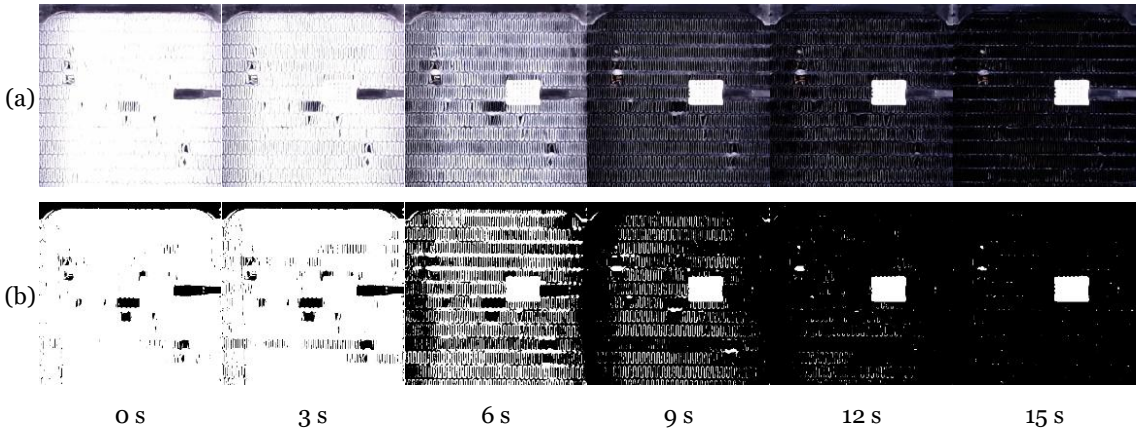

Figure 143 – 15 *s* sequence of the RGB (a) and respective binarized (b) images of the HX during defrosting.

The settings of the Logitech C920 webcam were fixed manually in the MATLAB application to prevent automatic corrections from altering the captured images over the course of an experiment. Consumer-grade webcams are equipped with automatic functions such as auto-exposure, auto-gain, auto-white-balance, and auto-contrast, which continuously adjust the image according to scene brightness or colour temperature. While beneficial for general video capture, these automatic adjustments introduce unwanted variability in measurements, resulting in frost measurement conditions that may appear differently across frames. Fixing all relevant parameters to the values presented in Table 42, resulted in each frame being recorded under identical conditions.

Table 42 – Logitech C920 settings set in the MATLAB application.

Parameter	Setting
Resolution	1280 × 720 px
Exposure	−6
Gain	64
White balance	3200 K
Contrast	50
Saturation	128
Backlight compensation	1
Sharpness	0
Brightness	70

Although the illumination was kept constant throughout each test, the subject of the image changed over time, transitioning from the dark HX surface to the white frosted background. This contrast reinforces the importance of maintaining fixed acquisition parameters, so that differences in pixel intensities are due to physical frost growth rather than camera-driven exposure compensation. A consequence of this approach is that some white regions may appear overexposed, but this is acceptable in the present context, since these regions correspond precisely to frost, and their overexposure does not compromise the objective of detecting and quantifying frost coverage.

After capture, the image is processed in MATLAB, as detailed in Annex B.2, where the corresponding code is provided for reference. The captured frame is cropped to a predefined region of interest corresponding exclusively to the HX, thereby eliminating elements of the wind tunnel that would otherwise introduce noise into the analysis. In the developed MATLAB application, this region was defined by the rectangle `[x = 479, y = 225, width = 350, height = 350]`, resulting in a square image of 350×350 pixels.

The cropped image is first converted to grayscale, yielding an intensity map in which each pixel is assigned a luminance value between 0 and 255 (or, in MATLAB's normalized format, between 0 and 1). A global fixed threshold of $T = 0.5$ is then applied to this map, classifying pixels with intensity ≥ 0.5 as white (frost) and those with intensity < 0.5 as black (no frost). This transformation produces a binary image, where each pixel can only take one of two possible values and which serves as the basis for frost-coverage quantification.

The proportion of white pixels within the cropped region of interest is then calculated by dividing the number of white pixels by the total number of pixels. This ratio provides a normalized estimate of frost coverage between 0 and 1. To facilitate a direct comparison with the resistive sensor data, which is read through the Arduino's $10-bit$ ADC, and therefore with values ranging from 0 to 1023, this ratio is multiplied by 1023 and rounded to the nearest integer. The result is a frost-coverage signal expressed in the same numerical range as the resistive sensor output. In this way, both signals can be plotted on the same scale, facilitating comparison of the resistive sensor response against the independent CV metric. The calculated frost value is appended at each acquisition cycle to the data matrix M, and is subsequently written to the experiment's CSV file together with the original and binarized images, in separate folders, so that the CV data remains synchronized and available for both real-time visualization and post-processing analysis. The full sequence of operations implemented in the MATLAB application is summarized in the flowchart of Figure 144.

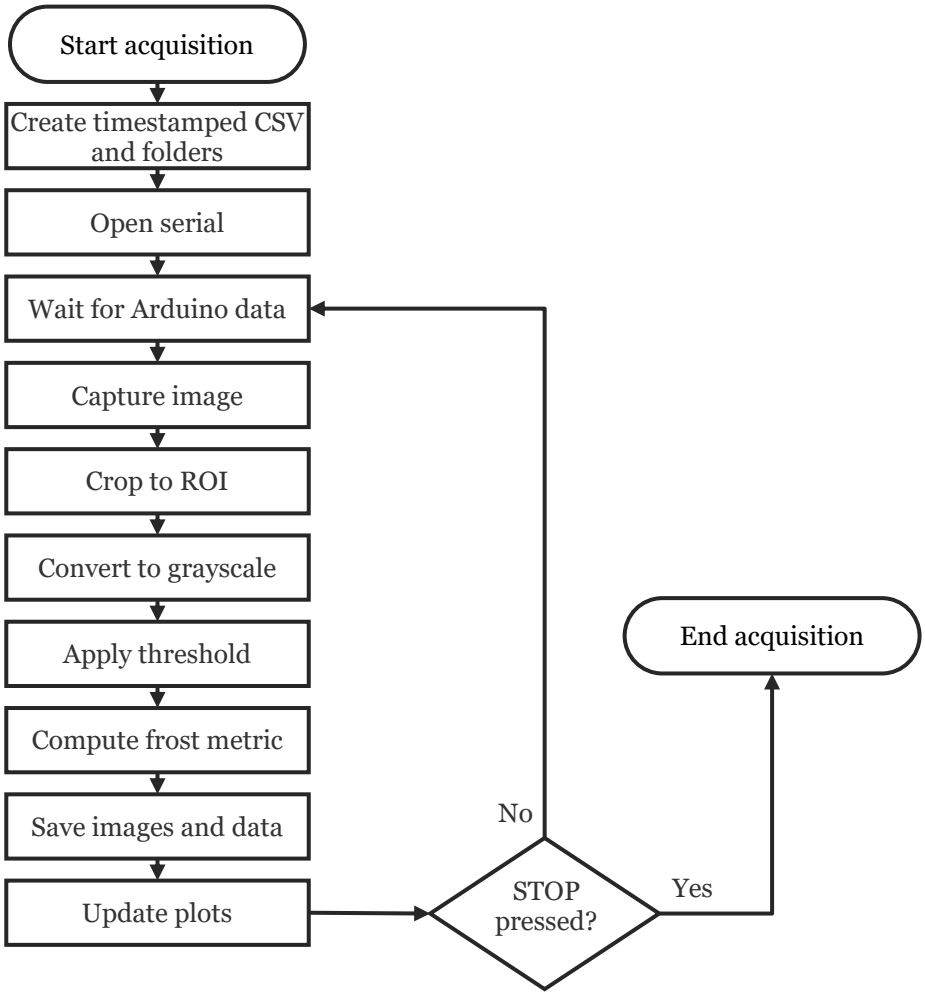

Figure 144 – Flowchart of the CV image-processing pipeline.

For each acquisition cycle, both the original and the processed binarized images are stored, and the calculated frost metric is logged in synchrony with the resistive sensor data. This allows the two signals to be plotted simultaneously in real-time, providing a direct visual and quantitative means of comparing resistive sensor behaviour with the independent metric obtained through the CV method.

5.4. Frost–defrost cycle metering using the computer vision method

To assess the performance of the CV method, three frost–defrost cycles were conducted. Each test highlights aspects of frost evolution and removal dynamics. In Test 1, defrosting was initiated once the global CV metric (CVG), which monitors the whole intake area of the AL-HX reached the threshold of 950, enabling evaluation of the method over a typical frosting cycle with controlled termination. Test 2 was allowed to proceed for an extended period of 95 min, providing insight into the maximum frost accumulation that can be captured by the method and into the behaviour of the frost curve. Finally, Test 3 was performed with the same threshold as Test 1, however the whole system was already cooled and prone to accelerated frost formation, allowing observation of the method under conditions of faster growth.

5.4.1. Test 1 of the CV method

The first test was conducted under controlled conditions, with defrosting triggered at the predefined CV threshold (CV_{th}) of 950. Figure 145 presents the time series of the CVG for Test 1, with markers corresponding to specific points along the curve, that will be detailed below.

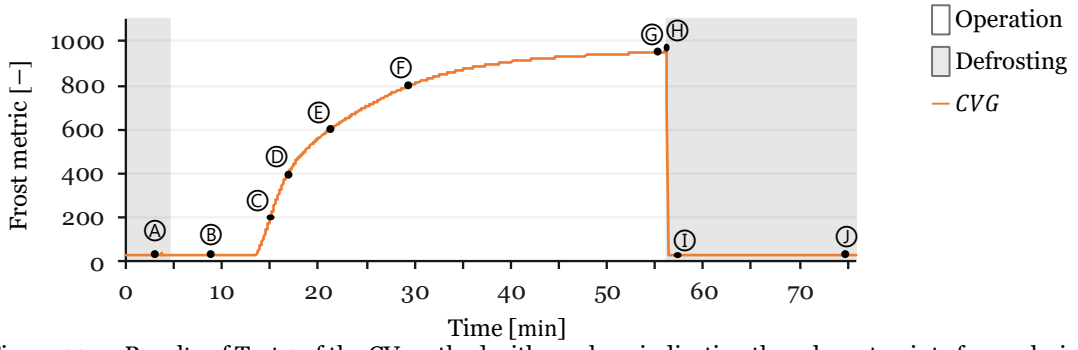

Figure 145 – Results of Test 1 of the CV method with markers indicating the relevant points for analysis.

Figure 146 displays binarized snapshots of the HX surface taken at those markers, enabling direct visual correlation between the CV metric and the frost evolution.

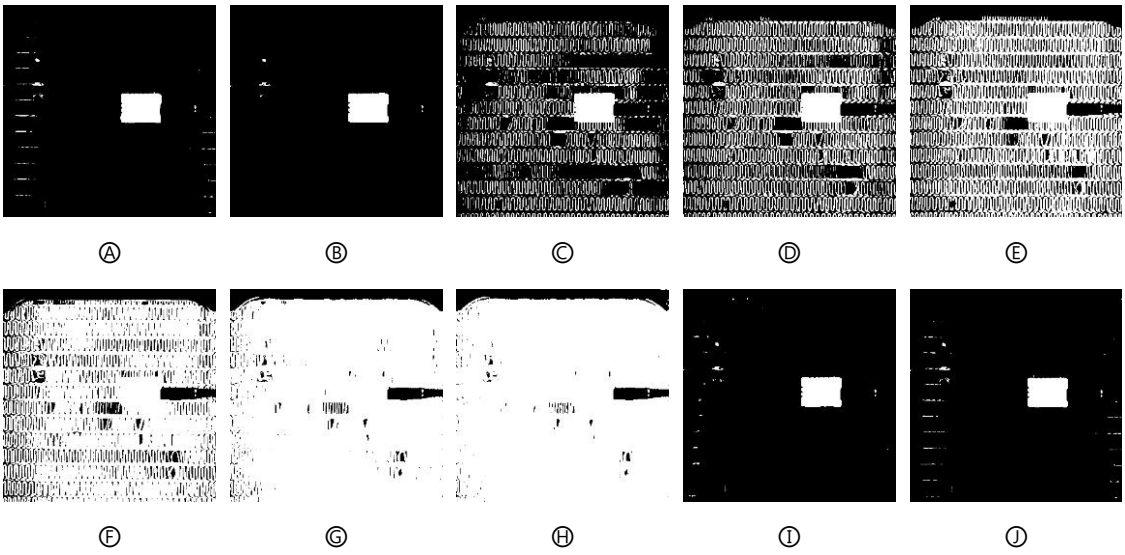

Figure 146 – Binarized snapshots of the HX ROI for the points of interest indicated in Figure 145.

The curve in Figure 145 is smooth and continuous, without noise or fluctuations, confirming the robustness of the CV metric. Marker 1 corresponds to the initial condition when the system was in defrosting mode and the fan was running at maximum speed. After startup, the CV signal exhibited a slight drop. This subtle decrease, though small, is visible in Figure 146, from Ⓐ to Ⓑ, as some fin lines that appeared bright in Ⓐ disappeared in Ⓑ. This occurs because the dry HX surface is slightly reflective, whereas once condensation forms during startup, the surface reflectance diminishes, and the fins appear darker.

Frost was first detected at $t = 13.5$ min, followed by a progressive increase marked as ©–Ⓕ in Figure 145. Marker © ($CVG = 200$) was reached 1.5 min after first detection, and , marker Ⓓ ($CVG = 400$) further 1.8 min afterward. This steep, nearly linear rise corresponds to the onset of frost formation in the HX, as nucleation does not occur simultaneously across all regions; this portion of the curve therefore represents the frost nucleation region. Marker Ⓔ ($CVG = 600$) was reached at $t = 21$ min , taking an additional 4 min to reach, already indicating a transition from nucleation to growth. Marker Ⓕ ($CVG = 800$) appeared at $t = 30$ min, i.e., an additional 9 min, confirming a progressive reduction in slope, and a transition to the densification region. Finally, the predefined threshold of $CVG = 950$ (marker Ⓖ) was reached at 56 min , requiring a further 26 min . Thus, the time intervals increased progressively: from ~1 to 2 min between the first thresholds up to > 25 min for the last interval. This trend reflects the transitions between frost nucleation, growth and densification. Additionally, as the HX surface becomes increasingly covered with frost, the optical contrast becomes less

sensitive to incremental changes, contributing to the characteristic decelerating curve that tends towards saturation (1023 = fully white).

Immediately after reaching marker ©, defrosting was initiated. Marker Ⓗ occurred only a few seconds later and a slight spike to $CVG = 956$, a value ~6 points higher than the threshold. This transient increase lasted for three frames (~9 s total), with CVG values of $956 \rightarrow 955 \rightarrow 955$, before returning to 950 and then falling to $699 \rightarrow 37 \rightarrow 29$ in the following frames. The effect is explained by the opening of the wind tunnel doors at the start of the defrost sequence: the sudden inflow of warmer, more humid ambient air, in contact with the supercooled AL-HX surface causes a rapid increase in frosting, before the frost temperature increases sufficiently to start melting.

Subsequently, as the defrost cycle advanced and the fan reached maximum speed, frost melted rapidly. The CVG metric dropped sharply from ~950 to 29 in the next frames, indicating the transition from a frost-covered to a water-covered HX surface. This was marker ①, where the HX surface was wet and thus less reflective, producing lower CV values. Finally, as the defrost completed and the HX surface dried, the CV metric recovered slightly. Marker ② showed the HX returning to its slightly reflective dry state, with values only marginally higher than those during the water-covered stage, consistent with the initial pre-frost condition shown at Ⓐ.

5.4.2. Test 2 of the CV method

The second test was performed over a significantly longer period, with the frost–defrost cycle lasting 115 min in total. For consistency with the previous and following tests, Figure 147 is cropped to 103 min, excluding most of the 20 min defrosting phase, which did not add relevant information beyond what was already observed in Test 1.

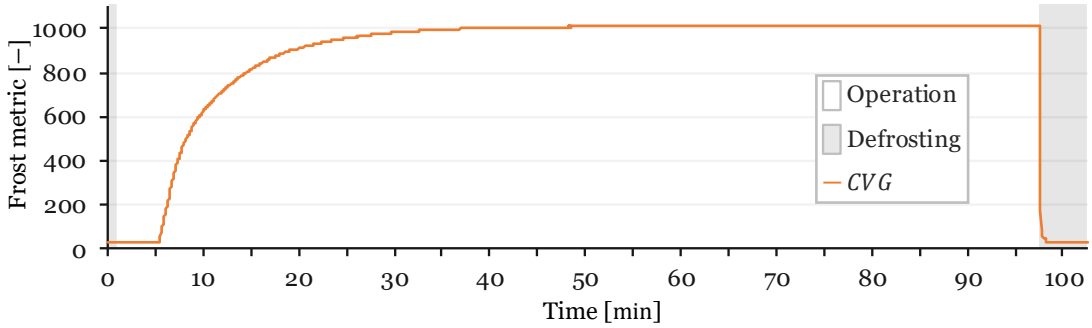

Figure 147 – Results of Test 2 of the CV method.

At the beginning of the test, the CV metric again exhibited a short initial decrease upon system startup, after which frost formation was first detected at 5 min. The frost coverage grew rapidly, surpassing 800 by $t = 15$ min, and reaching $CVG = 950$—the threshold value used to terminate Tests 1 and 3—at $t = 24$ min. Had this been a threshold-based cycle, defrosting would have been triggered at this point. Instead, the test was allowed to continue to observe the asymptotic behaviour of the metric.

The frost-coverage value reached $CVG = 1000$ units at $t = 37$ min, and increased only marginally thereafter, reaching $CVG = 1012$ units at $t = 98$ min. This near plateau indicates that once the AL-HX front surface is saturated with frost, further densification, increase in frost thickness and volume contribute little to the CVG value. This saturation of the CV method does not represent a practical limitation. When the frontal view of the HX becomes completely white, it indicates that the fin spacing is entirely filled with frost, corresponding to a critical blockage condition. The method remains effective and reliable for quantifying frost accumulation up to the point of full blockage, beyond which further measurement has little practical relevance for defrost control.

5.4.3. Test 3 of the CV method

The third test was performed after the system had already reached a lower temperature, which facilitated faster frost formation. The total duration, including defrosting, was 50 min, with the system starting operation at $t = 5$ min and defrosting initiated at $t = 35$ min, giving 30 min of operation before defrosting.

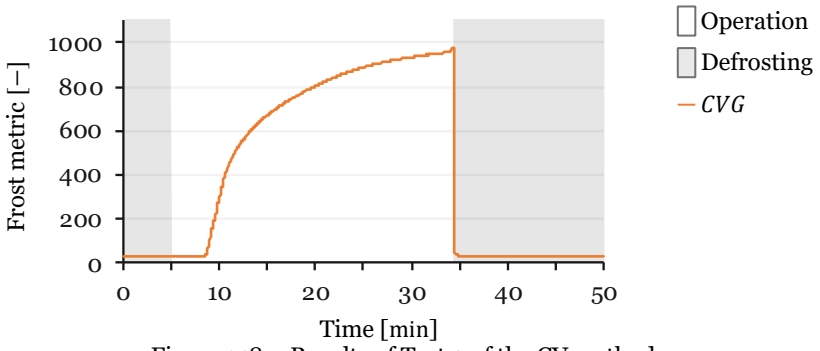

Figure 148 – Results of Test 3 of the CV method.

The curve obtained in this test, shown in Figure 148, exhibited the same smooth behaviour as in the previous tests. Frost was first detected at $t = 9$ min, and within just two minutes, at $t = 11$ min, $CVG = 400$. At the end of the frosting stage, when the threshold of 950 was reached, the curve exhibited a short spike to $CVG = 976$ before melting commenced. This overshoot was slightly larger than the one observed in Test 1, most likely because the AL-HX was colder when the doors were opened. The inflow of

warmer outside air with higher AH briefly caused a spike in frost growth at the cost of increasing the HX surface temperature, until the melting point was achieved, and defrosting actually commenced. Moreover, at a CVG of 950, the AL-HX surface is not yet fully saturated with frost, which makes this transient effect observable. In Test 2, where the CVG metric was already close to saturation, such an effect could not be detected.

The three tests presented demonstrate that the CV method provides a means of monitoring frost for demand defrosting applications. In all cases, the CV metric produced smooth, interpretable curves that reflected the frost level in the AL-HX intake surface throughout the frost–defrost cycles. The method proved effective in monitoring frost through nucleation, growth and densification, tracking its progression across different operating conditions, and capturing the rapid transitions associated with defrosting.

A caveat must be noted, however. The AL-HX intake contains several elements that act as sources of visual noise and evolve differently over time. Because the present method evaluates the entire HX surface, the resulting metric represents an average of all regions. This global approach would be suitable for real-time demand-based defrost control using CV. Nevertheless, in the present study, the CV method is used to validate FDS, whose performance depends on its placement, as was made evident in previous chapters. Since frost formation is spatially heterogeneous, averaging across the entire surface can obscure local behaviour at the sensor's location. For this reason, a more localized CV approach could improve accuracy.

5.5. Zone-specific frost formation

Frost formation on the AL-HX is heterogeneous. As illustrated in in Figure 149, different regions of the surface exhibit distinct behaviours. Certain elements within this area, highlighted in Figure 149 (a), introduce visual noise into the image analysis. The intake DHT sensor ① appears consistently white, while its cable ②, extending to the right, is consistently black in the binarized image. Additional sources of noise include damaged fins, as dented fins ③, or fins bent to allow the placement of larger sensors, as the AGRS4 ④, and fins dislodged from the refrigerant tube ⑤, which lose thermal contact with the HX and therefore do not accumulate frost at the same rate, leaving dark regions in early nucleation stages.

Beyond these artefacts, localized variations in frost growth also occur. Regions with increased ⑥ or decreased ⑦ frost accumulation can arise due to factors such as HX geometry, non-uniform working fluid and airflow distribution, or localized variations in

surface temperature due to varying efficiency in conduction of heat between working fluid and fin surface.

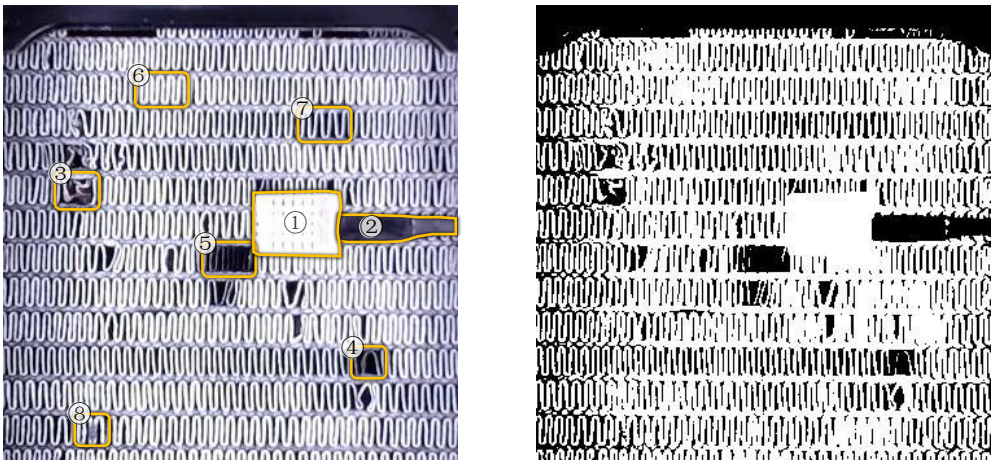

(a) (b)

Figure 149 – RGB image of the intake end of the HX with highlighted elements that create noise (a) and result of the binarized image (b).

Furthermore, the FDS itself ⑧, can produce a visible silhouette. These obstructions alter the local white-to-black pixel ratio in the affected regions, as shown in the binarized image in Figure 149 (b). Because some of these contributions vary over time, they can influence the CVG, which is the global CV metric. This highlights the need for a more localized analysis that focuses on smaller regions of the AL-HX surface, particularly around the resistive sensor, to minimize the influence of unrelated artefacts and spatial heterogeneities.

5.5.1. Sweep grid tile analysis

A direct way to address the spatial heterogeneity of frost growth is to subdivide the HX surface into smaller regions and analyse them independently. The simplest implementation of this idea is to superimpose a regular grid over the region of interest, effectively slicing the AL-HX into a set of tiles that can be processed separately. In this work, a 12 × 12 grid was adopted, yielding 144 tiles in total. This division was selected so that each tile corresponds to a physically meaningful portion of the surface, while still providing sufficient spatial resolution to capture local variations in frost growth. Figure 150 illustrates a binarized image of the AL-HX is with the 12 × 12 grid overlaid, where rows are identified by numbers and columns by letters, allowing each tile to be referenced. For example, the resistive frost detection sensor visible in this image occupies the bottom-left corner of tile $c12$, while the intake DHT sensor saturates tiles $h6$ and $i6$ completely and partially affects tiles $g6$, $g7$, $h7$, and $i7$.

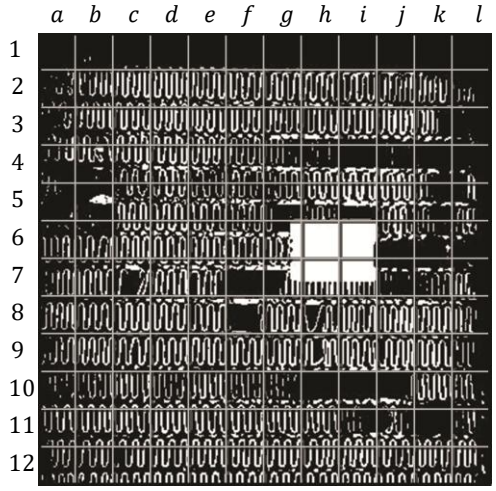

Figure 150 – Image of the HX, with a grid overlaid that delineates the tiles.

The advantage of this approach is that, instead of producing a single global value representing the entire HX surface, frost accumulation can now be quantified tile by tile. This enables the assessment of spatial variability and allows comparisons between regions with different behaviours. At this stage, the subdivision is purely geometric, meaning that all tiles are considered equally, without regard to defects, airflow anomalies, or sensor placement. Nevertheless, the resulting dataset provides a picture of how frost formation differs across the AL-HX surface, beyond what a global average can reveal. Ultimately, the purpose of introducing this tile-based approach is to enable analyses in smaller, localized regions that can be directly compared with the frost-resistive sensor. By focusing on the tiles in the vicinity of the sensor, the CV method can provide a more representative benchmark for validating sensor performance.

For this, a script to post-process the test data was developed in MATLAB, as detailed in Annex B.3, following the logic explained in the flowchart in Figure 151. After creating timestamped output directories and opening the results CSV file, the program gathers all images in the `/Images` folder and validates their availability. The outer loop iterates over the image sequence. For each frame, the trimmed, binarized ROI is partitioned into a 12×12 lattice of tiles. Columns are labelled $a - l$ (left to right) and rows $1 - 12$ (top to bottom), so that each tile has a unique chess-style identifier (e.g., $a1 \ldots l12$). The inner loop sweeps these tiles systematically. For each tile, the program computes the frost amount and maps it to a 10 *bit* frost metric. The tile's binary image is written as a lossless PNG to a folder named after that tile, while the corresponding metric is appended to an in-memory row buffer in the order $a1 \ldots a12, b1 \ldots b12, \ldots, l1 \ldots l12$. Once all 144 tiles of the current frame are processed, the program writes a single row to the CSV—filename, $a1, \ldots, l12$ capturing the complete spatial frost snapshot for that frame.

When the final frame has been written, the CSV handle is closed, and the script prints the output locations.

Figure 151 – Flowchart for the MATLAB image to tile analysis sweeping script.

The result from the processing of Test 1 using this method is shown in Figure 152. Each orange curve corresponds to the frost metric from one tile over time, while the black curve represents the average across all tiles (same curve as shown in Figure 145), which is equivalent to the whole–HX average analysed previously. The plot makes clear that the behaviour of individual tiles can vary substantially. While most tiles follow a pattern closely, or at least with the same shape as the average, some remain at very high frost metric values throughout the entire test, regardless of the operating phase. Others display a steep rise at the beginning, in contrast with tiles that progress more gradually and never exhibit such an initial slope. There are also tiles that only start increasing at later stages.

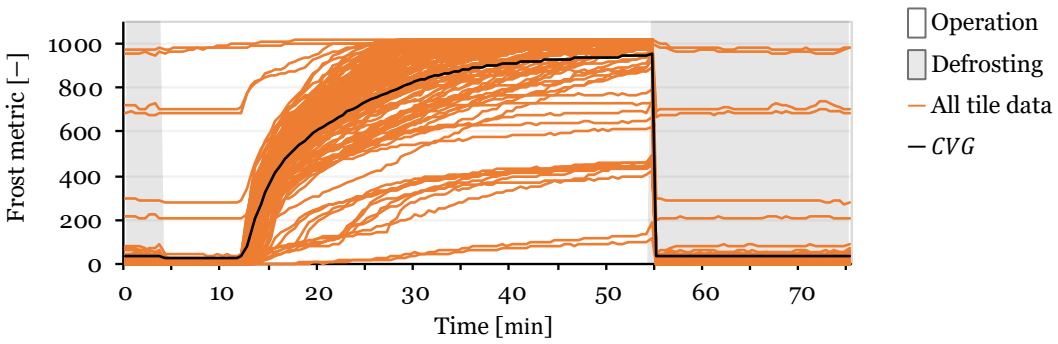

Figure 152 – Frost measurement from all the 144 tiles.

This representation also makes the separation between the dry state and the condensation stage more evident for some of the tiles than when considering only the average. Before the operation, tile values in regions that are reflective towards the camera are higher. Once the operation begins, condensation occurs, the AL-HX surface becomes more matte, and these tiles drop in value of CV tile frost metric (CVT), highlighting the transition more clearly. This tool can be further processed to better understand how frost forms in the HX surface.

5.5.2. Frost formation map of the HX surface

Another extension of the sweep grid tile analysis is the reconstruction of the CSV output into Frost Formation Map (FFM) frames. In this implementation, the CSV file generated by the 12 × 12 grid tile post-processing script (available in Annex B.3) is taken as the starting point. For each frame, the 144 tile values are read sequentially ($a1 - a12, b1 - b12, \dots, l1 - l12$) and reshaped into a 12 × 12 matrix (as the example in Figure 153 (a)), where each element represents the frost metric, which is then converted to an 8 bit grayscale value, as represented in Figure 153 (b).

5	21	34	35	47	27	15	2	0	0	0	0
190	344	501	513	511	498	533	516	501	465	398	146
237	356	499	549	508	473	482	506	466	594	445	118
199	264	425	485	470	416	405	395	305	387	285	164
213	201	423	459	404	438	339	524	491	568	401	255
294	248	506	502	490	410	585	1019	991	326	247	189
288	406	421	505	432	244	490	882	853	266	322	219
331	394	453	502	482	253	527	443	595	585	528	327
257	409	455	451	484	489	516	532	574	541	516	286
174	326	409	387	444	362	342	270	226	276	450	286
314	382	463	439	483	451	445	466	349	375	293	288
253	292	353	394	429	454	438	437	498	423	439	364

(a)

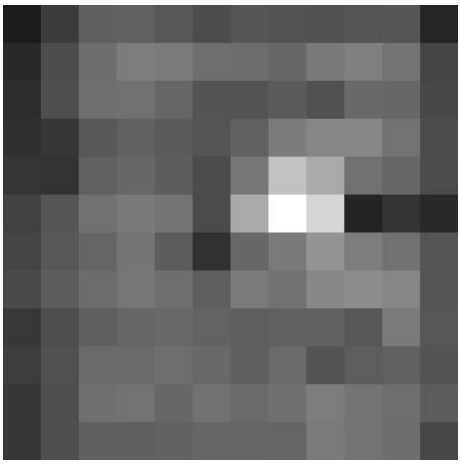

(b)

Figure 153 – Matrix values (a) and resulting map frame (b) after conversion from 10-bit tile metric to 8-bit grayscale, for a single test snapshot.

These matrices are stored over the entire sequence, forming a three-dimensional dataset in which the third dimension corresponds to time. When averaged, this 3D matrix is flattened into a frost map, which is characteristic of the HX in study. This process is represented in Figure 154.

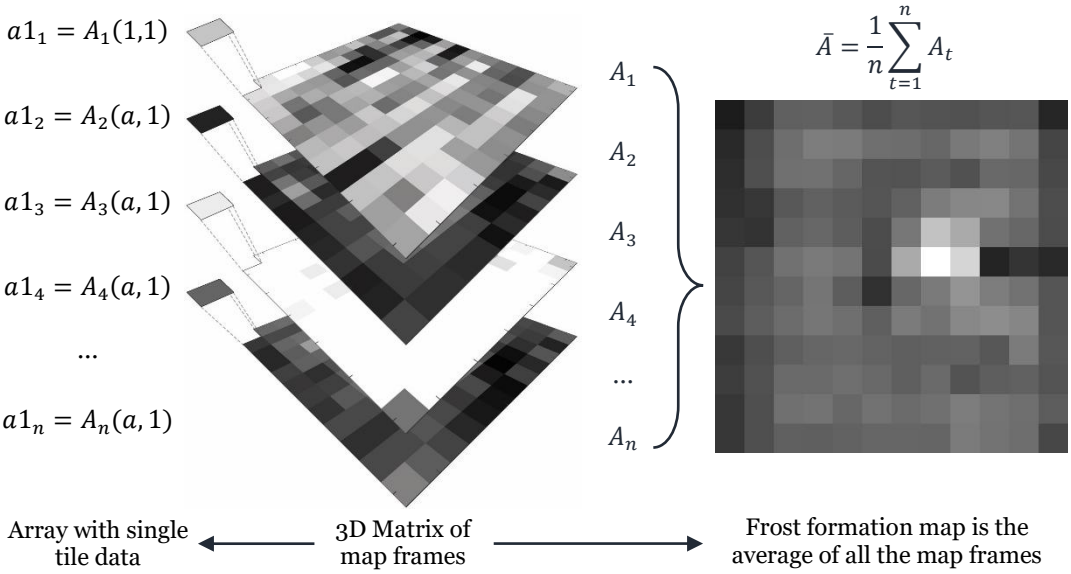

Figure 154 – Visual representation of the formation of the flattened frost map.

For this effect, a post-processing script was developed in MATLAB, with the pipeline represented in the flowchart of Figure 155, and available for analysis in Annex B.4). As illustrated, the process begins with the user selecting the CSV and the creation of output directories. Each row of the CSV is then processed in a loop: the tile values are converted from the original 10 bit range $(0 - 1023)$ into a 8 bit grayscale scale $(0 - 255)$, upscaled,

and written as a block-style image in the map frames folder. In this way, each experimental frame is represented by a frost-distribution map that simplifies the visual inspection of how frost develops across the HX surface.

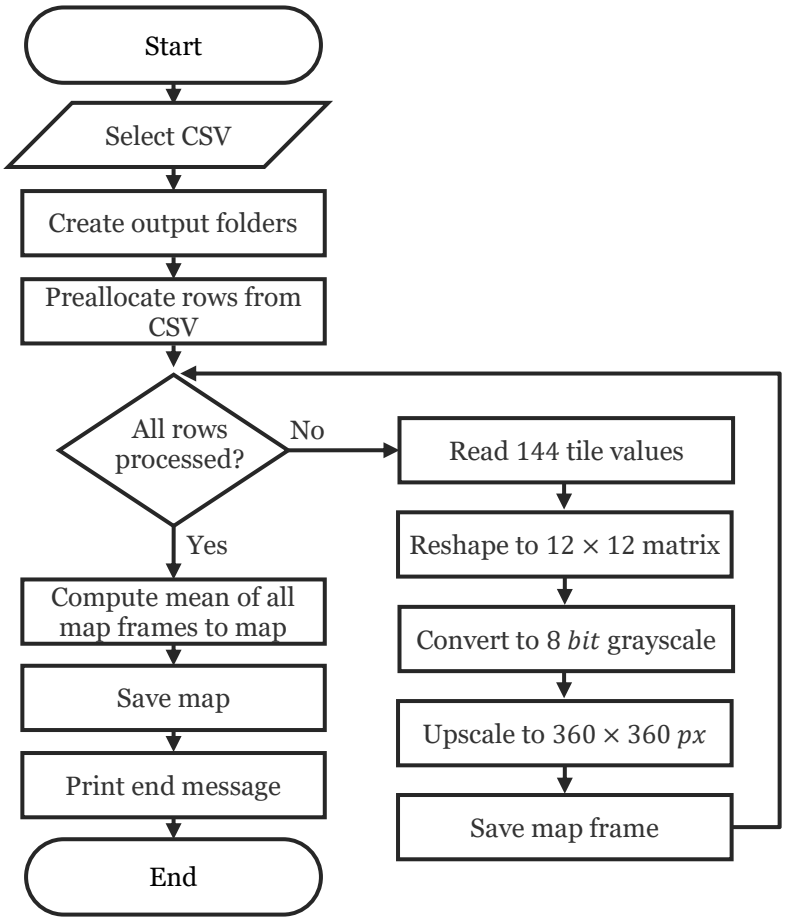

Figure 155 – Flowchart for the MATLAB CSV to FFM post-processing script.

Once all map frames have been processed, a second loop computes the average across the temporal dimension. This produces a composite 12×12 matrix in which each element corresponds to the mean frost coverage of its respective tile throughout the entire test. The resulting map is saved as a grayscale image, as shown in Figure 156 for Test 1.

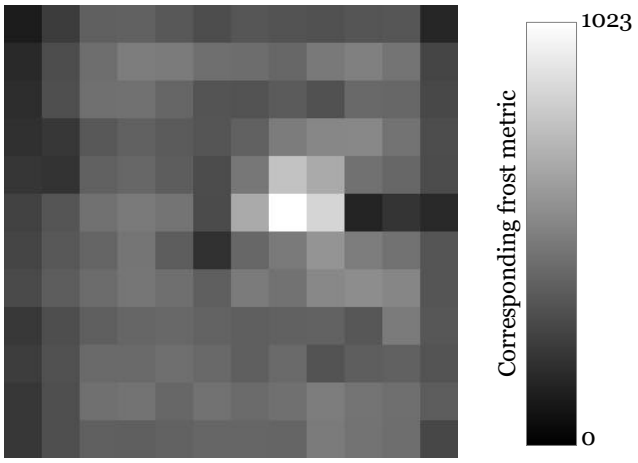

Figure 156 – Frost formation map for Test 1.

This FFM provides a global view of regions systematically more or less prone to frost accumulation. This representation condenses the visual analysis of frost growth on the HX, offering a simplified understanding of the frost-formation dynamics characteristic of this specific HX. It also provides simplified information for sensor placement, as regions with consistently high or low frost coverage can be identified, enabling sensors to be positioned either to maximize sensitivity to frost or to minimize the risk of early detection. Regions that appear constantly black or white should be avoided, as these indicate malfunctioning or atypical zones of the HX (e.g., damaged fins, poor thermal contact, or sensor obstructions), which could compromise the accuracy of the measurements.

Beyond guiding sensor positioning, this mapping approach can also provide diagnostic value, as contrasts revealed in the maps can expose localized malfunctions or performance anomalies.

The variability across tiles shows the limitations of relying on a single measurement point. A sensor located in a region that only develops frost later, or that maintains consistently high values, may give a signal that is not in pair with a general HX surface frost metric. Furthermore, it yields a representation of the overall HX condition. For this reason, it becomes necessary to consider approaches that account for the behaviour of surrounding regions when defining sensor placement. A mean curve, or a frost formation map provides a useful reference, but direct comparison with tiles that deviate strongly from it underlines the importance of capturing local variability rather than assuming surface homogeneity.

5.5.3. Targeted tile post-processing analysis

To address the non-specificity of a fixed, blind grid, a targeted tile approach was implemented in which only the tiles necessary for analysis are processed. This method operates from a user-defined coordinate on a ROI preview whose interface is shown in Figure 157. This is so that the tile is centred on the sensor location rather than straddling a tile boundary (as previously observed in Figure 150). By restricting computation to the neighbourhood of interest, the workflow becomes lighter and faster while yielding measurements that are directly representative of the sensor's local environment.

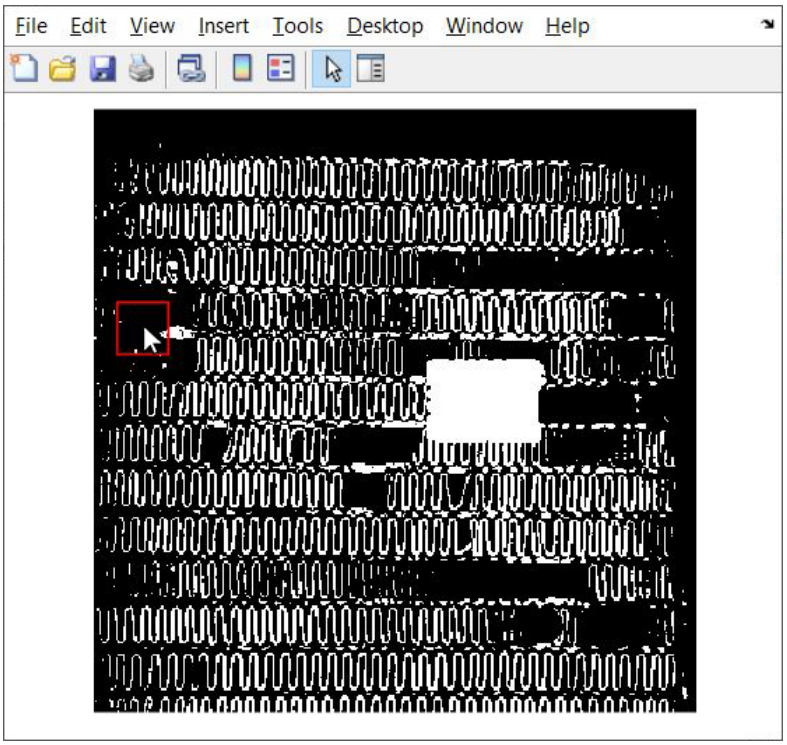

Figure 157 – Interface for the selection of the tile, where the mouse is tracked by a red box that represents tile boundary is shown.

The MATLAB script presented in Annex B.5 follows the logic outlined in the flowchart of Figure 158. After initialization, the interface is loaded, and a red square representing the tile area is displayed, following the cursor in real time. The user selects the tile centre, in a way that the sensor is properly centred within the tile. Once this selection is made, the same square tile is consistently extracted from every frame in the dataset. For each frame, the script calculates the white-pixel ratio and its 10-bit equivalent, saves the cropped tile as a lossless binary PNG, and records the corresponding metric in a CSV file.

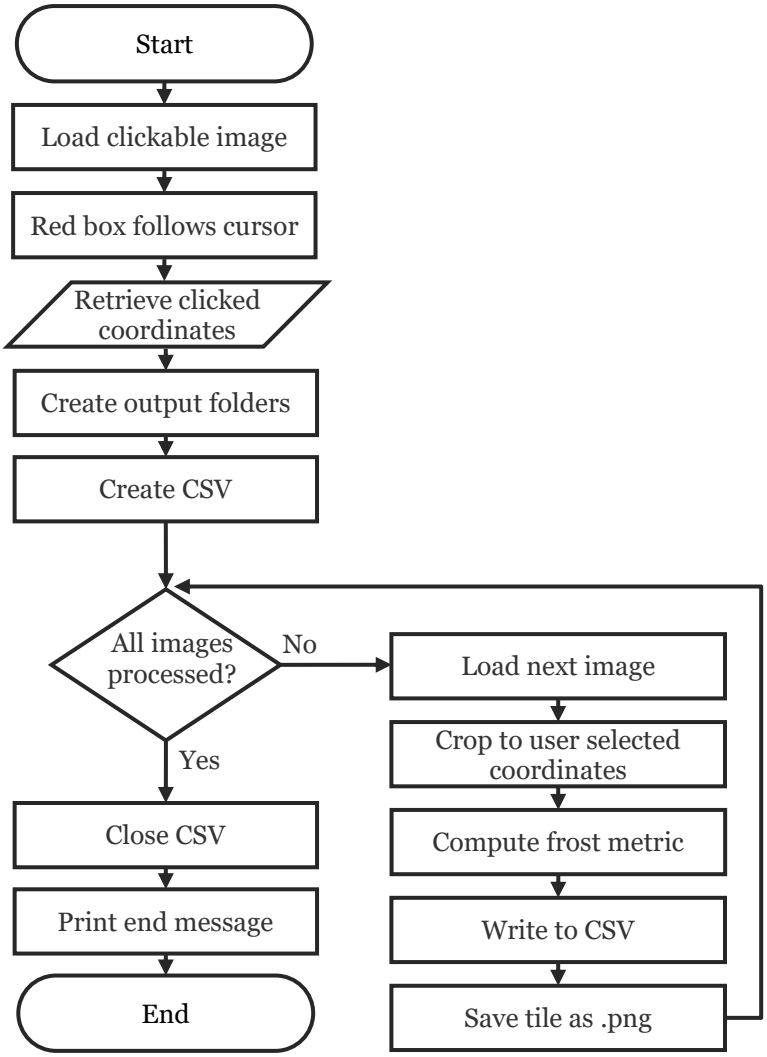

Figure 158 – Flowchart for the MATLAB targeted tile analysis script.

This targeted approach was then applied to the same eight regions previously identified in Figure 149 (a). That figure, as discussed earlier, shows the intake face of the HX with several areas highlighted that either introduce visual noise or exhibit distinct frost-formation behaviours. Figure 159 presents the same intake view of the HX with the corresponding to the tiles extracted using the clickable interface described previously. Each tile was selected by clicking on the region's centre.

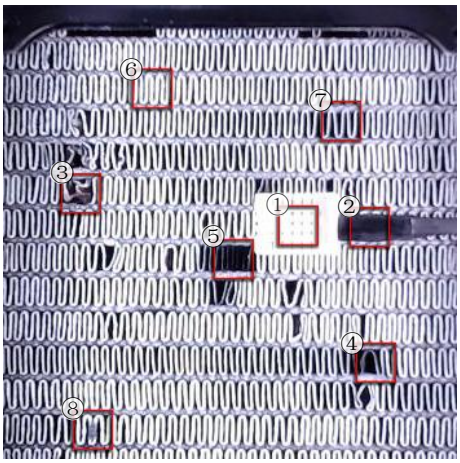

(a)

Figure 159 – RGB image of the intake end of the HX with highlighted artifacts.

The highlighted regions include artifacts caused by obstructions or damage, such as the intake DHT sensor ①, its cable ②, dented ③ or widened ④ fins, and fins dislodged from the refrigerant tube ⑤, as well as naturally occurring heterogeneities, with areas of increased ⑥ or decreased ⑦ frost accumulation, and the location of the FDS ⑧.

The results are organized into two groups. The first encompasses damage and obstruction, which includes artifacts caused by sensors, cables, or mechanical deformation of the fins. The second addresses frost-formation amplitude, which contrasts tiles located in regions prone to high or low frost accumulation, with the tile corresponding to the resistive sensor. This separation allows us to evaluate, on one hand, the effect of physical obstructions and defects on the CV metric, and on the other, the extent to which sensor placement in regions of different frost intensity influences its representativeness of overall HX behaviour.

The analysis of the targeted tiles corresponding to damage and obstruction is presented in Figure 160, where their frost-formation curves are compared against the global average curve previously shown in Figure 145. This average represents the overall frost accumulation on the HX surface, without tile separation, and serves here as a reference.

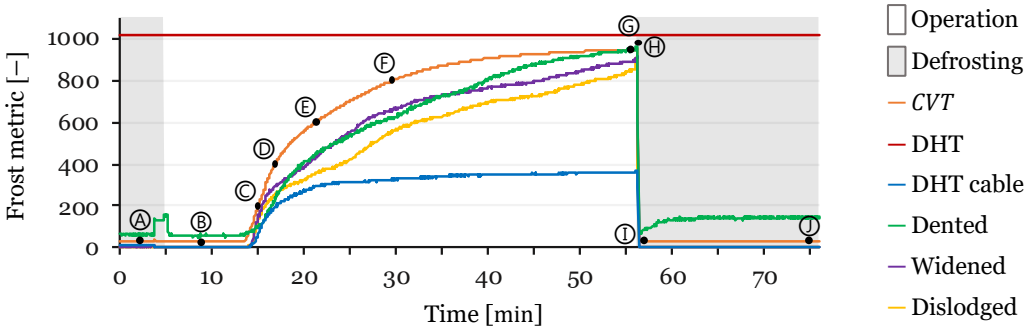

Figure 160 – Results of the damage and obstruction tiles compared to the averaged curve.

The targeted tile evolution is further illustrated in Figure 161, where the binarized images of each tile are shown over time across the same ten timestamped markers (Ⓐ – Ⓙ) defined in Test 1. These markers, overlaid on the average curve in Figure 160, indicate key stages such as the onset of operation (Ⓐ-Ⓑ), progressive frost accumulation Ⓒ – Ⓖ, the start of defrosting Ⓗ, complete melting Ⓘ, and the dried HX condition Ⓙ.

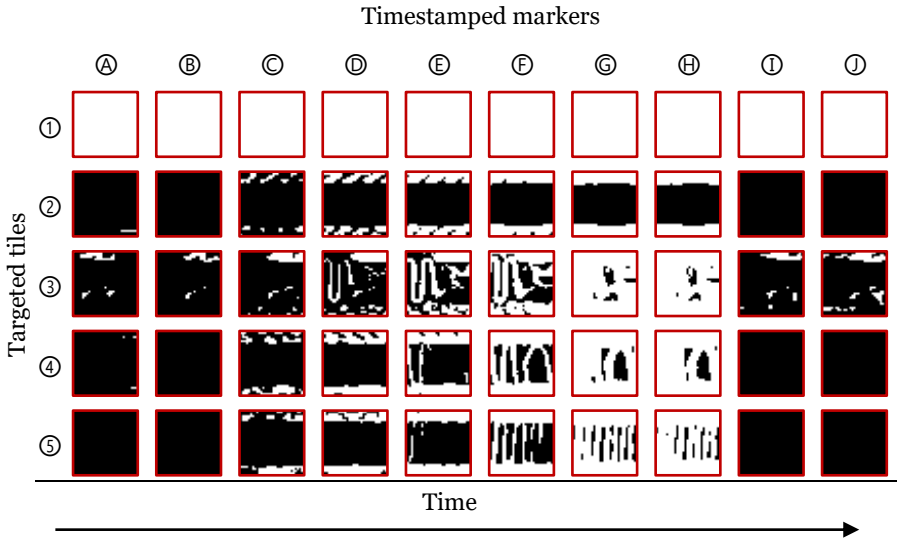

Figure 161 – Evolution of frost formation on the damage and obstruction tiles over time.

The first tile corresponds to the DHT sensor surface. As expected, this tile is fully saturated throughout the test due to its uniformly white surface, yielding a flat curve consistently at the saturation level. This behaviour is also evident in Figure 161, where the tile remains completely white from start to finish. The second tile, covering the DHT sensor cable, shows the opposite behaviour. It is predominantly black, with only small margins of frost formation detected at the upper and lower edges where the HX surface is still visible. As a result, its frost metric remains below $CVT \cong 400$ for the entire test.

The third tile, corresponding to dented fins, exhibits the highest degree of noise. The irregular fin geometry and surface defects amplify condensation and frost dynamics, leading to a fluctuating signal. Interestingly, during the defrosting stage, this tile shows a behaviour distinct from the average. While the CVG drops abruptly to a value close to 30, the dented tile decreases only to about 70 and then rises again towards $CVT \cong 140$ as the AL-HX dries. This secondary rise, which is not evident in the average curve, highlights how localized geometrical defects affect both frosting and drying visibility using this method. Figure 161 further confirms this irregularity, as the dented tile never becomes fully saturated with frost, leaving partially visible regions throughout the test.

The fourth tile, associated with widened fins, shows a smoother evolution than the dented case but still differs from the average curve. The frost accumulation slope is initially steep, then slows down, before declining again. This progression reflects the time-dependent surface phenomena visible in Figure 161, where frost first covers the refrigerant tubing, then gradually spreads to the fins but does not saturate the entire tile. The widened geometry leaves gaps that remain visible throughout, preventing full coverage and explaining the lower plateau compared to intact fins.

The fifth tile, covering fins dislodged from the refrigerant tube, presents another distinctive behaviour. Frost initiation occurs nearly simultaneously with the other tiles, but a visual inspection in Figure 161 reveals that this is driven by frost forming on the adjacent refrigerant tubing (at the top and bottom of the tile) rather than on the fins themselves. The fin surfaces only begin to show frost accumulation around the marker Ⓔ, by which point the global average curve has already advanced significantly. After this initial spike caused by frost in the refrigerant tubing, frost accumulation in this tile slows markedly, resulting in the lowest frost metric among all obstruction-related tiles (apart from the sensor cable). This reduced accumulation persists throughout the test, indicating impaired thermal performance of the dislodged fins. Notably, just before defrosting is triggered Ⓖ – Ⓗ, this tile shows one of the few slight increases in frost level, attributable to transient frosting, as outside air enters the system.

The targeted analysis of obstruction and damage-related tiles confirms that these features introduce localized deviations from the global frost-formation curve. While the DHT sensor surface and cable tiles show predictable saturation and suppression, respectively, the dented and widened fin tiles highlight the impact of structural irregularities on condensation, frosting, and drying behaviour. The dislodged fin tile, meanwhile, reveals the influence of impaired thermal contact, with frost preferentially forming on the tubing rather than the fin surfaces. Such tile-level differences, though

minor in some cases, demonstrate how geometric and material imperfections translate into measurable deviations in the CV frost metric.

The second group of tiles, associated with sensor placement and frost-formation amplitude, is compared to the global average curve in Figure 162, These tiles capture regions of the HX that accumulate frost faster (over frosted), slower (under frosted), and in the vicinity of the resistive sensor. As in the previous group, all curves display slightly greater variability than the global average, reflecting the reduced sample size of the tile-level method.

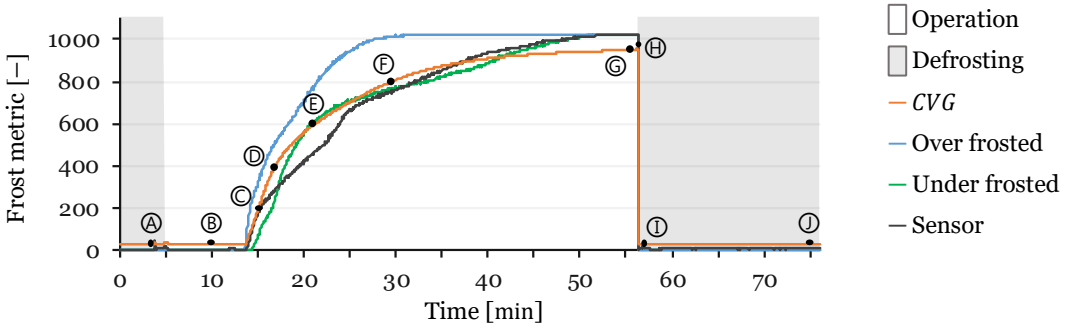

Figure 162 – Results of the frost formation amplitude and sensor tiles compared to the averaged curve.

Figure 163 complements this analysis by showing the evolution of the three tiles in this group across the ten timestamped markers Ⓐ – Ⓙ. As with the previous cases, these illustrate the progressive changes in the binarized tiles during frost growth, defrosting, and drying, now focused on the over-frosted, under-frosted, and sensor tiles.

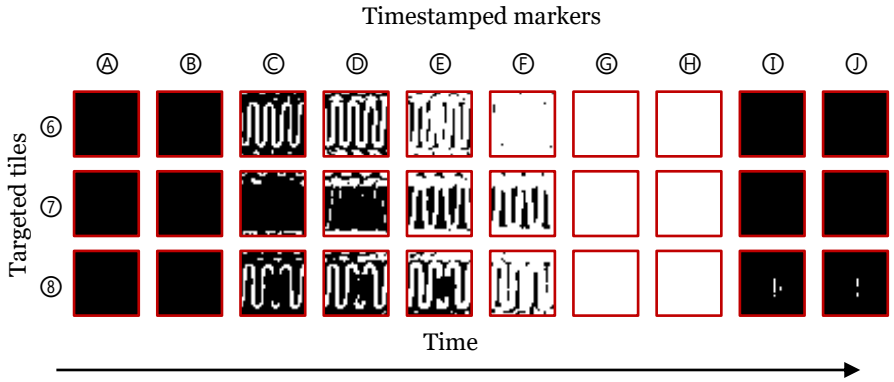

Figure 163 – Evolution of the frost formation amplitude and sensor tiles over time.

The over-frosted tile ⑥ demonstrates the steepest frost accumulation curve of this group. Frost initiation occurs at approximately the same time as the average, but growth is significantly faster: the frost metric reaches 950 at $t = 25\,\text{min}$, whereas the global average attains the same level only at $t = 56\,\text{min}$, a difference of 31 min. This rapid

progression is also evident in Figure 163, where significant frost is already visible at all the fins in marker ©, partial saturation occurs by Ⓕ, and full saturation (1023) is achieved slightly after Ⓕ and before Ⓖ.

The under-frosted tile ⑦ exhibits delayed frost initiation. The first detectable rise occurs nearly one minute after the over-frosted tile, with a sharp increase attributed to frost forming initially on the refrigerant tubing. At this stage, the frost metric temporarily surpasses the average, at $t \cong 10$ min, coinciding with visible accumulation on the fins in Figure 163 at marker Ⓔ. Beyond this point, frost growth slows, and the average curve overtakes it at $t \cong 25$ min. The under-frosted tile again converges with the average at 41 minutes and eventually reaches full saturation by $t = 52$ min, four minutes before defrosting is triggered. This behaviour indicates a fin that is thermally functional but accumulates frost less aggressively than neighbouring regions, ultimately leading to complete blockage by the end of the cycle.

The tile corresponding to the sensor location ⑧ shows an intermediate behaviour. Its curve begins with a steep rise, briefly exceeding a frost metric of 200, before declining slightly and then resuming growth. This reflects the absence of frost directly on the sensor surface until approximately $t = 23$ min, when a distinct increase is observed, corresponding to frost finally accumulating on the sensor surface. Thereafter, the curve progresses steadily and saturates at the same time as the under-frosted tile, close to the initiation of defrosting. Throughout most of the test, the sensor tile remains below the global average, only surpassing it after $t = 37$ min. Between $t = 17$ min and $t = 31$ min, it is temporarily overtaken by the under-frosted tile, after which it remains higher until both converge at saturation. Figure 163 illustrates this behaviour clearly: during markers © – Ⓔ, frost is visible on the fins while the sensor itself remains dark. At the marker Ⓕ, frost has also accumulated on the sensor surface, resulting in the subsequent rapid increase.

In summary, this group highlights the contrasting behaviours that arise from local variations in frost-formation dynamics. The over-frosted tile reaches saturation long before the average, the under-frosted tile lags but ultimately blocks fully, and the sensor tile demonstrates a mixed response influenced by both its surroundings and the frost dynamics of its own surface. An additional consideration is that tiles directly containing the sensor may be affected by the sensor's silhouette in the image, slightly biasing the calculated frost metric. For this reason, adjacent tiles that exclude the sensor shadow

may provide a more representative measurement of the frost relevant to sensor operation.

5.6. Concluding remarks

This chapter demonstrated that a CV approach can serve as a tool for frost detection. By transforming camera images into binary masks and quantifying the proportion of white pixels, the method provided frost–defrost curves, capturing both the gradual growth of frost and the rapid transitions during defrosting. For testing purposes, the global CV metric proved sufficient to initiate defrosting, as the progression of the average curve consistently mirrored the overall blockage state of the HX.

Beyond this global metric, zone-specific analyses confirmed that frost formation is not uniform but follows a repeatable spatial pattern across cycles. This heterogeneity was visualized through the FFM derived from the sweep grid tile analysis, which confirmed differences across the surface and highlighted regions of consistently faster or slower frost accumulation. The FFMs are relevant for sensor placement, as selecting a zone that frosts too quickly may lead to premature triggering, while zones that frost too slowly may delay detection. In principle, prior knowledge of a system's FFM could also be incorporated into control logic, allowing the state of the whole HX to be extrapolated from one or a few strategically placed sensors.

The analysis of zone-specific frost formation using the targeted tile analysis confirmed that frost formation across the HX is persistently heterogeneous, though it follows repeatable patterns across cycles. For overall defrost control, the CVG remains sufficient, as HX blockage can be inferred consistently from the average behaviour. However, when evaluating sensor behaviour in post-processing, local analysis becomes relevant. Frost formation near the sensor, rather than across the entire HX, dictates its response. FFM therefore serves both as proof of this heterogeneity and as a practical tool to guide sensor placement. While grid analysis provides a complete view of spatial dynamics, targeted-tile analysis offers a more efficient way to isolate specific regions without processing unnecessary data, ensuring tiles align with features of interest rather than straddling arbitrary boundaries.

The work also showed the complementarity of different analysis scales: global averages are useful for control and benchmarking, while tile-level analysis provides diagnostic insight into local behaviour, and targeted-tile analysis offers an efficient means of examining relevant regions without unnecessary processing or grid position constraints.

Finally, some limitations and opportunities should be noted. The method was tested on an HX coated in black paint, which maximized contrast with white frost. Performance on untreated metallic surfaces may be lower. This can be mitigated by optimizing illumination geometry or using alternative wavelengths to enhance scattering contrast. While CV is not as compact, rugged, or low-cost as dedicated resistive sensors, its suitability for research environments is clear, and falling costs of imaging and embedded systems may make it viable for broader applications, such as refrigerated rooms, cold storage warehouses, or transport refrigeration units.

Overall, the CV method provided an objective, repeatable, and insightful tool to characterize frost dynamics, enabling both the validation of resistive sensors and the broader understanding of spatially heterogeneous frost formation in HXs.

Chapter 6

Frost detection using resistive sensors

This chapter presents the results obtained with the FMRS4, together with the development of algorithms to process its signal and extract reliable indicators of frost nucleation and defrost completion. It begins by outlining the operating principle of resistive frost detection, and the typical behaviour of the sensor during a complete frost–defrost cycle. The discussion then moves to the signal processing framework, where the transformations applied to the raw data are explained and the logic of the frost nucleation and defrost completion detectors is established. With this foundation, the chapter proceeds to the experimental results: first describing how the tests were conducted and presenting the Design of Experiment (DoE), then an overview of the performance of the experimental setup during the tests to contextualise frost formation. On this basis, the results of frost nucleation and defrost completion detection across multiple experiments are presented and analysed. Finally, the chapter concludes with a discussion of the findings, considering both the capabilities and the limitations of the FDS detection approach.

The performance of the signal processing framework and the reliability of the frost detection algorithms are validated through an uncertainty analysis. This analysis quantifies the uncertainty of the primary processed signals that serve as the foundation for detecting frost nucleation and defrost completion. As detailed in Annex C, the standard uncertainty of the final processed resistive sensor signal is approximately 0.15 LSB in the frost nucleation regime and 0.29 LSB during defrost completion. For the validation metrics, the standard uncertainty of the CVG was determined to be approximately 1.1 LSB, while the smoothed AH difference signal, used to independently verify defrost completion, has a standard uncertainty of approximately 0.11 g/m^3. The complete uncertainty budget for all detectors and their associated derived quantities is detailed in the annex.

6.1. Signal processing framework for frost detection and validation

The principle underlying frost detection using the FDS has been discussed throughout this work: the electrical resistivity of water, air, and ice differs significantly, and this allows phase changes to be identified using a resistive FDS. When the refrigeration

system is switched on, the sensor resistance initially decreases as condensation forms on the electrode surface, creating a more conductive water film. As this water freezes and frost accumulates, the effective conductivity decreases, leading to an increase in resistance. The signal then stabilises at a plateau as the sensor surface saturates with frost, remaining relatively constant until a defrosting operation is triggered. Defrosting produces the opposite behaviour: the sudden release of liquid water drives the sensor to its lowest values, after which the signal increases again as the HX dries.

To illustrate this behaviour, Figure 164 shows a schematic representation of a complete frost–defrost cycle. The figure does not display raw sensor data but rather a representative curve that highlights the simplified representation of the evolution of the resistive signal.

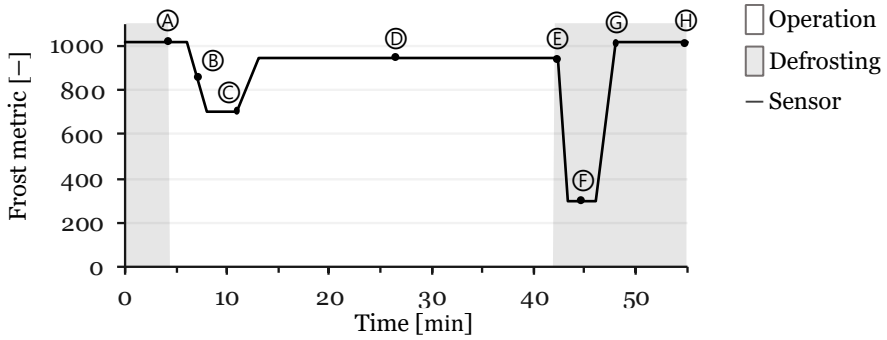

Figure 164 – Representative curve of the FDS signal during a full frost-defrost cycle.

Overlaid on this curve are labelled points (Ⓐ–Ⓗ), each corresponding to specific phases of the cycle. Points Ⓐ–Ⓔ represent the operation phase: with the start of operation Ⓐ, the mid-point of condensationⒷ, the onset of frost nucleation©, frost growth Ⓓ (between frost nucleation and defrosting trigger), and the end of the operation phase Ⓔ, and the initiation of the defrosting. Points Ⓔ–Ⓗ represent the defrosting phase, with the defrost trigger Ⓔ, lowest resistance Ⓕ corresponding to the maximum liquid water, sensor-detected dry HX Ⓖ, and the end of the defrost cycle Ⓗ. This provides a reference framework for interpreting the more irregular experimental signals presented later in the chapter.

It is clear from this simplified representation that the key events to be identified, and used for control, are the transition phases within the curve. Two points are of particular importance: © and Ⓖ. Point © marks the onset of frost nucleation. After the initial drop caused by condensation and the subsequent stabilization once condensation ceases, the resistive signal begins to rise as frost starts to form. Detecting this transition requires

identifying a sustained positive slope, which indicates the beginning of frost growth. Point © corresponds to the termination of defrosting. Following the sharp drop in signal due to liquid water accumulation, the signal rises again as the HX dries. To identify defrost completion, the signal must not only recover from its minimum but also reach a value at least close to that observed before defrost initiation, within a defined margin. This accounts for the local fluctuations often present during drying, such as temporary maxima associated with dripping or uneven evaporation. A further requirement is that all event detections rely exclusively on past data. This constraint ensures that the detection of both frost nucleation and defrost completion can be implemented in real time, since future values are not available during operation. By restricting the analysis to causal information, the methods developed here remain directly transferable from post-processed datasets to embedded control applications.

In summary, the objective is to detect frost nucleation and defrost completion by identifying these transitional behaviours in the resistive signal. The following section introduces the signal processing framework developed to extract these events.

6.1.1. Pre-processing of resistive frost detection sensor data

To enable identification of frost nucleation and the dry HX indicating completion of defrosting cycles, the raw output of the resistive frost detection sensor must be mathematically transformed before being subjected to event detection algorithms. In this work, the resistive sensor data were sampled every $\tau = 3\ s$ using a 10-bit ADC, and the outlet air temperature of the AL-HX ($TA2$) was adopted as the reference channel for temperature compensation. A sequence of pre-processing steps was applied to the acquired signal, beginning with temperature compensation, followed by moving-average smoothing, and finally the calculation of a finite-difference slope. These pre-processed quantities form the basis of the subsequent resistive frost nucleation detector and resistive defrost completion detector, which are both implemented on the same conditioned signal stream.

Temperature compensation reduces temperature-induced fluctuations in resistivity, partially compensating for their effect in the signal and minimizing their influence. This is performed using Equation (48), which can also be represented as Equation (49):

$$\widetilde{ADC_n} = \frac{1023 \cdot ADC_n}{\left(1 + \alpha \cdot \left(TA2_n - T_{ref}\right)\right) \cdot \left(1023 - ADC_n\right) + ADC_n} \tag{49}$$

Where:

- $\widetilde{ADC}_n$ is the temperature-compensated ADC value [−],
- ADC_n is the raw ADC data [−],
- $TA2_n$ is the HX air outlet temperature used for temperature compensation [°C],
- T_{ref} is the reference temperature [°C],
- α is the temperature coefficient [$°C^{-1}$].

As previously calculated, in this work, $T_{ref} = 2.22$ °C from Equation (45), and $\alpha = -0.045\ °C^{-1}$ from Equation (43).

A moving average was also applied according to Equation (50). The objective is to smooth the signal, thereby reducing short-term irregularities, while introducing a predictable latency of approximately $W \cdot \tau$. For real-time applicability, the moving average must be causal, and, in the present post-processing implementation, a centred average could be used, as both past and future samples are accessible. However, for the approach to remain directly transferable to real-time control, the moving average was implemented as a trailing window that shifts forward with the current sample.

$$\overline{ADC}_n = \frac{1}{W} \cdot \sum_{i=0}^{W-1} \widetilde{ADC}_{n-i} \tag{50}$$

Where:

- $\overline{ADC}_n$ is the moving-averaged, temperature-compensated ADC signal,
- W is the moving average window.

In this work, $W = 30$, corresponding to a smoothing horizon of $W \cdot \tau = 90\ s$ given the acquisition interval of $\tau = 3\ s$.

Next, a local finite-difference approximation of the local of the smoothed signal $\overline{ADC}$ was calculated as a proxy for the true derivative, using Equation (51), which enables detection of growth dynamics. Importantly, the finite-difference method is also causal, relying only on the current and immediately preceding values, which makes it directly suitable for future real-time monitoring and control applications. This is particularly relevant in the present context, where the slope of the resistive signal can vary rapidly during transitions between wet, frost, and dry surface states.

$$\Delta\overline{ADC}_n = \overline{ADC}_n - \overline{ADC}_{n-1} \tag{51}$$

Where $\Delta\overline{ADC}_n$ is a local finite-difference slope of $\overline{ADC}$.

It is relevant to note that, because the acquisition interval in this work is $\tau = 3\ s$, the finite-difference slope corresponds to a two-point slope over a 3 s horizon. This results in sudden fluctuations in slope in regions of the signal that are not in high dynamic changes, even after the smoothing. To compensate, the previous K slopes are averaged using Equation (52):

$$\Delta\overline{ADC}_n^{avg} = \frac{1}{K}\sum_{i=0}^{K-1} \Delta\overline{ADC}_{n-i} \tag{52}$$

In which,

- $\Delta\overline{ADC}_n^{avg}$ is the average of slopes over a K window,
- K is the average slope window.

For this work, K = 10 consecutive slope values were averaged to obtain a more stable slope estimate. This averaged slope was then processed using a classifier, shown in Equation (53). Values greater than θ were mapped to $+1$, values smaller than $-\theta_s$ were mapped to -1, and values within the interval $[-\theta_s, \theta_s]$ were mapped to 0.

$$C_n^{ADC} = \begin{cases} -1, \Delta\overline{ADC}_n^{avg} \leq -\theta_s \\ 0, \left|\Delta\overline{ADC}_n^{avg}\right| < \theta_s \\ 1, \Delta\overline{ADC}_n^{avg} \geq \theta_s \end{cases} \tag{53}$$

In which,

- θ_s is the slope threshold,
- C_n^{ADC} denotes the classified output of the averaged slope, mapped to $-1, 0,$ or $+1$ according to the threshold criterion.

In this work, a threshold of $\theta_s = 0.15$ was applied for frost nucleation detection and $\theta_s = 0.30$ for identifying a defrost completion. The pre-processing of the resistive frost detection sensor data pipeline is represented in the flowchart of Figure 165.

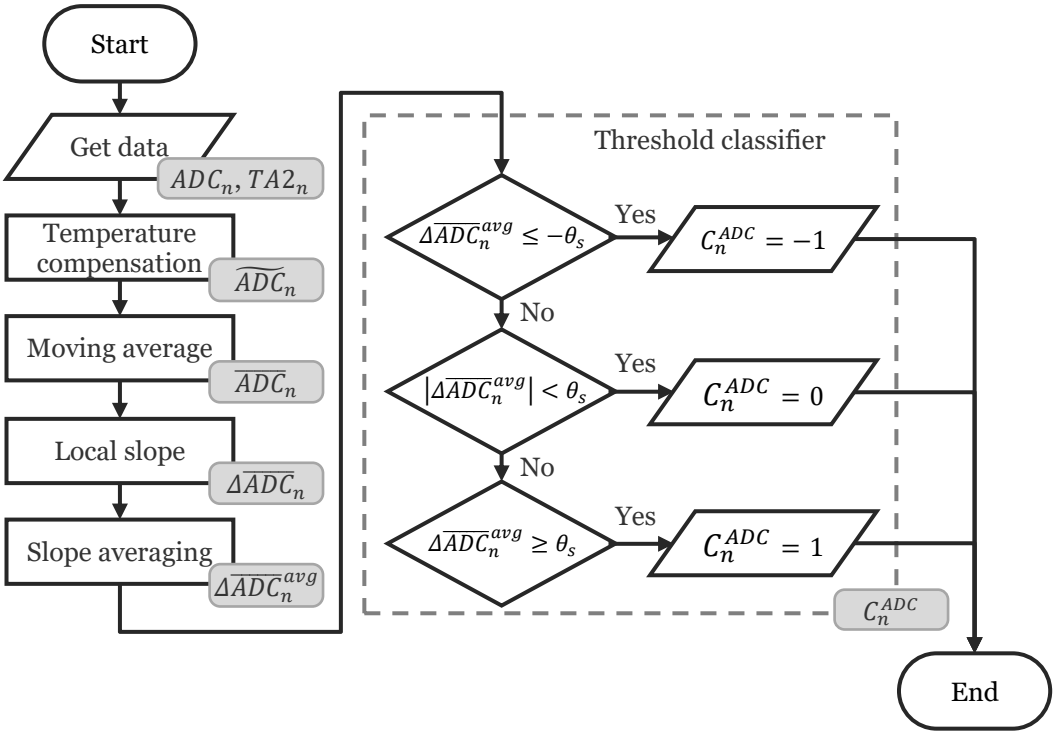

Figure 165 – Flowchart of the pre-processing of resistive frost detection sensor data pipeline.

This way, the output of the pre-processing of the resistive frost detection sensor data pipeline is a three-state variable that indicates if the temperature-compensated sensor measurement is significantly rising, significantly falling, or relatively stable. The type of event detected depends on the defrosting state: when the system is in defrost mode, the algorithm searches for cues indicating that the HX surface has dried, whereas when defrosting is inactive, the algorithm monitors for the onset of frost formation. With the pre-processed signals established in this section, the detectors can be defined.

6.1.2. FND - Frost Nucleation Detector

The frost nucleation detector (FND) returns a binary pulse when nucleation is detected. Its operation relies on identifying a slope rise following a sustained slope fall. To evaluate whether a sufficiently long negative trend has occurred, a negative-run condition is obtained from Equation (54)

$$NR_n^{FND} = 1 \cdot \left\{ \sum_{i=0}^{P-1} 1 \cdot \{C_{n-i}^{ADC} = -1\} = P \right\} \tag{54}$$

Where:

- P is the persistence window

- NR_n^{FND} returns 1 if and only if the classifier has remained in the negative state for the entire window of length P.

For this work, a persistence length of $P = 20$ samples was selected, as it is wide enough to filter out local slope fluctuations, but not so long that nucleation events were overlooked in tests with limited condensation.

Once the persistence condition is met, a state variable is introduced to lock the signal into a negative-trend state until a subsequent rising slope indicates frost nucleation. The update rule for the state variable φ_n^{FND} is shown in Equation (55):

$$\varphi_n^{FND} = \begin{cases} 0, & DOS_n = 1, \\ +1, & (\varphi_{n-1}^{FND} = -1) \wedge (C_n^{ADC} = +1) \\ -1, & (\varphi_{n-1}^{FND} = -1) \vee (NR_{n-1}^{FND} = +1 \wedge C_n^{ADC} \in \{0, +1\}) \\ 0, & otherwise \end{cases} \tag{55}$$

Where:

- DOS_n is the door-open sensor state, which directly indicates defrost ($DOS_n = 1$ during defrosting).
- φ_n^{ADC} is the state variable storing whether the system remains in a locked negative-trend condition or has transitioned to a positive slope.

The update rule for φ_n^{FND} ensures that the state behaves consistently across different operating phases. During defrost, identified by $DOS_n = 1$, the state is forced to zero so that no nucleation detection can occur. When the system is not defrosting, a $+1$ pulse is generated if the previous state was locked at -1 and the slope classifier transitions to $+1$, which marks the onset of nucleation. The state remains at -1 either if it was already locked in that condition in the previous sample, or if the negative-run condition has been satisfied while the current classifier is non-negative. This mechanism guarantees that once a negative slope has been established, the lock persists even if the signal stabilises around zero, so that a subsequent positive slope still produces a nucleation event. In all other cases, the state defaults to zero.

Because the state variable defaults to zero, the output assumes the value one only at the instant when nucleation is detected, after which it immediately returns to zero. The nucleation trigger is therefore obtained by identifying the positive value of φ_n^{FND}, as formally defined in Equation (56):

$$FND_n = 1 \cdot \{\varphi_n^{FND} = +1\} \tag{56}$$

Where the FND_n is a binary flag that yields a pulse whenever a nucleation event is detected.

The complete FND pipeline, from the slope classifier through the negative-run condition and state update to the nucleation trigger, is summarised in the flowchart of Figure 166:

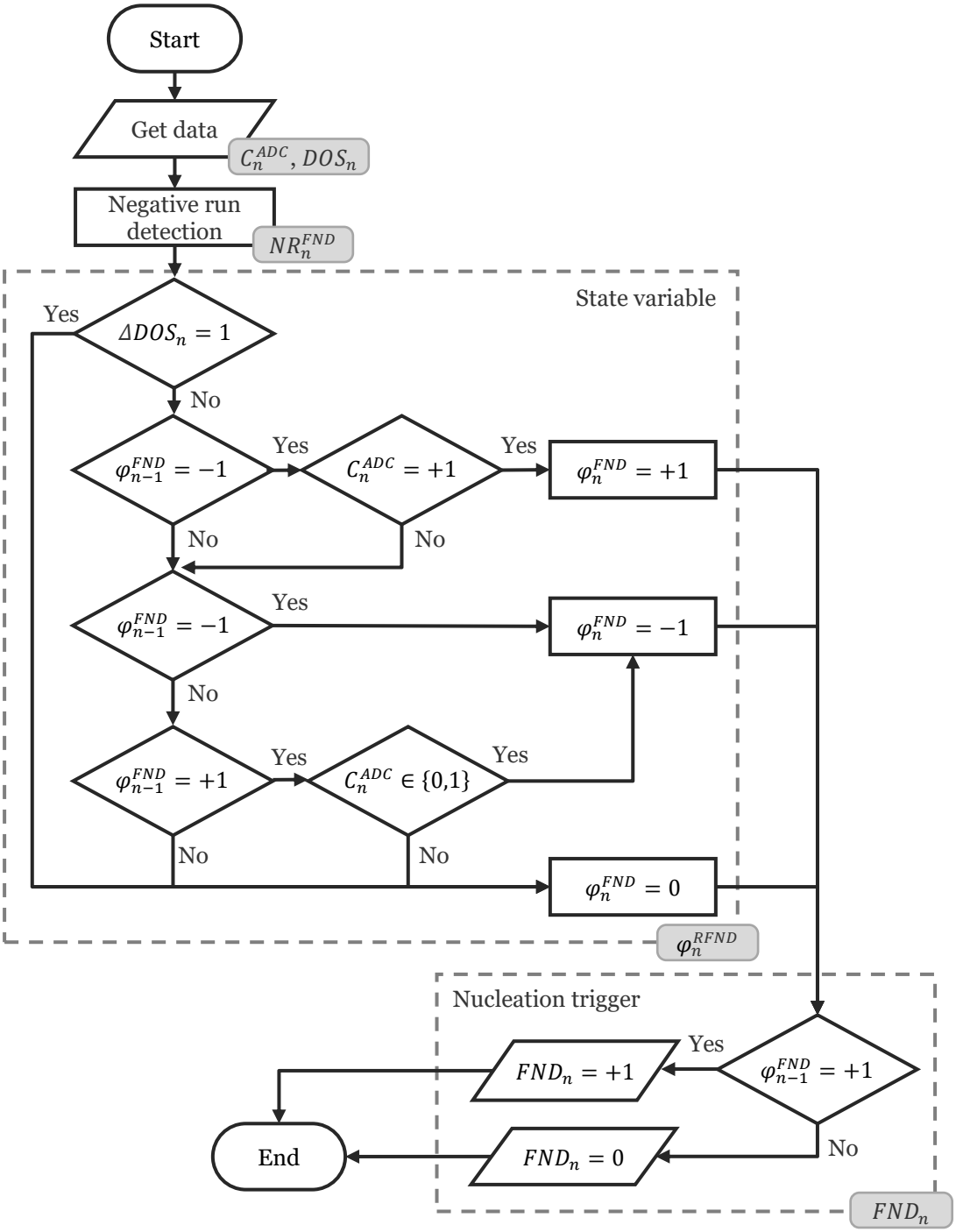

Figure 166 – Flowchart of the resistive frost nucleation detector data pipeline.

For this analysis, the nucleation pulse is displayed in the test plots as an artificial 1 min pulse rather than the actual $\tau = 3\ s$ sample pulse. This extension is purely cosmetic, intended to improve visibility in the figures. In a real application, a single-sample pulse would be sufficient or, alternatively, a pulse could be held high until defrosting is confirmed to have started. Once defrosting is triggered, however, it is also important to determine when to stop the operation, which is the focus of the next section.

6.1.3. DCD - Defrost Completion Detector

The defrost completion detector (DCD) is designed to determine when the AL-HX has sufficiently dried after a defrosting operation, thereby indicating the appropriate moment to stop defrosting. As previously discussed, during defrosting, the sensor first experiences a sharp signal drop caused by the sudden presence of liquid water. This is sometimes followed by a short stabilization at low levels, or, in other cases, the signal begins rising almost immediately as drying progresses. This intermediate stabilization can be disregarded, as it does not consistently appear across cycles, whereas the remaining signal states—sharp fall, subsequent rise, and final stabilization—are used for characterising the completion of defrosting. True completion is only reached when the slope transitions from negative to positive and then stabilizes at a high level, close to the pre-defrost value of a fully frosted sensor.

To formalise this detection, the process begins with Equation (57), which defines the consensus classifier CC_n^{DCD}. This quantity evaluates the last M values of the slope classifier C^{ADC} and updates its state only when all values are identical. This consensus mechanism suppresses minor fluctuations, local extrema, or irregularities, so that only persistent slope behaviours are propagated to the subsequent state variable.

$$\bar{C}_n^{ADC} = \frac{1}{M} \cdot \sum_{i=0}^{M-1} C_{n-i}^{ADC}, \qquad CC_n^{DCD} = \begin{cases} \bar{C}_n^{ADC}, & \bar{C}_n^{ADC} \in \{-1, 0, +1\} \\ CC_{n-1}^{DCD}, & otherwise \end{cases} \tag{57}$$

Where:

- $\bar{C}_n^{ADC}$ is the moving average of the last M slope classifier values.
- CC_n^{DCD} is the consensus classifier of the DCD, which updates only when the last classifier values are identical.
- M is the averaging window length used for the consensus classifier

In this work, a window size of $M = 20$ was selected, as it provided a balance between rejecting noise and still responding adequately to slope transitions during defrosting.

The next step is to store the $\overline{ADC}_n$ at the instant defrosting begins. When a defrosting operation is triggered, identified by the transition of DOS from 0 to $+1$, the trigger reference is updated as shown in Equation (58):

$$ADC_n^{trig} = \begin{cases} \overline{ADC}_n - \zeta, & DOS_{n-1} = 0 \wedge DOS_n = +1 \\ ADC_{n-1}^{trig}, & Otherwise. \end{cases} \quad (58)$$

Where:

- ADC_n^{trig} is the stored reference value of $\overline{ADC}_n$ at the instant a defrosting operation begins.
- ζ is the tolerance around ADC_n^{trig}

In all other cases, it retains its previous value. This stored value is later used as a benchmark, with a margin that for this work was selected to be $\zeta = 25$ for determining when the drying phase has progressed sufficiently, regardless of slope sequence.

Once the defrost trigger value is stored, a state variable is introduced to encode the sequence of slope behaviours during defrosting. The variable φ_n^{DCD} assumes -1 during the drainage phase, switches to $+1$ during the drying phase, and returns to 0 once stabilization is detected. The event of interest is the falling edge from $+1$ to 0, which occurs only after the negative, positive, and stabilization phases have been completed. The update rule for φ_n^{DCD} is shown in Equation (59).

$$\varphi_n^{DCD} = \begin{cases} 0, & (DOS_{n-1} = 0) \vee (CC_n^{DCD} = 0 \wedge \varphi_{n-1}^{DCD} = +1), \\ +1, & CC_n^{DCD} = +1 \wedge \varphi_{n-1}^{DCD} = -1 \vee \varphi_{n-1}^{DCD} = +1 \\ -1, & CC_n^{DCD} = -1 \vee \varphi_{n-1}^{DCD} = -1, \\ 0, & otherwise. \end{cases}, \quad (59)$$

Where:

- φ_n^{DCD} is the state variable that encodes the sequence of slope behaviours, locking negative, positive or neutral slopes after being detected in sequence

Finally, the defrost completion detector is defined in Equation (60). This equation produces a positive pulse when the state variable undergoes a falling edge, provided that the door-opening sensor indicates that defrosting is still active. In all other cases, the detector output is zero.

$$DCD_n = 1 \cdot \left\{ \varphi_{n-1}^{DCD} = +1 \wedge \varphi_n^{DCD} = 0 \wedge DOS_n = +1 \wedge \overline{ADC}_n > ADC_n^{trig} \right\} \quad (60)$$

Where:

- DCD_n is the defrost completion detector output, which issues a pulse when the falling edge of φ_n^{DCD} is detected under active defrosting conditions.

The explicit check of the door-opening sensor is necessary to avoid false positives: when defrosting is terminated by external control, forcing the state variable to drop from +1 to 0 even though the HX has not fully dried. Without this additional condition, such control-driven transitions would be incorrectly interpreted as defrost completion events. The ADC check allows for the DCD trigger to only be activated when the $\overline{ADC}_n$ is above the stored ADC_n^{trig}, that includes a tolerance ζ. This is to avoid a premature DCD trigger caused by stabilization mid drying.

The pipeline of the DCD is shown in the flowchart in Figure 167.

This graphical representation highlights the hierarchical structure of the algorithm: each stage depends on the stability and persistence of the preceding one, so that only robust slope transitions produce a completion signal. By enforcing this chain of logic, the DCD avoids false positives caused by transient fluctuations or control-driven terminations and tries to identify the true drying of the HX surface.

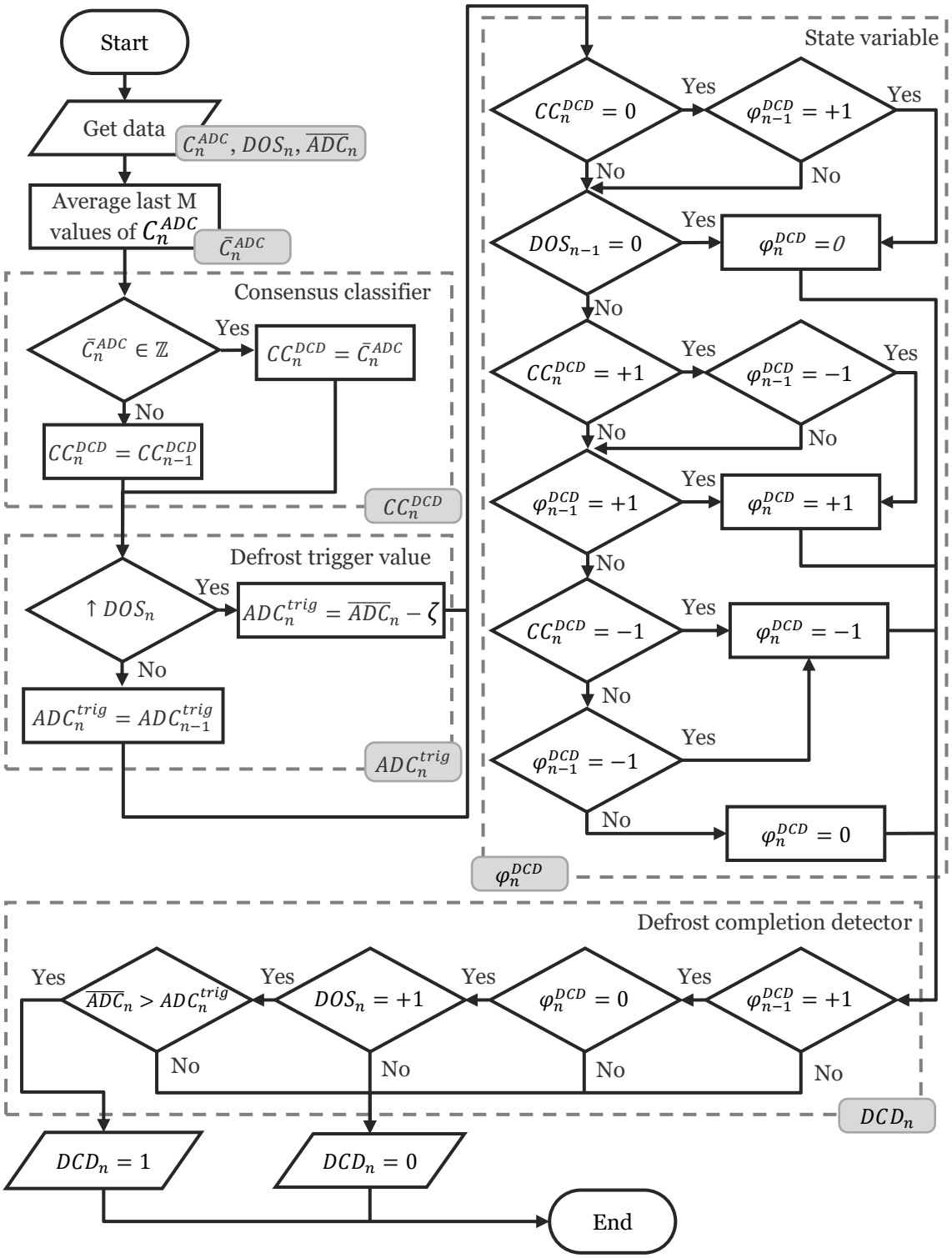

Figure 167 – Flowchart of the defrost completion detector data pipeline.

While the *FND* and *DCD* establish the core framework for identifying frost nucleation and defrost completion using the FDS data, their outputs must be validated against independent references. To this end, two validation metrics were extracted in post-

processing. The first addresses frost nucleation, defined as the initial appearance of frost detected by the CVT, and the second addresses the condition of a dry HX, derived from DHT RH measurements. These metrics provide external benchmarks against which the FND and DCD outputs can be evaluated.

6.1.4. CVFND - Computer Vision derived Frost Nucleation Detector

To provide an independent reference for the onset of frost formation, a computer-vision-based nucleation detector (CVFND) was defined using the CVT. The procedure was implemented in post-processing with a slope estimate obtained as the finite difference over a h sample window, as shown in Equation (61)

$$\Delta CVT_n = CVT_n - CVT_{n-h} \tag{61}$$

Where:

- ΔCVT_n is the local slope estimate of the targeted tile CV metric,
- CVT_n is the targeted tile CV frost metric obtained from the post-processing script in Annex B.5,
- h is the slope horizon used for the slope estimate.

For this work, a slope horizon of $h = 5$ was applied. A nucleation trigger, denoted as $CVFND_n$ was declared when the averaged slope over an update window of length U exceeded a fixed threshold θ_{CV} units, as shown in Equation (62). This suppresses isolated fluctuations and requires a sustained increase.

$$CVFND_n = 1 \cdot \left\{ \frac{1}{U} \cdot \sum_{i=0}^{U-1} CV_{n+1-i}^{Tile} \geq \theta_{CV} \right\} \tag{62}$$

Where:

- $CVFND_n$ is the CV frost nucleation detector output,
- U is the averaging update window length,
- θ_{CV} is the local slope estimate threshold for nucleation detection.

For this work, values of $U = 3$ and $\theta_{CV} = 20$ were adopted, as they provided the best compromise between detection accuracy and robustness against noise. $CVFND_n$ outputs a binary value that returns 1 when nucleation is detected, and 0 otherwise. The

timestamp of the first trigger is extracted for each test and compared with the FND output using Equation (63)

$$\Delta t_{nuc} = t_{FND} - t_{CVFND} \tag{63}$$

Where:

- t_{FND} is the timestamp of resistive nucleation detection [min]
- t_{CVFND} is the timestamp of computer-vision nucleation detection [min]
- Δt_{nuc} is the time difference between FND and $CVFND$ events [min]

This completes the definition of the $CVFND$, which provides an external reference for validating the FDS derived FND. It serves solely as an auxiliary validation metric and is not intended for real-time control.

6.1.5. HBDCD – Humidity-Based Defrost Completion Detector

A Humidity-Based Defrost Completion Detector ($HBDCD$) was defined in post-processing to provide an independent reference for the dry HX state. The method compares AH at the HX inlet and outlet, then applies smoothing and a stability check gated by the DOS.

The DHT measured RH was not used directly because AL-HX inlet and outlet temperatures are mostly different during testing. AH is expressed as the mass of water vapour per unit volume of air, therefore providing a temperature-independent measure of moisture content. By comparing inlet and outlet AH, the influence of temperature is removed, allowing the detector to reliably indicate whether the AL-HX is still releasing moisture or has reached a dry state.

AH was calculated from RH and air temperatures using the empirical formulation from Equation (16). Therefore, the AH at the inlet of the HX, denoted $AH1_n$, was calculated from the measured $TA1$, and $RH1$ according to Equation (64).

$$AH1_n = \frac{2.1674 \cdot RH1_n \cdot 6.112 \cdot e^{\frac{17.67 \cdot TA1_n}{TA1_n + 243.5}}}{TA1_n + 273.15} \tag{64}$$

Where:

- $AH1_n$ is the calculated absolute humidity at the HX inlet [g/m^3],

- $TA1_n$ is the air temperature at the HX inlet [°C],
- $RH1_n$ is the relative humidity at the HX inlet [%].

The absolute humidity at the outlet of the HX, denoted AH_2, was obtained in the same way, using the measured $TA2$, and $RH2$, as shown in Equation (65):

$$AH2_n = 1324.45 \cdot \frac{RH2_n}{100} \cdot \frac{exp\left(\frac{17.67 \cdot TA2_n}{TA2_n + 243.5}\right)}{TA2_n + 273.15} \tag{65}$$

Where:

- $AH2_n$ is the calculated absolute humidity at the HX outlet [g/m^3],
- $TA2_n$ is the air temperature at the HX outlet [°C],
- $RH2_n$ is the relative humidity at the HX outlet [%].

To reduce noise in the inlet absolute humidity signal, a centred moving average was applied over a window of length N, yielding the smoothed inlet absolute humidity $\overline{AH1}_n$ shown in Equation (66).

$$\overline{AH1}_n = \frac{1}{N} \cdot \sum_{i=0}^{N-1} AH1_{n+\frac{N}{2}-i} \tag{66}$$

Where:

- $\overline{AH1}_n$ is the smoothed inlet absolute humidity [g $\cdot$ m^{-3}],
- N is the length of the moving average window.

For this work, a centred moving average with $N = 10$ samples was applied, corresponding to a smoothing horizon of 30 s given the acquisition interval of 3 s.

The outlet absolute humidity was smoothed in the same manner, resulting in the averaged series in Equation (67):

$$\overline{AH2}_n = \frac{1}{N} \cdot \sum_{i=0}^{N-1} AH2_{n+\frac{N}{2}-i} \tag{67}$$

Where:

- $\overline{AH2}_n$ is the smoothed outlet absolute humidity [g · m^{-3}],

The same value of $N = 10$ samples was used here to maintain consistency between inlet and outlet signals.

The difference between the smoothed outlet and inlet absolute humidity was then computed in Equation (68)(69) as ΔAH_n

$$\Delta AH_n = \overline{AH2}_n - \overline{AH1}_n \tag{68}$$

Where:

- ΔAH_n is the difference in absolute humidity between the outlet and inlet [g · m^{-3}]

This difference reflects the amount of water vapour absorbed or released between the inlet and outlet. When positive, the HX is releasing moisture, and when negative, condensation and/or frosting is occurring. When close to zero, during defrosting, it signals the surface can be considered dry, as no mass transfer is occurring.

Finally, the difference signal ΔAH_n was smoothed using a second moving average over a window of length Q, giving the filtered series $\overline{\Delta AH}_n$ shown in Equation (69):

$$\overline{\Delta AH}_n = \frac{1}{Q} \cdot \sum_{i=0}^{Q-1} \Delta AH_{n+\frac{Q}{2}-i} \tag{69}$$

Where:

- $\overline{\Delta AH}_n$ is the smoothed difference in absolute humidity [g · m^{-3}],
- Q is the length of the moving average window applied to ΔAH

For this work, $Q = 20$ samples were used, corresponding to a smoothing horizon of 60 s. This ensured stability of the indicator while still allowing adequate responsiveness to the end of the drying phase.

Finally, the humidity-based defrost completion detector $HBDCD_n$ is defined in Equation (70) as a binary output:

$$HBDCD_n = 1 \cdot \begin{cases} 1, & |\overline{\Delta AH}_n| < \psi \wedge DOS_n = 1 \wedge |\overline{\Delta AH}_n - \overline{\Delta AH}_{n-1}| < \varepsilon \\ 0, & otherwise \end{cases} \quad (70)$$

Where,

- $HBDCD_n$ is the humidity based defrost completion detector,
- DOS_n is the door state sensor,
- ψ is the $\overline{\Delta AH}_n$ threshold for the AL-HX to be considered dry [$g \cdot m^{-3}$],
- ε is the stability tolerance threshold [$g \cdot m^{-3}$].

This requires $|\overline{\Delta AH}_n|$ to be below the threshold ψ, that for this work was selected to be $\psi = 0.5$. Additionally, defrosting ($DOS_n = 1$) must be active and the stability condition uses a stability tolerance threshold, that was set to be $\varepsilon = 0.001$ to separate false positives caused from transient fluctuations.

The timestamp of the first trigger is extracted for each test and compared with the DCD output using Equation (71).

$$\Delta t_{dry} = t_{DCD} - t_{HBDCD} \quad (71)$$

Where:

- t_{DCD} is the timestamp of resistive defrost completion detection [min]
- t_{HBDCD} is the timestamp of humidity-based defrost completion detection [min]
- Δt_{dry} is the time difference between DCD and $HBDCD$ events [min]

This completes the definition of the humidity-based defrost completion detector, which provides an external reference for validating the resistive DCD. It serves solely as an auxiliary validation metric and is not intended for real-time control.

This concludes the signal-processing framework. The two main FDS derived event detectors (FND and DCD), are two binary event flags that mark frost nucleation and defrost completion. In addition, two auxiliary validation metrics were defined ($CVFND$ and $HBDCD$). These provide independent external references for comparison with the FDS based detectors however are not intended for real-time control, although they hold that potential if adaptations to make them causal are made. Parameter choices such as window lengths and thresholds were fixed a priori and remained constant across tests to

ensure repeatability. With the detection logic and validation metrics established, the next section provides the Design of Experiment (DoE).

6.2. Design of experiment

This section defines the experimental conditions under which resistive frost detection was evaluated. It specifies sensor placement, acquisition and processing parameters, the test series, the control strategy used to initiate and terminate defrosting, and the variables monitored to characterise system behaviour during frosting–defrosting cycles. The objective is to provide a coherent framework that supports comparability across tests and traceability of the subsequent results.

6.2.1. Sensor placement

The first step in the DoE is to define the sensor location. This choice is made based on the FFM developed in the CV method for frost detection chapter, and shown in Figure 168. The FFM partitions the HX surface into a 12×12 matrix, allowing tiles to be referenced compactly. Lighter tiles correspond to stronger frost expression and darker tiles to weaker expression. The spatial non-uniformity of this pattern must be considered to obtain representative sensor measurements.

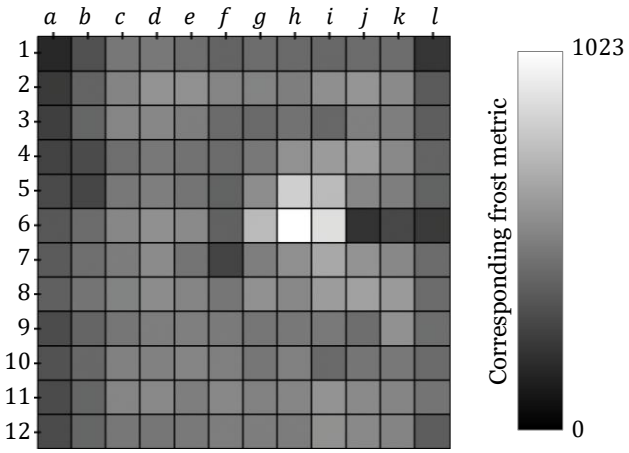

Figure 168 – Frost formation map.

Candidate locations are first pruned by excluding tiles that bias the analysis or complicate installation. Four classes, highlighted in Figure 169, are removed: (i) tiles with image defects, (ii) tiles occupied by the DHT sensor, (iii) tiles crossed by the DHT cable, and (iv) tiles that are either too dark or too bright, corresponding to the lowest and highest ends of the frost-intensity scale (i.e., low-frost and high-frost regions) were excluded based in FFM data.

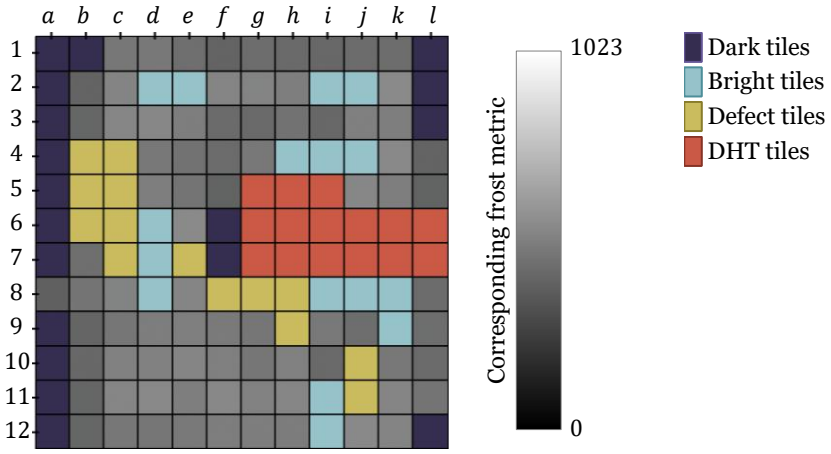

Figure 169 – Exclusion mask on the FFM.

Applying the full exclusion mask removes 63 tiles, leaving 81 valid candidates. Given the large number of valid tiles, an additional criterion is introduced to increase information content from co-located computer-vision measurements. Certain fin regions appear reflective only when dry, as shown in Figure 170 (a). During condensation, the surface becomes matte and those traces vanish, as shown in Figure 170 (b). This dry-only reflectiveness provides an auxiliary CV cue for condensation detection that complements the resistive signal.

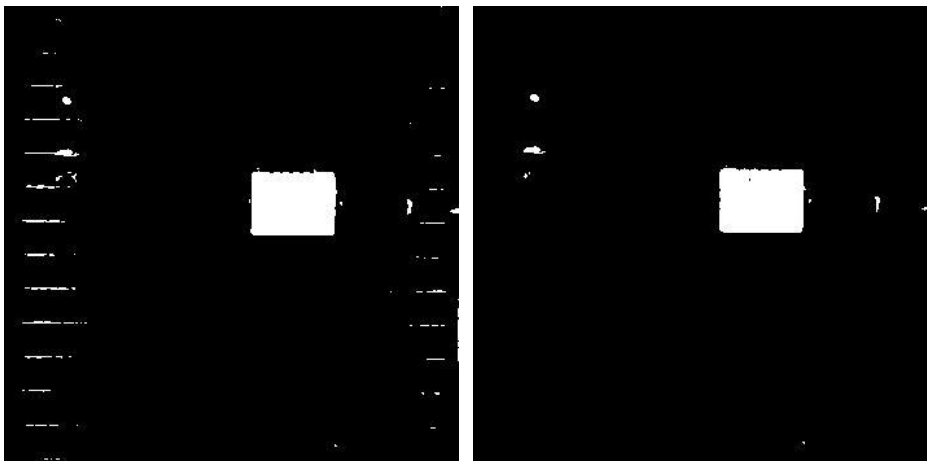

(a) (b)

Figure 170 –CV frames of the HX surface dry (a) and during condensation (b).

The FFM with highlighted tiles that exhibit these dry-only reflective regions is shown in Figure 171. Monitoring these highlighted regions makes it possible to achieve CV-based condensation detection.

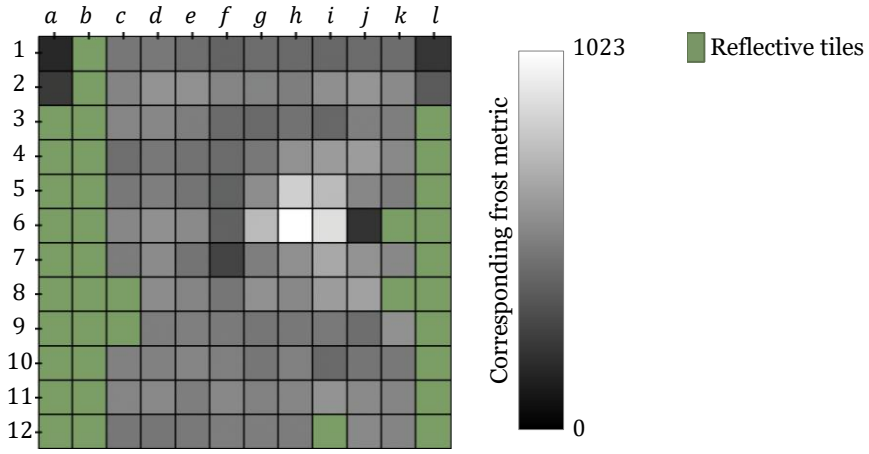

Figure 171 – FFM with reflective tiles highlighted.

Reflective tiles overlapping any exclusion were discarded and shown in Figure 172, leaving 17 reflective tiles in valid regions.

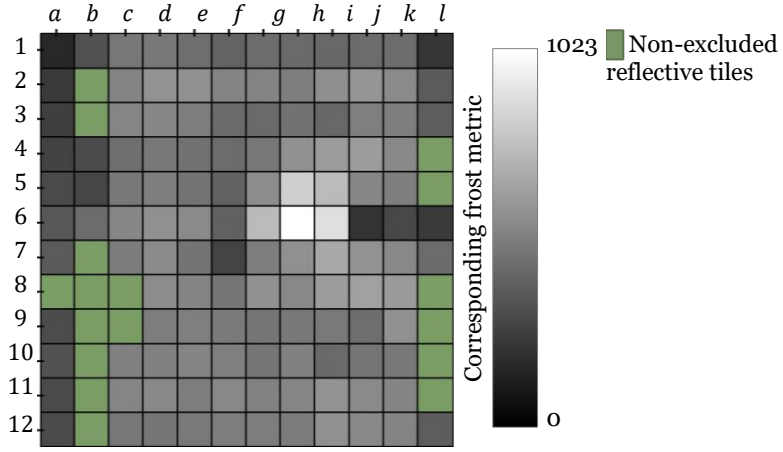

Figure 172 – FFM with non-excluded reflective tiles highlighted.

To reduce edge-related artefacts and simplify mounting, tiles adjacent to the outer border (column *a* and *l*, rows 1 and 12) were also removed. This yields 9 candidate tiles forming two compact clusters (one in the lower half and a smaller one in the upper top half). The upper cluster was preferred as it is less prone to drip-induced re-wetting during defrost, which stabilizes FDS measurements during defrosting. Within the upper cluster, two neighbouring tiles present comparable qualities and Tile *b*3 was selected for slightly easier mounting position.

After placement, the sensor is visible in the processed images of the HX and is highlighted in Figure 173(a). Because its presence introduces visual artefacts, the sensor itself should not be included in the targeted tile for post-processing analysis, so the targeted tile was defined immediately to the left of the sensor, providing a local reference

for frost formation while avoiding noise and obstruction caused by the sensor's visibility. This selected tile is shown in Figure 156 (b) and is used throughout this chapter for the computer-vision tile analysis comparison.

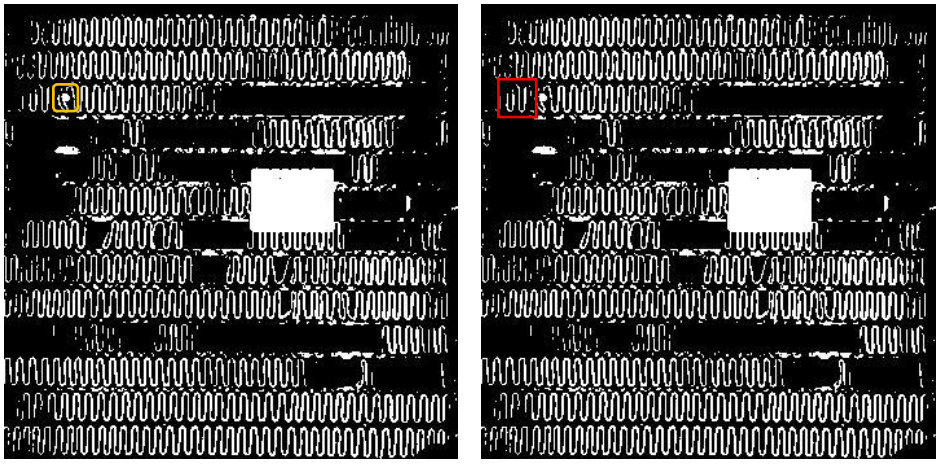

(a) (b)

Figure 173 – Sensor (a) and tile (b) location highlighted in the HX surface.

Although a targeted tile post-processing analysis is employed for result comparison throughout this chapter, the control actions during the experiments (stopping operation and initiating defrosting) were based on the CVG metric. This choice reflects the fact that, while the targeted tile analysis provides a more precise reference for comparison with the resistive sensor, it is the global frost accumulation that must guide system-level operation. The difference between the two indicators is minor within the operational window considered and therefore does not affect the validity of this approach.

To establish a clear basis for interpreting the experimental results, the next section outlines the operating parameters.

6.2.2. Experimental parameters

Several parameters were kept constant across all experiments to ensure comparability of results and to avoid introducing unnecessary variability in the analysis. These fixed parameters define both the data acquisition conditions and the processing framework used throughout the study. The acquisition settings and sensor configuration are summarised in Table 43.

Table 43 –Acquisition parameters and sensor configuration applied in all experiments.

Parameter		Value
Sampling interval [s]		3
Resolution		10-bit
Sensor placement tile		$b3$
Targeted CV coordinates [px]		$x = 28, y = 73$
Sensor used		FMRS4
Chiller set temperature [°C]		-6
Fan speed	Operation	Min
	Defrosting	Max
Wind tunnel state	Operation	Closed
	Defrosting	Open
Pumps state	Operation	Max
	Defrosting	Off
TE-HX power [W]	Operation	~ 250
	Defrosting	0
Illumination	Operation	On
	Defrosting	On

In addition to this, the FDS signal processing framework relied on the parameters, shown in Table 44 to obtain FND and DCD. As the values were fixed, they provided a reference for evaluating detection performance in a way that detector output arose solely from system behaviour.

Table 44 – Parameters of the signal processing framework.

Parameter	Value
Sensor signal	ADC
Temperature used for compensation	$TA2$
Temperature coefficient (α) [$°C^{-1}$]	-0.045
Reference temperature (T_{ref}) [°C]	2.22
Moving average window (W)[-]	30
Average slope window (K)[-]	30
Slope threshold (θ_s) for FND/DCD [-]	0.15/0.30
Persistence window (P) [-]	20
Tolerance around $ADC_n^{trig}(\zeta)$	25
FND/DCD pulse duration [s]	3
Cosmetic FND/DCD pulse duration [s]	60
Operation/defrosting indicator	DOS

Beyond the FDS-based detectors, the auxiliary $CVFND$ and $HBDCD$ were introduced to provide independent benchmarks. The parameters used to obtain them are presented in Table 45. These values were likewise kept constant throughout this chapter.

Table 45 – Parameters of auxiliary validation detectors.

Parameter	Value
Targeted tile CV frost metric	CVT
Slope horizon for CV metric (H) [-]	5
Averaging update window (U) [-]	3
CV nucleation slope threshold (θ_{CV}) [-]	20
Inlet air temperature [°C]	$TA1$
Inlet air RH [%]	$RH1$
Outlet air temperature [°C]	$TA2$
Outlet air RH [%]	$RH2$
AH smoothing window (N) [-]	10
ΔAH smoothing window (Q) [-]	20
ΔAH dryness threshold (ψ) [$g \cdot m^{-3}$]	0.5
Stability tolerance (ε) [$g \cdot m^{-3}$]	0.001
Operation/defrosting indicator	DOS

Together, these parameters allowed experiments to be conducted under consistent acquisition, environmental, and processing conditions. Holding these aspects constant means the analysis could focus on the influence of the dynamic variables, which are discussed in the following sections.

6.2.3. Control strategy

The overall control procedure of the experimental setup has already been described in the Frost formation experimental setup chapter and is displayed in the flowchart of Figure 59. However, the main points are recalled clarifying the operational sequence adopted in the present tests.

Before each test, the humidifier was saturated and placed inside the wind tunnel. The pumps and the four thermoelectric modules of the TE-HX were then activated, followed by the closure of the tunnel doors to initiate the operation stage under controlled airflow.

Defrosting was manually triggered once the CVG reached the predefined threshold, signalled by an alarm. The procedure consisted of sequentially switching off the TE-HX

and pumps, opening the wind-tunnel doors, and removing the humidifier. A timer was then started to maintain defrosting for the duration prescribed in the test design.

This control strategy allowed for repeatable frosting and defrosting conditions while maintaining consistency with the operational framework described earlier in this work.

6.2.4. Test series and operating conditions

To provide an overview of the experimental design, all tests are compiled in Table 46 according to their series, identifiers, and corresponding control parameters. The tests are organised in the order A, B, and C, reflecting their operating conditions.

Table 46 – Overview of test series and operating conditions.

Series	Test ID	CV_{th} [-]	Defrost [min]
A	T-A-01	960	15
A	T-A-02	960	15
A	T-A-03	960	15
A	T-A-04	960	15
B	T-B-01	1012	30
B	T-B-02	1012	30
B	T-B-03	1012	30
C	T-C-01	960	14
C	T-C-02	960	14
C	T-C-03	960	14
C	T-C-04	960	14
C	T-C-05	960	14

The A series represents the baseline condition, conducted with a CV_{th} of 960 and a defrost duration of 15 min. These values were selected because the CV_{th} corresponded to the visual observation of significant frost accumulation, while the defrost duration matched the time required to reach a dry HX with a safety margin. The four tests in this series provided the most consistent and reliable detections of nucleation and defrost completion, serving as the main reference for comparison.

The B series extended the operating window by applying a higher CV_{th} of 1012 and lengthening the defrost phase to 30 min. This regime was designed to explore the system under prolonged frosting and defrosting conditions, thereby testing the upper bounds of operation.

The C series used the same CV_{th} as the baseline but with a shorter defrost duration of 14 min, combined with a sub-optimal sensor placement. This configuration introduced challenges in achieving DCD, offering a robustness assessment of the detection method under non-ideal conditions.

Together, these series cover a representative range of operating regimes, providing the basis for the subsequent analysis of the FDS. With the test design and operating conditions established, the next subsection summarizes the monitored variables and derived metrics used to characterise system behaviour and sensor performance.

6.2.5. Monitored variables and derived metrics

To complement the resistive sensor measurements, several auxiliary parameters were monitored throughout all experiments. These signals provide context for interpreting sensor behaviour and for understanding the operating conditions of the experimental setup. Table 47 summarises the auxiliary monitored parameters. Among these, $TA2$ is used for temperature compensation of the resistive sensor, and together with $TA1$, $RH1$, and $RH2$ serve as references for assessing the dry state of the HX. The DOS provides a direct indication of whether the system is in operation or in defrosting mode. The remaining signals, such as working fluid temperatures, flow rates, and thermoelectric module currents, support the interpretation of operating conditions and help identify any anomalies in system behaviour.

Table 47 – Auxiliary monitored parameters.

Parameter	**Reference**
Working fluid temperatures [°C]	$TWF1$, $TWF2$, $TWF3$, $TWF4$
Working fluid flow [L/min]	$FS1$, $FS2$
TE-HX current [A]	$I1$, $I2$, $I3$, $I4$
Air temperature [°C]	$TA1$, $TA2$
Air relative humidity [%]	$RH1$, $RH2$
Wind tunnel door state [-]	DOS

The direct frost detection parameters are listed in Table 48. These represent the primary focus of the study. Both CV and FDS-derived metrics provide the raw input data against which the detection algorithms are applied and validated.

Table 48 – Frost detection parameters.

Parameter	Reference
FDS sensor data	ADC
Global CV metric	CVG
Targeted tile CV metric	CVT

In addition to the raw signals, several derived metrics were computed to enable event detection and comparative analysis. These are summarised in Table 49.

Table 49 – Derived metrics.

Parameter	Reference
Temperature compensated ADC	$\widehat{ADC}$
Smoothed temperature compensated ADC	$\overline{ADC}$
Frost nucleation detector	FND
Defrost completion detector	DCD
Humidity based defrost completion detector	$HBDCD$
CV derived frost nucleation detector	$CVFND$
Absolute humidity	$AH1$, $AH2$
Smoothed absolute humidity difference	$\overline{\Delta AH}_n$
Time difference between FND and $CVFND$ events	Δt_{nuc}
Time difference between DCD and $HBDCD$ events	Δt_{dry}

Only the principal derived quantities are included, as other intermediate calculations (such as slope estimates or intermediate moving averages) served as stepping stones rather than final targets of the analysis.

With these elements in place, the next section examines system performance during frost formation, where the monitored signals and derived metrics are plotted for a representative test to illustrate the behaviour of the experimental setup in operation.

6.3. System performance during frost formation

Before analysing the test results, it is necessary to establish how the system behaves during a representative frost–defrost cycle. This section provides the operational context in which the sensors operate, showing how the monitored variables evolve and interact. Such an overview helps in interpreting the dynamics involved in the frost-defrost states.

To contextualise the results presented in this section, it is useful to refer back to the schematic of the experimental setup shown in Figure 30 and in Figure 54, which

illustrates the placement of sensors and the arrangement of the fluid and airflow circuits. Together with this figure, Table 13 provides the corresponding sensor references, establishing the notation adopted here. Together, the schematic and table provide a comprehensive overview of the acquisition system, clarifying how each measured parameter is positioned within the setup.

6.3.1. Computer vision metrics

The CV metrics developed in this work are an auxiliary means of monitoring frost formation on the AL-HX surface. They quantify frost growth from either the entire surface (CVG) or from a targeted region of interest (CVT). This dual perspective allows both a system-level view that is used to control the initiation of defrosting and a locally sensitive measure for comparison with the FDS data.

In Figure 174, the CVG and CVT metrics are plotted together. The CVG produces a smoother curve, reflecting its insensitivity to local fluctuations, while the tile signal is more affected by local dynamics and thus appears slightly more irregular. Both detect nucleation shortly after operation begins, with the global detection occurring earlier than the tile. After nucleation, the global curve exhibits a smooth logarithmic-like shape, while the tile follows a piecewise-linear trajectory with a marked elbow. During defrost, both signals drop together.

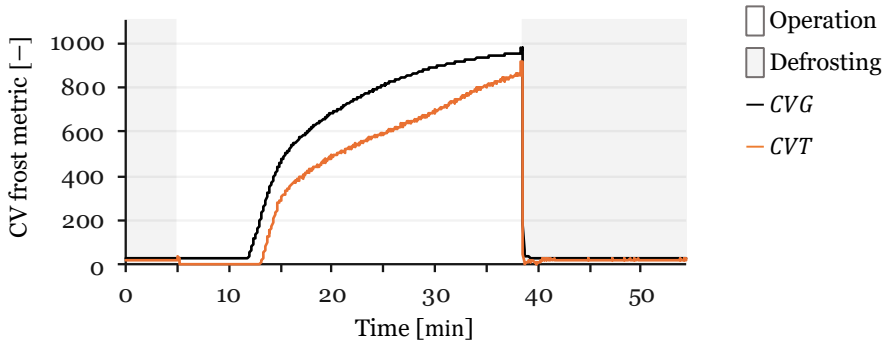

Figure 174 – CVG and CVT frost metrics during a frost–defrost cycle.

Figure 175 zooms in on the lower range of the CV metrics (0 – 100), which highlights their behaviour during condensation and early nucleation. The global curve drops modestly at the onset of condensation, whereas the tile metric falls to zero, reflecting the loss of reflectivity in the analysed region. This confirms the tile's higher sensitivity to surface condensation, even though it is unable to distinguish between liquid water and dry HX. Towards the end of defrost, the tile again exhibits a brief drop to zero followed

by a recovery before stabilising, which can be attributed to dripping intermittently at the start of defrosting, changing the reflectivity of the AL-HX surface. The CVG curve, in contrast, doesn't overshoot to zero, dropping to a low, stable value.

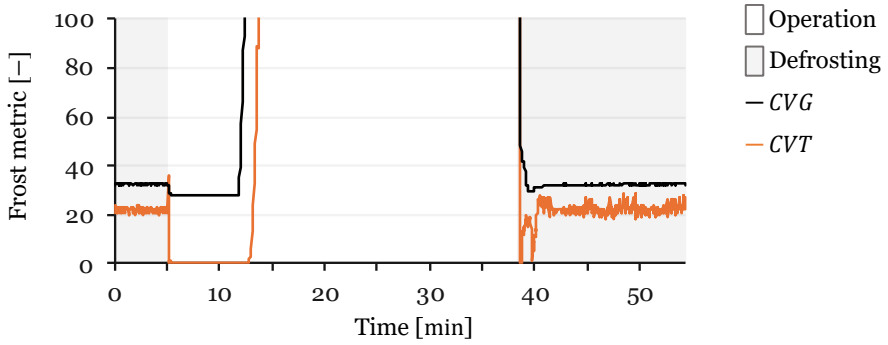

Figure 175 – Cropped view of the lower values for the Global and Tile CV frost metrics.

Overall, the CVG provides a system-level reference, while the CVT increases local sensitivity to phenomena close to the sensor location. The combination of the two strengthens the interpretation of surface conditions and validates the FDS measurements. With this visual baseline established, the analysis now turns to the resistive sensor metrics.

6.3.2. Resistive frost detection sensor metrics

FDS measurements form the core of the frost detection approach developed in this work. The FMRS4 responds to phase changes on the HX surface by shifting its resistance, which is sampled at the ADC. However, resistivity is also temperature-dependent, making raw measurements harder to interpret during rapid cooling and heating transitions if no compensation is performed. For this reason, temperature compensation and smoothing were applied, as described earlier, to obtain a signal suitable for the detection of nucleation and defrost completion.

In Figure 176, both the raw ADC signal and the temperature-compensated $\widetilde{ADC}$ are shown across a complete frost–defrost cycle. At first glance, the two signals appear similar, but closer inspection reveals that the compensated curve reduces distortions introduced by sudden temperature changes. Both curves capture the characteristic drop associated with condensation at the start of operation and the pronounced decline during defrost. Notably, the compensated curve maintains a clearer separation between dry and frosted states, whereas the raw curve tends to collapse these values into a closer range.

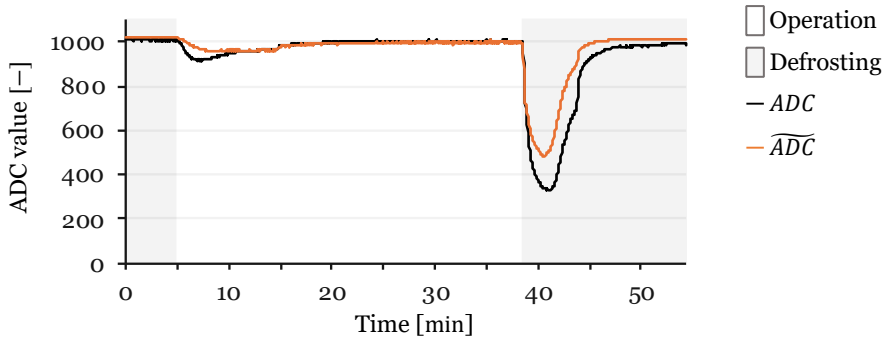

Figure 176 – Raw and temperature-compensated ADC values during a frost–defrost cycle.

Figure 177 zooms in on the region between ADC values of 910 and 1020, which highlights the subtle but important differences in behaviour. In this range, it is easier to see that the $\widetilde{ADC}$ shows higher values for dry HX than for frost saturation, reflecting the fact that air is more resistive than frost. The raw ADC, in contrast, often places dry values at or below frosted values, which can lead to misinterpretation. The zoom also shows condensation more clearly. In the $\widetilde{ADC}$ signal, condensation causes a drop that then stabilises as the sensor saturates with liquid water, whereas the raw ADC drops and then rises again, creating a false appearance of nucleation. This demonstrates the importance of compensation in avoiding false positives. During defrosting, the compensated curve rises above the raw curve because higher sensor temperatures reduce resistivity in the uncompensated signal. Small fluctuations visible in the higher ADC ranges also illustrate the limited resolution of the 10 -bit acquisition system, where a single ADC step corresponds to larger resistance changes at the upper end of the scale.

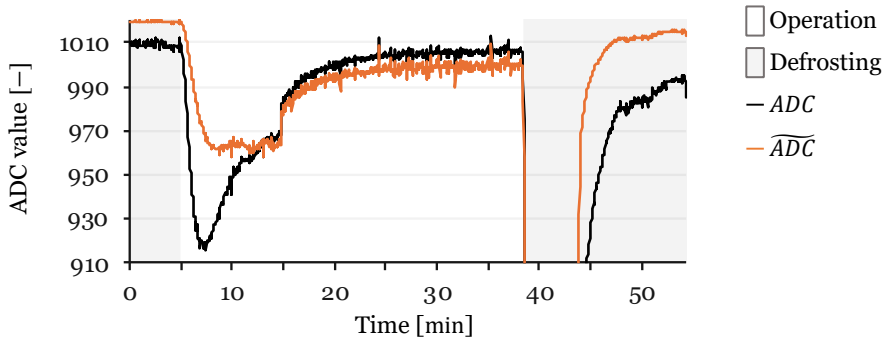

Figure 177 – Detail of raw and compensated ADC values during a frost–defrost cycle (910–1020 range).

Figure 178 overlays the $\widetilde{ADC}$ signal with its moving-average version, $\overline{ADC}$, again in the same zoomed region. The moving average almost overlaps the compensated curve, but with a slight temporal offset and reduced noise. This denoising is especially beneficial in the higher ADC range, where raw fluctuations would complicate the detection of stable plateaus. However, smoothing also softens the transitions between condensation and

frost, reducing sharpness at critical moments, although not critically due to a small window. This trade-off reflects the design choice of favouring robustness in event detection (particularly defrost completion) over fine temporal accuracy.

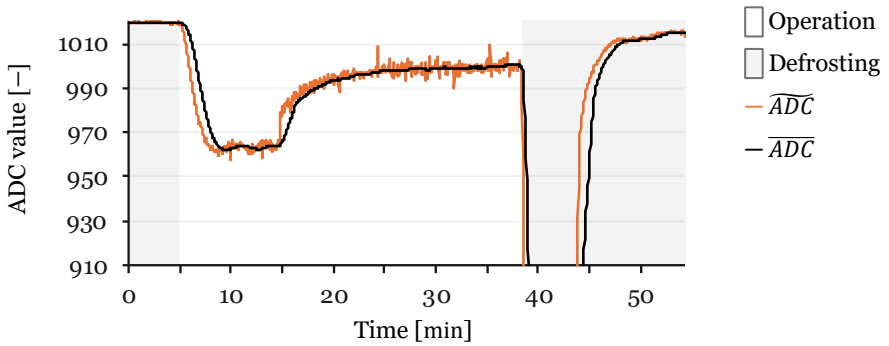

Figure 178 – Detail of temperature-compensated ADC signal with and without moving average.

Finally, Figure 179 displays the classified output of the averaged slope, C_n^{ADC} , together with the raw ADC signal. This comparison links the sensor readings to the discrete three-state variable used by the detection algorithms. During operation, the initial decrease in $\widetilde{ADC}$ is mapped as a negative slope, followed by a stable region during condensation and a positive classification when the signal begins to rise due to frost formation. During defrosting, the sharp decrease caused by liquid water is again classified as negative, while the subsequent drying phase produces a positive classification before returning to zero as the signal stabilises. This representation shows that C_n^{ADC} preserves the main transition information required by the FND and DCD, while suppressing minor fluctuations that are not relevant for event detection.

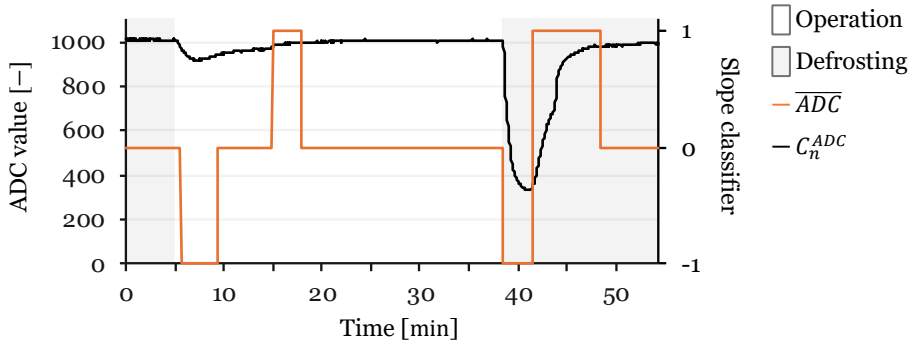

Figure 179 –Temperature-compensated ADC signal and classified slope during a frost–defrost cycle.

These plots show how temperature compensation corrects misleading behaviour in the raw ADC signal, allowing distinction between condensation, nucleation, and defrosting, while moving average filtering reduces noise at the cost of a slightly temporal shifted

curve. With the resistive sensor signals clarified, the analysis now turns to the thermal context of the system, examining air and fluid temperatures during operation.

6.3.3. Air and working fluid temperatures

Temperature signals provide the thermal context in which frosting and defrosting occur. They determine the phase state of water at the HX surface, and they were also used directly in the signal-processing framework for temperature compensation of the resistive signal.

In Figure 180, the inlet ($TA1$) and outlet ($TA2$) air temperatures are shown. The air temperatures begin near ambient conditions and $TA1$ remains the highest throughout the cycle, decreasing about 9 °C during operation. The $TA2$, in contrast, drops to values of -6 °C, which is 15 °C below the $TA1$ by the end of operation. This sharp gradient highlights the cooling effect of the AL-HX and explains again why $TA2$ was selected as the reference for compensation. When defrosting begins, both air temperatures rise sharply and converge approximately halfway through the defrost phase, reflecting the restoration of thermal equilibrium. This convergence confirms that airflow dominates the thermal response once active cooling ceases.

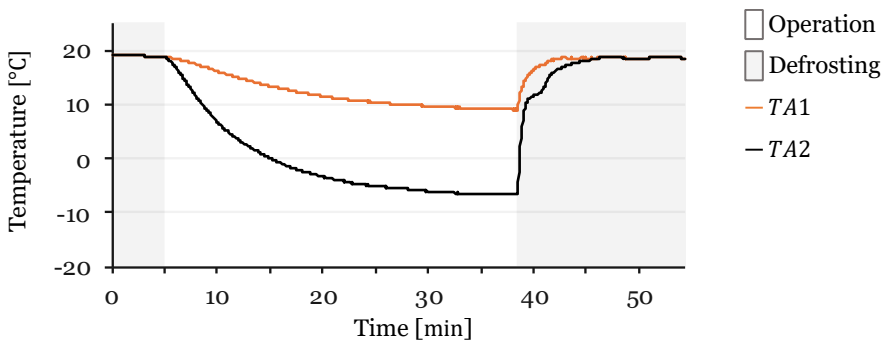

Figure 180 – Inlet and outlet air temperatures ($TA1$, $TA2$) during a frost–defrost cycle.

In Figure 181, the working fluid temperatures are shown for both circuits. For circuit 3, the inlet ($TWF1$) and outlet ($TWF2$) remain very close during operation, with a nearly constant offset of less than 1 °C. This indicates that the high flow rate keeps the HX nearly isothermal along its length, ensuring a uniform surface temperature. Over the course of the test, the overall drop is large (on the order of 15 – 20 °C), which approximates the shape of a negative logarithmic curve. Once defrosting starts, the pumps are switched off, and these readings no longer represent testing conditions.

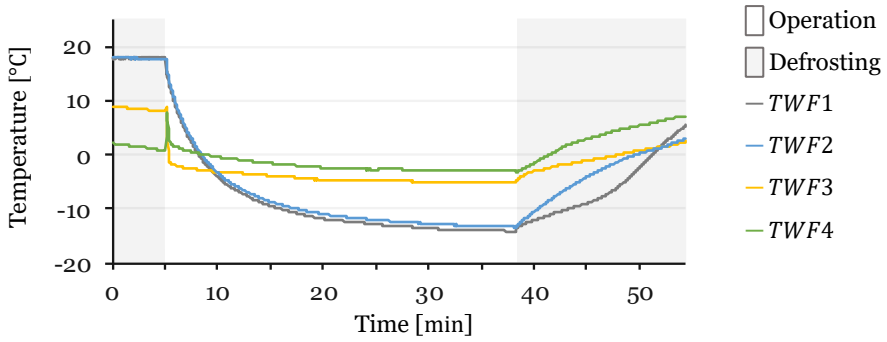

Figure 181 – Inlet and outlet working fluid temperatures of circuits 2 and 3 during a frost–defrost cycle.

Circuit 2, on the other hand, shows a different behaviour. Here, the inlet and outlet temperatures are farther apart, with a constant but larger ΔT across the circuit. This is a direct consequence of the smaller pump capacity, which reduces flow. The overall cooling trend across circuit 2 remains modest, with a net ΔT of around 3 °C over the test once the initial steep drop is excluded. This steep drop is moderated by the 200 litre reservoir whose thermal inertia initially causes a sudden temperature drop when circulation begins, followed by a gradual and steady decline. The spike observed in $TWF4$ is caused by liquid remaining in the TE-HX, which warms the working fluid even when it is switched off during defrosting. Once operation resumes, this warmed fluid is pumped past the temperature sensor, producing the transient increase.

These temperatures show how rapidly the AL-HX and airflow cool during operation and recover during defrost. They also justify the choice of outlet air temperature as the compensation reference for the FDS signal. With the thermal context established, the analysis now turns to humidity, which provides a complementary view of mass transfer and is particularly valuable for assessing the dry state of the HX.

6.3.4. Humidity metrics

Humidity signals complement the temperature and resistive sensor data by describing the mass transfer dynamics happening in the AL-HX. As presented earlier, two DHT sensors were placed at the inlet and outlet, providing relative humidity ($RH1$ and $RH2$).

In Figure 182, $RH1$ and $RH2$ are shown. Before operation, both sensors read approximately the same value, close to 50%, as inlet and outlet air are at the same temperature and moisture conditions. At the onset of operation, both sensors record a sharp increase, but their subsequent behaviours diverge: $RH1$ continues to rise, while $RH2$ quickly decreases back toward its initial value. The initial spike in $RH1$ is explained by two effects: the rapid cooling of the air at the inlet, which temporarily raises RH, and the fact that the closed tunnel recirculates the airflow after passing through the

humidifier, increasing moisture at the inlet. $RH2$, on the other hand, drops because condensation in the AL-HX removes moisture from the air. During defrost, $RH2$ shows a strong spike to saturation (100%), reflecting intense evaporation of meltwater from the HX surface. $RH1$ also increases, though less sharply, as warmer ambient air enters the tunnel and is cooled, raising its relative humidity temporarily.

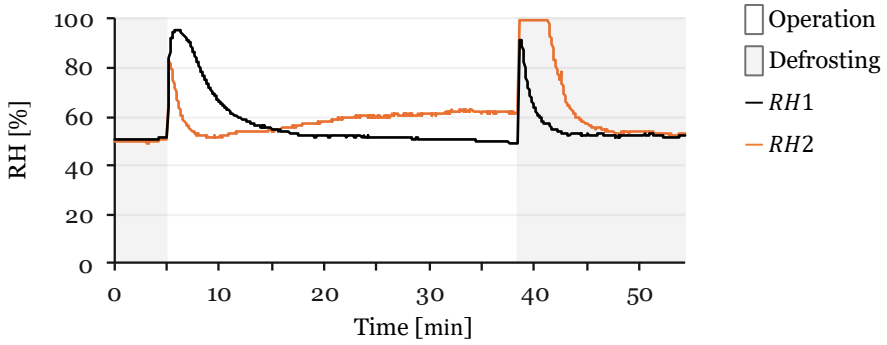

Figure 182 – RH at the inlet ($RH1$) and outlet ($RH2$) of the AL-HX during a frost–defrost cycle.

Figure 183 shows the corresponding absolute humidities, $AH1$ and $AH2$, computed from Equation (16). Unlike RH, which is strongly temperature-dependent, AH provides a direct measure of water vapour content. Both $AH1$ and $AH2$ decline steadily during operation, demonstrating that the airstream is gradually dehumidified as moisture is removed and deposited as frost, and the air lowers its temperature, decreasing its capacity to hold moisture. Their initial spikes differ in shape. $AH2$ shows a sharp peak followed by a logarithmic decay, while $AH1$ increases more slowly, forming a rounded maximum before also decreasing. This indicates that the air acquires moisture from the humidifier before reaching the inlet sensor, while at the outlet, moisture removal is immediate and sharp. During defrost, $AH1$ spikes due to the inflow of warmer air capable of holding more vapour, while $AH2$ rapidly surpasses $AH1$ as meltwater evaporates from the HX surface, causing the outlet air to hold more water vapour. This divergence continues until drying is complete, after which $AH1$ and $AH2$ converge again, signalling moisture equilibrium. This convergence justifies the use of AH as the basis for detecting the dry HX state.

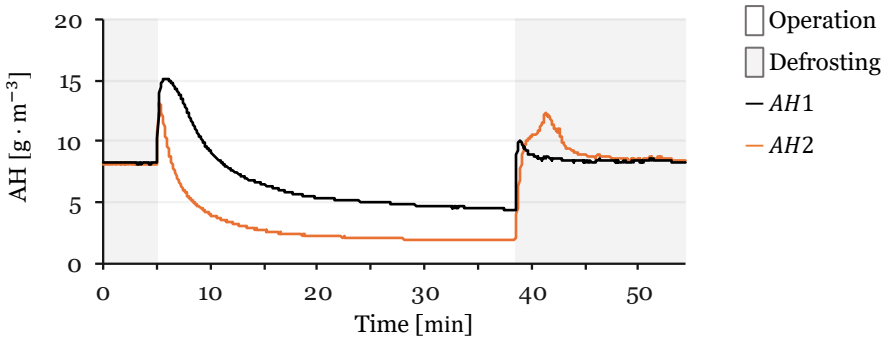

Figure 183 – Absolute humidity at the inlet (AH1) and outlet (AH2) of the HX during a frost–defrost cycle.

Finally, Figure 184 shows the moving-averaged difference between the outlet and inlet absolute humidities, $\overline{\Delta AH}_n$, computed from Equation (69). Before operation, this value is close to zero, indicating no significant mass transfer. Once operation begins, the curve drops steeply, stabilizing at a negative value meaning mass transfer to the AL-HX, which is absorbing moisture from the air (condensation or frost deposition). As the cycle continues, the difference stabilises at a negative offset, reflecting ongoing dehumidification. When defrost begins, a brief dip is observed due to the inlet spike, but shortly after, the signal crosses zero and becomes positive. This reversal marks the transition from moisture absorption to moisture release, as meltwater evaporates from the AL-HX. The curve then decays back toward zero, signalling that drying is complete and inlet and outlet vapour contents are again balanced. The sign of this signal thus directly indicates the mass transfer direction, negative during frosting, positive during defrosting.

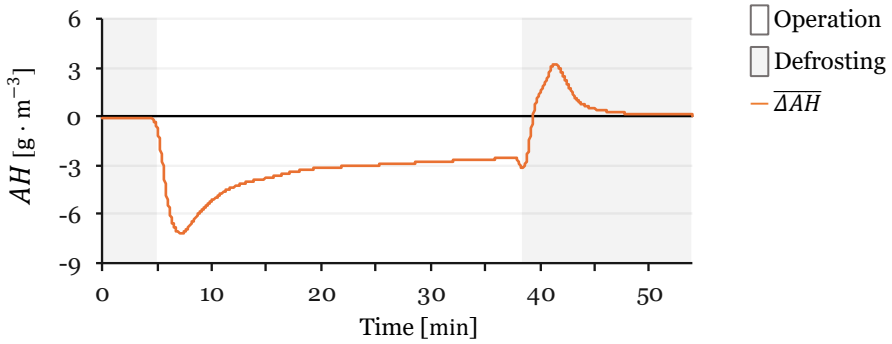

Figure 184 –Moving-averaged difference between outlet and inlet absolute humidities $\overline{\Delta AH}_n$, during a frost–defrost cycle.

The humidity metrics allow to retrieve information on air saturation from RH, while AH provides a measure of mass transfer through the $\overline{\Delta AH}$. With the moisture dynamics clarified, the analysis proceeds to the final set of ancillary signals: flow and viscosity.

6.3.5. Flow and viscosity

Fluid flow and viscosity provide complementary context for understanding the thermal and hydraulic behaviour of the working fluid circuits. While not direct indicators, they help explain how temperature changes propagate through the working fluids and how this, in turn, affects circulation stability.

In Figure 185, the flow rates measured by the two sensors are shown. $FS2$, connected to circuit 2, remains nearly constant across the entire cycle, with only a negligible decrease from its initial value. This stability reflects the smaller pump capacity and the nearly steady viscosity of the fluid in this circuit, which remains at low temperature throughout the test. A sharp but short-lived spike occurs at start-up, caused by the purge of warmer working fluid held in the TE-HX during the previous defrost. Once this liquid is purged by colder working fluid from the reservoir, the flow quickly drops and stabilises.

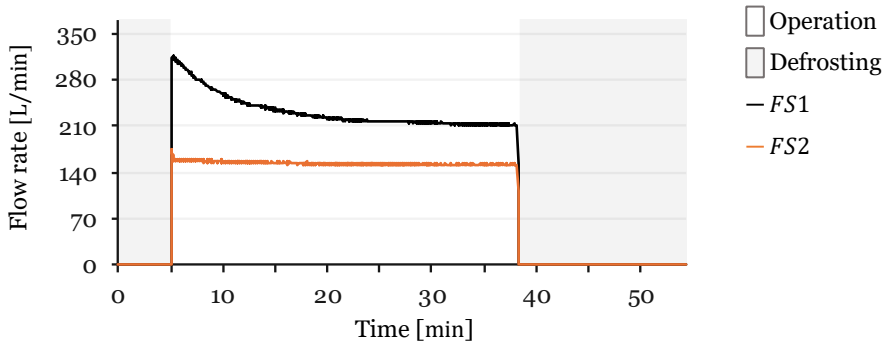

Figure 185 – Flow rates measured in the two working-fluid circuits during a frost–defrost cycle.

By contrast, $FS1$, connected to circuit 3, shows a steady decline across the operation phase, dropping by nearly one-third. This trend is linked to the gradual cooling of the working fluid in this circuit, which increases its viscosity and reduces pump throughput. This distinction between the circuits is consistent with the earlier temperature analysis. $TWF3$ and $TWF4$ from working fluid circuit 2 experience little temperature variation once cooled, while $TWF1$ and $TWF2$ from working fluid circuit 3 continues to lose heat throughout operation.

To further illustrate this relationship, Figure 186 compares the flow rate in circuit 3 with the corresponding viscosity. The viscosity data were fitted using the Andrade-type exponential correlation, as shown in Equation (72). This allowed the experimental results to be approximated to the tabulated reference data [142] for a 40% (v/v) ethylene glycol–water solution in the range of −5 to 20 °C:

$$\mu(T_n^{WFC2}) = 6.104 \cdot exp\,(-0.0390 \cdot T_n^{WFC2}) \tag{72}$$

Where:

- $\mu(T_n^{WFC3})$ is the dynamic viscosity [m$Pa \cdot s$]
- T_n^{WFC3} is the working fluid temperature in circuit 3, calculated by the average of $TWF1$ and $TWF2$.

The inverse relationship is immediately apparent, as viscosity increases with decreasing temperature, the flow rate decreases almost in mirror fashion. This confirms that the observed decline in circuit 3 flow is primarily a consequence of viscosity increase. During defrost, when circulation ceases, the viscosity values reflect stagnant fluid warming and are not representative of actual working fluid conditions.

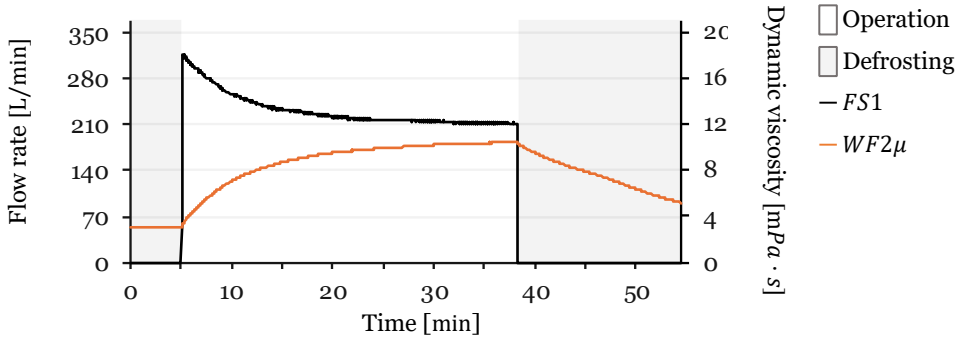

Figure 186 – Comparison of circuit 3 flow rate and viscosity, calculated from working-fluid temperature.

These results confirm that flow behaviour is coupled to fluid viscosity. While not directly tied to frost detection, these trends provide context for interpreting results. With the hydraulic background clarified, the system performance analysis is complete.

The set of signals analysed in this section together provides a representative picture of the experimental conditions under which all tests were performed. Although individual test runs show some variability, the trends presented here capture the typical behaviour of the system and form the basis for interpreting the results in later sections. With this comprehensive background established, the focus now shifts to the analysis of test results, where the performance of the FMRS4 is evaluated.

6.4. Experimental results: Performance of the FMRS4

The performance of the FMRS4 sensor was evaluated through three series with a total of 12 tests. Each test is identified using a code previously presented in Table 46 that combines the series designation with its sequential number within that series.

The analysis of each test within this section highlights the dynamic behaviour of frost formation, growth, and removal, and combines:

- Plots of FDS and CVT data, overlaid with FND and DCD markers, and indication of operation or defrosting phases.
- Image snapshots at eight key moments: Start, Condensation midpoint, $CVFND$ trigger, FND trigger, Frost growth midpoint, CVG defrost trigger, Water detection peak, and Defrost end.
- Table summarizing the experiment:
    - Test details (Operation time, Defrosting time, Total time, CV_{th}).
    - Computed metrics (CVT at t_{FND}, $\overline{\Delta AH}$ at t_{DCD}, Δt_{nuc}, Δt_{dry}).
    - Event timestamps (Start, Condensation midpoint, $CVFND$, FND, Frost growth midpoint, $CVG \geq CV_{Trsh}$, Water detection peak, $HBDCD$, DCD, Defrost end).

All tests followed a similar procedure, beginning with a 5 min start in defrost mode to standardize the initial conditions, followed by refrigeration system operation time until $CVG \geq CV_{th}$, and a timed defrosting phase. In none of the tests, t_{DCD} and t_{HBDCD} are possible to reliably distinguish in the CV snapshots.

6.4.1. Series A

Series A establishes the baseline conditions under which the system operated as intended. In these tests, the sensor provided a reference for how it performs under ideal conditions. The CV_{th} was set to 960, allowing frost to accumulate significantly on the HX surface without reaching full blockage. Defrosting periods were targeted at approximately 15 min, with slight variations due to manual operation.

6.4.1.1. T-A-01

The series A test 01, T-A-01, is representative of the baseline operating conditions defined for Series A, with consistent FND, $CVFND$, DCD and $HBDCD$ events captured across all monitoring methods. The cycle comprised an operating phase of 33.40 min followed by a 16.00 min defrosting phase, resulting in a total duration of 49.40 min.

In Figure 187, it is possible to observe that frost nucleation was detected by CV at $t_{CVFND} = 13.20$ min and by the sensor at $t_{FND} = 14.95$ min, resulting in a detection lag of $\Delta t_{nuc} = 1.75$ min. Defrost completion was detected by the humidity-based metric at $t_{HBDCD} = 48.30$ min and by the sensor at $t_{DCD} = 48.35$ min, resulting in a difference of

Δt_{dry} = 0.05 min, which indicates closeness of both detectors at the detection of the end of defrost. The FDS curve shows an early drop upon condensation, stabilising until nucleation occurs. The CVT signal also reflects condensation as a sharp decrease to zero, due to the reduced reflectivity of the selected tile region. CVT metrics rose during frost accumulation, while the FDS appears to maintain an almost saturated state after detection, but presented different values for dry, wet, and frosted saturation.

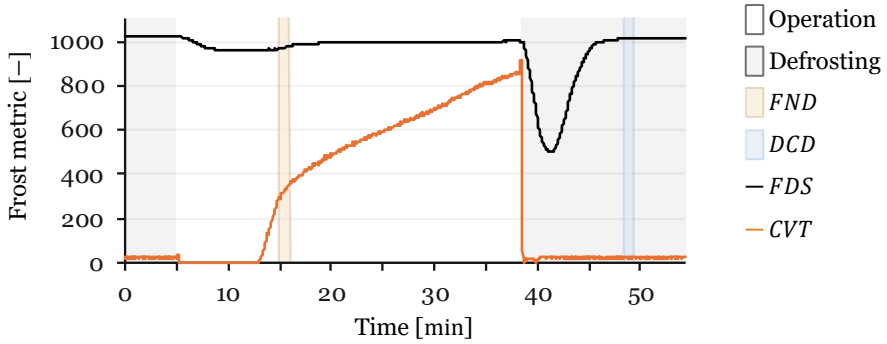

Figure 187 – Overall frost formation and defrosting cycle in test T-A-01.

It is notable that the DCD appears delayed in the plot, but this results from a low θ_s, that makes the algorithm more demanding for a stable slope, to consider dry HX. This effect is easier to understand in a plot that stretches the y-axis to amplify the slope. To this effect, Figure 188 crops the ADC range between 920 and 1030, improving the visibility of the FDS slope at the timing of the events. Within this detail, the impact of the slope criterion defining both nucleation and completion is understandable: FND is triggered at the onset of a sustained increase, and DCD is marked at the onset of stable recovery.

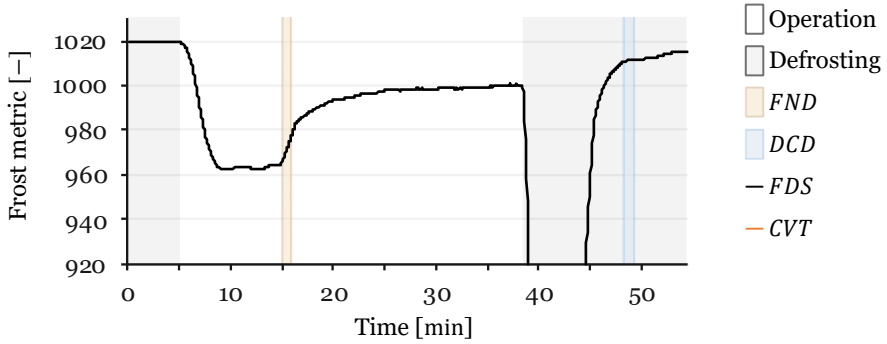

Figure 188 – Detail of the FMRS4 response for test T-A-01, cropped between 920–1030 ADC to highlight slope changes at FND and DCD.

Snapshots of the HX surface at the characteristic timestamps are presented in Figure 188. At the start ($t = 5.00$ min), reflective areas are visible in the tile region. During condensation ($t = 8.50$ min), the tile appears completely dark, consistent with condensation on the HX surface reducing reflectivity. At $t_{CVFND} = 13.20$ min, frost is evident across part of the HX surface and less so within the tile region. By the time FND is triggered ($t = 14.95$ min), frost coverage extends more widely, supporting the need for a local metric (CVT rather than CVG) to avoid capturing early nucleation in other HX regions.

At the frost-growth midpoint ($t = 26.70$ min), the HX appears already significantly white, reaching the CV_{th} at $t = 38.40$ min. During water detection peak ($t = 41.25$ min), the surface shows no apparent difference to the dry HX at the end of defrost ($t = 54.40$ min), with only minor local differences visible at the tile. These subtle local variations suggest potential for future use of CV for dryness assessment beyond frost detection.

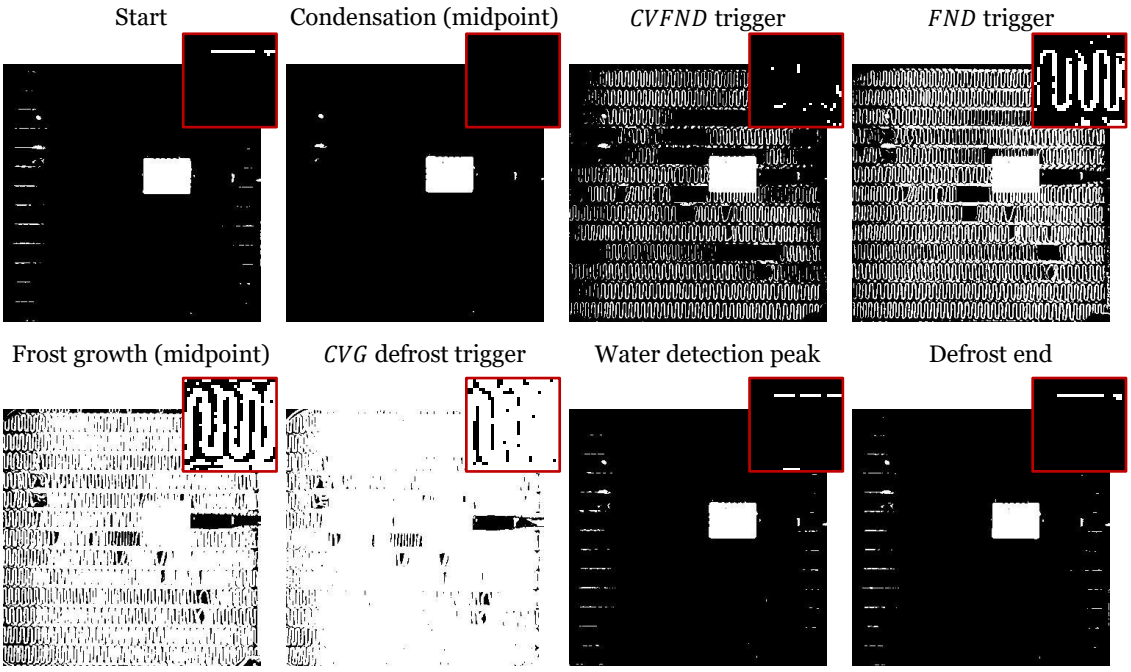

Figure 189 – Sequence of HX snapshots for test T-A-01, corresponding to characteristic timestamps.

Table 50 summarises the key timings and metrics extracted for T-A-01. At the moment of resistive nucleation detection, the CVT value was 293, showing the local tile intensity corresponding to the onset of frost bridging in the sensor electrodes. At DCD, the $\overline{\Delta AH}$ was 0.220 g · m^{-3}, consistent with the near-equilibrium state at the end of drying.

Table 50 – Summary of test T-A-01.

Test details		**Computed metrics**	
Operation time [min]	33.40	CVT at t_{FND} [−]	293
Defrosting time [min]	16.00	$\overline{\Delta AH}$ at t_{DCD} [g · m^{-3}]	0.220
Total time [min]	49.40	Δt_{nuc} [min]	1.75
CV_{th} [−]	960	Δt_{dry} [min]	0.05

Event timestamps [min]			
Start	5.00	$CVG \geq CV_{th}$	38.40
Condensation (midpoint)	8.50	Water detection peak	41.25
CVFND	13.20	HBDCD	48.30
FND	14.95	DCD	48.35
Frost growth (midpoint)	26.70	Defrost end	54.40

In summary, Test T-A-01 confirmed close agreement between the resistive sensor and CV methods, with nucleation and defrost completion detected within minimal time differences. These results validate the sensor's performance under baseline conditions.

6.4.1.2. T-A-02

Series A test number 2, T-A-02, was also able to identify nucleation and drying events across all detection methods. The cycle was comprised of 33.40 min of operation followed by a 16.00 min defrost, giving a total duration of 49.40 min.

The cycle behaviour is shown in Figure 190. During operation, a small condensation-induced dip appears shortly after the start, although at this ADC scale it is almost imperceptible. Despite the subtlety of this slope change, the computer-vision metric triggered frost nucleation detection at $t_{CVFND} = 9.30$ min, while the resistive sensor triggered at $t_{FND} = 10.95$ min, resulting in a difference of $\Delta t_{nuc} = 1.65$ min.

Later in the cycle, defrost completion was detected by the sensor at $t_{DCD} = 42.60$ min, slightly earlier than the humidity-based detector at $t_{HBDCD} = 43.20$ min, and resulting in a detection lag of $\Delta t_{dry} = -0.60$ min. The overall progression of the FDS and CVT signals is consistent with the previous test.

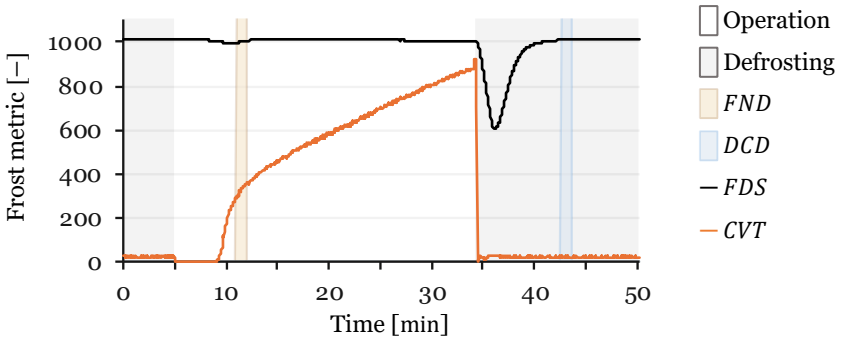

Figure 190 – Overall frost formation and defrosting cycle in test T-A-02.

Figure 191 crops the ADC range from 920 to 1030, amplifying the FDS slopes during events. In this closer view, the FND is seen to coincide with a sustained slope in the FDS curve. This visually confirms that the FND operated on a small but detectable signal change. The condensation and nucleation sequence in this test differs slightly from T-A-01, as the drop during condensation is followed by a direct increase, without the plateau observed previously.

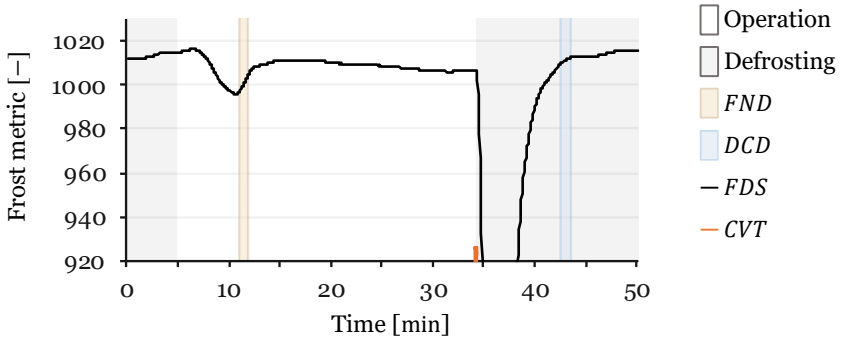

Figure 191 – Detail of the FMRS4 response for test T-A-02, cropped between 920–1030 ADC to highlight slope changes at FND and DCD.

Visual confirmation is provided in Figure 192 At the start ($t = 5.00$ min), reflections are visible across the surface. With condensation ($t = 6.85$ min), the tile becomes dark, losing reflectivity. Around the nucleation points, frost is visible in the HX surface and appears within the tile region ($t = 9.30$ min) after being present in a significant portion of the HX. At t_{FND} ($t = 10.95$ min) almost the whole HX surface has frost. During frost growth ($t = 22.65$ min) and at the defrost trigger ($t = 34.30$ min), the surface is predominantly white. At the water-detection peak ($t = 36.10$ min) and subsequent frames, reflections suggest localised liquid accumulation. Finally, at the dry end frame ($t = 50.15$ min), residual reflections are weaker than in the water detection peak.

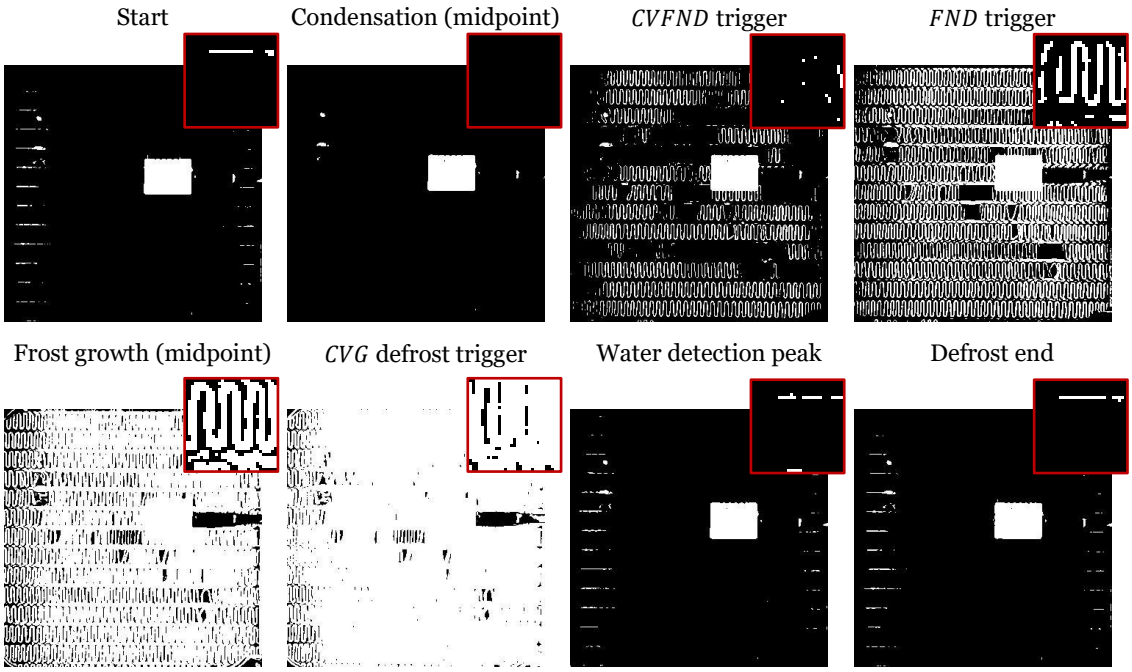

Figure 192 – Sequence of HX snapshots for test T-A-02, corresponding to characteristic timestamps.

The results for this test are summarised in Table 51. The CVT at t_{FND} was 295, closely matching the value obtained in test T-A-01. $\overline{\Delta AH}$ at t_{DCD} was 0.000 [g · m^{-3}], reflecting an equilibrium state in which no further mass transfer was taking place, confirming that the HX surface was already dry and the $HBDCD$ trigger was only awaiting stabilization.

Table 51 – Summary of test T-A-02.

Test details		**Computed metrics**	
Operation time [min]	29.30	CVT at t_{FND} [−]	295
Defrosting time [min]	15.85	$\overline{\Delta AH}$ at t_{DCD} [g · m^{-3}]	0.000
Total time [min]	45.15	Δt_{nuc} [min]	1.65
CV_{th} [−]	960	Δt_{dry} [min]	−0.60
Event timestamps [***min***]			
Start	5.00	$CVG \geq CV_{th}$	34.30
Condensation (midpoint)	6.85	Water detection peak	36.10
CVFND	9.30	HBDCD	43.20
FND	10.95	DCD	42.60
Frost growth (midpoint)	22.65	Defrost end	50.15

Test T-A-02 confirmed the alignment between detectors, with consistent identifications across methods. The cycle behaviour remained coherent with the baseline conditions of Series A.

6.4.1.3. T-A-03

Series A test number 3, T-A-03, likewise captured both nucleation and drying detectors across all monitoring methods. The cycle included 24.20 min of operation followed by a 16.25 min defrost, resulting in a total duration of 40.45 min.

In Figure 193, the onset of frost nucleation detected by the computer-vision metric occurred at $t_{CVFND} = 9.55$ min, and by the sensor at $t_{FND} = 10.70$ min. These were separated by a gap of $\Delta t_{nuc} = 1.15$ min. Later in the cycle, humidity-based dry HX detection was obtained at $t_{HBDCD} = 37.15$ min, while the sensor measurements triggered DCD almost simultaneously at $t_{DCD} = 37.20$ min, giving a detection offset of $\Delta t_{dry} = 0.05$ min.

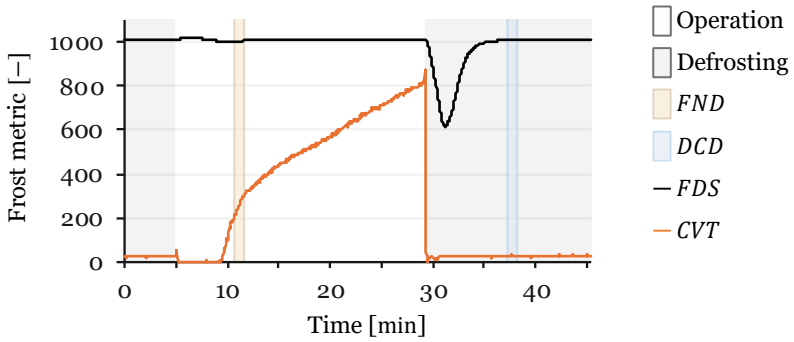

Figure 193 – Overall frost formation and defrosting cycle in test T-A-03.

Figure 194 crops the *ADC* range between 920 and 1030. This closer view highlights the slope that triggered *FND*. The compensated *ADC* curve shows a small but sustained change. The zoom also confirms that the *DCD* did not occur late but corresponded to a low-slope region better visible when magnified.

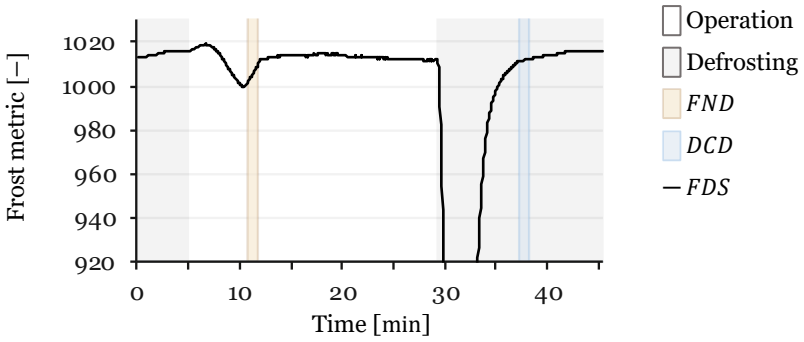

Figure 194 – Detail of the FMRS4 response for test T-A-03, cropped between 920–1030 *ADC* to highlight slope changes at *FND* and *DCD*.

Figure 195 presents the visual snapshots of the HX surface with the tile view highlighted. At the start ($t = 5.00$ min), the tile shows slight reflections on its surface. During condensation ($t = 6.90$ min), the surface becomes uniformly dark. Frost first appears in the tile at $t_{CVFND} = 9.55$ min, while the *FND* trigger ($t_{FND} = 10.70$ min) occurs slightly later, when frost is already more evenly distributed across a larger portion of the HX surface. At the frost growth midpoint ($t = 19.95$ min), the HX surface approaches near-complete coverage, and by the defrost trigger ($t = 29.20$ min) it appears predominantly white. The water detection peak ($t = 31.20$ min) highlights surface wetting during early defrost, and the final dry snapshot ($t = 45.45$ min) presents a similar appearance. As in all cases, t_{DCD} and t_{HBDCD} are not visually distinguishable in these images.

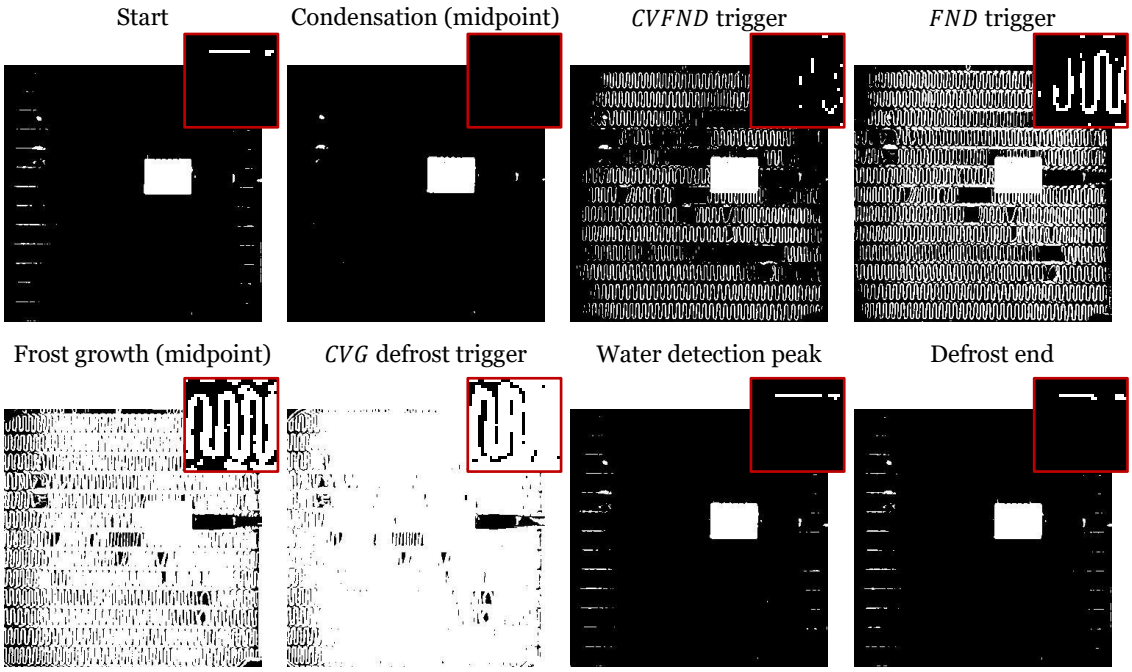

Figure 195 – Sequence of HX snapshots for test T-A-03, corresponding to characteristic timestamps.

Table 52 summarises the computed metrics and event times of test T-A-03. The CVT at t_{FND} was 213, lower than in the earlier Series A tests. The $\overline{\Delta AH}$ at t_{DCD} was 0.154 g · m^{-3}, showing that although the HX surface was approaching dryness, some residual mass exchange was still occurring.

Table 52 – Summary of test T-A-03.

Test details		**Computed metrics**	
Operation time [min]	24.20	CVT at t_{FND} [−]	213
Defrosting time [min]	16.25	$\overline{\Delta AH}$ at t_{DCD} [g · m^{-3}]	0.154
Total time [min]	40.45	Δt_{nuc} [min]	1.15
CV_{th} [−]	960	Δt_{dry} [min]	0.05

Event timestamps [***min***]			
Start	5.00	$CVG \geq CV_{th}$	29.20
Condensation (midpoint)	6.90	Water detection peak	31.20
CVFND	9.55	HBDCD	37.15
FND	10.70	DCD	37.20
Frost growth (midpoint)	19.95	Defrost end	45.45

Test T-A-03 again shows close correspondence between detectors, with the zoomed plot clarifying low-slope triggers and snapshots aligning with the observed transitions.

6.4.1.4. T-A-04

Test T-A-04 confirmed the baseline behaviour of Series A, with both nucleation and defrost completion events consistently captured by the detectors. The cycle comprised 30.20 min of operation followed by a 15.35 min defrost, for a total of 45.55 min.

In Figure 196, frost nucleation was first detected by the CV method at $t_{CVFND} = 9.45$ min, followed by the resistive sensor at $t_{FND} = 10.50$ min, with a lag of $\Delta t_{nuc} = 1.05$ min. Drying was recorded at $t_{DCD} = 43.65$ min for the resistive sensor and at $t_{HBDCD} = 44.40$ min for the humidity-based detector, producing $\Delta t_{dry} = -0.75$ min. The overall signal evolution matches the established behaviour for this series, with nucleation and drying events consistently detected by both methods.

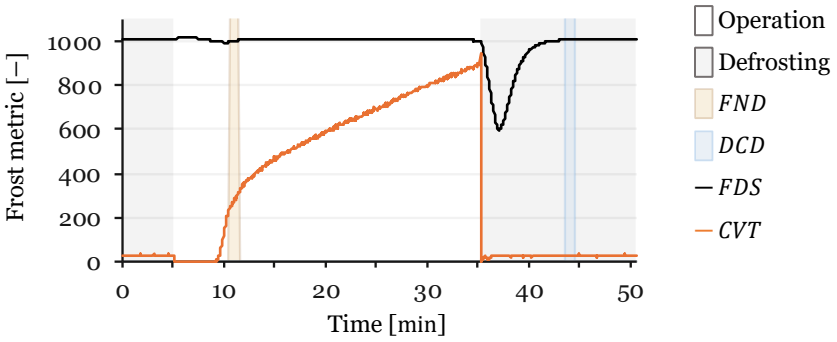

Figure 196 – Overall frost formation and defrosting cycle in test T-A-04.

Figure 197 crops the ADC range between 920 and 1030. The zoomed representation again makes visible the small slope that triggered frost nucleation detection in the resistive signal, which is not easily distinguished in the full plot. This detailed view also clarifies the behaviour of the compensated ADC signal near the end of defrost, where low-slope regions remain identifiable despite their subtlety.

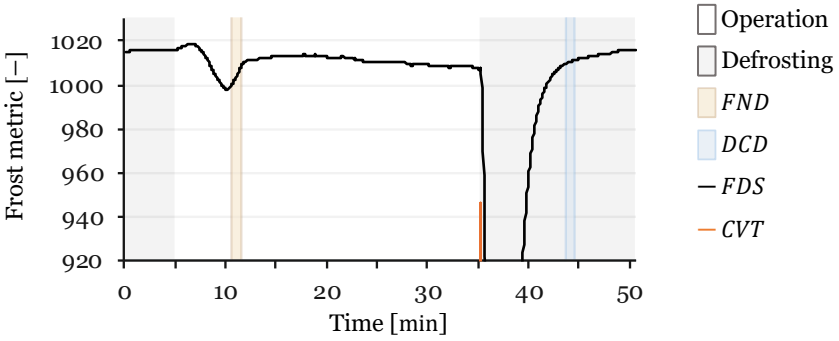

Figure 197 – Detail of the FMRS4 response for test T-A-04, cropped between 920–1030 ADC to highlight slope changes at FND and DCD.

Figure 198 shows the visual progression of the HX surface. At the start ($t = 5.00$ min), the reflective tile is observable. During condensation ($t = 6.95$ min), the tile darkens entirely. Frost becomes visible in the tile at $t_{CVFND} = 9.45$ min, while the FND trigger ($t_{FND} = 10.50$ min) occurs slightly later, when frost is more widely distributed across the HX surface. At the frost growth midpoint ($t = 22.85$ min), the HX surface shows near-complete coverage, and by the global defrost trigger ($t = 35.20$ min) it is almost fully white. The water detection peak ($t = 37.00$ min) corresponds to liquid presence during defrost, which is not visible, and the final dry frame ($t = 50.55$ min) appears visually similar to the water detection peak snapshot. As in all tests, t_{DCD} and t_{HBDCD} are not directly visible in the images.

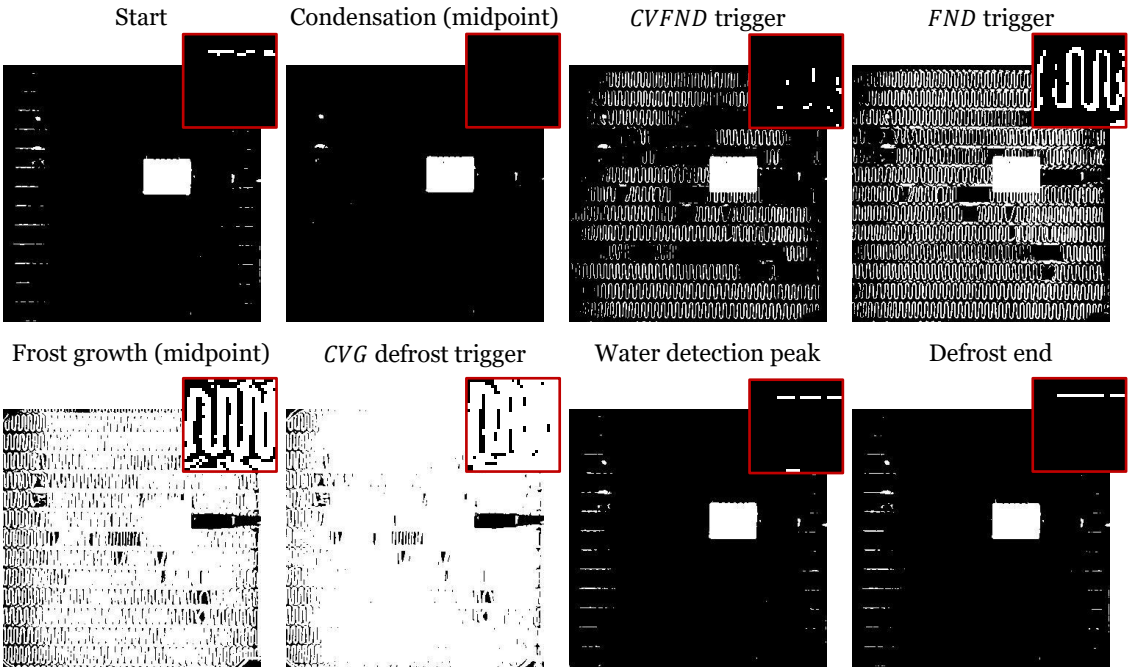

Figure 198 – Sequence of HX snapshots for test T-A-04, corresponding to characteristic timestamps.

Table 53 summarises the computed metrics for this test. The CVT at t_{FND} was 240, and the $\overline{\Delta AH}$ at t_{DCD} was 0.186 $\mathrm{g \cdot m^{-3}}$. These values are consistent with the other tests in Series A and confirm the stability of detection performance within the baseline conditions.

Table 53 – Summary of test T-A-04.

Test details		**Computed metrics**	
Operation time [min]	30.20	CVT at t_{FND} [−]	240
Defrosting time [min]	15.35	$\overline{\Delta AH}$ at t_{DCD} [$\mathrm{g \cdot m^{-3}}$]	0.186
Total time [min]	45.55	Δt_{nuc} [min]	1.05
CV_{th} [−]	960	Δt_{dry} [min]	−0.75
Event timestamps [***min***]			
Start	5.00	$CVG \geq CV_{th}$	35.20
Condensation (midpoint)	6.95	Water detection peak	37.00
CVFND	9.45	HBDCD	44.40
FND	10.50	DCD	43.65
Frost growth (midpoint)	22.85	Defrost end	50.55

Test T-A-04 consolidates the Series A baseline, confirming repeatable detection behaviour and consistent correspondence between signals and imagery.

6.4.2. Series B

Series B was conducted with a higher CVG_{th} of 1012, and a longer defrosting time of 30 min. This condition aimed to reach frost saturation and achieve full blockage of the HX, requiring longer defrosting periods to fully melt and dry the accumulated frost. The resulting tests were therefore considerably longer than those in Series A. These experiments provide insight into how both the FDS and CV metrics respond when larger amounts of frost are present, and the system is driven closer to its operational limits.

6.4.2.1. T-B-01

Series B test number 1, Test T-B-01, was the longest of all the performed tests, with extended frost accumulation phase. The cycle lasted 100.95 min in operation and 34.30 min in defrost, giving a total of 135.25 min. This test was the only one that did not include a 5 min initial period in defrosting mode, due to the absence of data collection prior to the starting point.

The first test of series B introduces longer operating and defrosting cycles compared with series A. In this case, the operation lasted 100.95 min and was followed by a 34.30 min defrost, giving a total duration of 135.25 min. The CVG threshold for defrost initiation was set at 1012 instead of 960, extending the operation phase until the HX surface reached a nearly saturated condition.

In Figure 199, frost nucleation was detected by the sensor at $t_{FND} = 10.75$ min and by the $CVFND$ at $t_{CVFND} = 10.85$ min, with a $\Delta t_{nuc} = -0.10$ min detection offset between the two methods. This close alignment shows both detectors responding almost simultaneously to the onset of frost. The defrost completion events were later recorded at $t_{DCD} = 116.05$ min for the sensor and $t_{HBDCD} = 116.70$ min for the humidity based detector, with a lag of $\Delta t_{dry} = -0.65$ min between them. The extended operation period is characterised by a long plateau, where the resistive signal slope continues to increase slowly but steadily. During defrosting, the FMRS4 signal exhibits a drop, a small rise, and then stabilises at a low level before rising again, showing a multi-step drying progression, probably caused by the increased amount of water released during defrosting.

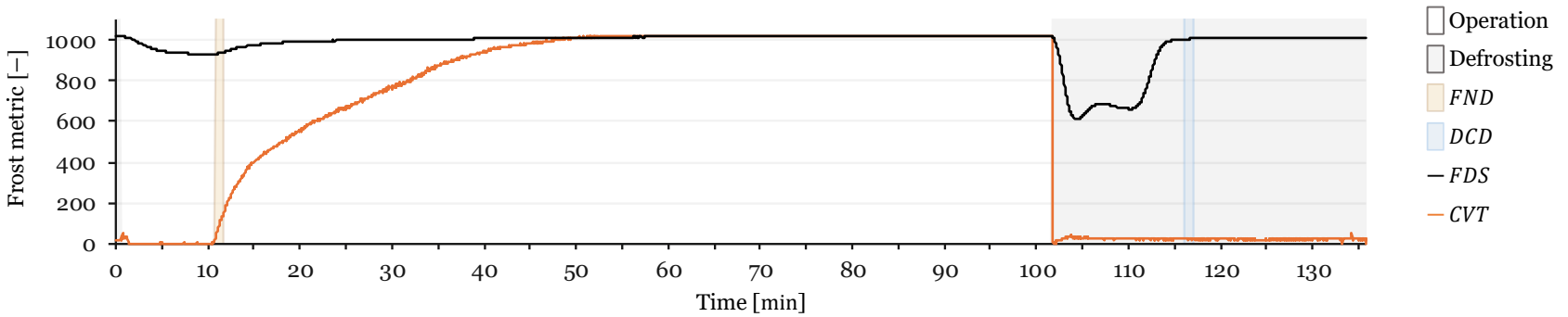

Figure 199 – Overall frost formation and defrosting cycle in test T-B-01.

Figure 200 crops the *ADC* range between 920 and 1030. The condensation phase produces the lowest compensated ADC value observed so far across the tests. FND is clearer in this zoomed region, as the slope change is more distinguishable here. It can be observed that the sensor signal continues to rise, albeit at a very low rate, even after the *CVT* has reached saturation. What appears at first to be stabilization in saturation still shows a gradual increase beyond the point where the CV metric saturates. The FMRS4 measurement before defrosting shows higher resistivity than after defrost completion, contrary to the trend observed in Test A, indicating an increase in resistivity during severe frost accumulation.

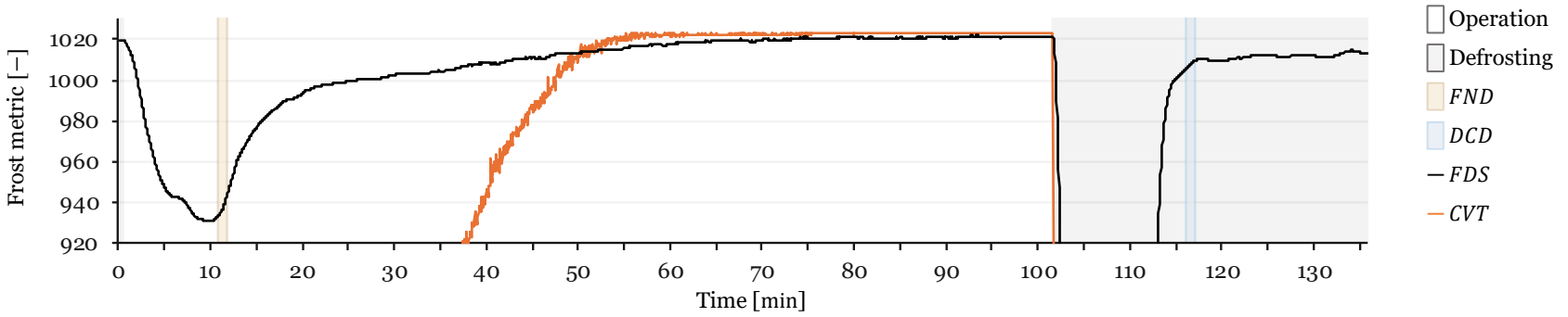

Figure 200 – Detail of the FMRS4 response for test T-B-01, cropped between 920–1030 *ADC* to highlight slope changes at *FND* and *DCD*.

In Figure 201 at the start ($t = 0.60$ min), the reflective tile region is visible, however, as in previous tests, during condensation ($t = 5.30$ min), the tile darkens fully. The $CVFND$ trigger occurs at $t_{CVFND} = 10.85$ min, when frost first becomes visible within the tile region, while the FND trigger ($t_{FND} = 10.75$ min) follows almost simultaneously, at a stage when frost has not yet extended across the whole HX surface. By the frost growth midpoint ($t = 56.15$ min), the HX surface is nearly fully covered, and at the global defrost trigger ($t = 101.55$ min), the surface appears completely frosted, consistent with the long operating phase. During defrost, the water detection peak ($t = 104.30$ min) is captured, and the final dry snapshot ($t = 135.85$ min) shows the HX surface returning to a dry appearance. As in all the other tests, t_{DCD} and t_{HBDCD} are not distinguishable in the images.

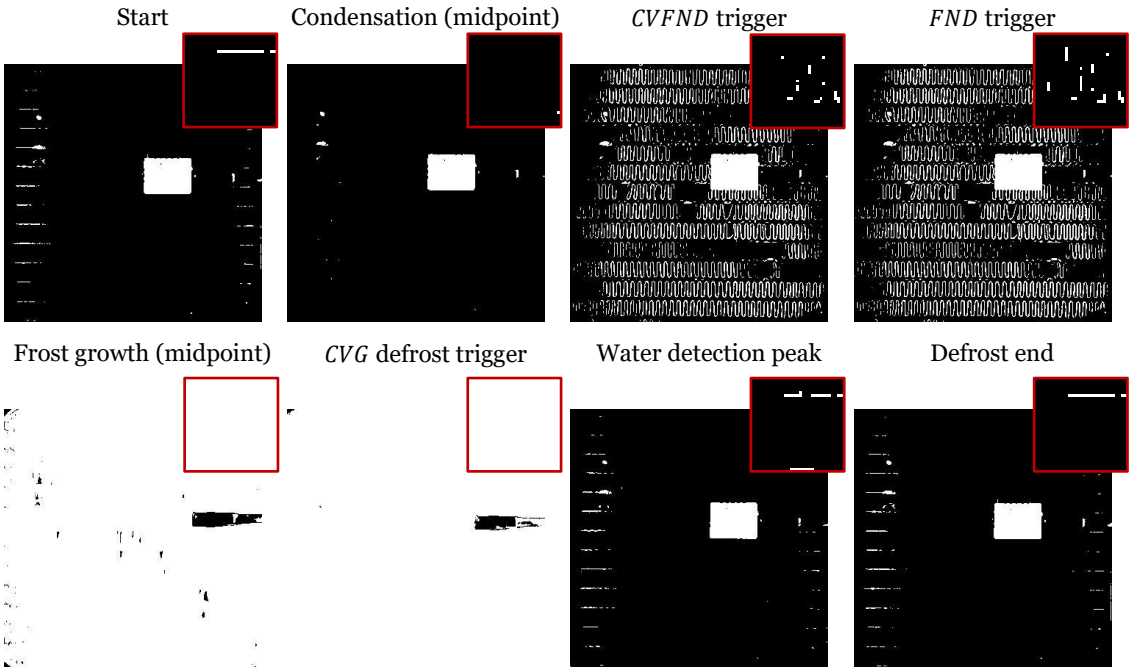

Figure 201 – Sequence of HX snapshots for test T-B-01, corresponding to characteristic timestamps.

Table 54 summarises the computed metrics. The CVT at t_{FND} was 20, a low value that is a consequence of the FND triggering before the $CVFND$ while the $\overline{\Delta AH}$ at t_{DCD} was 0.516 g · m^{-3}, a higher value when comparing to the trend of Series A, which is a likely consequence of the evaporation of water from the HX still happening when the FDS detected dry HX.

Table 54 – Summary of test T-B-01.

Test details		**Computed metrics**	
Operation time [min]	100.95	CVT at t_{FND} [−]	20
Defrosting time [min]	34.30	$\overline{\Delta AH}$ at t_{DCD} [g · m^{-3}]	0.516
Total time [min]	135.25	Δt_{nuc} [min]	−0.10
CV_{th} [−]	960	Δt_{dry} [min]	−0.65

Event timestamps [min]			
Start	0.60	$CVG \geq CV_{th}$	101.55
Condensation (midpoint)	5.30	Water detection peak	104.30
CVFND	10.85	HBDCD	116.70
FND	10.75	DCD	116.05
Frost growth (midpoint)	56.15	Defrost end	135.85

Test T-B-01 characterises the long-cycle regime of Series B: detections by FDS and CVT were achieved, and both plots and snapshots corroborate the extended frost load and staged drying behaviour.

6.4.2.2. T-B-02

Test T-B-02 also reflects the extended duration characteristic of Series B and was the second longest of all the test durations. The test included 96.45 min of operation and 31.95 min of defrosting, amounting to a total of 128.40 min.

In Figure 202 it is possible to observe nucleation detection by the CV detector at $t_{CVFND} = 10.10$ min and by the resistive sensor at $t_{FND} = 11.00$ min, producing a detection discrepancy of $\Delta t_{nuc} = 0.90$ min. Both detections occurred despite the condensation and frost transition not being very pronounced. Drying was recorded by the sensor at $t_{DCD} = 116.05$ min and by the humidity based detector at $t_{HBDCD} = 113.95$ min, giving a significant detection lag of $\Delta t_{dry} = 2.10$ min, which was a likely consequence of the extended defrosting operation phase resulting in a longer drying time, as more water was released from the HX during defrost.

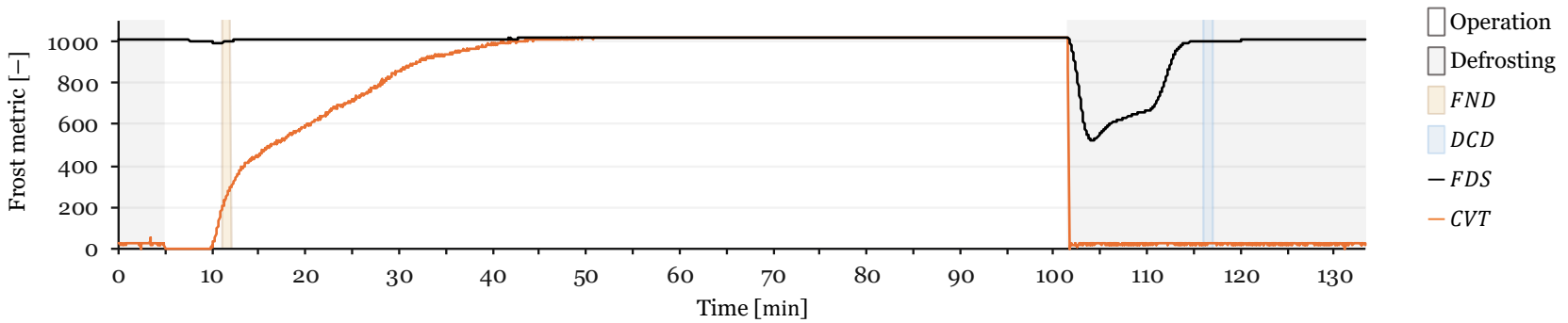

Figure 202 – Overall frost formation and defrosting cycle in test T-B-02.

Figure 203 crops the *ADC* range between 920 and 1030. The slope leading to FND is visible despite reduced magnitude compared to earlier tests. The zoom also shows fluctuations in the compensated *ADC* during the stable post-defrost phase, more evident here than in the full-plot view. These oscillations did not affect event detection. The sensor signal maintains a slight upward trend even after the *CVT* has saturated. What seems to be a stable plateau in the vision metric is, in fact, still accompanied by a slow increase in the sensor response. This effect also makes it so that just as before in this series, the resistivity at the end of the operation phase is higher than that of the defrost completion phases.

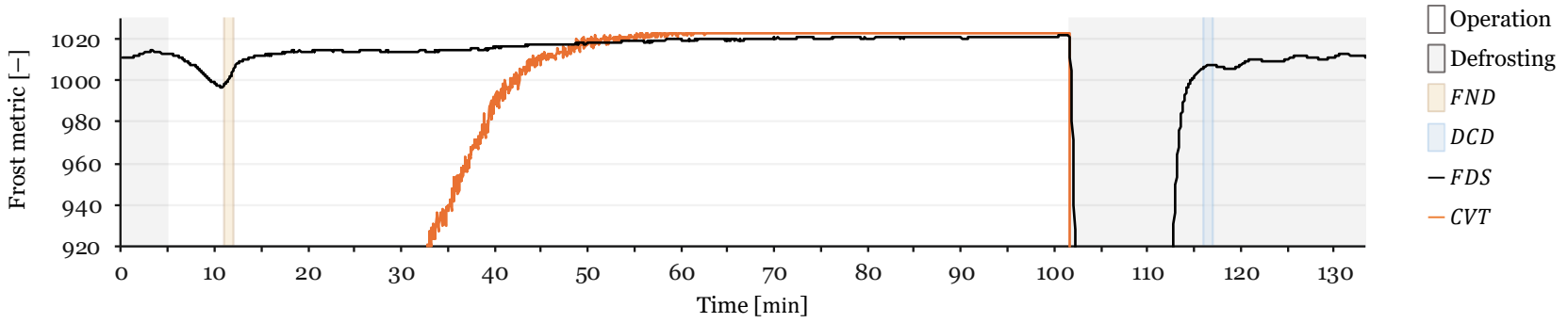

Figure 203 – Detail of the FMRS4 response for test T-B-02, cropped between 920–1030 *ADC* to highlight slope changes at *FND* and *DCD*.

Figure 204 shows the sequence of snapshots. At the start ($t = 5.00$ min), the tile shows signs of reflection, while condensation ($t = 7.25$ min) causes it to turn black. Frost is first detected by $CVFND$ at $t_{CVFND} = 10.10$ min, when frost becomes visible on the tile, and by the FDS at $t_{FND} = 11.00$ min, once frost distribution is more uniform. At the frost growth midpoint ($t = 56.25$ min), the HX surface is nearly saturated with frost, showing more frost coverage than in Series A tests before defrost initiation. At the defrost trigger ($t = 101.45$ min), the HX surface is almost completely white, leaving only the DHT cable and a single defect visible. At the water detection peak ($t = 104.15$ min), a heavy accumulation of liquid is present, larger than in previous tests due to the greater frost load, however the final dry frame ($t = 133.40$ min) resembles the water peak, with only minor residual reflections.

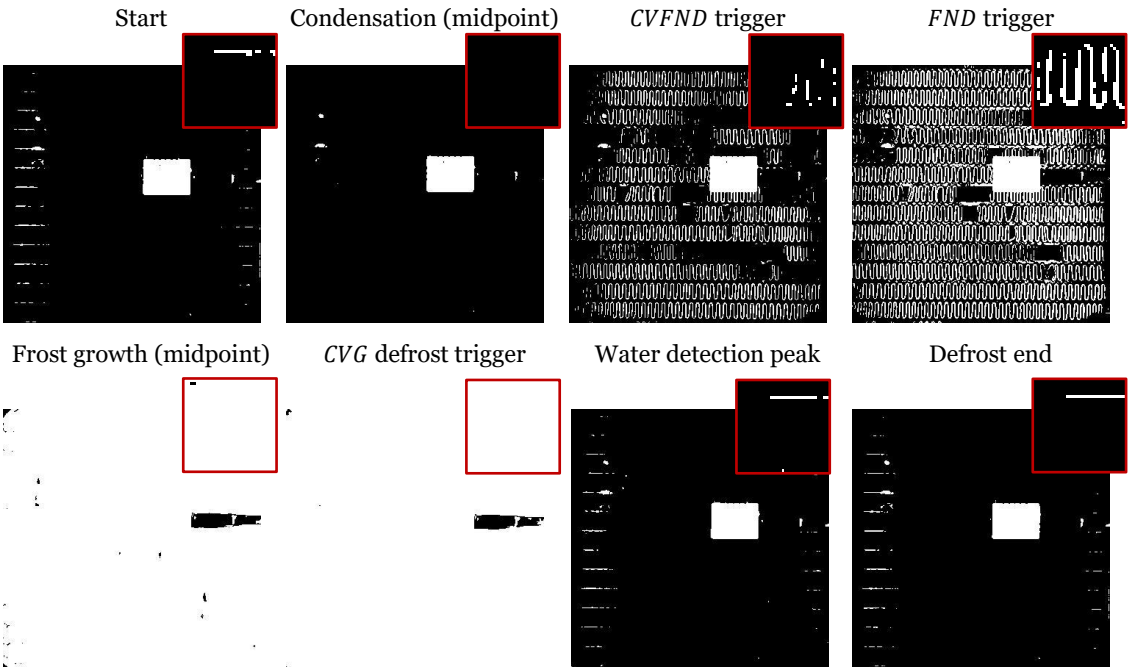

Figure 204 – Sequence of HX snapshots for test T-B-02, corresponding to characteristic timestamps.

Table 55 condenses the computed metrics. The CVT at t_{FND} was 196, a value closer to the trend of Series A while the $\overline{\Delta AH}$ at t_{DCD} was 0.016 g · m^{-3}, closer to zero and a symptom of a dryer HX at DCD.

Table 55 – Summary of test T-B-02.

Test details		**Computed metrics**	
Operation time [min]	96.45	CVT at t_{FND} [−]	196
Defrosting time [min]	31.95	$\overline{\Delta AH}$ at t_{DCD} [g · m^{-3}]	0.016
Total time [min]	128.40	Δt_{nuc} [min]	0.90
CV_{th} [−]	1012	Δt_{dry} [min]	2.10

Event timestamps [min]			
Start	5.00	$CVG \geq CV_{th}$	101.45
Condensation (midpoint)	7.25	Water detection peak	104.15
CVFND	10.10	HBDCD	113.95
FND	11.00	DCD	116.05
Frost growth (midpoint)	56.25	Defrost end	133.40

Test T-B-02 sustains the Series B pattern, with consistent event identification across methods and visual evidence supporting prolonged operation and recovery under the higher CV_{th}.

6.4.2.3. T-B-03

Test T-B-03 maintained the Series B trend of longer cycles, though with shorter operation and defrosting phases compared to the previous B series tests. It comprised 60.15 min of operation followed by 29.80 min of defrosting, resulting in 89.95 min overall.

In Figure 205, it is possible to observe that nucleation detections happened at $t_{CVFND} = 10.70$ min and $t_{FND} = 11.45$ min, for the CV and sensor based detectors respectively, which resulted in a detection lag of $\Delta t_{nuc} = 0.75$ min. Dry HX detection happened at $t_{HBDCD} = 80.20$ min, and $t_{DCD} = 81.25$ min for the humidity and sensor based detectors respectively, with a detection lag of $\Delta t_{dry} = 1.05$ min. Although the operation phase was shorter than in the previous series B, the defrost period remained long, consistent with the higher frost load accumulated prior to triggering. This behaviour suggests that the system accumulated frost at a rate higher than in prior cycles, which could be a consequence of the increased absolute humidity recorded for the test ambient conditions.

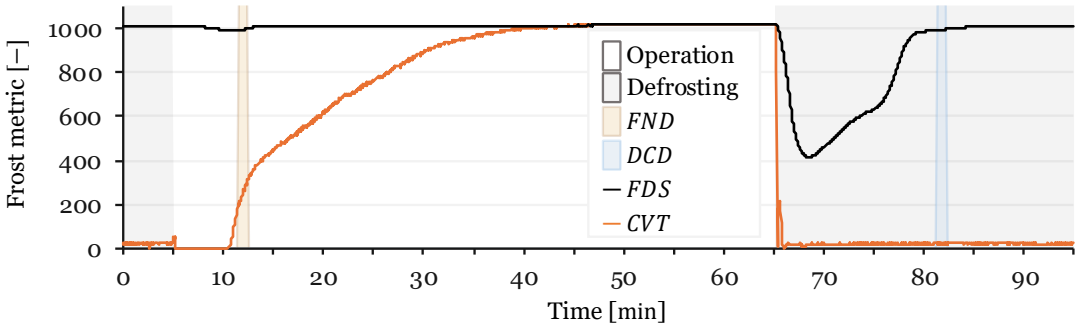

Figure 205 – Overall frost formation and defrosting cycle in test T-B-03.

Figure 206 crops the *ADC* range between 920 and 1030. Within this window, the early slope changes linked to condensation and nucleation are visible, though only marginally more pronounced than in the previous test. Both detection methods captured nucleation within proximity, and the compensated *ADC* signal shows an increased value at the end of the operation phase, compared to the defrost completion phase. This follows the trend of this series, which always measured higher resistivity for the end of the operation phase, with frost saturation, compared to the end of defrosting. This could be due to the residual moisture maintained in the sensor fabric being less resistive than the low-temperature frost accumulation. This goes along with the tendency of the FDS signal to rise throughout the growth and densification phases beyond the *CVT* saturation, despite the reduced duration of the cycle.

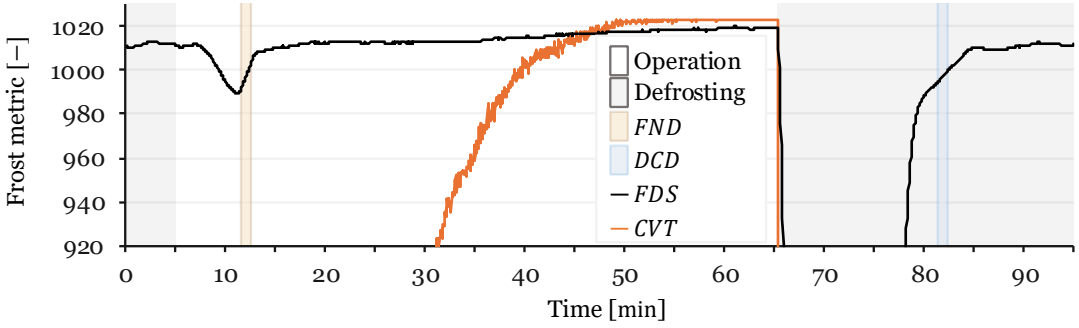

Figure 206 – Detail of the FMRS4 response for test T-B-03, cropped between 920–1030 *ADC* to highlight slope changes at *FND* and *DCD*.

Figure 207 presents the snapshot sequence with the tile view in each frame. At the start ($t = 5.00$ min), clear reflections are visible on the monitored tile. With condensation ($t = 7.50$ min), these reflections vanish as the surface darkens. Frost is already present across much of the HX at $t_{CVFND} = 10.70$ min, and by $t_{FND} = 11.45$ min nucleation extends across nearly the entire surface. At the frost growth midpoint ($t = 38.30$ min), the HX is already saturated with frost. By the defrost trigger ($t = 65.15$ min), the HX surface shows

almost complete white-out, apart from fixed artefacts such as the DHT cable. At the water detection peak ($t = 68.50$ min), a substantial meltwater layer forms but is not detected using the CV method, and consequently the final dry snapshot ($t = 94.95$ min) appears visually similar to the water peak, with surface reflectivity restored.

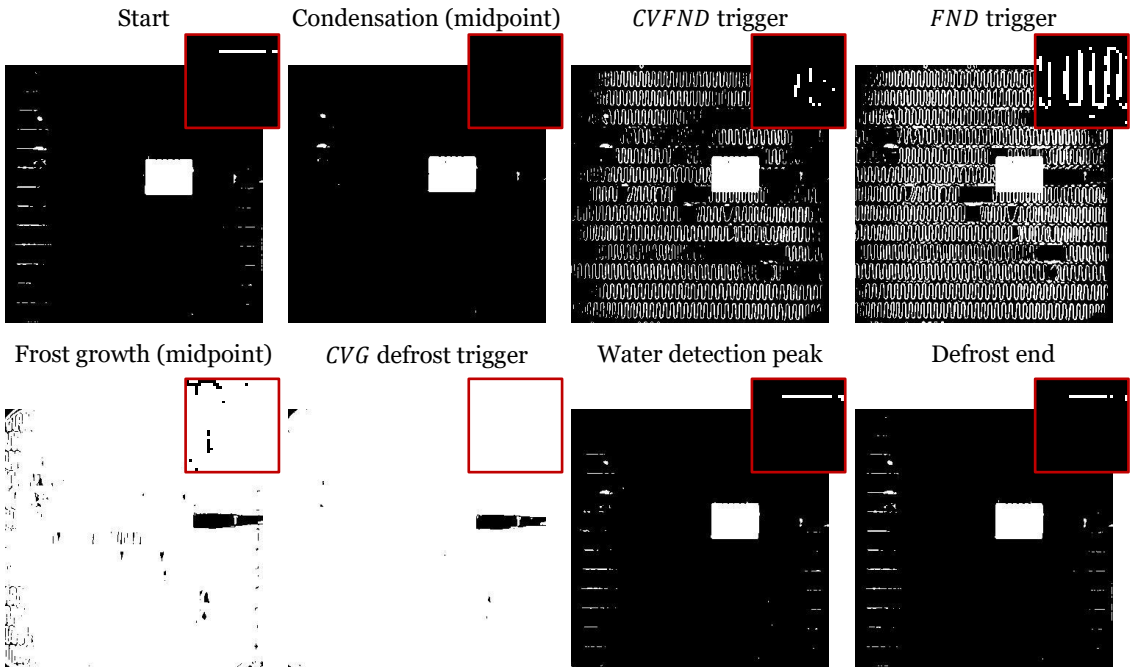

Figure 207 – Sequence of HX snapshots for test T-B-03, corresponding to characteristic timestamps.

Table 56 consolidates the computed metrics. The CVT at t_{FND} was 192, a value close to that of the previous test. The $\overline{\Delta AH}$ at t_{DCD} was 0.000 g · m^{-3}, reflecting a dry HX. The summary values demonstrate the repeatability of detection under extensive frosting and the sensitivity of the metrics to differences in frost accumulation and drying demand.

Table 56 – Summary of test T-B-03.

Test details		**Computed metrics**	
Operation time [min]	60.15	CVT at t_{FND} [−]	192
Defrosting time [min]	29.80	$\overline{\Delta AH}$ at t_{DCD} [g · m^{-3}]	0.000
Total time [min]	89.95	Δt_{nuc} [min]	0.75
CV_{th} [−]	1012	Δt_{dry} [min]	1.05

Event timestamps [***min***]			
Start	5.00	$CVG \geq CV_{th}$	65.15
Condensation (midpoint)	7.50	Water detection peak	68.50
CVFND	10.70	HBDCD	80.20
FND	11.45	DCD	81.25
Frost growth (midpoint)	38.30	Defrost end	94.95

Test T-B-03 confirms repeatable detection in the long-cycle setting, with signals and snapshots remaining coherent despite the shorter operation time relative to the other Series B tests.

6.4.3. Series C

Series C examines frost detection under non-ideal placement of the FDS within the fins, using the same CV_{th} of 960 and defrost periods of roughly 14 min. Under these conditions the FDS always failed to return to a dry baseline after defrosting, so DCD was never triggered, even though the $HBDCD$ indicated a dry HX within timings that go in accordance to the previous series. At the same time, nucleation remained captured by both $CVFND$ and the FND.

This series is therefore informative in two ways, it shows that frost nucleation can still be detected when local conditions around the sensor are non-ideal, and it highlights the importance of sensor placement for resolving the dry state.

6.4.3.1. T-C-01

Series C test number 1, Test T- C-01, marked the beginning of Series C, carried out under the non-ideal conditions that resulted in the lack of a DCD trigger. The cycle covered 33.95 min of operation followed by a 14.80 min defrost, for a total duration of 48.75 min.

The first test of series C differed from those in series A and B by failing to provide a valid DCD. The operation lasted 33.95 min, followed by a 14.80 min defrost, for a total cycle of 48.75 min. The shorter operation and defrost times go in line with those of Series A.

In Figure 208, $CVFND$ was triggered at $t_{CVFND} = 12.15\,\text{min}$, and FND at $t_{FND} = 12.10\,\text{min}$, showing almost coincident detections, with a lag of $\Delta t_{nuc} = -0.05\,\text{min}$. Defrost completion was not detected by the sensor ($t_{DCD} = n.d.$), while humidity based defrost completion was detected at $t_{HBDCD} = 48.15\,\text{min}$. During the defrosting phase, the resistive sensor signal dropped and partially recovered but did not return to its initial high plateau, instead remaining below the dry baseline. This behaviour explains the failure of the DCD algorithm, while the humidity-based detector still confirmed drying, which suggests dry HX was achieved, but the FDS failed in the detection.

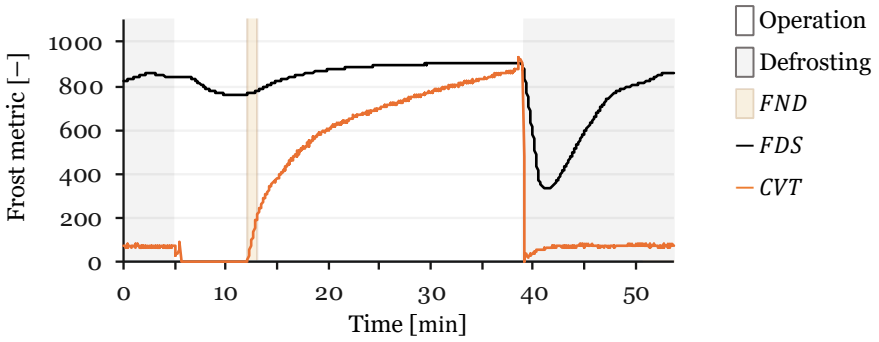

Figure 208 – Overall frost formation and defrosting cycle in test T-C-01.

Figure 209 crops the ADC range between 760 and 900, which is an atypical window of $\Delta ADC = 140$, as a $\Delta ADC = 110$ window was used in the cropped view of all the other tests. This wider window was necessary because the condensation minimum and frost maximum spanned a slightly larger amplitude. Within this range, the condensation detection appears as a distinct drop, followed by recovery and stabilization, while a small fluctuation is also visible at the very beginning of the test. The zoom confirms that the sensor response during defrost rises but falls short of re-establishing the dry reference level.

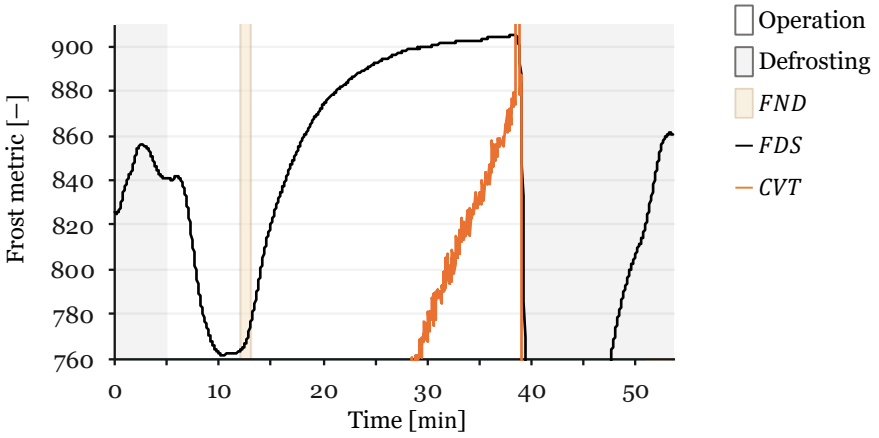

Figure 209 – Detail of the FMRS4 response for test T-C-01, cropped between 760–910 ADC to highlight slope changes at FND and DCD.

As with previous results, Figure 210 presents the image sequence of the HX surface, with the tile view included in each snapshot. At the start ($t = 5.00$ min), the reflective tile region is visible. During condensation ($t = 8.10$ min), the region darkens as expected. By $t_{CVFND} = 12.15$ min and $t_{FND} = 12.10$ min, the surface shows significant frosting, although not yet complete coverage across the HX. Frost coverage continues to increase, reaching partial but not fully saturated conditions at the frost growth midpoint ($t = 25.55$ min), and closer to saturation when CVG reaches the CV_{th} of 960 used for defrosting initiation. At the defrost trigger ($t = 38.95$ min), a substantial frost layer

remains but airflow is not yet fully blocked. The water detection peak ($t = 41.35$ min) and the defrost end ($t = 53.75$ min) appear similar, with only residual reflection differences. As in other series, DCD and $HBDCD$ cannot be directly distinguishable in these images.

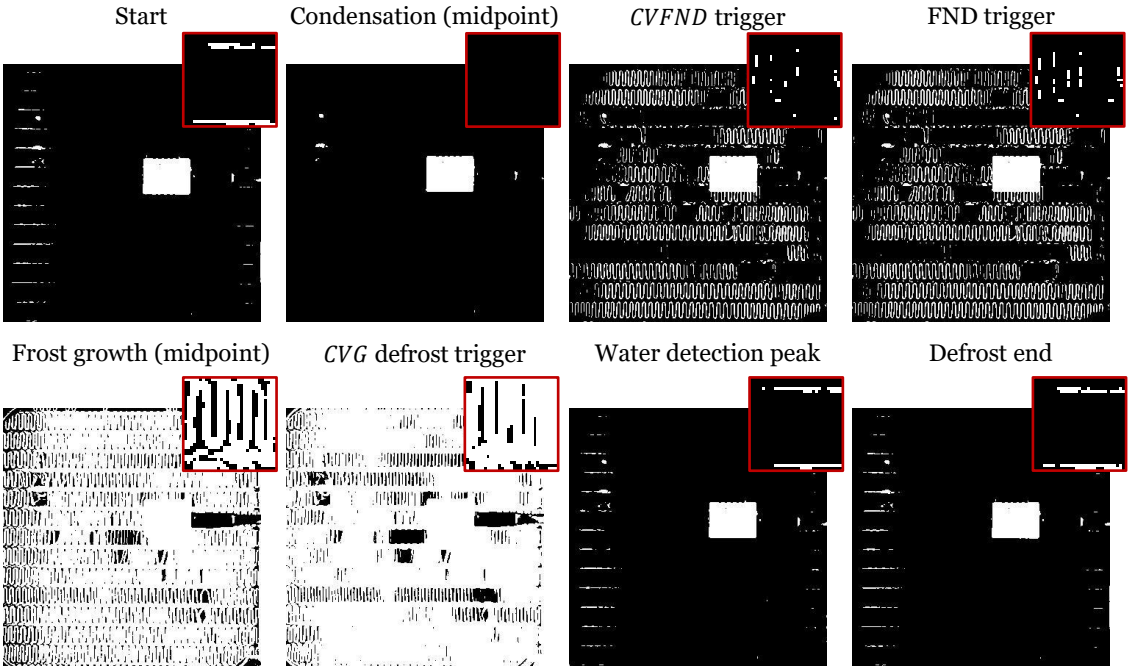

Figure 210 – Sequence of HX snapshots for test T-C-01, corresponding to characteristic timestamps.

Table 57 condenses the computed metrics. The CVT at t_{FND} was 10, far lower than the trend observed in previous Series, indicating that when the FDS detected nucleation, $CVFND$ was not triggered yet. The $\overline{\Delta AH}$ at t_{DCD} was not detected, consistent with the absence of DCD triggering in this series. This reflects the non-ideal placement and reduced sensitivity characteristic of Series C

Table 57 – Summary of test T-C-01.

Test details		**Computed metrics**	
Operation time [min]	33.95	CVT at t_{FND} $[-]$	10
Defrosting time [min]	14.80	$\overline{\Delta AH}$ at t_{DCD} $[\mathrm{g \cdot m^{-3}}]$	$n.d.$
Total time [min]	48.75	Δt_{nuc} [min]	-0.05
CV_{th} $[-]$	960	Δt_{dry} [min]	$n.d.$

Event timestamps [min]			
Start	5.00	$CVG \geq CV_{th}$	38.95
Condensation (midpoint)	8.10	Water detection peak	41.35
CVFND	12.15	HBDCD	48.15
FND	12.10	DCD	$n.d.$
Frost growth (midpoint)	25.55	Defrost end	53.75

Test T-C-01 starts the non-ideal regime of Series C. Nucleation was captured by both methods, but the FDS signal failed to recover to the dry baseline, preventing DCD. Nonetheless, $HBDCD$ was triggered within a window consistent with the trend of the previous series, indicating that the limitation was confined to the sensor response.

6.4.3.2. T-C-02

Test T-C-02 continued, with comparable cycle behaviour under the same placement conditions of series C, and consequent lack of DCD trigger. The test consisted of 29.65 min of operation and 13.10 min of defrosting, totalling 42.75 min.

In Figure 211, frost nucleation was detected closely by both methods at $t_{CVFND} = 8.15$ min and $t_{FND} = 8.50$ min for the CV and sensor based detectors respectively, resulting in a lag of $\Delta t_{nuc} = 0.35$ min. During defrosting, the sensor signal shows a reduced slope compared with earlier series. This trend reflects the gradual recovery of the sensor value without a clear stabilization at the dry baseline, consistent with moisture retention at the sensor position. Therefore, no defrost completion was detected by the sensor ($t_{DCD} = n.d.$), while the humidity-based detector reported drying at $t_{HBDCD} = 40.85$ min. As with T-C-01, the resistive signal failed to reach the dry reference level during defrost, which explains the absence of DCD detection.

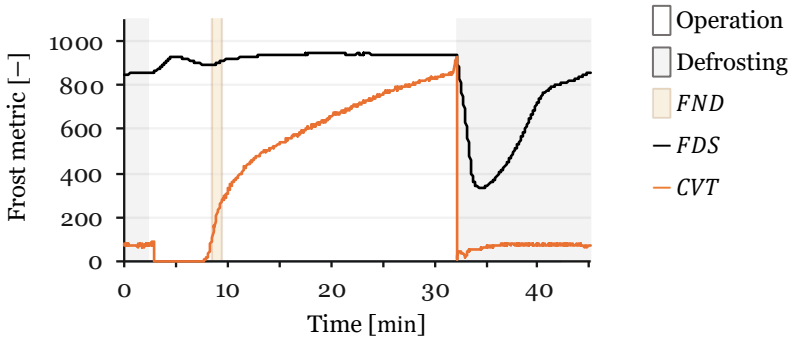

Figure 211 – Overall frost formation and defrosting cycle in test T-C-02.

Figure 212 crops the ADC range between 840 and 950. Within this zoomed region, the curve exhibits a short-lived rise at the onset of operation, a behaviour observable, but not seen as distinctly in T-C-01. This rise is most likely linked to the sensor surface being slightly damp at the start due to incomplete drying in the previous test. This results in the moist medium of the FMRS4 having better thermal contact with the HX, and the rapid cooling initially increases sensor resistivity. As the temperature compensation is based on outlet air ($TA2$) lags behind the actual cooling of the sensor itself at the start of the test. This difference in cooling rates is observed by comparing $TA2$ and $TWF2$ in the

previously discussed Figure 180 and Figure 181 respectively. The subsequent temperature compensation and condensation then dominate, driving the signal downward as expected. Despite this fluctuation, the FND was not affected, but it highlights the importance of the temperature selected for temperature compensation, requiring a fast response to temperature changes within the HX compared to that of the sensor. When properly dry, this effect is partially mitigated by the lower thermal contact between the sensor and the HX, before condensation.

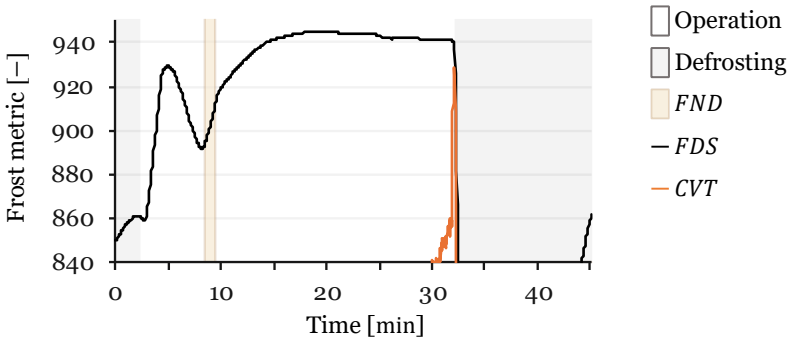

Figure 212 – Detail of the FMRS4 response for test T-C-02, cropped between 840–950 ADC to highlight slope changes at FND and DCD.

Figure 213 presents the image sequence of the AL-HX surface, with the tile view included in each snapshot. At the start ($t = 2.40$ min), the surface is reflective. During condensation ($t = 4.90$ min), the HX becomes less reflective and appears darker.

Frost nucleation is first visible at $t_{CVFND} = 8.15$ min in the tile and becomes slightly more visible when the sensor detects frost nucleation at $t_{FND} = 8.50$ min. Frost coverage intensifies toward the midpoint of growth ($t = 20.30$ min) and is extensive by the global defrost trigger ($t = 32.05$ min).

At the water detection peak ($t = 34.55$ min), surface wetting is evident in the sensor signal, but not observable through the CV method, appearing visually similar to the final dry-end snapshot ($t = 45.15$ min). As such, t_{DCD} and t_{HBDCD} are not directly distinguishable in these images.

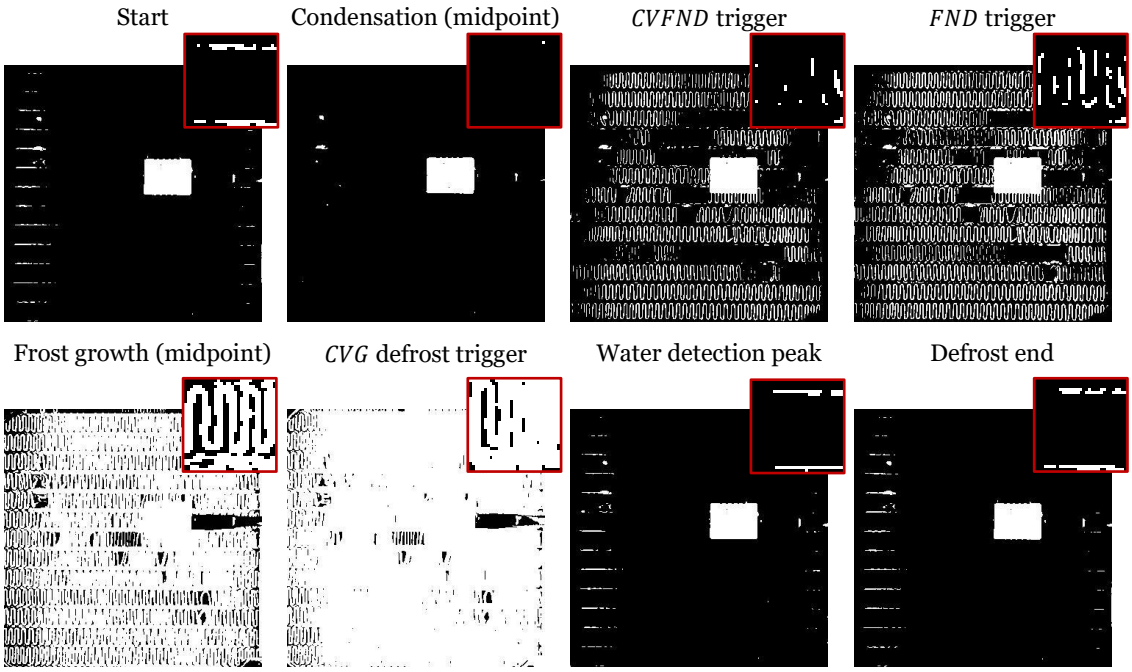

Figure 213 – Sequence of HX snapshots for test T-C-02, corresponding to characteristic timestamps.

Table 58 summarizes the test details. The CVT at t_{FND} was 110, higher than in T-C-01, but still much lower than values seen in series A and B, which shows earlier frost nucleation detection. $\overline{\Delta AH}$ at t_{DCD} was not detected, consistent with the absence of DCD in Series C tests. These results highlight that, although nucleation could be reliably captured with close agreement between CVT and FDS, the dry condition remained unresolved under this configuration.

Table 58 – Summary of test T-C-02.

Test details		**Computed metrics**	
Operation time [min]	29.65	CVT at t_{FND} [−]	110
Defrosting time [min]	13.10	$\overline{\Delta AH}$ at t_{DCD} [g · m^{-3}]	$n.d.$
Total time [min]	42.75	Δt_{nuc} [min]	0.35
CV_{th} [−]	960	Δt_{dry} [min]	$n.d.$

Event timestamps [***min***]			
Start	2.40	$CVG \geq CV_{th}$	32.05
Condensation (midpoint)	4.90	Water detection peak	34.55
CVFND	8.15	HBDCD	40.85
FND	8.50	DCD	$n.d.$
Frost growth (midpoint)	20.30	Defrost end	45.15

Test T-C-02 maintains the Series C pattern—close nucleation agreement, incomplete recovery during defrost, and no DCD despite $HBDCD$ indicating dry HX.

6.4.3.3. T-C-03

Test T-C-03 presented consistent results within Series C, without defrost completion detection achieved from the sensor data. This test had operation and defrosting periods of 33.15 min and 14.20 min respectively, giving a total duration of 47.35 min.

Test T-C-03 followed the same general pattern already observed in the earlier tests of series C. The operation lasted 33.15 min, followed by a defrosting period of 14.20 min, giving a total cycle time of 47.35 min. Condensation was identified at 7.65 min, The water detection peak occurred at 40.55 min, while drying was again not detected by the resistive sensor ($t_{DCD} = n.d.$), although the humidity-based method registered $t_{HBDCD} =$ 47.10 min.

In Figure 214, it is possible to observe that frost nucleation was detected again closely by both methods with $t_{CVFND} = 11.00$ min and $t_{FND} = 11.45$ min for the CV and sensor based detectors respectively, yielding a detection lag of $\Delta t_{nuc} = 0.45$ min. Regarding the dry HX detection, the sensor signal again fails to return to its dry baseline after defrosting, mirroring the behaviour of T-C-01 and T-C-02. The curve suggests a tendency toward stabilization but does not reach a plateau, remaining below the expected dry level. This incomplete recovery accounts for the absence of DCD detection ($t_{DCD} = n.d.$), while the $HBDCD$ reported drying at $t_{HBDCD} = 40.85$ min.

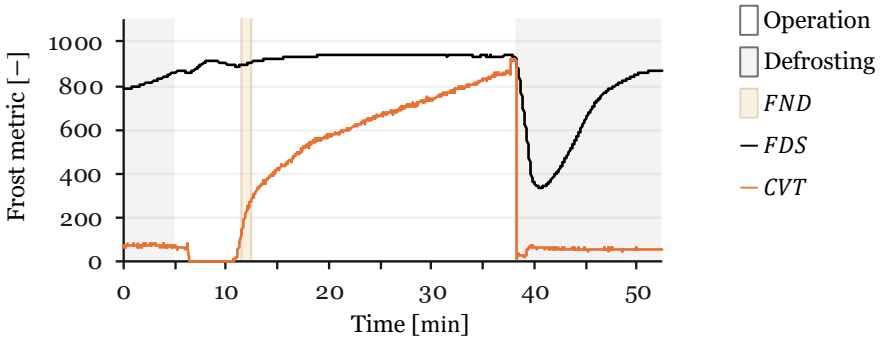

Figure 214 – Overall frost formation and defrosting cycle in test T-C-03.

Figure 215 shows the ADC range between 840 and 950. What initially appeared to be a stable plateau at the end of the defrosting phase in the full plot is revealed, as still relatively steep, confirming that the sensor never reached a condition representative of a dry HX. The behaviour at the start of operation was consistent with the previous test,

showing a brief rise before condensation and temperature compensation catch up and cause the expected signal drop.

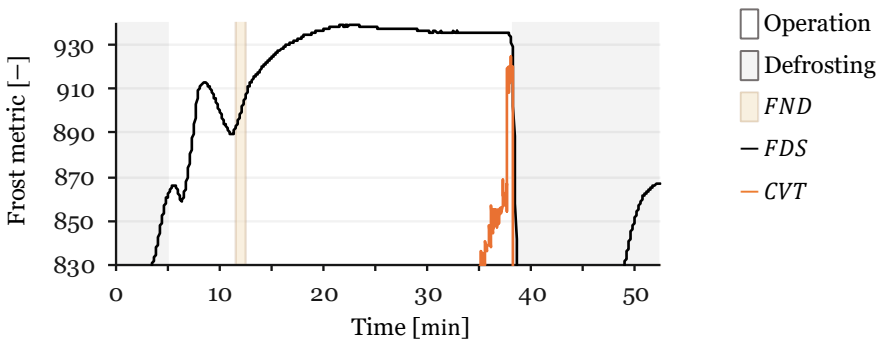

Figure 215 – Detail of the FMRS4 response for test T-C-03, cropped between 830–940 ADC to highlight slope changes at FND and DCD.

Figure 216 shows the sequence of snapshots from the CV method, each accompanied by the zoomed tile view. At the start ($t = 5.00$ min), the surface presents reflective areas. During condensation ($t = 7.65$ min), the AL-HX darkens uniformly. At $t_{\mathrm{CVFND}} = 11.00$ min frost becomes visible in the tile, and by $t_{FND} = 11.45$ min nucleation is apparent across much of the surface. Frost continues to grow, reaching extensive coverage by the midpoint of growth ($t = 24.80$ min), and the AL-HX is heavily frosted at the defrost trigger ($t = 38.15$ min). The water detection peak is measured by the FDS at $t = 40.55$ min. Finally, the defrost end frame ($t = 52.35$ min) appears visually similar to the water-peak snapshot, maintaining the trend.

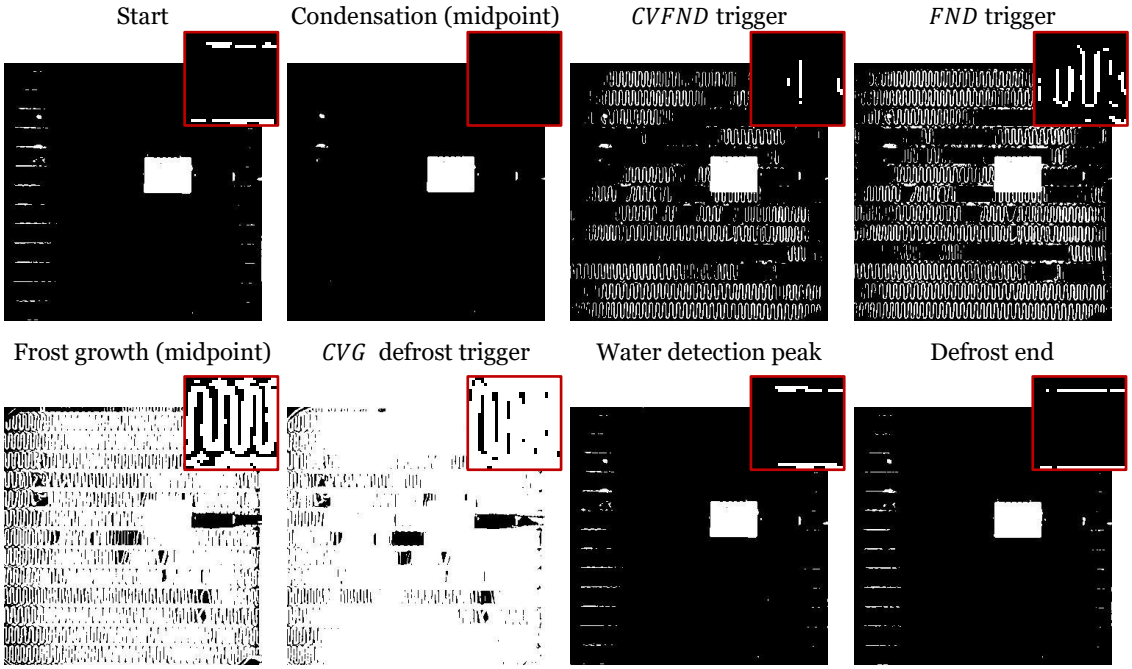

Figure 216 – Sequence of HX snapshots for test T-C-03, corresponding to characteristic timestamps.

Table 59 summarises the test metrics. CVT at t_{FND} was 130, somewhat higher than in T-C-02, but still below the trend seen in series A and B. The $\overline{\Delta AH}$ at t_{DCD} remain undetected, as in all series C tests. These results reinforce the pattern of nucleation detection but unresolved drying under non-ideal placement.

Table 59 – Summary of test T-C-03.

Test details		**Computed metrics**	
Operation time [min]	33.15	CVT at t_{FND} $[-]$	130
Defrosting time [min]	14.20	$\overline{\Delta AH}$ at t_{DCD} $[\mathrm{g \cdot m^{-3}}]$	$n.d.$
Total time [min]	47.35	Δt_{nuc} [min]	0.45
CV_{th} $[-]$	960	Δt_{dry} [min]	$n.d.$
Event timestamps [min]			
Start	5.00	$CVG \geq CV_{th}$	38.15
Condensation (midpoint)	7.65	Water detection peak	40.55
CVFND	11.00	HBDCD	47.10
FND	11.45	DCD	$n.d.$
Frost growth (midpoint)	24.80	Defrost end	52.35

Test T-C-03 reinforces the series behaviour, nucleation remains relatively well aligned across methods, while DCD is not achieved.

6.4.3.4. T-C-04

Test T-C-04 further extended the Series C set, maintaining the same experimental conditions, and consequently, lacking a DCD. The cycle lasted 34.45 min in operation and 13.25 min in defrosting, reaching 47.70 min in total.

In Figure 217, the condensation and nucleation phases are again visible but remain less pronounced than in series A and B. The CVT signal resulted in a frost nucleation detection at $t_{CVFND} = 9.45$ min, while the FDS signal shows a climb at the start followed a drop once the condensation and temperature compensation catch up. Nucleation detection was achieved at $t_{FND} = 10.90$. This resulted in a significant detection lag of $\Delta t_{nuc} = 1.45$ min inconsistent with the series. The behaviour during defrosting is once more incomplete, with the signal not recovering fully to the dry baseline ($t_{DCD} = n.d.$), while humidity-based detection occurred at $t_{HBDCD} = 48.90$ min.

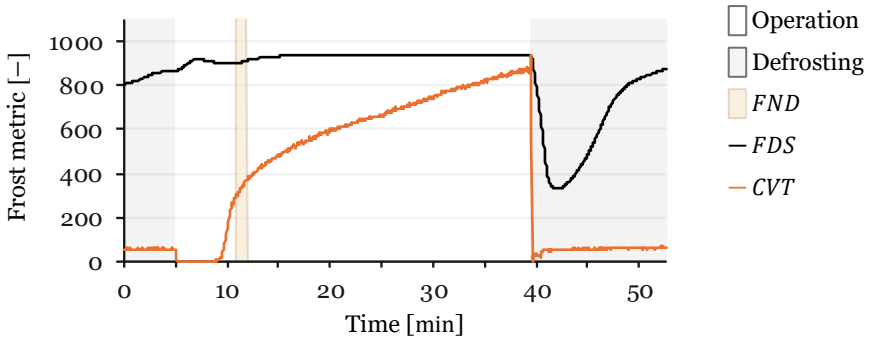

Figure 217 – Overall frost formation and defrosting cycle in test T-C-04.

Figure 218 crops the ADC range between 840 and 950. The zoom confirms that the slope following the apparent stabilization is still significant and does not flatten into a plateau. This aligns with the absence of t_{DCD} and reflects the same defrosting limitation present in the earlier series C tests.

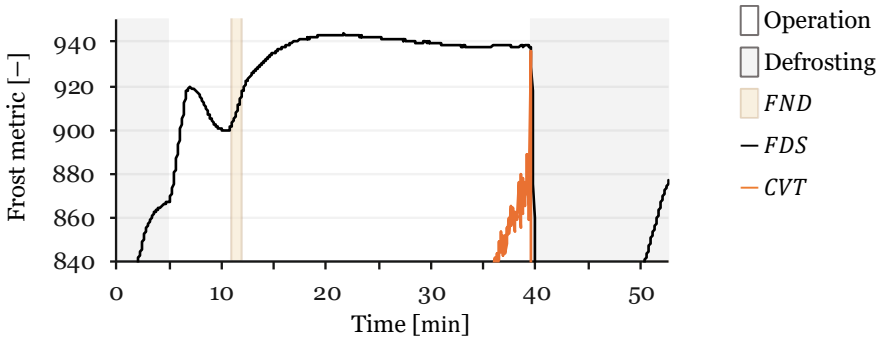

Figure 218 – Detail of the FMRS4 response for test T-C-04, cropped between 840–950 ADC to highlight slope changes at FND and DCD.

Figure 219 presents snapshots of the computer-vision analysis, each with its corresponding tile view. At the start ($t = 5.00$ min), surface reflections are visible. During condensation ($t = 7.00$ min), the surface becomes completely dark. Frost first appears in the tile at $t_{CVFND} = 9.45$ min, while at $t_{FND} = 10.90$ min frost already spreads across the AL-HX surface. By the midpoint of growth ($t = 25.20$ min), frost extends over most of the HX, progressing to significant frost accumulation by the global defrost trigger at $t = 39.45$ min. At the water detection peak ($t = 42.10$ min), the surface shows reflective areas associated with liquid accumulation. Finally, at the dry-end snapshot ($t = 52.70$ min), the AL-HX presents a visually similar state, continuing the trend of no distinction between dry and wet HX surface using CV.

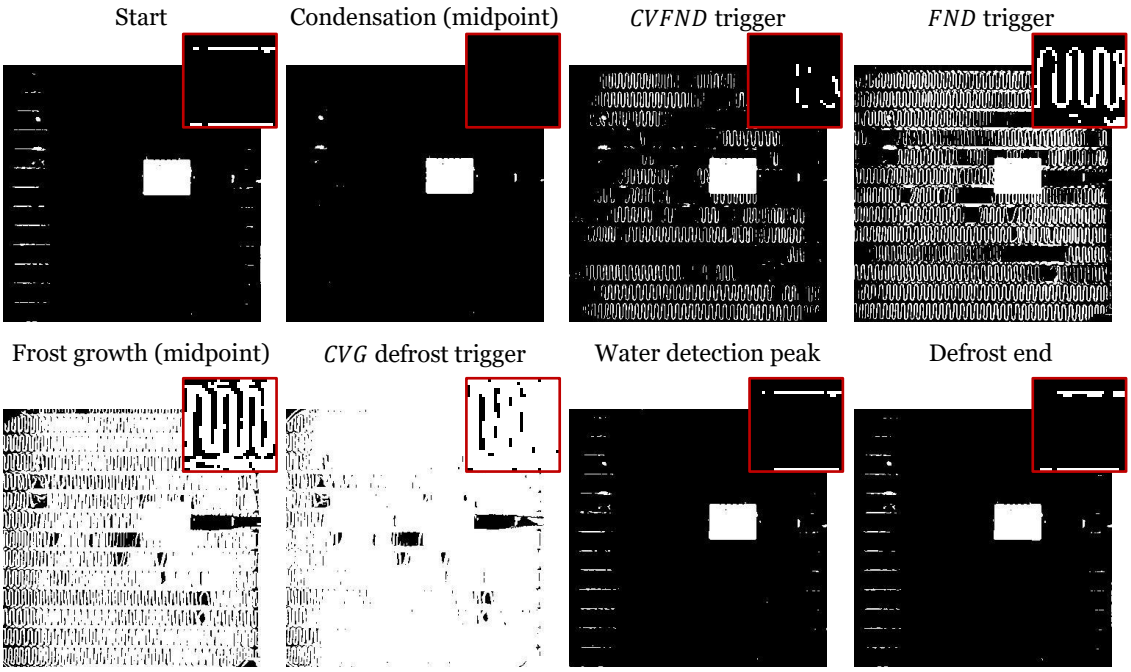

Figure 219 – Sequence of HX snapshots for test T-C-04, corresponding to characteristic timestamps.

Table 60 condenses the test metrics. The CVT at t_{FND} was 308, the highest value observed in all the Series. This elevated value suggests that the not fully dried sensor and/or its placement influenced the detection response, as the significant amplitude between CVT at t_{FND} values within this series means decreased reliability. The $\overline{\Delta AH}$ at $t_{DCD}$was not detected, consistent with the lack of DCD across all Series C tests.

Table 60 – Summary of test T-C-04.

Test details		**Computed metrics**	
Operation time [min]	34.45	CVT at t_{FND} [−]	308
Defrosting time [min]	13.25	$\overline{\Delta AH}$ at t_{DCD} [g · m^{-3}]	$n.d.$
Total time [min]	47.70	Δt_{nuc} [min]	1.45
CV_{th} [−]	960	Δt_{dry} [min]	$n.d.$

Event timestamps [min]			
Start	5.00	$CVG \geq CV_{th}$	39.45
Condensation (midpoint)	7.00	Water detection peak	42.10
CVFND	9.45	HBDCD	48.90
FND	10.90	DCD	$n.d.$
Frost growth (midpoint)	25.20	Defrost end	52.70

Test T-C-04 shows the highest delay in nucleation response within the series, and maintains the same limitation on DCD detection, with the FDS not reaching a stable dry level.

6.4.3.5. T-C-05

Test T-C-05 concluded Series C, again under non-ideal conditions and without triggering a DCD. It was comprised of 37.00 min of operation followed by 14.30 min of defrosting, summing to a total cycle of 51.30 min.

In Figure 220, the condensation and nucleation phases show the same pattern as earlier tests in this series. The FDS signal dropped at condensation and rose toward nucleation, with both $CVFND$ and FND detections occurring close together at $t_{CVFND} = 10.20$ min and $t_{FND} = 10.50$ min respectively, resulting in a signal lag of $\Delta t_{nuc} = 0.30$ min. Detection of a dry HX was again not achieved ($t_{DCD} = n.d.$), whereas the humidity-based method indicated $t_{HBDCD} = 52.80$ min, confirming the trend of this test series.

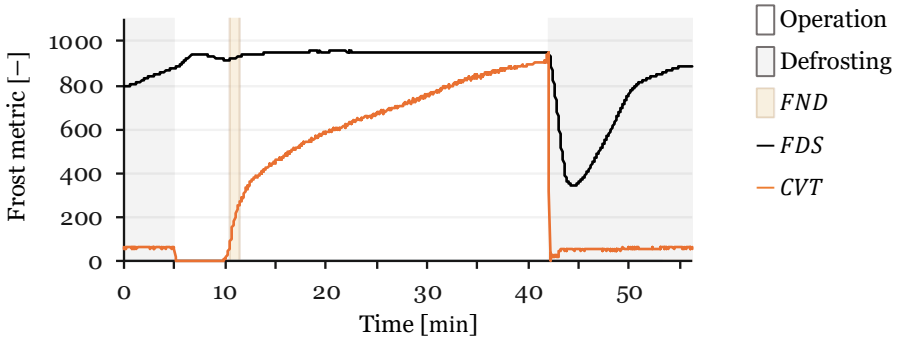

Figure 220 – Overall frost formation and defrosting cycle in test T-C-05.

Figure 221 crops the ADC range between 850 and 960. The zoom shows that the slope observed at the end of defrosting does not flatten into a plateau again, aligning with the missing DCD. The amplification also highlights the FDS signal spike preceding condensation detection, followed by a dip in condensation detection and a subsequent rise before nucleation, which is consistent with the series.

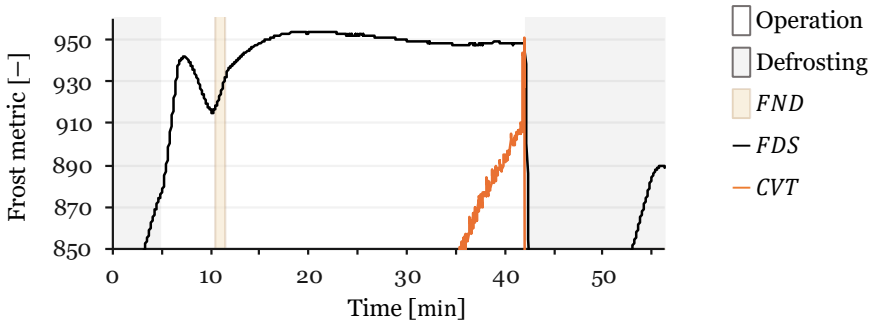

Figure 221 – Detail of the FMRS4 response for test T-C-05, cropped between 850–960 ADC to highlight slope changes at FND and DCD.

Figure 222 shows snapshots of the HX surface, each accompanied by a zoomed tile view in the top right corner. At the start (t = 5.00 min), surface reflections are clearly visible. During condensation (t = 7.20 min), the surface and tile appear dark, consistent with reduced reflectivity. At t_{CVFND} = 10.20 min, frost becomes visible within the analysed tile, while at t_{FND} = 10.50 min nucleation is evident across most of the HX surface, though not yet fully covering it. Frost coverage increases further by the midpoint of growth (t = 26.25 min), reaching near saturation before the global defrost trigger at t = 42.00 min. At the water detection peak (t = 44.45 min) the FDS reaches its lowest signal value, at the dry-end frame (t = 56.30 min), the HX surface shows a similar appearance to the previous snapshot. This is in line with all the previous tests, in which t_{DCD} and t_{HBDCD} are not directly distinguishable in these images.

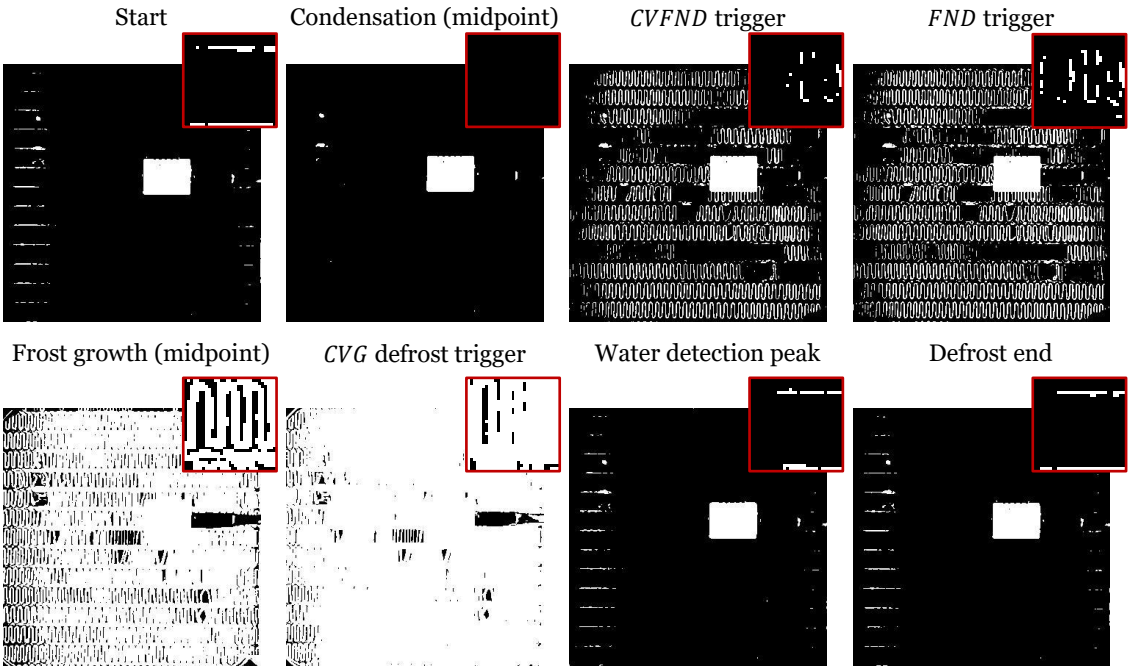

Figure 222 – Sequence of HX snapshots for test T-C-05, corresponding to characteristic timestamps.

Table 61 condenses the computed metrics. The CVT at t_{FND} was 87, a lower value that indicates FND close to CVT. The $\overline{\Delta AH}$ at t_{DCD} was not available, consistent with the absence of resistive dry detection in this series. These results reaffirm the trend across Series C: nucleation could still be captured, but drying remained unresolved under the testing conditions.

Table 61 – Summary of test T-C-05.

Test details		**Computed metrics**	
Operation time [min]	37.00	CVT at t_{FND} [−]	87
Defrosting time [min]	14.30	$\overline{\Delta AH}$ at t_{DCD} [g · m^{-3}]	$n.d.$
Total time [min]	51.30	Δt_{nuc} [min]	0.30
CV_{th} [−]	960	Δt_{dry} [min]	$n.d.$

Event timestamps [min]			
Start	5.00	$CVG \geq CV_{th}$	42.00
Condensation (midpoint)	7.20	Water detection peak	44.45
CVFND	10.20	HBDCD	52.80
FND	10.50	DCD	$n.d.$
Frost growth (midpoint)	26.25	Defrost end	56.30

Test T-C-05 concludes Series C with consistent nucleation detection and persistent failure of DCD. This series highlighted the importance of the sensor placement, however shows the method still holds repeatable FND under non ideal conditions.

6.5. Comparative analysis and discussion

Across all twelve tests, the FMRS4, CV and humidity-based metrics delivered consistent detections of frosting–defrosting dynamics. Series A ($CV_{th} = 960$; $\sim 24 - 33$ min operation time; $\sim 15 - 16$ min defrosting time) provided baseline behaviour with clean detections. Series B ($CV_{th} = 1012$; $\sim 60 - 101$ min operation time; $\sim 30 - 34$ min defrosting time) imposed higher frost loads and longer drying periods yet yielding clean detections in all detection metrics. Series C ($CV_{th} = 960$; $\sim 30 - 37$ min operation time; $\sim 13 - 15$ min defrosting time) documented non-ideal sensor placement, where dry HX detection based on the FDS was not achieved in any of the tests performed ($DCD = n.d.$), despite $HBDCD$ indicating an overall dry HX by the end of defrosting.

Table 62 summarises the computed metrics across all twelve tests. These values condense the comparative behaviour of the detectors, linking CVT at t_{FND}, the $\overline{\Delta AH}$ at DCD, and the trigger lags between FDS detectors and validation detection methods.

Table 62 – Summary of computed metrics from all tests.

Series	Test	CVT at t_{FND} [−]	$\overline{\Delta AH}$ at t_{DCD} $[g \cdot m^{-3}]$	Δt_{nuc} $[min]$	Δt_{dry} $[min]$
A	T-A-01	293	0.220	1.75	0.05
	T-A-02	295	0.000	1.65	-0.60
	T-A-03	213	0.154	1.15	0.05
	T-A-04	240	0.186	1.05	-0.75
B	T-B-01	20	0.516	-0.10	-0.65
	T-B-02	196	0.016	0.90	2.10
	T-B-03	192	0.000	0.75	1.05
C	T-C-01	10	n.d.	-0.05	n.d.
	T-C-02	110	n.d.	0.35	n.d.
	T-C-03	130	n.d.	0.45	n.d.
	T-C-04	308	n.d.	1.45	n.d.
	T-C-05	87	n.d.	0.30	n.d.

Table 63 presents detector trigger times normalised to the start of operation and to the initiation of defrosting. Expressing events relative to these cycle boundaries removes the effect of varying absolute cycle durations and deviations, as operation durations varied widely, from ~ 24 min in T-A-02 to ~ 101 min in T-B-01, justifying the need for this approach. Normalisation shows how quickly $CVFND$ and FND trigger after operation begins; and for drying, by reporting how long $HBDCD$ and DCD take after defrost initiation.

Table 63 – Detector trigger times relative to the operation and defrosting start for all tests.

Series	Test	$t_{CVFND} - t_{start}$ $[min]$	$t_{FND} - t_{start}$ $[min]$	$t_{HBDCD} - t_{CVG \geq CV_{th}}$ $[min]$	$t_{DCD} - t_{CVG \geq CV_{th}}$ $[min]$
A	T-A-01	8.20	9.95	9.90	9.95
	T-A-02	4.30	5.95	8.90	8.30
	T-A-03	4.55	5.70	7.95	8.00
	T-A-04	4.45	5.50	9.20	8.45
B	T-B-01	10.25	10.15	15.15	14.50
	T-B-02	5.10	6.00	12.50	14.60
	T-B-03	5.70	6.45	15.05	16.10
C	T-C-01	7.15	7.10	9.20	n.d.
	T-C-02	5.75	6.10	8.80	n.d.
	T-C-03	6.00	6.45	8.95	n.d.
	T-C-04	4.45	5.90	9.45	n.d.
	T-C-05	5.20	5.50	10.80	n.d.

The compiled data serve as the baseline for the comparative analysis that follows. The discussion is structured around two main aspects of sensor performance, frost nucleation detection and dry HX detection.

6.5.1. Nucleation detection: FND and CVFND

The time elapsed between the start of operation and nucleation detection showed average values of 5.38 ± 1.89 min ($mean \pm SD$) for $CVFND$ and 6.78 ± 2.12 min for FND in Series A, with corresponding medians of 4.50 min and 5.83 min. In Series B, the averages were 7.02 ± 2.82 min for $CVFND$ and 7.53 ± 2.28 min for FND, with medians of 5.70 min and 6.45 min. In Series C, detection occurred at 5.71 ± 1.00 min for $CVFND$ and 6.21 ± 0.60 min for FND, with medians of 5.75 min and 6.10 min.

The standard deviations observed across the series are primarily due to the first test in each set, where nucleation was delayed by 3 min to 4 min as the experimental setup takes time to cool even after the working fluid reaches its minimum temperature. When these first tests are excluded, the variability decreases as standard deviations reduce to 0.13/0.23 min in Series A, 0.42/0.32 min in Series B, and 0.69/0.40 min in Series C for $CVFND$ and FND respectively. This confirms that nucleation detection remains repeatable under stable operating conditions, while still being capable to capture onset even in different initial states.

FND and $CVFND$ were triggered in all the tests corresponding to a 100% detection rate. The temporal agreement between the two methods, expressed as Δt_{nuc}, showed average offsets of 1.40 ± 0.35 min in Series A ($n = 4$), 0.52 ± 0.54 min in Series B ($n = 3$), and 0.50 ± 0.56 min in Series C ($n = 5$). Median values followed the same trend, at 1.40 min, 0.75 min, and 0.45 min, respectively.

When considering all the tests ($n = 12$), the average Δt_{nuc} was 0.80 ± 0.63 min, (95% CI: $0.40 - 1.20$ min).All detection lags were within ± 1.75 min and 42% of detection lags were within ± 0.5 min, which shows the alignment between FND and $CVFND$ across all operating regimes.

The CVT curve shows a characteristic behaviour during frost nucleation. As frost begins to form on the thin frontal surfaces of the fins, the monitored tile undergoes a rapid visual transition, producing a steep rise in CVT values. This progression that goes from 0 to values close to 400 defines a nucleation region of the curve, indicating the region in which an adequate FND should occur. The CVT value at t_{FND} differed between series, although the FND consistently triggered within this nucleation region of CVT curve,

confirming that sensor-based detection coincides with the nucleation stage of frost accumulation observed via the CV method. In Series A, CVT value at t_{FND} values averaged 260 ± 40.5 with a median of 267 ($n = 4$). In Series B, the mean was 136 ± 100.5 with a median of 192 ($n = 3$). In Series C, the mean was 129 ± 109.9 with a median of 110 ($n = 5$). When considering all twelve tests, the average CVT at t_{FND} was 175 ± 103.4 (95% CI: $109 - 240$), which falls within the nucleation region of the curve, showing that numerical differences between series correspond to relatively modest absolute changes, consistent with the small detection lags previously analysed.

FND occurred after $CVFND$ in 10 out of the 12 tests, while the other 2 tests had FND earlier, although with very low negative detection lags of 0.10 min and 0.05 min. From a comparative standpoint, Series A exhibited slightly larger offsets between FND and $CVFND$, though still within a narrow range, reflecting its role as the clean baseline. In Series B, offsets remained similarly small despite longer cycles and higher frost loads, showing that extended operation did not compromise nucleation detection. Series C, despite the non-ideal sensor placement and the failure of DCD, still preserved close agreement between FND and $CVFND$, emphasising that nucleation remains reliably captured even under suboptimal sensor placement.

6.5.2. Dry detection: DCD and HBDCD

The time elapsed between the start of defrost and dry HX detection showed average values of 8.99 ± 0.81 min for $HBDCD$ and 8.68 ± 0.87 min for DCD in Series A with corresponding medians of 9.05 min and 8.38 min. In Series B, averages were 14.23 ± 1.50 min for $HBDCD$ and 15.07 ± 0.90 min for DCD, with medians of 15.05 min and 14.60 min, reflecting the longer melting and drying period under higher frost loads. In Series C, $HBDCD$ occurred at 9.44 ± 0.80 min, with a median of 9.20 min, while DCD was not detected ($n.d.$) in any test, a consequence of the non-ideal sensor placement. Series A and C show similar drying times when viewed from the $HBDCD$ perspective, while Series B required substantially longer to reach a dry HX, consistent with the higher frost load and extended removal needed under these operating conditions. The higher standard deviations observed in Series B reflect the larger volumes of meltwater generated, which introduce greater variability in how long residual moisture takes to drain and evaporate fully. However, when considered in proportion to the longer defrosting phase, this variability is not greater than in the other series, but rather consistent with the extended duration required for complete drying.

Across all tests, DCD was triggered in 7 of 12 cases, corresponding to 100% detection in Series A and B and 0% in Series C, for an overall detection rate of 58%. By contrast, $HBDCD$ was triggered in every test, achieving a 100% detection rate. Where both detectors triggered ($A + B, n = 7$), the Δt_{dry}, averaged 0.18 ± 1.05 min with a median of 0.05 min. By series, Δt_{dry} averaged -0.31 ± 0.42 min in Series A with a median of -0.27 min, indicating DCD was slightly earlier than $HBDCD$ and 0.83 ± 1.39 min in Series B with a median of 1.05 min indicating DCD was slightly later than $HBDCD$. All detected Δt_{dry} values lay within 0.18 ± 1.05 min, with $28\% \leq 0.5$ min and $71\% \leq$ 1.0 min, demonstrating close alignment between methods for series A and B even under extended cycles.

The absolute humidity difference, $\overline{\Delta AH}$ at t_{DCD}, remained close to zero, indicating a good agreement between dry HX detection methods. In Series A, the mean was 0.14 ± 0.10 g $\cdot$ m^{-3} (median $0.17\ g \cdot m^{-3}$); in Series B, $0.18 \pm 0.29\ g \cdot m^{-3}$ (median $0.02\ g \cdot m^{-3}$). Considering all detected cases ($A + B, n = 7$), the mean was $0.16 \pm 0.18\ g \cdot m^{-3}$ (median $0.15\ g \cdot m^{-3}$, 95% CI: $-0.01 - 0.33$). Contextually, the underlying $\overline{\Delta AH}$ values spanned wide intervals across series: in Series A from -7.65 to $3.32\ g \cdot m^{-3}$, in Series B from -9.39 to $1.68\ g \cdot m^{-3}$, and in Series C from -8.48 to $3.18\ g \cdot m^{-3}$. By contrast, the $\overline{\Delta AH}$ at t_{DCD} values at completion clustered close to zero, with values between $0.00 - 0.52\ g \cdot m^{-3}$ for Series A and B. This shows that the DCD marked defrost completion at a near-equilibrium state.

Overall, the dry HX detection exhibits two distinct behaviours. Series A and B demonstrate reliable performance of both detectors, with Δt_{dry} consistently below 1.5 min, confirming that the FDS aligns closely with the $HBDCD$ when placement is adequate. The negative offset in Series A indicates that the FDS tends to anticipate dryness slightly, while in Series B it lags modestly, reflecting the heavier frost load and longer drainage times. Series C highlights the importance of sensor placement: although $HBDCD$ confirmed overall dryness at timings comparable to Series A, the FDS failed to recover to its dry baseline, resulting in no DCD trigger. This divergence emphasises that while air-side drying is robustly captured, localised persistence of residual moisture at the sensor site can mask dry-state detection.

The low values of $\overline{\Delta AH}$ at t_{DCD} reinforce that both detectors converge at near-equilibrium conditions regardless of cycle duration or frost load. Series A and B thereby validate the reliability of DCD, while Series C demonstrates the FDS sensitivity to positioning, stressing that correct placement is essential to ensure detection

performance. This convergence across all conditions suggests that dry HX detection is the most accurate function of the FMRS4, granted it is well-positioned. Furthermore, unlike the $CVFND$, which evaluates a region close to the sensor using CVT instead of CVG, the $HBDCD$ does not perform a localized analysis. Instead, it monitors the system-level moisture balance. By contrast, the FDS-based DCD metric is localized and more sensitive to local dynamics.

6.6. Concluding remarks

Across the twelve tests, the FMRS4, CV, and AH-based metrics provided a coherent picture of frosting–defrosting dynamics. The normalised timing analysis allowed direct comparisons, while the computed metrics linked detector values to event timing in a consistent framework. Together, the datasets show that the three modalities are mutually reinforcing and, when interpreted jointly, capture both local and system-level phenomena across baseline (Series A), extended-load (Series B), and non-ideal FDS placement (Series C) conditions.

Nucleation detection was uniformly robust. FND and $CVFND$ triggered in every test, with small offsets that remained within narrow bounds across all operating regimes. $CVFND$ typically preceded FND, which is consistent with the role of CVT in tracking a locally sensitive nucleation region of the curve (from near-zero up to ~400), where the tile brightens rapidly as frost forms on the fin's frontal surface. All FND events occurred within—or immediately adjacent to—this region, confirming that the FDS-based detector responds during the early, nucleation stage captured via the CVT method. The first test in each series showed later nucleation due to an initially warmer system, but detection remained consistent thereafter, evidencing repeatability once conditions stabilised.

Dry HX detection exhibited a dual character that reflects the different scopes of the validation signals. The AH-based defrost completion detector, $HBDCD$, triggered in all tests and reported similar drying times in Series A and C, while Series B required longer drying following higher frost loads. The FDS-based defrost completion detector, DCD, aligned closely with $HBDCD$ when FDS placement was adequate (Series A and B) but did not trigger in Series C due to persistent local wetting at the sensor site. Apparent variability in the longer Series B cycles is largely a consequence of greater meltwater volumes; when considered relative to the longer defrost window, the dispersion is proportionate rather than excessive. Sensor placement proved decisive for detection reliability. The FFM method was used to identify optimal coordinates for placement, confirmed by Series A and B, however, the sensor cable, and its position within the fin

(i.e. twisted, or angled), is sufficient to cause it to behave differently. In Series C, slight sensor displacement during setup likely altered local airflow, hindering drying and preventing DCD triggering. Later tests with slight sensor adjustments restored proper operation, confirming that minor positioning variations within the dense fin pack can affect results. Future work will refine mounting and assess performance on HXs with wider fin spacing.

The moving-averaged absolute humidity difference, $\overline{\Delta AH}$, provided a physically interpretable reference of mass transfer: negative values during frosting correspond to net mass transfer from the air to the HX surface (condensation and frost accumulation), positive values during defrost reflect net mass transfer from the HX surface back to the air (melting and evaporation), and values near zero indicate equilibrium. Despite large absolute excursions of $\overline{\Delta AH}$ over each cycle, the $\overline{\Delta AH}$ values at DCD approached zero, showing that both detectors marked completion at a near-equilibrium state. This supports using $\overline{\Delta AH}$ at t_{DCD} as a quality flag.

Signal roles and processing choices underpinned this consistency. CVG served as a stable control reference for defrost initiation, while CVT emphasised local changes, such as increased sensitivity to condensation, and tile specific to nucleation detection. Temperature compensation reduced the raw ADC fluctuations that occur when the sensor undergoes thermal transitions between defrost and operation. Without this correction, rapid temperature changes at the sensor surface could induce drift or false nucleation events. The compensation applied here was calibrated for the moist state of the sensor, since this is the most critical and sensitive phase for nucleation detection. In Series C, however, the sensor was damper at the start of operation, resulting in higher thermal contact with the HX. Because the HX cooled faster than the surrounding air, a temporary increase in resistivity was observed before condensation detection, likely caused by a lag in the compensation temperature (TA2 relative to TWF2). Despite this effect, it did not compromise DCD or FND performance, as the compensation eventually caught up, providing a stable signal for FND.

In principle, optimal compensation would also require different corrections for the dry, moist, and frozen states, as the sensor material properties vary across these regimes. However, because the focus was on ensuring stable behaviour between the onset of moisture accumulation and nucleation, the moist-state calibration was prioritised. While some temperature-induced fluctuations may still arise due to dynamic material conditions, the applied correction proved effective: FND was always achieved within the expected window, confirming that the compensation scheme was adequate for this

application. Modest smoothing suppressed noise and stabilised DCD without re-tuning across tests, trading a small temporal smear for improved event detection.

Another important observation concerns the relative sensor resistance before and after defrosting. In Series A, where frosting exposure was significant but not excessive, the sensor resistance after defrosting was higher than at the end of operation. This behaviour is consistent with expectations, since frost has lower resistivity than air; once the sensor dries, the absence of conductive paths leads to a higher overall resistance. Nevertheless, both conditions correspond to high-resistance states, with the air-dry state being the most resistive. In contrast, Series B showed the opposite trend, with post-defrost resistance slightly lower than at the end of operation. This may indicate residual moisture retained in the fabric medium increases conductivity, while increasing frosting creates an increasingly high resistivity trend characteristic of the series B.

Practically, the results reinforce the FMRS4 sensor as a low-cost, compact solution capable of supporting both FND and dry DCD within a demand-defrost strategy. These metrics, derived directly from the sensor, were the primary focus of evaluation. The auxiliary CV and AH-based detectors served here as validation benchmarks, confirming whether the sensor-based triggers indeed corresponded to the frost nucleation and to a dry HX. While not intended as operational methods in this thesis, their performance also highlights that, in systems with available space for cameras or with design flexibility to include humidity monitoring, these alternatives could provide robust pathways for frost detection and defrost control, particularly where finer quantification or diagnostic insight is desired. CV, for instance, not only confirmed nucleation but also mapped frost coverage, offering diagnostic value such as identifying uneven growth or local defects. AH-based detection, meanwhile, tracked system-level moisture balance with resilience and, with the added capability of monitoring mass transfer in real time, could be used as a measure of condensation and frost formation.

Overall, the FMRS4 demonstrated a capability for FND in all tests and DCD when the sensor was appropriately placed. Complementary validation from $CVFND$ and $HBDCD$ metrics confirmed that both are effective, reliable, and independent methods for detecting frost and dry HX states and could themselves function as standalone approaches. While secondary to the sensor focus of this work, these findings provide a valuable baseline for interpreting sensor behaviour and may even open the door toward an alternative pathway for future development.

Chapter 7

Energy autonomous demand defrost control module

The previously discussed thermoelectric HX was developed to lower the refrigerant temperature by powering the TE modules with electrical energy. However, given the assembled setup and the potential for TE modules to operate as thermoelectric generators (TEG), it was considered relevant to investigate their use as an energy-harvesting solution. This investigation aimed to assess the feasibility of powering wireless frost-detection sensors, using the temperature differentials naturally present in refrigeration systems.

The work presented in this chapter resulted in a publication [143], which explored the concept of powering a frost detection sensor using a TE. The objective was to simplify installation by enabling local power generation, which, together with wireless data transmission, would eliminate the need for external wiring. The study analysed the power requirements of the sensor and compared them with the practical energy output obtained from the experimental testing results of the TEG. This assessment demonstrated the potential of thermoelectric energy harvesting to support autonomous frost-detection systems, paving the way for self-contained and easily deployable demand-defrost control solutions.

The assessment of the power generation capacity of the TEG-HX is supported by an uncertainty analysis to quantify the uncertainty in the derived quantities, such as the heat flow on both the hot and cold sides of the HX, and the final electrical power generated. As detailed in Annex C, the standard uncertainty for the heat flow measurements ranges from approximately 10 W to 15 W depending on test conditions, while the uncertainty of the generated electrical power is approximately 3.3 mW under the maximum power output scenario. This propagation of uncertainty shows that the conclusions regarding the feasibility of the energy-autonomous concept are based on measurements with defined confidence intervals.

7.1. Contextualization

In modern refrigeration systems, integrating Internet of Things (IoT) technologies can enhance operational efficiency and accuracy. IoT systems contain Wireless Sensor

Networks (WSNs) of interconnected devices that communicate and share data wirelessly. WSNs are components of IoT, consisting of spatially distributed sensors that monitor environmental conditions and transmit data to a central system. These sensors can provide real-time monitoring and control [144]. In the context of mitigating the problem of frost formation, IoT sensor networks can monitor refrigeration systems' working parameters, which can be used as data to feed decision-support tools for demand defrosting operations, such as demand defrost algorithms [140], digital twinning, deep learning, and AI [145].

Implementing a sensor within an HX presents several complexities, particularly in compact or remote HX applications. The availability of energy to power the sensing module, as well as issues related to cable management and the integration of the sensor into the existing system without causing disruption, make a wireless sensing module an interesting approach. Sensors such as the resistive sensor developed in this work have very low energy requirements due to their overall simplicity, and require a low acquisition rate, making them suitable for integration into low-power energy-autonomous wireless sensing modules.

Given the wide temperature gradients within refrigeration systems, a thermoelectric system presents an attractive solution as a power generation unit for wireless sensing modules. TEGs use the Seebeck effect to convert heat flow, which is driven by temperature gradients, into electrical energy. By tapping into these temperature gradients, thermoelectric systems can provide a sustainable and reliable power source for low-power applications [146], eliminating the need for repeated exchange of batteries or connection to an external PSU or extensive wiring.

In recent years, there has been a growing interest in the usage of thermoelectric systems for powering low-power devices. Research by Alvarez-Quintana [147] demonstrates the feasibility of using TEG modules to harvest electrical power from condenser heat in refrigeration systems, reaching close to 20 mW with a single commercial cell.

In another study, Attar et al. [148] designed and manufactured a HX with 16 TEG cells, implemented into refrigeration systems for de-superheating of refrigerants after the compression phase, demonstrating that the harvested energy could be used to power auxiliary systems, attaining power generations of 3 W to 12 W (average of 0.2 W to 0.7 W per cell), depending on the usage of a fan to increase heat transfer.

Due to a low electrical power to heat transfer ratio, implementation of TEGs requires careful study. Using a TEG between the evaporator and condenser would yield the higher temperature gradient, and therefore a higher electrical power generation. Nonetheless, this placement would be counterproductive, as it would introduce a significant thermal load, outweighing the benefits of a demand defrost system. Instead, these systems should be integrated where heat exchange is already intended, such as between the evaporator and intake air, between the condenser and refrigerating air, or in the liquid-to-suction line HX used to superheat the gas and subcool the liquid, such as the application in [148]. This approach ensures that the TEG system generates electrical power without adding undesired thermal loads.

The ability to convert heat flow into electrical energy for powering frost-detection sensors presents a dual potential for energy efficiency. On one hand, the sensor contributes to frost detection and defrosting operations. On the other hand, the power for this system could be obtained from the dissipation of waste heat, such as in the condenser, by extracting energy from a temperature gradient that the refrigeration system creates to discard the heat.

If waste heat is not available, a small amount of energy can be obtained from a location where heat flow is already desired, at the expense of introducing a small heat resistance to an HX. In such cases, the system should be designed to minimize disruption to normal system parameters, either by having a small footprint or by being placed in a way that its thermal resistance does not significantly impact the normal heat exchange process.

7.2. Experimental setup adaptation

The work presented in this chapter repurposes the experimental setup by converting the TE-HX into a TEG-HX configuration, to generate sufficient electrical power to operate a wireless, energy-autonomous demand defrost sensor. The cold circuit (blue dashed line), hot circuit (red dashed line) and its components are represented in Figure 223.

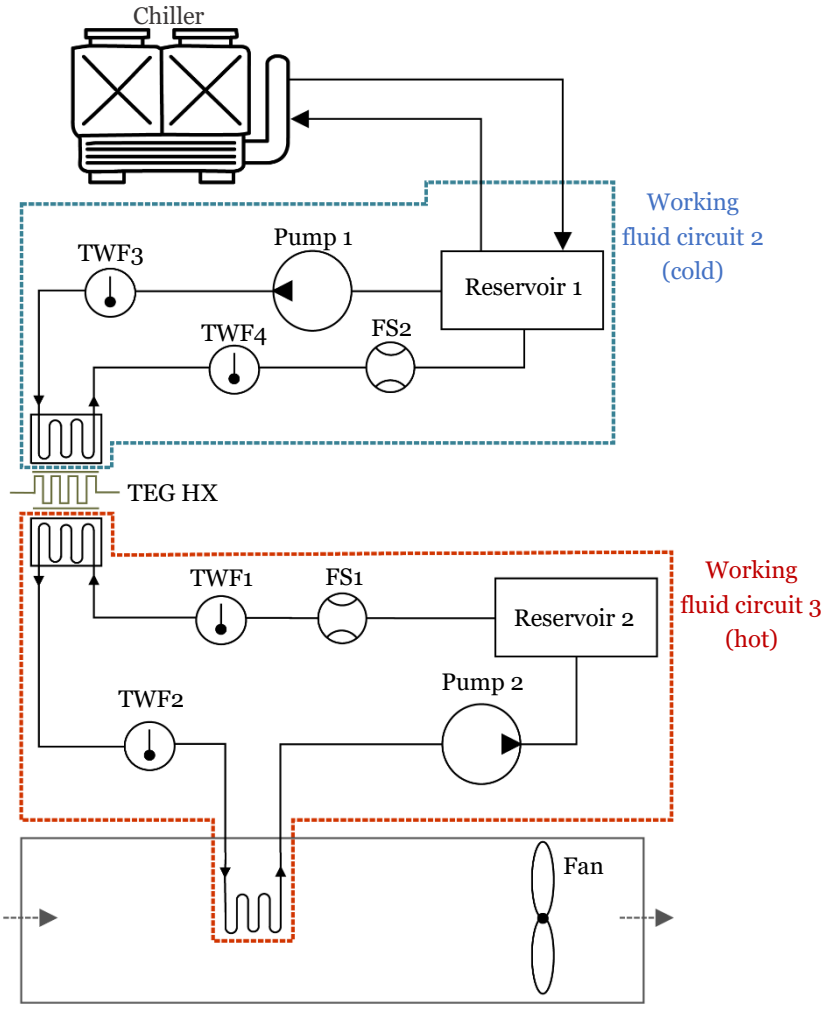

Figure 223 – Schematic of the experimental setup showing the conversion from TE-HX to TEG-HX.

The cold circuit is designed to absorb heat from the hot circuit and comprises some of the components already mentioned in Table 13. Within this context, a few things must be taken into consideration

- AL-HX is the heat source,
- $TWF1$ and $TWF2$ monitor the working fluid in the hot side of the TEG-HX, inlet and outlet temperatures respectively, with an accuracy of $\pm$ 0.5 °C.
- $TWF3$ and $TWF4$ monitor the working fluid in the cold side of the TEG-HX, inlet and outlet temperatures respectively, with an accuracy of $\pm$ 0.5 °C.
- $FS1$ and $FS2$ measures the flow rate of the cold working fluid, with an accuracy of $\pm$ 5%.

The TEG-HX, just like the TE-HX is comprised of four thermoelectric modules, as previously shown in Figure 38 which were disconnected from their respective PSUs and connected in series to a load, which will be discussed in the next section. All the

readapted components from the experimental setup can now be looked at from the point of view of the TEG-HX, where this analysis focuses.

7.3. Circuit, measurement and data acquisition

The series configuration was connected to a resistive load, with a microcontroller whose ADC is used to measure the voltage drop across the resistor terminals with an accuracy of $\pm$ 9.8 mV. For each test, a series of different resistors, ranging from 0.78 Ω up to 14861.44 Ω were tested using the circuit shown in Figure 224, to determine the maximum TEG power output.

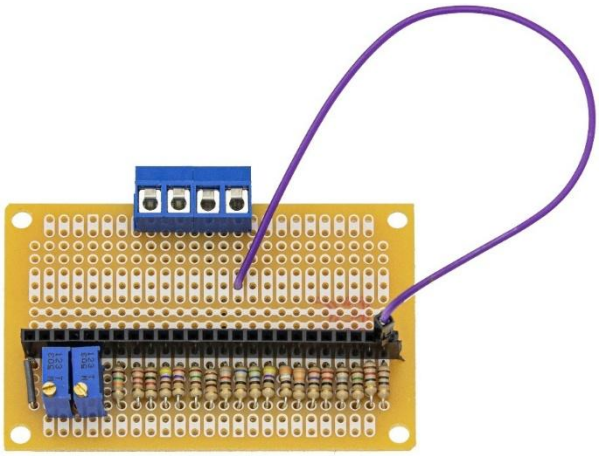

Figure 224 – Variable resistive load circuit.

The resistance values for each resistor tested were measured, including wiring resistance, with an accuracy of $\pm(0.05\%$ of the reading $+ 1\ LSD)$. The connection of the TEG modules and the load is represented in the schematic in Figure 225.

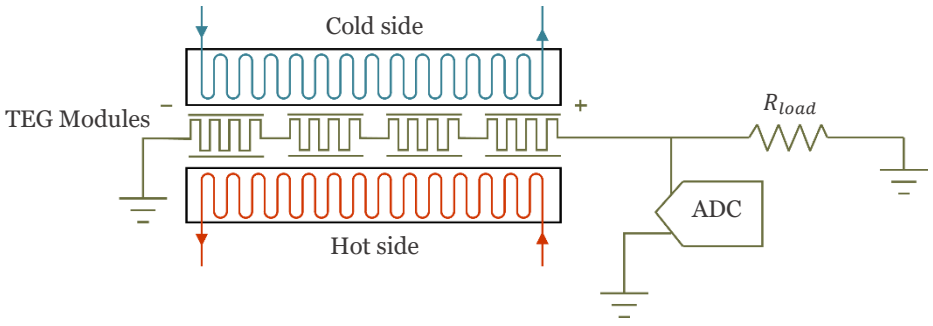

Figure 225 – Circuit of the connection between TEG modules, resistive load, and ADC.

The voltage drop across the resistor R_{load} is measured using a $10-bit$ ADC. Given the known resistance value for each resistor tested, the current and thus the power can be

calculated from these measurements. The following steps summarize the measurement process:

7.3.1. Electric power generation:

The ADC measures the voltage drop across the resistor, returning a value from 0 to 1023, that corresponds to a voltage of between 0 V and 5 V respectively. To calculate the voltage, this measurement is introduced into Equation (73):

$$V_{load} = \frac{ADC \cdot 5}{1023} \tag{73}$$

Where:

- V_{load} is the measured voltage drop across the R_{load} [V],
- ADC is the value returned by the ADC [-].

From here and knowing the value of R_{load}, the power can be calculated by replacing the known value of R_{load} and V_{load} in Equation (74)

$$P_{elec} = \frac{{V_{load}}^2}{R_{load}} \tag{74}$$

Where:

- P_{elec} is the generated power [W]

Resulting in Equation (75):

$$P_{elec} = \frac{\left(\frac{ADC \cdot 5}{1023}\right)^2}{R_{load}} \tag{75}$$

Which is directly calculated in the acquisition system, returning the electrical power generated (P_{elec})

7.3.2. Heat transfer

The heat flow ($\dot{Q}$) for both the cold and hot sides can be calculated using Equation (76) and Equation (78):

For the cold side:

$$\dot{Q}_c = \dot{V}_c \cdot \rho_c \cdot C_{p,c} \cdot \Delta T_c \tag{76}$$

In which ΔT_c can be obtained from Equation (77):

$$\Delta T_c = TWF4 - TWF3 \tag{77}$$

For the hot side:

$$\dot{Q}_h = \dot{V}_h \cdot \rho_h \cdot C_{p,h} \cdot \Delta T_h \tag{78}$$

In which ΔT_h can be obtained from Equation (79):

$$\Delta T_h = TWF2 - TWF1 \tag{79}$$

Where:

- $\dot{Q}_c$ and $\dot{Q}_h$ are the heat flows at the cold and hot sides respectively, [W].
- $\dot{V}_c$ and $\dot{V}_h$ are the volumetric flow rates for the cold and hot working fluids, respectively, [$c\mathrm{m}^3/s$].
- ρ_c and ρ_h are the cold and hot working fluid density, respectively [g/$c\mathrm{m}^3$].
- $C_{p,c}$ and $C_{p,h}$ are the specific heat capacities for the cold and hot working fluids, respectively [J/g. K].
- ΔT_c and ΔT_h are the difference between inlet and outlet temperatures for cold side and hot side, respectively, [K].
- $TWF1$, $TWF2$, $TWF3$ and $TWF4$ are the working fluid temperatures, measured at the inlet and outlet for the hot and cold sides respectively, [°C].

The average temperature for all the tests is -1.05 °C for the cold side, and 26.85 °C for the hot side. At these temperatures, and for the working fluid water-glycol mixture, the density at the average cold side temperature is 1.068 g/$c\mathrm{m}^3$, and at the average hot side temperature is 1.053 g/$c\mathrm{m}^3$. The specific heat capacities at these temperatures are 3.630 J/g · K for the cold side and 3.717 J/g · K for the hot side. With this in mind, $\dot{Q}_c$ and $\dot{Q}_h$ are calculated using Equations (80) and (81) respectively:

$$\dot{Q}_c = \dot{V}_c \cdot 1.068 \cdot 3.630 \cdot (TWF4 - TWF3) \quad (80)$$

And

$$\dot{Q}_h = \dot{V}_h \cdot 1.053 \cdot 3.717 \cdot (TWF2 - TWF1) \quad (81)$$

7.3.3. Energy requirements

The feasibility of powering an acquisition system with the generated power must consider the system's energy requirements. The conceptualized acquisition system comprises an ESP32 microcontroller and a voltage divider to read the FDS. According to the ESP32 Datasheet [149], power is given in mA, with the knowledge that the working voltage is 3.3 V Equation (82) can be applied to the datasheet values.

$$P_{op} = V_{op} \cdot I_{op} \quad (82)$$

Where:

- P_{op} is the electrical power consumption of the operation [mW],
- V_{op} is the operating voltage of the ESP32 [V],
- I_{op} is the electrical current drawn by the ESP32 during operation [mA].

This was used to calculate electric power consumption in mW, as presented in Table 64 for the different modes, together with the time required to execute each objective:

Table 64 – ESP32 power requirements in different modes, adapted from [149].

Mode	Objective	Execution time	Power consumption
Active	Data transmission	< 1 s	330 mW to 792 mW
Modem-sleep	Execute sensor readings	50 ms	66 mW to 224 mW
Light-sleep	Wait for next frost measurement	-	2.64 mW

The system's energy usage per operation is given by Equation (83)

$$E_{op} = P_{op} \cdot \Delta t_{op} \quad (83)$$

In which,

- E_{op} is the required energy for that operation [mJ],
- Δt_{op} is the operation execution time [s],

Based on frost formation studies [97], it is reasonable to assume a situation in which for worst-case scenarios, defrosting is required once per hour. Therefore, to implement an effective frost metering sensor, the minimum requirement would be to transmit data at least once per hour. If a measurement frequency of one reading every minute is applied, the evolution of frost formation could also be obtained, which could help assessing frost formation conditions and predict future defrosting needs.

To calculate the total energy used, Equation (84) was used:

$$E_{tot} = P_m \cdot \Delta t_m + P_t \cdot \Delta t_t + P_s \cdot \Delta t_s \quad (84)$$

Where:

- E_{tot} is the total energy consumption during the analysed period [mJ]
- P_m is the power consumption during the measurement phase [mW],
- Δt_m is the duration of the measurement phase [s],
- P_t is the power consumption during the data transmission phase [mW],
- Δt_t is the duration of the transmission phase [s],
- P_s is the power consumption during the sleep phase [mW],
- Δt_s is the duration of the sleep phase [s].

For the period of one hour (3600 s), there would be 60 measurements, taking a total of 3 seconds, and one transmission lasting 1 second. This leaves a sleep time of 3596 s. Applying these values to Equation (84) and using the upper bounds from Table 64, the result in Equation (85) is obtained:

$$E_{tot} = 224.00 \cdot 3 + 792.00 \cdot 1 + 2.64 \cdot 3596 = 10957\, mJ \cong 11.0\, J \quad (85)$$

In conclusion, the theoretical maximum energy requirement for the presented scenario is calculated to be 11.0 J per hour of operation. This estimation seeks to establish a value that the TEG must surpass so that the system can operate effectively under the specified

conditions, accounting for the necessary data transmission, sensor readings, and sleep periods. Because the power requirements will vary over time—with long periods of low power usage during sleep and peaks of power consumption during transmission—an electrical energy storage system, such as a small battery, will be needed as a buffer. This storage system will accumulate energy during sleep periods to cover the excess energy consumption during reading and transmission.

However, inefficiencies should also be accounted for. Small IoT devices with the ability to generate enough power to be self-sustainable such as the one developed by [150] are recommended to generate approximately $20 - 30\%$ more energy than the calculated requirements. This additional energy accounts for inefficiencies in the power management system and energy losses during rectification and storage, safeguarding reliable operation and sustainability. To ensure reliable operation by compensating for potential energy losses in accumulation and transmission, a 30% margin was selected. This adjustment increases the final power requirement to 14.3 J, which will be the value used for all subsequent calculations and analyses.

This estimation method provides a practical approach to determining the energy consumption of the acquisition system. It offers an approximate value that will vary depending on the system requirements. Some systems may necessitate more frequent measurements and transmissions, while others may require less. Nonetheless, this approach establishes a target value, providing a guideline for evaluating the feasibility of powering frost detection sensors using TE energy harvesting.

7.4. Results for the TEG-HX power generation

The experimental tests conducted comprised three distinct 30 min intervals, each executed within a stable regime, after the system reached thermal equilibrium and operated in a non-transitional state. During this period, inlet and outlet working fluid temperatures, volumetric flow in the hot and cold sides, and power generated in the TEG were measured and registered every 3 *s* intervals.

7.4.1. Working fluid temperatures

Figure 226 shows the inlet and outlet temperatures of the working fluids across all three tests. The inlet temperature on the cold side of the TEG HX remained constant at an average of $-2.65\,°C$, with a standard deviation of $0.17\,°C$. Conversely, the inlet temperature on the hot side was modulated as the variable parameter across the tests.

This parameter underwent incremental adjustments of 12.7 K and 14.6 K, respectively. Consequently, these adjustments yielded average temperature differentials between the hot and cold sides of the TEG HX ($\Delta T_{h-c\ AVG}$) of 16.3 K, 27.6 K, and 39.8 K, with standard deviations of 0.28 K, 0.23 K, and 0.48 K, respectively for the three tests. The different experiments aim to simulate conditions like those found in different regions of refrigeration systems, as previously discussed.

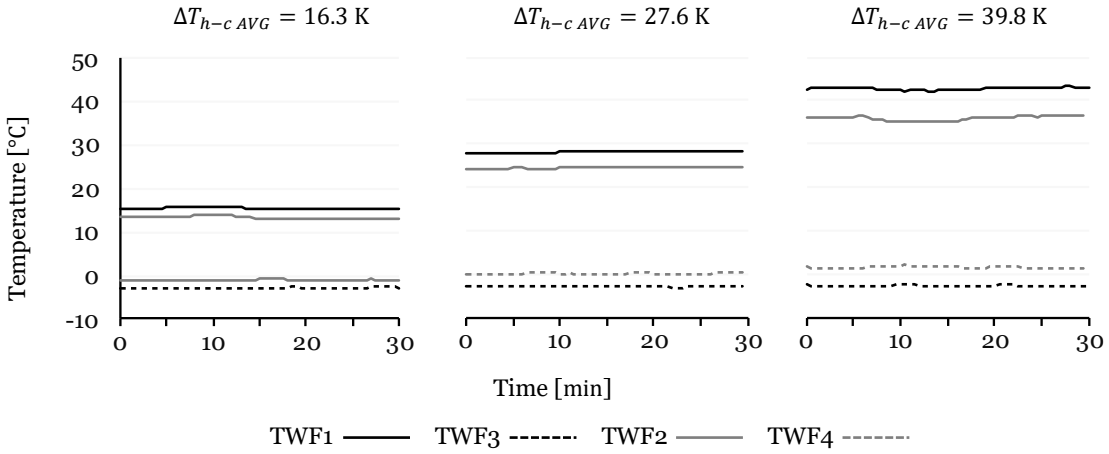

Figure 226 – TEG HX inlet and outlet temperatures for the cold and hot sides under the testing conditions.

The maintenance of the cold-side temperature and the incremental adjustments applied to the hot-side temperature between tests can be seen. While overall stability is observable, a slight temperature increase is discernible during the third test. During this test, a small increase of 0.37 K was measured from the start to the end of the test. Along with slight temperature fluctuations, this is reflected in the higher standard deviation values for Test 3 presented in Table 65. Nonetheless, the standard deviations remain within acceptable limits. These irregularities are mostly attributed to the hysteresis temperature control method of the thermostat on the hot side.

Table 65 – Average temperature differences between inlet and outlet and respective standard deviation for hot and cold sides across the three tests.

Test	ΔT_h **[K]**	$\sigma_{\Delta T_h}$ **[K]**	ΔT_c **[K]**	$\sigma_{\Delta T_c}$ **[K]**
Test 1: $\Delta T_{h-c\ AVG}$ = 16.3 K	−2.07	0.10	1.78	0.08
Test 2: $\Delta T_{h-c\ AVG}$ = 27.6 K	−3.65	0.06	3.04	0.09
Test 3: $\Delta T_{h-c\ AVG}$ = 39.8 K	−6.77	0.21	4.27	0.15

ΔT_c is consistently lower than. ΔT_h, this difference gradually increases from Test 1 to Test 3, primarily due to varying flow rates on the hot and cold sides during the tests.

7.4.2. Flow rates

The volumetric flow rate remained mostly constant throughout the data acquisition process for each of the tests; however, significant variations between tests are observable in Figure 227:

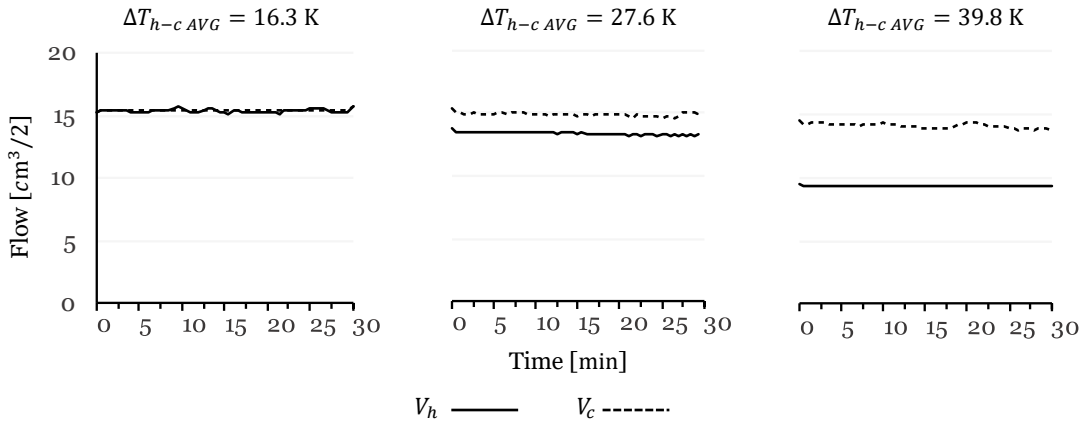

Figure 227 – TEG HX flow for the cold and hot sides under the three studied conditions.

Notably, there was a descending trend in the average volumetric flow rate on the hot side, although it remained mostly stable during testing, as confirmed by the standard deviation values presented in Table 66:

Table 66 – Average flow rates and respective standard deviation for hot and cold sides across the three tests.

Test	Vh $[cm^3/s]$	σVh $[cm^3/s]$	Vc $[cm^3/s]$	σVc $[cm^3/s]$
Test 1: $\Delta T_{h-c\,AVG}$ = 16.3 K	15.4	0.35	15.4	0.39
Test 2: $\Delta T_{h-c\,AVG}$ = 27.6 K	13.4	0.28	14.8	0.34
Test 3: $\Delta T_{h-c\,AVG}$ = 39.8 K	9.3	0.23	14.0	0.47

Conversely, the average volumetric flow rates on the cold side remained more stable during the three tests. A slight descending trend was observed in Test 3 due to a slow increase in working fluid pressure at the pump outlet. Nonetheless, volumetric flow rates remained relatively stable during testing, as confirmed by the standard deviation values.

The significant variations between tests stemmed from a decrease in the section of the flow limiter as the working fluid temperature increased. This was particularly observable

in the transition zones between tests. The low flow rate was intentional, to increase the temperature differential across the TEG HX. A low value of ΔT_c and ΔT_h can approach the temperature sensor's margin of error, resulting in a relatively large measurement uncertainty.

7.4.3. Heat flow

Utilizing the volumetric flow rates ($\dot{V}_c$ and $\dot{V}_h$), along with the calculated differences between measured inlet and outlet temperatures (ΔT_c and ΔT_h), the specific heat capacity ($C_{p,c}$ and $C_{p,h}$), and density of the hot and cold working fluid discussed in the preceding section, the heat flow ($\dot{Q}_c$ and $\dot{Q}_h$) was calculated. For this, Equations (80) and (81) were used for determining the heat flow on the cold and hot sides, respectively. The resulting plots depicting these calculations are illustrated in Figure 228.

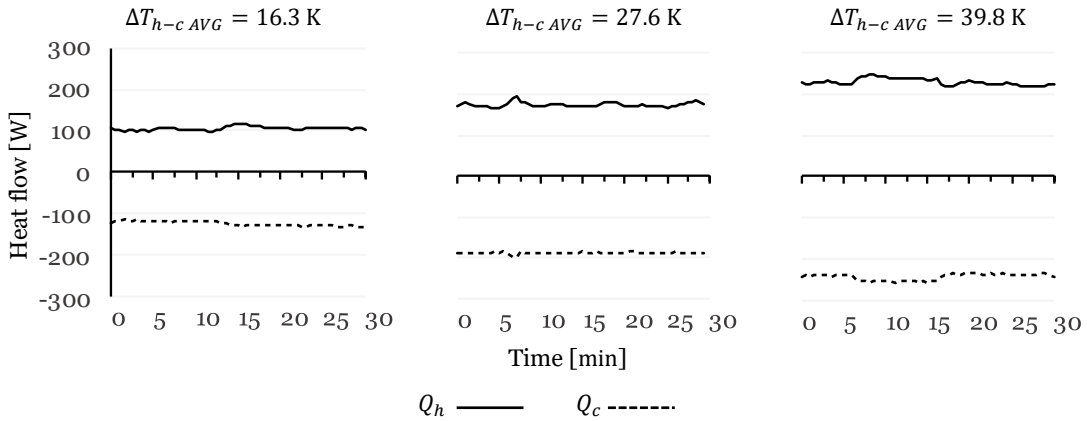

Figure 228 – Heat flow in the cold and hot sides for the three tests performed.

The results depicted in Figure 228 demonstrate that the heat flow differs significantly across tests. Heat flow remains relatively stable, on average. However, fluctuations are observed due to slight variations in temperatures and flow rates. The average heat flow for the hot and cold sides was as shown in Table 67.

Table 67 – Average heat flow rates and respective standard deviation for hot and cold sides across the three tests.

Test	$\boldsymbol{Q_h}$ $\boldsymbol{[W]}$	$\boldsymbol{\sigma_{Q_c}}$ $\boldsymbol{[W]}$	$\boldsymbol{Q_c}$ $\boldsymbol{[W]}$	$\boldsymbol{\sigma_{Q_c}}$ $\boldsymbol{[W]}$
Test 1: $\Delta T_{h-c\,AVG}$ = 16.3 K	−123.27	6.47	105.71	5.41
Test 2: $\Delta T_{h-c\,AVG}$ = 27.6 K	−187.94	4.69	174.14	6.82
Test 3: $\Delta T_{h-c\,AVG}$ = 39.8 K	−244.03	9.65	230.24	9.70

These results point towards a heat transfer rate slightly higher on the hot side compared to the cold side. The low value of the temperature differentials ΔT_c and ΔT_h makes the impact of even minor sensor reading inaccuracies relatively significant.

From Table 67, the average heat flow difference between the hot and cold sides for each one of the tests are 17.6 W for Test 1, 13.8 W for Test 2 and 13.8 W for Test 3.

These values are acceptable and are attributed to the heat power extracted by the TEG, thermal losses to the surroundings, and sensor accuracy.

7.4.4. Electric power generation

The power generated by the TEG during the tests is presented in Figure 229. The maximum generated power (P_{elec}) values of 0.20 W, 0.53 W and 0.93 W, were obtained for the respective tests with a R_{load} of 10.61 Ω. This graph illustrates the relation between the resistive load and power generation, for the different temperature differentials and a relatively low electrical output of the TEG under the given experimental conditions. While resistance values were tested up to 14861.44 Ω, only power measurements with R_{load} values up to 149.82 Ω are presented in Figure 229. Beyond this threshold, power generation slowly tends to zero (P_{elec} values for $R_{load} = 14861.44$ Ω were 0.21×10^{-3} W, 0.56×10^{-3} W and 1.01×10^{-3} W). Nonetheless, it is observed that, as expected, for every resistance value power increases with temperature difference, highlighting the TEG's capability to convert temperature differentials into electrical energy.

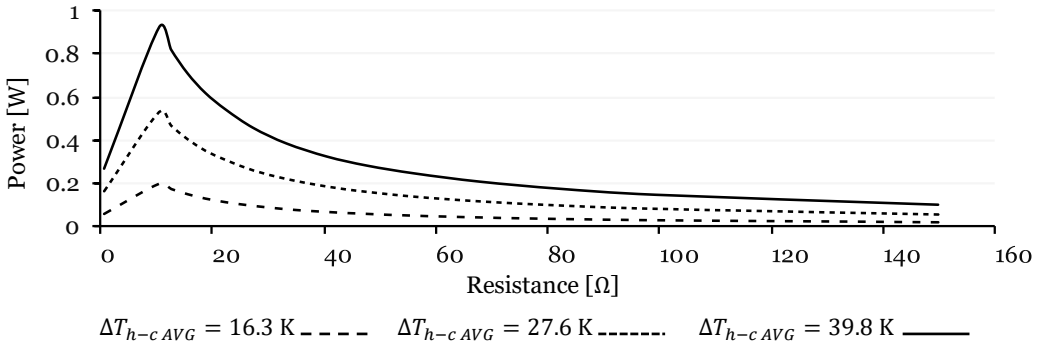

Figure 229 – Electric power generated using the TEG module for R_{load} values between 0.78 Ω and 149.82 Ω for each of the three tests performed.

When comparing the power involved in heat transfer with the power generated by the TEG, a significant difference in their magnitudes is observed, as shown in Table 68.

Table 68 – Maximum values of P_{elec} across the three $\Delta T_{h-c\,AVG}$ tests.

Test	$R_{P_{elec\,max}}$ [Ω]	$P_{elec\,max}$ [W]
Test 1: $\Delta T_{In\,h-c\,AVG} = 16.3$ K	10.61	0.20
Test 2: $\Delta T_{In\,h-c\,AVG} = 27.6$ K	10.61	0.53
Test 3: $\Delta T_{In\,h-c\,AVG} = 39.8$ K	10.61	0.93

The average heat transfer difference between the hot and cold sources ranged from 13.8 W to 17.6 W, while the TEG power ranged from 0.20 W to 0.93 W. This indicates that the TEG power is approximately two orders of magnitude smaller than the average heat flow difference between the hot and cold heat sources. Although this effect can be mitigated by implementing methods to reduce heat losses, and seeking more efficient TEG modules, the purpose of this study is not to find a very efficient method for energy production. Instead, the aim is to develop a method for powering a sensor in remote locations where a temperature differential already exists.

7.5. Discussion for the TEG-HX power generation results

The system detailed in the energy requirements section demands energy for six measurements and one transmission per hour, with the remaining time in a low-power sleep mode. This was calculated to require a total energy of 14.3 J per hour, which is 238.3 mW.

With this requirement in mind, and with results from the testing of the TEG HX it is now possible to assess whether this system can generate sufficient energy. Using the P_{elec} values obtained from Table 68, it is possible to determine the energy generated over a period of one hour using Equation (83). These calculations were performed, and the results are compiled in Table 69:

Table 69 – Energy generated over the period of one hour using the different tested conditions.

Test	Energy [J]
Test 1: $\Delta T_{In\,h-c\,AVG} = 16.3$ K	720.0
Test 2: $\Delta T_{In\,h-c\,AVG} = 27.6$ K	1914.5
Test 3: $\Delta T_{In\,h-c\,AVG} = 39.8$ K	3330.4

The energy generated by the TEG HX under the different tested conditions increases with the temperature differential. Even in the lowest temperature differential scenario (Test 1), the energy generated (720.0 J) exceeds by far the minimum energy requirement (14.3 J) necessary to power the frost measuring sensor system. As the temperature differential increases, the energy generation substantially surpasses the required power to maintain the sensing system active and transmitting data without the need to return to deep sleep, with Test 2 generating 1914.5 J and Test 3 generating 3330.4 J.

The tests were conducted using a TEG HX composed of four TE modules, each with an area of 50 × 50 mm. The findings indicate that a single TE module can generate 180.0 J of energy under the conditions of Test 1, 478.6 J under Test 2 conditions, and 832.6 J under Test 3 conditions. These values significantly exceed the minimum calculated energy requirement of 14.3 J. Based on the TE cell area (50 × 50 mm), the minimum required area per device can be extrapolated to be 14.1 × 14.1 mm for Test 1, 8.6 × 8.6 mm for Test 2, and 6.6 × 6.6 mm for Test 3. These calculations grossly assume that TEG energy production is a function of area not accounting for module uniformity, standard size availability, or variations in module efficiency. Thus, the actual required size would likely be larger. However, these estimates provide an indication of the potential for system miniaturization. This miniaturization is important as the implementation of a TEG HX will add a thermal resistance in a place where heat exchange is desired, which might be problematic. Nevertheless, a sensor with a TEG HX and a small footprint could have a negligible impact, especially in a larger industrial system.

These findings indicate that the TEG HX can generate sufficient energy to power the frost measuring sensor system under the tested conditions. This supports the feasibility of using a TEG for continuous operation of the system, assuming that potential losses in energy accumulation and transmission are adequately managed. The surplus energy generated, particularly in higher temperature differential scenarios, also provides a buffer to account for any additional inefficiencies or energy needs that may arise associated with higher transmission or measurement frequencies, or even allow adding an auxiliary system, such as a fan, to improve the efficiency of the TE module.

While the TEG HX can generate sufficient energy to power the frost measuring sensor system, it is important to note that this method is inherently inefficient. The TEG process captures only a very small fraction of the energy, with the majority being dissipated. This makes this method of powering the frost measuring sensors only viable if the primary goal of the system is heat transfer, and the generation of electrical energy is a secondary

benefit. In such cases, the TEG HX can be placed within the system to harness a minute portion of the heat, converting it into electrical energy to power low-energy devices, such as a demand defrost control sensor, without significantly impacting the primary heat transfer function of the HX.

7.6. Concluding remarks

This chapter aims to evaluate the feasibility of using a TE energy-harvesting module to power frost detection sensors in refrigeration systems. The experimental setup was adapted to simulate the conditions found in refrigeration units, in which TEG module could be applied. One side of the module was refrigerated while the other was heated, representing a temperature gradient where heat conduction is observed. The primary objective was to measure the power output of the TEG HX and assess its potential for remote sensor applications. The ability to convert heat flow into electrical energy for powering frost detection sensors presents a dual potential for energy efficiency. On one hand, the sensor contributes to frost detection for demand defrosting operations. On the other hand, the power for this system can be obtained from the dissipation of waste heat, such as in the condenser, by extracting energy from a temperature gradient that the refrigeration system creates to discard the heat. If waste heat is not available, a small amount of energy can be obtained from a location where heat flow is already desired, at the expense of introducing a small resistance to an HX. In such cases, the system should be designed to minimize disruption to normal system parameters, either by having a small footprint or by being placed in a way that its thermal resistance does not significantly impact the normal heat exchange process.

The TEG HX proved capable of producing enough energy to power the frost measuring sensor, with generated energy in all tested conditions exceeding the minimum required 14.3 J/h. Even under the smallest temperature differential, the energy output was far above the necessary threshold, showcasing the system's potential effectiveness across different scenarios, while leaving room for miniaturization.

The footprint reduction is therefore achievable, if extrapolating the results of this study, while disregarding other miniaturization considerations, the TEG HX module can be minimized to areas as small as 14.1 × 14.1 mm for Test 1, 8.6 × 8.6 mm for Test 2, and 6.6 × 6.6 mm for Test 3, reducing impact on overall system efficiency.

Despite its capability to generate sufficient electrical energy, this system is inefficient for electrical energy production compared to the amount of energy involved. This approach

is practical only in scenarios where heat exchange is already occurring and generating electrical energy is a secondary objective, such as placing a TEG between the evaporator and intake air, between the condenser and refrigerating air, or in the liquid-to-suction line HX used to superheat the gas and subcool the liquid, as demonstrated by Attar et al. [148]. This approach ensures that the TEG generates electrical power without adding undesired thermal loads to the refrigeration system, which would otherwise have a negative impact, surpassing any positive contribution a frost measuring sensor could bring.

Chapter 8

Conclusions and future works

This final chapter synthesizes the primary findings of the research, evaluates the extent to which the initial objectives were met, and outlines promising directions for future investigation. The conclusions are structured to address the main contributions of the thesis, covering the experimental setup, the development and validation of resistive frost detection sensors, and the role of the CV method as a verification tool.

8.1. General conclusions

Demand defrosting strategies are a way to improve refrigeration efficiency as traditional time-based controls are set for worst-case scenarios, leading to excessive and unnecessary defrost cycles, and excessive defrosting durations. The optimal time between defrosts can vary widely, depending mainly on ambient temperature and humidity, highlighting the inefficiency of a fixed-schedule defrost control. By adapting to actual system and environmental conditions, demand defrosting improves energy efficiency, enhances temperature stability, and increases system reliability.

To enable demand defrosting through direct frost measurement methods, the literature review identified several sensor technologies that could be implemented. Fiber-optic, piezoelectric, capacitive, computer-vision, and photoelectric methods were among the technologies found. The photoelectric sensor, in particular, demonstrated considerable potential. The TEPS operates by measuring frost accumulation as it blocks a light beam. A 24-hour comparative test confirmed its effectiveness, as the TEPS-controlled system initiated only eight defrost cycles, compared with the 30 cycles triggered by the default time-control method. The capacitive sensor also shows strong potential and currently represents one of the most mature approaches in frost detection research. Its measurements allow a clear distinction between different phases of frost accumulation and can be used to trigger defrost cycles based on a predefined threshold once a certain frost level is detected. Moreover, its ability to detect water provides an additional advantage, enabling the same sensor to monitor defrost completion.

Despite the proven success of such technologies, the resistive sensor was chosen as the focus of this thesis due to its compelling combination of cost-effectiveness, simplicity, and detection ability. These attributes make it an attractive candidate for practical application. The literature also indicated a relative scarcity of focused research on the

development of this specific sensor type, presenting an opportunity for a novel scientific contribution.

The primary objective of this thesis was therefore to contribute to the scientific progress of energy efficiency in refrigeration systems by investigating, developing, and experimentally testing cost-effective resistive sensors for the detection of frost formation, with the goal of future use in demand defrost applications. This work successfully achieved its goals by designing, fabricating, and validating several novel resistive sensor configurations against an objective ground truth provided by a custom-developed CV frost detection method, and AH based dry HX detector.

The key findings and contributions of this work can be summarized as follows:

Advancements in the development of resistive frost detection sensors by introducing and experimentally validating several configurations that demonstrated distinct improvements in robustness, reproducibility, and integration potential. These developments were complemented by the design of auxiliary validation tools, which combined CV and AH-based metrics to provide an objective reference for frost detection and defrost assessment.

In parallel, signal conditioning and processing strategies were developed to enhance sensor performance and reliability, covering temperature-compensation models and control methods to mitigate electrolysis-induced noise and sensor electrode degradation.

Beyond resistive sensing, the conceptual exploration of energy-autonomous modules demonstrated the feasibility of self-powered, wireless frost detection systems, extending the relevance of this research to energy-efficient refrigeration and its integration within WSN and IoT frameworks.

Finally, the results emphasized the importance of sensor placement and calibration, demonstrating that practical implementation must account for the spatial variability of frost formation on HX surfaces.

In conclusion, this thesis has demonstrated that cost-effective resistive frost detection sensors, when properly positioned and combined with suitable signal processing, can provide an effective solution for demand-defrost control in refrigeration systems. However, further development is required to improve robustness in sensor placement techniques before these sensors can be reliably applied in real-world systems.

8.2. Conclusions regarding the experimental setup

The custom experimental setup was important to the success of this research, providing a controlled and instrumented environment for the study of frost formation and detection. The level of sensorization within the experimental setup allowed for data to be used in ways not initially anticipated, such as for AH-based defrost completion detection, temperature compensation, or even evaluating the feasibility of developing an energy-autonomous demand-defrost control module.

The setup enabled the reproducible generation of frosting and defrosting cycles under multifactor monitoring. Incorporating a TE-HX allowed for achieving lower temperatures in the working fluid and for testing energy generation using the same TE-HX as a thermoelectric generator.

It served as a versatile platform for the iterative development and validation of sensor prototypes. The ability to mount, test, and replace different sensor configurations, combined with the capacity for rapid frost generation, proved valuable for comparing the designs of the AGRS, FMRS, and AMRS under similar conditions.

The $HBDCD$ is one such example, as is the ability to monitor parameters such as flow and temperature, which supported not only straightforward analysis but also troubleshooting and understanding testing issues. Cross-referencing these variables revealed the dependence of the resistive-sensor signal on temperature, which initially masked phase-change phenomena. To address this, an analysis was performed using temperature data from four points of the setup ($TA1$, $TA2$, $TWF1$, and $TWF2$), confirming that nearly all signal variation could be explained by these temperatures ($R^2 = 0.998$). Among them, the outlet-air temperature was identified as the most representative variable, leading to the development of a simplified linear compensation model that avoided the need for four additional sensors in the system. This reduction in instrumentation complexity was an important step toward practical implementation, as adding multiple sensors would increase cost, complexity and maintenance requirements. However, this simplification reduced the sensor's ability to respond on time to rapid temperature changes in the HX, due to the inherent lag between the AL-HX and outlet-air temperature measurements. Nevertheless, this analysis concluded that compensation based on a single outlet-air temperature measurement was sufficient. The resulting model reduced the influence of temperature variation and produced an improved sensor signal that more accurately represented the resistive response to frost nucleation and melting.

The GUI was also useful in guiding and monitoring the experiments, enabling real-time control of experimental parameters and facilitating troubleshooting when needed. Providing continuous data visualization supported informed decision-making during testing.

Ultimately, the experimental setup proved to be a necessary tool that enabled the validation of the resistive sensors against an objective, quantitative ground truth provided by the auxiliary sensors and integrated CV system.

8.3. Conclusions regarding resistive sensor design and development

The core of this thesis was the design, development, and testing of resistive frost detection sensors. The iterative process led to several conclusions regarding their design and performance.

The first phase of experimental development focused on the AGRS. These sensors consisted of two exposed electrodes separated by a small air gap and relied on condensation droplets bridging the gap between electrodes to form a conductive path. Reliable operation required effective thermal coupling with the HX, which was challenging when the sensor electrodes lacked electrical insulation. In addition, consistent droplet formation between electrodes was difficult to maintain under vibration or strong airflow, and poor thermal contact or droplet precipitation often resulted in inaccurate or missed readings. Configurations with poor thermal coupling, such as the AGRS3, failed to detect condensation and frost. Among the developed AGRS designs, the AGRS5 achieved the most consistent detection performance by combining a thermally coupled clamp electrode with a front-facing cylindrical electrode, confirming the potential of compact, low-cost resistive sensors. It successfully detected condensation, frost, and defrost completion in 4 out of 5 tests.

Sensor position in regions more prone to dripping during defrosting also causes inaccurate detections of a dry HX. Examples of this are highlighted in sensors that were especially sensitive to excessive moisture, such as the AGRS4, which, due to its design and placement position, was too sensitive to water accumulation, especially if placed in lower regions of the HX more prone to water accumulation during defrosting.

The AGRS family highlighted the recurring challenge of maintaining a stable liquid bridge under airflow and vibration, emphasizing the need for a medium capable of retaining moisture between electrodes. To address this limitation, the next concept

investigated the usage of porous mediums with non-electrically conductive and good thermal conductor properties. These mediums were explored to be included between electrodes, starting with the CMRS. Porous alumina was chosen for its high electrical resistivity, good thermal conductivity, and ability to absorb water within its microstructure. While the ceramic medium successfully formed conductive bridges and responded rapidly to moisture, its rigid nature made it unsuited for repeated freeze–thaw cycling. Samples fractured after only a few cycles, proving mechanically unreliable for frosting environments. This finding motivated a shift toward more flexible and compliant materials that could accommodate volumetric expansion during freezing.

The subsequent development of the FMRS built upon this understanding, sacrificing some of the thermal conductivity of the medium. Cotton was selected for its electrical insulation when dry, high capillarity, and mechanical resilience under repeated frost-defrost cycles. The fabric medium enabled water retention and redistribution between electrodes through capillary action, forming stable conductive bridges during both frosting and defrosting. Various configurations were tested, differing in electrode number, spacing, and fabric wrapping method. Among these, FMRS4 demonstrated the most consistent and reliable performance, successfully detecting all five frost–defrost cycles with clear signal transitions. Its loosely tied cotton string partially exposed the electrodes, improving both heat transfer and moisture uptake, while maintaining electrical insulation. The signal morphology also provided diagnostic value: different curve shapes characterized frosting, while defrosting yielded smooth, and more severe signal drops due to water retention and drying within the fibres.

Following this, the AMRS1 explored the potential of flexible conductive polymers produced through FFF. Using a multi-material approach with conductive and insulating TPU, the AMRS1 achieved complete frost–defrost detection cycles with consistent repeatability. A distinctive feature was its signal behaviour: ADC values initially dropped at frost onset before gradually rising as frost thickened, suggesting an increased sensitivity to temperature changes. The sensor demonstrated the feasibility of additive manufacturing for globally reproducible, low-cost frost detection sensors, remaining a strong candidate for future research.

Among the different sensor technologies evaluated, the configuration that achieved the best overall performance was the FMRS4. The AMRS1 also demonstrated strong potential, ranking second, and thus stands out as a promising candidate for future developments due to its reproducibility and adaptability through AM. Based on these

results, the FMRS4 was selected as the reference sensor for the subsequent developments and validation procedures conducted in this work.

Data acquisition must consider electrolysis, as it will affect sensor readings if not addressed. This effect also causes electrode degradation and the generation of ions that disrupt readings. The implementation of a PWM-based reading method, with a duty cycle of 1.7%, mitigated this issue by minimizing the sensor medium exposure to an electric field, thereby preventing ion and gas formation and consequently allowing stable, repeatable measurements. Other techniques could be implemented such as alternating electrode polarity, however, the low duty cycle and consequent data acquisition rate of three seconds proved more than enough to detect frost, and future applications that do not require the depth of analysis of this work, such as commercial applications could even reduce this duty cycle by lowering the acquisition rate by one or even two orders of magnitude. Using noble metals such as gold or platinum for the sensor electrodes could also mitigate electrolysis effects and electrode degradation with time, as these materials will stop the release of ions into the water caused from oxidation reactions. Given the very small electrode volume ($\approx 0.0015\ \text{mm}^3$), the added cost would remain minimal.

Applying smoothing filters also improves signal readability, however, the most critical aspect of signal conditioning is temperature compensation. Ideally, compensation should be derived from at least the HX outlet air temperature, which was found to most accurately represent the thermal conditions influencing the sensor. While this introduces slight complexity by requiring an additional temperature measurement, the system remains cost-effective, as existing temperature sensors within the refrigeration unit can often be repurposed, and if an extra sensor is needed, its implementation adds minimal cost relative to the overall system. In future implementations, compensation could be performed algorithmically by estimating temperature variation from operating time and calibrated system parameters. Since temperature compensation does not need to be perfect, and only sufficiently accurate to prevent false triggers from thermal fluctuations, such an approach could eliminate the need for additional hardware while preserving detection accuracy.

8.4. Conclusions regarding the computer vision method

The CV method developed in this thesis served as an objective tool for validating the performance of the resistive sensors. What began as an idea to compare image-based measurements against sensor data evolved into a comprehensive method for analysing frost formation and accumulation on the HX surface. Through spatial processing using

a 12 × 12 tile grid, the method produced frost formation maps and revealed the inherent heterogeneity of frost growth across the HX surface. This capability proved valuable for optimizing sensor placement, helping to avoid regions that frost too quickly, too slowly, or are affected by HX defects. The same analysis also allowed the study of recurring frost formation patterns, supporting diagnostic evaluation of HX behaviour and guiding ideal sensor positioning, a significant step to achieve frost detection and defrost completion using the resistive FDS developed in this work.

The CV method proved to be robust, repeatable, and computationally efficient, providing a reliable ground truth for frost coverage that surpassed subjective visual inspection. By converting images to binary frost masks and quantifying the pixel ratio, it produced smooth and consistent frost-growth curves across all tests, granted constant illumination with sufficient power to overwhelm potential external noise was provided. Beyond validation, the technique emerged as an independent, lightweight method for frost detection and is currently being evaluated as a standalone solution, as will be discussed in the Complementary works section of this chapter.

While highly effective as a laboratory tool, the CV method has practical requirements for broad commercial implementation. It requires a fixed camera position, controlled illumination or an illumination calibration procedure, and a minimum focal distance from the HX separated by a clear line of sight, which can be challenging in compact or enclosed refrigeration units. Nevertheless, its low processing demands and modest resolution requirements make it feasible to explore cost-effective embedded cameras capable of operating in confined spaces. This approach may be suited to large, refrigerated chambers, where physical space is less restrictive and the relative cost of a camera-based system becomes negligible compared with the efficiency gains it enables.

The performance of the method, however, also depends on the optical contrast provided by the HX surface. For highly reflective or bright HX materials, alternative image-processing thresholds or illumination wavelengths may be required. Future improvements could explore the use of multispectral imaging, infrared, ultraviolet, or other spectral bands, where the differences in reflectance between metal surfaces, water films, and frost layers can be more pronounced, potentially enabling even the detection of thin water layers.

Although the current CV method does not directly detect the presence of water, evidence from the uncertainty analysis presented in Annex C.4 indicates that it is possible to make it sensitive to drying and condensation phenomena, as well as to variations in frost

accumulation. For this purpose, thresholds closer to the extremes must be employed. As this approach leads to a loss of information, it should be used in conjunction with the developed method to broaden its scope, rather than replace it, thereby preserving its frost detection capability.

In summary, the CV method proved to be a valuable research tool that validated the resistive-sensor technology by detecting the frost accumulation within the HX with a high degree of reliability. Furthermore, this method provided deeper insight into the spatial dynamics of frost formation, informing improved sensor design and placement strategies. It also shows clear potential to evolve into a standalone, vision-based method for frost detection and defrost control in HXs.

8.5. Conclusions regarding frost detection using resistive sensors

To quantify the performance of the FMRS4, the sensor was evaluated in three series of tests. Acquisition and processing parameters were held constant across all test runs, changing only defrost initiation threshold and defrost duration between series so that results could be compared directly, and event times were analysed both absolutely and normalised to the starts of operation and defrost.

To assess the sensor's capability to detect frosting events and to support real-time control, two FDS-derived detectors were implemented. FND and DCD. Both operate causally on the conditioned sensor signal (temperature-compensated, smoothed, and converted to a finite-difference slope). Because they rely exclusively on past values, they are directly applicable for live operation without future data access. FND identifies nucleation by locking on a sustained negative trend followed by a persistent positive slope change, issuing a single pulse at onset. DCD supervises defrost termination by requiring a sequence of stable trends (fall, rise, stabilise) and validating that the recovered level matches the pre-defrost reference within a tolerance, issuing a pulse when the dry state is reached.

To complement this analysis and provide independent references, two auxiliary indicators were developed. $CVFND$, derived from the CV pipeline on a targeted tile close to the sensor, yields a nucleation timestamp that can be compared directly with FND. Because the computer-vision method, as used here, does not detect liquid water during defrost, the $HBDCD$ was introduced. It uses the inlet–outlet AH balance, with smoothing

and stability checks gated by defrost state, to mark the moment the HX becomes dry and thus to validate DCD.

The system performance during frost formation was also evaluated to contextualize sensor behaviour within the broader dynamics of the experimental setup. This analysis compared multiple measurement domains to understand how frost evolution influences and is reflected across them. CV metrics from both CVG and CVT were analysed, raw and temperature-compensated FDS outputs, and smoothed versus unsmoothed signals, to assess the effect of signal conditioning on clarity and event detection accuracy. Air and working fluid temperature profiles, together with relative humidity and its conversion to absolute humidity, were also examined. The absolute humidity difference (ΔAH) between HX outlet and inlet air proved a valuable quantitative indicator of mass transfer processes. Additionally, flow rate variations were observed, as working fluid viscosity changes with temperature directly affect overall heat exchange conditions. Establishing this experimental context allowed a clearer interpretation of FDS performance during testing and improved understanding of sensor readings within the system's operational behaviour.

The experimental procedure comprised three series. Series A established the baseline, Series B intentionally pushed the system to heavier frost loads and longer defrosting periods. Series C maintained the conditions of Series A, but due to a non-ideal sensor position, it had difficulty detecting defrost completion. This staging provided clean baseline data from Series A, extended-load behaviour from Series B, and an adverse placement condition from Series C to probe robustness.

The FND performed robustly. Across all twelve tests it triggered in every cycle, close to the $CVFND$, in ten tests $CVFND$ preceded FND, in the remaining two, FND was earlier by 0.05 min and 0.10 min. The CVT values at t_{FND} always lay within the nucleation region of the curve, indicating that the FDS-derived FND consistently occurred during nucleation. If excluding the first test of each series—where the experimental setup was still cooling—normalised detection times showed low dispersion, confirming that FND delivers repeatable, causal nucleation cues. The first test, however, allowed for analysis of system performance under slightly different conditions, which was adequate, only slightly changing both detector timings as expected.

The DCD also aligned closely with its auxiliary reference when the sensor was well placed. In Series A and B, DCD triggered in every test, and the average timing offset to the $HBDCD$ was low. Series A showed a slight tendency for DCD to anticipate $HBDCD$, while

Series B showed a modest lag, consistent with heavier frost loads and longer drainage/evaporation periods. Importantly, the $\overline{\Delta AH}$ at t_{DCD} approached zero in both series, indicating termination near mass-balance equilibrium. In Series C, DCD did not trigger in any test even though $HBDCD$ consistently indicated dryness at timings comparable to Series A. The local FDS signal failed to re-attain its dry plateau after defrost. This isolates sensor placement as the dominant factor governing dry detection reliability, because the auxiliary, system-level metric still returned a coherent dryness time.

Taken as a whole, the campaign demonstrates that FMRS4, when adequately placed and coupled with the established FND and DCD pipelines, consistently identifies the frost nucleation and the defrost completion with small lags to independent references under both baseline and extended-load regimes. The missed DCD in Series C was attributable to non-ideal placement that sustained local post-defrost wetting despite system-level dryness, underscoring that correct positioning within the fins is essential to guarantee dry-state resolution. However, even in this state, it managed to detect frost nucleation and trigger FND.

The design, development, and testing of the resistive sensors also highlighted the importance of sensor placement. Good thermal contact between the sensor and the HX surface promotes condensation and frosting directly on the electrodes. The selected location must be representative of the overall HX behaviour, avoiding regions prone to delayed or premature frosting, manufacturing defects, or areas with reduced airflow that lead to non-representative frost accumulation. Furthermore, care must be taken during placement so that the sensor is not in a position that shields water resulting from defrosting, which could cause failure in the detection of a dry HX. Finally, sensor position in regions more prone to dripping during defrosting might cause noise and delayed DCD.

The FMRS4 and its derived detectors provide a compact, cost-effective, and causal foundation for demand-defrost control. With proper placement, the system detects frost nucleation and defrost completion under near-equilibrium conditions, as demonstrated by 12/12 successful nucleation detections and 7/12 dry-HX detections—rising to 7/7 when excluding cases of poor sensor placement. $CVFND$ and $HBDCD$ independently validated these events. For future applications, an algorithm capable of deriving excessive frost accumulation directly from sensor data will be required to enable fully autonomous defrost control. These results confirm that the FMRS4 has the potential to constitute a practical solution for demand-defrost systems.

8.6. Technological maturity and intellectual property

The research conducted throughout this thesis led to the development of several technologies at different stages of maturity, some of which resulted in intellectual property protection.

8.6.1. Technology readiness level

To assess the technological maturity of the developments in this work, Technology Readiness Levels (TRLs) were assigned following the European Commission framework [151]. The TRL scale ranges from level 1, observation of basic scientific principles, to level 9, for a fully proven system operating in its intended environment.

In addition to the main developments presented in the previous chapters, several complementary and exploratory concepts described later in the Complementary works section of this chapter were also included in this assessment for completeness, as they were conceived and evaluated within the same research framework. The classification presented in Table 70, therefore, reflects the overall experimental validation status, robustness, and integration potential of all technologies developed in this thesis.

Table 70 – Estimated TRLs of the developed systems and methods.

System / Concept	TRL	Details
CMRS1	2	Conceptual design only
Energy-Autonomous Frost Sensing Module	3	Laboratory validation of thermoelectric generation demonstrated feasibility, partial functional testing
AGRS1 to AGRS6, FMRS1 to FMRS3, FMRS5, EMRS1 and EMRS2	4	Conceptualized, fabricated, and tested in a laboratory environment, but with limited success.
CV for demand defrosting in refrigerated chambers		Conceptual prototype designed for industrial application, not fabricated or experimentally validated.
Air AH based DCD	6	Developed and validated using experimental data. Effective $HBDCD$. Not yet embedded in control system.
CV method for frost detection		Developed, tested, and validated across multiple experiments. Accurate and robust frost detection.
Additive manufacturing resistive sensor AMRS1		Concept validated and prototype fabricated. Not integrated or long-term tested.
Fabric medium resistive sensor FMRS4		Most mature sensor design. Tested and validated under repeated cycles.

The technologies developed in this work span a wide range of readiness, from early conceptual designs (TRL 2–3) to validated prototypes operating in relevant laboratory environments (TRL 6). The FMRS4 and the CV method for frost detection are the most advanced, though the *HBDCD* and AMRS1 reached similar TRL levels after successful experimental validation. Overall, the work evolved from conceptual exploration to pre-operational prototypes, establishing a solid basis for future implementation.

8.6.2. Patents and patent applications

Two patent filings were submitted in the course of this work, both originating directly from the developments achieved in this research. The first, already published at the national level, protects the foundational concept of FMRS as summarized in Table 71.

Table 71 – Granted national patent (PT 116073 A) on the resistive frost detection sensor.

Title:	RESISTIVE SENSOR FOR FROST DETECTION
Number:	116073 A
Applicant:	UNIVERSIDADE DA BEIRA INTERIOR
Inventors:	PEDRO MIGUEL DE FIGUEIREDO DINIS OLIVEIRA GASPAR, MARTIM LIMA DE AGUIAR, PEDRO NUNO DINHO PINTO DA SILVA
Date:	Application - January 23, 2020 Publication: July 23, 2021
Summary:	The invention relates to a resistive sensor for detecting the deposition of water and the formation of ice on heat exchangers. It consists of a sensor body (1) separating two or more electrodes (2). A porous, non-conductive material (3) can be used between the electrodes to facilitate the creation of a water or ice bridge. The sensor is designed to be connected to a controller via terminals (4).
Image:	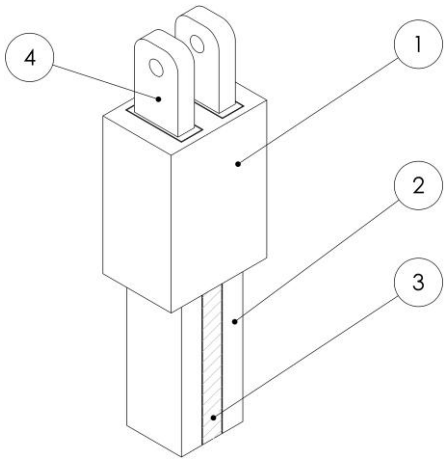

The patent PT 116073 A corresponds to the first medium-based resistive sensor developed in this research. As earlier AGRS had been reported, this patent protects sensors that include a medium material between electrodes. The patent text was formulated to include other potential media beyond frost for broader applicability. A second filing, currently registered as a provisional patent application, is summarized in Table 72.

Table 72 – provisional patent application (n.º 20242006661751) on the additive manufacturing-based resistive sensor.

Title:	ADDITIVE MANUFACTURING-BASED RESISTIVE SENSOR FOR FROST DETECTION
Number:	Application number 20242006661751
Applicant:	UNIVERSIDADE DA BEIRA INTERIOR
Inventors:	MARTIM LIMA DE AGUIAR, PEDRO MIGUEL DE FIGUEIREDO DINIS OLIVEIRA GASPAR, PEDRO NUNO DINHO PINTO DA SILVA
Date:	Filing: November 20, 2024
Status:	This provisional application establishes a priority date for the invention. A definitive patent application must be filed by November 20, 2025, to maintain this priority.
Summary:	The invention relates to a resistive sensor, fabricated via additive manufacturing, for detecting the deposition of water and the formation of frost on heat exchangers. The sensor is produced through a dual material fused filament fabrication process. It consists of a flexible non-conductive layer (1) made of insulating TPU, which serves as the base substrate. Printed onto this base is a conductive layer (2) with an interdigitated pattern that forms the left electrode (3) and the right electrode (4). These electrodes are separated by a small gap (5) to facilitate the creation of a water or ice bridge for detection. The sensor is designed to be connected to a controller via cable connection holes (6). For secure installation, securing holes (7) at each end allow the flexible sensor to be stretched and fastened around a fin, improving thermal contact.
Image:	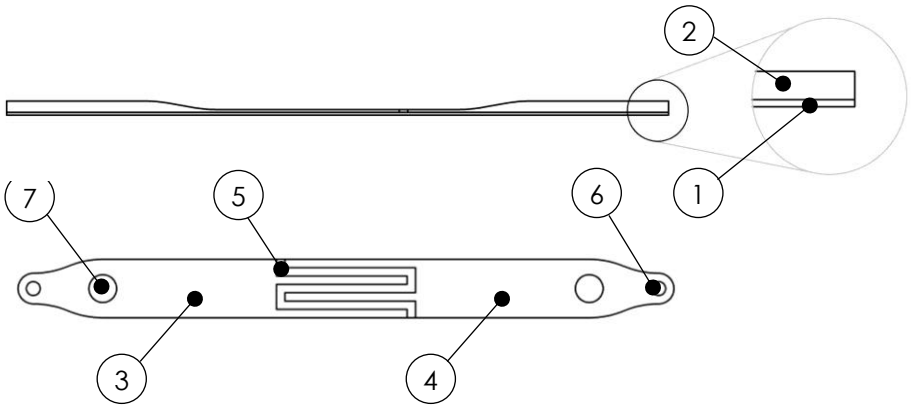

This second filing extends the principles defined in PT 116073 A to a new generation of sensors fabricated by additive manufacturing using conductive thermoplastic polyurethane. This invention introduces a fully 3D-printed, flexible, and cost-effective sensor capable of conforming to the fin geometries while maintaining the same detection principle. By integrating conductive and non-conductive layers in a single printing process, the design improves replicability, mechanical robustness, and integration potential for application.

8.7. Future works

This research has demonstrated the viability of FDS-based, CV-based and AH-based frost detection and defrost completion, opening several avenues for future investigation and development.

The next logical step in this research is to integrate the most promising sensor—FMRS4—into a commercial refrigeration unit. This transition from laboratory validation to real-environment testing will elevate its technological readiness from TRL 6 to TRL 7, demonstrating the sensor's functionality under operational conditions. In such an implementation, the processed sensor output would be linked to the unit's control system to enable true demand-defrost operation. Long-term field trials should be conducted to quantify energy savings compared to conventional time-based defrosting, while also assessing the sensor's durability, reliability, resistance to environmental contaminants, operational wear and behaviour under different frost formation conditions and morphologies.

For this application, further signal-processing development will be required. Although the current system detects frost nucleation, effective demand-defrost control depends on identifying not only the onset of frost but also its progression and the point of excessive accumulation. Future algorithmic development should therefore focus on expanding detection logic to classify multiple frost levels, enabling control systems to trigger defrost when needed. This could be achieved through mathematical modelling of signal morphology or through the application of machine-learning approaches that learn and classify characteristic signal patterns and curve shapes associated with different frost states. Such advancements would allow the system to autonomously infer frost severity and optimize defrost timing, further improving energy efficiency and operational reliability.

Future work on the computer-vision method should aim to make it more accurate and adaptable for real-world applications. One direction is to apply machine-learning models

that can automatically identify the state of the HX surface—dry, wet, or frosted—based on image data. These models could be trained using synchronized information from the resistive sensors and AH measurements to provide reference values during training.

In addition, building on the results of the visual sensitivity analysis (Annex C.4), future work could explore a dynamic or adaptive thresholding strategy. Such a method would binarize the snapshot with different *FT*, with higher values to focus on well-defined frost accumulation and lower values to enhance sensitivity to condensation events or even to enable a CV-based defrost-completion detection. This would expand the CV method into a comprehensive monitoring tool capable of tracking the full cycle.

Improvements in image acquisition could also be explored, including testing different lighting conditions, calibration routines, camera types, and viewing angles to enhance the contrast between frost, water, and dry metal surfaces. This is particularly important for untreated aluminium HXs commonly used in refrigeration systems, where reflections and low contrast will make detection more difficult. Higher-resolution cameras or lenses with optical zoom could also be used to increase image detail and allow more precise identification of frost density and distribution. In addition, future studies could explore using smaller analysis regions or even pixel-level FFM instead of large tiles to give a more detailed representation of frost growth. Finally, a dedicated prototype module could be developed for real installations, combining a compact camera, lighting system, and processing unit, to test its operation in commercial refrigeration systems and evaluate its performance as a demand-defrost control method in practical environments.

Another promising direction for future work lies in the integration of AH-based demand defrosting control by continuously measuring humidity at both the inlet and outlet of the evaporator, it becomes possible to estimate the rate of mass transfer occurring within the HX. During frost formation, the reduction in outlet AH relative to the inlet reflects the quantity of water vapour being deposited as frost. Once this mass transfer rate over time surpasses a predefined mass threshold, it could serve as a criterion to initiate defrosting. Conversely, during defrosting, monitoring the ratio between inlet and outlet absolute humidity can provide insight into the progression of evaporation and the return to a dry state. This presents a potential standalone research avenue, as it would enable frost and defrost monitoring through indirect mass transfer assessment using only cost-effective humidity and temperature measurements.

Additively manufactured sensors remain an attractive path even though FMRS4 was selected as the reference in this work. Future studies could explore new AMRS designs

and materials. Electrode layouts that use continuous toolpaths (no retractions) to avoid seam defects and reduce signal noise. Printing with smaller nozzles and thinner layers could enable slimmer, more closely spaced interdigitated electrodes and smaller overall footprints.

Beyond AM, sensor media and electrode materials offer further opportunities. Porous polymers, such as sintered or foamed structures, could combine the mechanical stability of a moulded medium with capillarity properties closer to textiles, while accommodating embedded metal electrodes. Using less reactive electrodes would also be worth testing to further suppress residual electrochemical effects and extend service life. Preliminary trials with carbon-fibre–based resistive elements showed promising behaviour; a more systematic evaluation of carbon fabrics, yarns, or printed carbon tracks could open an additional sensing route.

Because frost growth is spatially non-uniform, a logical next step is to replace the single-point measurement with an array of sensors distributed across the HX. An array would quantify location-dependent behaviour and, within a single run, provide multiple internal replicates that improve statistical power. It would also enable placement studies and simple voting or weighting schemes for robust triggering. For a specific HX model in a given product, such an array could be installed and tested under different operating conditions to identify which sensor positions are most representative of overall frost formation. Once identified, it would be possible to establish a correlation between that representative sensor and the remaining positions across the HX. This calibration could then allow future systems to rely on a single, optimally placed sensor while maintaining accuracy comparable to that of a full array. Although a similar spatial analysis can be achieved through CV, implementing it with distributed resistive sensors offers an alternative for systems that cannot accommodate a camera.

Building on the proof-of-concept demonstrated for the TEG-HX, future work could focus on developing a fully integrated, energy-autonomous sensor module. This prototype would combine a miniaturized thermoelectric generator, an optimized power-management circuit with energy storage (such as supercapacitors or compact batteries), and a low-power microcontroller with wireless communication capabilities. Further research should aim to improve overall efficiency, reduce system size, and explore more effective TE modules, as other studies have shown the potential for greater power generation, though still limited. Additionally, efficient energy storage and voltage regulation systems must be developed to enable the practical implementation of such a self-sustaining solution.

The experimental setup developed for this work reached a mature configuration through several iterative improvements, each implemented to support new experimental needs. While the final version enabled testing and data collection, it now provides a strong foundation for a new version. A future version could be redesigned from the ground up to integrate lessons learned and to improve experimental control, precision, and automation. One key area for improvement lies in the air humidification system. The current passive approach could be replaced by a more active humidification system to ensure consistent and controllable humidity levels. Additionally, employing a metallic HX similar to those used in commercial refrigeration systems would enhance representativeness and improve realism. Slightly increasing the HX dimensions could also facilitate sensor installation and accessibility between testing. The airflow path could benefit from greater uniformity by extending the wind tunnel length and optimizing flow, ensuring more homogeneous conditions across the HX. The image acquisition system could also be upgraded with optical zoom capabilities to capture finer spatial details without the need for digital cropping. Adding air pressure sensors at the AL-HX inlet and outlet could provide an additional metric for detecting excessive frost formation, since frost accumulation at the HX inlet increases airflow resistance and thus causes a measurable pressure differential. From a control standpoint, the next iteration of the experimental setup could be fully automated. Automatic actuation of doors, pumps, and thermoelectric modules would enable more precise and repeatable test sequences, eliminating manual intervention and associated delays and human error. Such automation would also make it possible to implement and test a pilot demand-defrost control loop, where defrost initiation and termination are triggered autonomously based on real-time sensor data. Finally, improving the thermal performance and air sealing of the tunnel would minimize heat losses and external air infiltration, allowing tighter regulation of temperature and humidity and, consequently, higher experimental reproducibility.

The voltage divider circuit used throughout this work proved to be a simple yet effective method for resistive sensing. However, future developments could explore more advanced signal-conditioning architectures to enhance sensitivity and discrimination between states such as frost, water, and air. For example, incorporating a high-input-impedance operational amplifier in an in-line configuration could amplify the minute current variations across the sensor, improving resolution in the high-resistance range where air and frost conditions are most difficult to distinguish. Additionally, implementing adaptive measurement ranges could automatically adjust the reference

resistance or gain according to the measured range, ensuring optimal sensitivity across the sensor's operating spectrum.

Ultimately, the evolution of this technology demands a multidisciplinary approach. Advancements in materials, sensor design, and signal conditioning must progress in parallel. Each improvement reveals new interdependencies: enhancing the sensor medium improves sensitivity but can expose new electrochemical challenges; mitigating hydrolysis stabilizes the signal but raises the need for finer thermal or electrical control. The development path, therefore, must remain iterative and integrative—continuously refining every subsystem as new requirements emerge from the interaction between heat transfer, mechanical design, electronics, and materials.

8.8. Complementary works

During the course of this work, several exploratory developments were undertaken that, while falling within the scope of the thesis, were not pursued to completion or did not evolve into consolidated results. These efforts are nonetheless relevant, as they reflect both the creative process inherent in research and the iterative path through which the main contributions of this work were shaped.

Some of these developments originated from external collaborations or preliminary design hypotheses that proved either too complex, too resource-intensive, or insufficiently aligned with the main research line. Despite not reaching a stage of full validation, they generated insights that influenced the direction of the thesis and highlighted promising opportunities for future exploration.

By documenting these unfinished developments, this section provides a more comprehensive account of the research process, underlining both the breadth of directions investigated and the role of failed or partial outcomes in shaping the consolidated contributions of this thesis.

8.8.1. Computer vision system for demand defrosting control in refrigerated chambers

Following the presentation of a work related to the CV method at the 26th IIR International Congress of Refrigeration [139], a multinational company specialized in the design and manufacturing of air heat exchangers expressed interest in the adaptation of this method for application in large, refrigerated chambers operating at ultra-low temperatures. This motivated the development of a conceptual prototype, designed to

extend the laboratory-scale method into a configuration suitable for testing under industrial conditions.

The proposed design enhanced the image acquisition method by introducing embedded processing capabilities, modularity, integrated lighting, and thermal insulation, enabling reliable operation under ultra-low-temperature conditions. It was based on off-the-shelf electronic components integrated within custom 3D-printed enclosures fabricated from low-temperature-resistant polymers and represented the first step toward the development of a dedicated, fully embedded architecture. The main system specifications are summarized in Table 73.

Table 73 – Main specifications.

Feature	Specification
Frost detection	Different levels of frost detection, adjustable defrosting trigger
Operational Temperature	Ultra-low temperatures
Field of View	120° wide angle or 75°
Illumination	Overwhelm external illumination noise
Thermal Insulation	Allows ambient temperature for electronic components. Low power.
Calibration & Adjustment	Adjustable mount, automatic calibration routines, debugging port
Processing	Local processing, expandable to networked or server processing
Rate of acquisition	Customizable up to 3 s

These specifications were defined with a focus on the adaptability and robustness of the system when operating under the extreme temperature conditions. The wide and configurable field of view allows the camera to monitor either the entire evaporator surface or selected regions of interest, while the synchronized LED illumination allows for consistent image quality regardless of external lighting. The inclusion of a customizable acquisition rate up to 3 *s* provides the necessary flexibility to balance data resolution and processing load, depending on the application scale. The local processing architecture reduces network dependency, improving reliability, whereas the possibility of remote or server-based processing enables future scalability and integration into more advanced and resource-intensive processing algorithms. The double-enclosure structure with embedded heating resistors allows safe temperatures for the system operation without requiring expensive low-temperature capable systems and protects against condensation, complementing the adjustable mount and calibration features that

facilitate both installation and maintenance. Figure 230 (a) displays the system assembled, in the purposed configuration, and Figure 230 (b) shows the cut view of the system allowing for the visualization of the inner enclosure.

(a) (b)

Figure 230 – Assembled CAD drawing of the whole system (a) and a cut view showing the inside the first enclosure (b).

The proposed prototype integrates the components summarized in Table 74, which outlines the function of each subsystem within the architecture.

Table 74 – System components.

No.	Function	Component
①	Control/ processing	Raspberry Pi Zero 2W
②	Image acquisition	Pi Camera Module 3
③	Thermal management	Internal heating element
④	Enclosures	3D-printed
⑤	Defogging	Heating element in window
⑥	Illumination	4 × 3 W LEDs

This architecture establishes a scalable foundation for a computer-vision-based frost-detection system capable of operating in ultra-low-temperature environments. The numbered components correspond to those shown in the exploded view of Figure 231.

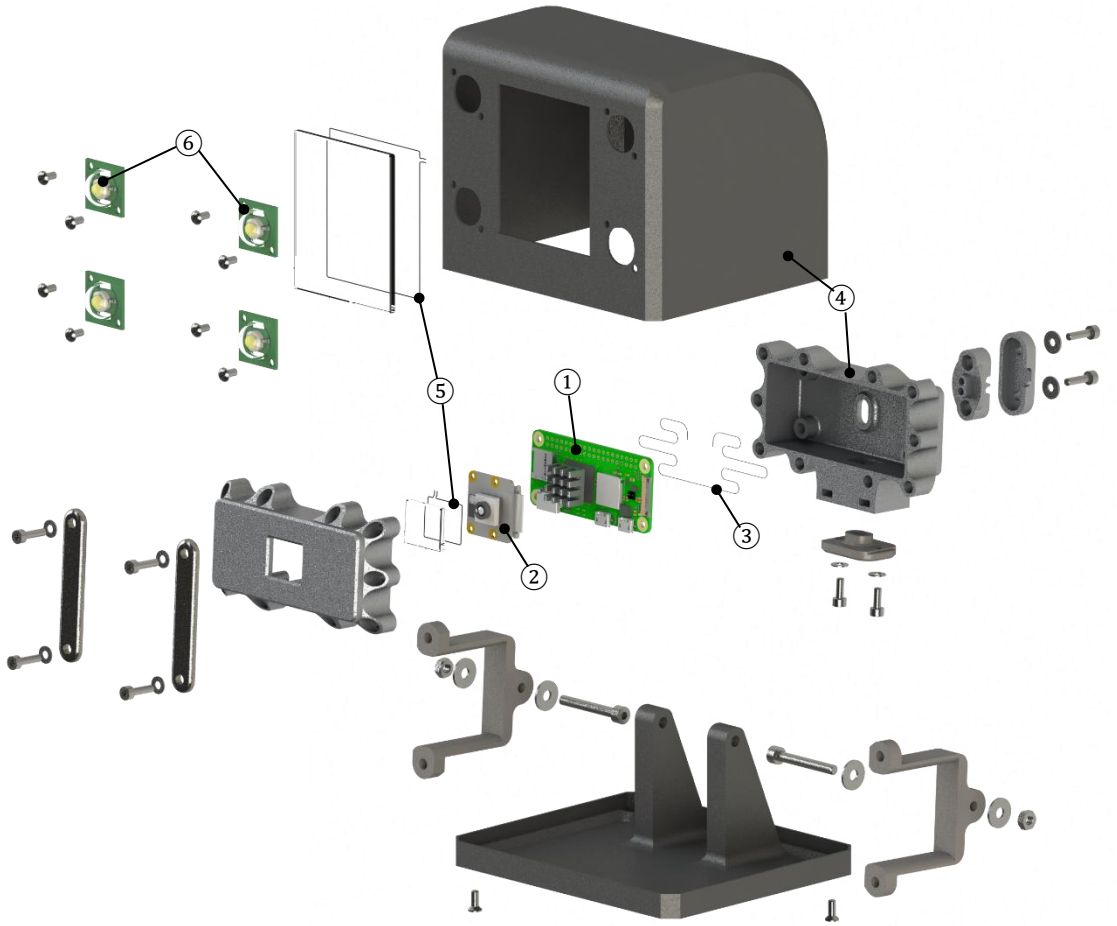

Figure 231 – Exploded view of the first proposed prototype.

The exploded view highlights how the processing unit, imaging system, and support hardware integrate within a compact assembly. The Raspberry Pi Zero 2W (①) serves as the local processing and control module, using the Pi Camera Module 3 (②), for image capture of the evaporator surface through the optical window. Surrounding these components, the internal heating element (③) maintains the temperature of the electronics within the operating range, preventing low temperature induced system failures. The entire system is housed inside custom 3D-printed enclosures (④), designed with a double-wall configuration that provides both mechanical support and thermal insulation. The transparent windows include a defogging heater (⑤) that prevents condensation and preserves image clarity, while four integrated 3 W LEDs (⑥) provide controlled illumination synchronized with image focus and acquisition.

These subsystems form a compact, low-cost, and modular device capable of image capture and processing in demanding thermal environments. Although this design did

not progress beyond the conceptual stage, it demonstrates a pathway toward the integration of computer-vision-based demand-defrosting in industrial refrigeration systems.

8.8.2. EWRS - Encapsulated Water medium Resistive Sensors

The encapsulated water medium resistive sensor (EWRS) concept was developed as an exploratory approach to indirectly detect frost formation through the phase change of a confined water volume. Two design variants were proposed and produced. The first, EWRS1, employed two internal electrodes and is shown as a complete model in the rendered view of Figure 232 (a) and with a cutaway of the capsule in Figure 232 (b). The second, EWRS2, featured a single central electrode surrounded by a conductive outer casing that served as the second electrode; it is shown as a complete rendered model in Figure 232 (c) and with the capsule sectioned in Figure 232.

Figure 232 – Rendered view (a) and rendered cut view (b) of the EWRS1, and rendered view (c) and cut view (d) of the EWRS.

The operating principle of this sensor is based on measuring the electrical conductivity of the water sealed within the enclosure. As the system cools, the resistivity between the electrodes increases sharply once the encapsulated water freezes. This effect effectively defines two states, liquid and solid, which act as detection thresholds analogous to a two-point temperature sensor, where the switching points correspond to the phase transitions of water.

The intended placement of the sensor was at the front of the evaporator, positioned a short distance away from the fins rather than in direct contact with them. This configuration was chosen so that the progression of frost from the fins toward the air stream would eventually bridge the gap and reach the sensor only when the frost layer

had reached a critical, pre-calibrated thickness. Consequently, the distance between the sensor and the HX defined the acceptable frost accumulation limit.

In normal operation, and exclusively in systems in which the air temperature entering the HX remains above the freezing point of water, the encapsulated medium stays in the liquid phase, and no frost detection occurred. Once the frost layer advances and contacts the sensor, thermal conduction through the frost triggers freezing of the encapsulated water, which was then detected electrically as a resistive transition. The concept, therefore, offered a potential means to detect excessive frost formation (rather than nucleation) without directly embedding the sensor into the fins.

Figure 233 illustrates this effect through two different calibration distances for the same encapsulated sensor. In Figure 233 (a), the sensor is positioned farther from the HX surface, and although the frost layer has formed, it has not yet reached the sensor, resulting in a negative frost-detection condition. In contrast, in Figure 233 (b), the sensor is calibrated closer to the HX, and under the same frost thickness, the frost now surrounds the sensor capsule, producing a positive detection condition and triggering a demand defrost signal.

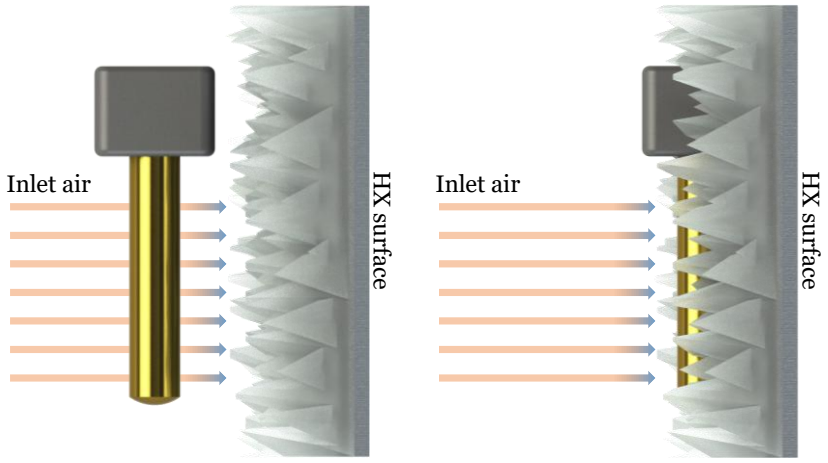

Figure 233 – Negative (a), and positive (b) frost-detection condition using the EWRS.

Although both EWRS1 and EWRS2 sensor variants were fabricated, as shown in Figure 234 (a) and (b) respectively, they yielded inconsistent results, their experimental evaluation revealed a limitation.

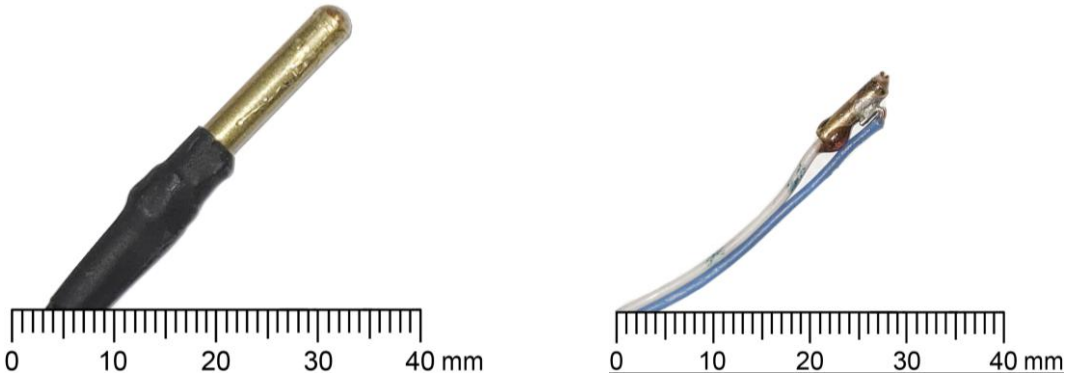

(a) (b)

Figure 234 – Picture of the EWRS1 (a) and EWRS2 (b) sensors produced

During early trials, the sensors were able to register correct early frost-detection events before eventually failing. The failures occurred after short operating periods due to internal pressure buildup that caused the casings to rupture. This behaviour was attributed to electrolysis, which, although minimal, became relevant when the electrodes were continuously immersed in water. The slow accumulation of gases inside the sealed chamber led to a gradual rise in internal pressure, ultimately resulting in over-pressurization and mechanical failure of the sensors.

Despite its premature termination, this experiment provided valuable insight into the electrochemical phenomena occurring in resistive frost-detection sensors. It exposed the need for a dedicated control approach to mitigate electrolysis, such as the PWM-based signal modulation, which was later implemented and proved decisive for improving sensor reliability.

From a conceptual standpoint, the encapsulated water medium sensor could still find potential application as a two-point phase-change sensor, effectively detecting the transition between liquid and solid states rather than absolute temperature. However, within the context of this thesis, its main contribution was methodological, as it highlighted the need to correct the influence of electrolysis on sensor performance and directly informed the design and control strategies adopted in subsequent sensor generations.

8.9. Final Remarks

This work established a foundation for frost detection and demand-defrost control through the integration of mechanical design, thermodynamics, sensing, and data processing. From fundamental principles to experimental validation and intellectual property protection, each stage contributed to transforming a conceptual idea into

demonstrable technology. The combined development of resistive sensors, auxiliary detection methods, and the supporting experimental infrastructure provides a comprehensive understanding of frost dynamics and a practical framework for future innovation in refrigeration efficiency. Beyond the technological advances, this research has also produced scientific contributions through publications in journals and international conferences, fostering knowledge exchange and consolidating the relevance of this field within the broader scientific community.

In the end, this work stands on the shoulders of giants, striving to add one more thin layer — an effort to raise the view just a little higher, so that we may see further still.

Acknowledgements

This work has been supported by:

- Project Centro-01-0145-FEDER-000017 - EMaDeS - Energy, Materials and Sustainable Development, co-financed by the Portugal 2020 Program (PT 2020), within the Regional Operational Program of the Center (CENTRO 2020) and the European Union through the European Regional Development Fund (ERDF).
- Project "PrunusPós - Optimization of processes for the storage, cold conservation, active and/or intelligent packaging and food quality traceability in post-harvested fruit products", project n.º PDR2020-101-031695, Partnership n.º 87, initiative n.º 175, promoted by PDR 2020 and co-funded by FEADER within Portugal 2020.
- ROBOTA SUDOE - Robotics, Automation, and Digitalization as Engines of Competitiveness and Growth for SMEs | Ref. INTERREG SUDOE 2021-2027, Priority 2, Specific Objective 1.1.
- Fundação para a Ciência e Tecnologia (FCT)
- R&D Unit C-MAST, "Center for Mechanical and Aerospace Science and Technologies", under project UIDB/00151/2020.
- University of Beira Interior

The author extends sincere gratitude for the essential financial backing and institutional opportunities provided by these entities, which were indispensable for the realization of this research and the completion of this dissertation.

References

[1] World Meteorological Organization, “State of the Global Climate 2024,” WMO, Geneva, 2025.

[2] S. R. Weart, The Discovery of Global Warming, Revised and Expanded ed., Cambridge, Massachusetts: Harvard University Press, 2008.

[3] N. Abas, A. R. Kalair, N. Khan, A. Haider, Z. Saleem and M. S. Saleem, “Natural and synthetic refrigerants, global warming: A review,” *Renewable and Sustainable Energy Reviews,* vol. 90, pp. 557-569, 7 2018.

[4] M. P. Chipperfield and S. Bekki, “Opinion: Stratospheric ozone – depletion, recovery and new challenges,” *Atmospheric Chemistry and Physics,* vol. 24, no. 4, pp. 2783-2802, 3 2024.

[5] European Parliament, “Interactive timeline: a guide to climate change negotiations,” 2025. [Online]. Available: https://www.europarl.europa.eu/infographic/climate-negotiations-timeline/index_en.html#event-2012.

[6] United Nations Framework Convention on Climate Change, “New collective quantified goal on climate finance (Decision text / overview materials),” UNFCCC, Baku, 2024.

[7] W. Bank, “A Water-Secure World for All.,” The World Bank Group, Washington, DC, 2019.

[8] Food and Agriculture Organization of the United Nations, The State of Food Security and Nutrition in the World 2025 – Addressing high food price inflation for food security and nutrition, Rome: FAO; IFAD; UNICEF; WFP; WHO;, 2025.

[9] United Nations Department of Economic and Social Affairs Population, “World Population Prospects 2024 Summary of Results,” United Nations, New York, 2024.

[10] T. Searchinger, R. Waite, C. Hanson and J. Ranganathan, “Creating a Sustainable Food Future,” World Resources Institute, Washington, DC, USA, 2019.

[11] D. Lin, L. Wambersie and M. Wackernagel, “Estimating the Date of Earth Overshoot Day 2025,” Global Footprint Network, Oakland, CA, USA, 2025.

[12] A. Galli, M. Antonelli, L. Wambersie, A. Bach-Faig, F. Bartolini, D. Caro, K. Iha, D. Lin, M. S. Mancini, R. Sonnino, D. Vanham and M. Wackernagel, “EU-27 ecological footprint was primarily driven by food consumption and exceeded regional biocapacity from 2004 to 2014,” *Nature Food,* vol. 4, no. 9, pp. 810-822, 9 2023.

[13] United Nations, “Transforming our world: the 2030 Agenda for Sustainable Development,” United Nations, New York, USA, 2015.

[14] United Nations, “The Sustainable Development Goals Report,” United Nations DESA, New York, USA, 2022.

[15] United Nations Environment Programme, “Food Waste Index Report,” United Nations, Nairobi, 2024.

[16] C. Mbow, C. Rosenzweig, L. G. Barioni, T. G. Benton, M. Herrero, M. Krishnapillai, E. Liwenga, P. Pradhan, M. G. Rivera-Ferre, T. Sapkota, F. N. Tubiello and Y. Xu, “Food Security. In: Climate Change and Land: an IPCC special report on climate change, desertification, land degradation, sustainable land

management, food security, and greenhouse gas fluxes in terrestrial ecosystems," Cambridge University Press, Cambridge, UK, 2019.

[17] G. A. González-Aguilar, J. F. Ayala-Zavala, G. I. Olivas, L. A. de la Rosa and E. Álvarez-Parrilla, "Preserving quality of fresh-cut products using safe technologies," *Journal für Verbraucherschutz und Lebensmittelsicherheit,* vol. 5, no. 1, pp. 65-72, 2 2010.

[18] International Institute of Refrigeration, "The Carbon Footprint of the Cold Chain (Informatory Note)," IIR, Paris, 2022.

[19] H. Hoang, T. Brown, E. Indergard, D. Leducq and G. Alvarez, "Life cycle assessment of salmon cold chains: comparison between chilling and superchilling technologies," *Journal of Cleaner Production,* vol. 126, pp. 363-372, 7 2016.

[20] L. Dumitraşcu, A. I. Nicolau, C. Neagu, P. Didier, I. Maître, C. Nguyen-The, S. E. Skuland, T. Møretrø, S. Langsrud, M. Truninger, P. Teixeira, V. Ferreira, L. Martens and D. Borda, "Time-temperature profiles and Listeria monocytogenes presence in refrigerators from households with vulnerable consumers," *Food Control,* vol. 111, p. 107078, 5 2020.

[21] A. Urquiola, G. Alvarez and D. Flick, "Frost formation modeling during the storage of frozen vegetables exposed to temperature fluctuations," *Journal of Food Engineering,* vol. 214, pp. 16-28, 12 2017.

[22] T. G. Hoffmann, A. F. Ronzoni, D. L. da Silva, S. L. Bertoli and C. K. de Souza, "Impact of household refrigeration parameters on postharvest quality of fresh food produce," *Journal of Food Engineering,* vol. 306, p. 110641, October 2021.

[23] L. Paravisini and D. G. Peterson, "Mechanisms non-enzymatic browning in orange juice during storage," *Food Chemistry,* vol. 289, pp. 320-327, 8 2019.

[24] P. Pourashouri, M. J. Chapela, M. Atanassova, A. G. Cabado, J. M. Vieites and S. P. Aubourg, "Quality loss assessment in fish-based ready-to-eat foods during refrigerated storage," *Grasas y Aceites,* vol. 64, no. 1, pp. 22-29, 3 2013.

[25] D. Coulomb, "Refrigeration and cold chain serving the global food industry and creating a better future: two key IIR challenges for improved health and environment," *Trends in Food Science & Technology,* vol. 19, no. 8, pp. 413-417, 8 2008.

[26] L. Manzocco, S. Calligaris, D. Mastrocola, M. C. Nicoli and C. R. Lerici, "Review of non-enzymatic browning and antioxidant capacity in processed foods," *Trends in Food Science & Technology,* vol. 11, no. 9-10, pp. 340-346, 9 2000.

[27] I. Dinçer and M. Kanoğlu, Refrigeration Systems and Applications, Second ed., Chichester: John Wiley and Sons, Ltd., 2010.

[28] K. Z. Skačanová and A. Gkizelis, "Technical report on energy efficiency in HFC-free supermarket refrigeration," Environmental Investigation Agency (EIA) & shecco, London, UK, 2018.

[29] UNEP, "United for Efficiency (U4E). Model Regulation Guidelines for Commercial," Nairobi, 2021.

[30] JARN, "World Refrigeration Equipment Market," *Japan Air Conditioning, Heating & Refrigeration News, Ltd.,* vol. https://www.ejarn.com/article/detail/85196, 9 2024.

[31] H. Demirpolat, "The energy efficiency and environmental analysis of open-type commercial display cabinet with a multi-flow air curtain design," *Sustainable Energy Technologies and Assessments,* vol. 60, p. 103555, 12 2023.

[32] A. Tunç, "Multideck Refrigerated Display Cabinet - CAD model," *GrabCAD,* 2016.

[33] P. D. Gaspar, L. C. C. Gonçalves and R. A. Pitarma, "Detailed CFD Modelling of Open Refrigerated Display Cabinets," *Modelling and Simulation in Engineering,* vol. 2012, pp. 1-17, 2012.

[34] S. Mariano Nascimento, G. Galdi Heidinger, P. Dinis Gaspar and P. Dinho Silva, "Experimental Evaluation of the Influence of Consumers' Passing Velocity on the Thermal Performance of Open Refrigerated Display Cabinets," in *16th International Refrigeration and Air Conditioning Conference at Purdue, 2016*, West Lafayette, IN, USA, 2016.

[35] C. J. L. Hermes, J. Boeng, D. L. da Silva, F. T. Knabben and A. D. Sommers, "Evaporator Frosting in Refrigerating Appliances: Fundamentals and Applications," *Energies,* vol. 14, no. 18, p. 5991, 9 2021.

[36] J. Cai, J. B. Jensen, S. Skogestad and J. Stoustrup, "On the trade-off between energy consumption and food quality loss in supermarket refrigeration systems," in *2002 American Control Conference*, Seattle, WA, USA, 2008.

[37] M. L. d. Aguiar, P. D. Gaspar and P. D. d. Silva, "Frost Measurement Methods for Demand Defrost Control Systems: A Review," in *IAENG World conference on engineering 2018*, London, 2018.

[38] M. L. d. Aguiar, P. D. Gaspar and P. D. d. Silva, "Frost Measurement Sensors for Demand Defrost Control Systems: Purposed Applications in Evaporators," in *Transactions on Engineering Technologies*, Singapore, Springer Singapore, 2019, pp. 159-171.

[39] M. L. d. Aguiar, P. D. Gaspar and P. D. d. Silva, "Frost Measuring and Prediction Systems for Demand Defrost Control," in *Novel Technologies and Systems for Food Preservation*, Hershey, PA, IGI Global Scientific Publishing, 2019, pp. 24-50.

[40] M. L. d. Aguiar, P. D. Gaspar and P. D. d. Silva, "Current status and future trends of computational methods to predict frost formation," in *+AGRO 2018 - International Congress on Organizational Management, Energy Efficiency and Occupational Health and Safety in Agrifood Industry*, Castelo Branco, 2018.

[41] J. Wu, G. Ouyang, P. Hou and H. Xiao, "Experimental investigation of frost formation on a parallel flow evaporator," *Applied Energy,* vol. 88, no. 5, pp. 1549-1556, 5 2011.

[42] R. O. Piucco, C. J. Hermes, C. Melo and J. R. Barbosa, "A study of frost nucleation on flat surfaces," *Experimental Thermal and Fluid Science,* vol. 32, no. 8, pp. 1710-1715, 9 2008.

[43] F. Wang, C. Liang and X. Zhang, "Research of anti-frosting technology in refrigeration and air conditioning fields: A review," *Renewable and Sustainable Energy Reviews,* vol. 81, pp. 707-722, 1 2018.

[44] D. Li and Z. Chen, "Experimental study on instantaneously shedding frozen water droplets from cold vertical surface by ultrasonic vibration," *Experimental Thermal and Fluid Science,* vol. 53, pp. 17-25, 2014.

[45] C. J. L. Hermes, R. O. Piucco, J. R. Barbosa Jr. and C. Melo, "A study of frost growth and densification on flat surfaces," *Experimental Thermal and Fluid Science,* vol. 33, pp. 371-379, 2009.

[46] L. Kwan-Soo, K. Woo-Seung and L. Tae-Hee, "A one-dimensional model for frost formation on a cold flat surface," *Heat and Mass Transfer,* vol. 40, no. 18, pp. 4359-4365, 1997.

[47] A. Z. Şahin, "An analytical study of frost nucleation and growth during the crystal growth period," *Heat and Mass Transfer,* vol. 30, pp. 321-330, 1995.

[48] D.-K. Yang, K.-s. Lee and D.-J. Cha, "Frost formation on a cold surface under turbulent flow," *International Journal of Refrigeration,* vol. 29, pp. 164-169, 2006.

[49] A. Lüer and H. Beer, "Frost deposition in a parallel plate channel under laminar flow conditions," *International Journal of Thermal Sciences,* vol. 39, pp. 85-95, 2000.

[50] D. L. d. Silva, C. J. Hermes and C. Melo, "Experimental study of frost accumulation on fan-supplied tube-fin evaporators," *Applied Thermal Engineering,* vol. 31, no. 6-7, pp. 1013-1020, 5 2011.

[51] W. Wang, J. Xiao, Q. C. Guo, W. P. Lu and Y. C. Feng, "Field test investigation of the characteristics for the air source heat pump under two typical mal-defrost phenomena," *Applied Energy,* vol. 88, p. 4470–4480, 2011.

[52] C. Melo, C. J. Hermes and D. L. Silva, "Effect of frost morphology on the thermal-hydraulic performance of fan-supplied tube-fin evaporators," *Applied Thermal Engineering,* pp. 1060-1068, 2017.

[53] B. Na and R. L. Webb, "A fundamental understanding of factors affecting frost nucleation," *International Journal of Heat and Mass Transfer,* vol. 46, no. 20, pp. 3797-3808, 9 2003.

[54] T. Aihara, H. Gakumasawa, S. Maruyama and M. Hongoh, "Frost formation and defrosting on tube-array evaporators in a fluidized bed and an impinging jet," *Experimental Thermal and Fluid Science,* vol. 2, no. 1, pp. 65-71, 1 1989.

[55] W. Sheng, L. Pengpeng, D. Chaobin and L. Guixin, "Review of restraint frost method on cold surface," *Renewable and Sustainable Energy reviews,* pp. 806-813, 2017.

[56] A. B. Olcay, P. Avci, E. Bayrak, A. S. Dalkılıç and S. Wongwises, "Experimental investigation of frost issue on various evaporators having different fin types," *International Communications in Heat and Mass Transfer,* vol. 86, pp. 190-198, 2017.

[57] Y. Liu and F. A. Kulacki, "An experimental study of defrost on treated surfaces: Effect of frost slumping," *International Journal of Heat and Mass Transfer,* vol. 119, pp. 880-890, 2018.

[58] F. Chu, X. Wu and Y. Zhu, "Defrosting on horizontal hydrophobic surfaces and the shrink angle," *International Journal of Refrigeration,* vol. 71, pp. 1-7, 2016.

[59] F. Wang, C. Liang, Y. Zhang and X. Zhang, "Defrosting performance of superhydrophobic fin-tube heat exchanger," *Applied Thermal Engineering,* vol. 113, pp. 229-237, 2017.

[60] X. Liu, J. Yu and G. Yan, "A numerical study on the air-side heat transfer of perforated finned-tube heat exchangers with large fin pitches," *International Journal of Heat and Mass Transfer,* vol. 100, pp. 199-207, 2016.

[61] X. Wu, S. Hu and F. Chu, "Experimental study of frost formation on cold surfaces with various fin layouts," *Applied Thermal Engineering,* pp. 95-105, 2016.

[62] C. M. Joppolo, L. Molinaroli, S. De Antonellis and U. Merlo, "Experimental analysis of frost formation with the presence of an electric field on fin and tube evaporator," *International Journal of Refrigeration,* vol. 35, pp. 468-474, 2012.

[63] Y.-J. Gou, Z.-L. Liu, Y.-M. Liu, L.-Y. Huang and M. Zhang, "The study of frost formation under magnetic field," *Journal of Engineering Thermophysics,* vol. 30, no. 3, pp. 465-467, 2009.

[64] D. Li, Z. Chen and M. Shi, "Effect of ultrasound on frost formation on a cold flat surface in atmospheric air flow," *Experimental Thermal and Fluid Science,* vol. 34, pp. 1247-1252, 2010.

[65] F. R. Ameen, J. E. R. Coney and C. G. W. Sheppard, "Experimental study of warm-air defrosting of heat-pump evaporators," *International Journal of Refrigeration,* vol. 16, no. 1, pp. 13-18, 1993.

[66] H.-J. Yin, Z. Yang, A.-Q. Chen and N. Zhang, "Experimental research on a novel cold storage defrost method based on air bypass circulation and electric heater," *Energy,* vol. 37, pp. 623-631, 2012.

[67] M. Song, S. Deng, D. Oan and N. Mao, “An experimental study on the effects of downwards flowing of melted frost over a vertical multi-circuit outdoor coil in an air source heat pump on defrosting performance during reverse cycle defrosting,” *Applied Thermal Engineering,* vol. 67, pp. 258-265, 2014.

[68] N. K. Anand, J. S. Schliesing, D. L. O'Neal and K. T. Peterson, “Effects of Outdoor Coil Fan Pre-Start on Pressure Transients during the Reverse Cycle Defrost of a Heat Pump,” *ASHRAE Transactions,* vol. 95, no. 2, pp. 699-704, 1989.

[69] H.-J. Choi, B.-S. Kim, D. Kang and K. C. Kim, “Defrosting method adopting dual hot gas bypass for an air-to-air heat pump,” *Applied Energy,* vol. 88, pp. 4544-4555, 2011.

[70] R. M. Abdel-Wahed, M. A. Hifni and S. A. Sherif, “Hot water defrosting of a horizontal flat plate cooling surface,” *International Journal of Refrigeration ,* vol. 6, no. 3, pp. 152-154, 1983.

[71] N. Snobe, K. Fukiba, S. Sato and Y. Yoshimura, “Method for defrosting heat exchangers using an air-particle jet,” *International Journal of Refrigeration,* vol. 60, pp. 261-269, 2015.

[72] H. Tan, G. Xu, T. Tao, S. Zhang and A. Luo, “Investigation on the ultrasonic propagation mechanism and its application on air-source heat pump defrosting,” *Applied Thermal Engineering,* vol. 107, pp. 479-492, 2016.

[73] L. Barelli, G. Bidini and S. Moraglia, “Development of an Innovative Defrosting System for Commercial Chiller Evaporators Through Piezoelectric Elements Application,” in *International Mechanical Engineering Congress and Exposition*, Anaheim, California USA, 2004.

[74] M. Amer and C.-C. Wang, “Review of defrosting methods,” *Renewable and sustainable energy reviews,* vol. 73, no. 2, pp. 53-74, 2017.

[75] J. Xiao, W. Wang, Q. C. Guo and Y. H. Zhao, “An experimental study of the correlation for predicting the frost height in applying the photoelectric technology,” *International Journal of Refrigeration,* vol. 33, pp. 1006-1014, 2010.

[76] Y. Jiang, J. Dong, M. Qu, S. Deng and Y. Yao, “A novel defrosting control method based on the degree of refrigerant superheat for air source heat pumps,” *International journal of refrigeration,* vol. 36, pp. 2278-2288, 2013.

[77] S. A. Tassou, D. Datta and D. Marriott, “Frost formation and defrost control parameters for open multideck refrigerated food display cabinets,” *Proceedings of the Institution of Mechanical Engineers - Part A - Power & Energy,* vol. 215, no. 2, pp. 213-222, 2001.

[78] B. A. Fricke and V. Sharma, “Demand Defrost Strategies in Supermarket Refrigeration Systems,” Oak Ridge National Laboratory, Oak Ridge, TN, 2011.

[79] K. Nawaz, B. Fricke and E. Ahmed, “A Critical Literature Review of Defrost Technologies for Heat Pumps and Refrigeration Systems,” Oak Ridge National Laboratory, Oak Ridge, TN, 2018.

[80] T. R. Buick, J. T. McMullan, R. Morgan and R. B. Murray, “Ice detection in heat pumps and coolers,” *Energy Research,* vol. 2, pp. 85-98, 1978.

[81] J. H. Jarrett, “A New Demand Defrost Control for Domestic Forced Draft Refrigerator Freezers and Freezers,” *IEEE Transactions on Industry Applications,* Vols. IA-8, no. 3, pp. 356-364, 1972.

[82] J. M. W. Lawrence and B. C. Parker, “Defrost control method and apparatus”. United States of America Patent 5,813,242, 29 September 1998.

[83] E. D. Muller, “A new concept for defrosting refrigeration plants,” *Kalte,* vol. 28, no. 2, pp. 52-54, 1975.

[84] J. Cui, W. Z. Li, Y. Liu and Z. Y. Jiang, "A new time- and space-dependent model for predicting frost formation," *Applied Thermal Engineering,* vol. 31, pp. 447-457, 2011.

[85] V. Bagyaveereswaran, S. S. Subramanian and R. Anitha, "Smart Defrost Control for Refrigeration System," *International Journal of Applied Engineering Research,* vol. 12, no. 22, pp. 12202-12207, 2017.

[86] Z.-K. Cao, C.-X. Zhang and B. Gu, "Application of a support vector machine algorithm for improving effects of defrosting of commercial refrigerated display cabinets in supermarkets," *HVAC&R Research,* vol. 19, no. 3, pp. 230-241, 2013.

[87] S. A. Kalogirou, "Applications of artificial neural-networks for energy systems," *Applied Energy,* vol. 67, pp. 17-35, 2000.

[88] D. Datta, S. A. Tassou and D. Marriott, "Frost prediction on evaporator coils of supermarket display cabinets using artificial neural networks," in *Proceedings of Clima 2000 Conference*, Brussels, 1997.

[89] W. Wang, J. Xiao, Y. Feng, Q. Guo and L. Wang, "Characteristics of an air source heat pump with novel photoelectric sensors during periodic frost–defrost cycles," *Applied Thermal Engineering,* vol. 50, no. 1, pp. 177-186, 1 2013.

[90] J. Ge, L. Ye and J. Zou, "A novel fiber-optic ice sensor capable of identifying ice type accurately," *Sensors and Actuators A: Physical,* vol. 175, pp. 35-42, 2012.

[91] Z. Li, W. Wang, Y. Sun, S. Wang, S. Deng and Y. Lin, "Applying image recognition to frost built-up detection in air source heat pumps," *Energy,* vol. 233, p. 121004, 10 2021.

[92] A. Troiano, E. Pasero and L. Mesin, "New System for Detecting Road Ice Formation," *IEEE Transactions on Instrumentation and Measurement,* vol. 60, no. 3, pp. 1091-1101, 3 2011.

[93] S. Roy, A. Izad, R. G. DeAnna and M. Mehregany, "Smart ice detection systems based on resonant piezoelectric transducers," *Sensors and Actuators A,* vol. 69, pp. 243-250, 1998.

[94] P. D. Gaspar, P. D. Silva, J. Nunes and L. P. Andrade, "Monitoring device of ice formation in evaporator surface of refrigeration systems," in *VI Ibero-American Refrigeration Sciences and Technologies*, Coimbra - Portugal, 2016.

[95] S. Sengupta, S. A. Sherif and K. V. Wong, "Empirical heat transfer and frost thickness correlations during frost deposition on a cylinder in cross-flow in the transient regime," *International Journal of Energy Research,* vol. 22, no. 7, pp. 615-624, 6 1998.

[96] M. Kandula, "Frost growth and densification on a flat surface in laminar flow with variable humidity," *International Communications in Heat and Mass Transfer,* vol. 39, no. 8, pp. 1030-1034, 10 2012.

[97] Y. Ge, Y. Sun, W. Wang, J. Zhu, L. Li and J. Liu, "Field test study of a novel defrosting control method for air-source heat pumps by applying tube encircled photoelectric sensors," *International Journal of Refrigeration,* vol. 66, pp. 133-144, 6 2016.

[98] Y.-H. Tai, A. S. A. Kamal, Y.-J. Park, P.-C. Tsai, Y.-L. Ho, P.-K. Wei, H. Daiguji and J.-J. Delaunay, "Real-Time Monitoring of Frost/Defrost Processes Using a Tapered Optical Fiber," *IEEE Sensors Journal,* vol. 21, no. 5, pp. 6188-6194, 3 2021.

[99] Z. Gao, J. Brechtl, K. Nawaz, B. Fricke, K. Gluesenkamp, N. Iavrik, P. Boudreaux and K. Li, "Advanced Frost Sensor for HVAC Applications," in *2024 ASHRAE Winter Conference*, Chicago, IL, 2024.

[100] Texas Instruments, "Capacitive Frost or Ice Detection Reference Design," 2017. [Online]. Available: https://www.ti.com/tool/TIDA-01465.

[101] Z. Gao, “Smart Frost Sensor for Frost Diagnostics and Defrosting Control [Poster],” in *Oak Ridge National Laboratory (ORNL)*, Oak Ridge, TN, USA, 2021.

[102] Y. Shen and S. Wang, “Condensation frosting detection and characterization using a capacitance sensing approach,” *International Journal of Heat and Mass Transfer,* vol. 147, p. 118968, 2 2020.

[103] S. Roy, R. G. DeAnna, M. Mehregany and E. Zakar, “A Capacitive Ice Detection Microsensor,” *Sensors and Materials,* vol. 12, no. 1, pp. 1-14, 2000.

[104] D. Caetano, P. D. Gaspar and P. D. da Silva, “Experimental testing of a resistive sensor for monitoring frost formation in refrigeration systems,” in *X Iberian Congress & VII congress on Ibero-American Refrigeration Sciences and Technologies*, Valencia, 2018.

[105] Stratasys Inc., “ GrabCAD Community Library,” 2024. [Online]. Available: https://grabcad.com/library. [Accessed 09 07 2024].

[106] Atmel Corporation, “ATmega328P Datasheet,” 2015. [Online]. Available: https://ww1.microchip.com/downloads/en/DeviceDoc/Atmel-7810-Automotive-Microcontrollers-ATmega328P_Datasheet.pdf.

[107] Arduino, “Arduino® UNO R3 User Manual,” 2025. [Online]. Available: https://docs.arduino.cc/resources/datasheets/A000066-datasheet.pdf.

[108] Maxim Integrated, “DS18B20 Programmable Resolution 1-Wire Digital Thermometer,” 2019. [Online]. Available: https://www.analog.com/media/en/technical-documentation/data-sheets/ds18b20.pdf.

[109] Arduino, “OneWire | Arduino Documentation,” [Online]. Available: https://docs.arduino.cc/libraries/onewire/. [Accessed 2021].

[110] Arduino, “DallasTemperature | Arduino Documentation,” [Online]. Available: https://docs.arduino.cc/libraries/dallastemperature/. [Accessed 2021].

[111] PTrobotics, “FS300A - G3/4 Water Flow sensor,” 2019. [Online]. Available: https://hi-ip.com/text/FS300A.pdf.

[112] Allegro MicroSystems, “ACS712ELC-20A - Fully Integrated, Hall Effect-Based Linear Current Sensor IC,” 2019. [Online]. Available: https://www.allegromicro.com/~/media/files/datasheets/acs712-datasheet.ashx. [Accessed 2022].

[113] Aosong Electronics Co., Ltd., “Digital humidity and temperature sensor AM2302,” 2015. [Online]. Available: https://cdn.sparkfun.com/assets/f/7/d/9/c/DHT22.pdf. [Accessed 2022].

[114] Arduino, “DHT sensor library | Arduino Documentation,” [Online]. Available: https://docs.arduino.cc/libraries/dht-sensor-library/. [Accessed 2021].

[115] D. Bolton, “The Computation of Equivalent Potential Temperature,” *Monthly Weather Review,* vol. 108, no. 7, pp. 1046-1053, 7 1980.

[116] Panasonic, “AVT3/AVL3 (FS-T) Switches Datasheet,” 2024. [Online]. Available: https://na.industrial.panasonic.com/file-download/762. [Accessed 2024].

[117] M. L. d. Aguiar, P. D. Gaspar and P. D. d. Silva, “Further development and experimental testing of a resistive sensor for monitoring frost formation in refrigeration systems,” in *The 25th IIR International Congress of Refrigeration (ICR 2019)*, Montréal, Canada, 2019.

[118] M. L. d. Aguiar, P. D. Gaspar and P. D. d. Silva, “Optimization and further experimental testing of a resistive sensor for monitoring frost formation in refrigeration systems,” in *6th IIR International Conference on Sustainability and the Cold Chain (ICCC 2020)*, Nantes, 2020.

[119] M. L. d. Aguiar, P. D. Gaspar, P. D. d. S. A. P. Silva and A. M. Martinez, "Medium materials for improving frost detection on a resistive sensor," *Energy Reports,* vol. 6, no. 12, pp. 263-269, 12 2020.

[120] M. L. d. Aguiar, P. D. Gaspar and P. D. d. Silva, "Testing of a resistive sensor with fabric medium for monitoring frost formation in refrigeration systems," in *Procedia Environmental Science, Engineering and Management*, Online conference, 2020.

[121] M. L. d. Aguiar, P. D. Gaspar and P. D. d. Silva, "Additive Manufacturing of a Frost-Detection Resistive Sensor for Optimizing Demand Defrost in Refrigeration Systems," *Sensors,* vol. 24, no. 24, p. 8193, 12 2024.

[122] M. L. d. Aguiar, P. D. Gaspar and P. D. d. Silva, "Mitigating Electrochemical Effects in Resistive Frost-Detection Sensors," *Applied Sciences,* vol. 15, no. 8, p. 4110, 4 2025.

[123] C. Jaccard, "Mechanism of the Electrical Conductivity in Ice," *Annals of the New York Academy of Sciences,* vol. 125, no. 2, pp. 390-400, 10 1965.

[124] T. Smolinka, "Fuels – Hydrogen Production | Water Electrolysis," in *Encyclopedia of Electrochemical Power Sources*, Elsevier, 2009, pp. 394-413.

[125] K. Qi and H. Huang, "Electrochemical migration behavior of copper under a thin distilled water layer," *Corrosion Communications,* vol. 11, pp. 52-57, 9 2023.

[126] Y. Cudennec and A. Lecerf, "The transformation of Cu(OH)2 into CuO, revisited," *Solid State Sciences,* vol. 5, no. 11-12, pp. 1471-1474, 11 2003.

[127] BullionByPost, "Platinum Price in EUR per Gram for Last 5 Years," 11 june 2024. [Online]. Available: https://www.bullionbypost.eu/platinum-price/5year/grams/EUR/.

[128] M. Hayashi, "Temperature-Electrical Conductivity Relation of Water for Environmental Monitoring and Geophysical Data Inversion," *Environmental Monitoring and Assessment,* vol. 96, no. 1-3, pp. 119-128, 8 2004.

[129] J. J. Barron and C. Ashton, "The Effect of Temperature on Conductivity Measurement [Technical paper]," *Reagecon Diagnostics Ltd,* no. TSP-07, 3, p. 5, 2007.

[130] Recreus, "Filaflex TPU 95A filament," Recreus, [Online]. Available: https://recreus.com/en/products/filaflex-95a. [Accessed 18 August 2023].

[131] Recreus, "Conductive Filaflex TPU filament," Recreus, [Online]. Available: https://recreus.com/en/products/filaflex-conductivo. [Accessed 18 August 2023].

[132] L. Huang, X. Lv, Y. Tang, G. Ge, P. Zhang and Y. Li, "Effect of Alumina Nanowires on the Thermal Conductivity and Electrical Performance of Epoxy Composites," *Polymers,* vol. 12, no. 9, p. 2126, 9 2020.

[133] Z. Živcová, E. Gregorová, W. Pabst, D. S. Smith, A. Michot and C. Poulier, "Thermal conductivity of porous alumina ceramics prepared using starch as a pore-forming agent," *Journal of the European Ceramic Society,* vol. 29, no. 3, pp. 347-353, 2 2009.

[134] M. Yang, J. Pan, A. Xu, L. Luo, D. Cheng, G. Cai, J. Wang, B. Tang and X. Wang, "Conductive Cotton Fabrics for Motion Sensing and Heating Applications," *Polymers,* vol. 10, no. 6, p. 568, 5 2018.

[135] M. Slavinec, R. Repnik and E. Klemenčič, "The impact of moisture on thermal conductivity of fabrics," *Anali PAZU,* vol. 6, no. 1-2, pp. 8-12, 6 2022.

[136] A. Rodriguez, J. P. Fuertes, A. Oval and G. Perez-Artieda, "Experimental Measurement of the Thermal Conductivity of Fused Deposition Modeling Materials with a DTC-25 Conductivity Meter," *Materials,* vol. 16, no. 23, p. 7384, 11 2023.

[137] M. Nowka, K. Ruge, L. Schulze, K. Hilbig and T. Vietor, “Characterization of the Anisotropic Electrical Properties of Additively Manufactured Structures Made from Electrically Conductive Composites by Material Extrusion,” *Polymers,* vol. 16, no. 20, p. 2891, 10 2024.

[138] M. L. d. Aguiar, P. D. Gaspar and P. D. d. Silva, “Image recognition method for frost sensing applications,” *Energy Reports,* vol. 8, no. 3, pp. 234-240, 6 2022.

[139] M. L. d. Aguiar, P. D. Gaspar and P. D. d. Silva, “Analysis of the frost formation pattern in heat exchangers for proper placement of frost measuring sensors,” in *The 26th IIR International Congress of Refrigeration (ICR 2023)*, Paris, 2023.

[140] M. L. d. Aguiar, P. D. Gaspar and P. D. d. Silva, “Optimized Placement of Frost-Measuring Sensors in Heat Exchangers via Image Processing of Frost Formation Pattern,” *Sensors,* vol. 23, no. 11, p. 5253, 6 2023.

[141] Logitech, “C920s Pro HD Webcam Official Product Page,” 2020. [Online]. Available: https://www.logitech.com/en-us/shop/p/c920s-pro-hd-webcam. [Accessed 2022].

[142] American Society of Heating, Refrigerating and Air-Conditioning Engineers (ASHRAE), The 2017 ASHRAE Handbook—Fundamentals SI Edition, Atlanta, Georgia, USA: American Society of Heating, Refrigerating and Air-Conditioning Engineers (ASHRAE), 2017.

[143] M. L. d. Aguiar, P. D. Gaspar and P. D. da Silva, “Thermoelectric-Powered Remote Sensor for Frost Detection,” *Electronics,* vol. 13, no. 14, p. 2683, 7 2024.

[144] J. Gubbi, R. Buyya, S. Marusic and M. Palaniswami, “Internet of Things (IoT): A vision, architectural elements, and future directions,” *Future Generation Computer Systems,* vol. 29, no. 7, pp. 1645-1660, 9 2013.

[145] A. Di Meglio, N. Massarotti and P. Nithiarasu, “A physics-driven and machine learning-based digital twinning approach to transient thermal systems,” *International Journal of Numerical Methods for Heat & Fluid Flow,* vol. 34, no. 1, pp. 2229-2256, 4 2024.

[146] D. M. Rowe, Thermoelectrics Handbook, D. Rowe, Ed., Boca Raton, FL, USA: CRC Press, 2018.

[147] J. Alvarez-Quintana, “Energy production through residual heat harvesting from domestic/commercial fridges using nanostructured thermoelectric modules,” *Thermal Science and Engineering Progress,* vol. 42, p. 101952, 7 2023.

[148] A. Attar, M. Rady, A. Abuhabaya, F. Albatati, A. Hegab and E. Almatrafi, “Performance Assessment of Using Thermoelectric Generators for Waste Heat Recovery from Vapor Compression Refrigeration Systems,” *Energies,* vol. 14, no. 23, p. 8192, 12 2021.

[149] Espressif Systems, “ESP32 Series Datasheet.,” 2021. [Online]. Available: https://www.espressif.com/documentation/esp32_datasheet_en.pdf.

[150] Y. Kuang, T. Ruan, Z. J. Chew and M. Zhu, “Energy harvesting during human walking to power a wireless sensor node,” *Sensors and Actuators A: Physical,* vol. 254, pp. 69-77, 2 2017.

[151] European Commission, “Technology Readiness Levels (TRL): HORIZON 2020 — Work Programme 2014–2015, General Annexes, G. Technology Readiness Levels (TRL),” 2014. [Online]. Available: https://ec.europa.eu/research/participants/data/ref/h2020/wp/2014_2015/annexes/h2020-wp1415-annex-g-trl_en.pdf. [Accessed 2025].

[152] Joint Committee for Guides in Metrology (JCGM), *Evaluation of Measurement Data — Guide to the Expression of Uncertainty in Measurement,* 1 ed., Sèvres, France: BIPM: JCGM 100:2008, 2008.

[153] Atmel Corporation, “ATmega328P Datasheet,” 2015. [Online]. Available: https://ww1.microchip.com/downloads/en/DeviceDoc/Atmel-7810-Automotive-Microcontrollers-ATmega328P_Datasheet.pdf.

[154] R. Ariyamuthu, V. Rupa Albert and S. Je, “An Overview of Food Preservation Using Conventional and Modern Methods,” *Journal of Food and Nutrition Sciences,* vol. 10, no. 3, p. 70, 2022.

[155] International Renewable Energy Agency, “World Energy Transitions Outlook 2023: 1.5°C Pathway,” Abu Dhabi, 2023.

[156] P. D. Gaspar, L. C. Carrilho Gonçalves and R. A. Pitarma, “CFD Parametric Studies for Global Performance Improvement of Open Refrigerated Display Cabinets,” *Modelling and Simulation in Engineering,* vol. 2012, pp. 1-15, 2012.

[157] P. Gaspar, P. Silva, J. Nunes and L. Andrade, “Characterization of the Specific Electrical Energy Consumption of Agrifood Industries in the Central Region of Portugal,” *Applied Mechanics and Materials,* vol. 590, pp. 878-882, 6 2014.

[158] G. G. Heidinger, S. M. Nascimento, P. D. Gaspar and P. D. Silva, “Experimental study of the fins arrangement pattern of refrigerated display cabinet evaporator towards thermal performance improvement,” *Applied Thermal Engineering,* vol. 138, pp. 246-253, 6 2018.

[159] W. Wang, Y. Feng, J. Zhu, L. Li, Q. Guo and W. Lu, “Performances of air source heat pump system for a kind of mal-defrost phenomenon appearing in moderate climate conditions,” *Applied Energy,* vol. 112, pp. 1138-1145, 12 2013.

[160] P. D. Silva, P. D. Gaspar, J. Nunes and L. Andrade, “Specific Electrical Energy Consumption and CO₂ Emissions Assessment of Agrifood Industries in the Central Region of Portugal,” *Applied Mechanics and Materials,* Vols. 675-677, pp. 1880-1886, 10 2014.

[161] P. Lizák and S. C. Mojumdar, “Thermal properties of textile fabrics,” *Journal of Thermal Analysis and Calorimetry,* vol. 112, no. 2, pp. 1095-1100, 5 2013.

[162] B. Gin, M. M. Farid and P. K. Bansal, “Effect of door opening and defrost cycle on a freezer with phase change panels,” *Energy Conversion and Management,* vol. 51, pp. 2698-2706, 2010.

[163] T. G. Hovgaard, L. F. S. Larsen, M. J. Skovrup and J. B. Jørgensen, “Power Consumption in Refrigeration Systems-Modeling for Optimization,” in *2011 International Symposium on Advanced Control of Industrial Processes*, Hangzhou, P.R. China, 2011.

[164] J. L. Dupont, A. El Ahmar and J. Guilpart, “IIR, The Role of Refrigeration in Worldwide Nutrition, 6th Informatory Note on Refrigeration and Food,” International Institute of Refrigeration, Paris, France, 2020.

[165] J. Nunes, P. D. Silva, L. P. Andrade and P. D. Gaspar, “Characterization of the specific energy consumption of electricity in the Portuguese sausage industry,” *WIT Transactions on Ecology and the Environment,* vol. 186, no. , pp. 763-774, 12 2014.

[166] P. D. Gaspar, L. C. Carrilho Gonçalves and R. A. Pitarma, “Three-Dimensional CFD Modelling and Analysis of the Thermal Entrainment in Open Refrigerated Display Cabinets,” *Heat Transfer,* vol. 2, pp. 63-73, 1 2008.

Annex A

Resistive frost detection sensor results

A.1. AGRS2

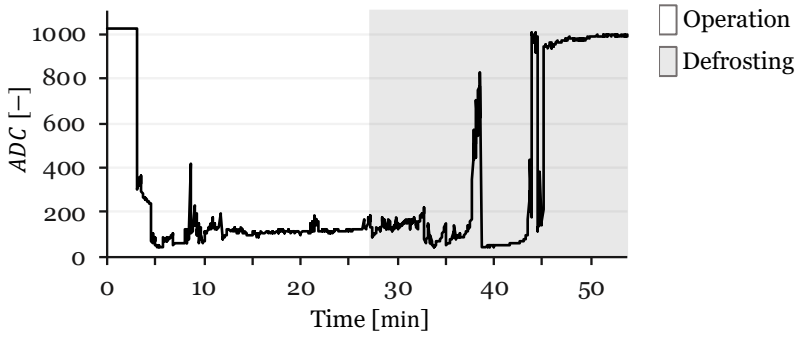

Figure 235 – Results for the third test of the AGRS2.

A.2. AGRS3

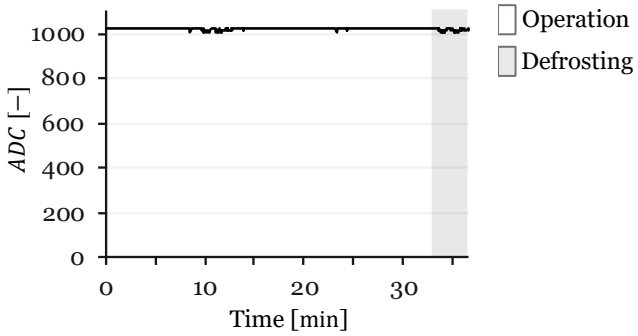

Figure 236 – Results for the second test of the AGRS3.

A.3. AGRS4

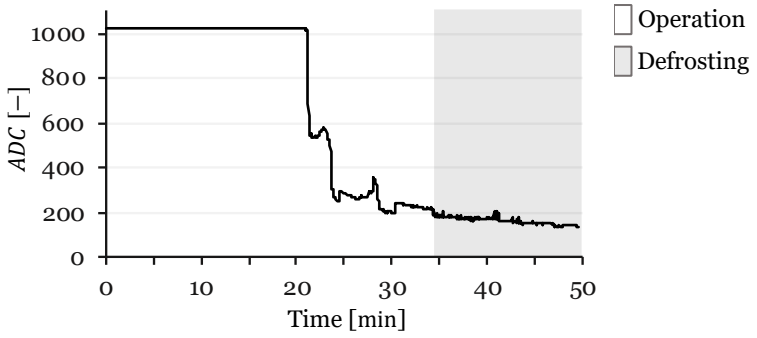

Figure 237 – Results for the second test of the AGRS4.

A.4. AGSR5

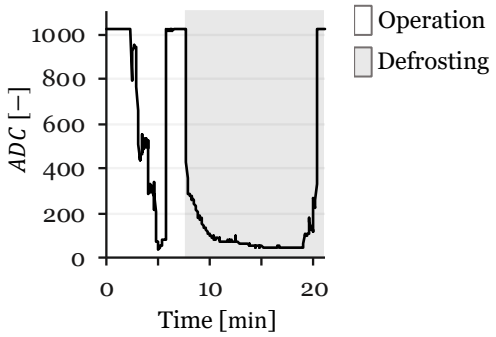

Figure 238 – Results for the first test of the AGRS5 sensor.

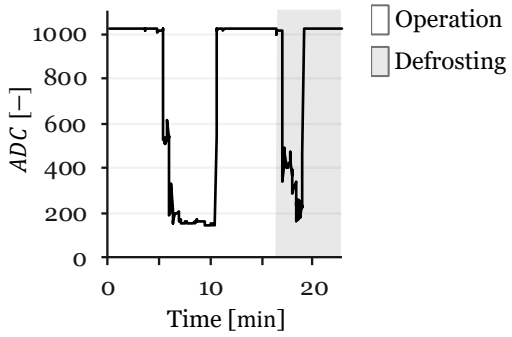

Figure 239 – Results for the fifth test of the AGRS5 sensor.

A.5. FMRS4

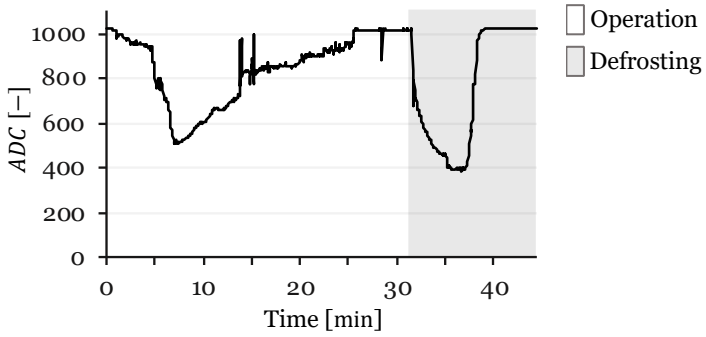

Figure 240 – Results for the second test of the FMRS4.

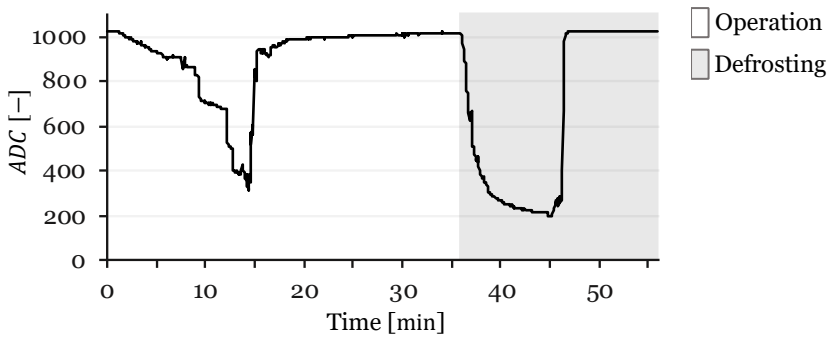

Figure 241 – Results for the fourth test of the FMRS4.

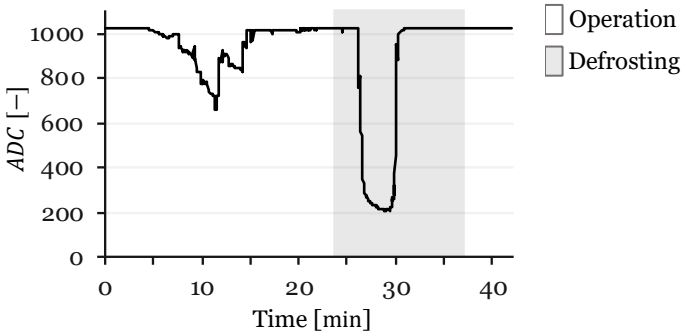

Figure 242 – Results for the fifth test of the FMRS4.

A.6. AMRS1

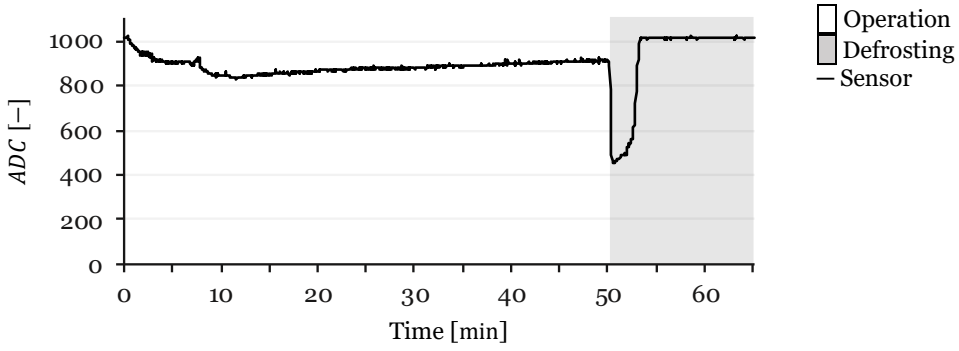

Figure 243 – Results for the second test of the AMRS1.

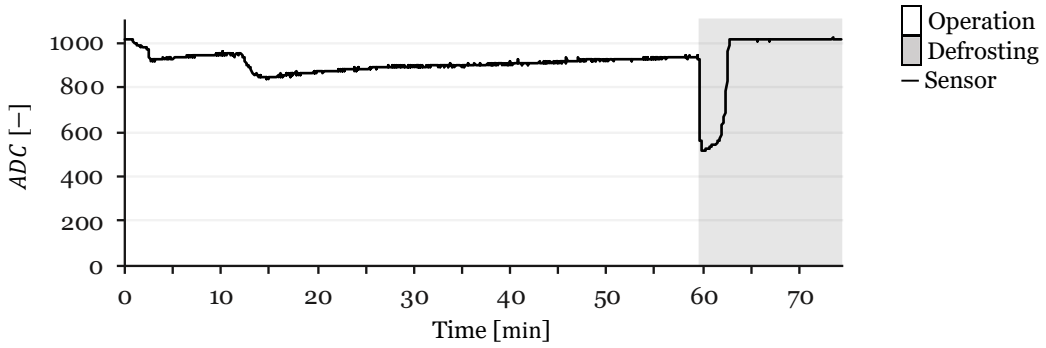

Figure 244 – Results for the third test of the AMRS1.

Annex B

Arduino and MATLAB code for data acquisition and post-processing

B.1. Arduino data acquisition firmware

Reads DS18B20 (TWF), DHT22 (TA and RH), FS300A (FS), ACS712-20A (I), frost sensor (FDS), and door switch (DOS). Publishes a 20-field CSV every 3 seconds in the fixed order aligned with Table 13, in the order of Equation (17)

```
//Setup DS1829
#include <OneWire.h>
#include <DallasTemperature.h>
#define ONE_WIRE_BUS 8  // All DS18B20 temperatureSensors are connected
to pin 8 on the Arduino
OneWire oneWire(ONE_WIRE_BUS);  // Creating a oneWire instance(object)
DallasTemperature temperatureSensors(&oneWire); // Pass oneWire object
reference to Dallas Temperature.
//Sensor adresses
uint8_t aT1[8] = {0x28, 0x5B, 0x55, 0x59, 0x38, 0x19, 0x01, 0x3F};
uint8_t aT2[8] = {0x28, 0x53, 0xB2, 0x32, 0x38, 0x19, 0x01, 0x11};
uint8_t aT3[8] = {0x28, 0x03, 0x46, 0x71, 0x38, 0x19, 0x01, 0xEE};
uint8_t aT4[8] = {0x28, 0xBF, 0xF3, 0x68, 0x38, 0x19, 0x01, 0xA2};

//Setup DHT
#include "DHT.h"
#define DHTPIN1 5     // Digital pin connected to the DHT sensor
#define DHTPIN2 4
#define DHTTYPE DHT22   // DHT 22
DHT dht1(DHTPIN1, DHTTYPE);
DHT dht2(DHTPIN2, DHTTYPE);

//Setup Flow Meter
volatile long flowFrequency1; // Measures flow sensor pulses
volatile long flowFrequency2; // Measures flow sensor pulses
unsigned int flowRate1; // Calculated litres/hour
unsigned int flowRate2; // Calculated litres/hour
unsigned char flowSensor1 = 2; // Sensor Input
```

```
unsigned char flowSensor2 = 3; // Sensor Input

unsigned long loopTime;

long t=3; //Measurement frequency in seconds  --------------------------
-------------------------------------------------------
String valueDelimiter=" , ";
float valueArray[20]; //Array values Sensor=0
Q2=1  Q4=2  t1=3  t2=4  t3=5  t4=6  t5=7  t6=8  h5=9  h6=10  I1=11  I2=12
 I3=13  I4=14  FAN=15 0 0 0 0

//Setup Fan
int Ftime;
int pinDoorSensor = 9;
bool doorState=0;
int pinArduino2=A0;//port used to signal defrosting procedure

//Setup Frost Sensor
int sensorpin = A5;
int sensorenablepin = 6;
int valorsensor;

//Setup Current sensor
int peltierVoltage = 5;
float currentSensor1;
float currentSensor2;
float currentSensor3;
float currentSensor4;
float currentSum1=0;
float currentSum2=0;
float currentSum3=0;
float currentSum4=0;
float currentValue1;
float currentValue2;
float currentValue3;
float currentValue4;
int currentSensorPin1 = A1;
int currentSensorPin2 = A2;
int currentSensorPin3 = A3;
int currentSensorPin4 = A4;
float potencia = 0;
int long currentReadings=0;

int i=0; //For variable NOV2023

//Flow sensor interrupt functions
void flow1 ()
{
   flowFrequency1++;
```

```
78  }
79  void flow2 ()
80  {
81     flowFrequency2++;
82  }
83
84  void setup(void) {
85
86    //Start serial
87    Serial.begin(9600);
88
89    //Start DS1829 sensors
90    temperatureSensors.begin();
91
92    //Start DHT sensors
93    dht1.begin();
94    dht2.begin();
95
96    //Setup door switch
97    pinMode(pinDoorSensor, INPUT_PULLUP);
98    pinMode(pinArduino2, OUTPUT);
99
100   //Set pin mode and start values for flow sensor
101   pinMode(flowSensor1, INPUT);
102   digitalWrite(flowSensor1, HIGH);
103   pinMode(flowSensor2, INPUT);
104   digitalWrite(flowSensor2, HIGH);
105   attachInterrupt(0, flow1, RISING); // Setup Interrupt
106   attachInterrupt(1, flow2, RISING); // Setup Interrupt
107   sei(); // Enable interrupts
108
109   //Set pin mode and start values for frost sensor
110   pinMode(sensorenablepin, OUTPUT);
111   digitalWrite(sensorenablepin, LOW);
112
113   //Set counters
114   loopTime = millis();
115 }
116
117 void loop(void) {
118
119   temperatureRead(); //read T1-T4 sensor values to average over a t
120 period
121   currentRead(); //read current sensor values to average over a t period
122
123   if(millis() >= (loopTime + (t*1000))){ // Every t seconds, calculate
124 and print sensor values
125
126     loopTime = millis(); // Updates loopTime
```

```
127       digitalWrite(sensorenablepin, HIGH);
128       flowCalc();
129       DHTCalc();
130       temperatureCalc();
131       currentCalc();
132       fanCalc();
133       pressureCalc();
134       frostRead(); //frostRead has to be the last value to be read so that
135   the procesing time of other readings is enough for the sensorenablepin to
136   get high
137       digitalWrite(sensorenablepin, LOW);
138
139       for(i=0; i<=19; i++){
140         Serial.print(valueArray[i]); //print all the array values
141         if (i<=18){ //so that the array print does not end with a value
142   delimiter
143           Serial.print(valueDelimiter); //print a value delimiter to
144   separate vaues
145           }
146       }
147       Serial.println();
148     }
149   }
150
151   float currentRead(){ //current sensor measurements
152     currentSensor1=((analogRead (currentSensorPin1)+0)*0.004887586-
153   2.5)/0.1;
154     currentSensor2=((analogRead (currentSensorPin2)+0)*0.004887586-
155   2.5)/0.1;
156     currentSensor3=((analogRead (currentSensorPin3)+0)*0.004887586-
157   2.5)/0.1;
158     currentSensor4=((analogRead (currentSensorPin4)+0)*0.004887586-
159   2.5)/0.1;
160     //Sensor value + calibration * voltage conversion value (5/1023) -2.5
161   because values between 0 and 2,5 are negative voltages and /0.1 because
162   it is a 20A sensor
163
164     currentSum1=currentSum1+currentSensor1;
165     currentSum2=currentSum2+currentSensor2;
166     currentSum3=currentSum3+currentSensor3;
167     currentSum4=currentSum4+currentSensor4;
168     currentReadings=currentReadings+1;
169   }
170
171   float currentCalc(){
172     currentValue1=currentSum1/currentReadings;
173     currentValue2=currentSum2/currentReadings;
174     currentValue3=currentSum3/currentReadings;
175     currentValue4=currentSum4/currentReadings;
```

```
    valueArray[11]=currentValue1;
    valueArray[12]=currentValue2;
    valueArray[13]=currentValue3;
    valueArray[14]=currentValue4;
    currentSum1=0;
    currentSum2=0;
    currentSum3=0;
    currentSum4=0;
    currentReadings=0;
  }

  float DHTCalc(){ //DHT sensor measurements
    // Reading temperature or humidity takes about 250 milliseconds!
    // Sensor readings may also be up to 2 seconds 'old'
    float h6 = dht1.readHumidity(); // Read temperature as Celsius (the
  default)
    float t6 = dht1.readTemperature(false);
    float h5 = dht2.readHumidity();
    float t5 = dht2.readTemperature(false);

    if (isnan(h5) || isnan(t5)) {
      valueArray[9]=0; //H5
      valueArray[7]=0; //T5
    }else{
      valueArray[9]=h5; //H5
      valueArray[7]=t5; //T5
    }

    if (isnan(h6) || isnan(t6)){
      valueArray[10]=0; //H6
      valueArray[8]=0; //T6
    }else{
      valueArray[10]=h6; //H6
      valueArray[8]=t6; //T6
    }
  }

  int flowCalc(){ //flow sensor measurements
    // Every t seconds, calculate and print litres/hour
    // Pulse frequency (Hz) = 7.5Q, Q is flow rate in L/min.
    flowRate1 = (flowFrequency1 * 60 / 7.5 / t); // (Pulse frequency x 60
  min) / 7.5Q = flowrate in L/hour
    flowFrequency1 = 0; // Reset Counter

    flowRate2 = (flowFrequency2 * 60 / 7.5 / t); // (Pulse frequency x 60
  min) / 7.5Q = flowrate in L/hour
    flowFrequency2 = 0; // Reset Counter

    if (flowRate1>0){
```

```
225       valueArray[1]=flowRate1; //Q2
226     }else{
227       valueArray[1]=0; //Q2
228     }
229
230     if (flowRate1>0){
231       valueArray[2]=flowRate2; //Q4
232     }else{
233       valueArray[2]=0; //Q4
234     }
235   }
236
237   int fanCalc(){ //door switch sensor measurements
238     doorState=digitalRead (pinDoorSensor); //Reads door sensor
239     valueArray[15]=doorState; //door state
240     digitalWrite(pinArduino2, doorState); //controll fan
241   }
242
243   int frostRead(){//Frost sensor measurements
244     valueArray[0]=analogRead(sensorpin); //Frost sensor
245     valueArray[0]=analogRead(sensorpin); //Frost sensor
246     valueArray[0]=analogRead(sensorpin); //Frost sensor
247     valueArray[0]=analogRead(sensorpin); //Frost sensor
248     valueArray[0]=analogRead(sensorpin); //Frost sensor
249   }
250
251   float temperatureCalc(){//get working fluid temperatures
252
253     valueArray[3]=temperatureSensors.getTempC(aT1);
254     valueArray[4]=temperatureSensors.getTempC(aT2);
255     valueArray[5]=temperatureSensors.getTempC(aT3);
256     valueArray[6]=temperatureSensors.getTempC(aT4);
257     }
258
259   float temperatureRead(){//working fluid temperature sensor measurements
260     temperatureSensors.requestTemperatures(); // Send the command to get
261   temperatures from all sensors.
262   }
```

B.2. MATLAB App for data acquisition during testing

This annex presents the MATLAB App Designer application developed for integrated acquisition, visualization, and logging of the frost–defrost experiments. The application opens a serial connection to the Arduino, initializes the Logitech C920 camera, and creates a time-stamped session folder for each run. At every acquisition cycle, it reads the 20-element `valueArray` from the Arduino, adds the host-side timestamp, computes the frost metric from the camera images, and constructs the record $b(t)$. These records are accumulated in the dataset M, continuously written to `data.csv`, and linked to synchronized RGB and binarized image folders. The GUI provides start/stop control, displays current values, plots time histories, and shows the camera view alongside the processed image. When the session is stopped, all files remain organized within the output folder. Only the essential acquisition callbacks are shown here; autogenerated interface code is omitted for clarity.

```
% Inside App Designer class (methods block)
% Core mapping used by GUI for b(t) = [ t_s , z(t) , CV_Frost ]
%   b(1)  = t_s                 % host-side timestamp (s)
%   b(2)  = FDS                 % frost sensor (ADC)
%   b(3)  = FS2                 % flow circuit 2 (L/h)
%   b(4)  = FS1                 % flow circuit 3 (L/h)
%   b(5)  = TWF1                % AL-HX outlet WF temp (DS18B20)
%   b(6)  = TWF2                % AL-HX inlet  WF temp (DS18B20)
%   b(7)  = TWF3                % TE-HX inlet  WF temp (DS18B20)
%   b(8)  = TWF4                % TE-HX outlet WF temp (DS18B20)
%   b(9)  = TA1                 % AL-HX inlet air temp (DHT22)
%   b(10) = TA2                 % AL-HX outlet air temp (DHT22)
%   b(11) = RH1                 % AL-HX inlet RH (DHT22)
%   b(12) = RH2                 % AL-HX outlet RH (DHT22)
%   b(13) = I1                  % TE1 current (A, window-avg)
%   b(14) = I2                  % TE2 current (A, window-avg)
%   b(15) = I3                  % TE3 current (A, window-avg)
%   b(16) = I4                  % TE4 current (A, window-avg)
%   b(17) = DOS                 % door/fan state (0=closed/min,
1=open/max)
%   b(18) = RES1                % reserved (0)
%   b(19) = RES2                % reserved (0)
%   b(20) = RES3                % reserved (0)
%   b(21) = RES4                % reserved (0)
%   b(22) = CV_Frost            % computer-vision frost metric (0..1024)

function StartButtonPushed(app, event)
    % --- init session state
    clear('M'); Frost = 0; app.READ = 1;

```

```
    % --- open Arduino serial (legacy API as in app)
    s = serial('COM4');     % set COM port here
    fopen(s);

    % --- configure camera (HD Pro Webcam C920) and session folder
structure
    cam = webcam('HD Pro Webcam C920');
    cam.Resolution         = '1280x720';
    cam.Exposure           = -6;
    cam.ExposureMode       = 'manual';
    cam.WhiteBalanceMode   = 'manual';
    cam.WhiteBalance       = 3200;
    cam.BacklightCompensation = 1;
    cam.Sharpness          = 0;
    cam.Saturation         = 128;
    cam.Brightness         = 70;
    cam.Gain               = 64;
    cam.Contrast           = 50;

    % Root output folder = Desktop\YYYY.MM.DD_HH.MM
    outRoot = 'C:\Users\Marti\Desktop\';
    outRoot = [outRoot,
datestr(now,'yyyy.mm.dd'),'_',datestr(now,'hh.MM')];
    mkdir(outRoot);
    mkdir(outRoot, 'Monochromatic Bitmap');
    mkdir(outRoot, 'Color');
    mkdir(outRoot, 'Files');
    dirCSV = [outRoot, '\Files\'];

    % --- prime one serial frame, start host timer, seed dataset M
    v   = fscanf(s);
    num = textscan(v,'%f','Delimiter',',');
    a   = cell2mat(num);                    % 20×1 Arduino vector z(t)
    tic
    b   = [toc, a.', Frost];                % 1×22 record = [t_s, z(t),
CV_Frost]
    M   = b;

    % --- acquisition loop (until STOP)
    countW = 1;                             % image index
    while app.READ == 1
        % ---- grab image & compute CV metric
        img    = snapshot(cam);
        imgRGB = imcrop(img, [479 225 350 350]);         % ROI at HX
intake
        imgGray= rgb2gray(imgRGB);
        imgBin = imbinarize(imgGray, 0.5);
        Frost  = round( (nnz(imgBin)*1024) / numel(imgBin) );  % 0..1024
scale
```

```
80          app.Frost = Frost;
81
82          % ---- update GUI image panes
83          imshow(imgRGB, 'Parent', app.UIAxes_2);          % RGB pane
84          imshow(imgBin, 'Parent', app.UIAxes_11);         % binarized pane
85
86          % ---- persist images
87          imwrite(img,    [outRoot,
88  '\Color\img_',            num2str(countW,'%05.f'), '.jpeg']);
89          imwrite(imgBin, [outRoot, '\Monochromatic Bitmap\imgBin_',
90  num2str(countW,'%05.f'), '.jpeg']);
91
92          % ---- read one Arduino CSV line and append one record
93          v   = fscanf(s);
94          num = textscan(v,'%f','Delimiter',',');
95          a   = cell2mat(num);                 % 20×1, strict schema/order
96          b   = [toc, a.', Frost];             % 1×22
97          M   = [M; b];                        % dataset grows by one row
98
99          drawnow;
100         countW = countW + 1;
101
102         % ---- continuously persist the session CSV (rolling save)
103         csvwrite([dirCSV,'data.csv'], M);          %#ok<CSVWR>
104     end
105
106     % --- stop: close and clean
107     fclose(s); delete(s);
108 end
109
110 function STOPButtonPushed(app, event)
111     % Signal the acquisition loop to exit; StartButtonPushed does the
112 cleanup.
113     app.READ = 0;
114 end
```

B.3. MATLAB script for 12×12 grid tile post-processing

The following MATLAB function was developed to automate the processing of image sequences into a structured dataset of tile-level metrics. The code reads the original frames, extracts a predefined region of interest, converts it to grayscale, and applies a fixed binarization threshold. The region is then divided into a 12×12 grid, generating 144 tiles that follow a chessboard-like naming convention (columns $a - l$, rows $1 - 12$). Each tile is stored as a binary image, and a numerical metric proportional to the fraction of white pixels (scaled to a 10-bit range) is computed. The results are written to a wide-format CSV file, with one column per tile.

```
function process_all_tiles_12x12()
% PROCESS_ALL_TILES_12x12

%% ---------------- CONFIG ----------------------------------
ROI_xywh     = [479, 225, 350, 350];   % [x y w h] (same as app)
THRESH_01    = 0.5;                    % threshold in [0,1]
TILE_ROWS    = 12;                     % rows = 12
TILE_COLS    = 12;                     % cols = 12  (a..l)
MIN_SPECKLE  = 0;                      % remove CC < N px after bin (0 =
off)
OUT_ROOTNAME = 'tiles_12x12_output';
% ----------------------------------------------------------------

rootDir = fileparts(mfilename('fullpath'));
imgDir  = fullfile(rootDir, 'Images');

% Collect originals
exts = {'*.jpg'};
files = [];
for k = 1:numel(exts)
    files = [files; dir(fullfile(imgDir, exts{k}))]; %#ok<AGROW>
end

% Make output folders
timestamp = datestr(now,'yyyy.mm.dd_HH.MM.SS');
outRoot   = fullfile(rootDir, [OUT_ROOTNAME '_' timestamp]);
tilesRoot = fullfile(outRoot, 'tiles');
resDir    = fullfile(outRoot, 'results');
mkdir(tilesRoot); mkdir(resDir);

% Build tile names (columns a..l; rows 1..12)
colLetters = arrayfun(@(c) char('a'+(c-1)), 1:TILE_COLS, 'UniformOutput',
false);
rowNums    = arrayfun(@num2str, 1:TILE_ROWS, 'UniformOutput', false);
```

```
tileNames  = cell(1, TILE_ROWS*TILE_COLS);
idx = 1;
for c = 1:TILE_COLS
    for r = 1:TILE_ROWS
        tileNames{idx} = [colLetters{c} rowNums{r}];  % a1..a12, b1..b12,
... l1..l12
        idx = idx + 1;
    end
end

% Pre-create per-tile folders
for i = 1:numel(tileNames)
    tFolder = fullfile(tilesRoot, tileNames{i});
    if ~exist(tFolder,'dir'), mkdir(tFolder); end
end

% CSV header (filename + a1..l12)
csvPath = fullfile(resDir, 'tiles_12x12_metrics.csv');
fid = fopen(csvPath, 'w');
fprintf(fid, 'filename');
for i = 1:numel(tileNames)
    fprintf(fid, ',%s', tileNames{i});
end
fprintf(fid, '\n');

% ----- Determine trim strategy from first frame (consistent for all) ---
--
firstPath = fullfile(files(1).folder, files(1).name);
I0 = imread(firstPath);
if ndims(I0)==3, I0g = rgb2gray(I0); else, I0g = I0; end
Iroi0 = imcrop(I0g, ROI_xywh);
Iroi0 = im2double(Iroi0);
Ibin0 = Iroi0 >= THRESH_01;
if MIN_SPECKLE>0, Ibin0 = bwareaopen(Ibin0, MIN_SPECKLE); end
[H, W] = size(Ibin0);

% Compute exact divisible size
tileH = floor(H / TILE_ROWS);
tileW = floor(W / TILE_COLS);
H2 = tileH * TILE_ROWS;
W2 = tileW * TILE_COLS;

% ----- Process each frame -----
for kf = 1:numel(files)
    fname = files(kf).name;
    fpath = fullfile(files(kf).folder, fname);

    % ROI + grayscale + binarize
    I = imread(fpath);
```

```
    if ndims(I)==3, Ig = rgb2gray(I); else, Ig = I; end
    Iroi = imcrop(Ig, ROI_xywh);
    Iroi = im2double(Iroi);
    Ibin = Iroi >= THRESH_01;
    if MIN_SPECKLE>0, Ibin = bwareaopen(Ibin, MIN_SPECKLE); end

    [Hc, Wc] = size(Ibin);
    IbinT = Ibin(1:H2, 1:W2);   % trimmed ROI used for tiling

    % Compute per-tile metric in column-major order (a1..a12, b1..b12,
...)
    rowVals = zeros(1, numel(tileNames), 'double');
    idx = 1;
    for c = 1:TILE_COLS
        c1 = (c-1)*tileW + 1; c2 = c*tileW;
        for r = 1:TILE_ROWS
            r1 = (r-1)*tileH + 1; r2 = r*tileH;

            tileBIN = IbinT(r1:r2, c1:c2);
            white_ratio = nnz(tileBIN) / numel(tileBIN);
            frost10 = round(white_ratio * 1023);
            rowVals(idx) = frost10;

            % Save tile image
            tName   = tileNames{idx};
            tFolder = fullfile(tilesRoot, tName);
            [~, base, ~] = fileparts(fname);
            outName = sprintf('%s_%s_BIN.png', base, tName);
            imwrite(tileBIN, fullfile(tFolder, outName), 'png');

            idx = idx + 1;
        end
    end

    % Write CSV row
    fprintf(fid, '%s', fname);
    fprintf(fid, ',%d', rowVals);
    fprintf(fid, '\n');

end

fclose(fid);
fprintf('Done.');
end
```

B.4. MATLAB script for frost post-processing map analysis

The MATLAB function presented in this annex was developed to reconstruct frost maps directly from the CSV file generated by the MATLAB script for 12×12 grid tile processing (Annex B.3). The code takes the numerical frost metrics of each tile ($a1 - l12$) and reshapes them into a 12×12 matrix for every frame, producing a grayscale representation in which intensity is proportional to frost coverage. Each frame is saved as an upscaled block-style image in a dedicated folder, allowing the spatial distribution of frost to be visualized over time. In addition, the script computes the per-tile average across all frames, generating a composite frost-formation map that highlights regions systematically more or less prone to frost accumulation. This map is exported both as an image and as a companion CSV file containing the average values for all tiles, providing a tool for analysing frost patterns and supporting sensor placement decisions.

```
function csv_tiles_to_images_and_map(csvPath)

UPSCALE_FACTOR = 30;   % pixels per tile (final image = 12*30 = 360 px)
ROUND_OUTPUT   = true; % round values before saving

if nargin < 1 || ~isfile(csvPath)
    [f,p] = uigetfile('*.csv','Select tiles_12x12_metrics.csv');
    if isequal(f,0), return; end
    csvPath = fullfile(p,f);
end

T = readtable(csvPath, 'TextType','string');

% Detect tile columns a..l □ 1..12 in proper order
cols = strings(0,1);
letters = char('a':'l');
for c = 1:numel(letters)
    for r = 1:12
        cols(end+1,1) = sprintf('%c%d', letters(c), r); %#ok<AGROW>
    end
end

% Verify columns exist
missing = cols(~ismember(cols, string(T.Properties.VariableNames)));
if ~isempty(missing)
    error('Missing columns: %s', strjoin(missing.', ', '));
end

csvDir = fileparts(csvPath);
timestamp = datestr(now,'yyyy.mm.dd_HH.MM.SS');
outRoot = fullfile(csvDir, ['CSV_tiles_to_images_' timestamp]);
```

```
framesDir = fullfile(outRoot, 'frames');
mapDir    = fullfile(outRoot, 'map');
mkdir(framesDir); mkdir(mapDir);

nFrames = height(T);
allFrames = zeros(12,12,nFrames, 'double');

toMat = @(v) reshape(v, [12,12]);

for i = 1:nFrames
    v = zeros(144,1);
    for k = 1:144
        v(k) = T.(cols(k))(i);
    end
    if ROUND_OUTPUT, v = round(v); end

    M10 = toMat(v);                        % 0..1023
    M8  = uint8( round(M10 / 1023 * 255) ); % 0..255

    M8_big = imresize(M8, UPSCALE_FACTOR, 'nearest');

    if ismember("filename", string(T.Properties.VariableNames))
        base = string(T.filename(i));
        if base == "", base = sprintf('row_%05d', i); end
    else
        base = sprintf('row_%05d', i);
    end
    imwrite(M8_big, fullfile(framesDir, sprintf('%s_tiles.png', base)));

    allFrames(:,:,i) = double(M10);
end

Mmean10 = mean(allFrames, 3, 'omitnan');   % 12×12, still 0..1023 scale
if ROUND_OUTPUT, Mmean10 = round(Mmean10); end
Mmean8  = uint8( round(Mmean10 / 1023 * 255) );

Mmean8_big = imresize(Mmean8, UPSCALE_FACTOR, 'nearest');
imwrite(Mmean8_big, fullfile(mapDir, 'map.png'));

avgRow = reshape(Mmean10, 1, []);  % 1×144 in same a1..l12 order
avgTbl = array2table(avgRow, 'VariableNames', cellstr(cols.'));
writetable(avgTbl, fullfile(mapDir, 'averages.csv'));

legendImg = repmat(uint8(linspace(0,255,256)), UPSCALE_FACTOR, 1);
imwrite(legendImg, fullfile(mapDir, 'legend_0to1023_gray.png'));

fprintf('Done.\nFrames: %s\nMap: %s\n', framesDir, mapDir);
end
```

B.5. MATLAB script for targeted tile extraction post-processing analysis

The MATLAB function presented in this annex was developed to enable targeted tile extraction based on user input. Instead of processing all of the 144 tiles in a blind grid, this approach allows the user to define a tile interactively by clicking on a preview image (clickable.jpeg). A red square follows the cursor to indicate the tile boundaries, and once confirmed, the same centered tile is extracted consistently from every frame in the dataset. The proportion of white pixels within the tile is calculated, converted to a 10-bit metric, and recorded in a CSV file together with the tile coordinates and size. In parallel, the binary tile images are saved as lossless .PNG, and a context image showing the selected tile location is produced. This method reduces computational load by processing only the region of interest and ensures that the tile is centred on the sensor location, thereby providing a more direct and accurate comparison between the CV metric and the resistive frost sensor signal.

```
function batch_tile_from_clickable_ROI_bin()
% BATCH_TILE_FROM_CLICKABLE_ROI_BIN

%% ---------------- USER CONFIG ----------------------------------
ROI_xywh        = [479, 225, 350, 350];   % [x y w h] (same as app)
THRESH_01       = 0.5;                    % grayscale threshold in [0,1]
TILE_SIZE_PX    = 30;                     % default square tile size (px)
MIN_SPECKLE     = 0;                      % remove CC < N pixels after
bin (0 = off)
% ---------------------------------------------------------------

rootDir  = fileparts(mfilename('fullpath'));
clickPath = fullfile(rootDir, 'clickable.jpeg');
imgDir    = fullfile(rootDir, 'Images');

if ~exist(clickPath,'file'), error('Missing clickable.jpeg in: %s',
rootDir); end
if ~exist(imgDir,'dir'),    error('Missing Images/ folder in: %s',
rootDir); end

% ----- 1) Prepare clickable: crop ROI + binarize (what you will click
on) -----
Ic = imread(clickPath);
if ndims(Ic)==3, Ic = rgb2gray(Ic); end
Ic_roi = imcrop(Ic, ROI_xywh);
Ic_roi = im2double(Ic_roi);                % [0,1]
Ic_bin = Ic_roi >= THRESH_01;              % fixed threshold
if MIN_SPECKLE>0, Ic_bin = bwareaopen(Ic_bin, MIN_SPECKLE); end
```

```
29
30  [Hc, Wc] = size(Ic_bin);
31
32  % ----- 2) Live preview on ROI-binarized clickable (CLICKABLE!) -----
33  f  = figure('Color','w','Name','Select tile center on ROI-binarized
34  clickable');
35  ax = axes('Parent',f);
36  hImg = imshow(Ic_bin, 'Parent', ax, 'InitialMagnification','fit');  %
37  clickable target
38  axis(ax,'image'); set(ax,'YDir','reverse'); hold(ax,'on');
39
40  % Make sure clicks reach us:
41  set(hImg, 'ButtonDownFcn', @onClick,
42  'PickableParts','all','HitTest','on');
43  set(ax,   'ButtonDownFcn', @onClick);
44  set(f,    'WindowButtonDownFcn', @onClick);
45  set(f,    'WindowButtonMotionFcn', @onMove);
46  set(f,    'KeyPressFcn', @onKey);
47
48  % Red 1px preview box
49  S    = TILE_SIZE_PX;
50  rect = rectangle(ax, 'Position',[1 1 S S], 'EdgeColor','r',
51  'LineWidth',1);
52
53  uiwait(f);  % wait until you click or cancel
54
55  if ~exist('confirmed','var') || ~confirmed
56      disp('Selection canceled.');
57      return;
58  end
59
60  % ----- 3) Batch process: ROI + bin + extract same tile on every frame --
61  ---
62  timestamp = datestr(now,'yyyy.mm.dd_HH.MM.SS');
63  outRoot = fullfile(rootDir,
64  sprintf('Tiles_from_clickable_x%04d_y%04d_s%03d_%s', xc, yc, S,
65  timestamp));
66  tilesDir = fullfile(outRoot,'tiles');  resDir =
67  fullfile(outRoot,'results');
68  mkdir(tilesDir); mkdir(resDir);
69
70  csvPath = fullfile(resDir, sprintf('metrics_x%04d_y%04d_s%03d.csv', xc,
71  yc, S));
72  fid = fopen(csvPath,'w');
73  fprintf(fid,'filename,center_x,center_y,tile_size_px,r1,r2,c1,c2,total_px
74  ,white_px,black_px,white_ratio,frost_10bit\n');
75
76  % Collect originals
77  exts={'*.png','*.jpg','*.jpeg','*.tif','*.tiff','*.bmp'};
```

```
78  files=[]; for k=1:numel(exts), files=[files; dir(fullfile(imgDir,
79  exts{k}))]; end %#ok<AGROW>
80  if isempty(files), fclose(fid); error('No images found in: %s', imgDir);
81  end
82
83  for i=1:numel(files)
84      fname = files(i).name; fpath = fullfile(files(i).folder, fname);
85      I = imread(fpath);
86      if ndims(I)==3, Ig = rgb2gray(I); else, Ig = I; end
87
88      % Crop ROI then binarize like the preview
89      Iroi = imcrop(Ig, ROI_xywh);
90      Iroi = im2double(Iroi);
91      Ibin = Iroi >= THRESH_01;
92      if MIN_SPECKLE>0, Ibin = bwareaopen(Ibin, MIN_SPECKLE); end
93
94      % Ensure current ROI matches clickable ROI size
95      [H,W] = size(Ibin);
96      if H~=Hc || W~=Wc
97          error('Frame "%s" ROI size [%dx%d] differs from clickable ROI
98  [%dx%d].', fname, H,W, Hc,Wc);
99      end
100
101     % Crop the same centered tile
102     half = floor(S/2);
103     r1 = max(1, yc - half); r2 = min(H, yc + half);
104     c1 = max(1, xc - half); c2 = min(W, xc + half);
105
106     % Adjust to try to keep SxS near borders
107     if (r2-r1+1) < S
108         d = S - (r2-r1+1);
109         r1 = max(1, r1 - ceil(d/2));
110         r2 = min(H, r1 + S - 1);
111     end
112     if (c2-c1+1) < S
113         d = S - (c2-c1+1);
114         c1 = max(1, c1 - ceil(d/2));
115         c2 = min(W, c1 + S - 1);
116     end
117     r1=max(1,min(r1,H)); r2=max(1,min(r2,H));
118     c1=max(1,min(c1,W)); c2=max(1,min(c2,W));
119
120     tileBIN = Ibin(r1:r2, c1:c2);
121
122     % Metrics
123     total_px    = numel(tileBIN);
124     white_px    = nnz(tileBIN);
125     black_px    = total_px - white_px;
126     white_ratio = white_px / total_px;
```

```
        frost_10bit = round(white_ratio * 1023);

        % Save tile (lossless pure binary PNG)
        [~, base, ~] = fileparts(fname);
        tileName = sprintf('%s_x%04d_y%04d_s%03d_BIN.png', base, xc, yc, S);
        imwrite(tileBIN, fullfile(tilesDir, tileName), 'png');

        % CSV row
        fprintf(fid,'%s,%d,%d,%d,%d,%d,%d,%d,%d,%d,%d,%.6f,%d\n', ...
            fname, xc, yc, S, r1, r2, c1, c2, total_px, white_px, black_px,
    white_ratio, frost_10bit);
    end
    fclose(fid);

    % Save a context image (the clickable ROI bin with rectangle)
    ctx = repmat(uint8(Ic_bin)*255,1,1,3);
    x1 = max(1, xc - floor(S/2)); x2 = min(Wc, x1 + S - 1);
    y1 = max(1, yc - floor(S/2)); y2 = min(Hc, y1 + S - 1);
    ctx([y1 y2], x1:x2, 1) = 255; ctx([y1 y2], x1:x2, 2:3) = 0;  % top/bottom
    ctx(y1:y2, [x1 x2], 1) = 255; ctx(y1:y2, [x1 x2], 2:3) = 0;  % left/right
    imwrite(ctx, fullfile(outRoot,
    sprintf('context_clickable_ROI_x%04d_y%04d_s%03d.png', xc, yc, S)));

    fprintf('Done.\nTiles: %s\nCSV: %s\n', tilesDir, csvPath);

    %% ---------- nested callbacks ----------
        function onMove(~,~)
            % Update the preview rectangle to follow the cursor
            cp = get(ax,'CurrentPoint'); x = round(cp(1,1)); y =
    round(cp(1,2));
            if x>=1 && x<=Wc && y>=1 && y<=Hc
                half = floor(S/2);
                x1 = max(1, x - half); y1 = max(1, y - half);
                w  = min(S, Wc - x1 + 1); h = min(S, Hc - y1 + 1);
                rect.Position = [x1, y1, w, h];
            end
        end

        function onClick(~,~)
            % Left-click confirms; right-click cancels
            sel = get(f,'SelectionType');
            if strcmpi(sel,'normal') % left click
                cp = get(ax,'CurrentPoint'); x = round(cp(1,1)); y =
    round(cp(1,2));
                if x>=1 && x<=Wc && y>=1 && y<=Hc
                    xc = x; yc = y; confirmed = true;
                    uiresume(f); close(f);
                end
            else
```

```
176             confirmed = false;
177             uiresume(f); close(f);
178         end
179     end
180 
181     function onKey(~,evt)
182         % ESC cancels; +/- resizes the box
183         if strcmpi(evt.Key,'escape')
184             confirmed = false;
185             uiresume(f); close(f);
186         elseif any(strcmpi(evt.Key, {'add','equal'}))      % '+' to grow
187             S = min(S+1, max(Hc,Wc)); onMove();
188         elseif any(strcmpi(evt.Key, {'subtract','hyphen'}))% '-' to
189 shrink
190             S = max(S-1,1); onMove();
191         end
192     end
193 end
194 
```

Annex C

Error and Uncertainty Analysis

C.1. Uncertainty modelling and combination methods

The uncertainty analysis in this thesis follows the methodology of the Guide to the Expression of Uncertainty in Measurement (GUM) approach [152]. The main principles and formulas applied are summarized below.

C.1.1. Standard Uncertainty

All individual uncertainty components, regardless of their method of evaluation (Type A or Type B), are expressed as a standard uncertainty (u), which is equivalent to one standard deviation (1σ).

C.1.2. Type B Uncertainty (from datasheets)

For instrument specifications given as a symmetric range of $\pm X$ with no stated confidence level, the value is assumed to follow a rectangular distribution. The standard uncertainty is calculated by treating X as the half-width of the distribution, as presented in Equation (86) (GUM, 4.3.7, [152]).

$$u = \frac{X}{\sqrt{3}} \tag{86}$$

C.1.3. Type B uncertainty (from digital resolution)

The uncertainty due to the finite resolution of a digital instrument with a step width of a is also modelled as a rectangular distribution. The error is assumed to be $\pm a/2$. The standard uncertainty is therefore shown in Equation (87) (GUM, F.2.2.1, [152]).

$$u_{res} = \frac{a}{\sqrt{12}} \tag{87}$$

C.1.4. Uncertainty of a mean

When averaging n independent samples to reduce random effects, the standard uncertainty of the average (u_{avg}) is the standard uncertainty of a single measurement (u) divided by $\sqrt{n}$, as per Equation (88) (GUM, 4.2.3).

$$u_{avg} = \frac{u}{\sqrt{n}} \tag{88}$$

C.1.5. Law of propagation of uncertainty

The combined standard uncertainty (u_y) for a derived quantity $y = f(x_1, \ldots, x_n)$ is calculated using the law of propagation of uncertainty. For uncorrelated input quantities, this is the root-sum-of-squares (RSS) of the individual contributions, as presented in Equation (89) (GUM, 5.1.2, Eq. 10).

$$u_y^2 = \sum_i \left(\frac{\partial f}{\partial x_i} \cdot u_{x_i} \right)^2 \tag{89}$$

C.1.6. Expanded uncertainty

Where required, an expanded uncertainty (U) is reported to define an interval with a high level of confidence (typically 95%). It is calculated by multiplying the combined standard uncertainty by a coverage factor k, as shown in Equation (90) (GUM, Clause 6).

$$U = k \cdot u_y \tag{90}$$

For this work, a coverage factor of $k = 2$ is used, which corresponds to an approximate 95% confidence level for a normal distribution (GUM, 6.3.3).

C.1.7. Inclusion rule

In this annex, the contribution from resolution (u_{res}) is explicitly included in the uncertainty budget only when it is non-negligible relative to other sources, defined as per Equation (91).

$$u_{res} \geq 0.1 \cdot u_{dom} \tag{91}$$

Where u_{dom} is the largest other standard uncertainty for the same measurand.

With these conventions, each input of the acquisition system is treated by converting ADC or counting effects to the sensor's physical units and combining them with the respective datasheet accuracy.

C.2. Sources of measurement uncertainty

The total uncertainty in experimentally derived results arises from the combined effects of the measuring instruments and the data acquisition system. Therefore, this analysis begins with the identification and characterization of the primary sources of measurement error.

C.2.1. ADC resolution and quantization error

The analog-to-digital conversion of sensor signals in this system is performed by the 10-bit ADC integrated in the ATmega328P microcontroller of the Arduino Uno Rev3. This ADC operates at a 5 V reference voltage, resulting in a nominal resolution of 4.88 mV per least significant bit (LSB). The specifications relevant to error analysis are summarized in Table 75.

Table 75 – ATmega328P specifications relevant to the error analysis [153, 107].

Specification	Value
Operating voltage [V]	5
ADC bit depth [bits]	10
ADC integral non-linearity [LSB]	± 0.5
ADC absolute accuracy [LSB]	± 2

Although the ADC introduces multiple sources of error such as quantization, integral non-linearity, and offset, the manufacturer specifies an absolute accuracy of ± 2 LSB. This value encompasses all dominant non-idealities and represents the maximum expected deviation between the true input and its digital representation under standard operating conditions.

Given its conservative and comprehensive nature, the ± 2 LSB bound is adopted in this thesis as the total ADC uncertainty, corresponding to an uncertainty of 9.76 mV. Following the GUM methodology outlined in section A.2, this is treated as an uncertainty with a rectangular distribution. The standard uncertainty in LSB counts, u_{ADC}, is therefore as presented in Equation (92).

$$u_{ADC} = \frac{2}{\sqrt{3}} \approx 1.155\ LSB \tag{92}$$

The standard uncertainty, $u_{ADC,V}$, is presented in Equation (93).

$$u_{ADC,V} = \frac{9.76}{\sqrt{3}} \approx 5.635\ mV \tag{93}$$

This standard uncertainty value will be used for all subsequent error propagations involving analog sensor readings.

C.2.2. Auxiliary sensor uncertainty analysis

The primary instruments used for monitoring the system's operating conditions each have a manufacturer-specified accuracy. These values represent the systematic or random errors inherent to the sensor itself and are summarized in Table 76.

Table 76 – Summary of instrumental uncertainties.

Sensor	Parameter	Accuracy	Resolution
DHT22	Temperature	± 0.5 °C	0.1 °C
	RH	± 2 % *RH*	0.1% *RH*
DS18B20	Temperature	± 0.5 °C	0.0625 °C
FS300A	Liquid flow rate	± 2 %	2.67 L/h
ACS712ELC-20A	Current	± 1.5 %	48.8 mA

The resolution for the FS300A flow sensor is determined by the duration of the acquisition period Δt, since the sensor outputs a discrete number of pulses proportional to flow rate. Assuming a minimum detectable change of one output pulse, the resolution was derived from Equation (12), introduced in the experimental setup chapter, and is simplified below as Equation (94).

$$\Delta Q = \frac{8}{\Delta t} \tag{94}$$

Where:

- ΔQ is the flow rate resolution [L/h],
- Δt is the acquisition period [s].

For a Δt of 3 s, this equation yields a resolution of 2.67 L/h

For the current sensor, the resolution was derived from the sensitivity, S, which is 0.1 mV/mA . Because these sensors are read through the ADC, and for the abovementioned ADC resolution of 4.88 mV, ΔI can be obtained from Equation (95).

$$\Delta I = \frac{\Delta V}{S} = \frac{4.88}{0.1} = 48.8\ mA \tag{95}$$

Where:

- ΔI is the current resolution [mA],
- ΔV is the ADC step [mV],
- S is the sensor sensitivity [mV/mA];

All the remaining table values were obtained from the respective sensor datasheets. With this, a per sensor analysis of relevance of each error and resulting uncertainty is required.

C.2.3. DHT22 – Air temperature uncertainty

The DHT22 reports temperature digitally which means that there is no ADC contribution to uncertainty. The datasheet gives ±0.5°C without a confidence level. Therefore per GUM it is treated as rectangular, as shown in Equation (96).

$$u_{acc_{TA}} = \frac{0.5}{\sqrt{3}} = 0.289\ °C \tag{96}$$

The stated resolution is 0.1 °C, also modelled as a rectangular step, as shown in Equation (97).

$$u_{res_{TA}} = \frac{0.1}{\sqrt{12}} = 0.0289\ °C \tag{97}$$

Combined effect of the two uncertainties can be obtained from Equation (98).

$$u_{TA} = \sqrt{u_{acc_{TA}}^2 + u_{res_{TA}}^2} = \sqrt{0.289^2 + 0.0289^2} \approx 0.291°C \tag{98}$$

The resolution term changes the result by < 1% and is therefore negligible relative to the accuracy. In line with the stated inclusion rule, the resolution term is discarded, and for propagation $u_{TA} = 0.289$ °C will be used.

C.2.4. DHT22 – Relative humidity uncertainty

The DHT22 reports RH digitally, without requiring the Arduino ADC. The datasheet gives $\pm 2\%$ RH without a confidence level, so per the methods section this is treated as rectangular, as shown in Equation (99).

$$u_{acc_{RH}} = \frac{2}{\sqrt{3}} = 1.155\%\ RH \tag{99}$$

The stated resolution is 0.1% RH, also modelled as a rectangular step in Equation (100).

$$u_{res_{RH}} = \frac{0.1}{\sqrt{12}} = 0.0289\%\ RH \tag{100}$$

And Equation (101) is obtained by applying the law of propagation of uncertainty.

$$u_{RH} = \sqrt{u_{acc_{RH}}^2 + u_{res_{RH}}^2} = \sqrt{1.155^2 + 0.0289^2} \approx 1.156\%\ RH \tag{101}$$

As the resolution term is negligible relative to the accuracy, it was discarded. For propagation, $u_{RH} = 1.155\%$ RH will be used.

C.2.5. DS18B20 – Working fluid temperature uncertainty

The DS18B20 reports temperature digitally, therefore the ADC contribution is not applicable. The datasheet states ± 0.5 °C without a confidence level thus per the methods section is treated as rectangular and obtained according to Equation (102).

$$u_{acc_{TWF}} = \frac{0.5}{\sqrt{3}} = 0.289°C \tag{102}$$

The stated resolution is 0.0625°C, also modelled as a rectangular step, as shown in Equation (103).

$$u_{res_{TWF}} = \frac{0.0625}{\sqrt{12}} = 0.018\,°C \tag{103}$$

Combining both, u_{TWF} is obtained from Equation (104).

$$u_{TWF} = \sqrt{u_{acc_{TWF}}^2 + u_{res_{TWF}}^2} = \sqrt{0.289^2 + 0.018^2} \approx 0.290\,°C \tag{104}$$

The resolution term is negligible relative to the accuracy and is discarded. For propagation $u_{TWF} = 0.289$ °C will therefore be adapted.

C.2.6. FS300A – Working fluid flow rate uncertainty

An accuracy of ±2% is obtained from Table 76. As this value does not have a confidence level, it is treated as rectangular. The resolution has also been calculated for a Δt of 3 to be 2.67 L/h.

From this, the standard uncertainty from accuracy is obtained from Equation (105).

$$u_{acc_F} = \frac{0.02 \cdot F}{\sqrt{3}}\ [L/h] \tag{105}$$

And the standard uncertainty from resolution is also obtained through Equation (106).

$$u_{res_F} = \frac{2.67}{\sqrt{12}} = 0.771\ L/h \tag{106}$$

Combining standard uncertainty, u_F is obtained from Equation (107).

$$u_F = \sqrt{u_{acc_F}^2 + u_{res_F}^2}\ [L/h] \tag{107}$$

For most of this work the flow operated in the 140 L/h to 350 L/h range (see Figure 185) with a measurement window of $\Delta t = 3\ s$. In this regime u_{res_F} is constant, while the u_{acc_F} scales with flow. To keep propagation simple and conservative across the full range, a single worst-case standard uncertainty is adopted at the upper bound ($F = 350$ L/h), which yields an $u_F = 4.12$ L/h.

For Chapter 7, the flows are lower, in the range of 30 L/h to 55 L/h (see Figure 227) and the relative impact of the counting term at $\Delta t = 3\ s$ would be excessive. As tests were performed in steady state, a centred moving average with $\Delta t = 30\ s$ was applied in post-processing, increasing the flow rate resolution by a factor of 10 from the previously calculated value in Equation (94) of 2.67 L/h to a 0.27 L/h. With this $u_{res,TEG}$ is recalculated to 0.077 L/h. However, the accuracy term remains that of Equation (105), which for a 30 L/h to 55 L/h range yields u_{acc_F} between 0.346 L/h and 0.635 L/h. Applying Equation (107) gives a combined $u_{F,TEG}$ between 0.355 L/h and 0.640 L/h. As the resolution term is negligible in this regime, a conservative, flow-independent value $u_{F,TEG} = 0.64$ L/h is adopted for Chapter 7.

C.2.7. ACS712ELC-20A – Current uncertainty

The TE-HX current consumption is measured per TE module with four ACS712ELC-20A sensors. The typical operating range of the TE modules spans roughly from 10.0 A to 12.5 A in the measured tests. Two contributions are considered, the sensor accuracy ($\pm 1.5\%$ of reading) and the Arduino ADC absolute accuracy (± 2 LSB) mapped to ampere via the transfer sensitivity of $S = 0.1$ mV/mA. The 1 LSB step (48.8 mA) is not added, since the ± 2 LSB bound already envelopes quantization. The datasheet specifies an accuracy without indicating a confidence level, therefore, following the approach defined in the methods section, it is treated as a rectangular distribution, with the corresponding standard uncertainty obtained from Equation (108).

$$u_{acc_I} = \frac{0.015 \cdot |I|}{\sqrt{3}}\ [A] \tag{108}$$

And standard uncertainty from ADC absolute accuracy mapped to current for $V_{ref} = 5$ V, and a bit depth of $n = 10$ is obtained in Equation (109).

$$u_{ADC_I} = \frac{2 \cdot \frac{V_{ref}}{2^n}}{\sqrt{3} \cdot S} \approx 0.0564\ [A] \tag{109}$$

Combining the standard uncertainties, Equation (110) is obtained.

$$u_I = \sqrt{u_{acc_I}^2 + u_{ADC_I}^2}\ [A] \tag{110}$$

u_{acc_I} is dependent on the measured current, as the sensor accuracy is defined as a percentage of the reading. Consequently, its contribution increases proportionally with the measured current amplitude, while the u_{ADC_I} remains constant. Although higher currents correspond to larger output voltages and slightly greater uncertainty, the TE modules operate within a narrow and stable power range, corresponding to maximum and minimum operating currents of approximately 12.5 A and 10.0 A, respectively. For a current of 10 A, $u_{acc_I} = 0.0866\ A$, resulting in $u_I = 0.103\ A$, and for 12.5 A, $u_{acc_I} = 0.1083\ A$ with $u_I = 0.122\ A$. The small variation in u_I across this operating range confirms that a current-dependent uncertainty model is unnecessary. Therefore, a single conservative value of $u_I = 0.122\ A$ is adopted for this work.

C.3. Propagation of uncertainty in derived quantities

This section applies the standard uncertainties to the key physical quantities calculated throughout the thesis. The standard uncertainties have been derived for each sensor which have been calculated in this annex, and that are compiled in Table 77.

Table 77 – Summary of adopted standard uncertainties (k = 1).

Sensor	Measurement	Symbol	Adopted u
ATmega328P ADC	Counts	u_{ADC}	1.155
	Voltage	$u_{ADC,V}$	5.635 mV
DHT22	Temperature	u_{TA}	0.289°C
	RH	u_{RH}	1.155% RH
DS18B20	Temperature	u_{TWF}	0.289°C
FS300A	Flow rate (Main)	u_F	4.12 L/h
	Flow rate (Chapter 7)	$u_{F,TEG}$	0.64 L/h
ACS712ELC-20A	Current	u_I	0.122 A

This process, known as propagation of uncertainty, determines the final confidence interval for each result.

C.3.1. Uncertainty in the FDS signal and FDS based detection algorithms

This section analyses the uncertainty of the processed signal from the FDS and evaluates the robustness of the event detection algorithms that operate on it, the FND and the DCD. The analysis begins with the temperature-compensated signal and follows the full signal processing chain, quantifying how each step affects the signal's uncertainty.

C.3.1.1. Uncertainty of the temperature-compensated signal

The temperature compensation model, presented in Equation (49) is a deterministic formula applied as a pre-processing step to the raw FDS signal (ADC) to correct for thermal drift. The final compensated signal, $\widetilde{ADC}$, is a function of two measured inputs: the raw ADC reading and the outlet air temperature ($TA2$). Therefore, the uncertainty of the compensated signal, $u_{\widetilde{ADC}}$, is found by propagating the standard uncertainties of these two inputs through the compensation formula.

Following the GUM methodology, the combined uncertainty, $u_{\widetilde{ADC}}$, is given in Equation (111) by the root-sum-of-squares of these independent contributions:

$$u_{\widetilde{ADC}}^2 = \left(\frac{\partial \widetilde{ADC}}{\partial ADC} \cdot u_{ADC}\right)^2 + \left(\frac{\partial \widetilde{ADC}}{\partial TA2} \cdot u_{TA}\right)^2 \quad (111)$$

The partial derivatives represent the sensitivity of the result to the uncertainty in each input measurement. The full theoretical derivations for these sensitivity coefficients, based on Equation (49), are as shown in Equation (112) and in Equation (113).

$$\frac{\partial \widehat{ADC}}{\partial ADC} = \frac{1023^2 \cdot \left(1 + \alpha \cdot \left(TA2 - T_{ref}\right)\right)}{\left(\left(1 + \alpha \cdot \left(TA2 - T_{ref}\right)\right) \cdot (1023 - ADC) + ADC\right)^2} \tag{112}$$

$$\frac{\partial \widehat{ADC}}{\partial TA2} = -\frac{1023 \cdot ADC \cdot \alpha \cdot (1023 - ADC)}{\left(\left(1 + \alpha \cdot \left(TA2 - T_{ref}\right)\right) \cdot (1023 - ADC) + ADC\right)^2} \tag{113}$$

These equations show that the sensitivity coefficients are non-linear, and their values depend on the ADC and $TA2$ values. To visualize this behaviour, the total standard uncertainty $u_{\widehat{ADC}}$ was calculated across the full operational range of the sensor, as shown in Figure 245.

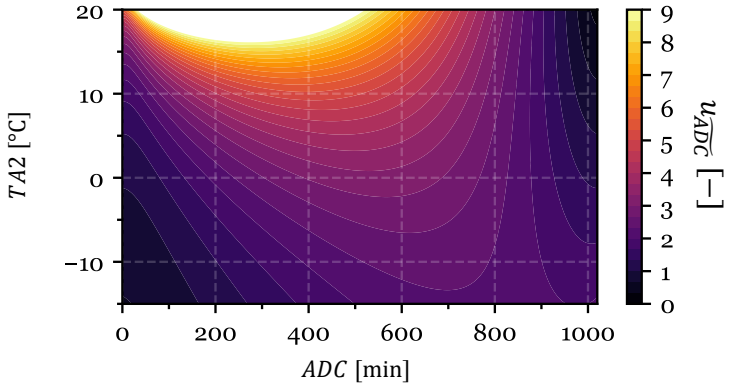

Figure 245 – Standard uncertainty of the compensated ADC signal as a function of raw ADC and $TA2$.

The plot provides several key insights. The uncertainty is highest in wet conditions (low ADC values), where the signal is most sensitive to temperature. Conversely, in the high-ADC range, the uncertainty is significantly lower and more stable.

For the tests performed in this work, two distinct detectors are used, each operating in a different physical regime. The FND occurs when the signal is in the high-ADC range, typically $ADC > 900$. Within this region, the uncertainty plot shows that the uncertainty increases as the temperature decreases. Since nucleation occurs close to 0°C, the point $ADC = 900, TA2 = 0$°C was selected to evaluate the conservative uncertainty for the FND's operational regime. Conversely, the DCD operates during the drying phase of a

defrost cycle. Based on the experimental data, a representative conservative operating point for this phase is $ADC = 500, TA = 20°C$. The uncertainty analysis for each detector must therefore be performed under its own specific conditions. At the FND's operating point, the sensitivity coefficients are evaluated numerically:

C.3.1.2. Robustness of the FND

At $ADC = 900$ and $TA2 = 0°C$, the sensitivity coefficients are evaluated numerically as presented in Equation (114).

$$\frac{\partial \widetilde{ADC}}{\partial ADC} = \frac{1023^2 \cdot \left(1 - 0.045 \cdot (0 - 2.22)\right)}{\left(\left(1 - 0.045 \cdot (0 - 2.22)\right) \cdot (1023 - 900) + 900\right)^2} \approx 1.074\ LSB/LSB \quad (114)$$

And as shown in Equation (115) for $TA2$:

$$\frac{\partial \widetilde{ADC}}{\partial TA2} = \frac{1023 \cdot 900 \cdot -0.045 \cdot (1023 - 900)}{\left(\left(1 - 0.045 \cdot (0 - 2.22)\right) \cdot (1023 - 900) + 900\right)^2} \approx 4.755\ LSB/°C \quad (115)$$

Using the standard uncertainties from Table 77 ($u_{ADC} \approx 1.155$ LSB and $u_{TA2} = 0.289°C$), the squared uncertainty contributions are shown in Equation (116) for ADC:

$$\left(\frac{\partial \widetilde{ADC}}{\partial ADC} \cdot u_{ADC}\right)^2 = (1.074 \cdot 1.155)^2 \approx 1.539 \quad (116)$$

And as shown in Equation (117) for $TA2$:

$$\left(\frac{\partial \widetilde{ADC}}{\partial TA2} \cdot u_{TA2}\right)^2 = (4.755 \cdot 0.289)^2 \approx 1.888 \quad (117)$$

Combining these contributions using the law of propagation of uncertainty from Equation (89), the result in Equation (118) is obtained

$$u_{\widetilde{ADC}}^2 = \left(\frac{\partial \widetilde{ADC}}{\partial ADC} \cdot u_{ADC}\right)^2 + \left(\frac{\partial \widetilde{ADC}}{\partial TA2} \cdot u_{TA2}\right)^2 \tag{118}$$

$$u_{\widetilde{ADC}} = \sqrt{1.539 + 1.888} = 1.851\ LSB$$

This analysis demonstrates that even under the worst-case conditions within the critical region for frost detection, the standard uncertainty of the compensated signal is approximately 1.85 $ADC\ counts$.

The FDS signal processing framework applies a moving average with a window of $W = 30$ samples to the compensated signal, as shown in Equation (50) to reduce noise. This averaging process reduces the random uncertainty by a factor of $\sqrt{W}$. The resulting standard uncertainty of the smoothed signal, $u_{\overline{ADC}}$, which is the direct input to the slope calculation, is therefore as calculated in Equation (119):

$$u_{\overline{ADC}} = \frac{u_{\widetilde{ADC}}}{\sqrt{W}} = \frac{1.851}{\sqrt{30}} \approx 0.338\ LSB \tag{119}$$

This initial smoothing step reduces the signal's standard uncertainty by more than a factor of five, preparing it for processing in the FND algorithm.

The FND algorithm operates by classifying the average slope of the smoothed signal, $\Delta\overline{ADC}^{avg}$, against a threshold of $\theta_s = 0.15$, as shown in Equation (53). To assess the FND robustness, this threshold should be compared to the uncertainty of the average slope measurement itself.

First, the local slope is calculated as a finite difference between two consecutive points of the smoothed signal, as shown in Equation (51). The uncertainty of this local slope, $u_{\Delta\overline{ADC}}$, is propagated in Equation (120) from the two independent $\overline{ADC}$ values used in the finite difference calculation:

$$u_{\Delta\overline{ADC}} = \sqrt{u_{\overline{ADC}}^2 + u_{\overline{ADC}}^2} = \sqrt{2} \cdot u_{\overline{ADC}} = \sqrt{2} \cdot 0.338 \approx 0.478\ LSB \tag{120}$$

Next, the algorithm averages K = 10 of these local slope values to get the final average slope, $\Delta\overline{ADC}^{avg}$ from Equation (52). This second averaging step further reduces the

uncertainty of the final slope measurement that is fed to the classifier, as shown in Equation (121):

$$u_{\Delta\overline{ADC}^{avg}} = \frac{u_{\Delta\overline{ADC}}}{\sqrt{K}} = \frac{0.478}{\sqrt{10}} \approx 0.151\ LSB \tag{121}$$

This shows that the standard uncertainty of the average slope measurement $u_{\Delta\overline{ADC}^{avg}}$ is almost identical to the detection threshold, $\theta_s = 0.15$. This indicates that after mapping the $\Delta\overline{ADC}^{avg}$ to the classifier C^{ADC} the algorithm operates at the limit of its sensitivity, where the signal's noise level is comparable to the threshold used for detection. This explains the necessity of the subsequent logic in the FND algorithm, by smoothing with a persistence window of P=20, which acts as an additional filter so that the FND is only triggered by a sustained trend rather than by random noise momentarily crossing the threshold.

For the DCD, the analysis must be performed under its own distinct operating conditions, where the uncertainty is significantly higher.

C.3.1.3. Robustness of the DCD

The DCD operates under a different physical regime than the FND. During a defrost cycle, the sensor becomes saturated with meltwater, causing the raw ADC signal to drop to a low range, while the air temperature rises significantly. This change in operating point requires a separate uncertainty analysis. Based on the experimental data, a conservative operating point for the DCD is $ADC = 500$ and $TA2 = 20$°C.

At this point, the sensitivity coefficients are calculated from the theoretical derivatives in Equations (122) and (123).

$$\frac{\partial\widetilde{ADC}}{\partial ADC} \approx 0.978\ LSB/LSB \tag{122}$$

$$\frac{\partial\widetilde{ADC}}{\partial T} \approx 11.45\ LSB/°C \tag{123}$$

Propagating the standard uncertainties from Table 77 ($u_{ADC} \approx 1.155$ LSB and $u_{TA} = 0.289$ °C) gives the squared uncertainty contributions shown in Equations (124) and (125).

$$\left(\frac{\partial \widetilde{ADC}}{\partial ADC} \cdot u_{ADC}\right)^2 = (0.978 \cdot 1.155)^2 \approx 1.277 \tag{124}$$

$$\left(\frac{\partial \widetilde{ADC}}{\partial TA2} \cdot u_{TA2}\right)^2 = (11.45 \cdot 0.289)^2 \approx 10.956 \tag{125}$$

The combined uncertainty squared for the compensated signal during defrosting is therefore presented in Equation (126).

$$u_{\widetilde{ADC}}^2 = \left(\frac{\partial \widetilde{ADC}}{\partial ADC} \cdot u_{ADC}\right)^2 + \left(\frac{\partial \widetilde{ADC}}{\partial TA2} \cdot u_{TA2}\right)^2$$
$$u_{\widetilde{ADC}} = \sqrt{1.277 + 10.956} = 3.498\ LSB \tag{126}$$

This is a substantial result. The standard uncertainty of the compensated signal in the wet, warm defrosting regime ($u_{\widetilde{ADC}} = 3.50$ LSB) is nearly double the uncertainty in the cold, high-ADC regime used for the FND.

At the likes of the FND, this uncertainty is then propagated through the same two-stage filtering process ($W = 30, \mathrm{K} = 10$) to find the uncertainty of the final average slope measurement, starting with the uncertainty of the smoothed signal in Equation(127).

$$u_{\overline{ADC}} = \frac{u_{\widetilde{ADC}}}{\sqrt{W}} = \frac{3.498}{\sqrt{30}} \approx 0.639\ LSB \tag{127}$$

The local slope is then calculated as a finite difference between two consecutive points of the smoothed signal, as shown in Equation (51). The uncertainty of this local slope is presented in Equation (128).

$$u_{\Delta\overline{ADC}} = \sqrt{u_{\overline{ADC}}^2 + u_{\overline{ADC}}^2} = \sqrt{2} \cdot u_{\overline{ADC}} = \sqrt{2} \cdot 0.639 \approx 0.286\ LSB \tag{128}$$

Next, the algorithm averages K = 10 of these local slope values to get the final average slope, $\Delta\overline{ADC}^{avg}$ from Equation (52). This reduces the uncertainty of the final slope measurement that is fed to the classifier, as shown in Equation (129).

$$u_{\Delta\overline{ADC}^{avg}} = \frac{u_{\Delta\overline{ADC}}}{\sqrt{K}} = \frac{0.286}{\sqrt{10}} \approx 0.286\ LSB \tag{129}$$

The final, fully processed signal that the DCD evaluates has a standard uncertainty of approximately 0.286 LSB. When comparing its specific slope threshold of $\theta s = 0.30$ to this uncertainty, the analysis yields an interesting conclusion. Just like the FND, the DCD operates at the very limit of its sensitivity. The characteristic noise of the signal it monitors is almost as large as the detection threshold itself. This finding highlights the importance of the DCD's subsequent consensus classifier logic ($M = 20$), which requires a highly stable trend for M consecutive samples before a DCD is triggered.

The sufficiency of this level of precision is proven empirically by the experimental results in Chapter 6. The FND and DCD algorithms demonstrated success rate in all valid tests ($12/12$ for FND, $7/7$ for DCD in Series A and B). This performance confirms that the inherent uncertainty in the compensated signal is below the magnitude of the signal changes that the algorithms are designed to detect, allowing for event detection.

C.3.2. Uncertainty in AH and the HBDCD

The AH is calculated from the temperature and RH using Equation (16). The uncertainty in AH is found by propagating the standard uncertainties of the DHT22 sensor, which are given in Table 77 as $u_{TA} = 0.289$°C and $u_{RH} = 1.155\%\ RH$. The combined uncertainty, u_{AH}, is therefore given by the root-sum-of-squares of the contributions from each variable, as shown in Equation (130).

$$u_{AH}^2 = \left(\frac{\partial AH}{\partial TA} \cdot u_{TA}\right)^2 + \left(\frac{\partial AH}{\partial RH} \cdot u_{RH}\right)^2 \tag{130}$$

The partial derivatives of the AH equation define the sensitivity of the result to the uncertainty in each input. The partial derivative with respect to RH is presented in Equation (131).

$$\frac{\partial AH}{\partial RH} = \frac{AH}{RH} \tag{131}$$

The partial derivative with respect to T is more complex. Based on the structure of Equation (16), the full theoretical derivation generates Equation (132).

$$\frac{\partial AH}{\partial TA} = AH \cdot \left(\frac{4302.595}{(TA + 243.5)^2} - \frac{1}{273.15 + TA} \right) \tag{132}$$

Substituting these two sensitivity coefficients into the propagation formula of Equation (130) gives the complete theoretical expression for the squared standard uncertainty of Absolute Humidity, presented in Equation (133).

$$u_{AH}^2 = \left(AH \cdot \left(\frac{4302.595}{(TA + 243.5)^2} - \frac{1}{273.15 + TA} \right) \cdot u_{TA}^2 \right)^2 + \left(\frac{AH}{RH} \cdot u_{RH} \right)^2 \tag{133}$$

This equation provides the standard uncertainty u_{AH} as a function of the measured AH, TA, and RH, and the known constant sensor uncertainties u_{TA} and u_{RH}. To visualize this behaviour, the total standard uncertainty u_{AH} was calculated across the full operational range of the sensor, as shown in Figure 246.

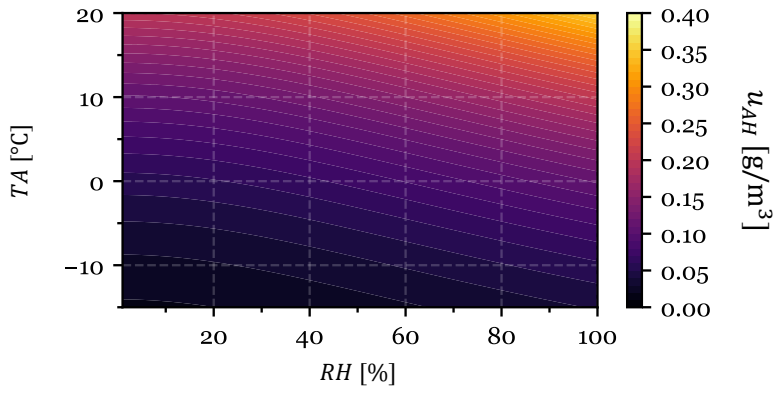

Figure 246 – Standard uncertainty of the AH signal as a function of RH and TA.

The plot reveals that the uncertainty in AH is not constant; it increases with both higher temperatures and higher RH. This is particularly relevant for the HBDCD, which operates during the defrost phase. In this phase, air temperatures rise, and the evaporation of meltwater causes humidity to spike, pushing the system into the high-uncertainty region shown in the plot.

To provide a conservative estimate for the uncertainty, the analysis will proceed by evaluating u_{AH} at the worst-case point within this operational regime: $TA = 20°C$ and $RH = 100\%$. At this condition, the AH is calculated by substituting these values into Equation (16), resulting in the expression shown in Equation (134).

$$AH = \frac{2.1674 \cdot 100 \cdot 6.112 \cdot e^{\frac{17.67 \cdot 20}{20+243.5}}}{273.15 + 20} \approx 17.29\ g/m^3 \tag{134}$$

Next, the sensitivity coefficients are evaluated at this point, for RH in Equation (135).

$$\frac{\partial AH}{\partial RH} = \frac{17.29}{100} = 0.1729\ (g/m^3)/\%RH \tag{135}$$

And for TA in Equation (136).

$$\frac{\partial AH}{\partial TA} = 17.29 \cdot \left(\frac{4302.595}{(20 + 243.5)^2} - \frac{1}{273.15 + 20}\right) \approx 1.012\ (g/m^3)/°C \tag{136}$$

Using the standard uncertainties from Table 77 ($u_{TA} = 0.289°C$ and $u_{RH} = 1.155\%RH$), the squared uncertainty contribution for TA is presented in Equation (137).

$$\left(\frac{\partial AH}{\partial TA} \cdot u_{TA}\right)^2 = (1.012 \cdot 0.289)^2 \approx 0.0856 \tag{137}$$

And for RH in Equation (138):

$$\left(\frac{\partial AH}{\partial RH} \cdot u_{RH}\right)^2 = (0.1729 \cdot 1.155)^2 \approx 0.0399 \tag{138}$$

Combining these contributions Equation (139) is obtained with the final standard uncertainty:

$$u_{ah} = \sqrt{0.0856 + 0.0399} \approx 0.354\ g/m^3 \tag{139}$$

The $HBDCD$ relies on the difference in absolute humidity, from Equation (68). Its uncertainty, $u_{\Delta AH}$, depends on the uncertainties of the two independent AH measurements. Assuming the errors of the two DHT22 sensors are uncorrelated, $u_{\Delta AH}$ can be obtained from Equation (140).

$$u_{\Delta AH} = \sqrt{u_{AH1}^2 + u_{AH2}^2} \tag{140}$$

Using the conservative worst-case value of u_{AH} calculated above, the result is found in Equation (141).

$$u_{\Delta AH} = \sqrt{0.354^2 + 0.354^2} \approx 0.501\ g/m^3 \tag{141}$$

This uncertainty value is nearly identical to the $HBDCD$'s stability threshold of $\varepsilon = 0.5\ \mathrm{g/m^3}$, which would imply that the detector operates at the very limit of its reliability, where measurement noise could be easily mistaken for a stable signal.

However, the $HBDCD$ algorithm does not operate on this raw signal. Instead, it employs a two-stage filtering process to ensure robustness. First, the AH signals are individually smoothed with a moving average of $N = 10$, as shown in Equations (66) and (67). This initial filtering step reduces the standard uncertainty of each smoothed signal, $u_{\overline{AH}}$, as follows in Equation (142).

$$u_{\overline{AH}} = \frac{u_{AH}}{\sqrt{N}} = \frac{0.354}{\sqrt{10}} \approx 0.112\ g/m^3 \tag{142}$$

The algorithm then calculates the difference between these two already-smoothed signals. The uncertainty of this intermediate difference signal, $u_{\Delta AH}$, is therefore calculated in Equation (143).

$$u_{\Delta AH} = \sqrt{u_{A\tilde{H}}^2 + u_{A\tilde{H}}^2} = \sqrt{0.112^2 + 0.112^2} \approx 0.158\ g/m^3 \tag{143}$$

Which is already significantly lower than that of the value obtained without the smoothing shown in Equation (141). This difference signal is smoothed again with a second moving average of $Q = 20$, as shown in Equation (69), before being evaluated by the detector. This second averaging step reduces the uncertainty of the final monitored signal, $u_{\overline{\Delta AH}}$, even further in Equation (144).

$$u_{\overline{\Delta AH}} = \frac{u_{\Delta AH}}{\sqrt{Q}} = \frac{0.158}{\sqrt{20}} \approx 0.035\ g/m^3 \tag{144}$$

The two-stage filtering process reduces the final signal's standard uncertainty to approximately 0.035 g/m^3. This demonstrates that the stability threshold, $\varepsilon = 0.5$ g/m^3, is approximately 14 times larger than the characteristic noise of the signal being monitored. This confirms that the *HBDCD* is a robust detector with a substantial safety margin, making it unlikely that measurement noise could be mistaken for a stable signal. The successful performance of the detector in the experimental tests validates this conclusion.

C.3.3. Uncertainty in TE-HX power consumption

The total power consumption of the TE-HX is calculated from the sum of the currents drawn by the four thermoelectric modules, multiplied by the operating voltage, as shown in Equation (15), and simplified in Equation (145) for the case of the TE-HX with 4 TE modules.

$$P = U \cdot (I_1 + I_2 + I_3 + I_4) \tag{145}$$

The uncertainty in the total power, u_P, is propagated from the uncertainty in each current measurement, u_I. The operating voltage U is supplied by a regulated 5V PSU and its uncertainty is considered negligible in comparison. Following the GUM methodology, the combined uncertainty squared, and assuming the errors in the four current sensors are uncorrelated, u_P^2, is given in Equation (146) by the root-sum-of-squares of the contributions from each measured current:

$$u_P^2 = \left(\frac{\partial P}{\partial I_1} \cdot u_I\right)^2 + \left(\frac{\partial P}{\partial I_2} \cdot u_I\right)^2 + \left(\frac{\partial P}{\partial I_3} \cdot u_I\right)^2 + \left(\frac{\partial P}{\partial I_4} \cdot u_I\right)^2 \quad (146)$$

The sensitivity coefficient for each current I_n is the partial derivative of the power equation with respect to that current, which is simply the operating voltage U, as shown in Equation (147).

$$\frac{\partial P}{\partial I_n} = U \quad (147)$$

The standard uncertainty for each current measurement as per Table 77 is $u_I = 0.122\ A$. Since the sensitivity and uncertainty are the same for all four measurements, the propagation formula simplifies to Equation (148).

$$u_P^2 = 4 \cdot (U \cdot u_I)^2 \quad (148)$$

For an operating voltage of $U = 5$ V, the total variance is calculated as in Equation (149).

$$u_P^2 = 4 \cdot (5 \cdot 0.122)^2 = 4 \cdot 0.61^2 = 1.4884 \quad (149)$$

The final standard uncertainty in the total power consumption is the square root of this value, calculated in Equation (150).

$$u_P = \sqrt{1.4884} \approx 1.220\ W \quad (150)$$

This value of $u_P \approx 1.22$ W represents the standard uncertainty in the total power consumption of the TE-HX.

C.3.4. Uncertainty in heat flow

The heat flow ($\dot{Q}$) in the TEG-HX study is calculated using Equations (80) and (81), which are functions of the volumetric flow rate ($\dot{V}$) and the temperature difference ($\Delta T = T_{out} - T_{in}$). The uncertainty in $\dot{Q}$ is therefore propagated from the standard uncertainties of the FS300A flow sensor and the two DS18B20 temperature sensors.

The values used for this calculation are the average values for $\dot{V}$ and ΔT taken over the steady-state period of each test, as reported in Table 65 and Table 66. This averaging reduces the influence of random fluctuations (Type A uncertainty) during the

measurement. However, the propagation of uncertainty must still account for the instrumental (Type B) uncertainty of the sensors themselves.

First, the standard uncertainty in the temperature difference, $u_{\Delta T}$, is calculated in Equation (151) from the standard uncertainty of the two independent DS18B20 sensor measurements, $u_{TWF} = 0.289°C$ from Table 77:

$$u_{\Delta T}^2 = u_{T_{out}}^2 + u_{T_{in}}^2 = 2 \cdot u_{TWF}^2$$
$$u_{\Delta T} = \sqrt{2 \cdot 0.289^2} \approx 0.409°C \quad (151)$$

For a multiplicative formula like the heat flow equation, the combined uncertainty is most clearly expressed in relative terms. The squared relative uncertainty of the heat flow, is given in Equation (152) by the root-sum-of-squares of the relative uncertainties of the measured variables:

$$\left(\frac{u_{\dot{Q}}}{\dot{Q}}\right)^2 = \left(\frac{u_{\dot{V}}}{\dot{V}}\right)^2 + \left(\frac{u_{\Delta T}}{\Delta T}\right)^2 \quad (152)$$

This equation reveals that the relative uncertainty of the heat flow is non-linear. To visualize this behaviour, the absolute standard uncertainty $u_{\dot{Q}}$ can be plotted as a function of the operating conditions $\dot{V}$ and ΔT. The absolute uncertainty is calculated by rearranging the relative uncertainty formula in Equation (153)

$$u_{\dot{Q}} = Q \cdot \sqrt{\left(\frac{u_{\dot{V}}}{\dot{V}}\right)^2 + \left(\frac{u_{\Delta T}}{\Delta T}\right)^2} \quad (153)$$

Substituting the full expression for heat flow ($\dot{Q} = \dot{V} \cdot \rho \cdot C_p \cdot \Delta T$) gives the final Equation (154) used to generate the uncertainty plot.

$$u_{\dot{Q}} = (\dot{V} \cdot \rho \cdot C_p \cdot \Delta T) \cdot \sqrt{\left(\frac{u_{\dot{V}}}{\dot{V}}\right)^2 + \left(\frac{u_{\Delta T}}{\Delta T}\right)^2} \quad (154)$$

Plotting this equation generates the contour plot of the absolute standard uncertainty shown in Figure 247.

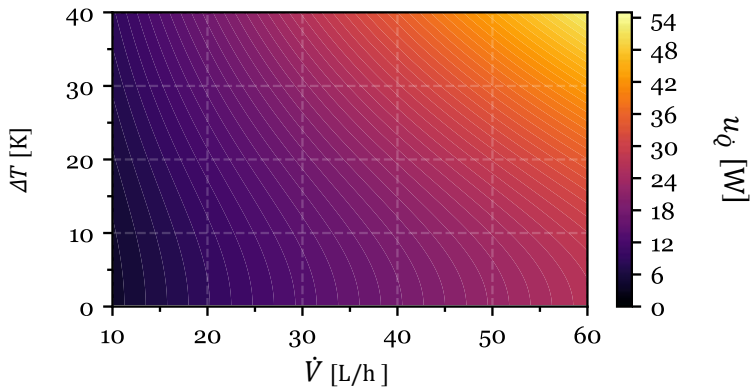

Figure 247 – Standard uncertainty of the $\dot{Q}$ as a function of $\dot{V}$ and ΔT.

The plot illustrates that the absolute uncertainty $u_{\dot{Q}}$ increases with both higher $\dot{V}$ and larger ΔT, as the total measured heat flow $\dot{Q}$ increases. However, the relative uncertainty is highest at low values of ΔT, where the constant uncertainty of the temperature sensors ($u_{\Delta T} \approx 0.409$ °C) represents a larger fraction of the measured difference.

Given this complex behaviour, a single worst-case value is insufficient. To provide the most accurate and transparent results, a per-test uncertainty analysis is performed using the average operating conditions for each of the three tests from Chapter 7.

The calculation is demonstrated here for Test 1. The average operating parameters for the hot side in this test were $|\Delta T_h| = 2.07$ K and $\dot{V}_h = 55.44$ L/h . The standard uncertainty of the flow rate for these tests was previously determined and adopted in section C.2.6 as the conservative value $u_{\dot{V}} = 0.64$ L/h . The relative uncertainty contributions are calculated in Equation (155) for the relative uncertainty from flow rate

$$\frac{u_{\dot{V}}}{|\dot{V}|} = \frac{0.64}{55.44} \approx 0.0115 \; (or \; 1.15\%) \tag{155}$$

And in Equation (156) for the relative uncertainty from temperature difference

$$\frac{u_{\Delta T}}{|\Delta T|} = \frac{0.409}{2.07} \approx 0.1976 \; (or \; 19.76\%) \tag{156}$$

In Equation (157) these values are combined in quadrature (by replacing the values in Equation (152)), from which the total relative standard uncertainty is obtained as the square root of this value:

$$\left(\frac{u_{\dot{Q}}}{\dot{Q}}\right)^2 = \left(\frac{0.64}{55.44}\right)^2 + \left(\frac{0.409}{2.07}\right)^2$$

$$\frac{u_{\dot{Q}}}{\dot{Q}} \approx \sqrt{0.0115^2 + 0.1976^2} \approx 0.1979 \; or \; 19.79\% \tag{157}$$

For the measured average heat flow of $\dot{Q}_h = -123.27$ W in Test 1, the absolute standard uncertainty is calculated in Equation (158).

$$u_{\dot{Q}} = 0.1979 \cdot |-123.27| \approx 24.4 \; W \tag{158}$$

This same procedure was applied to the average operating conditions of Test 2 and Test 3. The complete results for all three tests are summarized in Table 78.

Table 78 – Per-Test Uncertainty Analysis for $\dot{Q}_h$.

Test	$\|\Delta T_h\|$ $[K]$	$\dot{V}_h$ $[L/h]$	$u_{\dot{V},rel}$ **[%]**	$u_{\Delta T,rel}$ **[%]**	$u_{\dot{Q},rel}$ **[%]**	$\dot{Q}_h$ $[W]$	$u_{\dot{Q}}$ $[W]$
Test 1	2.07	55.44	1.15	19.76	19.79	−123.27	± 24.4
Test 2	3.65	48.24	1.33	11.21	11.29	−187.94	± 21.2
Test 3	6.77	33.48	1.91	6.04	6.33	−244.03	± 15.5

This per-test analysis confirms that the uncertainty contribution from the temperature difference, ΔT, is the dominant source of error in all experimental cases. This is particularly evident in Test 1, where the small temperature difference of $|\Delta T_h| = 2.07$ K results in a very high relative uncertainty of nearly 20%. As the temperature difference increases in subsequent tests, the relative precision of the measurement improves significantly, with the total relative uncertainty dropping to just over 6% in Test 3. Consequently, the absolute uncertainty, $u_{\dot{Q}}$, is also highest for Test 1, confirming that the heat flow measurements taken at the smallest temperature differentials are the least reliable. Ultimately, this analysis quantifies the specific standard uncertainty for each experimental condition, providing a precise and transparent confidence interval for each of the reported heat flow measurements.

C.3.5. Uncertainty in TEG electrical power

The electrical power, P_{elec}, generated by the TEG is calculated using Equation (74). The uncertainty primarily arises from the ADC's measurement of the voltage across the load resistor, V_{load}. The uncertainty in the value of the load resistor R_{load} is assumed to be negligible.

The propagated uncertainty is given by Equation (159).

$$u_{P_{elec}} = \left|\frac{\partial P_{elec}}{\partial V_{load}}\right| u_{V_{load}}$$
$$u_{P_{elec}} = \left|\frac{2 \cdot V_{load}}{R_{load}}\right| \cdot u_{V_{load}} \quad (159)$$

The standard uncertainty of the voltage measurement, $u_{V_{load}}$, is that of the ADC itself. As established in Table 77, this value is $u_{ADC,V} = 5.635$ mV. This analysis is performed for the peak power measurement in Test 3, where $P_{elec} = 0.93$ W was achieved with a load resistor of $R_{load} = 10.61\ \Omega$. The corresponding voltage is obtained in Equation (160).

$$V_{load} = \sqrt{P_{elec} \cdot R_{load}} = \sqrt{0.93 \cdot 10.61} \approx 3.14\ V \quad (160)$$

Propagating the uncertainty is given in Equation (161).

$$u_{P_{elec}} = \left|\frac{2 \cdot 3.14}{10.61}\right| \cdot 0.005635 \approx 0.0033\ W \quad (161)$$

The uncertainty in the power measurement is low. The result can be stated with high confidence as shown in Equation (162).

$$P_{elec} = 0.930 \pm 0.003\ W \quad (162)$$

This confirms that the conclusion in Chapter 7, that the generated power is more than sufficient to meet the calculated requirement of 14.3 J/h, is robust and not significantly impacted by measurement uncertainty.

C.4. Uncertainty in the CV method

The uncertainty of the CV method is evaluated through a combination of a visual sensitivity analysis and an empirical stability test. This dual approach is necessary because, unlike a simple sensor, the CV method's performance is dependent on algorithmic parameters and environmental conditions.

C.4.1. Visual Sensitivity Analysis

The most significant algorithmic parameter in the CV processing pipeline is the binarization threshold, FT, which is nominally set to 0.5. To visualize the impact of this parameter, a sensitivity analysis was performed on a representative test cycle. The CVG metric was re-calculated for the entire cycle using FT values ranging from 0.0 to 1.0 in steps of 0.1. The resulting family of curves is shown in Figure 248.

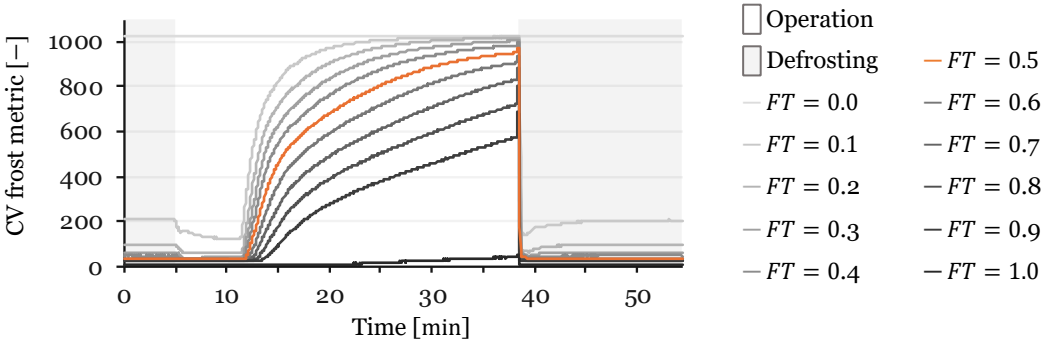

Figure 248 – Sensitivity of the CVG metric to the binarization threshold (FT).

The plot shows that while the general shape of the frost-defrost curve is preserved, the absolute amplitude of the CVG metric is sensitive to the choice of FT. Extreme values of $FT = 0$ and FT=1 are not useful for measurement. For the intermediate values, a trade-off, as lower FT detects frost onset earlier but saturates quickly, while higher FT lags slightly yet allows extended frost quantification. This suggests potential for future work using a multi-FT approach, where different thresholds could be used to optimize the detection of different events. The plot also demonstrates that the timing of the initial steep slope, which is used by the $CVFND$ algorithm, is relatively consistent across the central range of FT values. This indicates that slope-based nucleation detection is robust to the choice of FT. A different threshold would yield a consistently different slope, which could be compensated for with a minor adjustment to the $CVFND$'s slope threshold.

This visual analysis is further supported by Figure 249, which shows a grid of binarized snapshots at characteristic timestamps of the cycle for different FT values.

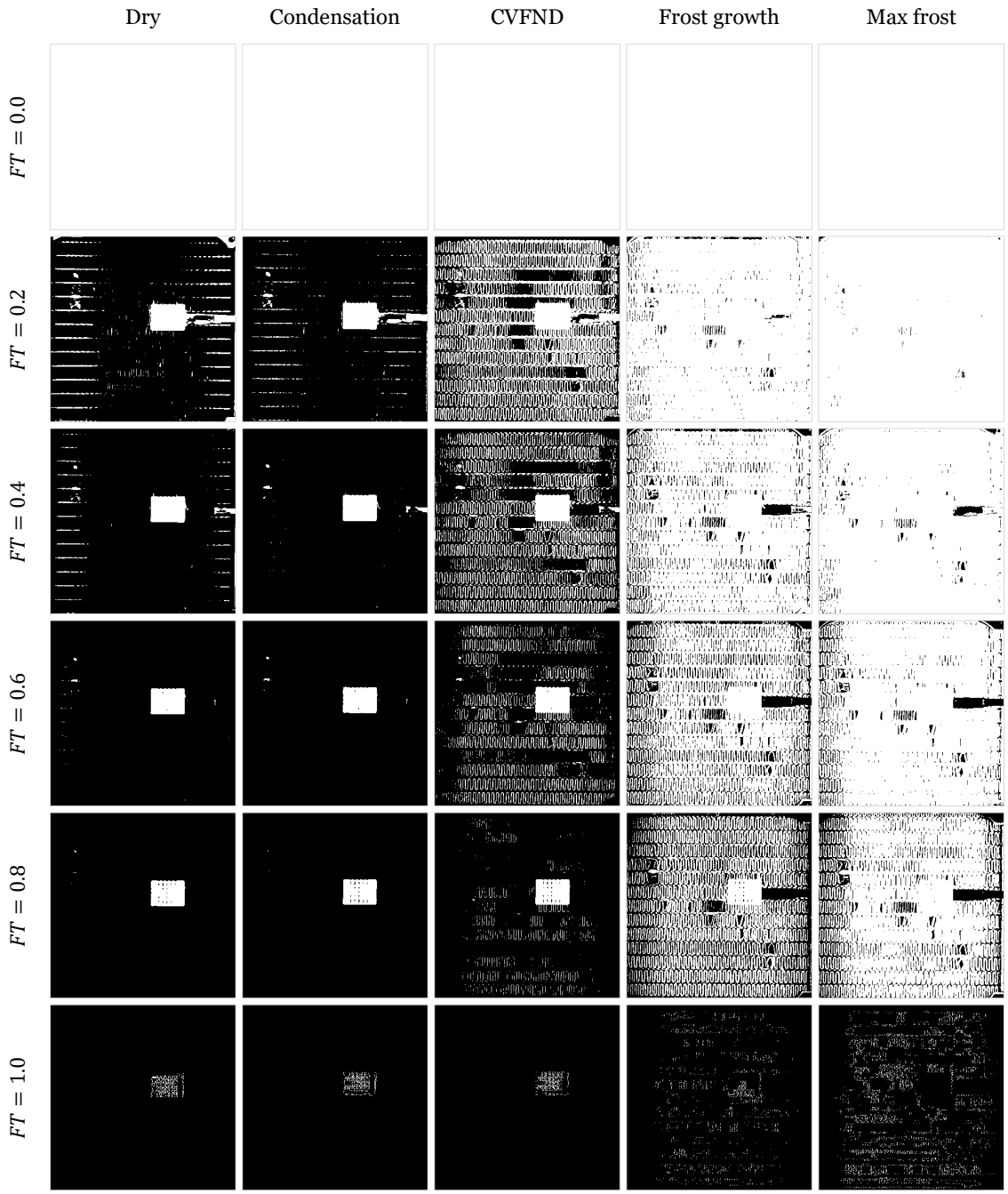

Figure 249 – Grid of binarized snapshots at different FT values for characteristic timestamps of a frost-defrost cycle.

As expected, this visualization confirms that higher *FT* values result in darker images, while lower values produce lighter ones. Importantly, it shows that for all non 0 or 1 *FT* values, frost is visible at the timestamp corresponding to the *CVFND* trigger. This confirms that the algorithm could be adjusted to reliably detect nucleation at that moment, regardless of the specific *FT* chosen within this reasonable range.

C.4.2. Empirical Measurement of System Stability and Noise

A quantitative measure of the system's uncertainty is still required. Empirical method was used to measure the combined effect noise sources, such as illumination fluctuations and camera sensor noise.

Two 45-minute stability tests were conducted to empirically measure the system's noise floor. The CVG signal was recorded while the system was off and the heat exchanger remained in a dry state. This condition was chosen, as a dry surface provides a stable target for isolating the system's intrinsic noise. Attempting to maintain a constant state of frost or condensation would introduce its own physical variations, confounding the measurement of the system's baseline uncertainty. The dry, painted HX surface is the most prone to reflections, a conservative scenario for sensitivity to stray light.

The experimental setup's controlled LED lighting was active for both tests. The first test was conducted with normal laboratory lighting and movement (Lights On) to simulate typical experimental conditions, while the second was conducted at night with all other lights off (Lights Off) to measure the baseline stability and test the system's resilience to ambient light. The test measurements are plotted in Figure 250

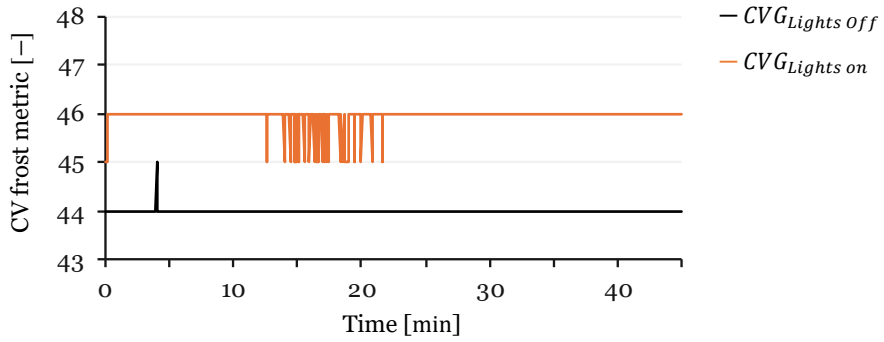

Figure 250 – Stability test of the CVG in Lights On and Lights Off conditions.

The standard deviation of the CVG signal during the steady-state tests provides a direct measure of the system's noise floor. Converted to the 10-bit ADC scale, the results were $\sigma_{Lights\ Off} = 0.033$ LSB and $\sigma_{Lights\ On} = 0.204$ LSB. The Lights Off test confirms negligible baseline noise, while the Lights On test shows that ambient light and movement increase it by about six times, though the level remains very low. The small offset in average CVG values (45.96 vs. 44.00) indicates a minor, acceptable effect of ambient light. To remain conservative, the higher Lights On value ($u_{CVG} = 0.204$) is adopted as the standard uncertainty for the CV method. This small value relative to the 10 –bit range (1023) confirms the method's stability and for FDS validation.